UNIVERSITY OF CALIFORNIA,
IRVINE

Shell Model Methods, Statistical Nuclear Reactions, and Beta-delayed Neutron Emission

DISSERTATION

submitted in partial satisfaction of the requirements
for the degree of

DOCTOR OF PHILOSOPHY

in Computational Science

by

Oliver C. Gorton

Dissertation Committee:
Professor Calvin W. Johnson, Co-chair
Professor Filipp Furche, Co-chair
Professor Daniel Whiteson
Professor Steven White
Professor Andrew Cooksy

2024

DEDICATION

To Mom, Cole, August, and Elliot

TABLE OF CONTENTS

LIST OF FIGURES

viii

LIST OF TABLES

LIST OF ALGORITHMS

ACKNOWLEDGMENTS

To Prof. Calvin Johnson and Dr. Jutta Escher for teaching me how to be a physicist and all that entails;

to the staff, postdocs, and students of the Nuclear Data and Theory Group at Lawrence Livermore National Laboratory, who for the last six years have welcomed me into their offices, meetings, and lunches, for their support and informal training which has been like a second graduate education;

to my collaborators and coauthors, modern physics is an entirely collaborative effort:

K. Bergstrom, E. Chimanski, E. Churchman, N. Cooper, A. M. Clark, J. E. Escher, C. Harris, S. L. Henderson, E. J. In, C. Jiao, C. W. Johnson, S. E. Kelly, R. Kelmar, M. Kruse, P. Millican, F. Naqvi, J. Nikoleyczik, O. Olivas-Gomez, A. Palmisano, S. Perrotta, S. Peru, C. Pruitt, R. Rahman, C. S. Reingold, D. Robertson, E. Shinkle, A. Simon, A. Spyrou, E. Stech, W. P. Tan, A. Thapa, and W. Younes;

to my partner, family, and friends for their support and for tolerating my absences;

to the Committee for taking the time to read this manuscript;

and to my financial support[†], **thank you**.

VITA

Oliver C. Gorton

EDUCATION

Doctor of Philosophy in Computational Science   **2024**
University of California, Irvine   *Irvine, California*
San Diego State University   *San Diego, California*

Master of Science in Physics   **2018**
San Diego State University   *San Diego, California*

Bachelor of Arts in Physics   **2016**
University of California, Berkeley   *Berkeley, California*

REFEREED JOURNAL PUBLICATIONS

Proton-neutron entanglement in the nuclear shell model   **2023**
C. W. Johnson and O. C. Gorton. Journal of Physics G: Nuclear and Particle Physics
50 (4) 045110.

`dmscatter`: **A Fast Program for WIMP-Nucleus Scattering**   **2023**
O. C. Gorton, C. W. Johnson, C. Jiao, J. Nikoleyczik. Computer Physics Communications 284, 108597.

Cross sections for neutron-induced reactions from surrogate data: **2023**
Reexamining the Weisskopf-Ewing approximation for (n, n') **and**
$(n, 2n)$ **reactions**
O. C. Gorton and J. E. Escher. Physical Review C: Nuclear Physics 107 (4), 044612.

Measurements of proton capture in the $A = 100 - 110$ **mass region:**   **2020**
Constraints of the ^{111}**In**$(\gamma, p)/(\gamma, n)$ **branching point relevant to the**
gamma-process
O. Olivas-Gomez, A. Simon, O. Gorton, J. E. Escher, E. Churchman, P. Millican, R.
Kelmar, C. S. Reingold, A. M. Clark, N. Cooper, C. Harris, S. L. Henderson, S. E. Kelly,
F. Naqvi, A. Palmisano, D. Robertson, E. Stech, A. Spyrou, and W. P. Tan. Physical
Review C: Nuclear Physics 102 (5), 055806.

REFEREED CONFERENCE PUBLICATIONS

A Problem in the Statistical Description of Beta-Delayed Neutron Emission
2023

O. C. Gorton, C. W. Johnson, and J. E. Escher. EPJ Web of Conferences 284, 03013

Improving nuclear data evaluations with predictive reaction theory and indirect measurements
2023

J. Escher, K. Bergstrom, E. Chimanski, O. Gorton, E. J. In, M. Kruse, S. Peru, C. Pruitt, R. Rahman, E. Shinkle, A. Thapa, W. Younes. EPJ Web of Conferences 284, 03012

Neutron capture cross sections from surrogate reaction data and theory: connecting the pieces with a Markov-Chain Monte Carlo approach
2021

O. C. Gorton and J. E. Escher. Springer Proceedings in Physics, vol 254, pages 229-231

ABSTRACT OF THE DISSERTATION

Shell Model Methods, Statistical Nuclear Reactions, and Beta-delayed Neutron Emission

By

Oliver C. Gorton

Doctor of Philosophy in Computational Science

University of California, Irvine, 2024

Professor Calvin W. Johnson, Co-chair

Professor Filipp Furche, Co-chair

An ongoing problem in nuclear physics is our ability to predict the rate of neutron and gamma emission of short-lived nuclei. This is especially true for beta-delayed neutron emission, an important but understudied reaction relevant to r-process nucleosynthesis and the decay of fission fragments. In this dissertation, I examine three hypotheses to explain this puzzling discrepancy between our models and experimental results. To improve our predictive capabilities, I have developed a suite of new computational tools which combine nuclear structure from the shell model with statistical reaction codes. Finally, I argue in favor of such a unified framework, and I use the beta-delayed neutron emission of ^{94}Rb as a case study.

Prologue

When asked, "what are you pursing a Ph.D. in?", I say "*computational science*, which is another way of saying scientific computing, and my chosen science is nuclear physics".

The computational science doctoral program is an interdisciplinary science department. In practice, this department is concerned with the application of computing to the sciences. Its students take courses in mathematical modeling, parallel computing, machine learning, statistics, and finally a number of courses in their field of interest. I took courses in physics and statistics. Ph.D. candidates inevitably fall into ranks with practicing scientists of some field of physical, social, or applied science. I have been trained as a nuclear physicist and this dissertation is about computational nuclear physics. The purpose of this dissertation is to demonstrate that I have developed expertise in the application of computational science to nuclear physics.

Several chapters of this dissertation are based on journal papers or other published works. In such cases, I include a paragraph beginning with *italics* to point to the original publication, and to say something about what my contributions to the work were. I also omit material from those publications when appropriate, e.g. if I did not contribute to it.

This dissertation has three parts, reflecting the three domains of my research: (I) Shell model Methods (and applications), (II) Statistical Nuclear Reactions, and (III) Beta-delayed Neutron Emission. Each part reports contributions I have made that stand alone in their

merit and interest to their sub-field. However, throughout Parts I and II, I will reveal connections to and foreshadowing of Part III, which in many ways represents the unification of the methods and tools I develop in the first two thirds of the dissertation. It is therefore worth presenting the following overview of Parts I, II, and III in order to prepare the reader for what to expect from each chapter, and for what relationships to look for among the various chapters and parts.

In reverse, Part III: Beta-delayed Neutron Emission attempts to resolve a mystery in applied nuclear reaction theory. There has been a discrepancy between measured and predicted particle counts in a process called beta-delayed neutron emission. This process relies on the nuclear structure of the nuclei involved, and is described in part by a statistical nuclear reaction. The methods and tools I have developed are uniquely suited to address this. Part II: Statistical Nuclear Reactions covers my contributions to statistical nuclear reactions and in particular uncertainty quantification tools to improve our evaluation of and constraints on phenomenological models. These underlying phenomenological models of nuclear structure, which feed our understanding of statistical nuclear reactions, can in turn be informed by microscopic models of nuclear structure. Thus Part III and Part II draw crucial theoretical inputs from Part I: Shell Model Methods. This first part covers the foundational understanding of nuclear structure from the shell model perspective, and covers new developments in computational methods to improve its usefulness for nuclear reactions, and the unified picture of nuclear structure and reactions presented in Part III.

Part I: Shell Model Methods

The main application of nuclear structure to other areas of nuclear physics is the calculation of matrix elements of nuclear transition operators. What are the bound states of systems of interacting nucleons and with what probability do transitions occur between those bound

states?

Chapter 1: My work in nuclear structure has been both in the development of tools for computing and in the application of calculations to other questions in physics. I begin Part I of the dissertation with a brief introduction to the nuclear shell model in Chapter 1. The shell model will be used throughout Part I, and again in Part III.

Chapter 2: In Chapter 2, I showcase a project I undertook early in my studies on a modern application of nuclear structure: the search for dark matter. This chapter also has significant relevance to Part III: the formalism of the electroweak theory of dark matter is identical to that of the complete treatment of beta decay, and especially relevant for higher order corrections to the usual first approximations.

Chapters 3, 4, and 5: Next, I move on and discuss the main tool I developed with my advisor: a new approximate shell model code, PANASh (proton and neutron approximate shell model). The method behind this code was inspired by similar efforts, and motivated by investigations into proton-neutron entanglement from my masters work. This is reviewed along with more recent results in Chapter 3. Then in Chapter 4 I discuss the method itself and demonstrate its effectiveness with results. I conclude the discussion of PANASh in Chapter 5 where I detail the computational methods and analysis that went into its programming.

Chapter 6: In the final chapter of Part I, I cover developments I have made to use the shell model to calculate statistical quantities relevant to the nuclear reaction theory covered in Part II: gamma-ray strength functions and nuclear level densities. This development, combined with the new shell model truncation scheme described in Chapter 4, is the cornerstone for the structure calculations required in Part III. I also propose a new formula for shell-model gamma ray strength functions which differs from the accepted definition.

Part II: Statistical Nuclear Reactions

The second part of the dissertation covers my contributions to statistical nuclear reactions and in particular an uncertainty quantification (UQ) tool I developed to improve evaluation of and constraints on phenomenological models. This code, COMMCAS, is now in use by multiple staff members at LLNL. These developments were first motivated by the work of Dr. Jutta Escher on surrogate reaction theory, which enables indirect measurements to constrain our models of nuclear reactions. I extended Escher's work showing the breakdown of certain approximations which would otherwise bypass the need for a more involved theoretical treatment of such measurements. I also demonstrate the application of COMMCAS to a problem in nuclear astrophysics.

Chapter 7: The first chapter introduces the main concepts of nuclear reaction theory relevant to my work. These are the concepts of low-energy nuclear reaction theory, compound nuclear reactions, and the underlying phenomenological nuclear structure models.

Chapters 8 and 10 : Next I report my contributions to the surrogate reaction theory. First, in a paper with Escher which demonstrates that the Weisskopf-Ewing approximation is not valid for fast-neutron reactions. This extends prior work by Escher and others who showed the same for neutron-capture and fission reactions. The breakdown of this approximation thus motivates the need for more advanced reaction theory, and the need for more sophisticated statistical methods (parameter inference and uncertainty quantification) for evaluating indirect experimental measurements. Chapter 10 briefly presents an application of full surrogate reaction method from a conference proceeding I published with Escher. This used new parameter inference tools I developed.

Chapters 9 and 11: The need for new parameter inference and uncertainty quantification tools brought about by the surrogate reaction method led to my development of a new code for the task. The code's fairly generic title, Computational Model Monte Carlo Sampler

(COMMCAS), indicates its applicability to a wide range of Monte Carlo sampling tasks for a wide class of computational models. The code has evolved over several years and has seen contributions from two other graduate students and one postdoc. COMMCAS is discussed in Chapter 9. Chapter 11 follows a direct application of COMMCAS: I initiated a collaboration between Escher, myself, and a group of experimentalists performing an inverse reaction measurement aimed at constraining a certain process in the astrophysical production of proton-rich nuclei. Using COMMCAS (or rather, an early version of its current form), I was able to improve the model agreement with the data and provide quantified uncertainties for their nucleosynthesis predictions.

Part III: Beta-delayed Neutron Emission

A subtitle for Part III would be: "where structure and reactions meet", because in fact this work was born out of an effort between my Ph.D. advisor, my Livermore mentor, and myself to craft a project that combines our expertise in nuclear structure and reactions.

Chapter 12: The problem of the missing neutrons: I introduce the main problem of the final part of the dissertation. This is a discrepancy between the statistical description of beta-delayed neutron emission and the measured ratio of gammas to neutrons emitted from the products of beta decay.

Chapter 13: This chapter introduces the theory of beta decay required for our description of beta-delayed neutron emission, including treatment of the lepton (electron and antineutrino) phase space factor with leading order Coulomb corrections.

Chapters 14, 15, and 16: These are the main results of the dissertation: a treatment of beta delayed neutron emission by combining the nuclear shell model structure with Hauser-Feshbach statistical reactions. Along the way, I introduce a new method for treating Porter-

Thomas width fluctuations, which to my knowledge has never been done before.

Chapter 17: The last chapter of the dissertation lays out the theory necessary for the next major development of this work: full treatment of the electroweak theory of beta decay within the framework of the nuclear shell model.

Part I

SHELL MODEL METHODS

Chapter 1

Low-energy Nuclear Structure

What are the properties of a bound system of interacting nucleons? What is the probability for transitions between those states when subjected to an external field? These questions are the day job of nuclear structure. I am interested in the application of nuclear structure to fundamental physics, such as the search for the dark matter or neutrinoless double-beta decay, as well as applications to nuclear astrophysics through the calculation of nuclear reaction rates.

To address most of these needs, it is sufficient to restrict our theories to a low-energy regime where the nuclear transitions are weak compared to the energy holding the nucleus together. This allows us to use the main results of time-dependent perturbation theory: Fermi's Golden Rule number 2 [253] states that the probability for a transition from an initial nuclear state $|\Psi_i\rangle$ to a final one $|\Psi_f\rangle$ is proportional to the squared matrix-element of the external field $\hat{H}_{\text{ext}}$:

$$T_{i \to f} = \frac{2\pi}{\hbar} |\langle \Psi_f | \hat{H}_{\text{ext}} | \Psi_i \rangle|^2. \tag{1.1}$$

This introduction will review the methods used in this work to model realistic wave functions
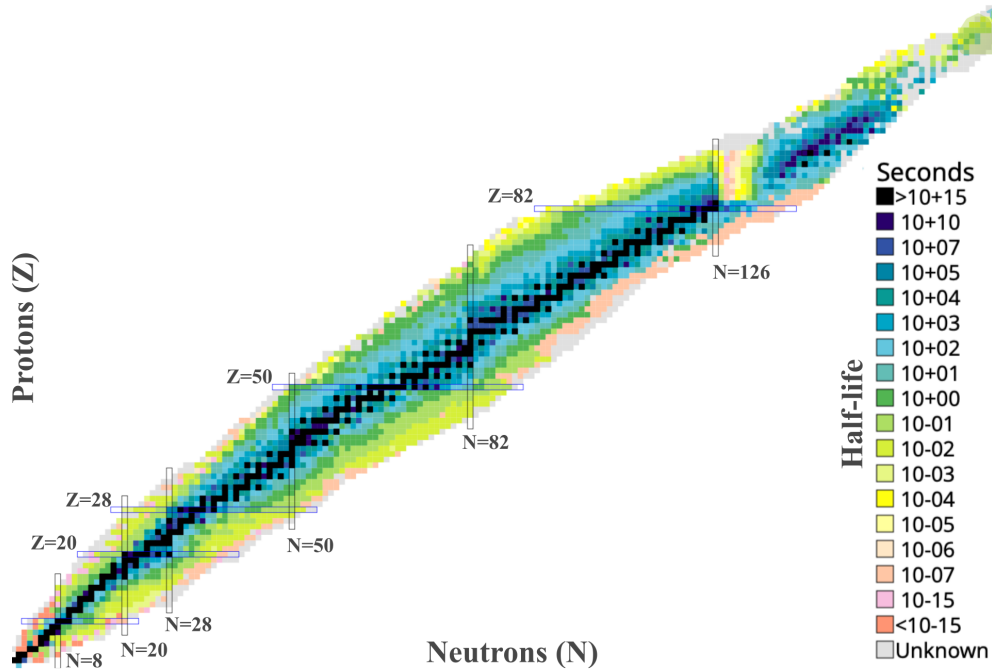
Figure 1.1: Chart of nuclei colored according to their ground state's half-life. Stable nuclei have an infinite half life (shown in black squares).

$|\Psi\rangle$ by solving the time-independent Schrödinger equation.

1.1   Accounting of bound states

There are more than 3,300 known nuclei, each with a unique number of protons (Z) and neutrons (N). These are organized on the chart of nuclei in Figure 1.1. Only about 250 of these are stable in their ground state configurations. These are the black squares in Figure 1.1 and they make up the center of the "Valley of Stability". Move away from this valley and the half-life decreases rapidly until it vanishes and no bound states can form. Unstable nuclei decay spontaneously in any time between the life-time of the universe and 10^{-20} seconds, although a more typical half-life is perhaps 10^{-1} seconds for a nucleus not too far from stability.

Most neutron rich nuclei ($N > Z$) decay when one of their neutrons turns into a proton and

emits an electron and an electron anti-neutrino:

$$n \rightarrow p + e^- + \bar{\nu}_e. \tag{1.2}$$

This process, β^- decay, arises from the weak nuclear force and can also be treated with equation (1.1). Other decay modes for ground-state nuclei are α decay and spontaneous fission, which will not be covered here.

So far, I have only discussed the properties of nuclear ground states. But nuclei can absorb a large amount of energy before coming unbound, and meanwhile can exist in a finite number of discrete internal configurations. While very light nuclei can have only a small number of bound configurations (^{1}H: 1, ^{8}B: 5), medium-mass nuclei such as ^{56}Fe can have hundreds of bound states. The lifetime of these states is measured in picoseconds (10^{-12}), with decay modes being entirely dominated by electromagnetic transitions to lower states via the emission of gamma photons. The energy levels of these excited states are typically millions of electron volts (MeVs). Above the threshold energy called the neutron separation energy, the nucleus has enough average energy for a neutron to escape. This might not happen right away, however. Quasi-bound states in this regime are called resonances, and they can be studied in some approximation with the same methods as bound states.

1.2 Observables

In the previous section I discussed some basic facts about the bound states of nuclei. These inform the kinds of observables we would like our nuclear structure models to predict: nuclear binding energies (equivalently, the nuclear masses), energies of excited states, and half-lives of those excited states.

The basic approach of modern nuclear structure models is to use the language of many-body

quantum mechanics to define a Hamiltonian $\hat{H}_0$ operator whose eigenstates $|\Psi\rangle$ are the bound states of the nucleus, and whose eigenvalues are the binding energies of the ground state and excited states. To first order, this Hamiltonian contains only the effective nuclear strong force and the repulsive proton Coulomb interaction. To compute transition probabilities between those excited states, we assume that, for example, the electromagnetic interaction is weak compared to the nuclear binding force, and can be treated perturbatively: $\hat{H} = \hat{H}_0 + \hat{H}_{EM}$. In short, we take the pure eigenstates $|\Psi\rangle$ of $\hat{H}_0$, and compute Fermi's Golden Rule:

$$T_{i\to f} = \frac{2\pi}{\hbar}|\langle\Psi_f|H_{EM}|\Psi_i\rangle|^2. \tag{1.3}$$

Basic energy arguments restrict this approximation to transitions of energies small compared to the nuclear binding energy. I will also sometimes write in terms of decay widths which are inversely related to the half life of the initial state:

$$\Gamma_{i\to f} = \frac{\hbar}{t_{1/2}} = \hbar T_{i\to f}. \tag{1.4}$$

The transition amplitude for a general operator $|\langle f|\hat{\mathcal{O}}|i\rangle|^2$ is a squared matrix element. We will see later that many of the operators we are interested in can be seen as one-body operators (usually because we are assuming some sort of impulse approximation). Such operators can be written:

$$\hat{\mathcal{O}} = \sum_{ab} O_{ab}\hat{c}_a^\dagger\hat{c}_b, \tag{1.5}$$

where $\hat{c}_a$, $\hat{c}_b^\dagger$ are one-body creation, annihilation operators and $O_{ab} = \langle a|O|b\rangle$ are the matrix elements of O in the one-body basis. The matrix elements of one-body operators can be

11

written as

$$\langle\Psi_f|\hat{\mathcal{O}}|\Psi_i\rangle = \sum_{ab} O_{ab}\langle\Psi_f|\hat{c}_a^\dagger\hat{c}_b|\Psi_i\rangle = \sum_{ab} O_{ab}\rho_{ab}^{fi}, \tag{1.6}$$

where $\rho_{ab}^{fi} \equiv \langle\Psi_f|\hat{c}_a^\dagger\hat{c}_b|\Psi_i\rangle$ are called one-body density matrices, or one-body transition density (OBTD) matrices. They are a reduced and compact form of the information stored in the wave functions. For this reason, the OBTD matrices are a key product of nuclear structure models.

The two most important groups of transition operators for this text are the electromagnetic (E1, E2, M1) and weak (Fermi and Gamow-Teller) transition operators. In both cases, we rely on the long-wavelength (low-energy) limit to use only the leading-order terms in a multipole expansion of the perturbing external fields (electromagnetic or electroweak). Each will be defined in detail as needed, but a summary following Suhonen's text [272], Brusssard and Glaudeman's text [46], and Fox's dissertation [94] follows below.

The standard form for a multipole electromagnetic transition probability, for $X = M$agnetic or Electric character of order L from an initial state i to a final state f is

$$T_{fi}^{XL} = \frac{8\pi}{\hbar}\frac{(L+1)}{L[(2L+1)!!]^2}\left(\frac{E_\gamma}{\hbar c}\right)^{2L+1} B(XL; i \to f), \tag{1.7}$$

where B is the reduced transition probability (B-value),

$$B(XL; i \to f) \equiv \frac{1}{2J_i+1}|\langle\Psi_f||\mathcal{M}_{XL}||\Psi_i\rangle|^2 \tag{1.8}$$

$$= \frac{1}{2J_i+1}\sum_{m_f m_i M}|\langle\Psi_f(m_f)|\mathcal{M}_{XLM}|\Psi_i(m_i)\rangle|^2. \tag{1.9}$$

This is a strength function which assumes orientation-independent operators and has been summed over all final magnetic substates and averaged over all initial magnetic substates. The double-bar || denotes the reduced matrix elements following the Wigner-Eckart the-

orem [74]. One computes the reduced B-values in (1.8) using the single-particle operator expansion (1.6).

The electric one-body operators have the form:

$$\mathcal{M}_{ELM} = e_p M_{LM}(q\vec{x}) \equiv e_p j_L(qx) Y_{LM}(\Omega_x), \tag{1.10}$$

where e_p is the proton charge, $j_L(qx)$ are spherical Bessel functions and $Y_{LM}(\Omega_x)$ are spherical harmonics. Electromagnetic transitions can be highly collective, involving many nucleons. Because we often work in a truncated single-particle space (treating only single particle states near the Fermi surface), this operator is often modified empirically to estimate the effects of the truncated space. In particular, one introduces effective charges, endowing neutrons with a charge. For example, one might set $e_p = 1.4$ and $e_n = 0.4$ relative to the proton charge.

The magnetic one-body operators are:

$$\mathcal{M}_{MLM} = \frac{\mu_N}{\hbar c} \left[\frac{2}{L+1} g_l \boldsymbol{l} + g_s \boldsymbol{s} \right] \cdot \nabla M_{JM}, \tag{1.11}$$

where the gyromagnetic ratios g_l and g_s modify the couplings to orbital angular momentum and spin relative to the nuclear magneton (in Gaussian units):

$$\mu_N = \frac{e\hbar}{2m_p} = 0.10515 \ ec \ \text{fm}. \tag{1.12}$$

For protons $g_l = 1$, $g_s = 5.586$ and for neutrons $g_l = 0$, $g_s = -3.826$. The matrix elements of these operators in a harmonic oscillator basis (the usual choice for shell model theory) have standard integral forms that can be found in many references [31, 46, 272]. Some of these are given in later chapters.

1.3 The nuclear shell model

The nuclear shell model treats the nucleus as a many-body system of interacting Fermions with two species: protons and neutrons. The original shell model consisted of a mean-field model, approximating the A-body nuclear interaction as a system of A non-interacting particles in a mean-field potential produced by the $A-1$ nucleons. Today, the shell model refers to the interacting shell model, or configuration interaction shell model. While the individual nucleons are placed in a fixed set of single-particle configurations, these configurations interact via 1- and 2-body matrix elements which account for the residual, beyond the mean-field interactions. In the interest of brevity, I omit discussion of the many stepping stones between mean-field methods and the full configuration interaction (FCI) shell model. These are the classic beyond-mean field methods, still in widespread use today, such as the Tamm-Dancoff and the random phase approximations. To summarize these methods, they modify the mean field by including either real or quasi (non-particle number conserving) excitations about the Fermi surface. They include mixtures of Slater determinants, but only a handful of specially crafted particle-hole states. FCI considers all possible configurations within a finite set of single-particle states. First I will discuss the form of the wave functions composed of these configurations.

We will consider factorized wave functions for our nuclear basis:

$$|\phi\rangle = |p\rangle |n\rangle, \tag{1.13}$$

where $|p\rangle$ are many-proton wave functions, and $|n\rangle$ are many-neutron wave functions. Each of these, in turn, is a product of properly normalized and anti-symmetric products of single-proton(neutron) wave functions, otherwise known as Slater determinants. As we work in second quantization, these are represented by strings of fermion creation operators $a_i^\dagger$ acting

on a vaccuum state. A 3-proton wave function (Slater determinant) might be:

$$|p\rangle = \hat{a}_1^\dagger \hat{a}_2^\dagger \hat{a}_3^\dagger |0\rangle . \tag{1.14}$$

The vaccuum state may be either a true vaccuum (no particles), or a sea of fully-occupied states representing an inert core. The fermion nature of these states is encoded the anti-commutation relations of the operators [87]:

$$\{\hat{a}_i, \hat{a}_j^\dagger\} \equiv \hat{a}_i \hat{a}_j^\dagger + \hat{a}_j^\dagger \hat{a}_i, = \delta_{ij}$$
$$\{\hat{a}_j, \hat{a}_j\} = \{\hat{a}_i^\dagger, \hat{a}_j^\dagger\} = 0. \tag{1.15}$$

For example, two fermions cannot occupy the same state, $(\hat{a}_i^\dagger)^2 = 0$, and therefore the maximum occupancy of a state ϕ_i is one.

The state created by $\hat{a}_i^\dagger$ is an arbitrary fermion wave function. The most common choice is a harmonic oscillator (HO) state; in principle this is the solution to the three-dimensional, single-particle Schrodinger equation for the mean-field nuclear interaction. These states carry the HO quantum numbers:

- n_i: principle quantum number

- l_i: orbital angular momentum

- j_i: total angular momentum, $\boldsymbol{j} = \boldsymbol{l} + \boldsymbol{s}$

Each HO single-particle *level* (or *orbit*) $n_i l_j j_i$ has a parity -1^l and $2j + 1$ degenerate *states* with $j_z = m$ labels: $m = -j, -j + 1, ..., j - 1, j$.

The standard ordering of single particle levels and their quantum numbers are shown in Figure 1.2. One difference from single particle states in atomic physics is that states with higher-j have lower energy; the nuclear spin-orbit term is attractive. The exact ordering of

the single particle levels in terms of their energies depends on the nature of the effective interaction used. Energy gaps between groups of these levels result in *magic quantum numbers* of nucleons: 2, 8, 20, 28, 50, 82, 126, which have special properties such as especially strong binding energies.

To construct a finite shell model basis, we must truncate the infinite harmonic-oscillator space, for example, to some maximum oscillator quanta. Furthermore, for medium to heavy-mass nuclei (let's say, $A > 20$), we must resort to a 'frozen-core' shell model, hereafter referred to as the large-scale shell model (LSSM): one assumes that sufficiently large energy gaps between single-particle states allows for scale-separation of an active valence space from an inert core of nucleons. See Figure 1.3. In such cases, the interaction must be renormalized, and the description of highly-collective states may be lost.

1.3.1 The shell model Hamiltonian

To find wave functions for nuclei, we find low-lying states of a nuclear Hamiltonian by the configuration-interaction method in a shell-model basis [46, 44, 56]. Any many-body Hamiltonian can be written in second quantization formalism as a polynomial in creation and annihilation operators [245]:

$$\hat{H} = \sum_i \epsilon_i \hat{a}_i^\dagger \hat{a}_i + \frac{1}{4} \sum_{ijkl} V_{ijkl} \hat{a}_i^\dagger \hat{a}_j^\dagger \hat{a}_l \hat{a}_k, \tag{1.16}$$

where ϵ_i are single particle energies and V_{ijkl} are the two-body interaction matrix elements. The single-particle operators $\hat{a}_i^\dagger$ create spin-1/2 nucleons in simple harmonic oscillator states with quantum numbers: n_i (radial quantum number), l_i (orbital angular momentum), and j_i (total angular momentum). Many-body states are constructed as antisymmetrized products of these single particle states.

The most general form of the solution to the shell model Hamiltonian is not a pure Slater determinant,

$$|\Phi\rangle = \prod_{i=1}^{N} \hat{a}_{\alpha_i}^{\dagger} |0\rangle, \tag{1.17}$$

but a mixture:

$$|\Psi\rangle = \sum_i \Psi_i |\Phi_i\rangle. \tag{1.18}$$

In the full configuration interaction shell model, we begin with a finite list of single-particle states and construct a basis consisting of all possible Slater determinants.

To make calculations tractable, we limit the number of single particle valence states. For example, one might assume a fixed ^{16}O core and allow valence nucleons in the $1s_{1/2}$-$0d_{3/2}$-$0d_{5/2}$ orbits, colloquially known as the sd shell; other examples are the pf-shell (^{40}Ca core with valence orbits $1p_{1/2,3/2}$-$0f_{5/2,7/2}$) and the combined sd-pf shells. Starting from a finite single-particle valence space yields a finite many-body basis [53]:

$$|\Psi\rangle = \sum_\alpha c_\alpha |\alpha\rangle, \tag{1.19}$$

where we use the occupation representation of Slater determinants, that is, of the form $|\alpha\rangle = \prod_i \hat{a}_i^{\dagger} |0\rangle$. Furthermore, we factorize the basis into proton (p) and neutron (n) components, so that we can write:

$$|\alpha\rangle = |p\rangle \otimes |n\rangle. \tag{1.20}$$

Using Eq. (1.16) and the factorized basis (1.19) one can compute [53, 164] the matrix elements of the Hamiltonian in the many-body basis, $H_{\alpha,\beta} = \langle\alpha|\hat{H}|\beta\rangle$. Then the time-independent Schrödinger equation becomes a simple matrix eigenvalue problem: $\mathbf{H}\vec{c} = E\vec{c}$.

1.3.2 M-scheme versus J-scheme

In this work we work in either the M-scheme or the J-scheme. These are names for constraints we place on our basis states depending on which quantum numbers we choose to be fixed (total angular momentum J, or z-component of angular momentum $J_z \equiv M$). The Hamiltonian commutes with both of these operators:

$$\hat{J}^2 \ket{\Psi} = j(j+1)\hbar^2 \ket{\Psi} \tag{1.21}$$

$$\hat{J}_z \ket{\Psi} = m\hbar \ket{\Psi}, \tag{1.22}$$

and so neither quantum number will be changed by the action of the Hamiltonian. One can therefore construct a smaller basis with either of these quantum numbers fixed, but not both. Basis states will in general be in a superposition of the other quantum number. The advantage of the M-scheme is that the M quantum number is additive, which makes computing matrix elements simpler. This choice is one factor that contributes to the efficiency of BIGSTICK [164]. The J-scheme has the advantage of smaller basis dimensions than the M-scheme, but at the cost of more complicated angular momentum couplings. However, the J-scheme is the only choice when truncating in the many-body space, since a truncation in the M-scheme may leave the many-body basis states in a linear combination of total angular momenta. This will be important in Chapter 4.

1.3.3   Weight factor truncation in configuration space

Even with the double truncation of the single-particle space (exclusion of an infinite number of high-energy states and an inert core), one can easily reach computationally inaccessible matrix dimensions above 10^{16}, e.g., in the $sdpf$ valence space. This is due to the combinatorial growth of possible configurations for any given set of single-particle states (orbits).

Therefore, additional truncation is often required. One such method is to define a limited valence space by restricting the number of particles that can occupy some subset of the single particle states. (See Figure 1.3.) In the `BIGSTICK` shell model code, a general class of truncation schemes are implemented which encompasses both (1) the n-particle n-hole truncation from atomic physics and (2) the N_{max} truncation from the no-core shell model. This is done with the "weight-factor" truncation scheme [164]: each single particle state is assigned an artificial additive quantum number called the weight w. The many-body configurations are limited by their total weight $W = \sum_i w_i$ across all single particle states. For example all normal valence space orbits could be assigned a weight of 0, and a limited valence space defined by a set of orbits with a weight of 1. A $W_{\mathrm{max}} = 1$ truncation would allow for all configurations in the valence space, plus all configurations with one particle excited into the limited valence space.

1.3.4 Phenomenological interactions

The parameters ϵ_i and V_{ijkl} in Eq. (1.16) are input parameters of the Hamiltonian. In principle these matrix elements could be obtained as integrals of an effective operator from some *ab initio* theory of the nuclear force. In fact, many of the phenomenological interactions begin life as such, and are then adjusted to fit experimental data. For our calculations we use high-quality empirical interactions fitted separately in each model space to experimental spectra. For details see the reviews in [46, 44, 53].

Some of examples are the USDB, GX1A, JUN45, and glepn interactions used in this work. Each of these corresponds to a particular choice of single particle states, shown in Figure 1.2. Details on these and other interactions used in this work can be found in Appendix B.3.

1.3.5 Isospin

Isotopic spin, or "isospin" was introduced in nuclear physics to recognize the charge-independence of the nuclear force. These will become relevant when describing the charge-violating transitions of beta decay. Despite the important differences between protons and neutrons in other areas, including other areas of nuclear physics, it is convenient to treat protons and neutrons as two projections of a general nucleon particle of isospin-1/2. The isospin states are labeled $|T, T_z\rangle$ (sometimes $|T, M_T\rangle$). In the isospin Hilbert space, we take the convention that a proton is isospin-up:

$$|p\rangle = |\frac{1}{2}, +\frac{1}{2}\rangle = \begin{pmatrix} 1 \\ 0 \end{pmatrix}, \tag{1.23}$$

while the neutron is isospin-down:

$$|n\rangle = |\frac{1}{2}, -\frac{1}{2}\rangle = \begin{pmatrix} 0 \\ 1 \end{pmatrix}. \tag{1.24}$$

Analogously to normal spin, the isospin T is an approximate quantum number. We can add such states with the usual vector coupling arithmetic. In this work we won't concern ourselves with the modern definition in terms of quark states. We have the usual Pauli matrices, now for isospin:

$$\boldsymbol{\tau}_x = \begin{pmatrix} 0 & 1 \\ 1 & 0 \end{pmatrix}, \boldsymbol{\tau}_y = \begin{pmatrix} 0 & -i \\ i & 0 \end{pmatrix}, \boldsymbol{\tau}_z = \begin{pmatrix} 1 & 0 \\ 0 & -1 \end{pmatrix} \tag{1.25}$$

Later we will be interested in beta decay, which involves transitions between neutron and proton states. We can define the following operators:

$$\boldsymbol{\tau}_+ = \boldsymbol{\tau}_x + i\boldsymbol{\tau}_y = \begin{pmatrix} 0 & 1 \\ 0 & 0 \end{pmatrix}, \tag{1.26}$$

$$\boldsymbol{\tau}_- = \boldsymbol{\tau}_x - i\boldsymbol{\tau}_y = \begin{pmatrix} 0 & 0 \\ 1 & 0 \end{pmatrix}, \tag{1.27}$$

which have the important effects: $\boldsymbol{\tau}_+ \lvert n \rangle = \lvert p \rangle$, $\boldsymbol{\tau}_- \lvert p \rangle = \lvert n \rangle$.

N=6

s(l=0)
d(l=2)
g(l=4)
i(l=6)

12   1i 11/2   +   148
10   2g 9/2   +   136

ℏω

N=5

p(l=1)
f(l=3)
h(l=5)

2   3p 1/2   −   126
14   1i 13/2   +   124
4   3p 3/2   −   110
6   2f 5/2   −   106
8   2f 7/2   −   100
10   1h 9/2   −   92

ℏω

N=4

s(l=0)
d(l=2)
g(l=4)

4   2d 3/2   +   82
2   3s 1/2   +   78
12   1h 11/2   −   76
8   1g 7/2   +   64
6   2d 5/2   +   56

GCN5082

ℏω

N=3

p(l=1)
f(l=3)

10   1g 9/2   +   50
2   2p 1/2   −   40
6   1f 5/2   −   38
4   2p 3/2   −   32
8   1f 7/2   −   28

JUN45   GX1A   glepn

ℏω

N=2

s(l=0)
d(l=2)

4   1d 3/2   +   20
2   2s 1/2   +   16
6   1d 5/2   +   14

USDB

ℏω

N=1

p(l=1)

2   1p 1/2   −   8
4   1p 3/2   −   6

ℏω

N=0

s(l=0)

2   1s 1/2   +   2

Harmonic oscillator $\vec{l}\cdot\vec{s}$ $N_j = 2j+1$ nlj $\pi = (-1)^l$ $\sum N_j$

Figure 1.2: Brussaard and Glaudeman's [46] approximate ordering of the single-particle levels of a harmonic-oscillator potential, with annotations. The vertical lines right of the figure show the approximate location of the single-particle valence spaces of phenomenological interactions used in this work. The labels for cumulative maximum particle count, $\sum N_j$, are boxed at the magic numbers 2, 8, 20, 28, 50, 82, 126.
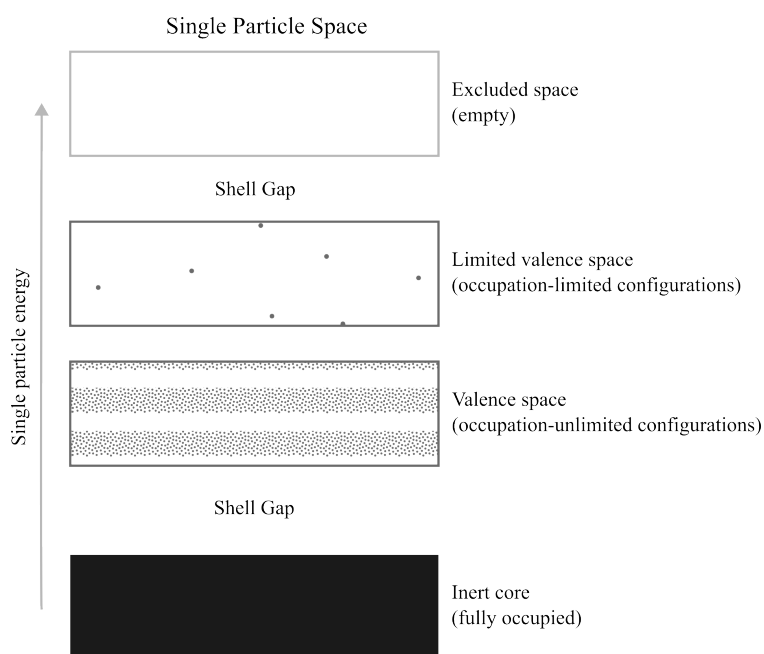
Figure 1.3: Shell model valence space with an inert core, active valence space, a limited valence space, and an infinite set of excluded orbits above.

Chapter 2

The Search for Dark Matter

This chapter is based on a paper I co-authored as first author with my advisor Calvin Johnson,
"dmscatter: A fast program for WIMP-nucleus scattering" by Oliver Gorton, Calvin Johnson,
Changfeng Jiao, and Jonathan Nikoleyczik". I will start by pointing out what I did not do: I
did not derive the effective field theory which determines the electroweak expansion of nuclear
form factors. I took as established the formalism for the effective field theory of WIMPs; the
domain of this contribution is in the application of nuclear structure to calculate the required
electroweak responses of the nuclei. I (1) designed and developed the code starting from a set
of subroutines written by then-postdoc Changfeng Jiao for computing single-particle matrix
elements of electroweak operators and nuclear response functions, (2) derived a form of the
dark matter event rate integral which could be numerically integrated in one dimension, and
(3) optimized the algorithm and code for parallel performance, resulting in a speedup of 2
to 3 orders of magnitude compared to the Mathematica equivalent. I wrote the majority of
the manuscript with edits from Johnson.

This chapter is a demonstration of the applications of low-energy nuclear structure to other
areas of physics, with ties to another topic in this dissertation, beta decay. One possible

candidate for dark matter is a new type of particle called weakly interacting massive particles (WIMPs). The 'weak' moniker here is not an insult to these elusive particles, but an indication that they may interact via the weak force with ordinary nucleons. Attempts to directly detect dark matter in the laboratory therefore rely on the electroweak theory of the nucleus, the same theory governing beta decay. The direct search for dark matter is an application of nuclear structure theory, and in particular the nuclear shell model which can provide microscopic descriptions of the nuclei used in WIMP detectors.

2.1   Introduction

The composition of the universe remains a fundamental puzzle to science. Astrophysical and cosmological evidence indirectly but strongly suggests that a substantial fraction (roughly a quarter) of the universe's mass-energy is made of some as-yet unidentified nonbaryonic particles [33, 27]. Substantial experimental effort has been and continues to be expended to directly detect this 'dark matter'. Because dark matter interacts with baryonic matter weakly and may be very massive compared to baryonic particles–WIMPs or *weakly interacting massive particles*–these experiments attempt to measure the recoil of nuclei from unseen and (mostly) elastic collisions [227, 86].

Originally it was assumed that dark matter particles would simply couple either to the scalar or spin densities of nucleons [108, 250]. But a few years ago Fitzpatrick *et al.* used effective field theory (EFT) calculations assuming Galilean invariance to identify upwards of 15 possible independent couplings between nonrelativistic dark matter and nucleons [89, 6, 289, 141].

The enlargement of the possible couplings motivates a variety of nuclear targets used in the detectors. More targets better constrain the actual coupling, but also complicate simula-

tions of detector responses. To aid such simulations, Anand, Fitzpatrick, and Haxton made available a script written in Mathematica computing the dark matter event rate spectra [6]; this script, `dmformfactor`, embodied the nuclear structure in a shell model framework and the user could choose the coupling to the EFT-derived operators. An updated Mathematica script has been developed and applied [305].

Not only did the EFT framework break new ground in the planning and analysis of dark matter direct detection experiments, the Mathematica script made the new framework widely accessible. Like many scripts in interpreted languages, however, `dmformfactor` is not fast, and scanning through a large set of parameters, such as exploring the effects of mixing two or more couplings or carrying out uncertainty quantification [94], ends up being time-consuming.

Inspired by the Mathematica script `dmformfactor`, we present here a fast modern Fortran code, `dmscatter`, for computing WIMP-nucleus scattering event rates using the previously proposed theoretical framework. The output is designed to align with practices of current dark matter searches. Intermediate results such as nuclear form factors can be easily accessed. With advanced algorithmic and numerical implementation, including the ability to take advantage of multi-core CPUs, our code opens up new areas of research: to rapidly explore the EFT parameter space including interference terms, and to conduct sensitivity studies to address the uncertainty introduced by the underlying nuclear physics models. Furthermore, we enhance the accessibility by including Python wrapper and example scripts which can be used to call the Fortran code from within a Python environment.

2.2 Theoretical Background

Although the formalism is fully developed and presented in the original papers [89, 6, 289, 141], for completeness and convenience we summarize the main ideas here.

The key product of the code is the differential event rate for WIMP-nucleus scattering events in number of events per MeV. This is obtained by integrating the differential WIMP-nucleus cross section over the velocity distribution of the WIMP-halo in the galactic frame:

$$\frac{dR}{dE_r}(E_r) = N_T n_\chi \int \frac{d\sigma}{dE_r}(v, E_r) \ \tilde{f}(\vec{v}) \ v \ d^3 v, \tag{2.1}$$

where E_r is the recoil energy of the WIMP-nucleus scattering event, N_T is the number of target nuclei, $n_\chi = \rho_\chi / m_\chi$ is the local dark matter number density, σ is the WIMP-nucleus cross section. The dark matter velocity distribution in the lab frame, $\tilde{f}(\vec{v})$, is obtained by boosting the Galactic-frame distribution $f(\vec{v})$: $\tilde{f}(\vec{v}) = f(\vec{v} + \vec{v}_{earth})$, where $\vec{v}_{earth}$ is the velocity of the earth in the galactic rest frame.

Next is the Halo model which describes the distribution of dark matter, encoded in the function $\tilde{f}(\vec{v})$. There are many models for the dark matter distributions of galaxies. We provide the Simple Halo Model (SHM) with smoothing, a truncated three-dimensional Maxwell-Boltzmann distribution:

$$f(\vec{v}) = \frac{\Theta(v_{esc} - |\vec{v}|)}{N_{esc} \pi^{3/2} v_0^3} \left\{ \exp\left[-(\vec{v}/v_0)^2\right] - \exp\left[-(v_{esc}/v_0)^2\right] \right\}, \tag{2.2}$$

where v_0 is some scaling factor (typically taken to be around 220 km/s), and N_{esc} renormalizes due to the cutoff [69, 98]. Halo distributions are not the focus of this paper, and we leave the implementation of more sophisticated halo models, such as SMH++ [82], to future work. The integral in equation (2.1) is evaluated numerically. Details can be found in 2.2.4.

The differential scattering cross section is directly related to the scattering transition probabilities $T(v, q(E_r))$:

$$\frac{d\sigma}{dE_r}(v, E_r) = 2m_t \frac{d\sigma}{dq^2}(v, q) = \frac{2m_T}{4\pi v^2} T(v, q). \tag{2.3}$$

The momentum transfer q is directly related to the recoil energy by $q^2 = 2m_t E_r$, where m_t is the mass of the target nucleus in GeV/c^2.

The WIMP-nucleus scattering event probabilities are computed as a sum of squared nuclear-matrix-elements:

$$T(v, q) = \frac{1}{2j_\chi + 1} \frac{1}{2j_T + 1} \sum_{M_i M_f} |\langle j_T M_f | \mathcal{H} | j_T M_i \rangle|^2 \tag{2.4}$$

$$= \frac{1}{2j_\chi + 1} \frac{1}{2j_T + 1} |\langle j_T \| \mathcal{H} \| j_T \rangle|^2 \tag{2.5}$$

which we have rewritten in terms of reduced (via the Wigner-Eckart theorem) matrix elements [74], as denoted by the double bars $\|$. Here v is the speed of the WIMP in the lab frame, q is the momentum transferred in the collision, and j_χ and j_T are the intrinsic spins of the WIMP and target nucleus, respectively. $\mathcal{H}$ is the WIMP-nucleus interaction.

The WIMP-nucleus interaction $\mathcal{H}$ is defined in terms of the effective field theory Lagrangian constructed from all leading order combinations of the following operators:

$$i \frac{\vec{q}}{m_N}, \ \vec{v}^\perp, \ \vec{S}_\chi, \ \vec{S}_N. \tag{2.6}$$

$\vec{v}^\perp$ is the relative WIMP-target velocity and $\vec{S}_\chi, \vec{S}_N$ are the WIMP and nucleon spins, respectively. There are fifteen such combinations, and $\mathcal{H}$ is specified implicitly by corresponding coupling constants c_i^x, (for $i = 1, ..., 15$), where $x = p, n$ for coupling to protons or neutrons

individually:

$$\mathcal{H} = \sum_{x=p,n} \sum_{i=1,15} c_i^x \mathcal{O}_i^x, \tag{2.7}$$

and the 15 momentum-dependent operators are:

$$\mathcal{O}_1 = 1_\chi 1_N \tag{2.8}$$

$$\mathcal{O}_2 = (v^\perp)^2 \tag{2.9}$$

$$\mathcal{O}_3 = i\vec{S}_N \cdot \left(\frac{\vec{q}}{m_N} \times \vec{v}^\perp \right) \tag{2.10}$$

$$\mathcal{O}_4 = \vec{S}_\chi \cdot \vec{S}_N \tag{2.11}$$

$$\mathcal{O}_5 = i\vec{S}_\chi \cdot \left(\frac{\vec{q}}{m_N} \times \vec{v}^\perp \right) \tag{2.12}$$

$$\mathcal{O}_6 = \left(\vec{S}_\chi \cdot \frac{\vec{q}}{m_N} \right) \left(\vec{S}_N \cdot \frac{\vec{q}}{m_N} \right) \tag{2.13}$$

$$\mathcal{O}_7 = \vec{S}_N \cdot \vec{v}^\perp \tag{2.14}$$

$$\mathcal{O}_8 = \vec{S}_\chi \cdot \vec{v}^\perp \tag{2.15}$$

$$\mathcal{O}_9 = i\vec{S}_\chi \cdot \left(\vec{S}_N \times \frac{\vec{q}}{m_N} \right) \tag{2.16}$$

$$\mathcal{O}_{10} = i\vec{S}_N \cdot \frac{\vec{q}}{m_N} \tag{2.17}$$

$$\mathcal{O}_{11} = i\vec{S}_\chi \cdot \frac{\vec{q}}{m_N} \tag{2.18}$$

$$\mathcal{O}_{12} = \vec{S}_\chi \cdot \left(\vec{S}_N \times \vec{v}^\perp \right) \tag{2.19}$$

$$\mathcal{O}_{13} = i \left(\vec{S}_\chi \cdot \vec{v}^\perp \right) \left(\vec{S}_N \cdot \frac{\vec{q}}{m_N} \right) \tag{2.20}$$

$$\mathcal{O}_{14} = i \left(\vec{S}_\chi \cdot \frac{\vec{q}}{m_N} \right) \left(\vec{S}_N \cdot \vec{v}^\perp \right) \tag{2.21}$$

$$\mathcal{O}_{15} = - \left(\vec{S}_\chi \cdot \frac{\vec{q}}{m_N} \right) \left(\left(\vec{S}_N \times \vec{v}^\perp \right) \cdot \frac{\vec{q}}{m_N} \right) \tag{2.22}$$

Operator 2 is generally discarded because it is not a leading order non-relativistic reduction of a manifestly relativistic operator [6]. Operators 1 and 4 correspond to the naive density-

and spin-coupling, respectively.

The EFT coefficients c_i^x can be expressed in terms of proton and neutron couplings $x = p, n$, or, equivalently, isospin and isovector couplings $\tau = 0, 1$. The relationship between the two is:

$$c_i^{\tau=0} = \frac{1}{2}(c^{x=p} + c_i^{x=n}) \tag{2.23}$$

$$c_i^{\tau=1} = \frac{1}{2}(c^{x=p} - c_i^{x=n}). \tag{2.24}$$

Our code accepts either specification and automatically converts between the two. (Note: while [6] specifies this same relationship, the Mathematica script distributed in Supplementary Material, `dmformfactor-prc.m`, also `dmformfactor-V6.m`, actually uses a different transformation, namely that $c_i^{\tau=0,1} = c_i^{x=p} \pm c_i^{x=n}$. Later versions [305] however, are consistent with the above relationship.)

The coefficients provided by the user should be in units of the weak interaction mass scale,

$$m_v = 256.2\text{GeV}. \tag{2.25}$$

2.2.1   Response functions

The summand of equation (2.4) is ultimately factorized into two factors: one containing the EFT content, labeled $R_i^{x,x'}$, and another containing the nuclear response functions, labeled $W_i^{x,x'}$ for each of the $i = 1, ..., 8$ allowed combinations of electro-weak-theory, discussed in the next section. The former are listed in 2.2.2.

There are eight nuclear response functions $W_i^{x,x'}$ considered here. The first six nuclear

response functions have the following form:

$$W_X^{x,x'} = \sum_J \langle\Psi||X_J^x||\Psi\rangle\,\langle\Psi||X_J^{x'}||\Psi\rangle, \tag{2.26}$$

with X selecting one of the six electroweak operators:

$$X_J = M_J, \Delta_J, \Sigma'_J, \Sigma''_J, \tilde{\Phi}'_J, \Phi''_J. \tag{2.27}$$

(further described in section 2.2.1) and Ψ being the nuclear wave function for the ground state of the target nucleus. The sum over operator-spins J is restricted to even or odd values of J, depending on restrictions from conservation of parity and charge conjugation parity (CP) symmetry.

As a check of normalization, the $J = 0$ contribution to $W_M^{xx'}$ is just the square of the Fourier transform of the rotationally invariant density. (For even-even targets, this is the only contribution to ground state densities.) This means, at momentum transfer $q = 0$, the $J = 0$ contribution to $W_M^{pp} = Z^2/4\pi$, $W_M^{nn} = N^2/4\pi$, and for isospin-format form factors, the $J = 0$ contribution to $W_M^{00} = \frac{1}{4\pi}\left(\frac{A}{2}\right)^2$. Such limits are useful when comparing to other calculations, to ensure agreement in normalizations.

Two additional response functions add interference-terms:

$$W_{M\Phi''}^{x,x'} = \sum_J \langle\Psi||M_J^x||\Psi\rangle\,\langle\Psi||\Phi_J^{''x'}||\Psi\rangle, \tag{2.28}$$

$$W_{\Delta\Sigma'}^{x,x'} = \sum_J \langle\Psi||\Sigma_J^{'x}||\Psi\rangle\,\langle\Psi||\Delta_J^{x'}||\Psi\rangle. \tag{2.29}$$

The transition probability is thus [89, 6]:

$$T(v,q) = \frac{4\pi}{2j_T+1}\sum_{x=p,n}\sum_{x'=p,n}\sum_{i=1}^{8} R_i^{x,x'}(v^2,q^2)W_i^{x,x'}(q), \tag{2.30}$$

where $i \rightarrow X$ for $i = 1, .., 6$, and $i = 7 \rightarrow M\Phi''$, $i = 8 \rightarrow \Delta\Sigma'$.

There are six basic operators, $M_J, \Delta_J, \Sigma'_J, \Sigma''_J, \tilde{\Phi}'_J, \Phi''_J$, describing the electro-weak coupling of the WIMPs to the nucleon degrees of freedom. These are constructed from Bessel spherical and vector harmonics [67]:

$$M_{JM}(q\vec{x}) \equiv j_J(qx)Y_{JM}(\Omega_x) \tag{2.31}$$

$$\vec{M}_{JML}(q\vec{x}) \equiv j_L(qx)\vec{Y}_{JLM}(\Omega_x), \tag{2.32}$$

where, using unit vectors $\vec{e}_{\lambda=-1,0,+1}$,

$$Y_{JLM}(\Omega_x) = \sum_{m\lambda} \langle Lm1\lambda| \,|(L1)JM_J\rangle\, Y_{Lm}(\Omega_x)\vec{e}_\lambda. \tag{2.33}$$

The six multipole operators are defined as:

$$M_{JM} \tag{2.34}$$

$$\Delta_{JM} \equiv \vec{M}_{JJM} \cdot \frac{1}{q}\vec{\nabla} \tag{2.35}$$

$$\Sigma'_{JM} \equiv -i \left\{ \frac{1}{q}\vec{\nabla} \times \vec{M}_{JJM} \right\} \cdot \vec{\sigma} \tag{2.36}$$

$$\Sigma''_{JM} \equiv \left\{ \frac{1}{q}\vec{\nabla} M_{JM} \right\} \cdot \vec{\sigma} \tag{2.37}$$

$$\tilde{\Phi}'_{JM} \equiv \left(\frac{1}{q}\vec{\nabla} \times \vec{M}_{JJM} \right) \cdot \left(\vec{\sigma} \times \frac{1}{q}\vec{\nabla} \right) + \frac{1}{2}\vec{M}_{JJM} \cdot \vec{\sigma} \tag{2.38}$$

$$\Phi''_{JM} \equiv i \left(\frac{1}{q}\vec{\nabla} M_{JM} \right) \cdot \left(\vec{\sigma} \times \frac{1}{q}\vec{\nabla} \right) \tag{2.39}$$

The matrix elements of these operators can be calculated for standard wave functions from second-quantized shell model calculations:

$$\langle \Psi_f| \,|X_J| \,|\Psi_i\rangle = \sum_{a,b} \langle a| \,|X_J| \,|b\rangle\, \rho_J^{fi}(ab), \tag{2.40}$$

where single-particle orbital labels a imply shell model quantum number n_a, l_a, j_a, and the double-bar $||$ indicates reduced matrix elements [74]. For elastic collisions, only the ground state is involved, i.e. $\Psi_f = \Psi_i = \Psi_{g.s.}$.

2.2.2 WIMP response functions

In the following, the EFT coefficients c_i^x are grouped according to how they couple to each of the eight nuclear responses $W_i^{x,x'}$. As a shorthand, $cl(j) \equiv 4j(j+1)/3$, and $v^{\perp 2} \equiv v^2 - (q/2\mu_t)^2$.

$$R_M^{xx'}(v,q) = \frac{1}{4}cl(j_\chi)\left[v^{\perp 2}(c_5^x c_5^{x'} q^2 + c_8^x c_8^{x'}) + c_{11}^x c_{11}^{x'} q^2\right] \tag{2.41}$$

$$+ (c_1^x + c_2^x v^{\perp 2})(c_1^{x'} + c_2^{x'} v^{\perp 2})$$

$$R_{\Sigma''}^{xx'}(v,q) = \frac{1}{16}cl(j_\chi)\left[c_6^x c_6^{x'} q^4 + (c_{13}^x c_{13}^{x'} q^2 + c_{12}^x c_{12}^{x'})v^{\perp 2} + 2c_4^x c_6^{x'} q^2 + c_4^x c_4^{x'}\right] \tag{2.42}$$

$$+ \frac{1}{4}c_{10}^x c_{10}^{x'} q^2$$

$$R_{\Sigma'}^{xx'}(v,q) = \frac{1}{32}cl(j_\chi)\left[2c_9^x c_9^{x'} q^2 + (c_{15}^x c_{15}^{x'} q^4 + c_{14}^x c_{14}^{x'} q^2 - 2c_{12}^x c_{15}^{x'} q^2 + c_{12}^x c_{12}^{x'})v^{\perp 2}\right. \tag{2.43}$$

$$\left. + 2c_4^x c_4^{x'}\right] + \frac{1}{8}(c_3^x c_3^{x'} q^2 + c_7^x c_7^{x'})v^{\perp 2} \tag{2.44}$$

$$R_{\Phi''}^{xx'}(v,q) = \frac{q^2}{16m_N^2}cl(j_\chi)(c_{12}^x - c_{15}^x q^2)(c_{12}^{x'} - c_{15}^{x'} q^2) + \frac{q^4}{4m_N^2}c_3^x c_3^{x'} \tag{2.45}$$

$$R_{\tilde{\Phi}'}^{xx'}(v,q) = \frac{q^2}{16m_N^2}cl(j_\chi)(c_{13}^x c_{13}^{x'} q^2 + c_{12}^x c_{12}^{x'}) \tag{2.46}$$

$$R_{\Delta}^{xx'}(v,q) = \frac{q^2}{4m_N^2}cl(j_\chi)(c_5^x c_5^{x'} q^2 + c_8^x c_8^{x'}) + 2\frac{q^2}{m_N^2}c_2^x c_2^{x'} v^{\perp 2} \tag{2.47}$$

$$R_{\Sigma'\Delta}^{xx'}(v,q) = \frac{q^2}{4m_N}cl(j_\chi)(c_4^x c_5^{x'} - c_8^x c_9^{x'}) - \frac{q^2}{m_N}c_2^x c_3^{x'} v^{\perp 2} \tag{2.48}$$

$$R_{M\Phi''}^{xx'}(v,q) = \frac{q^2}{4m_N}cl(j_\chi)c_{11}^x(c_{12}^{x'} - c_{15}^{x'} q^2) + \frac{q^2}{m_N}c_3^{x'}(c_1^x + c_2^x v^{\perp 2}) \tag{2.49}$$

It should be noted that the last two dark matter responses are composed entirely of interference terms, which is to say, they do not come into play unless certain combinations of EFT coefficients are simultaneously active. These are the coefficient pairs listed in Section 2.5.

For example, c_4 and c_5 together will activate $R_{\Sigma'\Delta}$, but not alone.

2.2.3   Nuclear structure

We assume a harmonic oscillator single-particle basis, with the important convention that the radial nodal quantum number n_a starts at 0, that is, we label the orbitals as $0s, 0p, 1s0d$, etc.., and *not* starting with $1s, 1p$, etc. By default, the harmonic oscillator basis length $b = \sqrt{\hbar/(m\omega)}$ is set to the Blomqvist and Molinari prescription [32]:

$$b^2 = 41.467/(45A^{-1/3} - 25A^{-2/3}) \text{ fm}^2, \tag{2.50}$$

where $A = Z + N$ is the number of nucleons. Other values can be set using the control words `hofrequency` or `hoparameter`. Then, the one-body matrix elements for operators $\langle a | |X_J^{(f)}| |b\rangle$, built from spherical Bessel functions and vector spherical harmonics, have closed-form expressions in terms of confluent hypergeometric functions [67].

The nuclear structure input is in the form of one-body density matrices between many-body eigenstates,

$$\rho_J^{fi}(ab) = \frac{1}{\sqrt{2J+1}} \langle \Psi_f | |[\hat{c}_a^\dagger \otimes \tilde{c}_b]_J| |\Psi_i\rangle, \tag{2.51}$$

where $\hat{c}_a^\dagger$ is the fermion creation operator (with good angular momentum quantum numbers), $\tilde{c}_b$ is the time-reversed [74] fermion destruction operator. Here the matrix elements are reduced in angular momentum but not isospin, and so are in proton-neutron format. These density matrices are the product of a many-body code, in our case BIGSTICK [164, 165], although one could use one-body density matrices, appropriately formatted (see 2.4), from any many-body code.

The theoretical formalism for computing the WIMP-nucleus form factors is largely the same

as in [89, 6]. In this paper we will therefore only provide the basic formalism which is necessary to understand the differences in our numerical and algorithmic approaches to the implementation.

2.2.4 Integrals

We use numerical quadrature to evaluate the integral in equation (2.1) for the velocity distribution (2.2). While there are analytic solutions [190, 90, 197] for specific forms for the cross section, namely with v^0 and v^2 dependence, we derive a general equation that can be used for any isotropic dark matter halo model, which to our knowledge has not been presented in publication. The integral has the form:

$$I = \int_{\Omega} d^3v \frac{d\sigma(v,q)}{dq^2} \; v \; f(\vec{v} + \vec{v}_E),\tag{2.52}$$

where the constraint Ω is that $v_{min}^2 < (\vec{v} + \vec{v}_E)^2 < v_{esc}^2$ and $f(\vec{v})$ is equation (2.2). Here we present only the result; the full derivation can be found in the manual. Switching to spherical coordinates and taking special care for the constraint Ω, one obtains:

$$I = \frac{1}{N} \int_{v_{min}}^{v_{esc}+v_E} dv \; \frac{d\sigma(v,q)}{dq^2} v^2 (I_{MB} - I_S),\tag{2.53}$$

where,

$$I_{MB} = \frac{\pi v_0^2}{v_E} \begin{cases} g(v - v_E) - g(v + v_E), & v < v_{low} \\ g(v - v_E) - g(v_{esc}), & otherwise \end{cases},\tag{2.54}$$

$$I_S = 2\pi g(v_{esc}) \begin{cases} 2v, & v < v_{low} \\ [v_{esc}^2 - (v - v_E)^2]/(2v_E), & otherwise \end{cases}.\tag{2.55}$$

with $v_{low} = v_{esc} - v_E$. $g(x)$ is a one-dimensional Gaussian form:

$$g(v) = e^{-v^2/v_0^2}. \tag{2.56}$$

The normalization factor is the same as previously derived [190, 90, 197]:

$$N_{sesc} = \pi^{3/2} v_0^3 \left[\text{erf}(z) - \frac{2}{\sqrt{\pi}} z \left(1 + \frac{2}{3} z^2 \right) e^{-z^2} \right], \tag{2.57}$$

with $z = v_{esc}/v_0$. I is a one-dimensional definite integral. We evaluate it with Gauss-Legendre quadrature.

The limits of the integral have physical constraints. The minimum speed is defined by the minimum recoil energy of a WIMP-nucleus collision at a momentum transfer q: $v_{min} = q/(2\mu_T)$, where μ_T is the reduced mass of the WIMP-nucleus system. In some approximations the upper limit is simply set to infinity. (Numerically, we approximate $\infty \approx 12 \times v_0$.) One can do slightly better by taking the maximum speed to be the galactic escape velocity: $v_{max} = v_{escape} \approx 550$ km/s.

2.2.5   Integrals in more detail

We provide the simplest model, a three-dimensional Maxwell-Boltzmann distribution,

$$f(\vec{v}) \propto e^{-\vec{v}^2/v_0^2}, \tag{2.58}$$

where v_0 is some scaling factor (typically taken to be around 220 km/s). This is called the Simple Halo Model (SHM) when a maximum value of the speed, due to the galactic escape

velocity v_{escape}, is taken into account [69, 98]:

$$f_{SHM}(\vec{v}) = \frac{\Theta(v_{esc} - |\vec{v}|)}{\pi^{3/2}v_0^3 N_{esc}}e^{-(\vec{v}/v_0)^2}, \tag{2.59}$$

where N_{esc} renormalizes due to the cutoff:

$$N_{esc} = \text{erf}\,(v_{esc}/v_0) - \frac{2v_{esc}}{\sqrt{\pi}v_0}\exp\{-(v_{esc}/v_0)^2\}. \tag{2.60}$$

With this distribution, the integral in the differential event-rate has the form:

$$I_{MB} = \int_\Omega d^3v \frac{d\sigma(v,q)}{dq^2}\,v\,e^{-(\vec{v}+\vec{v}_E)^2/v_0^2}, \tag{2.61}$$

where the constraint Ω is that $v_{min}^2 < (\vec{v} + \vec{v}_E)^2 < v_{esc}^2$.

To reduce to a one-dimensional integral, we make the conversion to spherical coordinates. Special care has to be taken to properly handle the truncated domain. Noting that $(\vec{v} + \vec{v}_{earth})^2 = \vec{v}^2 + \vec{v}_{earth}^2 + 2vv_{earth}\cos(\theta)$, with θ defining the angle between the two vectors, we make the substitution $d^3v = d\phi d(\cos\theta)v^2 dv$.

Now we follow the geometrical argument: Imagine constructing $\vec{v}_E + \vec{v}$. There are three cases to consider depending on the size of $\vec{v}$, and the implications for the allowed angles θ between $\vec{v}_E$ and $\vec{v}$ that satisfy the constraint $(\vec{v}_E + \vec{v})^2 < v_{esc}^2$.

- **Case 1:** "Small v", which we define as $v < v_{esc} - v_E$. Here there are no restrictions on θ since by construction the magnitudes together cannot exceed v_{esc}, so $\cos\theta$ is limited only by -1 and $+1$.

- **Case 2:** "Medium v", in which now $v > v_{esc} - v_E$, so not all angles are allowed. To keep the sum from exceeding v_{esc}, the angle must be restricted such that $\cos\theta < (v_{esc}^2 - v_E^2 - v^2)/2vv_E$. Case 2 also requires that $v < v_{esc} + v_E$ because we reach...

- **Case 3:** "Big v": It becomes impossible to satisfy the restriction once $v > v_{esc} + v_E$.

It follows that

$$\int_{(\vec{v}+\vec{v}_E)^2 < v_{esc}^2} d^3v = \int_0^{2\pi} d\phi \Big[\int_0^{v_{esc}-v_E} v^2 dv \int_{-1}^{+1} d\cos\theta \tag{2.62}$$

$$+ \int_{v_{esc}-v_E}^{v_{esc}+v_E} v^2 dv \int_{-1}^{(v_{esc}^2-v_E^2-v^2)/2vv_E} d\cos\theta \Big]. \tag{2.63}$$

Making the physically justified assumption that $v_{esc} - v_E > v_{min}$, we can simply shift the limit on the first integral from 0 to v_{min}. Along the way we will need to work out the angular integrals:

$$\int_{-1}^{+1} d\cos\theta\, e^{-2vv_E \cos\theta/v_0^2} = -\frac{v_0^2}{2vv_E} \left(e^{-2vv_E/v_0^2} - e^{2vv_E/v_0^2} \right); \tag{2.64}$$

$$\int_{-1}^{(v_{esc}^2-v_E^2-v^2)/2vv_E} d\cos\theta\, e^{-2vv_E \cos\theta/v_0^2} = -\frac{v_0^2}{2vv_E} \left(e^{-(v_{esc}^2-v^2-v_E^2)/v_0^2} - e^{2vv_e/v_0^2} \right). \tag{2.65}$$

Combining all of this together, and simplifying, we obtain a one-dimensional integral which we can evaluate with quadrature:

$$I_{MB} = \int_{v_{min}}^{v_{esc}+v_E} dv\, \frac{d\sigma(v,q)}{dq^2} v^2 \frac{\pi v_0^2}{v_e} \tag{2.66}$$

$$\{ \Theta_{v<v_{esc}-v_e} \left[g(v-v_E) - g(v+v_E) \right] + \Theta_{v>v_{esc}-v_E} \left[g(v-v_E) - g(v_{esc}) \right] \}, \tag{2.67}$$

where $g(v) = \exp(-v^2/v_0^2)$.

We then use Gauss-Legendre quadrature to evaluate I. There are analytic solutions for this integral in the form of error functions; we use quadrature since it makes easy to later modify the velocity distribution. For example, adding a velocity cut-off is as easy as changing the limit on the quadrature, with no need to write a whole new subroutine. While there

are analytic solutions for specific velocity-dependences of the cross section [190, 90, 197], our implementation favors a model-independent framework without the need to lock-in a particular form for the WIMP-nucleus cross section.

The limits of the integral, v_{min} and v_{esc}, have physical constraints. The minimum speed is defined by the minimum recoil energy of a WIMP-nucleus collision at a momentum transfer q:

$$v_{min} = q/(2\mu_T),\tag{2.68}$$

where $\mu_T = m_T m_\chi/(m_T + m_\chi)$ is the reduced mass of the WIMP-nucleus system. To use the simple Maxwell-Bolztmann distribution approximation, the maximum speed is taken to be $\infty \approx 12 \times v_0$. Otherwise, the maximum speed is taken to be the galactic escape velocity: $v_{esc} \approx 550$ km/s.

Note that as a function of momentum q, the integral is guaranteed to go to zero above some maximum momentum q_{max}. This happens when $v_{min} = v_{max} + v_{earth}$, which corresponds to:

$$q_{max} = 2\mu_T(v_{max} + v_{earth}),\tag{2.69}$$

$$E_{R,max} = q_{max}^2/2m_T = 2\mu_T^2 v_{max}^2/m_T.\tag{2.70}$$

With 150 GeV WIMPs and ^{29}Si, for example, $\mu_T = 23.031916$ GeV, $m_T = 27.209888$ GeV, $v_{max} = 550$ km/s $= 0.001834602$ GeV/c: $E_{R,max} = 265.2987$ keV.

2.3   Description of the code

The structure of the code and its inputs are outlined in Figure 2.1. The Fortran code replicates the capabilities of the earlier Mathematica script [6]. Notably, one can compute

the differential WIMP-nucleon scattering event rate for a range of recoil energies or transfer momenta, and any quantity required to determine those, such as the tabulated nuclear response functions.
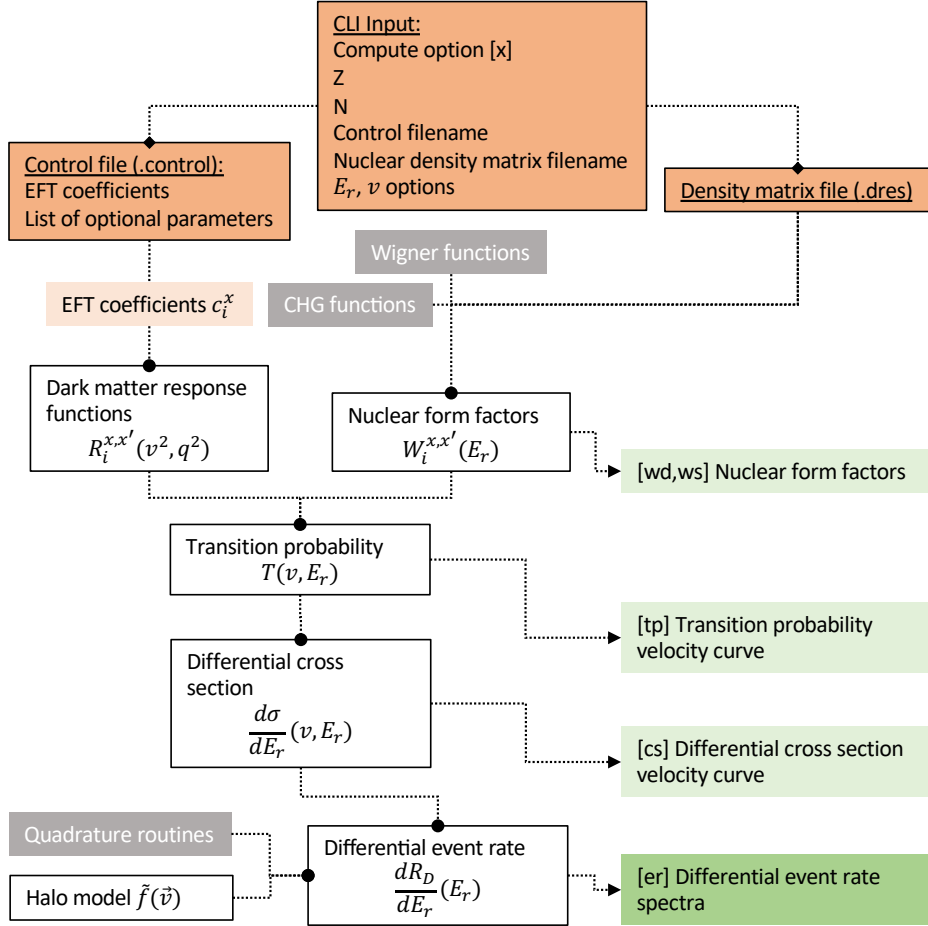
Figure 2.1: Flow of `dmscatter`. Orange boxes represent input files. Green boxes represent quantities the code can write to file. White boxes are important steps of interest and grey boxes are libraries built into the code. The inputs are: (1) the nuclear target information: target nucleus mass, spin, and one-body density matrix elements; (2) the non-relativistic EFT-specification of the WIMP-nucleon interaction; (3) the velocity distribution of WIMP particles in the laboratory frame.

We provide a detailed manual as part of the distribution package. The central engine, `dmscatter`, is written in standard modern Fortran and has OpenMP for an easy and optional parallel speed-up. While the distributed Makefile assumes the GNU Fortran compiler `gfortran`, the code should be able to be compiled by most recent Fortran compilers and does

not require any special compilation flags, aside from standard (and optional) optimization and parallel OpenMP flags.

To get started, one needs a modern Fortran compiler, the `make` tool, and, optionally, a Python interpreter (with NumPy, Matplotlib). We used the widely available GNU Fortran (`gfortran`) compiler, but we use only standard Fortran and our code should be able to be compiled by other Fortran compilers as well; the user will have to modify the makefile.

We provide a Python interface (a wrapper) for the Fortran code and a number of example scripts demonstrating its use. The wrapper comes with two Python functions EventrateSpectra, and NucFormFactor which can be imported from dmscatter.py in the Python directory. Each function has three required arguments:

1. number of protons Z in the target nucleus

2. number of neutrons N in the target nucleus

3. nuclear structure file name (.dres)

If no other arguments are provided, default values will be used for all of the remaining necessary parameters, including zero interaction strength. Default values are specified in the control file keyword table.

To calculate an event rate with a nonzero interaction, the user should also provide one or more of the optional EFT coupling coefficient arrays: `cp, cn, cs, cv`. These set the couplings to protons, neutrons, isoscalar, and isovector, respectively. The 0th index sets the first operator coefficient: `cp[0]` $= c_1^p$, etc. Finally, the user can also pass a dictionary of valid control keywords and values to the function in order to set any of the control words.

To compute the event-rate spectra for ^{131}Xe with a WIMP mass of 50 GeV and a $c_3^v = 0.0048$ coupling, one might call:

```
1  import dmscatter as dm
2  control_dict = {"wimpmass" : 50.0}
3  cv = np.zeros(15)
4  cv[2] = 0.0048
5  Erkev, ER = dm.EventrateSpectra(
6              Z = 54,
7              N = 77,
8              dres = "../targets/Xe/xe131gcn",
9              controlwords = control_dict,
10             cv = cv,
11             exec_path = "../bin/dmscatter")
```

This will return the differential event rate spectra for recoil energies from 1 keV to 1 MeV in 1 keV steps.

The file 'xe131gcn.dres' must be accessible at the relative or absolute path name specified (in this case '../targets/Xe/'), and contain a valid one-body density matrix for ^{131}Xe. Similarly, the `dmscatter` executable else the path to the executable should be specified, as in the above example (`exec_path = "../bin/dmscatter"`).

We have provided an additional option in `dmscatter` which computes these nuclear form factors from the target density-matrix and exports the results to a data file. This output may be useful for codes like WimPyDD [156], which compute the WIMP-nucleus event rate spectra starting from nuclear form factors (equation (2.26)) from an external source. (The DDCalc dark matter direct detection phenomenology package [38, 16] does have a fast Fortran90 central engine and predicts signal rates and likelihoods for ongoing dark matter experiments, but, unlike `dmscatter`, the nuclear structure input for the current version of DDCalc is fixed.)

The Python wrapper-function `NucFormFactor` runs the dmscatter option to export the nuclear response functions to file, and additionally creates and returns an interpolation function $W(q)$ which can be called. In the following code listing, the nuclear response function for ^{131}Xe is generated for transfer momentum from 0.001 to 10.0 GeV/c.

```
1  import dmscatter as dm
2  cwords = {"usemomentum": 1}
```

```
3  Wfunc = dm.NucFormFactor(
4          Z = 54,
5          N = 77,
6          dres = "../targets/Xe/xe131gcn",
7          controlwords = cwords,
8          epmin = 0.001,
9          epmax = 10.0,
10         epstep = 0.001)
11 Wfunc(0.001)
```

The final line returns an (8,2,2)-shaped array with the evaluate nuclear response functions at $q = 0.001$ GeV/c. Note that, had we not set the keyword `usemomentum` to 1, the function input values would have been specified in terms of recoil energy (the default) instead of transfer momentum.

2.4 Nuclear structure input

Users must provide nuclear one-body density matrix elements, either in isospin format,

$$\rho_{J,T}^{\Psi}(a,b) = (2J+1)^{-1/2}(2T+1)^{-1/2}\langle\Psi|||[\hat{c}_a^\dagger \otimes \tilde{c}_b]_{J,T}|||\Psi\rangle, \tag{2.71}$$

or proton-neutron format,

$$\rho_J^{\Psi}(a,b) = (2J+1)^{-1/2}\langle\Psi||[\hat{c}_a^\dagger \otimes \tilde{c}_b]_J||\Psi\rangle, \tag{2.72}$$

where Ψ is the nuclear-target wave function and $\hat{c}^\dagger$, $\hat{c}$ are the one-body creation, destruction operators. For proton-neutron format, the orbital indices a are distinct for protons and neutrons. Each label a corresponds to a radial quantum number $n_a = 0, 1, 2, ...$, orbital angular momentum l_a, and total angular momentum j_a.

The matrix elements must be stored in a file in a standard format produced by shell-model codes like BIGSTICK. The only assumption is that the single-particle basis states are har-

monic oscillator states. If density matrices are generated in some other single-particle basis, such as those from a Woods-Saxon potential or a Hartree-Fock calculation, that basis must be expanded into harmonic oscillator states. By using harmonic oscillator basis states one can efficiently compute the matrix elements. One can use either phenomenological or *ab initio* model spaces and interactions; as an example, we provide density matrices for ^{12}C, both from the phenomenological Cohen-Kurath shell model interaction [59], and from two no-core shell model interactions [75, 266]. A detailed description of the provenance of the supplied targets can be found in the included manual, and will be updated as more density matrices become available. We also include, for purposes of validation, the 'legacy' density matrices available in the original `dmscatter` script.

We supply a library of nuclear structure files (one-body density matrix files) for many of the common expected targets, as listed in Table 2.1. (We also include, for purposes of validation, some density matrices included with the original public Mathematica script [6].) These density matrix files are written in plain ASCII, using the format output by the nuclear configuration-interaction code BIGSTICK [164, 165]. The only assumption is that the single-particle basis states are harmonic oscillator states; the user must supply the harmonic oscillator single particle basis frequency Ω, typically given in MeV as $\hbar\Omega$, or the related length parameter $b = \sqrt{\hbar/M\Omega}$, where M is the nucleon mass.

Since standard one-body density matrices in phenomenological model spaces contain only matrix elements for orbitals in the valence space, it is necessary to infer the matrix elements for the core orbitals. Our code does this by default, but the user can disable this option using the `fillnuclearcore` control word.

For phenomenological interactions one typically has a 'frozen' core of nucleons which do not participate in the two-body forces of the Hamiltonian. In such cases the single-particle space listed in the .dres file consists only of the valence orbitals and the one-body density matrices are only specified for the valence orbitals.

Table 2.1: Table of nuclear data for targets we include with the program at time of publication. Each corresponds to a (.dres) density matrix file in the `targets` directory. The source indicates the nuclear Hamiltonian that was used to generate the wave function data. See the manual and GitHub repository for updates and full information on provenance. New targets may be added in future releases. * = density matrix used in original Mathematica script [6]

Nuclei	Isotopes	Source
He	4	[75, 266]
C	12	[59, 75, 266]
F	19	[301, 44]*,[42]
Na	23	[301, 44],[42]
Si	28, 29	[301, 44]*,[42]
Ar	40	[284]
Ge	70, 72, 73, 74, 76	[147]
I	127	[43]; unpublished used in [54, 55]
Xe	128, 129, 130, 131, 132, 134, 136	[43]; unpublished used in [54, 55]

DMFormFactor reads the valence space orbitals from the .dres file and infers the number of core nucleons by subtracting the number of valence protons and neutrons from the number of nucleons in the target nucleus. The core orbitals are assumed to be one of the standard shell model orbital sets associated with possible cores: ^{4}He, ^{16}O, ^{40}Ca, ^{56}Ni, ^{100}Sn.

The one-body density matrix elements for the core orbitals are then determined from the (full) occupation of the core orbitals. Because the orbitals are full and here we assume both proton and neutron orbitals filled, the core can contribute only to $J = 0, T = 0$ densities. Two formats are possible: proton-neutron format:

$$\rho^\Psi_{J,x=p,n}(a,b)_{(core)} = \delta_{a,b}\delta_{J,0}[j_a], \tag{2.73}$$

where $[y] \equiv \sqrt{2y+1}$ and j_a is the angular momentum of a-orbit, J is the total spin of the nuclear target state Ψ; and isospin format for a target state with good total isospin T:

$$\rho^\Psi_{J,T=0}(a,b)_{(core)} = \delta_{a,b}\delta_{J,0}\delta_{T,0}[1/2][j_a], \tag{2.74}$$

$$\rho_{J,T=1}^{\Psi}(a,b)_{(core)} = 0.0. \tag{2.75}$$

Internally the code expands densities in isospin format into proton and neutron densities. Note that our libraries only include isoscalar cores; if one had cores with $N > Z$ then one could also have $T = 1$ contributions.

When a density matrix is read in, `dmscatter` performs a test to validate the number of particles in the valence orbitals matches the declared number of valence particles at the top of the density matrix file. If this test fails, the code will stop. This is an indication that the density matrices being used were not fully converged, or have some other problem. The check is that

$$n_p = \sum_a \rho_{J=0,p}(a,a)[j_a]/[J_0] \tag{2.76}$$

$$n_n = \sum_a \rho_{J=0,n}(a,a)[j_a]/[J_0], \tag{2.77}$$

where n_p is the number of valence protons, j_a is the total angular momentum of the a-th valence orbital, and J_0 is the total angular momentum of the ground state of the nucleus. Similarly for the number of neutrons n_n.

2.5   Validation and performance

There are two sources of error in our calculation. The first is from the model uncertainty of the nuclear wave functions. This source of error is therefore also present in `dmscatter`. While phenomenological calculations can get energies within a few hundred keV [42], other observables often require significant renormalization of operators to agree with experiment, see, e.g., [244]. These errors in observables can have complex origins, arising both from truncations of the model space and higher-order corrections to the corresponding operators [122].

Errors in the numerical methods to solve the many-body problem given a set of input parameters are, by comparison, vanishingly small. Nonetheless, experience suggests that in most cases the renormalization is of order one. We have qualitative support of this fact from comparisons of event rate spectra from *ab initio* calculations with increasing model space dimension (scaling with N_{max}, the maximum excitation in an non-interacting harmonic oscillator basis, sometimes written as $N_{max}\hbar\omega$ excitations), and from different chiral effective-field theoretical interactions.

The second source of error is from the numerical integration. By comparison, the error from the numerical integration is expected to be many orders of magnitude smaller. Using an adaptive quadrature routine from a standard source [63], the code iteratively increases the complexity of the estimator until it achieves a desired relative uncertainty.

We validated our Fortran program `dmscatter` against the Mathematica script `dmformfactor` (version 6.0). We used ^{29}Si as a validation case since we have access to the same nuclear density matrix file provided in the `dmformfactor` package. With a $J = 1/2$ ground state, ^{29}Si also has non-zero coupling to all 15 operators.

We evaluated the differential event rate for recoil energies from 1 keV to 1000 keV in 1 keV increments for each coefficient individually c_i^x; for $i = 1, 3, 4, 5, ..., 15$; for linearly independent coupling pairs $c_a \cdot c_b = 1$ for $(a, b) = (1,2), (1,3), (2,3), (4, 5), (5,6), (8,9), (11,12), (11,15), (12,15)$, and for both $x = p, n$. An example is shown in Figure 2.2. In each case we reproduce the results of `dmformfactor`. Typical 'error' with respect to `dmformfactor` is shown in Figure 2.2. A full suite of validation plots are attached at the end of the manual.

The Fortran code has been optimized for multi-processor CPUs with shared memory architecture using OpenMP. As a result of this parallelism and the inherent efficiency of a compiled language, our program sees an extreme speedup when computing event-rate spectra compared to the Mathematica package `dmformfactor` version 6.
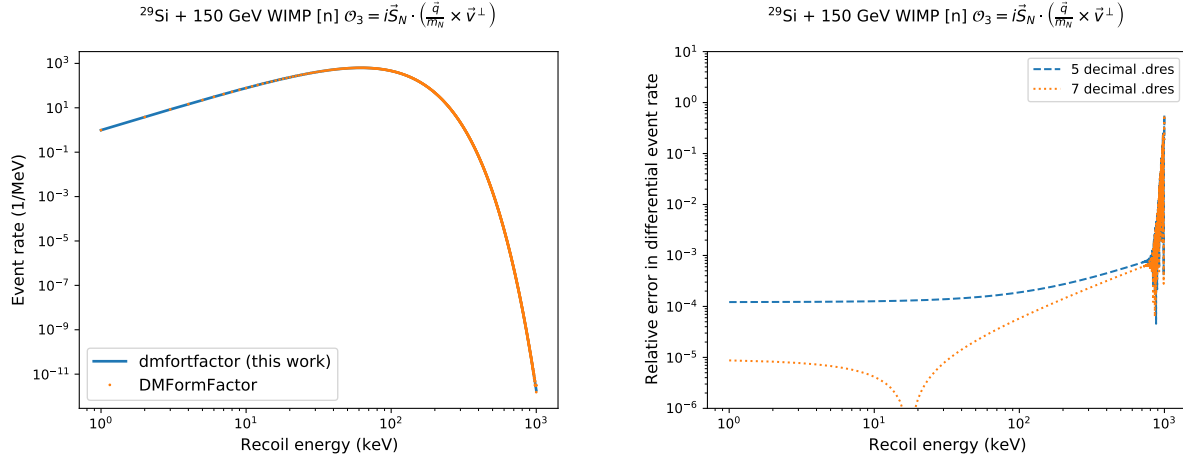
Figure 2.2: Left: Example differential event rate spectra for $c_3^n = 1$ with 150 GeV WIMPS on ^{29}Si computed with `dmscatter` (solid blue line) and with `dmformfactor` (orange dots). Right: Relative error of `dmscatter` with respect to the Mathematica script `dmformfactor` for the same example. The spike near recoil energy 10^3 keV is due to round-off error on zero; the event rate there is nearly zero. The (blue) dashed line was calculated with the `BIGSTICK`-standard 5 decimals of precision in the nuclear structure input (.dres file). The (orange) dotted line has 7 decimal places of precision, matching that used in the `dmformfactor` calculation.

We provide timing data for two benchmark cases: ^{29}Si and ^{131}Xe, shown in Table 2.2. The compute time of our code depends primarily on two sets of factors: the first is the number of elements in the nuclear densities matrices (which depends on the complexity of the nuclear structure for a given target nucleus), and the second is the number of nonzero EFT coefficients. We include logic to skip compute cycles over zero EFT coefficients.

The timing data in Table 2.2 provides a general indication of the compute time for basic calculations. We also ran a more complex benchmark calculation to represent the complexity of a practical application. In this calculation, we compute the differential event rate spectra for ^{131}Xe over a range of recoil energies from 1 keV to 1000 keV, and for a range of WIMP masses from 1 GeV to 300 GeV, in 1 GeV increments. We provide the Python script `exampleMassHeatPlot.py` used to generate this plot in the `python/` directory. The result is shown in the heat plot in Figure 2.3. This calculation represents 300 calculations of the type in Table 2.2, and so we estimate that generating the data for such a plot using the

Coupling	DMFormFactor	dmscatter	
		Serial	Parallel
Nuclear target: ^{29}Si			
c_1^n	3,800	0.5	0.2
c_3^n	3,800	1.3	0.5
c_4^n	3,700	1.5	0.5
c_5^n	3,700	0.9	0.3
c_6^n	3,700	0.8	0.3
Nuclear target: ^{131}Xe			
c_1^n	20,000	1.7	0.5
c_1^p		1.7	0.5
c_1^s	20,000	5.8	1.6
c_1^v		5.8	1.6
All nonzero	20,000	75	20

Table 2.2: Program execution time in seconds for a sample event-rate calculation with 1000 recoil energies with $m_\chi = 150$ GeV. The velocity distribution was taken to be Maxwellian with $v_{escape} \approx \infty$. All calculations were done on the same machine (Apple M1 processor, 2020). Multi-threaded execution was performed with 4 threads on the 8-core CPU. ^{29}Si has 23 matrix elements in its one-body density matrix, while ^{131}Xe has 67.

Mathematica package `dmformfactor` would require roughly 70 days of CPU time. Our calculation takes only 20 minutes of CPU time with serial execution (including overhead from the Python script running the code), and with parallel execution across 4 threads the wall time is 7 minutes.
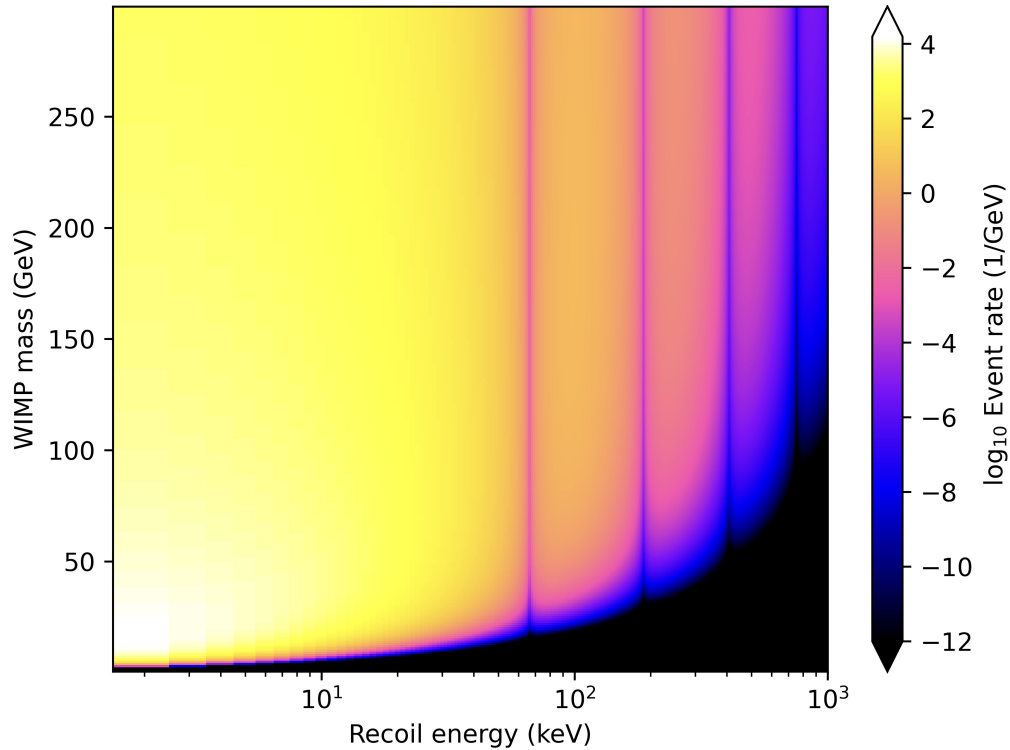
Figure 2.3: (Taken from [118].) Event rate as a function of WIMP mass and recoil energy for ^{131}Xe. 300 masses are represented in this figure (1000 recoil energies each; a slice along the horizontal axis is analogous to the calculation shown in Figure 2.2). Using our code, this consumed roughly 30 minutes of CPU time. We estimate that using `dmformfactor` to generate the same figure would take at least 70 days (300 curves, 20 000 seconds each). The EFT interaction used was vector isospin-coupling to operator-1 ($c_1^{\tau=1} = 0.00048$).

Chapter 3

Proton-neutron Entanglement Entropy

This chapter is based on a paper I co-authored with my advisor Calvin Johnson [162], as well as work from my master's thesis [115]. Johnson conceived of the idea and I ran the calculations. Eventually, I contributed by designing my own toy-model interactions in our attempts to understand the trends we saw in our calculations, although, none of these resulted in satisfying resolution. Johnson was the first author of the publication, writing the majority of the manuscript and also provided the final figures, with some edits from myself.

The interest of this chapter is twofold. First, many fields have recently seen fruitful results by applying quantum information theory to their respective complex systems. Concepts such as entropy and temperature can tell us about how a quantum system transitions from order to chaos, or from quantum to statistical. These are interests in their own right which can also be investigated for the nuclear many-body problem. The second interest is more practical: insights from quantum information may improve our computational methods. This chapter's second purpose is to serve as a justification for the new computational technique I have developed in the following two chapters: the weak entanglement approximation.

The entanglement entropy of a bipartite system measures the complexity of the coupling

between the two subsystems: an entropy of zero means we can factorize the wave function. We compute the proton-neutron entanglement entropy in the interacting nuclear shell model for a variety of nuclides and interactions. Some results make intuitive sense. For example, that the shell structure as governed by single-particle and monopole energies strongly affects the energetically available space and thus the entanglement entropy. We also find a surprising result: that the entanglement entropy at low excitation energy tends to decrease for nuclides when $N \neq Z$. While we provide evidence this arises from the physical nuclear force by contrasting with random two-body interactions which show no such decrease, the exact mechanism is unclear. Nonetheless, the low entanglement suggests that in models of neutron-rich nuclides, the coupling between protons and neutrons may be less computationally demanding than one might otherwise expect.

3.1 Introduction

The structure of atomic nuclei exhibits a mixture of simple and complex behaviors. What is meant by 'simple' can be subtle, but typically it means the behavior can be described by far fewer degrees of freedom than required by modeling the nucleus as a collection of A interacting nucleons; examples of simplicity include algebraic models [275] and mean-field pictures [245]. Of course, one must acknowledge that models themselves are not physical observables. Furthermore, complex models can mimic simpler ones, for example quasidynamic symmetries [19, 249, 20], where a Hamiltonian mixes symmetries yet observables such as spectra and ratios of transition strengths are consistent with 'simpler' symmetry-respecting models.

Entanglement is a concept describing whether the observable coordinates of a quantum system are independent; whether measurement of one generalized coordinate q_1 influences future measurements of another coordinate q_2 of a system $\psi(q_1, q_2, ...)$[5, 258]. Such correlations can

be described by the entanglement entropy, a concept which has become popular in recent years due to increasing interest in quantum information and the potential of quantum computing [148, 271]. It is trivial to write down states which are either separable (not entangled) or in a superposition of separable states (entangled), but the creation of entangled states in nature relies on the existence of an interaction that mixes the relevant degrees of freedom.

Here we consider the entanglement between the proton components and neutron components of configuration-interaction models of nuclei. Other recent work in entanglement entropy in nuclei addressed single-particle and seniority-mode entanglement [246, 180] as well as orbital entanglement revealing shell closures [279]; we note the first two papers reference unpublished versions of the research reported here.

A persistent phenomenon, however, is not so easily explained: realistic ground states of nuclides with $N \neq Z$ tend to have significantly smaller entanglement entropies than those with $N = Z$. We also show trends for entropies for all states. We can show this is related to some components of realistic nuclear forces by contrasting them with results using random interactions. While the mechanism for suppressing the entanglement eludes us, it is nonetheless worth reporting, not only as an apparently robust yet unexplained phenomenon, but also because it has a practical consequence: the low-lying states of neutron-rich nuclides have fewer nontrivial correlations between the proton and neutron components. This, in turn, suggests a practical approach for such nuclides, one which we are currently developing.

3.2   Entanglement entropy

The entanglement entropy is a fundamental tool in quantum information science [5, 148, 271]. Here we briefly review the development found in those sources.

For a pure quantum state $|\Psi\rangle$, the density operator is $\hat{\rho} = |\Psi\rangle\langle\Psi|$; in a basis $\{|\alpha\rangle\}$, i.e.,

Eq. (1.19), the density matrix elements are $\rho_{\alpha'\alpha} = c'_\alpha c^*_\alpha$. Because this is idempotent, $\rho^2 = \rho$, and thus has either 0 or 1 as eigenvalues, the von Neumann entropy, $S = -\operatorname{tr}(\rho \log \rho)$ vanishes.

Suppose we work in a bipartite Hilbert space, e.g. $\mathcal{H} = \mathcal{H}_\pi \oplus \mathcal{H}_\nu$. We can then write Eq. (1.19) explicitly as

$$|\Psi\rangle = \sum_{\mu,\sigma} c_{\mu,\sigma} |\mu_\pi\rangle \otimes |\sigma_\nu\rangle. \tag{3.1}$$

An unentangled state is one where one can transform to a basis where the amplitudes are separable, that is $c_{\mu,\sigma} = a_\mu b_\sigma$; in this case the state could be written as a simple product: $|\Psi\rangle = \left(\sum_\mu a_\mu |\mu_\pi\rangle\right) \otimes \left(\sum_\sigma b_\sigma |\sigma_\nu\rangle\right)$. States which do not satisfy this are entangled.

In the basis (3.1) the density matrix is $\rho_{\mu'\sigma',\mu\sigma} = c_{\mu'\sigma'} c^*_{\mu\sigma}$. This density matrix is idempotent. To get the *reduced* density matrix, one traces over one of the subspace indices:

$$\rho^{\text{red}}_{\mu',\mu} = \sum_\sigma c_{\mu'\sigma} c^*_{\mu\sigma}. \tag{3.2}$$

If the state is unentangled, the reduced density matrix will also be idempotent. For a general state the reduced density matrix need not be idempotent, and its eigenvalues can be between 0 and 1. Then the entanglement entropy [5]

$$S_{\text{entangled}} = -\operatorname{tr} \rho^{\text{red}} \ln \rho^{\text{red}} \tag{3.3}$$

can be nonzero. Because unentangled states must have zero entanglement entropy, non-zero entropy is a measure of entanglement [5]. The fact that the eigenvalues of ρ^{red} are real and non-negative, and independent of which subspace index we trace over, is a result of the singular value decomposition theorem; this is also called the Schmidt decomposition. The

maximum entropy possible is the natural logarithm of the smaller subspace dimensions,

$$S_{max} = \ln(\min(\dim_\pi, \dim_\nu)). \tag{3.4}$$

Because our codes are written using an explicit proton-neutron basis, it is easy to extract $c_{\mu,\sigma}$ for any calculated state and then compute the entanglement entropy.

To illustrate, let's consider a bipartite spin system $\mathcal{H}_{12} = \mathcal{H}_1 \otimes \mathcal{H}_2$. We can represent any wave function in this space as

$$|\Psi\rangle = \sum_{ab} \Psi_{ab} |a\rangle \otimes |b\rangle \rightarrow \Psi = \begin{bmatrix} \Psi_{\uparrow\uparrow} & \Psi_{\uparrow\downarrow} \\ \Psi_{\downarrow\uparrow} & \Psi_{\downarrow\downarrow} \end{bmatrix}, \tag{3.5}$$

where the basis vectors $|a\rangle$ and $|b\rangle$ are either $|\uparrow\rangle$ or $|\downarrow\rangle$, and where the elements of the matrix Ψ are the coefficients for the four possible bipartite basis states. Let's compute the entanglement entropy for two spin-1/2 particles which are not entangled:

$$|\Psi\rangle = |\uparrow\downarrow\rangle \rightarrow \Psi = \begin{bmatrix} 0 & 1 \\ 0 & 0 \end{bmatrix}. \tag{3.6}$$

The reduced density matrix of this wave function can be computed as the matrix product $\Psi\Psi^\dagger$:

$$\rho^{\text{red}} = \begin{bmatrix} 0 & 1 \\ 0 & 0 \end{bmatrix} \begin{bmatrix} 0 & 0 \\ 1 & 0 \end{bmatrix} = \begin{bmatrix} 1 & 0 \\ 0 & 0 \end{bmatrix}. \tag{3.7}$$

This density matrix is already diagonal, so we can compute its von Neummann entropy as

$$S_{\text{entangled}} = S(\rho^{\text{red}}) = -(1\ln(1) + 0\ln(0)) = 0. \tag{3.8}$$

Thus a non-entangled pair of spin-1/2 particles has zero entanglement entropy.

We can follow the same procedure for an entangled pair:

$$|\Psi'\rangle = \frac{1}{\sqrt{2}}(|\uparrow\downarrow\rangle - |\downarrow\uparrow\rangle), \tag{3.9}$$

which can be represented as a matrix using (3.5):

$$\Psi' = \frac{1}{\sqrt{2}}\begin{bmatrix} 0 & 1 \\ -1 & 0 \end{bmatrix}. \tag{3.10}$$

The reduced density matrix is

$$\rho' = \Psi'\Psi'^{\dagger} = \frac{1}{2}\begin{bmatrix} 1 & 0 \\ 0 & 1 \end{bmatrix}. \tag{3.11}$$

Thus this entangled pair has an entanglement entropy

$$S'_{\text{entangled}} = S(\rho') = -(\frac{1}{2}\ln(1/2) + \frac{1}{2}\ln(1/2)) = \ln 2, \tag{3.12}$$

which is the maximum entanglement entropy for a bipartite system with two-dimensional subspaces.

3.2.1   The calculations

We work in three different model spaces and with several different shell model interactions. All of our calculations are in the M-scheme, that is, a basis with fixed total J_z. We start with several studies of $N = Z$ nuclides in the sd-shell, where our results can be easily understood. We then look at cases in the sd, pf, and sd-pf spaces with $N \neq Z$, which leads to a surprise:

ground states with $N \neq Z$ have significantly lower entanglement entropies than those with $N = Z$. By comparing with randomly generated interactions we provide evidence that this phenomenon has its origin in physical forces; but beyond that, we have yet to understand the specific mechanism. Finally, we look at the behavior of the entropy over the entire spectrum.

3.2.2   Examples with $N = Z$ and the role of the shell structure

In this subsection we discuss some introductory results, focusing on $N = Z$ nuclides.

Our first examples in Fig. 3.1 are the ground state entanglement entropies for $N = Z$ nuclides in the so-called sd-shell, which has a fixed ^{16}O core and valence particles in the $1s_{1/2}$-$0d_{3/2}$-$0d_{5/2}$ orbitals. For convenience we give the $M = 0$ dimensions in Table 3.1. Here

Table 3.1: (Taken from [162].) $M = 0$ dimensions for the $N = Z$ nuclides in Fig. 3.1 with valence nucleons in the sd-shell. Because there are a maximum of 12 valence nucleons of either species, the dimensions have a particle-hole symmetry around $N, Z = 14$.

Nuclide	dimension
^{20}Ne, ^{36}Ar	640
^{22}Na, ^{34}Cl	6,116
^{24}Mg, ^{32}S	28,503
^{26}Al, ^{30}P	69,784
^{28}Si	93,710

the proton and neutron many-body spaces have equal dimensions. We use a high-quality empirical interaction, the universal sd-shell interaction, version B or USDB, which, like all similar empirical interactions, is represented as a list of single-particle energies and two-body matrix elements fitted to data [42].

We also show in Fig. 3.1(a) the entropies for ground states of the attractive isoscalar quadrupole-quadrupole (QQ) interaction, the attractive isovector (IV) pairing, that is, nucleons paired up to isospin $T = 1$, and the attractive isoscalar (IS) pairing, or nucleons paired up to $T = 0$. These schematic interactions are well-known in nuclear structure
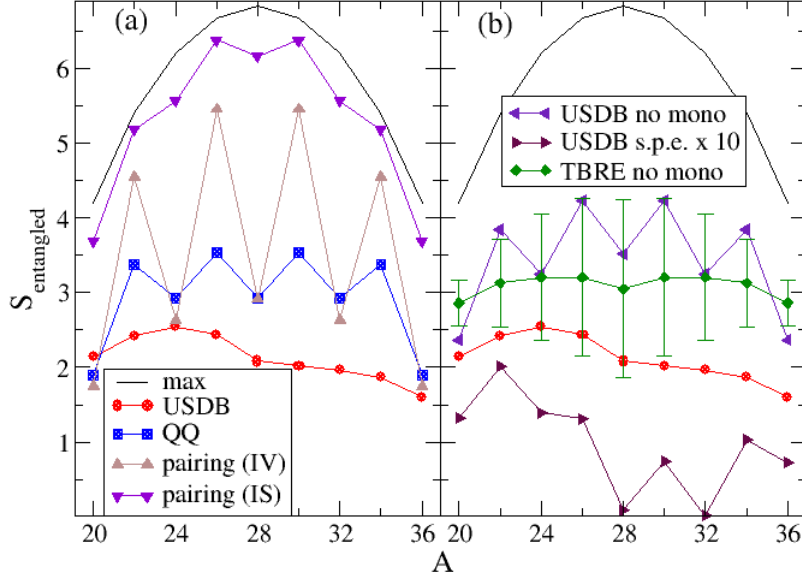
Figure 3.1: (Taken from [162].) Ground state entanglement entropy for $N = Z$ nuclides in the sd-shell. Both panels show results for USDB [42], a high-quality empirical interaction, and the maximum possible entanglement entropy. In panel (a) we show results for an attractive isoscalar quadrupole-quadrupole ('QQ') interaction; isovector (IV) and isoscalar (IS) pairing. In panel (b) we show results for USDB with single-particle energies and monopole interactions which have been set to zero, eliminating shell structure ('no mono'), and with single-particle energies were inflated by a factor of ten, amplifying shell structure ('s.p.e. x 10'). Additionally, panel (b) gives the average and standard deviation for calculations drawn from a two-body random ensemble [161], also with shell structure eliminated ('TBRE no mono'). See text for discussion.

physics [46, 245, 34]; we give their exact definitions:

Quadrupole-Quadrupole (QQ)

We construct a quadrupole operator

$$\hat{Q}_{2M,TM_T} = \sum_{ab} Q_{ab}[\hat{c}_a^\dagger \otimes \tilde{c}_b]_{2M,TM_T} \tag{3.13}$$

where a, b are indices for single-particle orbits defined by n, l, j; $[\cdot \otimes \cdot]_{JM,TM_T}$ indicates coupling by Clebsch-Gordan coefficients up to total angular momentum J (here $J = 2$) and z-component M and total isospin T and third component M_T; $\hat{c}_a^\dagger$ creates a particle in orbit a, $\tilde{c}_b$ is a time-reversed destruction operator [74] for a particle in orbit b; and finally the reduced matrix elements [74] of the quadrupole operator (which we compute in a harmonic-oscillator basis)

$$Q_{ab} = \langle a||r^2 Y_2||b\rangle, \tag{3.14}$$

where $Y_{lm}(\theta, \phi)$ is a spherical harmonic. The quadrupole-quadrupole Hamiltonian is

$$V_{QQ}\left[\hat{Q} \otimes \hat{Q}\right]_{00,00}, \tag{3.15}$$

where V_{QQ} is the strength of the interaction and is taken < 0 to make it attractive; because we only focus on the wave functions and not the energies, the magnitude of V_{QQ} is unimportant here. For our calculations we considered only the isoscalar (T=0) QQ interaction.

Pairing

The pairing operator is

$$\hat{P}_{TM_T}^\dagger = \sum_a \sqrt{2j_a + 1}[\hat{c}_a^\dagger \otimes \hat{c}_a^\dagger]_{00,TM_T}, \tag{3.16}$$

where j_a is the angular momentum of orbital a. The pairing Hamiltonian is

$$G \sum_{M_T} (-1)^{T-M_T} \hat{P}_{TM_T}^\dagger \hat{P}_{TM_T}, \tag{3.17}$$

where G is the strength of the pairing Hamiltonian, and is taken < 0 to make attractive. Here $T = 1$ yields isovector pairing and $T = 0$ isoscalar pairing.

Unsurprisingly, isoscalar pairing, which forces protons to pair with neutrons, has nearly maximal entanglement entropy. Isovector pairing shows a strong odd-even effect: odd-odd nuclides, where at least one proton and at least one neutron must pair up, has much higher entropy than the even-even cases. Ground states of the QQ interaction have a much weaker odd-even staggering, while USDB ground states have the lowest entropies of all and exhibit no odd-even staggering.

In Fig. 3.1(b), we further investigate the origin of some of these behaviors. The shell structure of nuclei is governed by the single-particle energies and the so-called monopole terms [53], that is, terms in the interaction of the form $\hat{n}_a \hat{n}_b$ where $\hat{n}_a$ is the number operator for orbital a. By setting the single-particle energies and monopole terms to zero, the ground state entanglement entropy increases, and shows an odd-even staggering comparable to QQ. Conversely, by inflating the standard USDB values of the single-particle energies ($\epsilon(1s_{1/2}) = -3.2079$ MeV, $\epsilon(0d_{3/2}) = 2.1117$ MeV, and $\epsilon(0d_{5/2}) = -3.9257$ MeV) by a factor of $\times 10$, we restrict the space energetically available and dramatically decrease the ground state entanglement entropy, reaching zero at shell closures. Finally, we considered two-body interactions drawn from a random ensemble (TBRE [161]), also removing single-particle energies and monopole terms. We used results from ten different members of the ensemble to get average entropies and corresponding standard deviations. From this we learn that, first, the shell structure, as encoded in single-particle energies and monopole terms, has a strong effect on the entanglement entropy, by energetically restricting the available model space and thus reducing the effective dimension. While the 'no mono' USDB results appear consistent with a randomly drawn interaction, it does show a nontrivial odd-even staggering. Later, we will see additional behaviors that strongly differ between USDB and randomly generated interactions.

From these numerical experiments we conclude the lower entanglement of the full USDB wave

functions is due to the shell structure, i.e., the monopole terms and single-particle energies. We speculate the lack of odd-even staggering in the entropies of full USDB calculations may be due to many small, quasi-random components in the interaction beyond pairing and QQ.

3.2.3 Away from $N = Z$

In the previous subsection we considered exclusively nuclides with $N = Z$. Here we compare entropies for nuclides with $N \neq Z$, and find systematically lower entropies–albeit when using physical forces. Because we use interactions which respect isospin as a good symmetry, we only consider here $N > Z$.

In Fig. 3.2 we compare the ground state entropies for 'triplets' of nuclides. These triplets are set in the same valence space, either sd or pf, and all members of a triplet have the same number of valence protons or proton holes, and the same number of valence neutrons or neutron holes. For example, we have ^{20}Ne, with 2 valence protons and 2 valence neutrons; ^{36}Ar, with 2 proton holes and 2 neutron holes (since the filled sd valence orbitals contain 12 particles of a given nuclear species); and ^{28}Ne, with 2 valence protons and 2 neutron holes. By this construction all members of a triplet have exactly the same dimensionalities. For the sd-shell cases in Fig. 3.2(a), following Fig. 3.1, we compare entanglement entropies from ground states computed with the full USDB interaction, USDB with monopole terms and single-particle energies set to zero, and finally entropies of ground states calculated from the two-body random ensemble (with monopole terms zeroed out). For the pf-shell cases in Fig. 3.2(b), we do the same but replace USDB with the GX1A interaction [146].

We see a strong and persistent trend: ground states of nuclides with $N \neq Z$ computed with realistic interactions have significantly lower entanglement than those with $N = Z$, a result we have replicated in other shell model spaces we do not show. To put this in perspective, an entropy difference of 1 corresponds to a difference in effective dimensionality
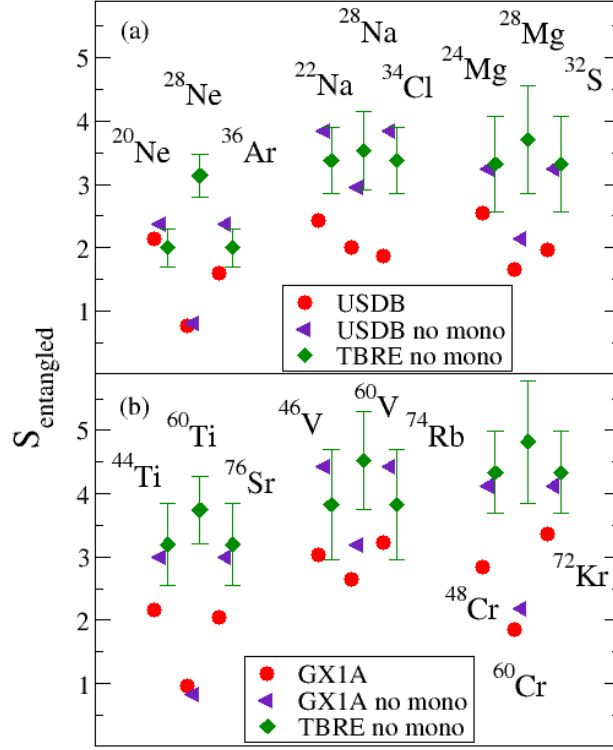
Figure 3.2: (Taken from [162].) Ground state entanglement beyond $N = Z$. We compare nuclide triplets with the same dimensionalities (same maximum entanglement entropy), with the same number of protons/proton holes and neutrons/neutron holes; not all cases correspond to physical nuclides. Panel (a) is for sd-shell nuclides, while panel (b) is for pf-shell nuclides. Here USDB [42] is an empirical interaction for the sd-shell while GX1A [144, 145, 146] is for the pf-shell. We also show the average and standard deviation for interactions drawn from the two-body random ensemble (TBRE). Finally, 'no mono' means the single-particle energies and monopole interaction terms have been set to zero, thus eliminating any shell structure [53].

of $e = 2.71 \ldots$. This trend is stronger for even-even nuclides and when the shell structure is removed. For ground states computed under the TBRE, however, that trend disappears and is even slightly reversed. While we have made attempts to devise a plausible model for these behaviors, for example why the $N \neq Z$ entropy is lower for realistic interactions but is higher for the TBRE, we have not succeeded.

Because this trend suggests a lower entanglement for neutron-rich nuclides (or, because of isospin symmetry for these interactions, proton-rich as well), we continue our investigation

in Fig. 3.3, where we consider cross-shell examples in the sd-pf space using the 'mu-db' interaction [155]. In order to compare with past results, we restrict the space so as to
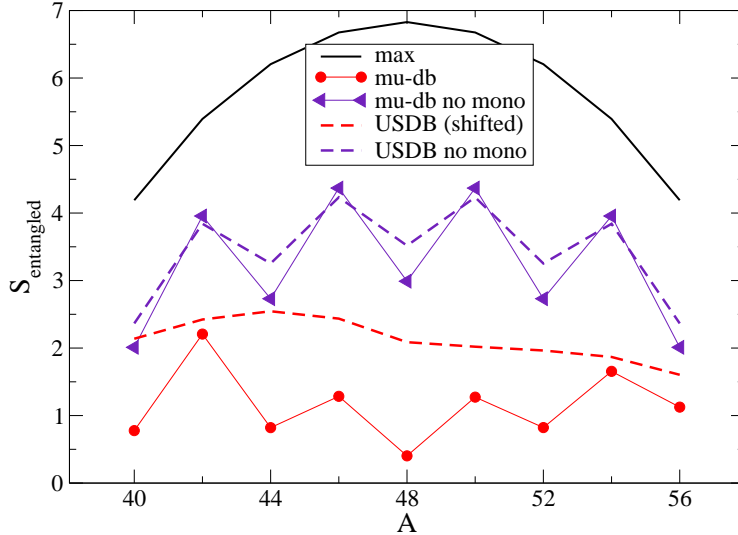
Figure 3.3: (Taken from [162].) Entanglement entropies for nuclides in the sd-pf space, from ^{40}Ne through ^{56}Ar. See text for a detailed description of the model space, which is truncated so that the dimensionalities are the same as for $N = Z$ sd-shell nuclides in Fig. 3.1. Here 'mu-db' is the interaction of Ref. [155], while 'max' and 'no mono' mean the same as in Fig. 3.1. We also include for comparison sd-shell results from Fig. 3.1 (dashed lines), shifted by $A = 20$

follow the dimensionalities of Fig. 3.1. Thus we restrict protons to the sd-shell, while for neutrons the sd-shell and the $0f_{7/2}$ orbitals are filled and frozen, leaving only $0f_{5/2}$-$1p_{3/2}$-$1p_{1/2}$ as the active space for neutrons. Finally, we restrict ourselves to the same number of active protons and neutrons. Thus the nuclides correspond to ^{40}Ne, ^{42}Na, ^{44}Mg, and so on, through ^{56}Ar. These restrictions are chosen so that the dimensionalities are the same as in Fig. 3.1. While somewhat artificial–we do not claim all these correspond to physical nuclides–this nonetheless allows us to make a clean investigation into the entanglement. For ease of comparison, we include the USDB and USDB monopole-subtracted ('no mono') results for $N = Z$ nuclides, shifted over by $A = 20$ (so that ^{20,40}Ne are superimposed, etc.). Again we see a low entanglement entropy, even lower than for the sd-shell examples in Fig. 3.1, although the 'no monopole' case shows much of this is driven by shell structure. Nonetheless

this provides evidence that the low-entanglement for $N \neq Z$ nuclides persists for cross-shell spaces.

It is important to note that this is not simply isospin. Although we do not show it, for a given N and Z, states of different J and T nonetheless show very similar trends. In other words, this behavior is related to T_z, not T. In the next section we investigate further.

3.2.4 Entanglement entropies of excited levels

In the previous results we focused on ground state entanglement. Here we look at systems where we can fully diagonalize and compute the entanglement entropy across the spectrum.

In Fig. 3.4 we present the entanglement entropy for all levels for several nuclides computed with empirical interactions that give a good description of the data. Specifically we con-
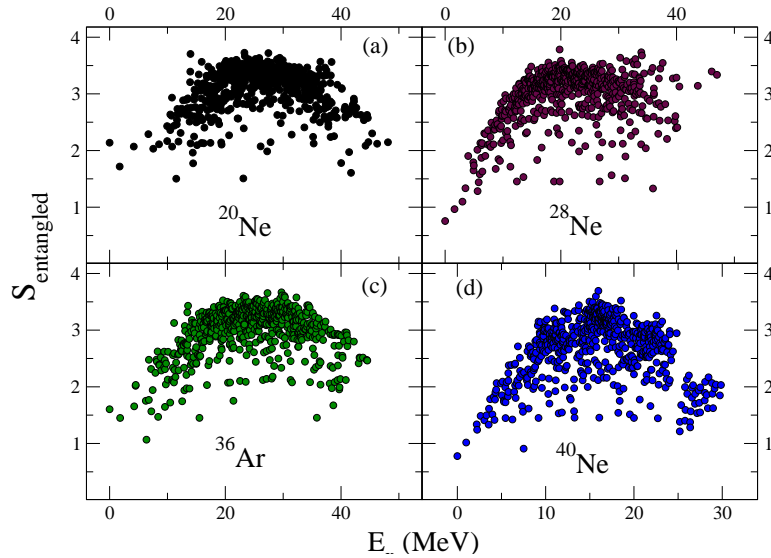
Figure 3.4: (Taken from [162].) Entanglement entropies for all levels as a function of excitation energy E_x. Panels (a), (b), and (c) are computed in the sd-shell using the USDB interaction [42]. Panel (d) is computed in the sd-pf space, using the 'mu-db' interaction [155]; certain orbits are frozen in order to make the dimensions for this case the same as the other three cases. The maximum entanglement entropy is at the top of each plot.

sider ^{20,28}Ne and ^{36}Ar, computed in the sd-shell with the USDB interaction [42], and ^{40}Ne

computed in a truncated sd-pf space, computed with a cross-shell interaction [155]; for the latter, we restricted the valence protons to the sd-shell, and froze all neutrons in the sd-shell and in the $0f_{7/2}$ orbital, so that we have only two valence neutrons in the $0f_{5/2}$-$1p_{3/2}$-$1p_{1/2}$ orbitals. These choices are made so that all four cases have exactly the same dimensionalities. While each plot has considerable scatter, there are a couple of noticeable features. The first is an overall curvature: on average, the entropy rises and then falls. The second feature is that the isospin-asymmetric nuclides, ^{28,40}Ne, are noticeably more asymmetric in the distribution of entropies compared to the isospin-symmetric nuclides, in particular the low entropy of the ground state as pointed out in the previous section.

To probe the origin of these behaviors, in Fig. 3.5 we recomputed the entropies for ^{20,28,40}Ne. In the top panels, Fig. 3.5(a)-(c), we set the single-particle energies and monopole interaction
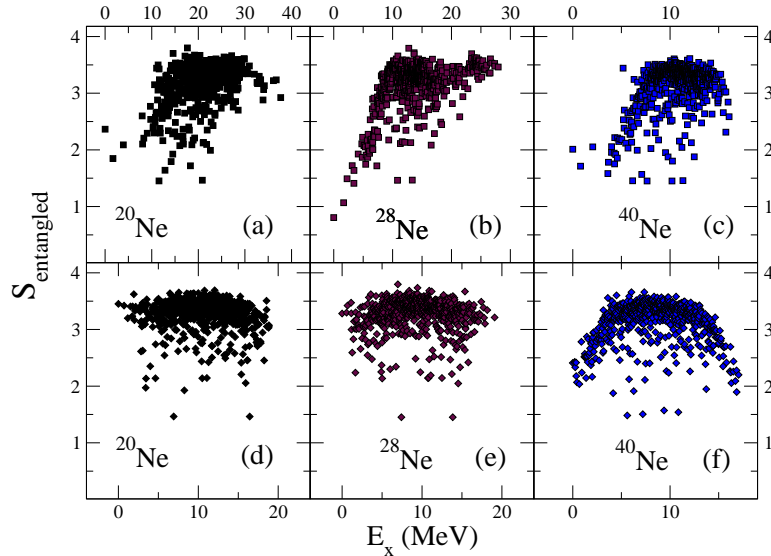
Figure 3.5: (Taken from [162].) Entanglement entropies for all levels as a function of excitation energy E_x. The top panels, (a)-(c), are computed with realistic interactions (USDB for panels (a) and (b), and 'mu-db' for panel (c)) but with all single-particle energies and monopole interaction terms set to zero, so as to remove shell effects. The bottom panels, (d)-(f), correspond to the same nuclides, but with a random two-body interaction. The maximum entanglement entropy is the top of each plot.

terms to zero. (Note that in such a scenario, there is a particle-hole symmetry, so that ^{36}Ar would be exactly the same as ^{20}Ne.) This has the effect of amplifying the asymmetry in

all three cases. In the bottom panels, Fig. 3.5(d)-(f), we instead generated a random set of two-body matrix elements, and also removed the monopole interaction terms. Here the asymmetry vanishes, and the curvature for ^{20,28}Ne is much reduced. An important lesson we learn is that the T_z dependence of the entropy appears to come out of the physical nuclear force, as it does not appear when using a randomly generated interaction.

3.2.5 Conclusion and outlook on entanglement

We have found that both schematic and realistic nuclear shell model Hamiltonians have low entanglement between the proton and neutron components of the wave function. This is particularly pronounced for states with high isospin. Part of the behavior is governed by the shell structure, which reduces the effective dimensionality, but, by using random two-body matrix elements, we can establish that the low entropy also is a feature of typical nuclear forces. While we have spent considerable effort to construct toy models to understand this behavior, so far none of them have provided convincing illumination.

A low entanglement means that one can get a good approximation to a wave function using a much smaller subset of basis states. This is the driving idea between the density matrix renormalization group methods [297, 298, 255], which have only been used sporadically in nuclear structure physics [279, 71, 248, 276, 186], partitioning on orbitals rather than between protons and neutrons. Closer to the present work is the proton-neutron singular-value decomposition analysis of shell model wave functions [217, 219]; ironically, the latter studies focused on $N \approx Z$ nuclides. One happy conclusion from our work presented here is that reduced basis methods, justified by low entanglement [296], may be even more effective for high-isospin nuclides, such as heavy nuclei, where the need for dimensional reduction is greatest. We have made progress in a systematic implementation of this idea in the following chapter.

3.3 Optimal factors and entropies

Suppose that the division of the Hilbert space is fixed, but we consider transformations within each subspace. Is there an optimal choice of such a transformation? By optimal I mean one that efficiently represents Ψ with the fewest number of nonzero elements. Let's assume a general bipartite wave function with a set of basis factors $|a\rangle$ and $|b\rangle$:

$$\Psi = \sum_{ab} \psi_{ab} |a\rangle |b\rangle . \tag{3.18}$$

Let $|a\rangle$ form the columns of a unitary matrix A and $|b\rangle$ form the columns of the unitary matrix B. It turns out that an optimal basis occurs when $|a\rangle$ and $|b\rangle$ are eigenstates of the reduced density matrices of Ψ, in which case:

$$\rho_a = \Psi\Psi^\dagger = ADD^\dagger A^\dagger \tag{3.19}$$

$$\rho_b = \Psi^\dagger\Psi = BDD^\dagger B^\dagger, \tag{3.20}$$

where $DD^\dagger = D^\dagger D$ is a diagonal matrix with the eigenvalues of the reduced density matrices ρ_a and ρ_b. For the wave function matrix ψ_{ab} this defines a transformation of each subspace that results in the so-called singular value decomposition:

$$\Psi = ADB^\dagger, \tag{3.21}$$

where D is diagonal with elements equal to the roots of the eigenvalues of the reduced density matrices. These are called the singular values of Ψ. In this basis we therefore have diagonal coefficient matrix elements:

$$\psi_{ab} = \psi_{ab}\delta_{ab}, \tag{3.22}$$

And a diagonal reduced density matrix:

$$\rho_{aa'}^{\text{red}} = \delta_{aa'} |\psi_{aa}|^2. \tag{3.23}$$

The entanglement entropy for the state in the optimal basis is therefore:

$$S_{\text{entangle}} = -\operatorname{Tr}\left(\rho^{\text{red.}} \ln \rho^{\text{red.}}\right) \tag{3.24}$$

$$= -\sum_{aa'} \delta_{aa'} (\delta_{aa'} |\psi_{aa}|^2) \ln\left(\delta_{aa'} |\psi_{aa}|^2\right) \tag{3.25}$$

$$= -\sum_{a} |\psi_{aa}|^2 \ln |\psi_{aa}|^2 \tag{3.26}$$

$$= -\sum_{\alpha} W_\alpha \ln W_\alpha, \tag{3.27}$$

where $W_\alpha \equiv |\psi_{aa}|^2$. This turns out to be exactly the von Neumann entropy [311]:

$$S_{\text{VN}} = -\sum_{\alpha} W_\alpha \ln W_\alpha, \tag{3.28}$$

where for a general set of wave function coefficients $W_\alpha \equiv |\psi_{ab}|^2$. This entropy measures the localization of the wave function in the basis. It is zero in the eigenbasis of the Hamiltonian that generates Ψ (one coefficient would be 1 and the rest 0). Its maximum is $\ln(\dim(\Psi))$.

We can conclude that the entanglement entropy is bounded by the von Neumann entropy. If the coefficient matrix has nonzero off-diagonal elements, then the entanglement entropy will be reduced relative to the von Neumann entropy.

We can also define another type of entropy, the projected von Neumann entropy:

$$S_{\text{PVN}}^a = -\sum_{a} W_a \ln W_a, \tag{3.29}$$

where $W_a \equiv \sum_b |\psi_{ab}|^2$. W_x is the projection of Ψ into the subspace labeled x. I showed

in earlier work [115] how these projections are exponentially distributed for realistic shell model wave functions when the basis factors are chosen to be eigenstates of the projected Hamiltonian. For example, see Figure 3.6.

Unlike the entanglement entropy, this projected von Neumann entropy is not symmetric: $S_{\text{PVN}}^a \neq S_{\text{PVN}}^b$, so we must be sure to label which subspace we have projected into. This entropy also reduces to the full von Neumann entropy in the optimal basis.

We now have three types of entropy to characterize our wave function coefficients. Some special cases are laid out in Table 3.2. There, I introduced the term 'singular' to describe a situation where a δ-function appears in desribing some aspect of the wave function. If the wave function is singular in some subspace, then I mean that all of its elements are zero except for one. In other words, it is an eigenvector expressed in its own eigenbasis within that subspace. If a wave function is singular in both spaces, it is an eigenvector in its own eigenbasis in the composite space. Correspondingly, its von Neumann entropy is zero.

Table 3.2: Some relations between bipartite wave function coefficients and their entropies. All entries with s_{VN} reduce to the form of the unprojected von Neumann entropy for some undetermined positive value that are equal within a given row.

Description	coefficients	S_{VN}	S_{PVN}^a	S_{PVN}^b	S_{entangle}	Wave function
Singular in both spaces	$\delta_{ai}\delta_{bi}\psi_{ab}$	0	0	0	0	$\psi_{ii}\,|i\rangle \otimes |i\rangle$
Singular in a-space only	$\delta_{ai}\psi_{ab}$	s_{VN}	0	s_{VN}	0	$|i\rangle \otimes (\sum_b \psi_{ib}\,|b\rangle)$
Singular in b-space only	$\delta_{ib}\psi_{ab}$	s_{VN}	s_{VN}	0	0	$(\sum_a \psi_{ai}\,|a\rangle) \otimes |i\rangle$
Jointly singular (SVD basis)	$\delta_{ab}\psi_{ab}$	s_{VN}	s_{VN}	s_{VN}	s_{VN}	$\sum_{aa} \psi_{aa}\,|a\rangle \otimes |a\rangle$
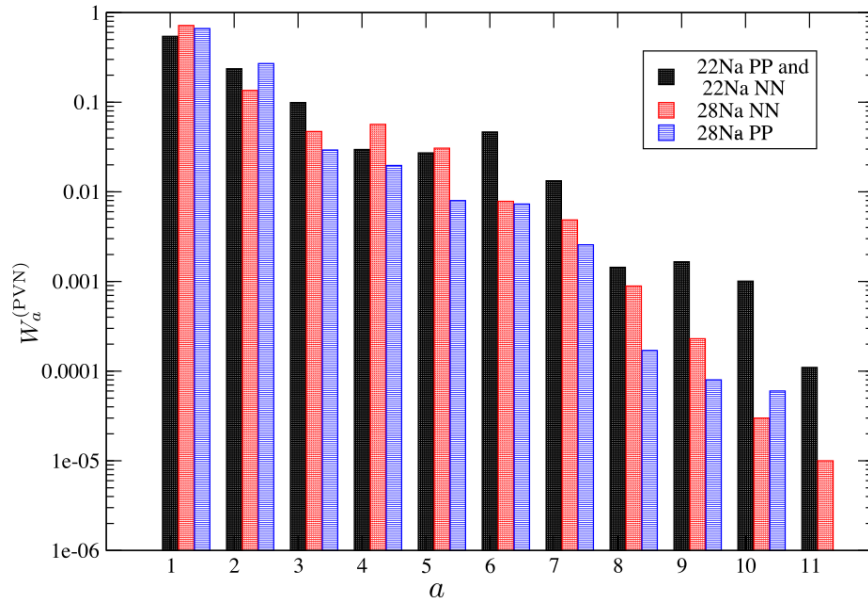
Figure 3.6: (Taken from [115].) Distribution of the amplitudes $W_a = \sum_b |\psi_{ab}|^2$ which are related to the projected von Neumann entropy given in equation (3.29). The specific examples here are proton-neutron decompositions of ^{22,28}Na computed with the USDB [42] interaction. In the case of ^{22}Na, both subspaces are identical, while for ^{28}Na they are unique.

Chapter 4

Weak Entanglement Approximation

4.1   Motivation

The current limit of exact diagonalization for low-lying states of sparse matrices, which is how we solve the nuclear many-body problem in the shell model framework, is dimension 10^{10} [92]. For applications to nuclear reaction theory it is useful to solve for thousands of eigenstates, which would naturally bring this dimensional limit even lower. There are numerous interesting cases which easily exceed dimension 10^{16}. This drives our need for basis-reduction methods that retain the physics we care about, including the collectivity needed for many observables.

Shell model calculations use a harmonic-oscillator-like single-particle basis to represent the single-particle states from which the many-nucleon states are constructed. Without any extra steps, this leads to an infinite basis. One must therefore truncate the single particle space to include only up to some maximum harmonic oscillator quanta. Calculations in such a basis are the no-core shell model (NCSM). This no-compromises basis includes the maximum number of correlated many-particle states but quickly exceeds the limits of sparse

matrix solvers around the p-shell.

To make shell model calculations of medium-to-heavy mass nuclei possible, we must resort to a 'frozen-core' shell model, hereafter referred to as the large-scale shell model (LSSM): one assumes that the energy gaps between major shells allow separation of an active valence space from an inert core of nucleons. See Figure 1.3. The interaction must be renormalized within the limited space, and the description of highly-collective states may be lost. In practice, an empirical interaction that has been fitted to experimental spectra and transition strengths is used.

In the LSSM, each many-body basis state is a product of anti-symmetrized creation operators (Slater determinants) acting on the frozen core. All possible configurations in the valence space are included so that the maximum number of Slater determinants is

$$
\binom{\sum_{n=1}^{N_o} 2j_n + 1}{N_{p/n}},
\tag{4.1}
$$

where N_o is the number of single-particle orbits (labeled n_i, l_i, j_i) and $N_{p/n}$ is the number of protons/neutrons in the nucleus.

Even with this double truncation of the single-particle space, one can easily reach computationally inaccessible matrix dimensions above 10^{16}, e.g., in the $sdpf$ valence space. This is due to the combinatorial (4.1) growth of possible configurations for any given set of single-particle states (orbits). We therefore seek additional means of basis reduction. Rather than continue to reduce the single particle space, inducing further re-normalization and loss of collectivity, we will seek an importance truncation in the many-body configuration space. That is, we will try to use properties of many-body configurations themselves to perform an importance truncation within a fixed set of single-particle states.

In the previous decade, two sets of promising methods for truncating LSSM calculations were

developed and tested: various density matrix renormalization group (DMRG) approaches [218, 276, 186] based on the original method developed for spin-chains [297, 298] and variational wavefunction factorization (VWF) truncations [217, 219, 218]. DMRG and VWF take insights from information theory [185]. As will be discussed in a later section, the truncation presented in this chapter is closely related to each of these, and builds upon a long history of related shell model truncation schemes.

4.2   Related shell model truncation methods

In addition to VWF and DMRG, there are some related methods to acknowledge from the long history of shell model truncation schemes. This is not meant to be a comprehensive review, rather the following list is meant to provide context for the present set of methods without an exhaustive comparison. This list is also specifically focused on methods which attempt to select the most important basis states based on some computed metric. These are built on top of either an N_{max} truncation in an *ab initio* framework, or on top of a truncation to a particular valence space in a phenomenological framework.

- **Hasper (1979)**: Diagonal percentage truncation (DPT) improves the diagonal energy truncation (DET); in both methods the diagonal elements of the Hamiltonian are used to reorder the basis states based on their energy [127].

- **Horoi et al. (1994-2003)**: Truncation based on moments of the Hamiltonian: extension of diagonal energy truncation (DET), taking into account the width of the diagonal matrix element distribution [149].

  "Chaotic Wave Functions and Exponential Convergence of Low-Lying Energy Eigenvalues" (1999) [151].

"Exponential convergence method: Nonyrast states, occupation numbers, and a shell-model description of the superdeformed band in ^{56}Ni" (2003) [150].

- **Andreozzi et al. (1999-2003)**: The single particle space is partitioned and the Hamiltonian is solved within each partition. The basis for the full space is constructed from these subspace solutions:

  "Truncation of Large Shell-Model Eigenproblems by Model Space Partitioning" (1999) [10].

  "A redundancy-free approach to the use of correlated bases in the truncation of large shell-model eigenproblems" (2001) [11].

  A subblock of the Hamiltonian is diagonalized. Then, in an iterative procedure, the matrix is expanded by incorporating new matrix elements with the already diagonalized subblock:

  "A simple iterative algorithm for generating selected eigenspaces of large matrices" (2002) [12].

  "An importance sampling algorithm for generating exact eigenstates of the nuclear Hamiltonian" (2003) [9].

- **Papenbrock et al. (2003-2005)**: SVD-themed truncation of the proton-neutron-factorized basis leads to coupled set of nonlinear equations for optimal basis components, which is solved iteratively [217, 219].

  "Density matrix renormalization group and wavefunction factorization for nuclei" (2005) [218].

- **Thakur et al. (2008)**: "Density matrix renormalization group study of ^{48}Cr and ^{56}Ni" (2008) [276].

- **Roth et al. (2009)**: A reference state is iteratively/perturbatively improved by adding np-nh configurations to the basis and tracking convergence with a perturbation theory importance measure. Importance truncation for large-scale configuration interaction approaches [247].

- **Weinstein et al. (2011)**: Lanczos-SVD for lattice Hamiltonians, motivated by en- tanglement entropy [296].

- **Kruse et al. (2013)**: Important truncation of the no-core shell model based on the Hamiltonian matrix element between an approximate solution and each expanded basis state [181].

- **Qi et al. (2014-2018)**: Particle number partitions are solved independently and then re-coupled to form a correlated-basis, and keeping only the lowest energy states. In this case, "partitions" are a set of configurations with the same number of particles in each involved orbit [158]. Implemented in a version of NuShellX [232].

A key takeaway from this list is that there have been many attempts over the years to create importance truncation schemes for the shell model. However, none of them have become standard for carrying out large scale calculations - many are published as a proof of concept and not taken further. Our goal is to go beyond proof of concept and normalize the use of our truncation scheme. We are encouraged by the simplicity of our approach which is not iterative and our expectation that its efficiency will increase for $N > Z$ nuclei. A recent paper [221] citing our work on proton neutron entanglement entropy has shed additional light on this matter. The authors of [221] demonstrated that proton and neutron orbitals have the lowest entanglement entropy among all possible equipartitions of the valence space.

4.3 Weak entanglement limit

Suppose we have a Hamiltonian $\hat{H}$ acting on a bipartite space $\mathcal{H} = \mathcal{A} \oplus \mathcal{B}$ such that

$$\hat{H}(\lambda) = \hat{A} + \hat{B} + \lambda \hat{H}^{(AB)}, \tag{4.2}$$

where $\hat{A} : \mathcal{A} \to \mathcal{A}$ and $\hat{B} : \mathcal{B} \to \mathcal{B}$ are operators acting within each subspace only, and $\lambda \hat{H}^{(AB)}$ is an operator acting on both subspaces. We define the *weak entanglement limit* as the fact that as $\lambda \to 0$, the subspace entanglement of eigenstates of $\hat{H}$ must also go to zero:

$$\lim_{\lambda \to 0} S_{AB}(\hat{H}(\lambda)) = 0. \tag{4.3}$$

The great use of this fact is that if we identify a bipartite system with low entanglement entropy, then we can use equation (4.2) as a recipe for a sort of perturbative expansion. This is what we have found is the case for the proton-neutron bipartite representation of realistic nuclear Hamiltonians [162] (see Chapter 3); this does lead to an effective method for basis reduction [115]. Furthermore, recent work [221] demonstrated that proton and neutron orbitals have the lowest entanglement entropy among all equipartitions of the nuclear valence space.

In the rest of this chapter, I discuss the application of this weak entanglement limit to the development and results of the proton and neutron approximate shell model code (PANASh) that I have co-developed with Johnson.

4.4   Proton and neutron approximate shell model

I now explain how the weak entanglement limit is used with a proton-neutron factorization to approximate exact shell model states.

The shell model Hamiltonian represents a system of interacting single-particle harmonic oscillator states with a mean-field (one-body) and effective two-body interaction:

$$\hat{H} = \sum_i \epsilon_i \hat{a}_i^\dagger \hat{a}_i + \frac{1}{4} \sum_{ijkl} V_{ijkl} \hat{a}_i^\dagger \hat{a}_j^\dagger \hat{a}_k \hat{a}_l. \tag{4.4}$$

The creation/destruction operators $\hat{a}_i^\dagger/\hat{a}_i$ create/destroy particles in the valence space orbital i, which has harmonic oscillator labels n_i, l_i, j_i.

With two species of particles, protons and neutrons, we have the following Hamiltonian:

$$\hat{H} = \hat{H}^{(p)} + \hat{H}^{(pp)} + \hat{H}^{(n)} + \hat{H}^{(nn)} + \hat{H}^{(pn)}, \tag{4.5}$$

where the superscript in parenthesis indicates the type of operator: (p) is a one-body proton operator, (pp) is a two-body proton operator, equivalently for neutrons (n), (nn), and finally there is the remaining proton-neutron two-body interaction (pn). The proton-only and neutron-only operators,

$$\hat{P} \equiv \hat{H}^{(p)} + \hat{H}^{(pp)} \tag{4.6}$$

$$\hat{N} \equiv \hat{H}^{(n)} + \hat{H}^{(nn)}, \tag{4.7}$$

each have the form of (4.4). Furthermore, each is an operator constrained to its own subspace: $\hat{P} : \mathcal{P} \to \mathcal{P}$ and $\hat{N} : \mathcal{N} \to \mathcal{N}$. The direct-product of these two subspaces is the bipartite proton-neutron space $\mathcal{H} = \mathcal{P} \otimes \mathcal{N}$, which is where the total Hamiltonian acts:

$$\hat{H} = \hat{P} + \hat{N} + \hat{H}^{(pn)}. \tag{4.8}$$

Each subspace operator has its own eigenstates and eigenenergies:

$$\hat{P}|p\rangle = E_p|p\rangle \tag{4.9}$$

$$\hat{N}|n\rangle = E_n|n\rangle. \tag{4.10}$$

The dimensions of these subspaces are orders of magnitude smaller than the full space, and in general can be solved without any truncation. See Figure 4.1 for an example of the *sd*-space. In the weak entanglement limit, these subspace eigenstates approximate the optimal

basis factors $|\tilde{p}_j\rangle , |\tilde{n}_j\rangle$, i.e. eigenstates of the exact reduced density matrix. This motivates a basis of products of these subspace eigenstates:

$$[|p\rangle \otimes |n\rangle]_{J^\pi} = |pn; J^\pi\rangle. \tag{4.11}$$

We choose the J-scheme, rather than the usual M-scheme, so that any truncation of this basis will produce wave functions with well-defined J.

Dimensions in the SD shell model space 0d(3/2), 0d(5/2), 1s(1/2)

	28Ca 1	29Ca 3	30Ca 14	31Ca 37	32Ca 81	33Ca 119	34Ca 142	35Ca 119	36Ca 81	37Ca 37	38Ca 14	39Ca 3	40Ca 1
	27K 3	28K 28	29K 128	30K 394	31K 822	32K 1290	33K 1469	34K 1290	35K 822	36K 394	37K 128	38K 28	39K 3
	26Ar 14	27Ar 128	28Ar 640	29Ar 1935	30Ar 4206	31Ar 6457	32Ar 7562	33Ar 6457	34Ar 4206	35Ar 1935	36Ar 640	37Ar 128	38Ar 14
	25Cl 37	26Cl 394	27Cl 1935	28Cl 6116	29Cl 13029	30Cl 20564	31Cl 23558	32Cl 20564	33Cl 13029	34Cl 6116	35Cl 1935	36Cl 394	37Cl 37
	24S 81	25S 822	26S 4206	27S 13029	28S 28503	29S 44133	30S 51630	31S 44133	32S 28503	33S 13029	34S 4206	35S 822	36S 81
	23P 119	24P 1290	25P 6457	26P 20564	27P 44133	28P 69784	29P 80115	30P 69784	31P 44133	32P 20564	33P 6457	34P 1290	35P 119
	22Si 142	23Si 1469	24Si 7562	25Si 23558	26Si 51630	27Si 80115	28Si 93710	29Si 80115	30Si 51630	31Si 23558	32Si 7562	33Si 1469	34Si 142
	21Al 119	22Al 1290	23Al 6457	24Al 20564	25Al 44133	26Al 69784	27Al 80115	28Al 69784	29Al 44133	30Al 20564	31Al 6457	32Al 1290	33Al 119
	20Mg 81	21Mg 822	22Mg 4206	23Mg 13029	24Mg 28503	25Mg 44133	26Mg 51630	27Mg 44133	28Mg 28503	29Mg 13029	30Mg 4206	31Mg 822	32Mg 81
	19Na 37	20Na 394	21Na 1935	22Na 6116	23Na 13029	24Na 20564	25Na 23558	26Na 20564	27Na 13029	28Na 6116	29Na 1935	30Na 394	31Na 37
	18Ne 14	19Ne 128	20Ne 640	21Ne 1935	22Ne 4206	23Ne 6457	24Ne 7562	25Ne 6457	26Ne 4206	27Ne 1935	28Ne 640	29Ne 128	30Ne 14
	17F 3	18F 28	19F 128	20F 394	21F 822	22F 1290	23F 1469	24F 1290	25F 822	26F 394	27F 128	28F 28	29F 3
	16O 1	17O 3	18O 14	19O 37	20O 81	21O 119	22O 142	23O 119	24O 81	25O 37	26O 14	27O 3	28O 1

Neutron dimensions in the SD shell model space 0d(3/2), 0d(5/2), 1s(1/2)

	28Ca 1	29Ca 3	30Ca 14	31Ca 37	32Ca 81	33Ca 119	34Ca 142	35Ca 119	36Ca 81	37Ca 37	38Ca 14	39Ca 3	40Ca 1
	27K 1	28K 3	29K 14	30K 37	31K 81	32K 119	33K 142	34K 119	35K 81	36K 37	37K 14	38K 3	39K 1
	26Ar 1	27Ar 3	28Ar 14	29Ar 37	30Ar 81	31Ar 119	32Ar 142	33Ar 119	34Ar 81	35Ar 37	36Ar 14	37Ar 3	38Ar 1
	25Cl 1	26Cl 3	27Cl 14	28Cl 37	29Cl 81	30Cl 119	31Cl 142	32Cl 119	33Cl 81	34Cl 37	35Cl 14	36Cl 3	37Cl 1
	24S 1	25S 3	26S 14	27S 37	28S 81	29S 119	30S 142	31S 119	32S 81	33S 37	34S 14	35S 3	36S 1
	23P 1	24P 3	25P 14	26P 37	27P 81	28P 119	29P 142	30P 119	31P 81	32P 37	33P 14	34P 3	35P 1
	22Si 1	23Si 3	24Si 14	25Si 37	26Si 81	27Si 119	28Si 142	29Si 119	30Si 81	31Si 37	32Si 14	33Si 3	34Si 1
	21Al 1	22Al 3	23Al 14	24Al 37	25Al 81	26Al 119	27Al 142	28Al 119	29Al 81	30Al 37	31Al 14	32Al 3	33Al 1
	20Mg 1	21Mg 3	22Mg 14	23Mg 37	24Mg 81	25Mg 119	26Mg 142	27Mg 119	28Mg 81	29Mg 37	30Mg 14	31Mg 3	32Mg 1
	19Na 1	20Na 3	21Na 14	22Na 37	23Na 81	24Na 119	25Na 142	26Na 119	27Na 81	28Na 37	29Na 14	30Na 3	31Na 1
	18Ne 1	19Ne 3	20Ne 14	21Ne 37	22Ne 81	23Ne 119	24Ne 142	25Ne 119	26Ne 81	27Ne 37	28Ne 14	29Ne 3	30Ne 1
	17F 1	18F 3	19F 14	20F 37	21F 81	22F 119	23F 142	24F 119	25F 81	26F 37	27F 14	28F 3	29F 1
	16O 1	17O 3	18O 14	19O 37	20O 81	21O 119	22O 142	23O 119	24O 81	25O 37	26O 14	27O 3	28O 1

Figure 4.1: (Left:) Basis dimensions of the M-scheme, full configuration interaction model in the sd-shell model space. (Right:) Basis dimensions of the neutron-only part of the Hamiltonian, $\dim(\hat{N})$, with the same single particle space.

We can write the matrix elements of the Hamiltonian in this basis as

$$\langle p_f n_f; J, \pi | \, \hat{H} \, | p_i n_i; J, \pi\rangle = \delta_{n_f n_i} E_p + \delta_{p_f p_i} E_n + \langle p_f n_f; J, \pi | \, \hat{H}^{(pn)} \, | p_i n_i; J, \pi\rangle, \tag{4.12}$$

where the matrix elements of $\hat{H}^{(pn)}$ are expressed in terms of one-body density matrices computed from the $|p\rangle$ and $|n\rangle$ eigenstates. The details for computing the proton-neutron matrix elements are given in section 4.5. By diagonalizing in a truncated basis set, we obtain

78

approximate solutions of the form:

$$|\tilde{\Psi}\rangle = \sum_{pn}^{m_n, m_p} \psi_{pn}|pn; J^{\pi}\rangle \approx |\Psi\rangle, \tag{4.13}$$

where $|\Psi\rangle$ is an exact eigenstate of $\hat{H}$. Before truncation, $m_p = d_p \equiv \dim(\hat{P})$ and $m_n = d_n \equiv \dim(\hat{N})$, with additional constraints for conservation laws, not shown. Because the only approximation we are performing is in leaving out certain basis states, our ground state solutions follow a variational principle. Consider the true ground state $|\Psi_0\rangle$ of $\hat{H}$ with energy $E_0 < E_i$ for all other eigenpairs $E_i, |\Psi_i\rangle$. In a complete and normalized basis for any other state $|\tilde{\Psi}_0\rangle = \sum_i \psi_i|\Psi_i\rangle$:

$$\langle\tilde{\Psi}_0|\hat{H}|\tilde{\Psi}_0\rangle = \sum_i |\psi_i|^2 E_i \geq E_0 \sum_i |\psi_i|^2 \geq E_0. \tag{4.14}$$

Meaning that leaving out basis factors can only increase the energy of the approximate ground state. While such a rigorous statement cannot be made for the excited states, the same result is found in practice: the first approximation of $\langle\tilde{\Psi}|\hat{H}|\tilde{\Psi}\rangle$ always improves by adding more terms. Some insight can be had by examining the expectation value of the Hamiltonian for a truncated wave function in this basis:

$$\langle\tilde{\Psi}|\hat{H}|\tilde{\Psi}\rangle = \sum_{pn}^{m_n, m_p} |\psi_{pn}|^2 (E_p + E_n + E_{pn}), \tag{4.15}$$

where E_{pn} is the residual energy from the proton-neutron interaction given by the last term in equation (4.12). In general, the E_n and E_p are all negative energy (bound) states and so $E_{p=1} < E_{p=2} < ... < E_{p=m_p}$ by construction (and also for $E_{n=1,...,m_n}$). It follows that as long as

$$|E_p + E_n| > |E_{pn}|, \tag{4.16}$$

that is, as long as the residual energy E_{pn} is a lesser contribution than the subspace energies, the energy will decrease with each additional term, even if E_{pn} is positive (repulsive). This is by no means guaranteed, but it is approximately true under the weak entanglement limit. As the proton-neutron entanglement entropy goes to zero, so too must the residual proton-neutron interaction.

Our code for performing shell model calculations in this truncated basis of proton and neutron states is called the Proton and Neutron Approximation (Sh)ell model, or PANASh.

4.4.1   Basis construction

In this section I will explain in more detail how the basis for PANASh is constructed. It will be shown that there are choices to be made about how factors are combined to create the coupled basis. I also discuss different choices for basis construction.

The PANASh basis is a set of coupled proton and neutron wave functions:

$$\{|i\rangle\} = \{[|p\rangle \otimes |n\rangle]_{J^\pi}\} = \{|pn; J^\pi\rangle\}, \tag{4.17}$$

where the proton $|p\rangle$ and neutron $|n\rangle$ states, called the subspace factors, are each a complete set of orthonormal many-body states. In particular, $\{|p\rangle\}$ and $\{|n\rangle\}$ are sets of eigenvectors of Hamiltonian operators.

The first step in basis construction is to generate the basis factors. Given the proton-neutron decomposition of the Hamiltonian as

$$\hat{H} = \hat{P} + \hat{N} + \hat{H}^{(pn)}, \tag{4.18}$$

we first diagonalize $\hat{P}$ and $\hat{N}$ to obtain its eigenpairs:

$$\hat{P}|p\rangle = E_p|p\rangle \tag{4.19}$$

$$\hat{N}|n\rangle = E_n|n\rangle. \tag{4.20}$$

We use `BIGSTICK` [165] for this, although any shell model code with agreeable output formats could be used. Each of these states has wave function coefficients in the basis $|\Phi_i\rangle$ used by the generating shell model code:

$$|p\rangle = \sum_i \psi_i^{(p)}|\Phi_i\rangle. \tag{4.21}$$

In the construction of the PANASh basis we do not use these wave function coefficients. In fact, we never use the $\psi_i^{(p)}$ directly. (To compute matrix elements in the coupled basis, we require only the one-body density matrices derived from $\psi_i^{(p)}$. This is discussed in section 4.5.2.) The basis is constructed using only information about the quantum numbers of each basis factor, and assuming that the factors are orthonormal. `BIGSTICK` produces eigenstates with well defined total angular momentum J, parity π, angular momentum projection $M = J_z$, energy E_p. We may label each state as:

$$|p\rangle = |p : E_p, j_p, m_p, \pi_p\rangle \tag{4.22}$$

However, we do not use the m_p quantum numbers of the factors.

Given two basis factors,

$$|p\rangle = |j_p, \pi_p\rangle \tag{4.23}$$

$$|n\rangle = |j_n, \pi_n\rangle, \tag{4.24}$$

a number of basis states can be constructed. The parity of the coupled state is fixed:

$\pi = \pi_p \pi_n$, and the angular momentum couple in the usual way: $|J_p - J_n| \leq J \leq J_p + J_n$. We can therefore generate a set of coupled states for each pair:

$$||j_p - j_n|, \pi_p \pi_n\rangle,$$
$$||j_p - j_n| + 1, \pi_p \pi_n\rangle,$$
$$... \tag{4.25}$$
$$|j_p + j_n - 1, \pi_p \pi_n\rangle,$$
$$|j_p + j_n, \pi_p \pi_n\rangle.$$

The Hamiltonian conserves both parity and total angular momentum J^π, and our basis states have definite J^π. This will make the Hamiltonian matrix block-diagonal. Each block can be diagonalized independently. We therefore can construct a separate basis for each J^π corresponding to each block of the Hamiltonian:

$$\{|i\rangle = |pn; J^\pi\rangle\}_{J^\pi}. \tag{4.26}$$

Algorithms for combining m_p, m_n factors

Given a set of m_p states $|p\rangle$ and m_n states $|n\rangle$, basis construction proceeds by looping over all $m_p m_n$ combinations of the basis factors and selecting the pairs which meet the requirements of each J^π basis, plus any other constraints one might like to apply. The maximum basis J value is twice the largest J of the basis factor states. To improve data locality when accessing vector coupling coefficients, the basis factors are first ordered by their quantum numbers: all factors with the same J_x, π_x are grouped together. So in actuality, first the set of unique quantum numbers are iterated, then all factors within that group are iterated.

Each factor $|p\rangle$ has four essential labels: its eigenstate index p, energy E_p, angular momentum

j_p, and parity π_p. If we keep $m_p \, |p\rangle$ factors and $m_n \, |n\rangle$ factors, and consider only combinations consistent with the conservation of angular momentum and parity, we are still left with a choice of which combinations to keep, and which to discard. We can visualize this choice with the help of the diagrams in Figure 4.2 which depicts four basic ways to select the proton and neutron factors to be used in the basis. Each horizontal axis indicates increasing either the cutoff in the maximum number N_p or energy E_p of proton factors used to construct the basis. The vertical axis indicates the same but for neutron factors. In each case, the area inside the dotted line indicates the combinations selected. Generally speaking, the number of states N_p available increases exponentially with the excitation energy E_p. Therefore, an area in N-space is transformed to a different area in E-space with the same number of factors.
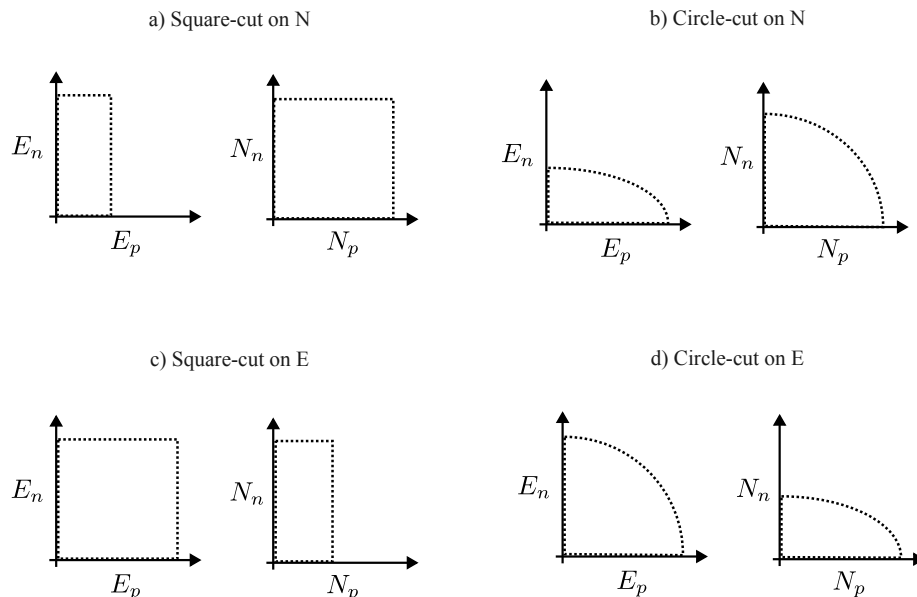
Figure 4.2: Four basic ways to truncate the many-body basis on the selection of proton and neutron factors. See text for discussion. Similar diagrams are found in [181].

We considered only two of the algorithms from Figure 4.2:

a) *Square-cut on N*: Take a fixed number of factors of each type and take every combination consistent with the conservation of angular momentum and parity. In cases with

unequal dimension, we actually take a fixed fraction of factors from each subspace.

d) *Circle-cut on E*: Take all factors with $E^{(x)} < \epsilon$ and construct every combination consistent with $E_p^2 + E_n^2 < E_{\text{cut}}^2$, and angular momentum and parity.

The first of these is the simplest conceivable truncation scheme. The second is inspired by perturbation theory; since the terms closest to the energy of the ground state are expected to have the largest contribution, one may hypothesise that those terms outside some circle of energy radius E_{cut} are significantly less important and can be dropped.

We compared the two schemes on two different metrics: Convergence of low-lying spectra as a function of (a) the number of basis factors, or (b) the dimension of the truncated basis. We found that the square-cut on factor number method optimizes metric (a), while the circle-cut on factor energy optimizes metric (b). An example with ^{49}Cr in the pf space is shown in Fig. 4.3. In this case, $d_p = 565$ and $d_n = 1651$. In the square-cut calculations, the same number of proton and neutron factors are used.

Which method one chooses thus depends on whether most of the computational cost comes from generating the factor wave functions, or from diagonalizing the Hamiltonian in the truncated basis. While the dimension of the coupled basis D is proportional to the product of m_p and m_n, we often only require a small number of solutions N_{sol}. Considering only the cost of a power-iteration type algorithm, the minimum cost scaling for obtaining N_{sol} solutions in the truncated space is $S \equiv N_{sol}(m_p m_n)^2$. On the other hand, obtaining the m_p and m_n factors has a minimum cost scaling $F \equiv m_p d_p^2 + m_n d_n^2$. Let's assume that $m_n \sim m_p$ and suppose $m_n^2 \sim d_n$. In this case, $S \sim N_{sol} d_n^2$ and $F \sim d_n^{2.5}$. For large d_n, the cost of factor generation increases faster.

Taking a more concrete example, let $m_n = d_n/10$ and $N_{sol} = 10^2$. Then, $F_{10\%} = d_n^3/10$ and $S_{10\%} = 10^2(d_n/10)^4 = d_n^4/10^2$.
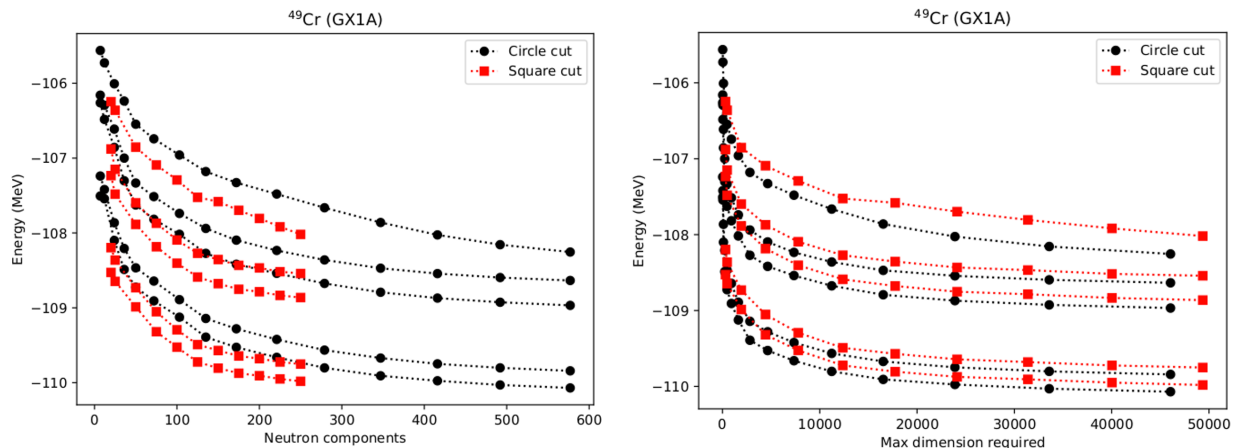
Figure 4.3: I compare two methods of constructing the coupled basis: fixed maximum excitation energy (circle cut) and fixed number of factors (square cut). Eigenvalues of the first five levels in ^{49}Cr as a function of (left) number of neutron factors used to construct the basis and (right) the dimension of the resulting eigenvalue problem. If factor generation is the limiting factor, then square-cut construction is most efficient. If diagonalizing in the truncated basis is the limiting factor, then circle-cut construction is more efficient.

In conclusion, in most applications where a significant truncation is required (for very large dimensional problems), the cost of generating the basis factors is greater than the cost of diagonalization in the truncated basis. Therefore, the square-cut basis construction method is preferred, since it maximizes the convergence per total compute cost.

4.5   Residual Hamiltonian matrix elements

In this section I derive the main results required to implement the weak entanglement approximation as a reduced-basis method: the residual proton-neutron Hamiltonian matrix elements.

4.5.1 Two-body operators

It is useful to define the two-body creation operator with fixed angular momentum [245]:

$$\hat{A}^{\dagger}_{ab;KM} \equiv [c^{\dagger}_a \otimes c^{\dagger}_b]_{KM} \tag{4.27}$$

Here, the angular momentum K and the azimuthal or magnetic quantum number $M = K_z$ are needed for the coupling of the two one-body creation operators, via Clebsch-Gordan coefficients [74]:

$$[c^{\dagger}_a \otimes c^{\dagger}_b]_{KM} = \sum_{m_a m_b} (j_a m_a, j_b m_b | KM) \hat{c}^{\dagger}_{j_a m_a} \hat{c}^{\dagger}_{j_b m_b}. \tag{4.28}$$

The two-body creation and annihilation operator with fixed K and M are thus, respectively:

$$
\begin{aligned}
A^{\dagger}_{ab;KM} &= \sum_{m_a m_b} (j_a m_a, j_b m_b | KM) c^{\dagger}_{j_a m_a} c^{\dagger}_{j_b m_b}, \\
A_{cd;KM} &= -[c_c \otimes c_d]_{KM} = \sum_{m_c m_d} (j_c m_c, j_d m_d | KM) c_{j_d m_d} c_{j_c m_c}.
\end{aligned}
\tag{4.29}
$$

These will be used later in the derivation of the proton-neutron interaction matrix elements. With these definitions, two-body states with proper normalization are [46]

$$|ab; KM\rangle \equiv \frac{1}{\sqrt{1 + \delta_{ab}}} \hat{A}^{\dagger}_{KM}(ab) |0\rangle. \tag{4.30}$$

The two-body (pn) part of the Hamiltonian is thus expressed as

$$\hat{H}^{(pn)} = \sum_{abcd} V_{abcd} \pi^{\dagger}_a \nu^{\dagger}_b \hat{\pi}_c \hat{\nu}_d = \sum_{abcd} \zeta_{ab} \zeta_{cd} \sum_{KM} V_{abcd;KM} A^{\dagger}_{ab;KM} A_{cd;KM}, \tag{4.31}$$

where $\zeta_{ab} \equiv \sqrt{(1 + \delta_{ab})}$ and a, c correspond to protons orbits and b, d correspond to neutron orbits.

4.5.2 Residual proton-neutron operator

To diagonalize the nuclear Hamiltonian $\hat{H} = \hat{P} + \hat{N} + \hat{H}^{(pn)}$ in the basis (4.11), we seek an explicit form in terms of proton and neutron one-body density matrices since these are a byproduct of the diagonalization of the subspace Hamiltonians (4.9).

The $\hat{P}$ and $\hat{N}$ operators will naturally be diagonal in our basis. The diagonal terms are $E^{(p)}$ and $E^{(n)}$. All that remains is to find the matrix elements of $\hat{H}^{(pn)}$ in terms of the original FCI single particle basis and matrix elements.

To calculate the matrix elements of $H^{(pn)}$, we refactor equation (4.31) into one-body density-like operators whose matrix elements can be computed from the density matrices found from solving the single-species terms of the full Hamiltonian. Equation (4.31) is written as a product of pair creation and annihilation operators. These can be reordered into one-body density operators. Doing so will introduce a nontrivial phase and a number of identities involving vector coupling coefficients will be applied.

We start with the general proton-neutron Hamiltonian in terms of two-body interaction matrix elements:

$$\hat{H}^{(pn)} = \sum_{abcd;K} V^{(pn)}_{abcd;K} \sum_M A^{\dagger}_{ab;KM} A_{cd;KM}$$

$$= \sum_{abcd;K} V^{(pn)}_{abcd;K} \sum_M \sum_{m_a m_b} (j_a m_a, j_b m_b | KM) c^{\dagger}_{j_a m_a} c^{\dagger}_{j_b m_b} \sum_{m_c m_d} (j_c m_c, j_d m_d | KM) c_{j_d m_d} c_{j_c m_c},$$

(4.32)

where $M' = m_a - m_c = -(m_b - m_d)$. We want to write this in terms of the the generalized one-body density operators:

$$\hat{\rho}^{(p)}_{a\tilde{c};K'\mu} \equiv \sum_{m_a m_c} (j_a m_a, j_c - m_c | K'\mu) \pi^{\dagger}_{j_a m_a} \tilde{\pi}_{j_c - m_c},$$

(4.33)

$$\hat{\rho}^{(n)}_{b\tilde{d};K'\mu} \equiv \sum_{m_b m_d} (j_b m_b, j_d - m_d | K'\mu) \nu^\dagger_{j_b m_b} \tilde{\nu}_{j_d - m_d}. \tag{4.34}$$

The two-body operators will need to be re-ordered and the coupling coefficients re-written. Using fermion relations:

$$\begin{aligned}
\pi^\dagger_{j_a m_a} \nu^\dagger_{j_b m_b} \nu_{j_d m_d} \pi_{j_c m_c} &= \pi^\dagger_{j_a m_a} \nu^\dagger_{j_b m_b} (\delta_{j_c m_c, j_d m_d} - \pi_{j_c m_c} \nu_{j_d m_d}) \\
&= -\pi^\dagger_{j_a m_a} \nu^\dagger_{j_b m_b} \pi_{j_c m_c} \nu_{j_d m_d} \ \ (\text{drop charge-changing term}) \\
&= -\pi^\dagger_{j_a m_a} (\delta_{j_b m_b, j_d m_d} - \pi_{j_c m_c} \nu^\dagger_{j_b m_b}) \nu_{j_d m_d} \\
&= \pi^\dagger_{j_a m_a} \pi_{j_c m_c} \nu^\dagger_{j_b m_b} \pi_{j_d m_d}, \ \ (\text{drop charge-changing term})
\end{aligned} \tag{4.35}$$

and time-reversal relations (cf. [46], eq. (14.56a)),

$$\pi_{j_c m_c} = (-1)^{j_c - m_c} \tilde{\pi}_{j_c - m_c}, \tag{4.36}$$

$$\nu_{j_d m_d} = (-1)^{j_d - m_d} \tilde{\nu}_{j_d - m_d}, \tag{4.37}$$

we can then write the two-body operators as:

$$\begin{aligned}
\sum_M A^\dagger_{ab;KM} A_{cd;KM} = \sum_M \sum_{m_a m_b m_c m_d} (j_a m_a, j_b m_b | KM)(j_c m_c, j_d m_d | KM) \\
(-1)^{j_c - m_c}(-1)^{j_d - m_d} \pi^\dagger_{j_a m_a} \tilde{\pi}_{j_c - m_c} \nu^\dagger_{j_b m_b} \tilde{\nu}_{j_d - m_d}.
\end{aligned} \tag{4.38}$$

To write this in the form of the density operators, a few coupling coefficient transformations are required. I will start from the identity (cf. [46] eq. (A.1.b13)):

$$\sum_M (j_a m_a, j_c - m_c | KM)(j_d m_d, j_b - m_b | KM)(-1)^{j_c - m_c}(-1)^{j_b - m_b} =$$

$$(-1)^{j_a + j_b + j_c + j_d}(2K + 1) \sum_{K'M'} \begin{Bmatrix} j_a & j_b & K' \\ j_d & j_c & K \end{Bmatrix} (j_b m_b j_a m_a | K'M')(j_c m_c j_d m_d | K'M').$$

$$\tag{4.39}$$

First, I relabel the states $|j_c - m_c\rangle \to |j_b m_b\rangle$ and $|j_b - m_b\rangle \to |j_c m_c\rangle$ to bring the left-hand side (LHS) of the above closer to our original expression.

$$\sum_M (j_a m_a, j_b m_b|KM)(j_d m_d, j_c m_c|KM)(-1)^{j_b+m_b}(-1)^{j_c+m_c} =$$

$$(-1)^{j_a+j_c+j_b+j_d}(2K+1)\sum_{K'M'}\begin{Bmatrix} j_a & j_c & K' \\ j_d & j_b & K \end{Bmatrix}(j_c - m_c j_a m_a|K'M')(j_b - m_b j_d m_d|K'M').$$

$$(4.40)$$

Second, I use the symmetry relations $(j_d m_d, j_c m_c|KM) = (-1)^{-j_d-j_c+K}(j_c m_c, j_d m_d|KM)$ and $(j_c - m_c j_a m_a|K'M') = (-1)^{j_c+j_a-K'}(j_a m_a j_c - m_c|K'M')$:

$$\sum_M (j_a m_a, j_b m_b|KM)(j_c m_c, j_d m_d|KM)(-1)^{j_d+j_c-K}(-1)^{j_b+m_b}(-1)^{j_c+m_c} =$$

$$(-1)^{j_a+j_c+j_b+j_d}(2K+1)\sum_{K'M'}\begin{Bmatrix} j_a & j_c & K' \\ j_d & j_b & K \end{Bmatrix}$$

$$\times (-1)^{j_c+j_a-K'}(j_a m_a j_c - m_c|K'M')(j_b - m_b j_d m_d|K'M'). \qquad (4.41)$$

Third, I use the symmetry $(j_b - m_b j_d m_d|K'M') = (-1)^{j_b+j_d-K'}(j_b m_b j_d - m_d|K' - M')$ and the interchange of rows in two columns of the six-J symbol:

$$\sum_M (j_a m_a, j_b m_b|KM)(j_c m_c, j_d m_d|KM)(-1)^{j_d+j_c-K}(-1)^{j_b+m_b}(-1)^{j_c+m_c} =$$

$$(-1)^{j_a+j_c+j_b+j_d}(2K+1)\sum_{K'M'}\begin{Bmatrix} j_a & j_b & K \\ j_d & j_c & K' \end{Bmatrix}$$

$$\times (-1)^{j_c+j_a-K'}(j_a m_a j_c - m_c|K'M')(-1)^{j_b+j_d-K'}(j_b m_b j_d - m_d|K' - M'). \qquad (4.42)$$

Finally, rearranging, cancelling certain phases and using properties such as $(-1)^{2n} = 1$ and

89

$(-1)^n = (-1)^{-n}$ for integer n,

$$\sum_M (j_a m_a, j_b m_b | KM)(j_c m_c, j_d m_d | KM) = (2K+1) \sum_{K'M'} (-1)^{K+j_b-j_d+m_b+m_c}$$

$$\times \begin{Bmatrix} j_a & j_b & K \\ j_d & j_c & K' \end{Bmatrix} (j_a m_a j_c - m_c | K'M')(j_b m_b j_d - m_d | K' - M'). \qquad (4.43)$$

With this identity, the definitions of the density operators, and $-M' = m_b - m_d$ (and again $(-1)^n = (-1)^{-n}$ for integer n) we can write (4.38) as:

$$\sum_M A^\dagger_{ab;KM} A_{cd;KM} = \sum_{K'M'} (-1)^{K+j_b+j_c-M'} \begin{Bmatrix} j_a & j_b & K \\ j_d & j_c & K' \end{Bmatrix} \hat{\rho}^{(p)}_{a\tilde{c};K'M'} \hat{\rho}^{(n)}_{b\tilde{d};K'-M'} \qquad (4.44)$$

The one-body density operators are proper spherical tensors, and we can recognize through some rearrangement that the above expression contains a scalar product of two such tensors [74]:

$$\rho^{(p)}_{ac;K'} \cdot \rho^{(n)}_{bd;K'} = = \sum_{M'} (-1)^{-M'} \rho^{(p)}_{a\tilde{c};K'M'} \rho^{(n)}_{b\tilde{d};K'-M'}. \qquad (4.45)$$

The (pn) Hamiltonian can thus be written:

$$H^{(pn)} = \sum_{abcd} \sum_K (-1)^{K+j_b+j_c}(2K+1)V^{(pn)}_{ab,cd;K} \sum_{K'} \begin{Bmatrix} j_a & j_b & K \\ j_d & j_c & K' \end{Bmatrix} \rho_{a\tilde{c}K'} \cdot \rho_{b\tilde{d}K'}. \qquad (4.46)$$

This representation can be further simplified if we define recoupled two-body interaction matrix elements (note the order of the indices):

$$W_{acbd;K'} \equiv \sum_K (-1)^{K+j_b+j_c}(2K+1) \begin{Bmatrix} j_a & j_b & K \\ j_d & j_c & K' \end{Bmatrix} V^{(pn)}_{abcd;K}. \qquad (4.47)$$

In terms of these new matrix elements, the final expression for the proton-neutron residual matrix elements are:

$$\hat{H}^{(pn)} = \sum_{abcd} \sum_{K'} W_{acbd;K'} \hat{\rho}^{(p)}_{a\tilde{c};K'} \cdot \hat{\rho}^{(n)}_{b\tilde{d};K'}. \tag{4.48}$$

4.5.3   Residual proton neutron interaction matrix elements

The expression (4.48) reveals that the (pn) part of the interaction is the scalar-product of two independent operators: $\hat{\rho}^{(p)}_{ac;K} \cdot \hat{\rho}^{(n)}_{bd;K}$. Standard vector-coupling relations tell us that matrix elements of this operator in a j-j-coupled basis can be expressed as products of matrix elements in the uncoupled basis:

$$\langle f| \hat{\rho}^{(p)}_{ac;K} \cdot \hat{\rho}^{(n)}_{bd;K} |i\rangle = (-1)^{j_{pi}+j_{nf}+J} \begin{Bmatrix} J & j_{nf} & j_{pf} \\ K & j_{pi} & j_{ni} \end{Bmatrix} \langle p_f || \hat{\rho}^{(p)}_{ac;K} || p_i \rangle \langle n_f || \hat{\rho}^{(n)}_{bd;K} || n_i \rangle, \tag{4.49}$$

where $|i\rangle = |p_i n_i; J\pi\rangle$ and $(J\pi)_i = (J\pi)_f = J\pi$. Finally, the pn matrix elements are:

$$\langle f| \hat{H}^{(pn)}_J |i\rangle = (-1)^{j_{pi}+j_{nf}+J} \sum_K \begin{Bmatrix} J & j_{nf} & j_{pf} \\ K & j_{pi} & j_{ni} \end{Bmatrix} \sum_{bd} (2K+1) \sum_{ac} \rho^{p_f p_i}_{ac;K} W^{(pn)}_{ac,bd;K} \rho^{n_f n_i}_{bd;K}. \tag{4.50}$$

4.6   Spectral calculations

First, we show how the low-lying spectra obtained from the weak entanglement factorization compare to the un-truncated, full configuration-interaction (FCI) calculations. Given specifications from the phenomenological interactions used, we can also compute the total binding energies of the states. We compare the most-bound levels for four benchmark nuclei. In each case, multiple calculations are performed. Each uses an increasing fraction of the proton and neutron subspace factors and therefore an increasing computational cost which

scales like the cube of the model space dimension. All calculations were performed with the square-cut algorithm, using all allowed combinations of the (m_p, m_n) basis factors.

We perform calculations in two model spaces. The first is the $0f_{7/2}, 1p_{3/2}, 0f_{5/2}, 1p_{1/2}$ space with the GX1A interaction [145], and the second is the $0f_{5/2}, 1p_{3/2}, 1p_{1/2}, 0g_{9/2}$ space with the JUN45 interaction [147]. The nuclei modeling in each space and their dimensions are shown in Table 4.1. These nuclei were selected to span a large range of M-scheme model

Table 4.1: PANASh benchmark calculations and their: interaction used (Int.), M-scheme FCI dimension in millions (Mdim), number of protons (Z), number of valence protons ($Z_{\text{val.}}$), proton subspace M-scheme dimension (Zdim), (the equivalent for neutrons), and properties for which the nucleus was selected as a benchmark.

Nucleus	Int.	Mdim. 10^6	$Z(Z_{\text{val.}})$	Zdim.	$N(N_{\text{val.}})$	Ndim.	Properties
^{78}Ge	JUN45	3.7	32(4)	701	46(18)	701	even-even, deformed
^{70}As	JUN45	760	33(5)	2,293	37(9)	36,998	odd-odd, deformed
^{60}Ni	GX1A	1090	28(8)	12,022	32(12)	12,022	even-even, spherical
^{79}Rb	JUN45	8600	37(9)	36,998	42(14)	24,426	odd-A, spherical

space dimensions (from 10^6 to 10^9), as well as breath of properties which affect the difficulty of capturing the many-body physics. Even-even nuclei tend to be simpler than odd-A (^{79}Rb) or odd-odd (^{70}As) nuclei, since the unpaired nucleon in the latter two cases lead to stronger mixing of the proton and neutron subspaces. We also have two even-even cases: one more spherical (^{60}Ni) which is expected to exhibit vibrational spectra, and one more deformed (^{78}Ge) which is expected to exhibit rotational spectra. (In a very simplistic liquid drop model, spherical nuclei can be thought of as perfect Harmonic oscillators yielding bands of equally spaced levels with $E = n\hbar\omega$, while deformed nuclei are like symmetric rotors with spacing as $E = \hbar^2 J(J+1)/2I_0$; for reference see Ring and Schuck [245], Fig. 1.12). The theoretical deformation of these nuclei can be estimated from beyond mean-field calculations tabulated in a database described in [138].

The binding energies are calculated using the formula:

$$BE(Z, N) = E_{\text{val}} + E_{\text{core}} + E_C(Z, N), \tag{4.51}$$

where E_{val} is the binding energy amongst the valence particles, determined by the eigenenergies of the model space Hamiltonian. E_{core} is the binding energy of the core nucleons, taken to be the experimental binding energy of the core nucleus. Finally, $E_C(Z, N)$ takes into account the binding energy correction due to the Coulomb interaction. For interaction JUN45 we use the empirical formula [147, 60],

$$E_C(Z_v, N_v) = \epsilon_C Z_v + \frac{1}{2} V_C Z_v (Z_v - 1) + \frac{1}{2} b_C Z_v + \Delta_{np} Z_v N_v, \tag{4.52}$$

where Z_v and N_v are the number of valence protons and neutrons, and $\epsilon_C = 9504$, $V_C = 228$, $b_C = 30$, and $\Delta_{np} = -36$ are parameters in keV taken from [60], as in [147]. The Coulomb term for the GX1A interaction is calculated using the formula and parameters from [145].

Since PANASh uses a J-scheme basis, each J^π block of the Hamiltonian can be solved independently with a much smaller basis, typically an order of magnitude or more smaller than the equivalent M-scheme basis The J-scheme matrix elements have a much higher cost per element, however, and the `BIGSTICK` code is far more efficient for a fixed basis-size. For this reason we use `BIGSTICK` to compute the FCI results for the un-truncated basis where the advantages of the weak-entanglement approximation are lost.

The results for ^{78}Ge, an even-even deformed nucleus, are shown in Figure 4.4. In each panel the PANASh basis is constructed with m proton and neutron factors with as an increasing fraction of the available subspace factors $d_n = d_p = 701$ (see also Table 4.1). Below each m is the d, the maximum J-scheme dimension which had to be solved to obtain the results in that panel. In the first panel, with 1% of the basis factors resulting in four orders of magnitude reduction in the dimension of the model space, we reproduce the spectral structure characteristic of a deformed, rotational nucleus: non-degenerate low-lying $0^+, 2^+, 4^+$ states. We also get the ground state binding energy well within the 1-percent level (1.6 MeV / 676 MeV). The last panel, $m = 1.0d_n$, has no basis factors left out of the basis and is equivalent
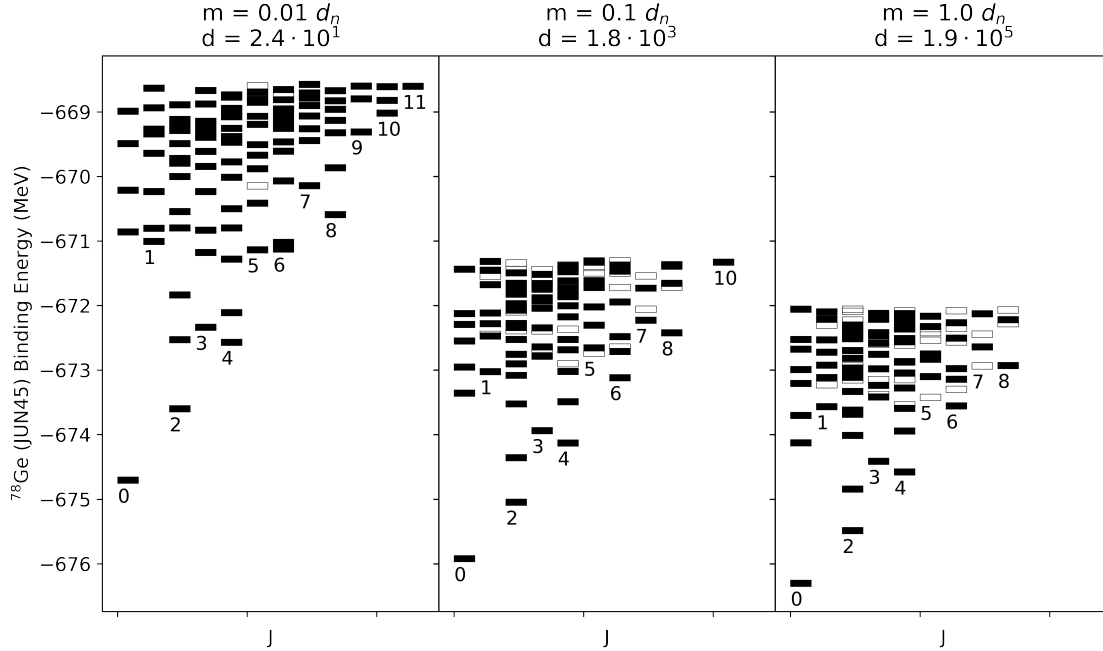
Figure 4.4: Binding energies of 100 levels of ^{78}Ge computed with the weak entanglement factorization approximation. Each panel has two labels: the number of components used as a fraction of the neutron subspace dimension, and the largest basis dimension required (across all spins). Each stack of bars is a set of levels with a given total angular momentum J; full bars are positive parity and empty bars are negative parity. All calculations are done with the square-cut basis method.

to the full configuration interaction (FCI) calculation. Unlike the next three benchmark cases, it is practical to compute the FCI results with PANASh, since the dimensions are relatively modest (10^5).

The results for ^{60}Ni, an even-even spherical nucleus, are shown in Figure 4.5. The format of the figure is the same as in Figure 4.4, except for the last panel showing the FCI calculation. Here it was not practical to get the FCI results using PANASh due to the large dimensions, and instead the FCI code `BIGSTICK` was used. Therefore, the dimension indicated is in the M-scheme rather than the J-scheme (which would have been about an order of magnitude smaller). The spectral structure here is not so different from ^{78}Ge, but we do see the indicator for a spherical nucleus [245]: 0^+ ground state, 2^+ first excited state, and a triplet $0^+, 2^+, 4^+$ degeneracy approximately twice the energy of the first 2^+ state. (Whereas in a deformed
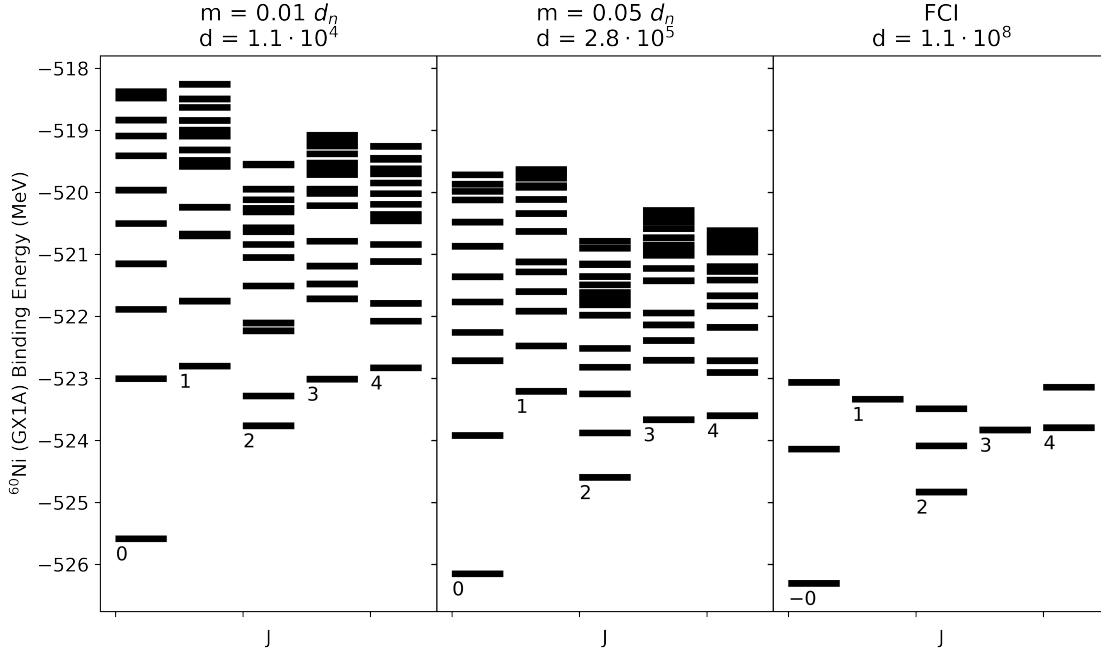
Figure 4.5: Same as figure 4.4 but for ^{60}Ni. The final panel, labeled FCI, was performed with the M-scheme code `BIGSTICK` at a dimension of $1.1 \cdot 10^9$, but lists the equivalent J-scheme dimension. See text for a full discussion.

nucleus the degeneracy is broken with the 2^+ and 4^+ brought down in energy.) The ground state binding energies obtained using only 1% of the basis factors (4 orders of magnitude reduction in dimension) is within 1 MeV, and the excitation energy of the first 2^+ state is about 350 keV too high, about twice the typical shell model uncertainty. Using 5% of the basis factors (still 3 orders of magnitude reduction), the ground state binding energy is within 160 keV of FCI, and the first 2^+ is within 81 keV.

The results for ^{70}As, an odd-odd, deformed nucleus, are shown in Figure 4.6. Unlike the even-even nuclei with a 0^+ ground state and orderly low-lying excitations, the spectra for the odd-odd ^{70}As is dense with a 4^+ ground state. The 1% calculation which in the previous two cases came very close to the final ground state binding energy, here the error is almost 3 MeV. This comports with our expectation that the odd proton and neutron are forced to couple, increasing the proton neutron entanglement entropy and reducing the effectiveness of the PANASh method. Despite this, we are still able to obtain the approximate ordering
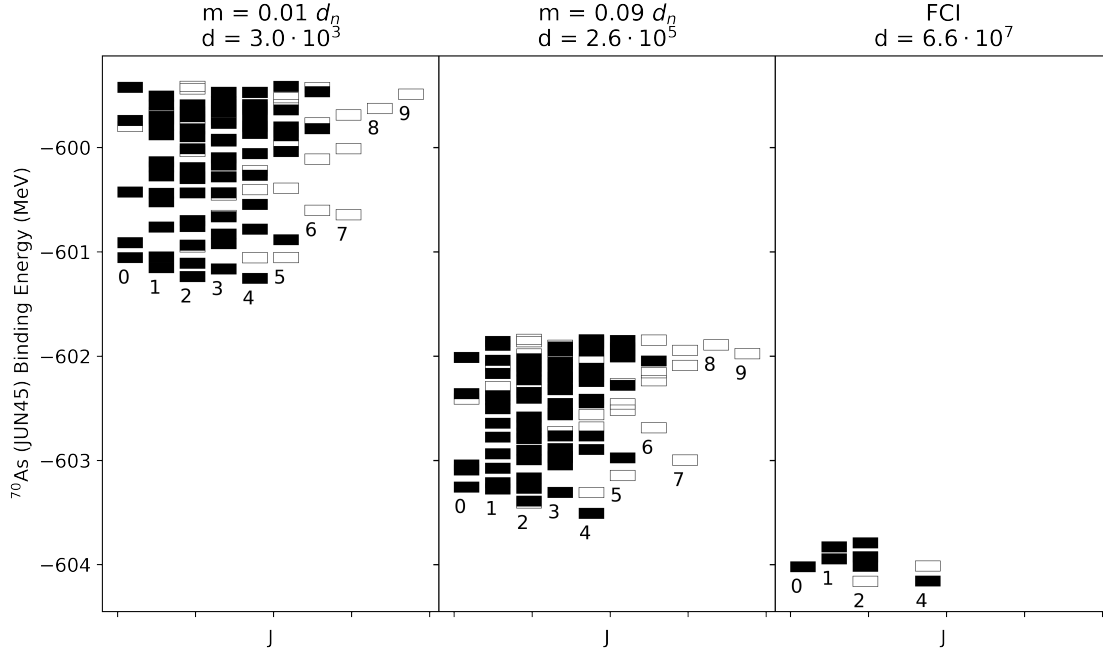
Figure 4.6: Same as figure 4.4 but for ^{70}As. The final panel, labeled FCI, was performed with the M-scheme code `BIGSTICK` at a dimension of $7.1 \cdot 10^8$, but lists the equivalent J-scheme dimension.

of the low-lying states and obtain hundreds of states where FCI can only manage a few with significant resources. For the 9% calculation, the 2^- ground state is off by 0.75 MeV and resolves above the first 4^+ MeV state which is nearly degenerate.

The results for ^{79}Rb, an odd-A, spherical nucleus, are shown in Figure 4.7. As an odd-A nucleus, there will be one unpaired nucleon leading to half-integer spins (represented in the figure in decimal values). The M-scheme dimension for this nucleus is $8.6 \cdot 10^9$, which is approaching the limits of our computing capabilities. Using `BIGSTICK`, we could only obtain the lowest four states of each parity in a reasonable amount of time. In the J-scheme it would have been $7.1 \cdot 10^8$. Using 1% of the basis factors, four orders of magnitude basis reduction, the ground state binding energy is too weak by 2.1 MeV, and the ordering of the first few states does not match the converged results. This is not too surprising given the high level density. Furthermore, this truncation error is comparable to the error of FCI compared to the experimental binding energy: $BE_{exp} = -679.5$ MeV, $BE_{FCI} = -680.7$
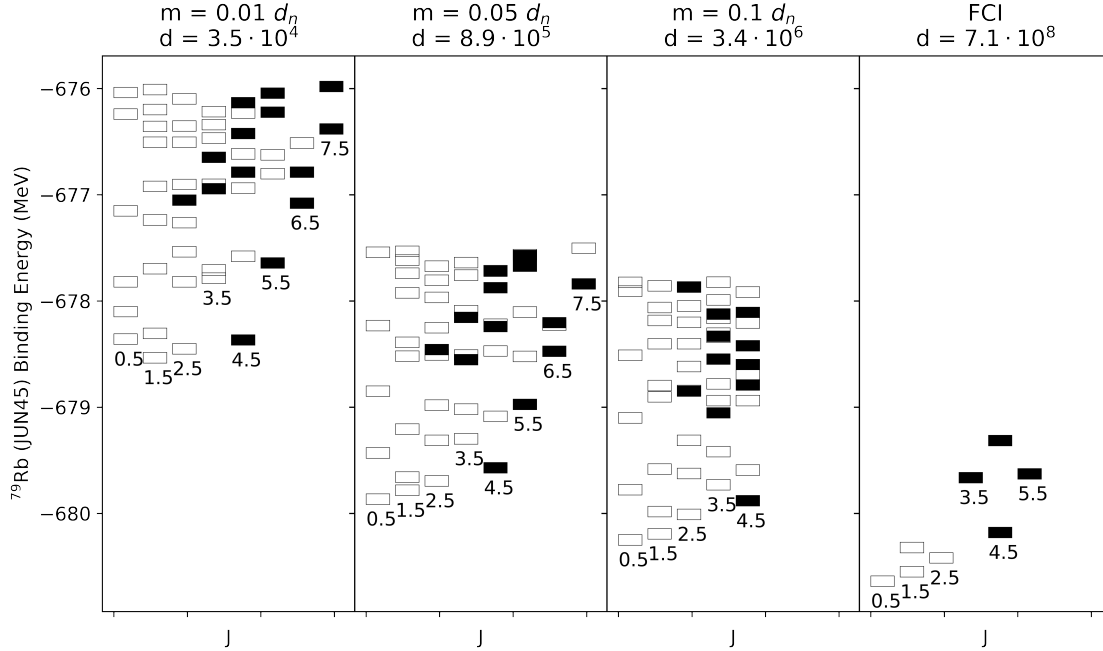
Figure 4.7: Same as figure 4.4 but for ^{79}Rb. The right-most panel was computed with the FCI code `BIGSTICK` at a dimension of $8.6 \cdot 10^9$, but lists the equivalent J-scheme dimension.

MeV (error = 1.2 MeV). Increasing to 5% of the basis factors and an order of magnitude increase in dimension, we get the right ordering of at least the first 5 states compared to FCI. The error in the ground state binding energy is 770 keV. Doubling the basis factors to 10% does not significantly improve convergence despite quadrupling the basis dimension. This is evidence that we can extract most of the physics from the lowest energy basis factors.

The significant basis reduction achieved by the weak entanglement approximation is useful in two extremes. The first, is that it makes possible calculations which cannot be attempted in FCI - we will be able to study the structure of a few low-lying states in model spaces that were previously computationally impossible. The second extreme can already be seen by the small number of levels in the FCI panel of last three figures: using this basis reduction method we can obtain a far greater number of states for a comparable computational cost. We can choose to sacrifice some quality for a larger quantity of states. This might not sound desirable, but for statistical quantities like average electromagnetic properties of highly excited states, it is exactly the right trade-off.

4.7 Transitions

Obtaining the eigenenergies and wave functions of the Hamiltonian is not enough. We are interested in the transition probabilities we can compute with the wave function solutions. The most common types of transitions can be cast as one-body operators and computed using the one-body transition density matrices computed from the original wave functions. This greatly speeds up the computations. The next two subsections present the main results required to compute one-body transitions using PANASh.

4.7.1 One-body transition density matrices

To compute basic observables, e.g. $E\lambda$ and $M\lambda$ multipole transition rates, we use one-body density matrices ($\boldsymbol{\rho}_K^{fi}$). These are efficient representations of the wave function content needed for computing one-body operator ($\hat{O}_{1b}$) matrix elements:

$$\langle \Psi^f | \hat{O}_{1b} | \Psi^i \rangle = \mathrm{Tr}\Big\{ \hat{O}_{1b} \boldsymbol{\rho}_K^{fi} \Big\}. \tag{4.53}$$

The trace is over all single-particle orbits in the single-particle model space. Once we have solutions Ψ for the Hamiltonian (4.5), the one-body density (1BD) matrices can be computed in a fashion similar to the matrix elements of the Hamiltonian: expressed in terms of the factor wave function 1BD matrices.

The proton and neutron 1BD operators are:

$$\hat{\rho}_{ab,K}^{(p)} = [\hat{\pi}_a^\dagger \hat{\pi}_b]_K \otimes 1 \tag{4.54}$$

$$\hat{\rho}_{ab,K}^{(n)} = 1 \otimes [\hat{\nu}_a^\dagger \hat{\nu}_b]_K, \tag{4.55}$$

where $\hat{\pi}_a$ and $\hat{\nu}_a$ are proton and neutron one-body operators, respectively. The matrix

elements of these operators for the eigenstates of the Hamiltonian in the coupled basis are:

$$\rho_{ac;K}^{fi(p)} = \langle \Psi^f || \hat{\rho}_{ac,K}^{(p)} || \Psi^i \rangle = \sum_{p_f n_f p_i n_i} \psi_{p_f n_f}^f \psi_{p_i n_i}^i \langle p_f n_f; J_f \pi | \hat{\rho}_{ac,K}^{(p)} | p_i n_i; J_i \pi \rangle \tag{4.56}$$

Using the identity for a tensor-product of a single-species operator with the identity, we obtain the matrix elements of the proton/neutron 1BD operators in terms of the 1BD matrices of the factor wave functions:

$$\langle f | \hat{\rho}_{ac,K}^{(p)} | i \rangle = (-1)^{J_i+K+j_{pf}+j_{ni}} \delta_{j_{nf} j_{ni}} [J_f][J_i] \begin{Bmatrix} j_{pf} & J_f & j_{ni} \\ J_i & j_{pi} & K \end{Bmatrix} \langle p_f || \hat{\rho}_{ac;K}^{(p)} || p_i \rangle \tag{4.57}$$

The Kronecker-delta acts to create a trace over the 'spectator' subspace. Combining, we obtain:

$$\rho_{acK}^{fi(p)} = (-1)^{J_i+K} [J_f][J_i] \sum_{p_f p_i} \sum_{n_f} (-1)^{j_{pf}+j_{nf}} \begin{Bmatrix} j_{pf} & J_f & j_{nf} \\ J_i & j_{pi} & K \end{Bmatrix} \psi_{p_f n_f}^{(f)} \psi_{p_i n_f}^{(i)} \rho_{acK}^{p_f p_i(p)} \tag{4.58}$$

We can rewrite to obtain:

$$\rho_{acK}^{fi(p)} = (-1)^{J_i+K} [J_f][J_i] \sum_{p_f p_i} P_{(K)}^{p_f p_i(fi)} \rho_{acK}^{p_f p_i(p)} \tag{4.59}$$

where, for efficiency, we pre-compute the sum

$$P_{(K)}^{p_f p_i(fi)} = \sum_{n_f} (-1)^{j_{pf}+j_{nf}} \begin{Bmatrix} j_{pf} & J_f & j_{nf} \\ J_i & j_{pi} & K \end{Bmatrix} \psi_{p_f n_f}^{(f)} \psi_{p_i n_f}^{(i)}. \tag{4.60}$$

This is done at each combination of f, i, K, and so m_p^2 memory is required. The total compute scaling is

$$S_p' = N_k N_s^2 m_p^2 (N_o^2 + m_n), \tag{4.61}$$

99

where N_s is the number of solution wave functions between which transitions are computed. An equivalent expression holds for S'_n. The speedup as a result of pre-computing (4.60) is

$$\frac{S}{S'} = \frac{N_k N_s^2 N_o^2 m_p^2 m_n}{N_k N_s^2 m_p^2 (N_o^2 + m_n)} = \frac{N_o^2 m_n}{N_o^2 + m_n}. \tag{4.62}$$

4.7.2 Charge-changing matrix elements

To compute the charge-changing one-body density matrices, one generalizes the expressions from the previous section to evaluate the reduced matrix elements of the tensor operator $\hat{\rho}_{ab,K}^{(pn)} = [\hat{\pi}_a^\dagger \otimes \tilde{\nu}_b]_K$:

$$\langle \Psi^f || [\hat{\pi}_a^\dagger \otimes \tilde{\nu}_b]_K || \Psi^i \rangle = [J_f][K][J_i] \sum_{p_f n_f p_i n_i} \psi_{p_f n_f}^f \psi_{p_i n_i}^i \begin{Bmatrix} j_{p_f} & j_{p_i} & j_a \\ j_{n_f} & j_{n_i} & j_b \\ J_f & J_i & K \end{Bmatrix} \langle p_f || \hat{\pi}_a^\dagger || p_i \rangle \langle n_f || \tilde{\nu}_b || n_i \rangle. \tag{4.63}$$

The proton one-body matrix element can be identified as the spectroscopic factor:

$$S_{p_f p_i; a} \equiv [j_{p_f}]^{-1} \langle p_f || \hat{\pi}_a^\dagger || p_i \rangle. \tag{4.64}$$

In this convention, a spectroscopic factor is the matrix element of a creation operator. To write the neutron one-body matrix element in the same way, we first apply the time-reversal identity:

$$\langle n_f || \tilde{\nu}_b || n_i \rangle = (-1)^{j_{n_f} - j_b - j_{n_i}} \langle n_i || \hat{\nu}_b^\dagger || n_f \rangle = (-1)^{j_{n_f} - j_b - j_{n_i}} [j_{n_i}] S_{n_i n_f; b}. \tag{4.65}$$

100

This means one has to compute the spectroscopic factor as a transition from the final neutron state to the initial neutron state. The complete expression is:

$$\langle \Psi^f || [\hat{\pi}_a^\dagger \otimes \tilde{\nu}_b]_K || \Psi^i \rangle = (-1)^{j_{n_f} - j_b - j_{n_i}} [J_f][K][J_i] \sum_{p_f n_f p_i n_i} \psi^f_{p_f n_f} \psi^i_{p_i n_i}$$

$$\times [j_{p_f}][j_{n_i}] \begin{Bmatrix} j_{p_f} & j_{p_i} & j_a \\ j_{n_f} & j_{n_i} & j_b \\ J_f & J_i & K \end{Bmatrix} S_{p_f n_i; a} S_{n_i n_f; b}. \tag{4.66}$$

4.8 Discussion of density matrix methods

We will briefly review the density matrix renormalization group (DMRG) and variational wavefunction factorization (VWF) methods to clarify how the weak entanglement limit compares. All three methods are based on a bipartite decomposition of the Hilbert space, followed by some sort of truncation, and can also be directly or indirectly related to a singular-value decomposition of the bipartite representation of the wave function.

4.8.1 DMRG

In a density matrix renormalization group (DMRG) approach to the nuclear shell model, one splits the single-particle space into subspaces, which are either iteratively increased in size (infinite algorithm), or swept through 'left and right' (finite algorithm) as information from distant orbitals is integrated into the truncated states. In either case, a product state representation of the true ground state is realized,

$$|\Psi\rangle \approx \sum_{lr}^{m} \psi_{lr} |l\rangle |r\rangle, \tag{4.67}$$

where $|l\rangle$ and $|r\rangle$ are many-body states constructed from the left and right subsets of orbitals. In [218] these were chosen to be conjugate pairs of proton and neutron orbits, ordered such that the orbits near the Fermi surface were in the middle of the chain. m is the truncation parameter which is ideally much smaller than the dimensions of the l and r subspaces.

At each iteration of the method, the ground state of the subspaces are found by exact diagonalization. The factors $|l\rangle$ and $|r\rangle$ approach their optimal values, which are the eigenstates of the reduced density matrices of each subspace:

$$\rho_L = \text{Tr}_R |\Psi\rangle \langle\Psi| \tag{4.68}$$

$$\rho_R = \text{Tr}_L |\Psi\rangle \langle\Psi|. \tag{4.69}$$

This is related to the fact that the optimal representation of (4.67) is given by its singular value decomposition (SVD): $\psi = usv^T$,

$$\psi_{lr} = \sum_j^m u_{lj} s_j v_{jr}, \tag{4.70}$$

where s_j are the singular values, and $u_{ll'}$ and $v_{rr'}$ are unitary matrices. If we insert (4.70) into (4.68), we see that the eigenvalues of the density matrix are the squares of the singular values of Ψ, and $u_{ll'}$ contain its eigenvectors. This is a key point that will come up again: the eigenvectors of the reduced density matrices diagonalize the wave function coefficient matrix.

To summarize, in each step of DMRG, (1) the effective interaction in a given subspace is diagonalized, (2) the approximate ground state's SVD is used to inform which states to keep in a truncation to m factors from that subspace, and (3) the solution to the full space is taken as a product state of the subspace solutions. Various flavors of DMRG deal with how to select the sites which define the subspaces, and how to change the subspaces at each iteration.

4.8.2 VWF

Variational wavefunction factorization (VWF), or simply wavefunction factorization (as called by its creators [217, 219]) is a method which seeks to find the optimal set of proton and neutron factors $|\tilde{p}\rangle$ and $|\tilde{n}\rangle$ which for $m << \min(d_p, d_n)$ yield a good approximation,

$$|\Psi\rangle \approx \sum_j^m |\tilde{p}_j\rangle |\tilde{n}_j\rangle. \tag{4.71}$$

Again, it is known that the optimal representation is given by an SVD, but it is generally too expensive to solve even the ground state of the systems. In VWF, the optimal factors are instead found by an iterative, variational procedure. One starts with an ansatz state comprised of random proton and neutron many-body wavefunctions. Next, a variational condition minimizing the Hamiltonian leads to a coupled set of nonlinear equations. These are solved as a generalized eigenvalue problem. A SVD of the updated matrix of factor coefficients $C_{ij} = \langle i|p_j\rangle$ restores orthonormality of the factors within each subspace: $C = UDV^T \rightarrow |p_j'\rangle = \sum_i U_{ij} |i\rangle$. After each iteration, the number of basis factors m is increased until satisfactory convergence is reached.

Like DMRG, VWF relies on the fact that the singular values of realistic shell model ground states fall off rapidly so that an accurate approximation can be achieved with only a small number of factors [218]. In practice, the spectra (including excited states [218]) tend to converge exponentially with the number of states m retained.

4.8.3 Weak entanglement approximation

We showed in previous work that projections of ground state wave functions onto the eigenstates of proton and neutron subspace Hamiltonians fall off exponentially with the eigenstate

number [115]. This mimics the behavior of singular values and indicates that a basis constructed from such factors would provide an efficient representation, without the need for iterative optimizers. Building upon this initial investigation, it has been shown that the entanglement between the proton and neutron subspaces is weak [162]. In a bipartite system $\mathcal{H} = \mathcal{P} \oplus \mathcal{N}$ with weak entanglement, there is a natural connection between the eigenstates of the subspace operators and the reduced density matrices. Namely, a state with zero entanglement entropy is a pure product of the eigenstates of the subspace operators:

$$|\Psi_{S_{\text{entangle}}=0}\rangle = |p\rangle |n\rangle. \tag{4.72}$$

The reduced density matrix of such a state is $\rho_{\mathcal{P}} = |p\rangle \langle p|$. For this special case, $|p\rangle$ and $|n\rangle$ are the optimal factors. It follows that for weak entanglement entropy, eigenstates of the proton and neutron subspace operators approximate the optimal basis factors.

4.8.4 Comparison

A major cost of both DMRG and VWF is the variational approach to finding the optimal basis factors, which has limited the widespread application of the methods beyond proof-of-concept calculations. We tackle this problem by making the following ansatz: that eigenstates of the proton and neutron subspaces are 'good-enough' approximations of the optimal factors.

We combine two ideas, one from DMRG and the other from VWF. First, as in DMRG, we solve each subspace to obtain a partial solution of the full space. However, rather than iteratively expanding (or sweeping) the single-particle subspaces, we maintain constant partitions. Second, as in VWF, our partitions are the proton and neutron bi-partitions with unaltered single-particle spaces, and the truncation deals with which many-proton and many-neutron configurations to use. We take the first m (or (m_p, m_n)) factors from each subspace, and

in some cases add further restrictions to the construction of the basis (see section 4.4.1). However, unlike VWF, we do not attempt to optimize a random ansatz. Instead, we assume that the eigenstates of the subspaces are good enough and that the lowest energy eigenstates are the most important.

Interestingly, our choice of metric for selecting the proton and neutron basis factors is reminiscent of Wilson's numerical renormalization group (NRG) [302, 71], the precursor to DMRG. The downfall of NRG (which DMRG overcame) is that its truncation is based only on the energy of the subspace solutions and ignores the coupling of the subspace to the rest of the system. It fails when long-range correlations exist. PANASh does not have this problem, since within each bipartition we include all orbitals, and it is known that the entanglement between the proton and neutron subspaces is weak [162].

4.9   Outlook

Future work should investigate the behavior of other important observables including electromagnetic transitions and weak transitions. We expect that these observables will not converge as easily as the eigenstates of the Hamiltonian. We therefore propose a modified proton and neutron approximation scheme where the basis factors are transformed by the operators $\hat{T}$ whose matrix elements we are trying to obtain:

$$|p'\rangle = \hat{T} |p\rangle \tag{4.73}$$

$$|n'\rangle = \hat{T} |n\rangle . \tag{4.74}$$

In general, $\hat{T}$ will act in $\mathcal{H}$, not only $\mathcal{P}$ or $\mathcal{N}$. This means that the matrix elements of the Hamiltonian will need to be modified since the proton and neutron subspace Hamiltonians will no longer be diagonal. This work is left for future work.

Chapter 5

Computational Methods

This chapter describes algorithms I have implemented in the PANASh shell model code, unless otherwise indicated.

5.1   Solving the Hamiltonian matrix equation

By selecting a basis, we can turn the many-body Schrödinger equation, a linear partial differential equation, into an eigenvalue problem. Therefore, finding the solutions to the Schrödinger equation reduces to finding the eigenvalues and eigenvectors of a Hermitian matrix $\boldsymbol{H}$:

$$\boldsymbol{H}\boldsymbol{\psi} = E\boldsymbol{\psi}, \tag{5.1}$$

where $(\boldsymbol{\psi}, E)$ are the eigenpairs which solve the matrix eigenvalue problem. The straightforward way to do this is to find the unitary transformation which diagonalizes the Hamiltonian

matrix $\boldsymbol{H}$:

$$\boldsymbol{D} = \boldsymbol{U}\boldsymbol{H}\boldsymbol{U}^T, \tag{5.2}$$

where $\boldsymbol{D}$ is diagonal and $\boldsymbol{U}$ is unitary. In this form, the diagonal elements of $\boldsymbol{D}$ contain all eigenvalues E, and the columns of $\boldsymbol{U}$ contain all eigenvectors of $\boldsymbol{H}$. This is only possible for a diagonalizable matrix, but all Hermitian matrices are diagonalizable.

There are numerous algorithms for diagonalizing matrices, but I will consider them in two categories: those which provide all eigensolutions, and those which provide only extremal eigensolutions.

The most important non-extremal method, that is, used for obtaining all eigenpairs, is the QR algorithm [104]. In modern implementations, the QR algorithm has two steps. First, $\boldsymbol{H}$ is made tridiagonal using Householder transformations. Then, the tridiagonal matrix is diagonalized by successive QR factorizations, that is to factorize it into an orthogonal matrix $\boldsymbol{Q}$ and an upper triangular matrix $\boldsymbol{R}$. At each successive iteration, one reverses the product of $\boldsymbol{R}$ and $\boldsymbol{Q}$, which is equivalent to a unitary transformation of $\boldsymbol{Q}\boldsymbol{R}$ by $\boldsymbol{Q}$. This is roughly how the LAPACK routines SSYEV and DSYEV work [8].

Extremal eigenpair solvers can all be thought of as extensions of power iteration methods. Starting from some initial vector $\boldsymbol{x}_0$, at each iteration a matrix-vector multiplication is applied so that

$$\boldsymbol{x}_{i+1} = \frac{\boldsymbol{H}\boldsymbol{x}_i}{||\boldsymbol{H}\boldsymbol{x}_i||}, \tag{5.3}$$

gives the next best approximation in the sequence. Ideally, the initial vector would be some approximation of the true eigenvector, otherwise a random initialization is used. The rate of convergence of power methods depends on the spectral distribution of the eigenvalues.

Spectra with nearly degenerate eigenvalues will converge more slowly, and the rate of convergence of the dominant eigenvalue goes like its ratio to the next largest eigenvalue: $|\lambda_2/\lambda_1|$. The most important power iteration type method used in nuclear many-body problems are variations of the Lanczos algorithm, which will be explained in depth in the next section.

5.1.1   Lanczos

There are many introductory texts covering this class of algorithm, see for example [104], or for the first application to nuclear physics see [299]. The idea behind the Lanczos algorithm is very similar to the humble power iteration method. In this case, a so-called Krylov subspace is constructed:

$$\mathcal{K}(\boldsymbol{H}, \boldsymbol{v}) = \text{span}\{\boldsymbol{v}, \boldsymbol{H}\boldsymbol{v}, \boldsymbol{H}^2\boldsymbol{v}, ..., \boldsymbol{H}^{m-1}\boldsymbol{v}\}, \tag{5.4}$$

where $\boldsymbol{v}$ is the initial Lanczos vector (Krylov subspace basis state), and the rest of the Lanczos vectors are defined as

$$\boldsymbol{v}_k \equiv \boldsymbol{H}^k\boldsymbol{v}, \tag{5.5}$$

with $k = 0, ..., m-1$. Projection of $\boldsymbol{H}$ into $\mathcal{K}$ by the transformation $\boldsymbol{V}^T\boldsymbol{H}\boldsymbol{V}$ is a tridiagonal matrix, where $\boldsymbol{V}$ has orthonormal columns $\boldsymbol{v}$. The dimensional check of this projection looks like this:

$$\boldsymbol{T}_{m\times m} = \boldsymbol{V}^T_{m\times n}\boldsymbol{H}_{n\times n}\boldsymbol{V}_{n\times m}. \tag{5.6}$$

The Lanczos algorithm allows us, with a few extra steps, to find the lowest m eigenpairs of the $n \times n$ matrix $\boldsymbol{H}$. In particular, If $(\lambda, \boldsymbol{x})$ is an eigenpair for $\boldsymbol{T}$, then $(\lambda, \boldsymbol{V}x)$ is an

eigenpair for H, since

$$\boldsymbol{T}\boldsymbol{x} = \lambda\boldsymbol{x} \tag{5.7}$$

$$\boldsymbol{V}^T\boldsymbol{H}\boldsymbol{V}\boldsymbol{x} = \lambda\boldsymbol{x} \tag{5.8}$$

$$\boldsymbol{V}\boldsymbol{V}^T\boldsymbol{H}(\boldsymbol{V}\boldsymbol{x}) = \lambda(\boldsymbol{V}\boldsymbol{x}) \tag{5.9}$$

$$\boldsymbol{H}(\boldsymbol{V}\boldsymbol{x}) = \lambda(\boldsymbol{V}\boldsymbol{x}). \tag{5.10}$$

The general approach is to use Lanczos iterations (Algorithm 1) to find the tridiagonal matrix $\boldsymbol{T}$, and then to fully diagonalize $\boldsymbol{T}$ using something like the QR algorithm in a standard library like LAPACK.

A key step in practical implementations of the Lanczos algorithm is re-orthogonalization. Due to finite numerical precision and the large number of matrix-vector prodcuts, round-off errors eventually accumulate and the Lanczos vectors lose their orthogonality. The remedy is to simply reorthogonalize. Although more sophisticated approaches have been studied in the literature, we simply reorthogonalize at each iteration. The additional cost is justified since the number of vectors tends to be very small compared to the cost of the matrix-vector product (and computation of the matrix elements themselves).

The computational complexity of the Lanczos algorithm scales like $2mn^2 + 2m^2n + 3mn$, where n is the dimension of the Hilbert space of $\boldsymbol{H}$ and m is the number of Lanczos iterations. The number of Lanczos iterations needed to converge l extremal eigenstates is at least l, and the exact number will depend on the density of the eigenvalues. The cost of reorthogonalization approximated here as $2m^2n$ comes from $2(m(m+1)/2*2n)$. When $m \ll n$, the mn^2 term of matrix-vector multiplication dominates. However, as m grows large, the cost of reorthogonalization grows quickly. For example, suppose $m = n/10$, then MatVec scales as $n^3/10$, and reorthogonalization scales as $n^3/50$, up to a fifth of the total compute. If one is seeking a large number of solutions, i.e. several hundred or several thousand, the

Algorithm 1 Lanczos iterator: This algorithm requires a method to generate the matrix-vector product $\boldsymbol{H}_{n\times n}\boldsymbol{v}_n$. The result of the algorithm are m Lanczos vectors $\boldsymbol{v}_k$, and the diagonal (α_k) and super-diagonal (β_k) elements of the tridiagonal matrix $\boldsymbol{T}$.

$\boldsymbol{v}_1 \sim \mathrm{U}^n$ $\triangleright$ i.e. random initialization
for k = 1, m **do** $\triangleright$ Important: reversing the order leads to instability.
    $\boldsymbol{w} = \boldsymbol{H}\boldsymbol{v}_k$ $\triangleright$ OPS: $2mn^2$
    for j = 1, k **do** $\triangleright$ Reorthogonalization step
       $\mathrm{R} = \boldsymbol{w}^T\boldsymbol{v}_j$ $\triangleright$ OPS: m^2n
       if $k == j$ **then**
          $\alpha_k = R$
       end if
       $\boldsymbol{w} = \boldsymbol{w} - R\boldsymbol{v}_j$ $\triangleright$ OPS: m^2n
    end for
    $\beta_k = ||w||_2$ $\triangleright$ OPS: $2mn$
    $\boldsymbol{v}_{k+1} = \boldsymbol{w}/\beta_k$ $\triangleright$ OPS: mn
end for

---

advantage of Lanczos can be diminished. Complete diagonalization algorithms like the QR algorithm have compute complexity scaling of order n^3. To obtain m solutions, a minimum of m Lanczos iterations will need to be performed, resulting in order $m^2n + m^2n$ operations. If the number of desired states m is much less than the dimension n, then clearly Lanczos is superior. However, if m is similar in magnitude to n, Lanczos becomes less efficient than complete diagonalization.

Lanczos iterations are usually applied in sets, starting with at least q iterations where q is the number of desired eigenpairs of $\boldsymbol{H}$. After q iterations, several (perhaps 1-10) iterations are applied, after which some convergence criterion is checked. A simplistic criterion would check the change in the eigenvalues since the last check and continue until a criterion is reached, such as:

$$\frac{1}{q + \mathrm{buffer}} \sum_{i=1}^{q+\mathrm{buffer}} |E_i - E_i^{\mathrm{prev}}| < \mathrm{tolerance}, \tag{5.11}$$

where typical values are buffer = 10 and tolerance = $1 \cdot 10^{-3}$.

A more sophisticated convergence check might track the overlap of the eigenvectors, but this

is computationally more expensive.

5.1.2   Block Lanczos

The Block Lanczos [105] algorithm (Algorithm 2) takes advantage of data locality and memory hierarchy to improve the performance of the Lanczos algorithm by using a block with b Lanczos vectors in place of a single Lanczos vector. It also supposedly improves performance for near-degenerate eigenspectra [265], which all power iteration methods suffer upon.

Algorithm 2 Block Lanczos iterator: This algorithm requires a method to generate the matrix-matrix product $\boldsymbol{H}_{n\times n}\left|V\right\rangle_{n\times b}$. The result of the algorithm are m Lanczos block vectors $\left|V_k\right\rangle$, and the diagonal $(\boldsymbol{\alpha}_k)$ and super-diagonal $(\boldsymbol{\beta}_k)$ blocks of the block-tridiagonal matrix $\boldsymbol{T}$.

$\quad\boldsymbol{V}_1 \sim \mathrm{U}^{nb}$ $\qquad\qquad\qquad\qquad\qquad\qquad$ ▷ i.e. b random orthonormal n-dim vectors

$\quad$**for** k = 1, m **do** $\qquad\qquad\qquad\qquad$ ▷ Important: reversing the order leads to instability.

$\qquad\boldsymbol{W} = \boldsymbol{H}\boldsymbol{V_k}$ $\qquad\qquad\qquad\qquad\qquad\qquad\qquad\qquad\qquad\qquad\qquad$ ▷ OPS: $2bmn^2$

$\qquad$**for** j = 1, k **do**

$\qquad\qquad\boldsymbol{R} = \boldsymbol{W}^T\boldsymbol{V_j}$ $\qquad\qquad\qquad\qquad\qquad\qquad\qquad\qquad\qquad\qquad$ ▷ OPS: bm^2n

$\qquad\qquad$**if** $k == j$ **then**

$\qquad\qquad\qquad\boldsymbol{\alpha}_k = \boldsymbol{R}$

$\qquad\qquad$**end if**

$\qquad\qquad\boldsymbol{W} = \boldsymbol{W} - \boldsymbol{R}^T\boldsymbol{V_j}$ $\qquad\qquad\qquad\qquad\qquad\qquad\qquad\qquad$ ▷ OPS: bm^2n

$\qquad$**end for**

$\qquad\boldsymbol{\beta}_k = \sqrt{\boldsymbol{W}^T\boldsymbol{W}}$ $\qquad\qquad\qquad\qquad\qquad\qquad\qquad\qquad\qquad\qquad$ ▷ OPS: $2bmn$

$\qquad\boldsymbol{V_{k+1}} = \boldsymbol{W}/\boldsymbol{\beta}_k$ $\qquad\qquad\qquad\qquad\qquad\qquad\qquad\qquad\qquad\qquad$ ▷ OPS: bmn

$\quad$**end for**

Just as the Lanczos algorithm can be thought of as a generalization of the power iteration method (by keeping all vectors generated at each power of matrix-vector multiplication), Block Lanczos can be thought of as a generalization of standard Lanczos. Block Lanczos, at each iteration, acts as the matrix $\boldsymbol{H}$ on a set (block) of initial vectors. At each subsequent iteration, another block $\boldsymbol{H}^k\boldsymbol{V}_0$ is obtained, where $\boldsymbol{V}_0$ is a matrix with the b initial vectors $\boldsymbol{v}_0$.

Because the basic operation is now matrix-matrix multiplication, rather than matrix-vector multiplication, a given matrix element of $\boldsymbol{H}$ is applied b times at each matrix-matrix multi-

plication. This leads to a significant performance increase, especially in the case of on-the-fly algorithms, since a matrix element is reused b times before it is destroyed. It also improves cache performance if the Lanczos Block is organized to apply the matrix element to sequential block elements in memory.

5.1.3 Even more variations on Lanczos

There are even more sophisticated and efficient versions of Lanczos which can be implemented, but I have not yet implemented them in PANASh.

Thick-Restart Block Lanczos [265] improves efficiency for obtaining a large number of eigenvalues by occasionally pausing the iterations, dropping all but the most recent Lanczos Blocks, and restarting using the kept Block as a new pivot (starting vector). This reduces the maximum number of Lanczos vectors stored in memory.

Bootstrapped Block Lanczos [309] is an extension of Thick-Restart Block Lanczos' principle of starting from a partially converged result. In this case, an improved starting block is obtained by first finding an approximate solution in a highly truncated space. The overlap with the exact wave function is what grants a speedup of two or more over a random pivot. This method will be especially useful for methods like PANASh where an iterative procedure could bootstrap a truncated solution with m basis factors to the next solution with $m + dm$ basis factors.

Block Lanczos tends to be more sensitive to numerical instability than standard Lanczos, due to the increased number of Lanczos vectors.

5.2 Memory management and data structures

This section deals with trade-offs between memory and time resources.

5.2.1 On-the-fly Matrix-Vector Products

Computers have two basic types of resources: time and memory. The types of computational problems we are dealing with push the bounds of both. Matrices take memory to store with a scaling of $\mathcal{O}(n^2)$, and obtaining m solutions takes time with a scaling of $\mathcal{O}(mn^2)$. (In fact, as I'll discuss in the next section, another important time cost for us is obtaining the matrix in the first place.)

While both time and memory are finite, our contemporary resource limits make memory the harder boundary. Often we can simply wait longer to get around time constraints, even when we are bound by a hardware-defined number of operations per second. To push our calculations beyond these in-memory constraints, we implement 'on-the-fly' matrix-vector products. This means that rather than computing all matrix elements at once and storing them in memory, we compute each matrix element only when it is called in our iterative solver, for example, when we need to multiply a Lanczos vector.

J^π	Dimension	Hamiltonian (GB)	Lanczos vectors (GB)
$1/2^+$	$8.9 \cdot 10^5$	3,100	9
$3/2^+$	$1.7 \cdot 10^6$	12,000	17
$5/2^+$	$2.4 \cdot 10^6$	24,000	24
$7/2^+$	$3.0 \cdot 10^6$	36,000	30

Table 5.1: Example J-scheme dimensions and potential memory usage of a PANASh calculation. We avoid memory cost of the Hamiltonian by computing its matrix elements on-the-fly. This example is for ^{79}Rb in the pfg space using $r = 3699$ proton factors and $s = 2442$ neutron factors (10% of each subspace). Space was allocated for up to 2500 Lanczos vectors.

The main advantage of the no-the-fly approach is that our dominant memory constraint drops

from $\mathcal{O}(n^2)$ to $\mathcal{O}(n)$, since we now only need to store a constant number of n-dimensional Lanczos vectors. A moderately large example is shown in Table 5.1. The main disadvantage is that now we must recompute the entire Hamiltonian at each Lanczos iteration.

5.2.2 Perils of derived types

Like all aspects of computational science, the choice of data structures comes down to a trade-off between time and memory. Many of the irreducible data structures of shell model calculations are very sparse. This makes custom data types attractive, but sometimes this can go awry.

The most extreme example I encountered came out of trying to store one-body transition densities more efficiently. These operator matrix elements have a minimum of 5 labels:

$$\boldsymbol{\rho}_{f,i,a,b,k} : \langle \psi_f | \, [\hat{c}_a^\dagger \otimes \hat{c}_b]_K \, | \psi_i \rangle \,, \tag{5.12}$$

where f and i label the initial and final state wavefunctions, a and b label the orbits each operator acts on, and k labels the angular momentum of the operator. The most memory-inefficient way to store this object would be in a rank-5 array. Due to symmetries (most significantly conservation of angular momentum) this array is extremely sparse. One is tempted to create a Fortran derived type with this sort of structure:

```
rho%states(i,f)%operator(a,b)%coupling(k)
```

since at each substructure, one could work out exactly how many objects to allocate based on the indices of the parent substructure. I.e. fixing i, f determines a subset of allowed a, b, and fixing i, f, a, b determines an an even smaller subset of allowed k.

The problem with this data structure is that it implicitly creates a very large number of

114

small allocatable arrays, and each of those arrays has a small memory overhead in the form of metadata. That metadata can be thought of as storing the data type and array bounds. Table 5.2 shows a minimal example using the code snippet shown below.

```fortran
type manyarrays
  real, allocatable, dimension(:) :: array
end type
type(manyarrays), allocatable, dimension(:) :: mymanyarrays

n = 2e8 ! number of arrays
m = 5   ! size of arrays

allocate(manyarrayobj(n))
do i = 1, n
  allocate(mymanyarrays(i)%array(m))
  manyarrayobj(i)%arr = i
end do
```

Table 5.2: Memory usage of many small allocatable arrays. Nominal memory usage is what would be expected if only the mn real (single precision) values were stored. System memory usage is the amount of memory used as reported by the operating system.

n arrays	m array size	Nom. (GB)	Sys. (GB)
1	10^9	4.0	4.0
10^3	10^6	4.0	4.0
10^8	10	4.0	11.1
$2 \cdot 10^8$	5	4.0	19.2
$1 \cdot 10^9$	1	4.0	95.7

In conclusion, storing sparse data structures as a very large number of small arrays is not necessarily a good idea. The data structure still used in PANASh for OBTD matrices is:

```fortran
rho%states(i,f)%coupling(k)%operator(a,b)
```

The operator array in this case is typically 3×3 in size, with order $100 \times 100 \times 10 = 10^5$ total number of such arrays. However, these data structures *are not* used in the core calculations, but are spooled into simple arrays. This is discussed in detail in section 5.3.

115

5.3 Precomputation and caching

5.3.1 Vector coupling coefficient caching

Profiling PANASh at run-time with tools like gprof reveals that the vector-coupling coefficients dominate the compute cost. This is because each matrix element requires many vector coupling coefficients, each taking many operations to compute. But there is a finite number of inputs, and by the organization of the nested loops, we can predict which subsets of inputs will be called within some fixed block of time. This leads to two general strategies, both involving the precomputation of vector coupling coefficients.

Large agnostic cache

First is the general approach of computing a large number of coefficients. This functionality is built into the Wigner library I wrote. One can initialize a large array of vector coupling coefficients and keep them in memory. There is then a lookup function for accessing the values, and a fallback to computation if the requested value falls outside of the available stored values. This method can still significantly slow down calculations since the check of the array bounds is expensive and hard for the compiler to optimize.

The Hamiltonian matrix elements are computed by coupling proton wave functions to neutron wave functions. This requires Wigner 6-j symbols and no other explicit vector coupling. These appear in both the transformed pn-interaction and in the coupling of the pn OBTD operators. The latter couples the angular momentum of the component wave functions and therefore requires larger angular momentum values. The 6-j symbol is

$$
\begin{Bmatrix} J & j_{nf} & j_{pf} \\ K & j_{pi} & j_{ni} \end{Bmatrix}
\tag{5.13}
$$

where $\boldsymbol{J} = \boldsymbol{j}_{nf} + \boldsymbol{j}_{pf}$. Once the basis has been constructed, I determine the exact maximum angular momentum couplings that will be required. The maximum symbol is therefore set by $M = \max(j_n, j_p)$:

$$
\begin{Bmatrix} 2M & M & M \\ 2M & M & M \end{Bmatrix}. \tag{5.14}
$$

For large calculations, storing all symbols up to the symbol (5.14) requires $S = 8(M + 1)^6$ floating point (4) numbers. For $M = 20$ that is approximately 2.7 GB of memory. Doubling to $M = 40$ requires 152 GB of memory. Somewhat arbitrarily I chose $M = 20$ as an upper limit for the pre-cached symbols, and so:

$$
M = \max(j_n, j_p, 20). \tag{5.15}
$$

Loop-optimized spooling

The second strategy follows the general theme of this section, which is to be clever about when each piece of data will be needed for the computation. Since PANASh is a J-scheme code, the matrix eigenvalue problem is solved independently for each J. This reduces the number of indices by one, so already the storage requirement is reduced to $S = 8(M + 1)^5$. For $M = 20$ that's 0.13 GB, already a significant reduction from the 2.7 GB before.

We can also improve the computational efficiency of accessing the cached data by improving data locality. In other words, I will arrange the data in an array so that values which are expected to be used sequentially are nearby in physical memory. Computing the matrix elements of the Hamiltonian is the most expensive operator in PANASh. I can examine the loop structure of this part of the calculation to determine what order the 6-j symbols should be arranged in memory. I call this process *spooling* (see Appendix A.3), which is a more

specific version of array flattening in computer science.

For the Hamiltonian matrix elements we need the symbols shown in equation (5.13). In the general cache the 6-j symbols are stored in a rank-6 array. I construct a new flattened (rank-1) array called 'sixjspool', and loop over all its 5+1 arguments: J, K, j_{pf}, j_{nf}, j_{pi}, j_{ni}. The loops are nested in order corresponding to the computation of the Hamiltonian matrix elements. The order is

$$j_{pf} < j_{nf} < j_{pi} < j_{ni} < K, \tag{5.16}$$

where $j_{pf} < j_{nf}$ means that j_{nf} is nested under j_{pf}; j_{nf} will increment more frequently than j_{pf}. I therefore spool the rank-6 array into the rank-1 array with the above index ordering.

5.3.2   Solution transition densities

In this section, I discuss the efficient calculation of the one-body transition densities for the solutions wave functions obtained by PANASh. To be clear, these are not the OBTD matrices used to compute the Hamiltonian matrix elements but are the OBTD matrices of the solutions of the Hamiltonian. These are used to compute the expectation values of operators on the solution wave functions.

The expressions for the one-body transition density (OBTD) matrices using PANASh formalism are:

$$\rho_{ack}^{fi(p)} = (-1)^{J_i+k}[J_f][J_i] \sum_{p_f p_i n_f} (-1)^{j_{pf}+j_{nf}} \begin{Bmatrix} j_{pf} & J_f & j_{nf} \\ J_i & j_{pi} & k \end{Bmatrix} \psi_{p_f n_f}^f \psi_{p_i n_f}^i \rho_{ack}^{p_f p_i(p)} \tag{5.17}$$

$$\rho_{ack}^{fi(n)} = (-1)^{J_f+k}[J_f][J_i] \sum_{n_f n_i p_f} (-1)^{j_{pf}+j_{ni}} \begin{Bmatrix} j_{nf} & J_f & j_{pf} \\ J_i & j_{ni} & k \end{Bmatrix} \psi_{p_f n_f}^f \psi_{p_f n_i}^i \rho_{ack}^{p_f p_i(n)}. \tag{5.18}$$

118

In these, we have already applied factors of $\delta_{nf,ni}$ in the first equation and $\delta_{pf,pi}$ in the second equation.

The scaling of this calculation can be understood by counting the orders of the indices. There is an implicit loop on a, c, k, f, and i. See Table 5.3.

Table 5.3: Scaling of each index appearing in equations (5.17) and typical values for their order-of-magnitude. The scaling parameters are: n = number of single-particle levels, N_k = number of couplings allowed by angular momentum conservation, N = number of wave functions for which transitions are calculated, m_p = number of proton basis factors, m_n = number of neutron basis factors.

Index	Scaling	Order
a	n	10
c	n	10
k	N_k	10
f	N	10^2 - 10^3
i	N	10^2 - 10^3
p_f	m_p	10^2 - 10^3
p_f	m_p	10^2 - 10^3
n_f	m_n	10^2 - 10^3

The nominal compute complexity for the proton OBTD matrices is

$$C^{(p)} = N_k N^2 m_p^2 m_n n^2, \tag{5.19}$$

where each symbol is explained in Table 5.3. I will work with the proton density explicitly. Equivalent arguments can be made for the neutron OBTD by exchanging p and n. Assuming $m_p \approx m_n$ (i.e. a similar number of proton and neutron factors), then the complexity $C = N_K N^2 m^3 n^2$.

Complexity is conserved, but we can often make some trade between compute complexity and memory complexity. In this case, I see a way to reduce the compute complexity at the cost of pre-computing one of the three sums: the n_f sum occurs less frequently than the

other two summed indices. I define:

$$P^{fi}_{kp_f p_i} = (-1)^{j_{pf}} \sum_{n_f} (-1)^{j_{nf}} \begin{Bmatrix} j_{pf} & J_f & j_{nf} \\ J_i & j_{pi} & k \end{Bmatrix} \psi^f_{p_f n_f} \psi^i_{p_i n_f} \tag{5.20}$$

$$N^{fi}_{kn_f n_i} = (-1)^{j_{ni}} \sum_{p_f} (-1)^{j_{pf}} \begin{Bmatrix} j_{nf} & J_f & j_{pf} \\ J_i & j_{ni} & k \end{Bmatrix} \psi^f_{p_f n_f} \psi^i_{p_f n_i}, \tag{5.21}$$

where $\psi^i_{p_i n_i}$ are the coefficients of the solution wave functions in the PANASh basis $\{|p\rangle |n\rangle\}$. From these, we obtain the much simpler expression for the densities in terms of these factors:

$$\rho^{fi(p)}_{ack} = (-1)^{J_i + k} [J_f][J_i] \sum_{p_f p_i} P^{fi}_{kp_f p_i} \rho^{p_f p_i (p)}_{ack} \tag{5.22}$$

$$\rho^{fi(n)}_{ack} = (-1)^{J_f + k} [J_f][J_i] \sum_{n_f n_i} N^{fi}_{kn_f n_i} \rho^{p_f p_i (n)}_{ack}. \tag{5.23}$$

The compute complexity of this calculation is reduced by a factor of m_p or m_n, so that the new complexity is:

$$C^{(p)'} = N_k N^2 m_p^2 n^2, \tag{5.24}$$

$$C^{(n)'} = N_k N^2 m_n^2 n^2. \tag{5.25}$$

Overall speedup

The compute complexity for N and P is spent "upfront", i.e. beforehand and stored in memory. Each has a compute complexity of

$$C^{(x)}_{\text{Upfront}} = N_k N^2 m_x^3, \tag{5.26}$$

where $x = n, p$.

To estimate the upfront cost of storing P and N, we compare it as a fraction of C':

$$\frac{C_{\text{Upfront}}}{C'} = \frac{m_x}{n^2}. \tag{5.27}$$

If $m_x = 1000$ and $n = 10$, then the upfront cost is about $10\times$ the density compute cost. The benefit of this large upfront cost comes from the overall complexity decrease:

$$\frac{1}{\text{Speedup}^{(x)}} = \frac{C^{(x)'} + C^{(x)}_{\text{Upfront}}}{C^{(x)}} = \frac{N_k N^2 m_x^2 n^2 + N_k N^2 m_x^3}{N_K N^2 m_x^2 m_{x'} n^2} = \frac{n^2 + m_x}{n^2 m_{x'}}. \tag{5.28}$$

For typical values of $n \approx 10$ and $m_x \approx 100$, this is a complexity reduction of 0.02. Under 'ideal conditions' this means a speedup of 50. In general, if n dominates, the speedup goes like m_x'; if m_x dominates, the speedup goes like n^2.

Induced memory cost

Whether this is a practical method also depends on the memory requirements of storing P and N. Storing all indices for $P^{fi}_{kp_f p_i}$ would require memory that scales like

$$S = N_k N^2 m_p^2. \tag{5.29}$$

For typical values, this could easily exceed $(10)(100^2)(1000^2)(4 \cdot 10^{-9})$ GB ≈ 400 GB. This is way too much. But we can get around this by computing subsets of $P^{fi}_{kp_f p_i}$ on-the-fly/*in-situ* in a loop nest with the density calculation. If we share the loops f, i, and k, then we are now dealing with

$$P^{(fik)}_{p_f p_i} = (-1)^{j_{pf}} \sum_{n_f} (-1)^{j_{nf}} \begin{Bmatrix} j_{pf} & J_f & j_{nf} \\ J_i & j_{pi} & k \end{Bmatrix} \psi^{(f)}_{p_f n_f} \psi^{(i)}_{p_i n_f} \tag{5.30}$$

$$N_{n_f n_i}^{(fik)} = (-1)^{j_{ni}} \sum_{p_f} (-1)^{j_{pf}} \begin{Bmatrix} j_{nf} & J_f & j_{pf} \\ J_i & j_{ni} & k \end{Bmatrix} \psi_{p_f n_f}^{(f)} \psi_{p_f n_i}^{(i)} \tag{5.31}$$

$$\tag{5.32}$$

where the indices in parenthesis (fik) are implicit based on the loop iteration and not stored. The storage scaling is now only m_x^2, e.g. something like $(1000^2)(4 \cdot 10^{-9})$ GB ≈ 4 kB.

5.3.3 Improved computation of residual p-n interaction

The preceding section explained in detail how we drastically improve the efficiency of computing the OBTD matrices of our solution wave functions. The same approach is also applied to improve the efficiency of the Hamiltonian matrix elements. This section explains the basic details but the principles are the same as above.

The matrix elements of the pn-part of the Hamiltonian (4.50) can be written in the simplified form:

$$\langle f | \hat{H}_J^{(pn)} | i \rangle = (-1)^{j_{pi} + j_{nf} + J} \sum_K \begin{Bmatrix} J & j_{nf} & j_{pf} \\ K & j_{pi} & j_{ni} \end{Bmatrix} \sum_{bd} (2K+1) \sum_{ac} \rho_{ac;K}^{p_f p_i} W_{ac,bd;K}^{(pn)} \rho_{bd;K}^{n_f n_i}$$

$$= (-1)^{j_{pi} + j_{nf} + J} \sum_K \begin{Bmatrix} J & j_{nf} & j_{pf} \\ K & j_{pi} & j_{ni} \end{Bmatrix} \sum_{bd} P_{bd;K}^{p_f p_i} \rho_{bd;K}^{n_f n_i} \tag{5.33}$$

where the reduced one-body density matrix elements of the factor wave functions $|x_\chi\rangle$ are defined as

$$\rho_{ij;K}^{\chi' \chi (x)} \equiv \langle x'_\chi || \hat{\rho}_{ij;K}^{(x)} || x_\chi \rangle / \sqrt{2K+1}, \tag{5.34}$$

and where the partial sum $P_{bd;K}^{p_f p_i}$ is defined as:

$$P_{bd;K}^{p_f p_i} = (2K+1) \sum_{ac} \rho_{ac;K}^{p_f p_i} W_{ac,bd;K}^{(pn)}. \tag{5.35}$$

The compute cost of all Hamiltonian matrix elements $\langle f | \hat{H}_J^{(pn)} | i \rangle$ scales like

$$C = N_K m_p^2 m_n^2 n^4, \tag{5.36}$$

where n is the number of single-particle orbits, $m_{(p/n)}$ is the number of proton/neutron-subspace factors, and N_K is the number of allowed angular momentum combinations. We pre-compute (5.35) at a compute cost of

$$C_{\text{Upfront}} = N_K m_p^2 n^4, \tag{5.37}$$

and memory cost

$$S = N_k m_p^2 n^2. \tag{5.38}$$

The remaining cost of the Hamiltonian matrix elements is

$$C' = N_K m_p^2 m_n^2 n^2. \tag{5.39}$$

The total compute scaling is then

$$C_{\text{Upfront}} + C' = N_k m_p^2 n^2 (n^2 + m_n^2), \tag{5.40}$$

which results in an overall speedup of

$$\text{Speedup} = \frac{C}{C_{\text{Upfront}} + C'} = \frac{m_n^2 n^2}{n^2 + m_n^2}. \tag{5.41}$$

5.4 Joining one-body transition density matrices

A key ingredient of the proton-neutron approximate shell model is the set of one-body transition density (OBTD) matrices of the component wave functions. OBTD matrices are used to calculate the interaction matrix elements of the proton-neutron part of the Hamiltonian. It is common to read the density matrices from multiple sources. There are both practical and physics-based reasons for this. First, it is sometimes not practical to obtain *all* matrix elements in one calculation due to resource restrictions. Sometimes they must be broken up into separate, smaller calculations. Second, for reasons discussed in the following subsection 5.4.1 it is sometimes not possible to obtain all OBTD matrix elements from a fixed-M calculation.

We have an established a need to combine sets of OBTD matrix elements from different sources, and so I have developed algorithms to do this in PANASh. We use another shell model code, `BIGSTICK`, to calculate the reduced matrix elements of the OBTD operators. A reduced matrix element of a tensor operator is a way to represent the matrix element of an operator without regard to the orientation in space. This is accomplished with the Wigner-Eckart theorem [74]. For a tensor operator $\hat{O}_{KM}$,

$$
\begin{aligned}
\langle J_f M_f | \, \hat{O}_{KM} \, | J_i M_i \rangle &= [J_f]^{-1} (J_i M_i K M | J_f M_f) \, \langle J_f | | \hat{O}_k | | J_i \rangle \\
&= (-1)^{J_f - M_f} \begin{Bmatrix} J_f & K & J_i \\ -M_f & M_K & M_i \end{Bmatrix} \langle J_f | | \hat{O}_k | | J_i \rangle \,,
\end{aligned}
\tag{5.42}
$$

where $[j] \equiv \sqrt{2j+1}$ and the six-argument array is the six-J symbol. In the case of OBTD operators,

$$
\langle J_f | \, | [\hat{c}_a^\dagger \otimes \tilde{c}_b]_K | \, | J_i \rangle = [J_f] (J_i M_i K M | J_f M_f)^{-1} \, \langle J_f M_f | \, [\hat{c}_a^\dagger \otimes \tilde{c}_b]_{KM} \, | J_i M_i \rangle \,,
\tag{5.43}
$$

where the fermion operators $\hat{c}$ create either proton or neutrons in pure or mixed isospin states. BIGSTICK prints these matrix elements to file in a plain text format described in Appendix B.4:

$$\rho_{abK}^{fi} = \frac{1}{\sqrt{2K+1}} \langle J_f || [\hat{c}_a^\dagger \otimes \tilde{c}_b]_K || J_i \rangle. \tag{5.44}$$

If we use multiple sources of OBTD matrix elements, we seek to find the joint set of those matrix elements to provide all required combinations of i, f, a, c, k:

$$\{\rho_{ac;K}^{fi}\} = \{\langle \Psi_1^f || \hat{\rho}_{ac;K} || \Psi_1^i \rangle\} \cup \{\langle \Psi_2^f || \hat{\rho}_{ac;K} || \Psi_2^i \rangle\}. \tag{5.45}$$

Level matching

When PANASh is run, the user first provides a list of single particles orbits $\{a : n_a, l_a, j_a\}$ and wave functions $\{i : E_i, J_i, \pi_i\}$. When the OBTD files are read in, the wave functions may have slightly different values of E_i, and in poorly converged solutions, slightly different J_i. PANASh first performs a level matching routine which tries to identify each level in the OBTD file to the reference levels. Some tolerance is set for the allowed difference in energy levels: $5 \cdot 10^{-6} \times E_i$. The level spins J_i are forced to be their nearest integer or half-integer values, and must match the reference level. The parity of the states must also match.

Read-in precedence

Currently, as PANASh reads in new OBTD files, logic is applied to find matrix elements which are missing and fill them in. Elements are 'missing' if their value is less than some

tolerance $\epsilon = 5 \cdot 10^{-6}$. The pseudo code each time a new OBTD is read-in is:

$$\{\rho_{ac;K}^{fi}\} = \begin{cases} \rho_{ac;K}^{fi}(\text{new}), & \rho_{ac;K}^{fi}(\text{old}) < \epsilon < \rho_{ac;K}^{fi}(\text{new}) \\ \\ \rho_{ac;K}^{fi}(\text{old}), & \text{elsewhere.} \end{cases} \tag{5.46}$$

All values less than ϵ are also forced to be zero. The code for this logic is something like:

```
! Where data is missing, fill it in
where (abs(rho_old) < density_tol .and. abs(rho_new) > density_tol)
    !rho_new = rho_new
elsewhere
    rho_new = rho_old
end where
```

In some cases which are fairly common, a phase difference exists between the old and new matrix elements. This must be corrected for. This is discussed later in section 5.4.2.

5.4.1 Accidental zeros in the Wigner-Eckart formula

This section describes a symmetry of vector coupling coefficients which causes the Wigner-Eckart theorem to lead us astray. This leads to the necessity to read in multiple OBTD matrices from different solutions of the Schrödinger equation.

A basic time-reversal symmetry of vector coupling coefficients is [74]:

$$(j_a m_a j_b m_b | JM) = (-1)^{j_a + j_b - J}(j_a - m_a j_b - m_b | J - M). \tag{5.47}$$

Consider the special case $m_a = m_b = M = 0$. Then,

$$(j_a 0 j_b 0 | J0) = (-1)^{j_a + j_b - J}(j_a 0 j_b 0 | J0), \tag{5.48}$$

and we are restricted to

$$(j_a 0 j_b 0 | J 0) = \begin{cases} (j_a 0 j_b 0 | J 0), & j_a + j_b - J \text{ is even} \\ \\ 0, & j_a + j_b - J \text{ is odd,} \end{cases} \tag{5.49}$$

since if $j_a + j_b - J$ is odd we have $X = -X$. This means that computing the reduced density matrix element $\langle J_f || \hat{O}_k || J_i \rangle$ with the Wigner-Eckart theorem in an $M = 0$ basis may give what is called an 'accidental zero'. In such cases, we must recalculate the reduced density matrix element in the $M = 1$ basis (since any M will satisfy the theorem). (We cannot compute only in the $M = 1$ basis, since then we would be missing all states with $J = 0$.)

Importantly, these accidental zeros only occur with even-A systems. This is clear when considering that J_i and J_f are the total angular momenta of the initial and final states of the system. An even number of particles always couple up to an integer total angular momentum, while an odd number of particles always couple up to a half-integer total angular momentum.

Our coupled-basis shell model calculations rely on the one-body transition densities of the basis factors. The preceding argument implies that for even numbers of protons or neutrons only, we must supply reduced density matrices with both $M = 0$ and $M = 1$ wave functions. For odd numbers of protons or neutrons, $M = 1/2$ is sufficient.

5.4.2 Phases inconsistencies between component wave functions

We must carefully consider the phases of the wave functions used to compute the component OBTD matrix elements. The overall sign of a solution to the Schrödinger equation is undetermined: if $|\Psi_1\rangle$ is an eigenstate of $\hat{H}$, then so is $|\Psi_2\rangle = -|\Psi_1\rangle$. This phase carries over into the OBTD matrix elements. If we use only one set of solutions of $\hat{H}$ to obtain the

OBTD matrix elements, then there is no problem.

Dealing with phase differences is nontrivial since for two different sets of matrix elements,

$$\{\rho_{ac;K}^{fi(1)}\} = \{\langle \Psi_1^f | |\hat{\rho}_{ac;K}| |\Psi_1^i\rangle\} \tag{5.50}$$

and

$$\{\rho_{ac;K}^{fi(2)}\} = \{\langle \Psi_2^f | |\hat{\rho}_{ac;K}| |\Psi_2^i\rangle\}, \tag{5.51}$$

we can have three distinct possible phase signatures. First, note that each of the four wave functions in a given comparison (Ψ_1^f, Ψ_2^f, Ψ_1^i, Ψ_2^i) has an independent and essentially random sign, but only the signs of the products $\Psi_1^f\Psi_1^i$ and $\Psi_2^f\Psi_2^i$ determine the overall phase of a set of matrix elements determine by f, i, a, c, K. We can therefore consider the matrix elements as belonging to blocks of fixed i, f, which I will denote $(fi1)$ and $(fi2)$. Matrix elements from block $(fi1)$ must have the same phase as block $(fi2)$. If solutions 1 and 2 are in phase or out of phase, then

$$\text{sign}(\rho_{ac;K}^{(fi1)} \cdot \rho_{ac;K}^{(fi2)}) = \pm 1. \tag{5.52}$$

In the case of a negative phase signature, we simply substitute $\rho_{ac;K}^{fi(2)} \rightarrow -\rho_{ac;K}^{fi(2)}$. However, if one of the matrix elements is missing due to accidental zeros (section 5.4.1), then we can have the situation that

$$(\rho_{ac;K}^{fi(1)} \cdot \rho_{ac;K}^{fi(2)}) = 0. \tag{5.53}$$

I construct a third array called the phase mask which is defined as:

$$M_{acK}^{(fi)} = \begin{cases} +1, & \rho_{acK}^{(fi1)}\rho_{acK}^{(fi2)} > \epsilon \\ -1, & \rho_{acK}^{(fi1)}\rho_{acK}^{(fi2)} < -\epsilon \\ 0, & |\rho_{acK}^{(fi1)}\rho_{acK}^{(fi2)}| < \epsilon. \end{cases} \tag{5.54}$$

A "+1" is found in cases where both matrix elements are present and in phase. A "-1" is found in cases where both matrix elements are present and out of phase. And importantly, a "0" is found in cases where one of the matrix elements is missing (zero) from the one of the data sets but is present in the other.

The phase mask array serves two purposes. The first is the trivial identification of phase mismatches. If M contains -1's, then the sign is opposite between the two density matrix blocks, and the newer one is updated to match the existing data. If M contains +1's, no change is needed.

Under ideal conditions, entries would be either all 1's and 0's (signs match and some missing matrix elements are filled in), or all -1's and 0's (signs must be corrected for the missing matrix elements that are filled in). However, due to rounding errors of very small matrix elements, it is routine to encounter a third case: *most* entries of M are all the same sign and zeros, but a few are of opposite signs: both 1's and -1's appear. I call this a phase inconsistency.

Phase inconsistencies indicate some sort of problem with the density matrices being analyzed. One possibility is that the density matrix results being read in are not fully converged. Another possibility is that levels in the file have been incorrectly identified. This is more likely for nearly degenerate states in a region of high level density. In some cases, highly excited states with large model spaces simply have such small amplitudes that rounding errors dominate.

When phase inconsistencies are encountered, it's best to reevaluate the data and check for signs of non-convergence. PANASh will continue running despite the presence of phase inconsistencies after printing appropriate warnings. To continue, a phase must be selected. To choose a phase, I simply compute the sum of the phase mask M, taking the phase of the majority of matrix elements:

$$\phi_{\text{inconsistent}} = \text{sign}(\sum_{acK} M_{acK}). \tag{5.55}$$

Phase inconsistency or not, the phase ϕ simply multiplies the new density matrix block before it is used to fill in the missing matrix elements in the existing data.

5.4.3 Binary format for one-body density matrices

In this section, I describe the new format I designed for storing OBTD matrix elements, and benchmark the results using code I wrote to convert between the old and the new format.

The number of OBTD matrix elements scales like $N^2 n^2 k$, where N is the number of wave functions, n is the number of one-body orbits, and k is the number of allowed couplings. In a typical case, we might have $N = 10^3$, $n = 10$, and $k = 10$. This results in something like 10^9 numbers or 4 GB of memory. The standard format for storing the OBTD matrices was designed to be human-readable and is therefore not very compact. It is also not very efficient to read and write these files. I found this particularly hindering when running on a large machine with a 24-hour runtime limit. I discovered that over an hour of that time was being used just to read in the component OBTDs for the calculation. I was motivated to find a more efficient data structure.

Tables 5.4 and 5.5 show some example times for a fairly large OBTD matrix. The examples are for the proton (matrices A and B) and neutron (matrix C) component wave functions

used for a PANASh calculation of ^{79}Rb in the pfg valence space. There are $r = 3,700$ of each type and $n = 4$ one-body orbits (single-particle states). The cumulative time to read in these three sets of density matrices from plain text format is roughly 58 minutes. By switching to the binary density format, the time is only 5 minutes. Most of this time is actually not reading the file, but parsing the sparse array into the data structure used within PANASh. The raw IO time is only about 20 seconds for all three files. The long IO time of the plain text file is in large part due to the complexity of the parsing required.

Table 5.4: Comparison of OBTD matrix file sizes using the standard human-readable format versus the simple binary format. The three cases A, B, and C are three different OBTD densities. All three are in the pfg model space. A and B are both $Z = 0$, $N = 14$ systems with $M = 0, 1$, respectively. C is $Z = 9$, $N = 0$ with $M = 1/2$. The columns are number of matrix elements in millions (#ME), Nominal storage for the matrix elements as kind=4 floats in gigabytes (Nom.), the actual storage used by the plain-text formatted file (Plain), the actual storage used by the binary formatted file (Plain), and the reduction factor for using the binary format over the plain-text format (reduction).

Density matrix	#ME ($\times 10^6$)	Nom. (GB)	Plain (GB)	Binary (GB)	Reduction
A	132	0.53	12.9	3.75	3.5
B	244	1.95	22.5	3.90	5.8
C	246	1.97	22.4	3.93	5.7

Table 5.5: Comparison of OBTD matrix I/O times using the standard human-readable format versus the simple binary format. The three cases A, B, and C are three different OBTD densities. All three are in the pfg model space. A and B are both $Z = 0$, $N = 14$ systems with $M = 0, 1$, respectively. C is $Z = 9$, $N = 0$ with $M = 1/2$.

Density matrix	#ME ($\times 10^6$)	Plain (s)	Binary (s)	Reduction
A	132	810	100	7.8
B	244	1400	110	13
C	246	1300	100	13

The plain-text format for OBTD as produced by the `BIGSTICK` shell model code is described in Appendix B.4. It can be noted that a significant number of characters are used to make the file easily readable. This comes at the cost of significant storage cost for the files, as well as significant time to read and write the files. The main source of improvement is simply using a binary-format (in Fortran, 'unformatted' files) and writing entire arrays with one command. In fact, these two features are so efficient that it becomes faster to store all of the

nontrivial zeros in the sparse OBTD matrix which are omitted from the plain-text format.

The conversion tool I wrote works by first reading in the the necessary inputs. These are (1) labels of the states involved, (2) labels of the single-particle orbits, and (3) the plain text density matrix. These are all read from the (.dres) file in the usual way with a plain-text parsing code. Then, the number of allowed matrix elements is counted. That is, the number of matrix elements after conservation of angular momentum and parity are taken into account. For a density matrix element

$$\rho_{ac;K}^{if} = \langle \Psi^f | |\hat{\rho}_{ac;K}| | \Psi^i \rangle , \tag{5.56}$$

that is all matrix elements which satisfy the triangle rules $\Delta(J_i, K, J_f)$, $\Delta(j_a, j_c, K)$, and parity conservation $\pi_i \pi_f = \pi_a \pi_c$. Next, one-index arrays are allocated to hold this number of elements for both the proton and neutron densities, and the matrix elements are transferred using nested loops. The order of the nested loops and the enforcement of the conservation rules takes this form:

```
m = 0
do i = 1, N
  do f = 1, N
    do a = 1, n
      do b = 1, n
        check_parity(i, f, a, b)
        do K = kmin, kmax
          check_triangle(i, f, k)
          check_triangle(a, b, k)
          m = m + 1
          rec_p(m) = rho_p%states(i,f)%coupling(K)%operator(a,b)
          rec_n(m) = rho_n%states(i,f)%coupling(K)%operator(a,b)
        end do
      end do
    end do
  end do
end do
```

Where 'rec_p' and 'rec_n' are the one-index arrays, previously allocated. In practice, the 'kmin' and 'kmax' are chosen to automatically satisfy the triangle rules, so the 'check_triangle' subroutines are not needed. Finally, four sets of unformatted write statements are made.

The pseudo code looks something like this:

```
write ( binfile ) nstates , norbits , ncombo
do state = 1 , nstates
   write ( binfile ) states ( state )%E, states ( state )%Ex, states ( state )%J,
      states ( state )%T
end do
do state = 1 , norbits
   write ( binfile ) orbits ( state )%i, orbits ( state )%n, orbits ( state )%l, orbits
      ( state )%jx2
end do
write ( binfile ) rec_p
write ( binfile ) rec_n
```

The read statement is equivalent. 'rec_p' and 'rec_n' contain the OBTD matrix elements with 'ncombo' number of kind=4 reals. 'states' and 'orbits' are Fortran derived types used to store the 'nstates' wave function and 'norbits' single-particle orbits labels.

5.5   Hybrid parallel implementation and performance

I parallelized PANASh from its original serial version using a hybrid approach. openMP is a shared memory specification for parallel programming that automatically handles thread creation and work sharing. Generally, core components of a code can be parallelized with openMP simply by placing directive statements around do loops. The Message Passing Interface (MPI) is a distributed memory framework that requires more careful implementation. It relies on independent copies of the program communicating with each other to distribute the work. By implementing both, a variety of architecture can be used more efficiently.

5.5.1 openMP

I implemented a fairly crude parallelization of the matrix-matrix product in the block-Lanczos algorithm of PANASh. The core operation which is parallelized is:

$$\boldsymbol{W} = \boldsymbol{HV}, \tag{5.57}$$

where $\boldsymbol{H}$ is the Hamiltonian matrix and $\boldsymbol{V}$ is the block of Lanczos vectors. The code for this operation (the in-memory-Hamiltonian version) is the following:

```
            !$OMP parallel do schedule(guided, 5)&
            !$OMP private(bra,pf,nf,pfj,nfj,sector2) &
            !$OMP private(ket,pi,pij,ni,sector4,phase,hij,a) &
            !$OMP private(thread_id)
            do bra = brastart, brastop, 1
#ifdef _openMP
               thread_id = omp_get_thread_num()
#endif
               do ket = 1, bra - 1
                 hij = ham(ket,bra)
                 ! bra, ket: w(a,bra) = sum_ket H(ket, bra) * vk(a, ket)
                 do a = 1, blocksize
                   w_dist(a, bra, thread_id) = w_dist(a, bra, thread_id) &
                         + hij * blvecs(a, ket, k)
                 end do
                 ! ket, bra: w(a, ket) = sum_bra H(ket, bra) * vk(a, bra)
                 do a = 1, blocksize
                   w_dist(a, ket, thread_id) = w_dist(a, ket, thread_id) &
                         + hij * blvecs(a, bra, k)
                 end do
               end do ! ket
               hij = ham(bra,bra)
               do a = 1, blocksize
                 w_dist(a, bra, thread_id) = w_dist(a, bra, thread_id) &
                         + hij * blvecs(a, bra,k)
               end do
             end do ! bra
```

There are several things to note. First, the transpose of the Hamiltonian is stored, so that the inner loop iterates consecutively through the row-major array in memory. This significantly improves cache performance. Second, the $\boldsymbol{W}$ array is fragmented into `omp_num_threads()` pieces, indicated by the final index of the rank-3 array. This allows each openMP thread to

work on its own partial sum without interfering with the others. Normally this could more efficiently be accomplished with openMP's built-in sum-reduction directive, but this tends to fail for very large arrays (more than 2^{31} elements). Third, the bra-ket nested loops are upper triangular, taking advantage of the Hermitian symmetry of the Hamiltonian.

Other sections of the code are also openMP parallel, such as the pre-computed partial sums discussed in previous section, as well as computation of the solution-OBTD matrices.

I provide some sample parallel scaling data to demonstrate typical parallel performance of PANASh. The following calculations were done on a workstation with 1TB of shared memory and two AMD EPYC 7643 48-Core Processors. For a benchmark case, I calculated the first 5 $J^\pi = 3^+$ states of Ce-132 with the GCN5082 model. The dimension is 128k and the block size is 10, iterating until 5 states are converged. Time total includes reorthogonalization steps and convergence checks. The total time depends on the total number of iterations performed, which has some randomness depending on the initial pivot block. Thus, the average time per iteration is a more reliable metric. Efficiency is the ratio of MatMat speedup to thread count.

Table 5.6: Performance of PANASh on a workstation computer with shared-memory architecture using openMP.

Hamiltonian stored in-memory. Peak memory: 67 GB			
openMP threads	Time total (s)	Time/Iter (s)	Efficiency
1	2200	67	1.0
2	1200	36	0.93
4	740	24	0.70
8	380	12	0.70
16	210	6.8	0.62
32	130	3.9	0.54
64	88	2.9	0.36
96	75	2.3	0.30
Hamiltonian computed on-the-fly. Peak memory: 5 GB			
openMP threads	Time total (s)	Time/Iter (s)	Efficiency
64	470	11	-
96	340	14	-

5.5.2 MPI

I use MPI to distribute the top-level loop of the matrix-matrix product previously discussed. The algorithm is currently designed assuming on-the-fly matrix elements which does not require much memory compared to storing the entire Hamiltonian. To make MPI practical for the in-memory solver, the Hamiltonian would need to be scattered amongst the ranks rather than replicated (broadcast) across all ranks, as is currently done. The benefit of this less sophisticated parallel algorithm (besides ease of implementation) is that we can take advantage of the Hermiticity of the Hamiltonian matrix, yields a nearly factor 2 speedup.

As mentioned, the top level loop is broken up amongst the MPI ranks. Each rank is responsible for a range of loop iterations. Hermiticity means we can skip almost half of the total iterations, but this makes load balancing is less straightforward. The approach I have adopted is to compute the a work-scaling factor for each outer-loop iteration as:

$$\text{nme(bra)} = \text{bra(bra}+1)/2, \tag{5.58}$$

which is the number of upper-triangular matrix elements in the bra$^{\text{th}}$ row. I compute the desired work per rank as $(1/nranks)\sum_{\text{bra}=1}^{\text{dim.}}\text{nme(bra)}$. Then for each MPI rank, I add assigned rows (bra's) to the rank until the desired amount of work is assigned. An example of this algorithm distributing the work of a dimension 128,277 problem with 16 MPI ranks:

```
                   begin - end     (toal nme)
Rank   1 assigned      1 -  32069 (514226415)

Rank   2 assigned  32070 -  45353 (514243566)

Rank   3 assigned  45354 -  55546 (514236850)

Rank   4 assigned  55547 -  64139 (514230899)

Rank   5 assigned  64140 -  71710 (514260175)
```

```
Rank   6 assigned  71711 -  78555 (514285385)

Rank   7 assigned  78556 -  84849 (514235535)

Rank   8 assigned  84850 -  90708 (514297161)

Rank   9 assigned  90709 -  96211 (514310380)

Rank  10 assigned  96212 - 101415 (514225454)

Rank  11 assigned 101416 - 106365 (514257975)

Rank  12 assigned 106366 - 111095 (514295265)

Rank  13 assigned 111096 - 115632 (514332468)

Rank  14 assigned 115633 - 119997 (514262475)

Rank  15 assigned 119998 - 124209 (514299942)

Rank  16 assigned 124210 - 128277 (513558558)
```

The memory scaling of this MPI algorithm for this example is roughly $4.5 + 1.4$ N (GB), where N is the number of MPI ranks. Of this 1.4 GB, about half are the Lanczos vectors. The rest are pre-computed factors such as vector coupling coefficients and OBTDs of the factor wave functions.

Table 5.7: Performance of PANASh on a workstation computer with shared-memory architecture using MPI.

Hamiltonian computed on-the-fly.				
MPI ranks	Time total (s)	Time/Iter (s)	Efficiency	Peak memory (GB)
1	15000	450	1.0	4.5
16	1000	34	0.83	26
32	580	20	0.70	48
64	310	11	0.64	94
96	280	8.5	0.55	130

While the advantages of the PANASh code lie in its physics-based approximation scheme, this chapter has shown how the computational aspects and implementation details be a deciding factor for the success of a shell model method. The performance effects of data structures, algorithms, and parallel programming can easily add up to the total gains of the approximation itself. This concludes the discussion of the computational aspects of PANASh.

Chapter 6

Statistical Properties of Nuclei

This chapter is concerned with nuclear level densities and gamma-ray strength functions, the two most important statistical properties of nuclei for the subject of the next part of this dissertation: statistical nuclear reactions. Nuclear level densities are the average number of levels available for a nucleus to occupy per unit MeV. Gamma-ray strength functions are a more complicated topic, but they are related to the average electromagnetic decay width, or probability, as a function of the energy of the transition. In this context "statistical" means we are dealing with energy-averaged quantities that describe typical behaviour of a nucleus without attention to specific states or transitions.

As will be discussed at length in Part II, statistical nuclear reactions fall under the theoretical umbrella of Hauser-Feshbach (HF) theory. What we need to know for this chapter on statistical properties of nuclei is that HF theory requires as input both nuclear level densities and gamma-ray strength functions. In the absence of experimental data, broad studies of nuclear reactions rely on systematic trends in these statistical quantities which are fit to data for nuclei near stability. To improve such models, we look to microscopic models like the shell model to provide theory predictions for these reaction model inputs, especially where

data are unavailable.

Both nuclear level densities (NLDs) and gamma-ray strength functions (GSFs) can be directly calculated starting from a complete list of the nuclear wave functions and their transition probabilities up to some maximum excitation energy. This means a sufficiently large shell model calculation can provide these statistical quantities by simply computing statistics on its solutions.

6.1 Nuclear level densities

Level densities can be thought of as a probability density function (PDF) for the number of levels (bound states or resonances) of a nucleus between two energies. For example, the cumulative number of levels as a function of excitation energy E_{ex}, spin (total angular momentum) J, and parity π of the levels is given by the cumulative level density (CLD):

$$\text{CLD}(E_{ex}, J^\pi) = \int_0^{E_{ex}} \rho(E, J^\pi) dE, \tag{6.1}$$

in terms of the level density $\rho(E, J^\pi)$. I say approximately because the nuclear level density is a continuous approximation of the integer number of levels.

In energy regimes and for nuclei where we can count levels (experimentally or from the shell model), the nuclear level density can itself be 'approximated' as the number of levels per energy bin of width ΔE. If each $\text{bin}(i)$ has a domain $(E_i, E_i + \Delta)$, then we count the levels with energies $\tilde{E}_j$ in each bin:

$$\rho(E_i, J^\pi) \approx \frac{1}{\Delta E} \sum_{\tilde{E}_j \in \text{bin}(i)} 1. \tag{6.2}$$

This will only work well where the level density is sufficiently high as to have a statistically

significant number of levels in each bin.

In this section I present an example calculation of nuclear level densities using both a full configuration interaction (FCI) shell model calculation and using PANASh. The main figure to note is Figure 6.1. The case is ^{78}Ge, which has 51 experimentally measured levels [48]. Of these, only 12 have a complete level scheme, and 5 have assigned spin and parity. This highlights the need for theoretical predictions of the nuclear level densities, which often have limited experimental data.

The model space used is the pfg model space ($f_{5/2}, p_{3/2}, p_{1/2}, g_{9/2}$ valence orbitals above a ^{56}Ni core) with the JUN45 interaction [147]. The FCI calculation includes all possible many-body configurations in the model space. The $M^\pi = 0^+$ calculation has dimension $1,831,531$ and the $M^\pi = 0^-$ has dimension $1,828,324$. Each were solved with Block Lanczos to obtain the 500 lowest states of each parity. The results are shown in Figure 6.1.

The same model and interaction was applied using our PANASh shell model code. The proton and neutron subspace dimensions are both 701. This is trivially solved even with an exact solver. The PANASh calculation presented uses 10% of each subspace: 70 proton and 70 neutron basis factors to compute the basis. All allowed combinations of these factors are used. Again, the results are shown in Figure 6.1.

For both methods, the model reproduces the cumulative level density (CLD) below about 3 MeV. Above this, the slope of the experimental CLD falls off. This indicates above this many of the states have not been observed. Above about 6 MeV, both models run out of levels: each calculation targeted the lowest 500 levels only. The PANASh method systematically underestimates the FCI level density. The missing states can be understood to be systematically shifted upward in energy; the ground state converges most quickly, and, due to the variational principle, the approximation of each state's energy is guaranteed to be greater than its un-truncated value.
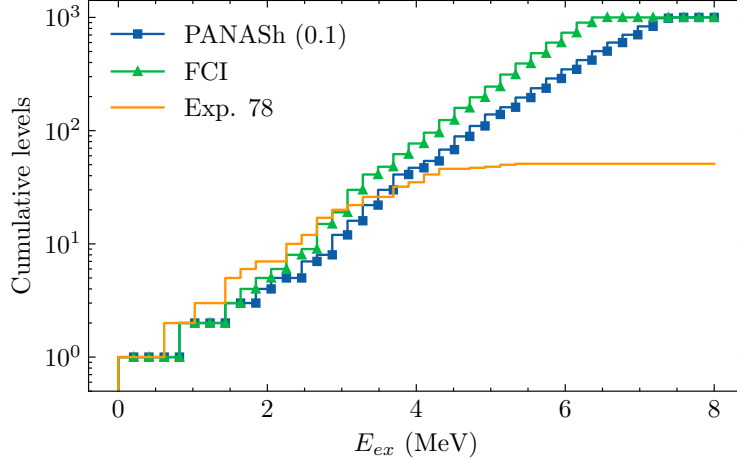
Figure 6.1: Cumulative level density for ^{78}Ge from experimentally reported levels [48], and using full configuration interaction (FCI) shell model, and our proton and neutron approximate shell model (PANASh) using 10% of the proton and neutron subspaces.

6.2 Gamma-ray strength functions

A gamma-ray strength function is a particular form of a simple quantity: the probability for a highly excited nucleus to de-excite by emitting a photon of a particular energy E_γ. In the shell model, this should be straightforward to calculate since one can compute the transition probability between any two states. Obtaining a gamma ray strength function needed by a reaction code should therefore be a simple matter of knowing what averages to take and what particular definition is needed. In this section I will tell a more complicated story.

For statistical reaction codes the standard is to use a simple function $f(E_\gamma)$ that describes the average, statistical probability for a nucleus to decay by emitting a gamma photon with E_γ. The form of these functions ignores the specific structure of individual states and resonances, and in factor often ignores everything except E_γ. These functions have simple parametric forms which are typically fit to systematic trends in measurable quantities like the photo-absorption cross section, or the average total radiative width in a given mass range.

The goal of this section is to be able to compute gamma-ray strength functions using the shell model which are suitable as inputs for statistical reaction codes. As it will be shown, there

is more than one definition or interpretation of what exactly a gamma-ray strength function is and how it should be related to measurements. I review the various definitions, then give my own derivation of one of these definitions. I then compare various interpretations and argue for a specific definition to be used as input for statistical reaction calculations which is not the one used in recent literature. If my argument holds, it points towards a significant increase in the the low-energy region of the gamma-ray strength function as compared to the currently accepted prescription.

6.2.1   Definitions

I claim that so far there are at least three distinct definitions of gamma-ray strength functions, which have been grouped together and often confused. The most important definition for this work is the definition in terms of *transmission coefficients*, to be defined below implicitly in terms of a photoabsorption cross section, and more fully explained later in Chapter 7. This is the definition I will continually refer back to because the purpose of gamma-ray strength functions (GSFs) in this work are as inputs for modeling statistical nuclear reactions.

The second definition comes from efforts to relate the transmission coefficient definition to some measurable observable. This was first done in terms of photo-absorption or Coulomb excitation of a nucleus - in either case, a nucleus in its ground state is excited by electromagnetic perturbation into a highly excited state, by perhaps tens of MeV. The GSF can then be related directly to the probability that the nucleus absorbs a fixed quanta of energy. It is then assumed that this is related by time-reversal symmetry and the principle of detailed balance to the probability for the same system to emit a photon of the same energy. The problem with this approach is that it may ignore transitions from the excited state to states other than the ground state. This is a significant omission since the number of possible final states will grow exponentially with the level density near the final state.

The third definition arises from efforts to relate the GSF to yet another measurable observable. The class of experimental techniques known as the Oslo method extracts gamma strength functions from coincidence measurements of nuclear excitation energy and emitted gamma energy. This method improves over ground-state excitation methods because it allows not only for decays to the ground state, but decays to any energy lower than the excitation energy of the initial state. This method also has its limitations. While the decay probabilities obtained from Oslo-type measurements include proportionality to the final state level density, they are normalized to one at each excitation energy [182] and so are not sensitive to the level density near the initial state. The raw results of the method yield a GSF with undetermined overall normalization [200].

Transmission coefficients

Gamma-ray strength functions find their use in modeling of compound nuclear reactions. I will postpone complete introduction of nuclear reactions until Chapter 7, and present only the relevant definitions here. The (energy averaged) photoabsorption cross section σ can be expressed in terms of a transmission coefficient $\mathcal{T}_\gamma$ as:

$$\langle \sigma_\gamma^{XL} \rangle = g\pi\lambda^2 \mathcal{T}_\gamma^{XL}, \tag{6.3}$$

where g is a (spin) statistical weight, and XL is the multipole type and order of the electromagnetic radiation. $\lambda = \lambda/2\pi = 1/k_\gamma$ is the reduced wavelength, which is related to the energy as $k_\gamma = E_\gamma/(\hbar c)$. For massive particles like neutrons, transmission coefficients are directly related to average total-widths of the neutron resonances Γ_n, and the average resonance spacing D [277]:

$$\mathcal{T}_n = \frac{2\pi\langle\Gamma_n\rangle}{D}. \tag{6.4}$$

This comes from Hauser-Feshbach theory which averages over many resonances. The probability of absorbing the particle into one of these resonances is approximately the average total resonance width times the number of resonances $(1/D)$. For photons, the transmission coefficients are expressed in terms of the *gamma-ray strength function* f:

$$\mathcal{T}_\gamma^{XL}(E_\gamma) = 2\pi E_\gamma^{2L+1} f^{XL}(E_\gamma), \tag{6.5}$$

which factors out a systemic energy dependence of the gamma widths. The origin of this expression can be traced to the theory of photo-absorption of a nucleus in terms of transition probabilities between individual levels which carry this energy dependence.

Formal strength functions and photo-absorption

The implicit definition of the gamma-ray strength function (GSF) differs from the more formal definition of a strength function [160]:

$$S(E_i, E_x) = \sum_f \delta(E_x - E_f + E_i)|\langle f|\hat{\mathcal{O}}|i\rangle|^2, \tag{6.6}$$

where E_i and E_f are the energies of the initial and final stats, and $E_x = E_f - E_i$ is the energy of the excitation[1]. Instead, the GSF can be thought of as related to the energy averaged strength function:

$$E_\gamma^{2L+1} f^{XL}(E_\gamma) \propto \frac{1}{\Delta E} \int_{E_i - \Delta E/2}^{E_i + \Delta E/2} dE_i S(E_i, E_\gamma), \tag{6.7}$$

where ΔE is the energy region of interest accessible by the transitions. The Brink-Axel hypothesis implicit in the energy-independent definition of the GSF requires that $S(E_i, E_\gamma)$ be independent of E_i.

---

[1]This definition comes from the study of *sum rules*, which place physical limits on the maximum value of these strength functions for certain operators [31].

We can compare these expressions to Ring and Schuck's expression [245, 285] for photoabsorption of dipole radiation:

$$\sigma_{\text{abs}}(E_\gamma) = \frac{16\pi^3 E_\gamma}{9\hbar c} S(E_i = 0, E_\gamma). \tag{6.8}$$

The definition of Bartholomew

Modern applications of the nuclear shell model to calculation of gamma-ray strength functions [97, 208, 184, 41, 260] nearly all refer to Bartholomew's 1973 definition [21]. Bartholomew's perspective is from that of an experimentalist trying to measure GSF's, in a time where photo-excitation was the main way to do so. The definitions therein are not derived, but stated as: "the distribution, as a function of γ-ray energy, of the average reduced width for transitions of a particular multipole type XL":

$$\overrightarrow{f}_{fiJ}^{XL}(E_\gamma) = E_\gamma^{-(2L+1)} \bar{\Gamma}_{fiJ}^{XL}(E_\gamma) \rho_J(E_f), \tag{6.9}$$

where the transition is upward from $i \to f$ ($E_f > E_i$), absorbing a gamma energy of E_γ. Usually i is the ground state. The average radiative width $\bar{\Gamma}_{fiJ}$ is averaged over large numbers of levels of the same spin and parity near E_f.

For compound nuclear reactions we need not the upward GSF, but the downward one, which can be used to describe the decay of a compound nucleus. Modern works have cited Bartholomew's definition for *the strength function for decay of levels of spin J within unit energy interval at E_i to a state E_f by emission of radiation type XL*[21]:

$$\overleftarrow{f}_{fiJ}^{XL}(E_\gamma) = E_\gamma^{-(2L+1)} \bar{\Gamma}_{fiJ}^{XL}(E_\gamma) \rho_J(E_i), \tag{6.10}$$

where now the transition is $E_i > E_f$. The average is over a large number of initial states near
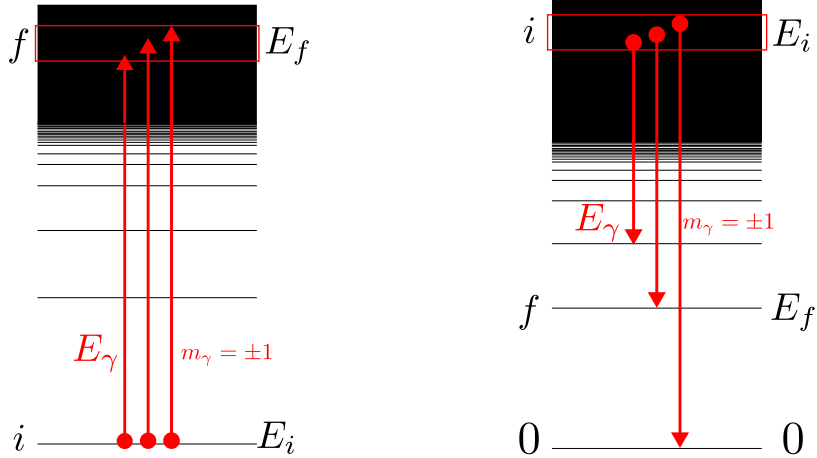
Figure 6.2: Photo-absorption (left) of an unpolarized beam of photons with energy $E_\gamma \pm \Delta E$ by a nucleus in its ground state. Photo-emission (right) of a nucleus shortly after absorbing an unpolarized beam of photons.

E_i; E_i is fixed and E_f describes a variable state. To obtain an energy-independent strength function, one needs to either sum or average over final states.

In his PhD thesis, Zeiser points out [310](pp.9-11) that (6.10) can be explained by applying the *principle of detailed balance*, which says that:

$$T_{i \to f} = \frac{\rho_f}{\rho_i} T_{f \to i}. \tag{6.11}$$

Zeiser thusly argues that Bartholomew's two definitions are linked. Equation (6.11) comes from time-dependent perturbation theory, in particular Fermi's Golden rule. So I will briefly introduce it here. Fermi's Golden Rule[2], as it is commonly called[3] plays an important role in the description of nuclear decay. It describes the transition probability per unit time of a quantum system from an initial state i to some closely spaced group of final states f[253]:

$$T_{i \to f} = \frac{2\pi}{\hbar} |H'_{fi}|^2 \rho_f, \tag{6.12}$$

---

[2]Actually, he called it "Golden Rule No. 2" [213]

[3]Although, Fermi cites the rule from Schiff's textbook [253] on quantum mechanics.

where H' is the perturbative operator leading to the transition, and ρ_f is the density of states near f. This approximation comes directly from time-dependent perturbation theory, with the following assumptions: (1) there is a group of states f that have nearly degenerate energies, and for which the matrix element is roughly constant; (2) the level density $\rho(f)$ is also sufficiently independent of f.

Oslo-measurement formula

The following expression is an interpretation of (6.10), which I will call the Oslo-measurement formula, since it was introduced to account for measurements made with the Oslo method in recent shell model calculations of the gamma-ray strength function [97, 208, 184, 40, 260]:

$$f_{\text{Oslo}}^{(M1)}(E_i, E_\gamma) = \frac{16\pi}{9(\hbar c)^{-3}} \langle B(E_\gamma) \rangle_i \rho(E_i), \tag{6.13}$$

where $\langle B(E_\gamma) \rangle_i$ is the average B-value (reduced matrix elements) and can be related to the average radiative width (the details will be explained later). Because this formula has been used in the context of the Oslo method of measuring gamma-ray strength functions, it has been interpreted in a particular way. Midtbo provides a derivation of this GSF in his dissertation [198] (Appendix A, pp. 147-150), starting from Bartholomew's expression of the average total radiative width as an integral of the gamma-ray strength function and the level densities at both the initial and final states. That is,

$$\langle \Gamma(E_i, J, \pi)^{XL} \rangle = \int_0^{E_i} \frac{E_\gamma^{2L+1} f^{XL}(E_i, E_\gamma, J, \pi)}{\rho(E_i, J, \pi)} \sum_{J_f=J-L}^{J+L} \rho(E_f, J_f, \pi_f) dE_\gamma. \tag{6.14}$$

In the Oslo method, gamma energies E_γ are measured in coincidence with the nuclear excitation energy $E_x = E_i$ and binned into a large matrix of decay probabilities $P(E_i, E_\gamma)$:

$$P(E_i, E_\gamma) \propto \mathcal{T}(E_\gamma)\rho(E_f) \tag{6.15}$$

Importantly, the matrix is normalized for each E_i [254]:

$$\sum_{E_\gamma} P(E_i, E_\gamma) = 1. \tag{6.16}$$

This decay matrix is in turn convoluted into a product of the final state nuclear level density and a gamma-ray strength function. The average B-value is computed by sorting the transitions into 100 keV bins on the initial energy $E_i = E_x$ and the transition energy $E_\gamma = E_i - E_f$, analogous to the probability matrix $P(E_i, E_\gamma)$, and dividing by the number of transitions in each two-dimensional bin, or 'pixel' [40].

6.2.2   Derivation of the upward strength function

To understand the origin of Bartholomew's expression (at least the *upward* definition), I follow Blatt and Weisskopf's (BW) text [31]. The following argument roughly follows chapter XII, sec. 7 discussing the nuclear photoeffect, and leads to the derivation of the photo-absorption cross section. To obtain the definition of Bartholomew (6.9), I then relate the cross section back to the strength function defined in Section 6.2.1.

First, BW restate that the probability for excitation of a nucleus from the ground state to some definite state f is given by the beam intensity $S(E_\gamma)$ times the spontaneous emission probabilities T, given in equations BW(3.25) and BW(3.21), respectively. It is assumed that the photon beam is not monochromatic. It has an intensity $S(E_\gamma)$ exciting many states in a region ΔE around $E_\gamma = E_f$. The unpolarized[4] light will have $m = \pm 1$. The probability of

[4]By this we mean that the photons have random spin alignment.

excitation by multipole radiation type XL is (BW(3.25)) then:

$$A^{XL} = \frac{\pi^2}{2k_\gamma^2}(2L+1)S(E_\gamma)[T^{XL}(m=-1)+T^{XL}(m=+1)], \tag{6.17}$$

where $k_\gamma = E_\gamma/(\hbar c)$. The constant factor is from normalizing the flux to the particular flux corresponding to one photon per vibration of the field at order L (see BW pp. 809-811). In our notation the reduced transition probability is (equivalent of BW(3.21)):

$$T_{fi}^{XL} = \frac{8\pi}{\hbar}\frac{(L+1)}{L[(2L+1)!!]^2}\left(\frac{E_\gamma}{\hbar c}\right)^{2L+1}B(XL; i \to f), \tag{6.18}$$

where B is the reduced matrix element (B-value), averaging over all orientations:

$$B(XL; i \to f) = \frac{1}{2J_i+1}|\langle\Psi_f||\mathcal{M}_{XL}||\Psi_i\rangle|^2. \tag{6.19}$$

Second, BW elaborate that with an incident gamma beam with a spread of energies, many states f will be excited. Then, the total excitation probability is a sum over those states, which can be approximated as an ensemble average:

$$A_{tot}^{XL} = \sum_{E_f=E_\gamma}^{E_\gamma+\Delta E} A_{0\to f}^{XL} \approx \langle A_{0\to f}^{XL}\rangle_{av}\rho_J(E_f)\Delta E, \tag{6.20}$$

where ΔE is the beam width and $\rho_J = D_J^{-1}$ is the level density of states near f which are populated by the photo-excitation. The average is over the final states f.

The approximation (6.20) is only valid if the average transition probability to the group of states f has low variance, and the level density does not vary too rapidly. (I.e. law of large numbers; the sum is the average times the number in the sum, not valid for 'long-tailed' distributions.) Similar arguments take place to arrive at Fermi's golden rule (6.12) from time-dependent pertubation theory [253], with similar constraints. In this context, however,
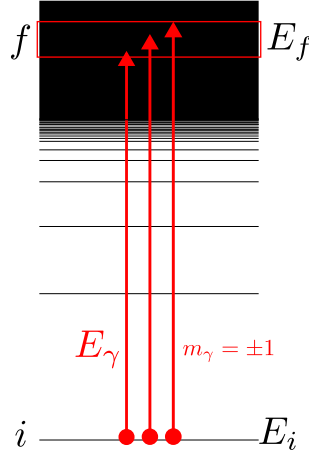
Figure 6.3: Photo-absorption of an unpolarized beam of photons with energy $E_\gamma \pm \Delta E$ by a nucleus in its ground state. The total probability of absorption is a sum over transition probabilities to states in the energy bin near E_f.

we do not *need* this approximation if in fact we know all of the states f. In deriving a modern definition of the GSF, I will drop this approximation.

Finally, to find the photo-absorption cross section, BW divide the excitation probability by the flux: number of photons in the beam per area per second, $S(E_\gamma)(\Delta E/\hbar)$.

$$\langle \sigma_{abs}^{XL} \rangle (E_\gamma) = \frac{A_{tot}^{XL}}{S(E_\gamma)(\Delta E/\hbar)} \approx \frac{\pi^2}{k_\gamma^2}(2L+1)\hbar \langle T_{0\to f}^{XL} \rangle_{av} \rho_J(E_\gamma). \tag{6.21}$$

The factor $1/2$ was combined with the sum over both values of m. This matches equation (49) of Carpenter [51], p.23, up to a statistical factor g. Note also that $E_f = E_\gamma$.

To relate (6.21) to the GSF, we take the definition (6.3), while summing over the final states spins J_f and averaging over the photon spins s to get the absorption cross section:

$$\langle \sigma_{abs}^{XL} \rangle (E_\gamma) = \frac{1}{w(s)} \sum_s \sum_{J_f} g(J_f, s) \frac{\pi}{k_\gamma^2} 2\pi E_\gamma^{2L+1} f^{XL}(E_\gamma), \tag{6.22}$$

where $w(j)$ is the number of states accessible by the spin (angular momentum) j. Only the spin factor g depends on J_f and s. This spin factor is proportional to the number of

accessible states of the final level J_f, and inversely to the number states formed by coupling s and J_i [31]:

$$g = \frac{w(J_f)}{w(s)w(J_i)}. \tag{6.23}$$

(A nice trick for counting angular momentum couplings is to remember that the number of states, i.e. the dimension, is conserved between the coupled and uncoupled basis. This is why the denominator of (6.23) is the product of $w(s)$ and $w(J_i)$.) We have the constraint $\mathbf{J_f} = \mathbf{J_i} + \mathbf{s} + \mathbf{L}$, where L is the orbital angular momentum of the projectile. Generally $w(j) = 2j + 1$, counting up the magnetic substates m in the usual way. In our case, $s = 1$, but for massless photons only $m = \pm 1$ are allowed, so $w(s) = 2$. Evaluating the average and sum in (6.22) for (6.23), we obtain:

$$\frac{1}{2}\sum_s \sum_{J_f} g = \frac{1}{2}\sum_s \sum_{J_f} \frac{2J_f + 1}{2(2J_i + 1)} = \frac{1}{2}(2L + 1); \tag{6.24}$$

This required $\sum_{J_f}(2J_f + 1) = (2L + 1)(2S + 1)$ from [31] where $\mathbf{S} = \mathbf{L} + \mathbf{s}$. Thus, the photoabsorption cross section for unpolarized radiation of multipole type XL is:

$$\langle \sigma_{abs}^{XL} \rangle (E_\gamma) = (2L + 1)\frac{\pi^2}{k_\gamma^2} E_\gamma^{2L+1} \overrightarrow{f}^{XL}(E_\gamma). \tag{6.25}$$

Using $\hbar T = \Gamma$ and equations (6.21) and (6.25), we have derived Bartholomew's gamma-ray strength function for absorption:

$$\overrightarrow{f}_{0\to f}^{XL}(E_\gamma) = E_\gamma^{-(2L+1)} \langle \Gamma_{0\to f}^{XL} \rangle_{av} \rho_J(E_\gamma). \tag{6.26}$$

Undoing the approximation as an ensemble average, this can also be written more explicitly

as:

$$\overrightarrow{f}^{XL}_{0\to f}(E_\gamma) = E_\gamma^{-(2L+1)} \frac{1}{\Delta E} \sum_{E_f=E_\gamma}^{E_\gamma+\Delta} \Gamma^{XL}_{0\to f} \tag{6.27}$$

$$= \frac{8\pi(L+1)}{L[(2L+1)!!]^2} \left(\frac{1}{\hbar c}\right)^{2L+1} \frac{1}{\Delta E} \sum_{E_f=E_\gamma}^{E_\gamma+\Delta} B(XL; 0\to f). \tag{6.28}$$

This form avoids any possible confusion about the definition of the level density in equation (6.26).

In summary, the photo-absorption strength function describes the total width from the ground state to an excitation energy near $E_f = E_\gamma$, assuming there are many nearby partial widths contributing. This is a quantity that is proportional to the level density near the final state. That is clear from the form (6.26). The only energy dependence is from the energy dependence of the level density, and any residual energy dependence in the reduced B values. The former grows exponentially, while the B-values are often assumed to be energy-independent according to the Brink-Axel hypothesis [39, 18]. However, shell model studies have shown that the Brink-Axel hypothesis is not quite true [160, 137].

6.2.3 Return to strength functions

Equation (6.27) is consistent with the form of the strength function expression for the photoabsorption cross section [245, 284]:

$$\sigma_{\text{abs}}(E_\gamma) = \frac{16\pi^3 E_\gamma}{9\hbar c} \sum_f B(E1; 0\to f)\delta(E_\gamma - E_f + E_0), \tag{6.29}$$

since if we select $L = 1$ and substitute $k_\gamma = E_\gamma/(\hbar c)$ into (6.25) and using (6.27) we get:

$$\langle\sigma_{abs}^{E1}\rangle(E_\gamma) = 3\frac{16\pi^3 E_\gamma}{9\hbar c} \frac{1}{\Delta E} \sum_{E_f=E_\gamma}^{E_\gamma+\Delta} B^{E1}(0\to f). \tag{6.30}$$

The factor of 3 comes from the assumption of unpolarized photons.

6.2.4 Photo-emission from an excited state

So far we have only discussed photo-absorption. What about photo-emission from a compound nucleus? In particular, what is the gamma-ray strength function used to calculate a transmission coefficient for decay from an initial state i? See Figure 6.4. If we are in
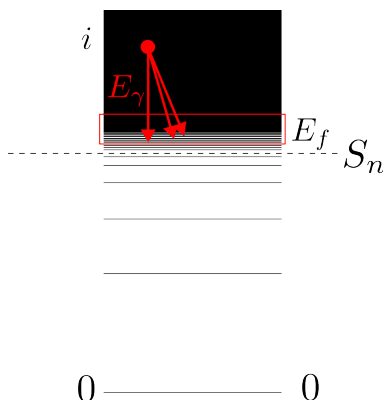

Figure 6.4: Photo-emission from a single state i to a bin near E_f. The total probability of decay is a sum over transition probabilities to states in the energy bin near E_f. S_n is the neutron separation energy around which the level density is usually high enough for a statistical description.

the continuum description of statistical decay, then the HF gamma-decay probability (to be defined in the next chapter) is proportional to the transmission coefficient times the level density near the final state. Recalling that the gamma-ray transmission coefficient should be written in terms of the gamma-ray strength function, we can write:

$$\mathcal{T}_\gamma^{XL}(E_\gamma = E_i - E_f)\rho(E_f)\Delta E = 2\pi E_\gamma^{2L+1} f^{XL}(E_\gamma)\rho(E_f)\Delta E. \tag{6.31}$$

From a microscopic perspective, the gamma-decay probability for a state i is proportional to the total decay width:

$$2\pi\Gamma_i = 2\pi \sum_{f \in E_f} \Gamma^{XL}_{i \to f} = 2\pi \langle \Gamma_{i \to f} \rangle_f \rho(E_f) \Delta E., \tag{6.32}$$

where $f \in E_f$ means all final states f within $\Delta E/2$ of E_f. And so we can write down an expression for the photo-emission gamma-ray strength function by equating the two numerators:

$$f^{XL}(i, E_\gamma) = E_\gamma^{-(2L+1)} \langle \Gamma_{i \to f} \rangle \tag{6.33}$$

$$= \frac{8\pi(L+1)}{L[(2L+1)!!]^2} \left(\frac{1}{\hbar c}\right)^{2L+1} \frac{1}{N_f} \sum_{f \in E_f} B^{XL}(i \to f) \delta_{\Delta E}(E_f - E_i + E_\gamma),$$

$$\tag{6.34}$$

where the 'softened' delta function $\delta_{\Delta E}(x)$ enforces the relation $x = 0 \pm \Delta E/2$, and N_f is the number of final states accessible. Finally, to compute a 'Brink-Axel' gamma-ray strength function [39, 18] independent of the initial energy, I average over all initial states above some minimum for the sum to have good statistics, e.g. $i > 100$. This type of gamma-ray strength function is illustrated in Figure 6.4.

To calculate what is measured in photo-absorption experiments (i.e. proportional to the total level width), we must multiply (6.33) by the number of accessible final states $\rho(E_f)$ to get a new function $F(i, E_\gamma)$:

$$F^{XL}(i, E_\gamma) = f^{XL}(i, E_\gamma) \rho(E_f) \tag{6.35}$$

$$= \frac{8\pi(L+1)}{L[(2L+1)!!]^2} \left(\frac{1}{\hbar c}\right)^{2L+1} \frac{1}{\Delta E} \sum_{f \in E_f} B^{XL}(i \to f) \delta_{\Delta E}(E_f - E_i + E_\gamma)$$

$$\tag{6.36}$$

Some regard $F^{XL}(i, E_\gamma)$ as the 'photon-strength function' and $f^{XL}(i, E_\gamma)$ as the 'gamma-ray strength function' [88], but this is not widespread.

Physically, equation (6.36) is expected to have a giant dipole resonance when the transition is of $E1$ type [285, 39, 18] and i is the ground state, which is often modeled with a Lorentzian shape. However, it is common practice in Hauser-Feshbach codes to instead model f^{XL} with Lorentzian type functions, fit to experimental data like average total radiative widths [215, 174].

6.2.5   Photo-emission to a final state

What about Bartholomew's formula for decay of levels near E_i to a final state f? That is, $\overleftarrow{f}^{XL}(f, E_\gamma) = E_\gamma^{-(2L+1)} \langle \Gamma_{i \to f}^{XL}(E_\gamma) \rangle_i \rho(E_i)$, which corresponds to the situation depicted in the right side of Figure 6.2. I propose the following interpretation of the Bartholomew formula:

$$F^{XL}(f, E_\gamma) = E_\gamma^{-(2L+1)} \langle \Gamma_{i \to f}^{XL} \rangle_i \rho_J(E_i) \tag{6.37}$$

$$= \frac{8\pi(L+1)}{L[(2L+1)!!]^2} \left(\frac{1}{\hbar c} \right)^{2L+1} \frac{1}{\Delta E} \sum_{i \in E_i} B^{XL}(i \to f) \delta_{\Delta E}(E_f - E_i + E_\gamma). \tag{6.38}$$

This is the total strength from many states near E_i to a final state f. This is in contrast to equation (6.36), which is a decay from a specific state i to a bin near E_f, shown in Figure 6.4. The state-independent GSF $F(E_\gamma)$ is obtained by an average over all final states. I have now defined four gamma-ray strength functions in this $f_x, F_x = f_x/\rho$ notation. To obtain a function which depends only on the gamma energy, we need to take one final average over the remaining free variable. These are given in Table 6.1. A comparison of the two expressions for both f_x and $F_x = f_x \rho$ is given in Figure 6.5.

Unsurprisingly, both f_i and f_f give similar values. In the end, we are averaging over both

Table 6.1: The various gamma-ray strength functions defined to far and the final average that must be taken to give the Brink-Axel equivalent GSF. F_i is the upward Bartholomew formula if $i = 0$ which can be related to the photoabsorption cross section. F_f is the downward Bartholomew formula.

Formula	GSF	Physical description	Final average
(6.33)	$f_i = f(i, E_\gamma)$	Average B-value from initial states	All initial states i
(6.35)	$F_i \equiv F(i, E_\gamma)$	Total strength from initial state	All nonempty bins E_i
-	$f_f \equiv f(f, E_\gamma)$	Average B-value to final states	All final states f
(6.37)	$F_f \equiv F(f, E_\gamma)$	Total strength to final state	All nonempty bins E_f

initial and final states. F_i and F_f give very different results. F_i has an exponential 'up-turn' at low energy. This is explained by the multiplication by the final state density: a single decaying state has many more low-energy transitions available to it. F_f is nearly flat. Here, the decaying strength f_f is countered by the exponentially growing number of initial states near E_i.

6.2.6 The Oslo GSF and the Bartholomew formula

How do expressions (6.35) and (6.33) compare to the literature? The following expression is an interpretation of (6.10), which I will call the Oslo formula, since it was introduced to account for measurements made with the Oslo method in recent shell model calculations of the gamma-ray strength function [97, 208, 184, 40, 260]:

$$f_{\text{Oslo}}^{(M1)}(E_i, E_\gamma) = \frac{16\pi}{9(\hbar c)^{-3}} \langle B(E_\gamma) \rangle_i \rho(E_i).$$

(6.39)

Because this formula has been used in the context of the Oslo method of measuring gamma-ray strength functions, it has been interpreted in a particular way.

In the Oslo method, gamma energies E_γ are measured in coincidence with the nuclear excitation energy $E_x = E_i$ and binned into a large matrix of decay probabilities $P(E_i, E_\gamma)$:
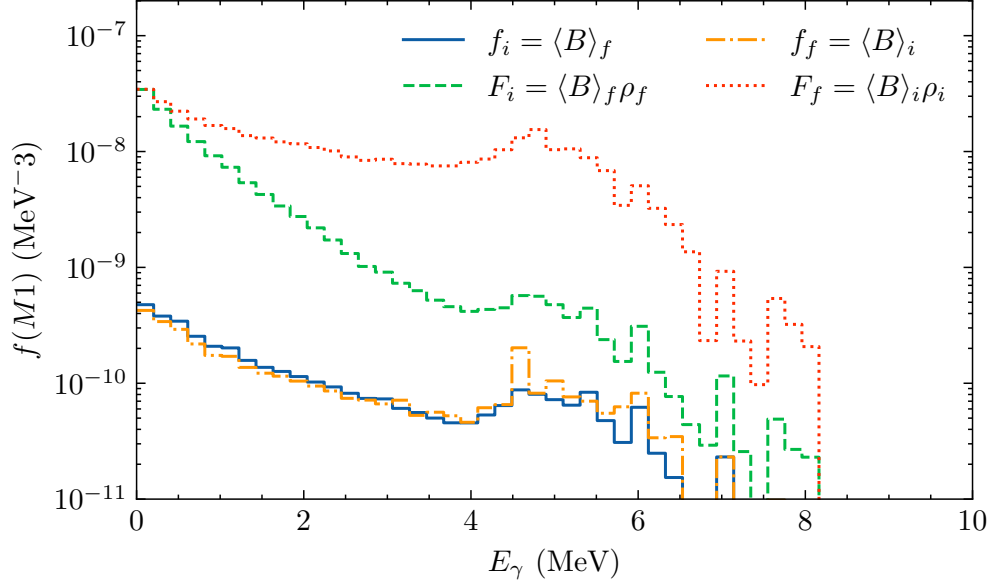
Figure 6.5: Calculated M1 gamma-ray strength function for ^{94}Sr computed using an approximate shell model with the *glepn* interaction [191]: a comparison of gamma-ray strength functions between a single state and an energy bin, depending on the direction of the decay. F_i is a decay from a state i to a bin E_f yielding a E_γ transition. F_f is the reverse: decay from a bin near E_i, downward E_γ, to state f.

$$P(E_i, E_\gamma) \propto \mathcal{T}(E_\gamma)\rho(E_f). \tag{6.40}$$

Importantly, the matrix is normalized for each E_i [254]:

$$\sum_{E_\gamma} P(E_i, E_\gamma) = 1. \tag{6.41}$$

This decay matrix is in turn convoluted into a product of the final state nuclear level density and a gamma-ray strength function. Equation (6.39) is then used to calculate an equivalent shell model GSF. The average B-value is computed by sorting the transitions into 100 keV bins on the initial energy $E_i = E_x$ and the transition energy $E_\gamma = E_i - E_f$, analogous to the probability matrix $P(E_i, E_\gamma)$, and dividing by the number of transitions in each two-

dimensional bin, or 'pixel' [40]. In terms of the B-values, this translates to:

$$\langle B(E_i, J_i, \pi_i, E_\gamma) \rangle = \frac{1}{N_{if}} \sum_{if \in E_i, E_\gamma} B^{M1}(i \to f) \delta_{100 \text{ kev}}(E_\gamma - (E_i - E_f)), \quad (6.42)$$

where N_{if} is the number of transitions in each pixel and the sum is over all transitions $i \to f$ satisfying $E_f = E_i - E_\gamma$ (all transitions in the pixel (E_i, E_γ)). This is equivalent to satisfying the 'softened' delta function. Next, one is to multiply by the initial state level density $\rho(E_i, J_i, \pi_i)$, which is the number of states in one row of fixed E_i in the (E_i, E_γ) matrix:

$$f_{\text{Oslo}}^{(M1)}(E_i, E_\gamma) = \frac{16\pi}{9(\hbar c)^{-3}} \langle B(E_\gamma) \rangle_{if} \rho(E_i) \quad (6.43)$$

$$= \frac{16\pi}{9(\hbar c)^{-3}} \rho(E_i, J_i, \pi_i) \frac{1}{N_{if}} \sum_{if \in E_i, E_\gamma} B^{M1}(i \to f) \delta_{100 \text{ kev}}(E_\gamma - (E_i - E_f)) \quad (6.44)$$

$$= \frac{16\pi}{9(\hbar c)^{-3}} \frac{N_i}{\Delta E} \frac{1}{N_{if}} \sum_{if \in E_i, E_\gamma} B^{M1}(i \to f) \delta_{100 \text{ kev}}(E_\gamma - (E_i - E_f)), \quad (6.45)$$

In the second equation, I have made the definition of the level density explicit in terms of the number of transitions N_i out of the bin with E_i. This number is counted by the number of nonzero B-values. This avoids the need to track the spins and parities of the 'level density' since the number of nonzero B-values automatically respect the appropriate selection rules. The i-independent function is obtained by a simple average over nonempty bins (E_i, J_i, π_i).

Figure 6.6 provides a numerical example comparing this Oslo-experiment formulation of the gamma-ray strength function to the average GSF for the decay states near E_i to a single state f, $F(f, E_\gamma)$.
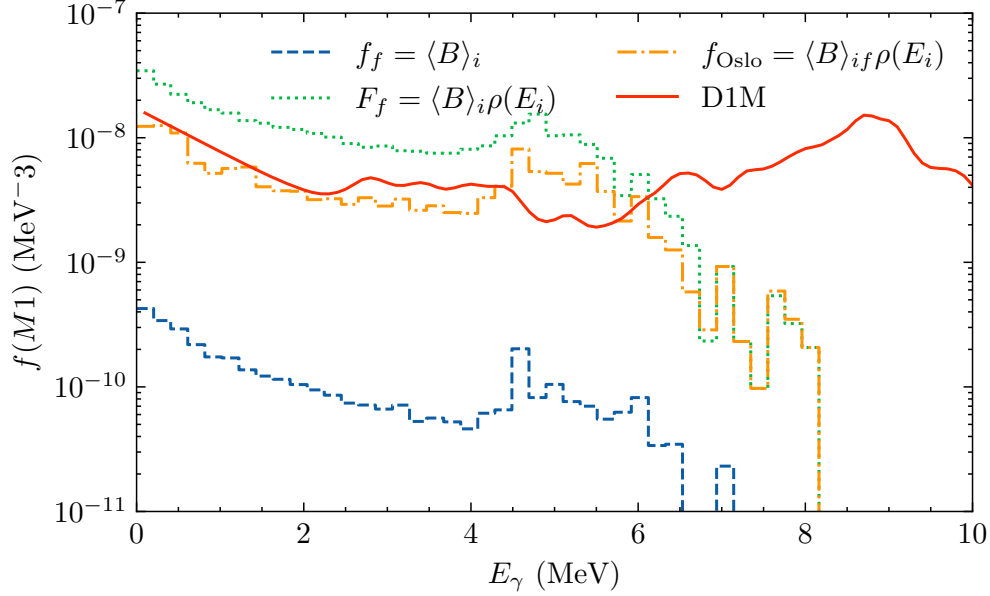
Figure 6.6: M1 gamma-ray strength function for ^{94}Sr computed using an approximate shell model with the *glepn* interaction [191]. The blue dashed line shows the decay strength from an initial bin E_i to a state f. The green dotted line shows the equivalent $F = f\rho$. The orange dash-dotted line shows the Oslo GSF formula (6.43) from recent literature [97, 208, 184, 40, 260]. The red solid line shows a composite model based on D1M+QRPA calculations [112, 110], which uses a mean field approach with realistic forces plus an empirical low-energy 'up-bend' fit to shell model calculations and low-energy data.

6.2.7 Hauser-Feshbach (bin to bin) decays

So far we have explored (1) decays from an initial state i to an energy bin E_f, (2) decays from an initial energy bin E_i to a final state f, and (3) decays from an initial energy bin E_i with a decay energy of E_γ simulating an Oslo-type measurement. So which expression should be used as inputs for a Hauser-Feshbach calculation? Hauser-Feshbach codes calculate the probability for decay from one energy bin to a lower energy bin. This is shown in Figure 6.7. To model a bin-to-bin transition, level densities in both the initial bins and the final bins will influence the total decay probability.

The expression for the decay probability from the initial bin near E_i can be obtained by
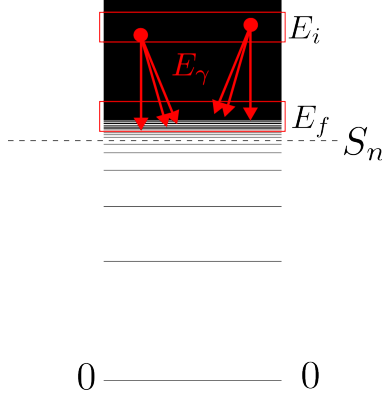
Figure 6.7: Photo-emission from a bin near E_i to a bin near E_f. The total probability of this decay is a sum over all states in the initial bin and over all transition probabilities to states in the energy bin near E_f.

summing the total decay widths for all levels in the initial energy bin:

$$P(E_i, E_\gamma) = 2\pi \frac{1}{\Delta E} \sum_{i \in E_i} \Gamma_i^{XL}(E_\gamma) \tag{6.46}$$

$$= 2\pi \frac{1}{\Delta E} \sum_{i \in E_i} \langle \Gamma_{i \to f} \rangle_f \rho(E_f = E_i - E_\gamma) \Delta E \tag{6.47}$$

$$\approx 2\pi \rho(E_i) \langle \Gamma_{i \to f} \rangle_f \rho(E_f) \Delta E, \tag{6.48}$$

where the approximate equality shows the proportionality to both initial and final state densities. It is approximate because it relies on the local Brink-Axel hypothesis for the total gamma decay widths: that all total widths near E_i are similar and thus the sum can be approximated by the average times the number of states.

There is an important difference between (6.46) and the Oslo-experiment formula presented in equation (6.40). The Oslo gamma matrix $P_{\text{Oslo}}(E_i, E_\gamma)$ is normalized to one at each E_i. In our case, it may be that $\sum_{E_\gamma} P(E_i, E_\gamma)$ depends on E_i. In fact, we can see from equation (6.48) that the HF decay probability depends on $\rho(E_i)$, which has an exponential E_i dependence. At higher excitation energy, there are more states per MeV, and thus more chances per MeV for the nucleus to decay out of that bin. Because the Oslo matrix is normalized to 1 at each E_i, this effect cannot be extracted from Oslo measurements.

Recall that the Hauser-Feshbach decay probability is defined as:

$$\mathcal{T}_\gamma^{XL}(E_\gamma = E_i - E_f)\rho(E_f)\Delta E = 2\pi E_\gamma^{2L+1} f^{XL}(E_\gamma)\rho(E_f)\Delta E. \tag{6.49}$$

We obtain the Hauser-Feshbach gamma-ray strength function by equating the two probabilities (6.46) and (6.49). The densities near E_f will cancel, along with a factor of $2\pi\Delta E$, leaving a dependence proportional to the density near $\rho(E_i)$. We therefore must accept the following definition of the Hauser-Feshbach gamma-ray strength function:

$$f_{\text{HF}}^{XL}(E_i, E_\gamma) = E_\gamma^{-(2L+1)}\frac{1}{\Delta E}\sum_{i\in E_i}\langle\Gamma_{i\to f}\rangle_f \tag{6.50}$$

$$= \frac{1}{\Delta E}\sum_{i\in E_i}\frac{8\pi(L+1)}{L[(2L+1)!!]^2}\left(\frac{1}{\hbar c}\right)^{2L+1}\frac{1}{N_f}\sum_f B^{XL}(i\to f)\delta_{\Delta E}(E_f - E_i + E_\gamma) \tag{6.51}$$

$$= \frac{1}{\Delta E}\sum_{i\in E_i}\overleftarrow{f}^{XL}(i, E_\gamma). \tag{6.52}$$

An equivalent expression holds for F_{HF}^{XL} in terms of $\overleftarrow{F}^{XL}(i, E_\gamma)$ using equation (6.36). The last equality relates the HF gamma-ray strength function to the gamma-ray strength function for photo-emission from a single state, given in equation (6.33). It is important to note that the average of the final states, and therefore the value of N_f, is determined by all final states accessible to a particular initial state i and transition energy $E_\gamma \pm \Delta E/2$.

If we were to use the Brink-Axel hypothesis, we would have the form:

$$f_{HF}^{XL} \approx E_\gamma^{-(2L+1)}\langle\Gamma_{i\to f}\rangle_f\rho(E_i), \tag{6.53}$$

which is different than equation (6.39) from recent literature [97, 208, 184, 40, 260].

Figure 6.8 shows this new expression for the HF gamma-ray strength function and compares it to the Bartholomew expression $F(f, E_\gamma)$ from equation (6.37). f_{HF} is significantly enhanced
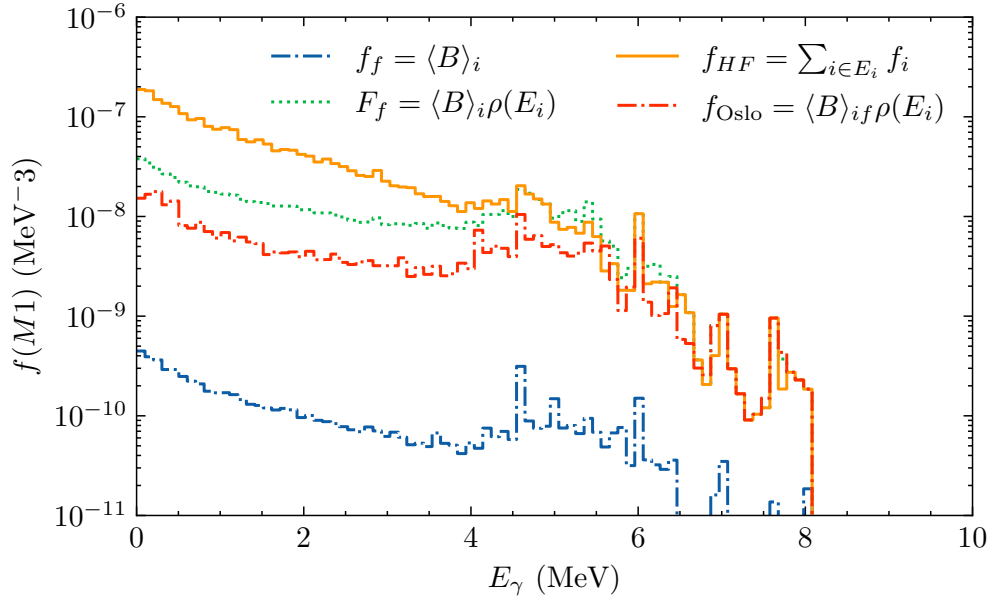
Figure 6.8: M1 gamma-ray strength function for ^{94}Sr computed using an approximate shell model with the *glepn* interaction [191]: A comparison of the Oslo formulation (6.43) of the gamma-ray strength function (GSF) and the Hauser-Feshbach (HF) GSF proposed in equation (6.50).

with respect to the Bartholomew expression (which treats each final state as independent). The HF expression f_{HF} first computes the average partial width of each initial state i to a local set of states near E_f, then sums over all initial states in the bin. The Bartholomew expression sums all strength from states near E_i to one final state f, then averages over all final states.

6.2.8 Conclusion

Our goal in computing gamma-ray strength functions is the generation of inputs for statistical reaction models. There have been multiple attempts to constrain GSF's using different experimental techniques: electromagnetic excitation of the ground state, Oslo-type measurements, and the surrogate reaction method, which has yet to be discussed (see Chapters 8 and 10). Relating these measurements to the theoretical formulation of the gamma-ray strength function has also been affected by confusion about the definitions [199]. In this chapter, I have

paid special attention to the microscopic significance of the gamma-ray strength function, and studied how different approaches for averaging transition probabilities can result in different definitions of the gamma-ray strength function. Finally, I have made an argument for a new microscopic definition of the gamma-ray strength function which differs from those used to analyze both ground-state excitation and Oslo-type measurements.

It is left to future work to make rigorous tests of this new definition and explore its consequences for reactions, especially those sensitive to the gamma-ray strength function like neutron capture reactions. One should compare these various GSF definitions, computed with a microscopic model, to the non-statistical method of computing nuclear decay. Since the microscopic model like the shell model provide the individual levels and their branching ratios, an *ab initio* model of the random decay can be carried out with the same methods as in [29]. The same calculation can then be carried out with a Hauser-Feshbach code, and the GSF definition which best reproduces the *ab initio* model should be considered. In parallel, experimental methods such as the surrogate method (see Chapter 10) can be used to cross-validate.

6.2.9   Supplemental tests

Results from PANASh compared to FCI

These results have appeared in a conference proceeding [117] from the 15th International Conference on Nuclear Data for Science and Technology (ND2022).

For demonstration of gamma-ray strength functions, we show preliminary results for ^{78}Ge in the pf-shell ($f_{5/2}, p_{3/2}, p_{1/2}, g_{9/2}$ valence orbitals above a ^{56}Ni core) with the JUN45 interaction [147]. To compute the M1 strength function, we follow the methods described in recent literature [97, 208, 184, 40, 260].

In this case, we take 20 percent of the proton and neutron eigenstates to construct the basis, yielding a maximum basis dimension 7,000, only 4-percent relative to the un-truncated dimension of 170,000. (This is the dimension of the largest J-basis, $J = 6$.) To calculate the M1 strength functions involved in the GSF, we use the standard magnetic moment operator with proton spin and orbital couplings $g_s = 5.586$, $g_l = 1$; and neutron couplings $g_s = -3.826$, $g_l = 0$. We used the usual quenching factor of $q = 0.7$ [147].

We compute the first 500 positive-parity states for use in the calculation, for $J = 0 - 10 \hbar$. The resulting level density and M1 photon strength function are shown in Figure 6.9. We find good agreement with recent results from [97], which used a similar interaction with the same single particle space. Although that calculation also included negative parity states, we find that these only slightly alter the GSF.

An important conclusion we can draw from Figure 6.9 is that the GSF converges far better than the nuclear level density. This can be understood in terms of the variational principle: the energy levels from a PANASh calculation are guarenteed to be larger than their converged results, and the ground state converges fastest. This explains why the PANASh level density is "shifted" to the right of the FCI level density: all the energies are larger than their converged values, and more so for higher energies. The GSF, on the other hand, does not follow a variational principle. It is the result of averaging over many incoherently perturbed matrix elements. The result, we can conclude from the figure, is a much better agreement with the un-truncated calculation.

Brink-Axel hypothesis

The Brink-Axel hypothesis [39, 18] claims that the gamma-ray strength function should be independent of the initial state excitation energy. It should be noted that this specifically refers to the photo-excitation energy from the ground state or low excited states. However, it
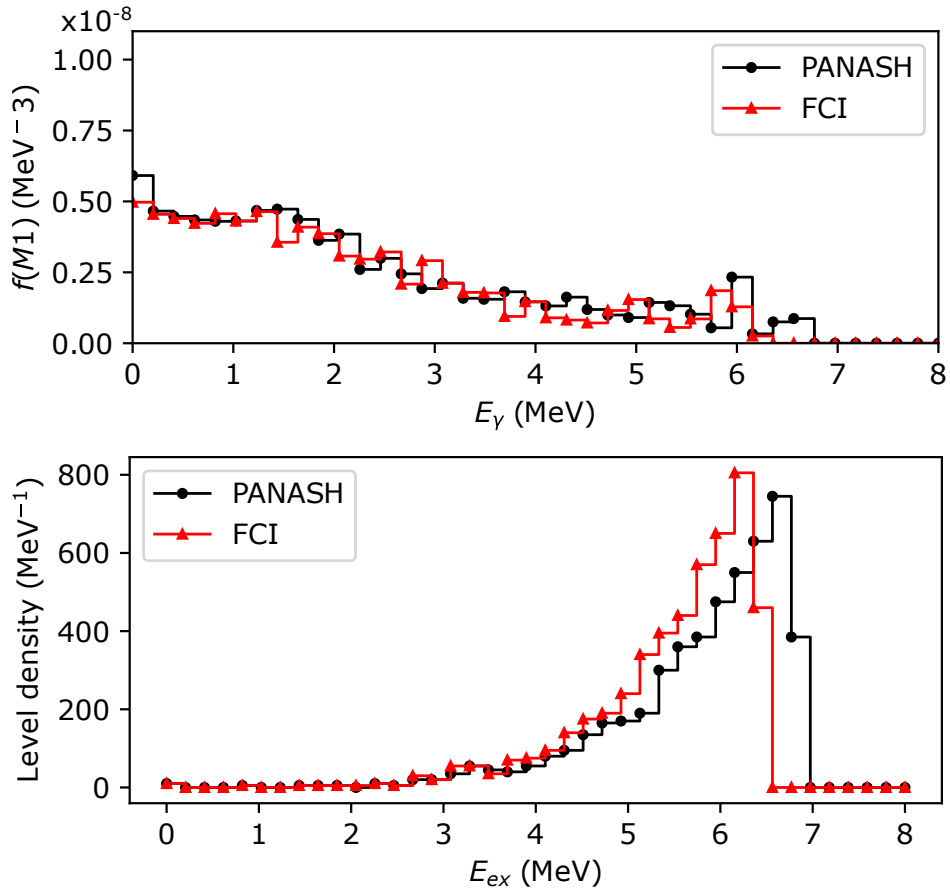
Figure 6.9: Preliminary calculations of gamma-ray strength functions (GSFs) (top panel) and nuclear level densities (NLDs) (bottom panel) using the PANASh code, with comparison to the full configuration interaction (FCI), untruncated model. In both cases, the first 500 positive-parity states were computed; the sudden drop of the level density above 6 MeV is a direct result of this. Energy bins are 0.2 MeV.

is important to examine the more broadly defined BA hypothesis as it is applied in Hauser-Feshbach theory: that the gamma ray strength function is completely independent of the initial excitation energy. We can easily test this with the shell model.

Figure 6.10 shows the same gamma ray strength function $F(i, E_\gamma)$ calculations shown in Figure 6.6, but for individual initial states $i = 100, 500, 1500, 1501, 15002$. The functions have also been smoothed by convolution with a Gaussian kernel with a width of $3\Delta E$, with $\Delta E = 0.05$ MeV being the bin width. We see evidence for the local BA hypothesis [137]: only states nearby in energy have similar strength functions. Even still, there is significant

variation from one level to the next.
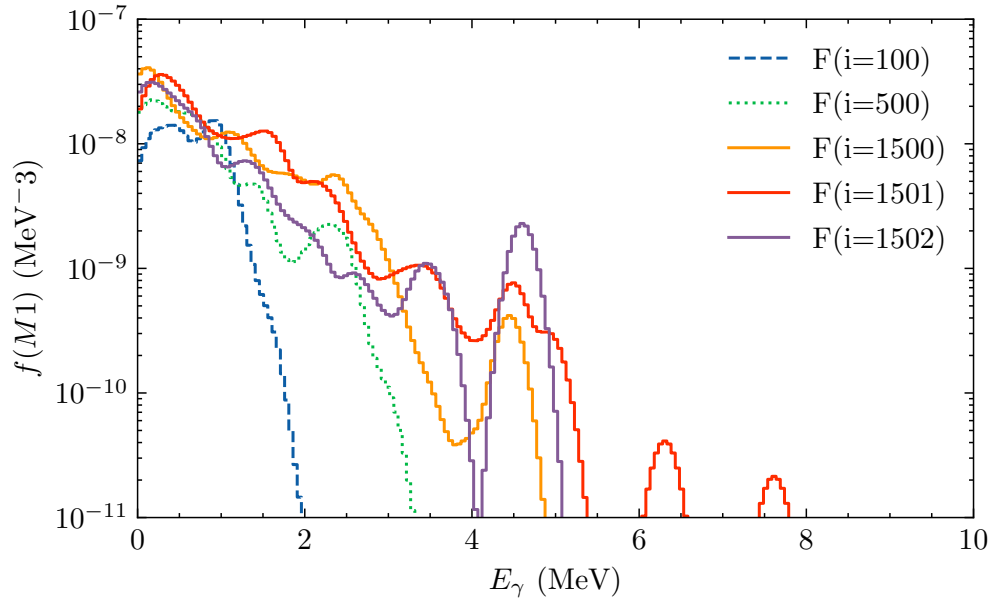
Figure 6.10: M1 gamma-ray strength function for ^{94}Sr computed using an approximate shell model with the *glepn* interaction [191] for different initial excitation states. In this model, $i = 100$ has $E_x = 4.69$ MeV, $i = 500$ has $E_x = 6.23$ MeV, and $i = 1500$ has $E_x = 7.55$ MeV. Levels 1500, 1501, and 1502 are degenerate in energy within 0.001 MeV, but have $J^\pi = 5^+, 1^+ 3^-$, respectively.

Part II

STATISTICAL NUCLEAR

REACTIONS

Chapter 7

Introduction to Reaction Theory

Modeling nuclear reaction networks for nuclear science applications and for simulations of astrophysical environments relies on cross section data for a vast number of reactions, many of which have never been measured. Cross sections for neutron-induced reactions on unstable nuclei are particularly scarce, since they are the most difficult to measure. Consequently, we must rely on theoretical predictions or indirect measurements to obtain the requisite reaction data. For compound nuclear reactions, the surrogate reaction method can be used to determine many cross sections of interest.

7.1   Basic concepts and terminology

Since nuclei are composed of protons and neutrons, we account for reactants and products in terms of their number of protons (Z) and neutrons (N). When labeling nuclei we name both their elemental symbol, e.g. U (Uranium, $Z = 92$), which uniquely specifies Z, and their atomic mass A ($\equiv Z + N$). Thus, ^{238}U uniquely identifies the nucleus Uranium-238, which is $Z = 92$ and $N = A - Z = 146$.

This notation is augmented to describe reactions among nuclei. For example, we can describe reaction in which (1) a neutron collides with a Uranium nucleus to (2) form a compound-nucleus with one additional neutron, (3) which then decays by emitting two neutrons, in the notation:

$$n +^{238} U \rightarrow^{239} U^* \rightarrow 2n +^{237} U. \tag{7.1}$$

This can be written compactly as: $^{238}U(n, 2n)$, since we can work out the other isotopes of U involved by conservation of Z and N. In this example, the neutron is the projectile and the uranium nucleus is the target. What nuclei are left over after the reaction are called the reaction products.

The rate at which a reaction will take place per unit volume may be written:

$$r_{A(a,b)} = \Phi_a n_A \sigma_{A(a,b)}, \tag{7.2}$$

where Φ_a is the incoming flux (particles/area/second) of projectile particles a, n_A is the density of target nuclei in the target (particles/volume), and $\sigma_{A(a,b)}$ is the microscopic cross section (units of area) of the target nucleus, which in general is simply called the cross section.

This chapter is primarily concerned with the acquisition of nuclear cross sections. Equation (7.2) alludes to experimental measurements of nuclear cross sections. But for many reactions of interest, it is not possible or practical to carry out the reaction in a laboratory setting. Theoretical calculations of these cross sections is possible, but proves insufficient, as will be discussed later. An intermediate option is to conduct what are called indirect measurements. These are measurements which when combined with a theoretical description of nuclear reactions, yield the desired cross section.

7.2 Types of reactions

Nuclear reactions fall into a number of categories depending on the relevant degrees of freedom of the nucleons involved. I will restrict the discussion to a limited number of these. First, we will deal mostly with neutron-induced reactions, with some exceptions, and mostly with nuclei with a relatively high level density near the neutron separation energy. Within these constraints, the main consideration for which mechanism will dominate is the energy of the projectile. *Inelastic* reactions transition one of the reacting nuclei to an excited state. So, below some threshold energy corresponding to the first excited state, all reactions will be *elastic*.

In this work we will focus on reactions from several hundred keV to several MeV incident energy. This roughly coincides with where the *compound nuclear reaction* mechanism is dominant. The other important mechanism is the *direct reaction* mechanism. These two mechanisms are on opposite ends of a spectrum. Direct reactions are fast, taking place in a time small compared to the mean-free-path of a nucleon within a nucleus, $\approx 10^{-22}$ seconds. They involve single-particle excitations in the target nucleus. Conversely, compound reactions take place over a much longer timescale $10^{-15} - 10^{-16}$ seconds and involve many-particle excitations. These can be thought of as reactions which form long-lived resonance states.

An essential aspect of modeling compound nuclear reactions is the Bohr Hypothesis. This is the idea that the compound nuclear reaction can be described by two independent processes: first, the absorption of the projectile by the target to form the intermediate resonance, the compound nucleus, and second, the decay of the compound nucleus. The Bohr hypothesis, roughly speaking, says that the compound nucleus forgets how it was formed, 'remembering' only its energy, spin, and parity. The second process, the decay, can therefore be described in purely statistical way, without regard to the specific nuclear states excited in the first

step. This approximation is far from perfect, and corrections are required.

7.3 Hauser-Feshbach theory

The Hauser-Feshbach (HF) statistical reaction formalism properly accounts for conservation of angular momentum and parity in compound-nuclear reactions. For a reaction with entrance channel $\alpha = a + A$ that forms the compound nucleus (CN) B^*, which subsequently decays into the exit channel $\chi = c + C$,

$$a + A \rightarrow B^* \rightarrow c + C,$$

the HF cross section can be written as

$$\sigma_{\alpha\chi}(E_a) = \sum_{J,\pi} \sigma_\alpha^{CN}(E_{ex}, J^\pi) G_\chi^{CN}(E_{ex}, J^\pi). \tag{7.3}$$

Here E_a and E_{ex} are the kinetic energy of the projectile a and the excitation energy of the compound nucleus B^*, respectively. They are related to each other via $E_a = \frac{m_A}{m_a + m_A}(E_{ex} - S_a)$, where S_a is the energy needed to separate the particle a from the nucleus B^*. m_a and m_A are the masses of the projectile and target, respectively. J and π are the spin and parity of the compound nucleus and $\sigma_\alpha^{CN}(E_{ex}, J^\pi)$ is the cross section for the forming the compound nucleus B^* with spin and parity J^π at energy E_{ex}. The $\sigma_\alpha^{CN}(E_{ex}, J^\pi)$ and their sum, the compound-formation cross section $\sigma_\alpha^{CN}(E_{ex}) = \sum_{J,\pi} \sigma_\alpha^{CN}(E_{ex}, J^\pi)$, can be determined using an appropriate optical model for the a-nucleus interaction. Width fluctuation corrections have been omitted to simplify the notation in Equation 7.3, but are included in the calculations.

Equation (7.3) expressed the idea introduced earlier that a compound nucleus 'forgets' how

it was formed. If in fact there were no correlation between the incoming and out-going particles, the total cross section (a probability-like quantity) would be the simple product of the formation cross section and decay probabilities. Being good physicists, we at least have to conserve angular momentum and parity, hence equation (7.3). As we will see later on, the essence of the Weisskopf-Ewing approximation is to give up even this.

$G_\chi^{CN}(E_{ex}, J^\pi)$ is the probability that the CN decays via the exit channel χ. It depends on the convolution of the transmission coefficient $T_{\chi l_c j_\chi}^J$ with the level density $\rho_{j_C}(U)$ for the residual nucleus, divided by analogous terms for all competing decay modes χ':

$$G_\chi^{CN}(E_{ex}, J^\pi) = \frac{\sum_{l_c j_\chi j_C} \int T_{\chi l_c j_\chi}^J \rho_{j_C}(U) dE_\chi}{\sum_{\chi' l_c' j_\chi' j_C'} \int T_{\chi' l_c' j_\chi'}^J (E_{\chi'}) \rho_{j_C'}(U') dE_{\chi'}}. \tag{7.4}$$

The quantities l_c and l_c' are the relative orbital angular momenta in the exit channels. $\vec{j}_\chi = \vec{j_c} + \vec{j_C}$ is the exit channel spin, related to the total spin $\vec{J} = \vec{l_a} + \vec{j_\alpha} = \vec{l_c} + \vec{j_\chi}$ by conservation of momentum with the entrance channel spin, $\vec{j_\alpha} = \vec{j_a} + \vec{j_A}$. $\rho_C(U, j_C)$ is the density of levels of spin j_C at energy U in the residual nucleus. Contributions from decays to discrete levels and to regions described by a level density have to be accounted for, as shown in the denominator of (7.4). All sums over quantum numbers must respect parity conservation, although this is not explicitly expressed here. A graphical representation of the decay of a compound nucleus is shown in Figure 7.1. In this example, the compound nucleus is ^{88}Y which is formed by neutron capture on ^{87}Y. The vertical gray bands represent the various sets of levels for different J. The dashes below are known discrete levels. The arrows represent various possible realizatons of decays, e.g. by gamma emission between excited states, or neutron emission to the neighboring nucleus. In a monte carlo HF code, decays continue until there are no more energetically favorable transitions.

We focus on neutron-induced reactions, i.e. $\alpha = n + A$. For such reactions, the optical model potential, used to calculate the first factor in (7.3), is well approximated by a one-body
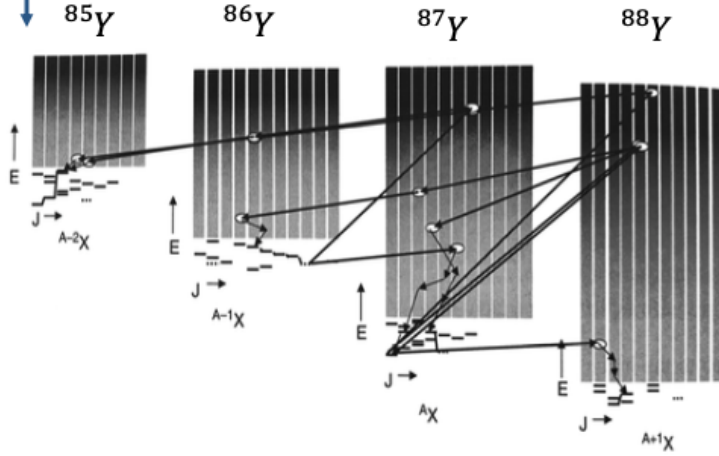
Figure 7.1: Figure of Hauser-Feshbach decay from "Nuclear Reactions for Astrophysics" Thompson and Nunes [278], originally attributed to Erich Ormand. In this case, a neutron captures on ^{87}Y to form the compound nucleus ^{88}Y, which subsequently decays statistically.

potential [100]. By far the greatest source of uncertainty comes from the decay probabilities, a fact that can be attributed to uncertainties in the nuclear structure inputs. *Ab initio* shell-model calculations can provide nuclear structure information for nuclei with only a dozen or so nucleons, and traditional shell-model calculations cover a limited number of nuclei, primarily near closed shells, containing up to around 100 nucleons. Mean-field and beyond-mean field approaches cover a wider range of nuclei, but calculating the relevant structure quantities (level densities and gamma-ray strength functions) is nontrivial. While much progress has been made toward achieving microscopic nuclear structure inputs for HF calculations of medium-mass and heavy nuclei, many isotopes needed for applications and for simulating stellar environments are currently out of reach.

A greatly simplified Hauser-Feshbach formula might be expressed in terms of a wave-number k_α and transmission coefficients T for the incoming and outgoing channels as:

$$\sigma_{\alpha\chi} = \frac{\pi}{k_\alpha} T_\alpha \frac{T_\chi}{\sum_{\chi'} T_{\chi'}}. \tag{7.5}$$

The right-most factor involving T_χ, when generalized to account for spins and continuous level density models yields equation (7.4). The transmission coefficients T_χ are related to

S-matrix elements connecting the incoming and outgoing particles:

$$T_\chi = 1 - |\langle S_{\chi\chi}\rangle|^2. \tag{7.6}$$

These must be available for all possible decay-channels. For nucleon emissions, these are assumed to be identical to the absorption transmission coefficients calculated using the optical model - again, these are well-constrained. A significant uncertainty enters, however, for the photon-transmission coefficients, which are especially relevant when the neutron-capture channel competes. In these reactions, the compound nucleus does not emit a nucleon, but is left in a highly excited state which must decay by electromagnetic transitions until it reaches its ground state.

7.3.1 Nuclear level density model

The level density model $\rho(E_x, J, \pi)$ is a mean description of the number of levels per unit energy available in the nucleus at excitation energy E_x and spin J. There are several models available for the description of the nuclear level density, but all are comparable to the model we will discuss here, the Gilbert-Cameron model [101], which combines the constant temperature model at low excitation with the back-shift Fermi-gas model at high temperature.

Closely paraphrasing the presentation of [215], the back-shifted Fermi gas model is

$$\rho_{FG}(E_x, J^\pi) = \frac{1}{12\sqrt{2}\sigma} \frac{\exp\left[2\sqrt{aU}\right]}{a^{1/4}U^{5/4}} P_J(E_x)P_\pi(E_x), \tag{7.7}$$

where $U = E_x - \Delta$, with Δ being the pairing parameter, σ is the spin cutoff parameter, and a is the single-particle, level-density parameter. The angular momentum distribution is

given by

$$P_J(E_x) = \frac{2J+1}{2\sigma^2} \exp\left[-\frac{(J+\frac{1}{2})^2}{2\sigma^2}\right], \tag{7.8}$$

while the parity fraction is generally taken to be $\frac{1}{2}$ for $\pi = \pm 1$. Both σ and a are functions of the excitation energy E_x. The energy dependence of the level-density parameter is

$$a(E_x) = \tilde{a}\left(1 + \delta W \frac{1 - \exp(-\gamma U)}{U}\right), \tag{7.9}$$

where $\tilde{a}$ is the asymptotic level density parameter, δW is the shell correction parameter, and γ is the shell damping factor. The spin cutoff parameter is taken to be of the form

$$\sigma^2(E_x) = \lambda A^{5/3} \sqrt{\frac{U}{a(E_x)}}, \tag{7.10}$$

where the constant is taken to be $\lambda = 0.01389$.

At low excitation energy, the level density is assumed to have the constant-temperature form:

$$\rho_{CT}(E_x, J^\pi) = \frac{1}{T} \exp\left[\frac{E_x - E_0}{T}\right] P_J(E_x) P_\pi(E_x), \tag{7.11}$$

where E_0 and T are fit to known low-lying discrete levels.

7.3.2 Gamma ray strength function model

For gamma transitions of a CN from relatively low-excitation energy, there are often gamma-ray transition probabilities available based on experimental measurements. For gamma transitions from highly excited states - far into the continuum description of the level density - no such measurements are available, and so phenomenological gamma-ray strength functions

(GSFs) are used. These functions were first understood in terms of photo-absorption and the observed giant dipole resonance. That phenomenon can be explained by strength functions which take modifications of the Lorentzian form:

$$f^{XL}(E_\gamma) = \frac{K_L}{E_\gamma^{2L-2}} \sum_i \frac{\sigma_{XL,i} E_\gamma \Gamma_{XL,i}^2}{(E_\gamma^2 - E_{XL,i}^2)^2 + E_\gamma^2 \Gamma_{XL,i}^2}, \tag{7.12}$$

where $K_L = 1/[(2L+1)\pi^2\hbar^2c^2]$ and $\sigma_{XL,i}$, $E_{XL,i}$, and $\Gamma_{XL,i}$ are the strength, energy, and width for each resonance. X and L define the type (electric or magnetic) and polarity of the transition.

For the E1 GSF, it is standard to add an additional energy-dependent term to the Lorentzians due to the work of Kopecky and Uhl [178] (again, closely paraphrasing the presentation in [215]):

$$f^{E1}(E_\gamma) = K_1 \sum_i \left[\frac{E_\gamma \Gamma_{E1,i}(E_\gamma)}{(E_\gamma^2 - E_{E1,i}^2)^2 + E_\gamma^2 \Gamma_{E1,i}^2(E_\gamma)} + \frac{0.7\Gamma_{E1} 4\pi^2 T^2}{E_{E1,i}^5} \right] \sigma_{E1,i} \Gamma_{E1,i}, \tag{7.13}$$

(note that both [215] and [177] have a typo in the second term, raising the denominator E_{E1} to the third power instead of the fifth, as it should be [178]) where the energy dependent width is given by

$$\Gamma_{E1,i}(E_\gamma) = \Gamma_{E1,i} \frac{E_\gamma^2 + 4\pi^2 T^2}{E_{E1,i}^2}, \tag{7.14}$$

and T is a nuclear temperature depending on the nuclear level density parameters and defined as

$$T = \sqrt{\frac{E_x - \Delta - E_\gamma}{a(S_n)}}, \tag{7.15}$$

where E_x is the excitation energy of the compound nucleus, Δ is the pairing gap, the $a(S_n)$ is the level-density parameter evaluated at the neutron separation energy S_n. An example

of this form is shown in Figure 7.2. This low energy enhancement of the E1 GSF represents
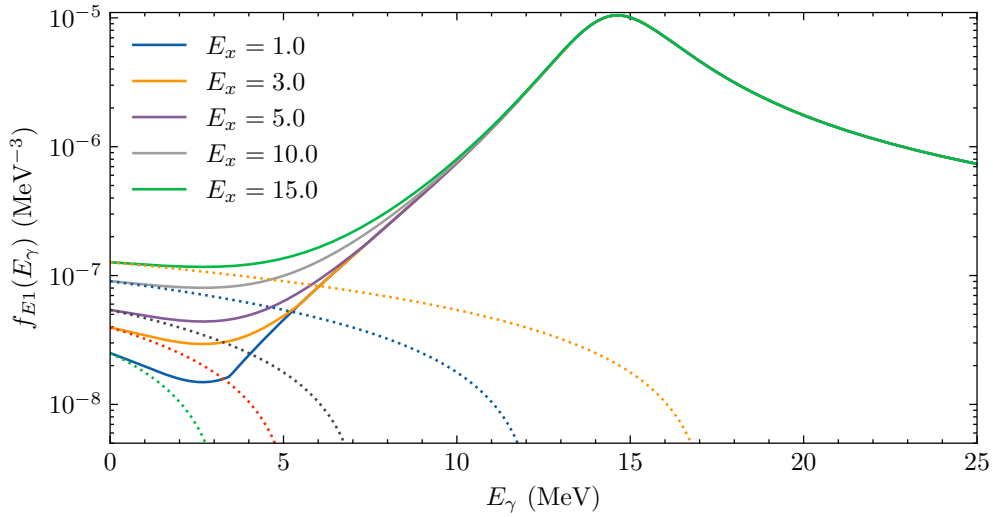

Figure 7.2: Kopecky-Uhl gamma-ray strength function: a standard Lorentzian centered at 15 MeV with a width of 4 MeV and the low-energy enhancement term (dotted lines) at various excitation energies E_x. The other parameters are $\Delta = -2.44$ MeV, $a(S_n) = 12.5$, $\sigma_{E1} = 180$ mb.

a break from the Brink-Axel hypothesis. The Kopecky-Uhl work [178] only included such a term in the E1 resonance because the energy regime they studied would not have been affected by additional terms in, e.g. the M1 GSF, which peaks between 5 - 10 MeV.

It is also common to include a second and weaker peak in the E1 somewhere around 5-10 MeV to model what is called the pygmy resonance (for a review, see [251]). This will not be considered in detail in this work.

Both the nuclear level densities and the gamma-ray strength functions follow systematic trends: nuclei which are neighbors on the nuclear chart are likely to have similar nuclear structures. Furthermore, there are databases such as the Reference Input Parameter Library (RIPL) [48] which store evaluated parameters, some of which are based on targeted studies of specific regions of the nuclear chart, and others based purely on global systematics.

However, these trends are not absolute, and since most global fits are based on measurements for nuclei near the valley of stability, it's expected that these models require special tuning

for any detailed study of particular nuclear reactions.

7.4 Hauser-Feshbach codes

Today's Hauser-Feshbach (HF) codes for reactions have evolved into multi-physics pack-ages that go beyond purely statistical [129] decay models. It's now routine to have an integrated software package that computes coupled-channel optical models, pre-equilibrium decays, width-fluctuation corrections, multi-chance fission, decays between hundreds of discrete states, and more [215, 177, 136].

Some examples of HF codes are TALYS [177, 173], EMPIRE [136], CoH [166], NON-SMOKER [239, 240], STAPRE [283] and YAHFC [215]. Each has different advantages, includes or omits certain approximations, and has favor with certain communities interested in statistical nuclear reactions. Some of the work presented in this part of the dissertation will use TALYS, STAPRE and YAHFC, while all calculations performed in Part III are performed with YAHFC.

YAHFC is a relatively new code developed at Lawrence Livermore National Laboratory by Erich Ormand (one of the original developers of the shell model code BIGSTICK). I have been able to participate in some of the development of YAHFC (mostly bug fixes). This has allowed me to extend its feature set when necessary for my applications. YAHFC is a Monte Carlo code, which means that the statistical decay calculations are carried out using random event generation with millions of events. This enables correlation and spectral analysis not possible with deterministic codes. For these reasons it is favored in this work.

Chapter 8

Surrogate Reactions I: Weisskopf-Ewing Approximation

This chapter is based on a paper I co-authored, "Cross sections for neutron-induced reactions from surrogate data: Reexamining the Weisskopf-Ewing approximation for (n, n') and $(n, 2n)$ reactions", by Oliver Gorton and Jutta Escher [116]. This is my first first-author journal paper. I did the majority of the work and writing, while my supervisor Jutta Escher designed the study (which was based on her previous studies of the Weisskopf-Ewing approximation for other reaction mechanisms), provided generous guidance and support, edited and helped write the manuscript, especially the introduction and discussion.

8.1   Surrogate reaction method

Nuclear reaction data are required for many applications in both basic and applied science, whether it be for modeling the origin of elements in the universe, the safe operation of a next-generation reactors, or for national-security applications [13, 133]. Nuclear reaction

libraries provide evaluated reaction data for many such applications [48]. These evaluations are based on nuclear reaction calculations anchored to experimental data and state-of-the-art nuclear theory. As many reaction cross sections of interest cannot be measured directly, due to short lifetimes or high radioactivity of the target nuclei involved, indirect methods are being developed [22, 282, 80, 182] to address the gaps and shortcomings in present databases.

In this chapter we focus on the "surrogate reaction method" [80, 77], an indirect approach for determining cross sections for compound-nuclear reactions. Compound-nuclear, or "statistical" reactions, proceed through the formation of an intermediate "compound" nucleus $n + A \rightarrow B^*$, followed by a decay into reaction products $B^* \rightarrow c + C$. The appropriate formalism for calculating cross sections for these reactions is the Hauser-Feshbach formalism [129, 99]. Hauser-Feshbach calculations are often quite limited in accuracy due to uncertainties in the nuclear physics inputs needed, in particular the nuclear structure inputs associated with the decay of the compound nucleus (CN).

In a surrogate reaction experiment, the CN of interest is produced via an alternative, experimentally accessible reaction, and the probability of decay into the reaction channel of interest is measured. From this data, constraints for the Hauser-Feshbach calculations can be obtained.

The surrogate method has some significant advantages over alternative indirect approaches: 1) the method does not require measurement of auxiliary nuclear properties that are not available for unstable nuclei and for which interpolation or extrapolation procedures are associated with uncontrolled uncertainties [81, 236], and 2) The method can be used for reactions that populate energies well above particle separation thresholds in the CN, i.e. it is applicable not only to (n, γ), but also to (n, n'), $(n, 2n)$, (n, p), (n, f) reactions (and similarly to charged-particle-induced reactions).

Alternative indirect approaches, in particular the Oslo and β-Oslo methods [182], aim at
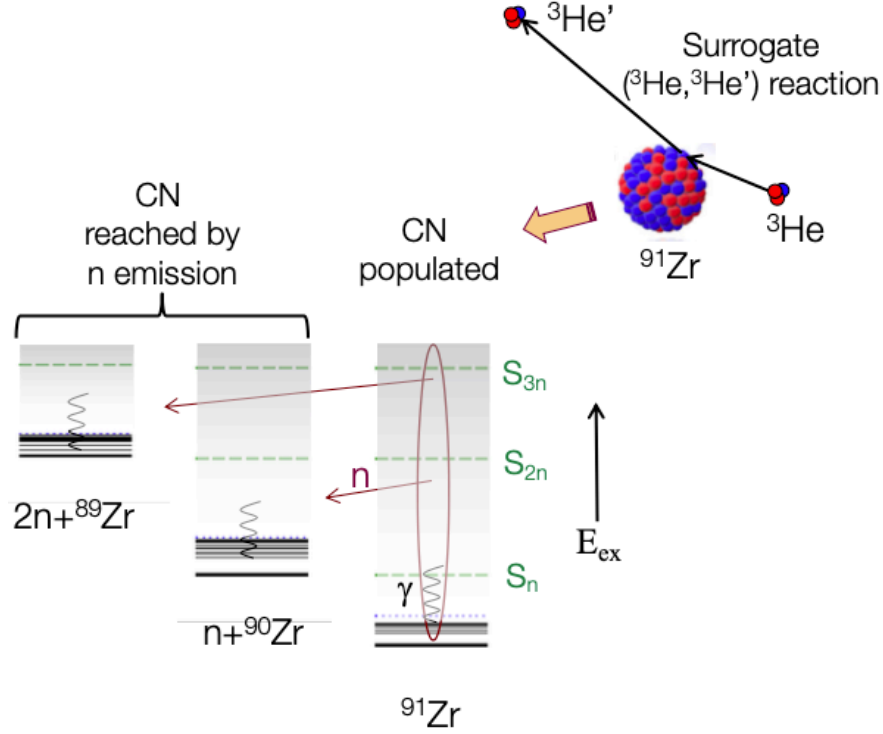
Figure 8.1: Surrogate reactions approach for the simultaneous measurement of ^{90}Zr(n,γ), ^{90}Zr(n,n'), and ^{90}Zr$(n,2n)$ cross sections. A recent inelastic scattering experiment produced the CN up to about 30 MeV, i.e. above the two-neutron threshold. Subsequent decay via emission of γs, one neutron, and two neutrons, produces final ^{91}Zr, ^{90}Zr, and ^{89}Zr nuclei, respectively. The example here displays a situation in which discrete γ transitions between low-lying states in three nuclei are used to determine the decay channel probabilities. A complementary decay measurement that focuses on the detection of neutrons is under development as well [154]. The ^{90}Zr experiment serves as a benchmark, since multiple neutron-induced reactions for the stable ^{90}Zr nucleus are known from direct measurements [263].

extracting level densities and γ-ray strength functions by populating a CN below the neutron separation energy via a transfer reaction or β decay, respectively, and measuring the resulting gamma emission. To separate the level density from the gamma-ray strength function, the Oslo-type analyses require the use of additional information; typically, this includes average neutron resonance spacings (D_0) and the average radiative widths, $\langle\Gamma_\gamma\rangle$. For neutron-induced reactions on unstable nuclei, however, these quantities are not available and are difficult to estimate reliably. In addition, the (n,n') and $(n,2n)$ reactions of interest here require CN decay information for excitation energies well above the neutron separation energy.

Both the surrogate method and the Oslo/β-Oslo methods require the calculation of the formation of the CN in the desired reaction. This involves, for neutron-induced reactions, knowledge of a neutron-nucleus optical model potential. For target nuclei near stability, global nucleon-nucleus optical models exist [176, 287], which are expected to be reliable at least a few isotopes away from stability. While these optical models are often applied far from stability, little is known about how well they work in these areas of the isotopic chart [163, 230, 134]. More theoretical work is needed to develop the next generation of optical model potentials. These need to display the proper dispersive properties and reflect the correct isospin dependence, and are ideally based on microscopic theories [65, 229, 300, 30]. In addition, new experiments at radioactive beam facilities are needed to constrain and test the optical models.

Applications of the surrogate method to (n, f) reactions have a long history [80] and in recent years scientists successfully used the approach to obtain neutron capture cross sections [81, 236, 222]. In this chapter, we focus on possible applications to (n, n') and $(n, 2n)$ reactions.

Figure 8.1 illustrates how the surrogate approach can be used to determine ^{90}Zr(n, γ), ^{90}Zr(n, n'), and ^{90}Zr$(n, 2n)$ cross sections from a surrogate inelastic scattering experiment. For incident neutron energies below a few MeV, neutron capture and inelastic neutron scattering compete with each other, above $E_n \approx 10$ MeV, one- and two-neutron emission compete with each other. Proton and α emission compete only weakly and have to be accounted for, but are not shown here. In actinides, fission may compete at all energies. If the surrogate reaction measurement is designed to cover a broad energy range, it becomes possible to determine cross sections for all three neutron-induced reactions in *one* experiment. The decay channel of interest is determined either by measuring γ transitions specific to one of the three decay products, or by detecting outgoing neutrons, in coincidence with the scattered ^{3}He particle. Experimentalists conducting these measurements have utilized discrete γ rays

and are currently developing the capability to use neutron measurements.

8.2   The Weisskopf Ewing approximation

In principle, a careful description of the surrogate reaction mechanism is required to obtain the cross section of the desired reaction. This is because one must account for the differences in the decay of the CN due to the angular-momentum and parity differences in the surrogate and desired reactions (the spin-parity mismatch). Indeed, (n, γ) reactions are very sensitive to spin effects, particularly in nuclei with low level density [58, 79, 93]. On the other hand, sensitivity studies for surrogate (n, f) applications have shown that neglecting the spin-parity mismatch yields reasonable results, except at low neutron energies [307, 308, 78]. Neglecting the spin-parity mismatch between the surrogate and desired reactions is known as the Weisskopf-Ewing approximation, and it greatly simplifies the extraction of the cross sections from surrogate data, as only a simple theoretical treatment is required.

It is the purpose of this chapter to investigate what is required to determine reliable cross sections for (n, n') and $(n, 2n)$ reactions from surrogate data. Specifically, we carry out sensitivity studies that examine the validity of the Weisskopf-Ewing approximation for these two reactions for several regions of the nuclear chart.

In the next section, we review the surrogate reaction formalism and provide details on the Weisskopf-Ewing approximation. In Section 8.4, we describe our procedure for testing the assumption of the approximation, and for investigating the consequences of applying the approximation in situations where its assumptions are not strictly valid. In Section 8.5, we present results for zirconium, gadolinium and uranium nuclei, which are representative of spherical and deformed nuclei, respectively. We summarize our findings and make recommendations in Section 8.6.

8.3 Weisskopf-Ewing formalism

Here we summarize the Hauser-Feshbach formalism for calculating the cross section of a compound-nuclear reaction and its relationship to the description of a surrogate reaction. This clarifies how surrogate reaction data can be used to constrain calculations for unknown cross sections. We outline the circumstances under which the Weisskopf-Ewing approximation can be used to simplify the analysis used to obtain the desired compound cross section.

8.3.1 Full modeling of the surrogate reaction

In a surrogate experiment, such as the one schematically shown in Figure 8.1, the compound nucleus B^* is produced by an inelastic scattering or transfer reaction $d + D \rightarrow b + B^*$, and the desired decay channel is observed in coincidence with the outgoing particle b at angle θ_b.

The probability for forming B^* in the surrogate reaction (with specific values for E_{ex}, J, π) is $F_\delta^{CN}(E_{ex}, J, \pi, \theta_b)$, where δ refers to the surrogate reaction $d + D \rightarrow b + B^*$. The quantity

$$P_{\delta\chi}(E_{ex}, \theta_b) = \sum_{J,\pi} F_\delta^{CN}(E_{ex}, J^\pi, \theta_b) \ G_\chi^{CN}(E_{ex}, J^\pi) \, , \tag{8.1}$$

which gives the probability that the CN B^* was formed with energy E_{ex} and decayed into channel χ, can be obtained experimentally by detecting a discrete γ-ray transition characteristic of the residual nucleus (or some other suitable observable).

The distribution $F_\delta^{CN}(E_{ex}, J, \pi, \theta_b)$, which may be very different from the CN spin-parity populations following the absorption of a neutron in the desired reaction, has to be determined theoretically, so that the branching ratios $G_\chi^{CN}(E_{ex}, J^\pi)$ can be extracted from the measurements.

In practice, the decay of the CN is modeled using a Hauser-Feshbach-type decay model and the $G_\chi^{CN}(E_{ex}, J^\pi)$ are obtained by adjusting parameters in the model to reproduce the measured probabilities $P_{\delta\chi}(E_{ex}, \theta_b)$. Subsequently, the sought-after cross section for the desired (neutron-induced) reaction can be obtained by combining the calculated cross sections $\sigma_{n+A}^{CN}(E_{ex}, J^\pi)$ for the formation of B^* (from $n+A$) with the extracted decay probabilities $G_\chi^{CN}(E_{ex}, J^\pi)$, see Eq. (10.1). Modeling the CN decay begins with an initial ("prior") description of structural properties of the reaction products (level densities, branching ratios, internal conversion rates), plus a fission model for cases which involve that decay mode. Finally, a procedure for fitting the parameters of the decay models, e.g. via a Bayesian approach as introduced in Ref. [81], needs to be implemented to determine the desired cross section, along with uncertainties.

This procedure was recently employed to determine cross sections for neutron capture on the stable ^{90}Zr and ^{95}Mo isotopes (for benchmark purposes), as well as for neutron capture on the unstable ^{87}Y nucleus [81, 236]. It was also used to simultaneously infer the (n, γ) and low-energy (n,f) cross sections for ^{239}Pu [222]

Such a full treatment of a surrogate experiment is challenging: It involves taking into account differences in the angular momentum J and parity π distributions between the compound nuclei produced in the desired and surrogate reactions, as well as their effect on the decay of the compound nucleus. Predicting the spin-parity distribution $F_\delta^{CN}(E_{ex}, J, \pi, \theta_b)$ resulting from a surrogate reaction is a nontrivial task since a proper treatment of direct reactions leading to highly excited states in the intermediate nucleus B^* involves a description of particle transfers, and inelastic scattering, to unbound states. In addition, a complete treatment should include consideration of width fluctuation corrections and the possible decay prior to reaching equilibrium.

For capture cross sections, it was shown that this type of approach is needed to account for the spin-parity mismatch in the surrogate experiment [79, 58], while for fission applications

it often suffices to employ the much simpler Weisskopf-Ewing or ratio approximations [78].

8.3.2 Weisskopf-Ewing approximation for neutron-nucleus reactions and surrogate coincidence probabilities

The Hauser-Feshbach expression for the cross section of the desired neutron-induced reaction, Eq. (10.1), conserves total angular momentum J and parity π. Under certain conditions the branching ratios $G_\chi^{CN}(E_{ex}, J^\pi)$ can be treated as independent of J and π and the cross section for the desired reaction simplifies to

$$\sigma_{n+A,\chi}^{WE}(E_a) = \sigma_{n+A}^{CN}(E_{ex}) \, \mathcal{G}_\chi^{CN}(E_{ex}) \tag{8.2}$$

where $\sigma_{n+A}^{CN}(E_{ex}) = \sum_{J\pi} \sigma_{n+A}^{CN}(E_{ex}, J^\pi)$ is the cross section describing the formation of the compound nucleus at energy E_{ex} and $\mathcal{G}_\chi^{CN}(E_{ex})$ denotes the $J\pi$-independent branching ratio for the exit channel χ. This is the Weisskopf-Ewing limit of the Hauser-Feshbach theory [100].

The Weisskopf-Ewing limit provides a simple and powerful approximate way of calculating cross sections for compound-nucleus reactions. In the context of surrogate reactions, it greatly simplifies the application of the method. In section 8.3.1 we described the process required to obtain the $J\pi$-dependent branching ratios G_χ^{CN} from measurements of $P_{\delta\chi}(E_{ex})$. In the Weisskopf-Ewing limit, and because $\sum_{J\pi} F_\delta^{CN}(E_{ex}, J^\pi) = 1$,

$$P_{\delta\chi}(E_{ex}) = \mathcal{G}_\chi^{CN}(E_{ex}). \tag{8.3}$$

Calculating the direct-reaction probabilities $F_\delta^{CN}(E_{ex}, J, \pi, \theta_b)$ and modeling the decay of the compound nucleus are no longer required in this approximation. (In actual applications,

experimental efficiencies have to be included when determining $P_{\delta\chi}(E_{ex})$; these are omitted for simplicity here, but are accounted for in the analysis of surrogate experiments.)

The conditions under which the approximate expressions (8.2)) and (8.3) are obtained from equations (10.1) and (8.1) are discussed in the appendix.

In addition, the Weisskopf-Ewing approximation can be used in situations in which the surrogate reaction produces a spin distribution that is very similar to that of the desired reaction, i.e.

$$F_{\delta}^{CN}(E_{ex}, J^{\pi}) \approx F_{n+A}^{CN}(E_{ex}, J^{\pi}) \equiv \frac{\sigma_{n+A}^{CN}(E_{ex}, J^{\pi})}{\sum_{J^{\pi'}} \sigma_{n+A}^{CN}(E_{ex}, J^{\pi'})}, \tag{8.4}$$

since the weighting of the J^{π}-dependent decay probabilities in the measured $P_{\delta\chi}(E_{ex})$ is the same as the weighting relevant to the desired reaction. While some intuitive arguments have been forwarded in favor of specific surrogate reaction mechanisms that might satisfy the condition (8.4), not much is actually known about what spin-parity distributions F_{δ}^{CN} are obtained when producing a CN at high excitation energies ($E_{ex} > 5$ MeV) via inelastic scattering or a transfer reaction. We therefore investigate both the dependence of realistic decay probabilities $G_{\chi}^{CN}(E_{ex}, J^{\pi})$ on spin and parity (Section 8.4.1) and the impact of using the Weisskopf-Ewing approximation in situations in which $G_{\chi}^{CN}(E_{ex}, J^{\pi})$ depends on spin and parity (Section 8.4.2).

8.3.3 Conditions of the Weisskopf-Ewing limit

As discussed in Section 8.3.2, if the decay probabilities $G_{\chi}^{CN}(E_{ex}, J^{\pi})$ are independent of spin and parity, or the surrogate reaction produces a compound nucleus spin distribution which is very similar to that produced by the neutron-induced reaction, the cross section for the

desired reaction can be obtained very simply as:

$$\sigma_{n+A,\chi}(E_n) = \sigma_{n+A}^{CN}(E_{ex}) P_{\delta\chi}^{CN}(E_{ex}), \tag{8.5}$$

where $P_{\delta\chi}^{CN}(E_{ex})$ is the coincidence probability determined from the surrogate measurement.

The latter of these options, the 'serendipitous' or 'matching' condition requires that $F_{\delta}^{CN}(J^{\pi}) \approx F_{n+A}^{CN}(E_{ex}, J^{\pi})$ holds. A comparison of $F_{n+A}^{CN}(E_{ex}, J^{\pi})$ for representative nuclei and energies E_{ex}, shown in Figure 8.2 of this chapter and in Figure 3 of Ref. [79], with realistic surrogate spin-parity distributions, such as those shown in Figure 8.3, indicates that it is difficult to identify and carry out a surrogate reaction experiment that can achieve this condition.

Here, we briefly review the conditions in which the decay probabilities become approximately independent of J^{π}, i.e. $G_{\chi}^{CN}(E_{ex}, J^{\pi}) \to \mathcal{G}_{\chi}^{CN}(E_{ex})$ (see also Refs. [100, 78]):

First, the energy of the compound nucleus has to be sufficiently high, so that almost all channels into which the nucleus can decay are dominated by integrals over the level density. In that case, the denominator in Eq. (10.2) does not include decays to discrete levels.

Second, correlations between the incident and outgoing reaction channels, which can be formally accounted for by including width fluctuation corrections [140], have to be negligible. These correlations enhance elastic scattering, at the expense of the inelastic and reaction cross sections, and are most prominent at the low energies relevant to capture reactions. Width fluctuations are negligible if the first condition (above) is satisfied.

Third, the transmission coefficients $T_{\chi'l_c'j_\chi'}^{J}$ associated with the available exit channels have to be independent of the spin of the states reached in these channels. This condition is sufficiently well satisfied since the dependence of transmission coefficients on target spin is very weak and, in fact, is ignored in many Hauser-Feshbach codes.

Fourth, the level densities ρ_{jC} in the available channels have to be independent of parity and their dependence on the spin of the relevant nuclei has to be of the form $\rho_{jC} \propto (2j_C + 1)$. While level densities are known to depend on parity, that dependence becomes weaker with increasing excitation energy and is often ignored in statistical reaction calculations. In addition, many successful applications use level densities that are parametrized in a form that is factorized (for each parity) as:

$$\rho_{jC}(U_C) = w(U_C)\frac{(2j_C + 1)}{2\sigma_C^2} \exp\left(\frac{-j_C(j_C + 1)}{2\sigma_C^2}\right), \tag{8.6}$$

where $w(U_C)$ contains the energy dependence of the level density and σ_C is the spin cut-off factor. At low energies ($E_{ex} \le 3$ MeV), typical values for σ_C^2 are 7-10 in the Zr region and 12-16 in the Gd region [290]. As E_{ex} increases from a few MeV to about 20 MeV, σ_C^2 can increase by a factor of 4 or more for these mass regions [291]. If we then assume that the spins populated in the residual nucleus are small compared to the σ_C, the level density can be written as

$$\rho_{jc}(U_C) \approx \frac{w_C(U_C)}{2\sigma_C^2}(2j_C + 1). \tag{8.7}$$

When the above conditions are satisfied, the decay probabilities from Eq. (10.2) take the form:

$$G_\chi^{CN}(E_{ex}, J^\pi) = \frac{\sum_{l_c j_\chi j_C} \int T_{\chi l_c j_\chi}^J w_C(U_C)(2j_C + 1)dE_\chi}{\sum_{\chi' l_c' j_\chi' j_C'} \int T_{\chi' l_c' j_\chi'}^J(E_{\chi'})w_{C'}(U_C')(2j_C' + 1)dE_{\chi'}}. \tag{8.8}$$

We can carry out the sum over j_C if we use the triangle rule $|j_\chi - j_c| < j_C < |j_\chi + j_c|$ to obtain the identity

$$\sum_{j_C}(2j_C + 1) = (2j_\chi + 1)(2j_c + 1), \tag{8.9}$$

189

analogously for the j_χ:

$$\sum_{j_\chi}(2j_\chi + 1) = (2J + 1)(2l_c + 1), \tag{8.10}$$

to obtain the spin-independent decay probabilities:

$$\mathcal{G}^{CN}_\chi(E_{ex}) = \frac{\left(\sum_{l_c}(2l_c + 1)T_{\chi l_c}\right)\int(2j_c + 1)w_C(U_C)dE_\chi}{\left(\sum_{\chi' l'_c}(2l_c + 1)T_{\chi' l'_c}(E_{\chi'})\right)\int(2j'_c + 1)w_{C'}(U'_C)dE_{\chi'}}. \tag{8.11}$$

In summary, in order for the $G^{CN}_\chi(E_{ex}, J^\pi)$ to become independent of spin and parity, the energy E_{ex} of the compound nucleus must be high enough so that decays to the continuum of residual nuclei dominate, and the reaction must populate spins that are small relative to the spin cutoff parameter. Since neutron-induced reactions and surrogate reactions can produce different spin distributions, it is possible that the conditions for the validity of the Weisskopf-Ewing approximation are satisfied for one type of reaction, but not the other.

8.4 Assessing the validity of the Weisskopf-Ewing approximation

As discussed in the previous section, there are two scenarios in which it is clearly valid to employ the Weisskopf-Ewing approximation in the analysis of a surrogate experiment: (a) The decay probabilities $G^{CN}_\chi(E_{ex}, J^\pi)$ are independent of $J\pi$ for the decay channel χ of interest; or (b) The surrogate and desired reactions produce identical spin distributions ("serendipitous" or "matching" approach [80]). In addition, there are some intermediate situations in which a Weisskopf-Ewing analysis can give a good approximation to the true cross section. For instance, it is possible that the decay probabilities $G^{CN}_\chi(E_{ex}, J^\pi)$ are only moderately sensitive to $J\pi$, and that the surrogate and desired reactions populate somewhat

similar compound nucleus spins and parities, so that violations of the Weisskopf-Ewing limit may have little impact on the extracted cross section. Investigations into the possibility of using the Weisskopf-Ewing approximation must therefore consider *both* the behavior of the decay probabilities $G_\chi^{CN}(E_{ex}, J^\pi)$ for the decay channel χ of interest *and* their influence in typical surrogate reaction analyses.

Earlier studies, which have done that, demonstrated that it is not *a priori* clear whether the Weisskopf-Ewing limit applies to a particular reaction in a given energy regime [78, 93, 79, 58]. For fission applications, it was found that using the Weisskopf-Ewing approximation gives reasonable cross sections, with violations of the Weisskopf-Ewing limit occurring primarily at low energies (E_n below 1-2 MeV) and at the onset of first and second-chance fission [78]. For neutron capture reactions, however, the $G_\gamma^{CN}(E_{ex}, J^\pi)$ were found to be very sensitive to the $J\pi$ and no circumstances have been identified so far in which the Weisskopf-Ewing limit can be used to obtain capture cross sections [79].

In the present study we focus on the proposed use of the surrogate method to determine (n, n') and $(n, 2n)$ cross sections. To study the validity of the Weisskopf-Ewing approximation, we proceed in two steps:

1. Investigation of the $J\pi$ dependence of the decay probabilities $G_\chi^{CN}(E_{ex}, J^\pi)$ for $\chi = 1n$ and $2n$, *i.e.* for one- and two-neutron emission.

2. Assessment of the impact of the $J\pi$ dependence of the $G_\chi^{CN}(E_{ex}, J^\pi)$ on cross sections extracted by using the Weisskopf-Ewing approximation.

8.4.1 Method for determining spin-parity dependence

In the first step, we obtain the $G_\chi^{CN}(E_{ex}, J^\pi)$ from well-calibrated Hauser-Feshbach calculations that involve the relevant decay channels. We selected $n+^{90}$Zr, $n+^{157}$Gd, and $n+^{238}$U

as representative cases for neutron reactions on spherical and deformed nuclei, with the uranium case representing a nucleus for which fission competes with particle evaporation and γ emission.

For each nucleus, we carried out a full Hauser-Feshbach calculation of the neutron-induced reaction and calibrated the model parameters to give an overall good fit of the known neutron cross sections. This local optimization of model parameters allows us to isolate the spin-parity effects from model uncertainties. Our optimization procedure accounted for pre-equilibrium effects using the two-exciton model [172], and other competing decay channels. This is necessary to accurately and realistically reproduce the data without biasing the model-space parameters. In contrast, the calculations described in this and the following section include only contributions from compound nucleus decay. This is consistent with the goal of investigating the ability to determine the compound cross section from a Weisskopf-Ewing analysis of surrogate data.

The calculations were carried out with Hauser-Feshbach codes STAPRE [283] and YAHFC [215]. The results discussed here are obtained using the latter. We extracted the branching ratios $G_{xn}^{CN}(E, J^\pi)$ for one- and two-neutron emission ($x = 1$ and 2, respectively) for a range of spin and parity values of the initially formed compound nuclei ^{91}Zr*, ^{158}Gd*, and ^{238}U*, and investigated their behavior as a function of the excitation energy E_{ex} of the CN. Our findings are discussed in Section 8.5.1.

8.4.2 Method for demonstrating impact of spin-parity dependence

In the second step, we employ the decay probabilities $G_{xn}^{CN}(E_{ex}, J^\pi)$ extracted above to simulate the results of possible surrogate measurements. This is done by calculating the co-incidence probabilities given by equation (8.1), which are ordinarily measured in a surrogate experiment, by multiplying the $G_{xn}^{CN}(E_{ex}, J^\pi)$ with several schematic spin-parity distributions

$F_\delta^{CN}(E_{ex}, J^\pi)$, summed over all relevant spins and parities:

$$P_{xn}^{sim}(E_{ex}) = \sum_{J\pi} F_\delta^{CN}(E_{ex}, J^\pi) G_{xn}^{CN}(E_{ex}, J^\pi). \tag{8.12}$$

We normalized the distributions $\sum_{J\pi} F_\delta^{CN}(E_{ex}, J^\pi) = 1$ and did not consider angle dependencies. Multiplication of these simulated coincidence probabilities $P_{xn}^{sim}(E_{ex})$ by the CN-formation cross section $\sigma_{n+A}^{CN}(E_{ex})$ then yields cross sections $\sigma_{(n,n')}^{WE}(E_n)$ and $\sigma_{(n,2n)}^{WE}(E_n)$ that correspond to a Weisskopf-Ewing analysis of the simulated surrogate measurement:

$$\sigma_{(n,xn)}^{WE}(E_n) = \sigma_{n+A}^{CN}(E_{ex}) P_{xn}^{sim}(E_{ex}) \tag{8.13}$$

for $x = 1, 2$. In Section 8.5.2, we compare the so extracted cross sections for various spin-parity distributions F_δ^{CN} to each other and to the known desired cross sections.

To select relevant $J\pi$ distributions for our study, we briefly summarize what is known about $J\pi$ distributions that typically occur in neutron-induced as well as surrogate reactions.

Spin-parity distributions in neutron-induced reactions.

Figure 8.2 shows spin-parity distributions relevant to neutron-induced reactions, as predicted by calculating the compound-formation cross sections for various spins and parities, at the energies indicated. For Zr, a spherical optical-model calculation is sufficient, while rare earths and actinides require coupled-channels treatments, which can be carried out by suitably deforming a spherical optical model, see Ref. [209, 210], or by using a coupled-channels scheme that is specifically adjusted for the nucleus or nuclear region of interest, see Refs. [267, 268, 196, 66, 79]. We have used the Koning-Delaroche optical model [176] for Zr and Gd, and Soukhovitskii [267, 268] for U.

For the (n, n') and $(n, 2n)$ applications considered here, neutron energies between about 5 and 20 MeV are relevant. The examples selected here involve target nuclei with low spins ($3/2^-$ for ^{157}Gd and 0^+ for the even-even ^{90}Zr and ^{238}U nuclei), so the spin-distributions are closely connected to the angular-momentum transferred in the reaction.

Panel (a) shows the population of positive and negative parity states for the n+^{90}Zr example, for several neutron energies E_n. At $E_n \approx 1$ MeV, p-wave capture dominates [93] and produces a distribution that favors negative-parity states within a narrow range of spins. As the energy increases, contributions from higher partial waves result in smoother distributions, centered at larger angular momentum values, and with a more equal partition between positive and negative spins.

Panels (b), for n+^{157}Gd, and (c), for n+^{238}U, are representative of the situations one encounters for deformed rare-earth and actinide nuclei, respectively. Overall, the distributions are smoother for the deformed nuclei than for the Zr case and involve larger values of angular momentum. With increasing E_n, the positive and negative parity distributions become similar, while at low energies, $E_n < 1$ MeV, the distributions can look quite different from each other [79].

Spin-parity distributions in surrogate reactions.

The findings of the following illustrate that it is *not* correct to assume that the spin-parity distribution of a compound nucleus produced in a surrogate reaction is given by the spin and parity behavior of the level density for that nucleus. The reaction mechanism plays a critical role in selecting which states act as doorways into the compound nucleus. The population of these doorway states determines the $J\pi$ distribution for the surrogate reaction.

Figure 8.1 illustrates schematically the excitation energies that a surrogate reaction has to populate in order to produce decay information relevant to (n, γ), (n, n') and $(n, 2n)$
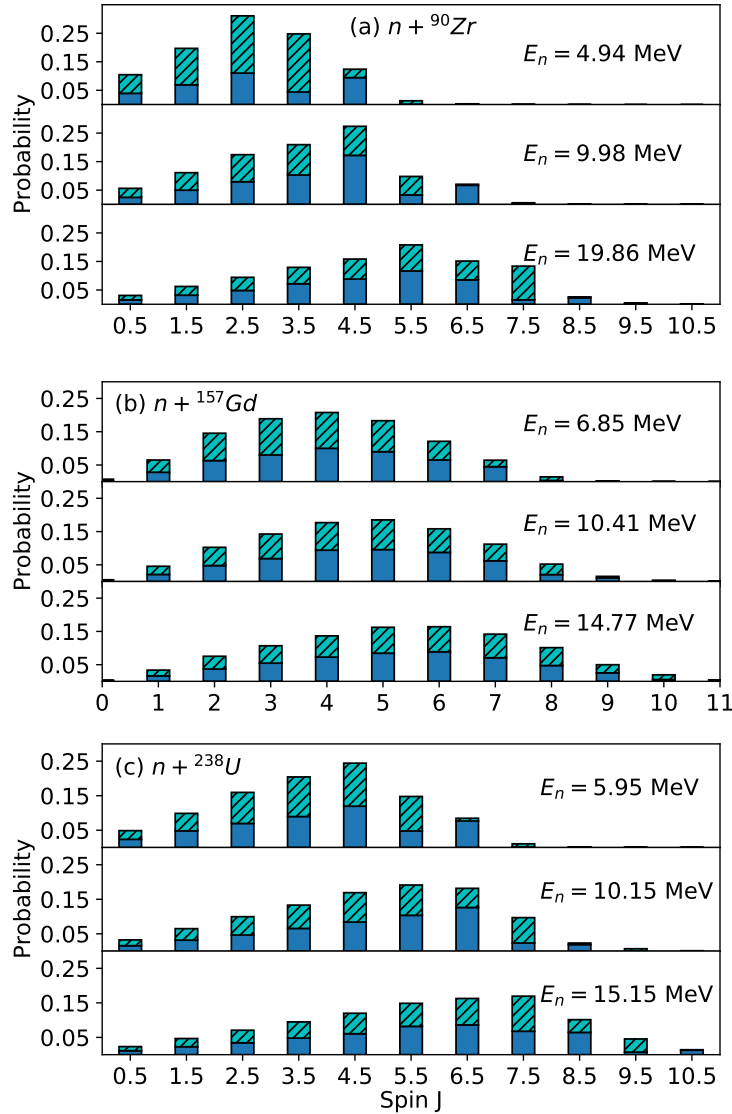
Figure 8.2: (Published in [116].) Spin-parity distributions for compound nuclei produced in neutron-induced reactions, for several neutron energies E_n. Solid bars are positive- and hatched bars are negative-parity probabilities. Panels (b) n+^{157}Gd and (c) n+^{238}U are representative of deformed rare-earth and actinide nuclei, respectively, while panel (a) presents the case of a near-closed shell nucleus, n+^{90}Zr. Neutron energies below 1 MeV are important for neutron capture reactions [79]. For the (n, n') and $(n, 2n)$ applications considered in this chapter, neutron energies between about 5 and 20 MeV are relevant.

reactions. For neutron capture, E_{ex} values between about 5 and 10 MeV have to be reached, for inelastic scattering, energies between approximately 10 and 20 MeV are relevant, and for $(n, 2n)$ reactions, $E_{ex} = 20$-30 MeV are important. These energy regimes exhibit high level

densities, and transfer reactions aiming to populate these energy ranges are very different from those used for traditional nuclear structure studies. It should therefore not surprise that standard DWBA or even coupled-channels calculations cannot be used to reliably calculate the direct (surrogate) reactions that produce such states.

Predicting the spin-parity distributions for these higher excitation energies requires taking into account both the surrogate reaction mechanism and the nuclear structure at these higher energies. For instance, to calculate the $J\pi$ population in the compound nucleus ^{91}Zr* that was produced via the ^{92}Zr(p,d) pickup reaction in a recent surrogate experiment with $E_p = 28.5$ MeV [81], it was necessary to consider the structure of deep neutron hole states, which exhibit considerable spreading [70, 80]. Furthermore, two-step mechanisms involving $(p, d')(d', d)$ and $(p, p')(p', d)$ combinations of inelastic scattering and pickup contribute significantly to the reaction. These have a strong influence on the final spin-parity distribution in ^{91}Zr* [81], which is shown for $E_{ex} = 7.25$ MeV in Figure 8.3(a). The influence of the reaction mechanism is reflected in the differences between the predicted spin-parity population (bars) and the spin distribution in a representative level density model at the same excitation energy (green curve).

Around the neutron separation energy, $i.e.$ in the energy region of interest to neutron capture, the angular behavior of the (p,d) cross section was found to be fairly structureless, and the $J\pi$ distribution was seen to vary little over several MeV around $E_{ex} = S_n(^{91}\text{Zr}) = 7.195$ MeV [72]. These observations reflect the fact that the surrogate reaction does not produce a simple single-particle excitation, but populates specific *doorway* states which mix with neighboring complex many-body states to form the compound nucleus.

The (d, p) transfer reaction, which – at first glance – seems to be a well-matched surrogate for neutron-induced reactions, turns out to involve non-trivial reaction mechanisms as well. The case of interest is that in which the deuteron breaks up in the combined Coulomb-plus-nuclear field, and the neutron is absorbed while the proton escapes and is observed

in a charged-particle detector. Calculating the resulting compound nucleus $J\pi$ distribution requires a theoretical description that separates elastic from nonelastic breakup and, in principle, one also needs to separate out inelastic breakup, rearrangement, and absorption. This challenge has generated strong interest in developing a more detailed formalism for inclusive (d, p) reactions [187, 188, 225, 50, 226]. This formalism was used to calculate the $J\pi$ distribution relevant to the ^{95}Mo(d, p) surrogate reaction described in Ref. [236]. The calculated $J\pi$ distribution, for excitation energies near the neutron separation energy in ^{95}Mo is shown in Figure 8.3(b). Here, again, the predicted spin-parity distribution (bars) does not follow the distribution of spins that are expected to be available at this energy, based on a representative level density model (green curve).

Inelastic scattering with charged light ions is a third type of reaction that has been employed in surrogate reaction measurements [262, 242, 153, 216, 222]. From these experiments, as well as from traditional studies of giant resonances [28, 35, 194], it is known that inelastic scattering can produce a compound nucleus at a wide range of excitation energies. There is evidence that this type of reaction is also likely to produce $J\pi$ distributions that are broad and may be centered at angular momentum values of 5-10 $\hbar$ [262, 222]. Furthermore, for inelastic α scattering, a staggering of even and odd parity populations is expected, since the reaction populates predominantly natural-parity states.

Schematic spin-parity distributions

In order to investigate the impact of a spin-parity mismatch between the desired and surrogate reaction on the cross section obtained from a Weisskopf-Ewing analysis, we employ the schematic distributions $F_\delta^{CN}(J^\pi)$ shown in Figure 8.4. We include distributions that are centered at both low and high angular-momentum values and allow for more spread-out distributions in the latter case. The distributions centered at low J values allow us to investigate situations in which the surrogate reaction populates lower spins than the desired
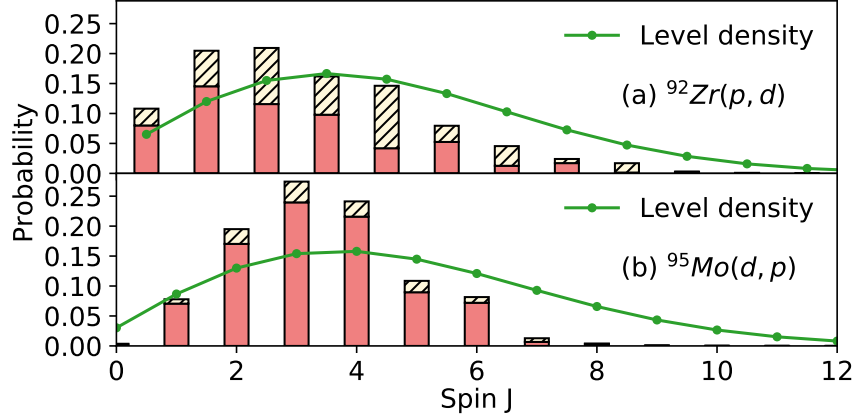
Figure 8.3: (Published in [116].) Spin-parity distributions (bars) near the neutron separation energy, as predicted for use with specific surrogate experiments. Solid bars are positive-parity and hatched bars are negative-parity probabilities. Panel (a) shows the half-integer J distribution in the compound nucleus ^{91}Zr* resulting from a ^{92}Zr(p,d) reaction with $E_p = 28.5$ MeV at $E_{ex} = 7.25$ MeV [81]. Panel (b) shows the integer valued result for ^{95}Mo(d,p) surrogate reaction with $E_d = 12.4$ MeV at $E_{ex} = 9.18$ MeV [236]. In both cases, the predicted spin-parity distributions were used in combination with models for the decay of the respective compound nuclei, leading to the successful determination of (benchmark) neutron capture cross sections. For comparison, the spin distribution calculated from an energy-dependent level density model, which assumes equal parity distribution, is given by the green solid curve [291].

reaction. Variations in parity are not explicitly considered for this part of the sensitivity study, as we found the decay probabilities to be less sensitive to parity than to variations in spin.

The distributions shown will be combined with the decay probabilities $G_\chi^{CN}(E_{ex}, J^\pi)$ extracted from our calibrated Hauser-Feshbach calculations (see Section 8.5.1) to simulate a range of possible surrogate data $P_{\delta\chi}(E_{ex}, \theta)$ using Eq. (8.1). For simplicity, we will neglect the energy dependence of the $J\pi$ distributions. This should be a reasonable approach for our sensitivity studies, as recent results indicate that these distributions vary slowly with energy [236, 81].
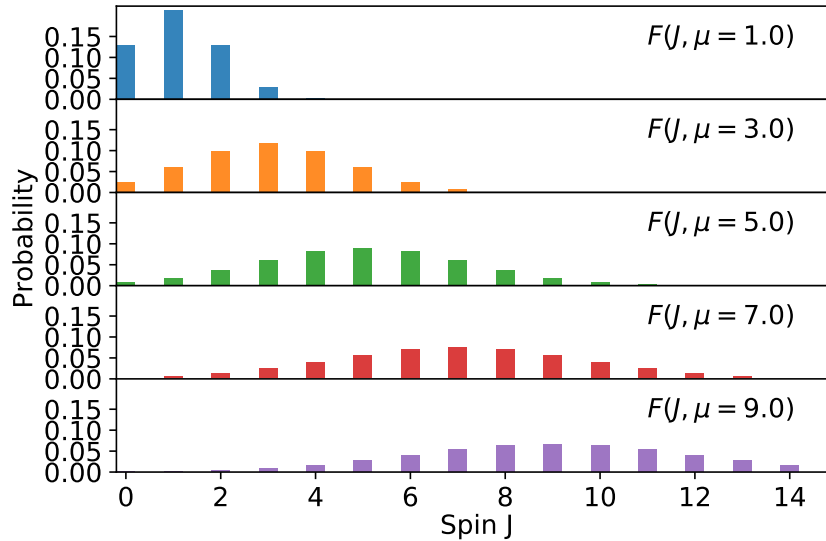
Figure 8.4: (Published in [116].) Schematic spin distributions employed in the current study. Each is of the form $F(J, \mu) \propto \mathcal{N}(m = \mu, sd = \sqrt{\mu})$, where $\mathcal{N}$ is a normal distribution and mean spin μ is indicated in the legend. The spin values J are either integer or half-integer, for even-A and odd-A nuclei, respectively, and equal probability is assigned to positive and negative parity states.

8.5 Results

We first demonstrate that the one- and two-neutron decay probabilities depend on the spin, and to a lesser extent, the parity of the compound nucleus. The dependence is strongest at low energies and for spherical nuclei, and lesser at higher energies and for deformed nuclei. Then, we show the impact of the Weisskopf-Ewing approximation on the outcome of simulated surrogate experiments, giving insight into the effect that the spin dependence has on predicted cross sections.

8.5.1 Decay probabilities for representative nuclei

$G_{xn}^{CN}(E_{ex}, J^\pi)$ for one- and two-neutron emission from the compound nucleus ^{91}Zr* are shown in Figure 8.5, for both positive and negative parities and a variety of spins. The behavior

of $G_{xn}^{CN}(E_{ex}, J^\pi)$ just above the CN separation energy, corresponding to $E_{ex} = S_n(^{91}\text{Zr})$ = 7.194 MeV, is governed by the interplay of the neutron-transmission coefficients and the low-energy structure of the residual nucleus ^{90}Zr which is reached by one-neutron emission. The situation is schematically illustrated in Figure 8.1. Due to the shell structure of the nucleus, the low-energy spectrum of ^{90}Zr is very sparse, with the first excited state occurring at 1.76 MeV. Since both the ground state and the first excited state have $J^\pi = 0^+$ and s- and p-wave neutron emission dominates at low energies, the residual nucleus can only be reached from low-spin states in the compound nucleus $^{91}\text{Zr}^*$. This suppression of neutron emission from all but the lowest spin states in $^{91}\text{Zr}^*$ is well known from earlier studies of neutron capture reactions, and a dependence on parity is observed as well [93, 80, 37].

As the excitation energy in $^{91}\text{Zr}^*$ increases, additional states in the residual nucleus become accessible and the decay probabilities $G_{xn}^{CN}(E_{ex}, J^\pi)$ for higher J values take on non-zero values. In the region between $E_{ex} = 15 - 20$ MeV, the one-neutron emission probability is essentially unity, because of the weakness of competing decay channels.

In the energy region between 20 and 27 MeV, we observe the transition from predominantly one-neutron emission to two-neutron emission. We see significant dependence of the branching ratio on the spins of the compound nucleus for $J \geq 6.5$, while there is much weaker dependence for $J \leq 6.5$. The decay probabilities are not very sensitive to parity.

Figure 8.6 shows the analogous one- and two-neutron emission probabilities for the decay of the rare-earth nucleus ^{158}Gd. Here, the dependence on spin is weaker than in the Zr case, especially near the one-neutron separation energy of the compound nucleus. This is primarily due to the significantly higher level density in the gadolinium nuclei: While the first excited state in ^{90}Zr is at 1.76 MeV, there are 15 levels below 0.5 MeV in ^{157}Gd. In general, the level densities in deformed nuclei are much higher, and the sensitivity of the compound nucleus decays to spin and parity is reduced. This is also true at higher energies: The competition between one- and two-neutron emission shows significant dependence on

Figure 8.5: (Published in [116].) robabilities for neutron emission from the ^{91}Zr* nucleus, as function of excitation energy, for various $J\pi$ values of the compound nucleus. Both decay channels exhibit a strong dependence on the spin of the compound nucleus. The variance is seen to be greatest at the onset of one-neutron emission, near $E_{ex} = S_n(^{91}\text{Zr}) = 7.194$ MeV.

the compound-nuclear spins, although the sensitivity is not as strong as in the zirconium case.

Figure 8.7 shows the one- and two-neutron emission probabilities for the ^{239}U nucleus. Like
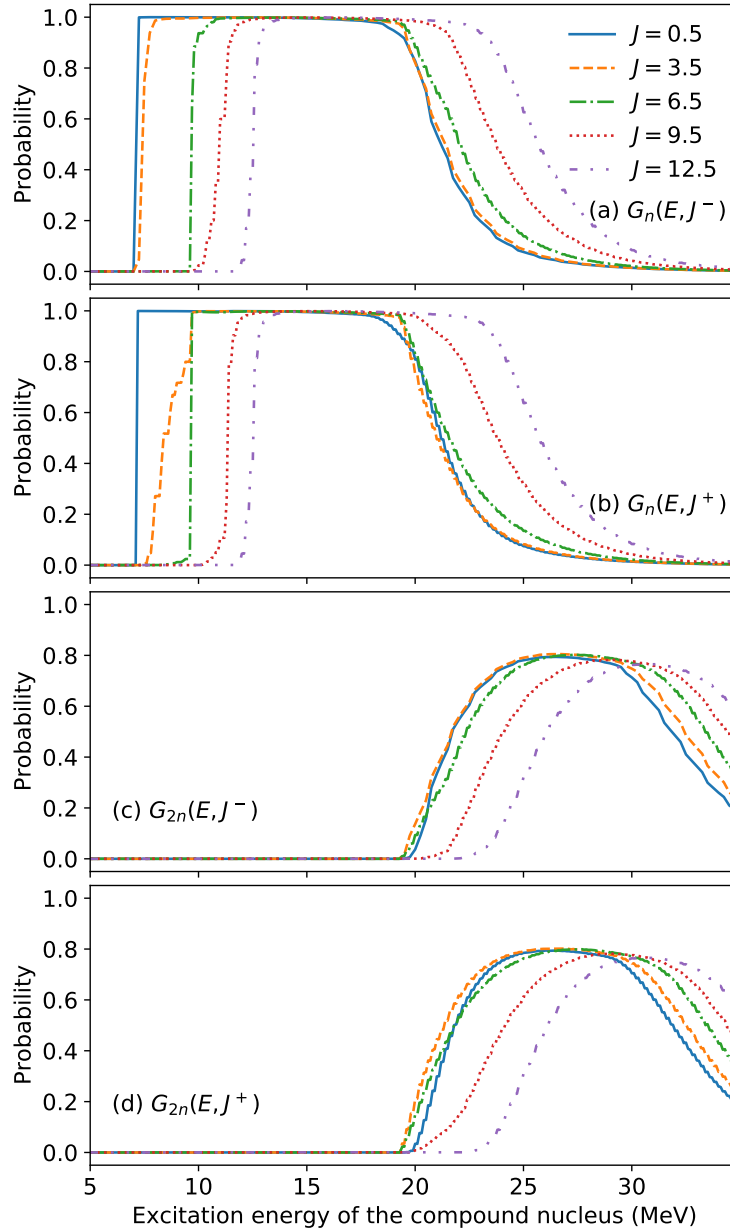
Figure 8.6: (Published in [116].) Probabilities for one-and two-neutron emission from the ^{158}Gd* nucleus, as function of excitation energy, for various $J\pi$ values of the compound nucleus. The decay probabilities for both channels are seen to depend on the angular-momentum states populated in the compound nucleus, at the onset of one-neutron emission near $E_{ex} = S_n(^{158}\text{Gd}) = 7.937$ MeV and in the transition region where the two-neutron channel opens.

the gadolinium case discussed, the uranium nuclei are deformed and have a much higher

level density than the zirconium nuclei: ^{238}U has 16 levels below 1 MeV. The transition from

one-neutron to two-neutron emission, which lies near the threshold for second-chance fission, is also sensitive to the angular momentum population of the compound nucleus. Multiple channels compete at all energies considered and no clear plateaus for the probabilities emerge, unlike in the other cases considered.
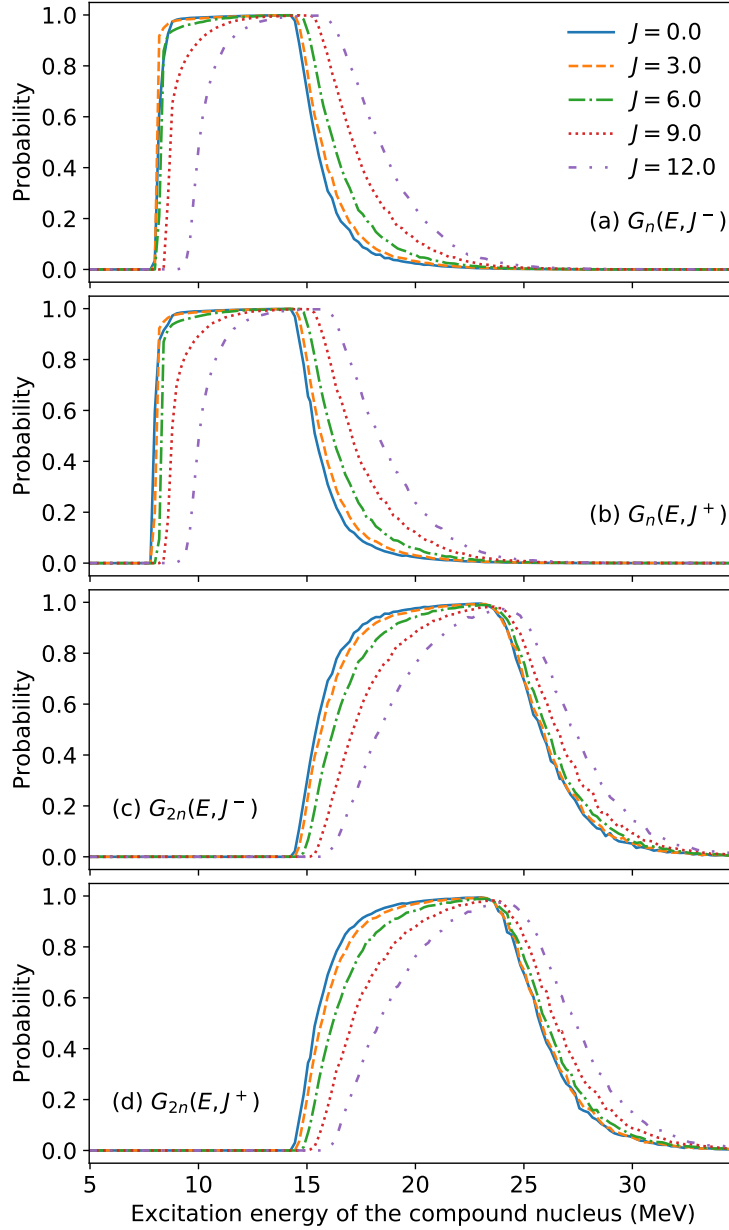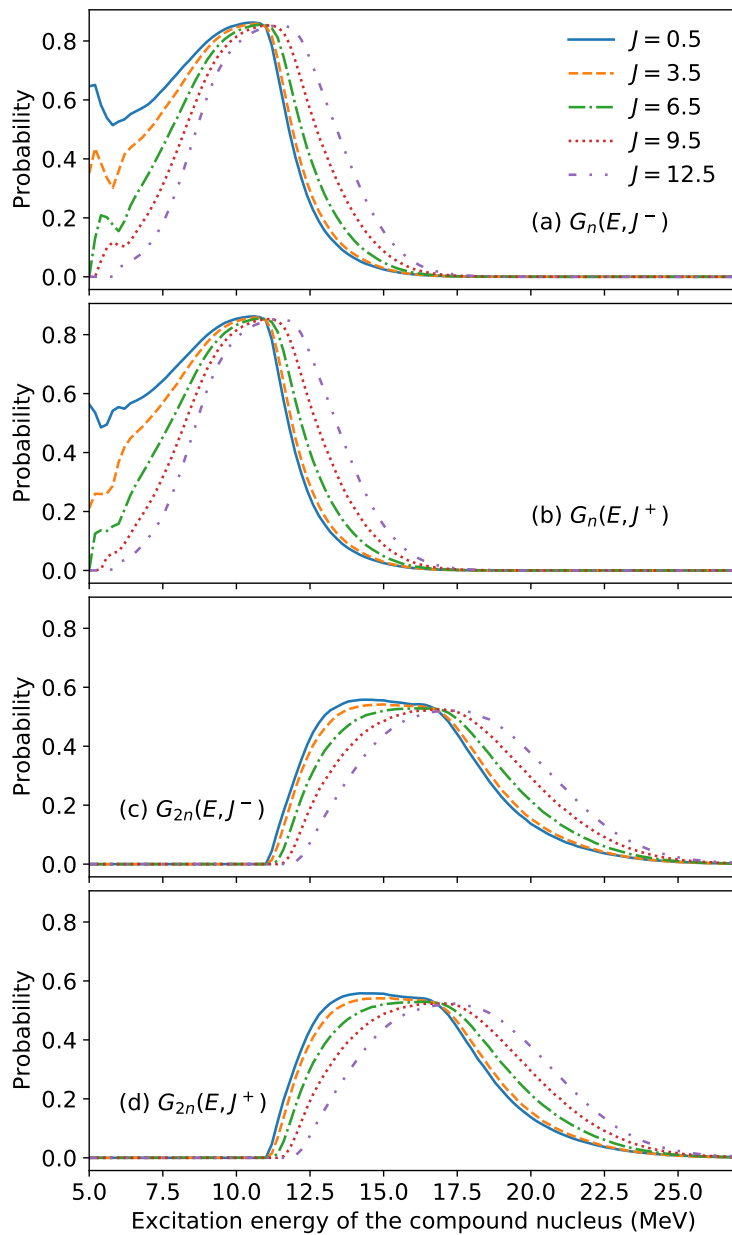

Figure 8.7: (Published in [116].) Probabilities for one- and two-neutron emission from the $^{239}U^*$ nucleus, as function of excitation energy, for various $J\pi$ values of the compound nucleus. We observe a strong spin- and parity-dependence of $G_{1n}^{CN}(E_{ex}, J^{\pi})$ near $E_{ex} = S_n(^{239}U) = 4.806$ MeV, which lies just below the threshold for fission.

For all three cases discussed, we have observed that there is enhanced sensitivity of the neutron emission probabilities near the thresholds. It can therefore be expected that a failure to account for the spin-parity mismatch in the analysis of surrogate reaction will result in extracted (n, n') and $(n, 2n)$ cross sections that do not reflect the true threshold behavior. This will be investigated in more detail in the next subsection.

8.5.2 Impact of spin dependence of 1n and 2n decay probabilities

In the previous section, we observed that the one- and two-neutron decay probabilities show a significant dependence on the spin of the compound nucleus and a lesser dependence on parity. Here we study the impact of this dependence on cross sections obtained under the assumption of the validity of the Weisskopf-Ewing approximation. We use the schematic spin distributions $F_\delta^{CN}(E_{ex}, J^\pi)$ discussed in Section 8.4.2. They are conveniently parameterized as discretized normal distributions with mean μ and variance $\sigma^2 = \mu$:

$$F_\delta^{CN}(E_{ex}, J^\pi) \propto \mathcal{N}(m = \mu, sd = \sqrt{\mu}). \tag{8.14}$$

The distributions are cut off above $J = 50$ and normalized to unity. For the even-even compound nucleus ^{158}Gd*, we consider the five distributions, $\mu = 1, 3, 5, 7, 9$, shown in Figure 8.4; for the odd nuclei ^{91}Zr* and ^{239}U* we use $\mu = 1.5, 3.5, 5.5, 7.5,$ and 9.5.

Results for ^{90}Zr(n, n') and ^{90}Zr$(n, 2n)$ cross sections obtained from a Weisskopf-Ewing analysis of the simulated surrogate data are shown in Figure 8.8. As expected, the threshold regions for both reactions are particularly sensitive to spin effects. At the onset of inelastic scattering, it is not possible to obtain a reliable (n, n') cross section; both shape and magnitude show a very large variance. Different spin distributions give the same magnitude of

this cross section in the region of the plateau, but there is again significant uncertainty in the region where the two-neutron channel opens up.
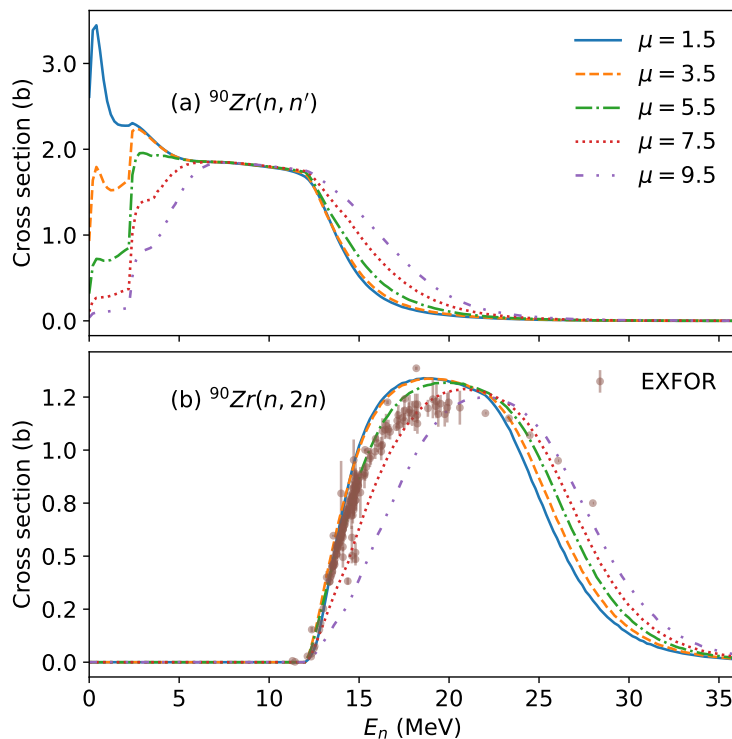
Figure 8.8: (Published in [116].) Cross sections for (a) ^{90}Zr(n, n') and (b) ^{90}Zr$(n, 2n)$, obtained from simulated surrogate data, using the Weisskopf-Ewing assumption. The underlying schematic spin-parity distributions used are indicated in the legend. The shape of the transition depends clearly on which simulated surrogate data is used, with the cross sections varying by $\pm 30\%$ at about $E_n = 15$ MeV. The ^{90}Zr$(n, 2n)$ cross section varies by $\pm 4\%$ near its maximum, which is located at about $E_n = 20$ MeV. For comparison, experimental data [312] for ^{90}Zr$(n, 2n)$ is shown in panel (b). The only data for the inelastic scattering case is for scattering to an isomeric state.

Given the findings in the previous section, we expect the situation to be better for the gadolinium case, shown in Figure 8.9. While the ^{157}Gd(n, n') cross section near the onset of inelastic scattering varies less than the analogous zirconium cross section, it is still quite unreliable. The value of the ^{157}Gd(n, n') cross section shows no dependence on the simulated spin-parity distribution in a region around $E_n = 5$ MeV. Not surprisingly, the Weisskopf-Ewing approximation for different sets of simulated surrogate data yields results that are

consistent with each other in an energy regime where there is little to no competition from other decay channels. The maximum for the ^{157}Gd$(n, 2n)$ cross section occurs near $E_n = 15$ MeV, where the different sets of surrogate data differ from each other by about 4%, which is an uncertainty that is similar to the error bands obtained from direct measurements. Overall, it appears that the Weisskopf-Ewing approximation might provide a very rough estimate of the $(n, 2n)$ cross section of a rare earth nucleus.

Figure 8.9: (Published in [116].) Cross sections for ^{157}Gd(n, n') and ^{157}Gd$(n, 2n)$, obtained from simulated surrogate data, using the Weisskopf-Ewing assumption and several schematic spin-parity distributions. In the energy region where the transition from one- to two-neutron emission occurs, the cross sections exhibit greater uncertainty, varying by $\pm 57\%$ for (n, n') and $\pm 13\%$ for $(n, 2n)$ at $E_n = 10$ MeV. The maximum for $(n, 2n)$ near $E_n = 15$ MeV, the variation is $\pm 62\%$ for (n, n') and $\pm 1\%$ for $(n, 2n)$. For comparison, directly measured data [312] is shown for the ^{157}Gd$(n, 2n)$ cross section; no data are available for the inelastic cross section.

For the uranium case, shown in Figure 8.10, we observe a further decrease in sensitivity to differences in spin. Even so, the shape of the ^{238}U(n, n') cross section cannot be reliably ex-

tracted at low energies. With increasing energy, the Weisskopf-Ewing approximation appears to become more reliable. In fact, the ^{238}U$(n, 2n)$ cross section obtained from the simulated data are in good agreement with available directly-measured data. At energies above 18 MeV, however, where no data exists, we see deviations from the ENDF evaluation[45]. We attribute this to the neglect of pre-equilibrium contributions, which are included in evaluations but neglected in standard WE analysis. We attribute the systematic discrepancy of the simulated WE prediction relative to the evaluated cross section [45] to pre-equilibrium contributions, which are not included in the WE analysis. Overall, it appears that the Weisskopf-Ewing approximation might provide a reasonable estimate of the $(n, 2n)$ cross section of an actinide nucleus if pre-equilibrium can be taken into account.
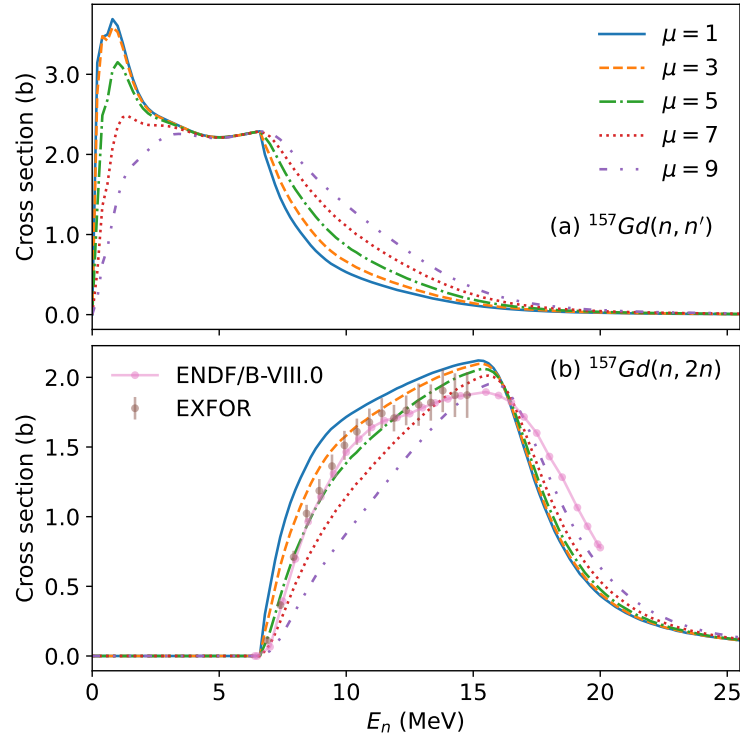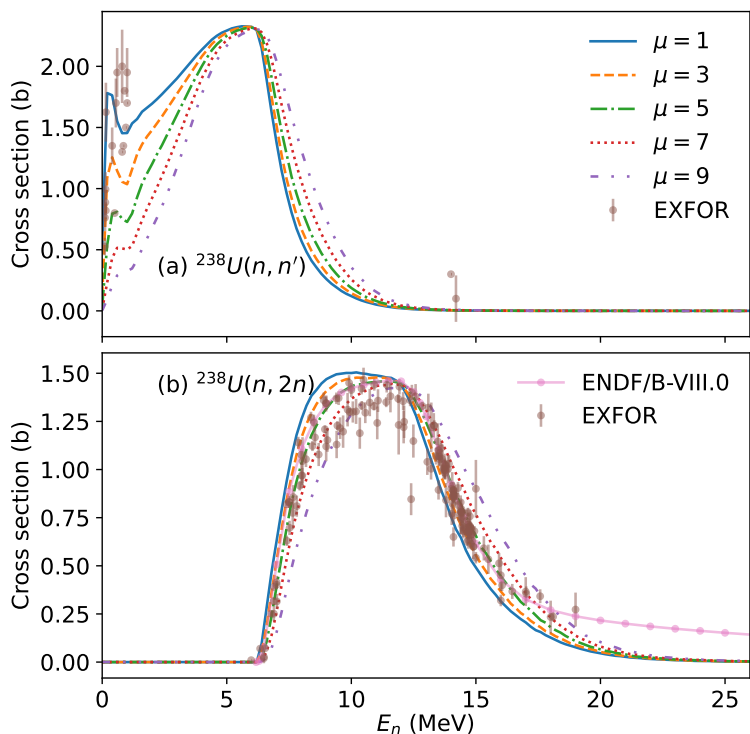

Figure 8.10: (Published in [116].) Cross sections for (a) ^{238}U(n, n') and (b) ^{238}U$(n, 2n)$, obtained from simulated surrogate data, using the Weisskopf-Ewing assumption and several schematic spin-parity distributions. The ^{238}U$(n, 2n)$ results agree reasonably well with the existing data [312]. For the inelastic case, data is only available data for low energies, where direct reaction mechanisms are known to contribute.

Overall, we find that the Weisskopf-Ewing approximation can provide rough first estimates for the $(n, 2n)$ cross sections of nuclei with large level densities, such as rare earth and actinide nuclei, while the low-energy behavior is much less reliable. Specifically, near thresholds there is clearly increased sensitivity of the decay to the underlying spin-parity distribution in the compound nucleus. As a result, the shape of the extracted cross sections do not reproduce the true cross sections very well. Notably, the Weisskopf-Ewing approximation fails at the onset of one-neutron emission. This is in line with earlier findings about the limitations of this approximation for neutron capture cross sections.

In addition, it should be stressed that we have focused on the compound contributions to the (n, n') and $(n, 2n)$ cross sections here. For inelastic scattering, it is well known that direct (pre-equilibrium) mechanisms provide significant additional contributions, which are not considered here. These contributions are known to affect the spins populated in the target nucleus [62, 169] and will exacerbate the deficiencies of the WE approximation. These have to be calculated separately and added to the cross section, similar to what is done for the direct-reaction component in an evaluation. Unfortunately, for many nuclei there is little data available for neutron inelastic scattering, and the calculations are challenging, so this reaction channel requires additional studies, both experimentally and theoretically.

8.6   Outlook

We have investigated the potential use of the Weisskopf-Ewing approximation for determining (n, n') and $(n, 2n)$ cross sections from surrogate reaction data. Earlier work for neutron-induced fission and radiative neutron capture demonstrated that this approximation yields reasonable approximations for the fission cross sections, but fails for capture, making it necessary to employ more detailed theoretical modeling in the latter case.

We modeled the nuclear structure properties that determine the decay of a compound nucleus via $1n$ and $2n$ emission, as well as the combined effect of the nuclear structure and the surrogate reaction mechanisms on the cross-section results that one obtains from a Weisskopf-Ewing analysis of the indirect data. We found that the Weisskopf-Ewing approximation fails to give consistent cross section shapes in the presence of a spin-parity mismatch between the desired and surrogate reactions. The outcomes are worse for nuclei with low level density, *i.e.* for lighter nuclei and for those in regions near closed shells. While rough estimates for the cross sections might be obtained for $(n, 2n)$ reactions on well-deformed rare-earth and actinide nuclei, we find that nuclei in the mass-90 region are more sensitive to the effects of spin and parity. Furthermore, inelastic neutron scattering cross sections are found to be quite sensitive to angular-momentum effects and thus require a detailed treatment of the reaction mechanism, similar to that recently used for extracting capture cross sections from surrogate data.

Suggestions to find a surrogate reaction that approximates the spin-parity distribution relevant to the desired reaction are well-motivated, as the use of the Weisskopf-Ewing approximation greatly simplifies surrogate applications. However, not enough is known about the angular momentum and parity of the compound states that are populated in a surrogate reaction to plan an appropriate experiment. Recent work has demonstrated that the surrogate reactions that produce a compound nucleus at the high energies of interest involve higher-order reaction mechanisms, which render inadequate the type of simple angular-momentum estimates that are often used in traditional nuclear structure studies. It is also not necessarily true that a surrogate reaction produces spins in a compound nucleus that are higher than those relevant to neutron-induced reactions. This means that in order to achieve cross section results with appropriate shapes and errors less than about 30%, surrogate reaction data will need to be combined with full modeling of the reaction mechanism, as described in section 8.3.1.

In light of our findings that the Weisskopf-Ewing approximation is insufficient for determining (n, n') and $(n, 2n)$ cross sections, we believe that further development of surrogate reaction theory is important for addressing existing nuclear data needs. Inelastic scattering (n, n') reactions in particular are poorly constrained by direct measurement techniques. Alternative indirect methods [183] do not address (n, n') and $(n, 2n)$ reactions. Recent surrogate reaction applications to neutron capture have demonstrated how to proceed to accurately extract cross sections from surrogate data in situations where the Weisskopf-Ewing approximation fails [81, 236, 222]. Given the limited utility of the Weisskopf-Ewing approximation for neutron induced one- and two- neutron emission reactions, we conclude that additional developments are needed in order to describe the relevant reaction mechanisms, such as those involved in the $(^3\text{He},^3\text{He}')$ scattering experiment described in Figure 8.1.

Chapter 9

Computational Model Monte Carlo Sampler (COMMCAS)

Markov Chain Monte Carlo (MCMC) methods are a subset of Monte Carlo methods: principally they are methods to sample probability distribution functions. To apply MCMC to the problem of fitting model parameters to data, the probability distribution that is sampled is the posterior probability distribution for some observable associated with the data. By defining a map between the observable and the parameters, e.g. by some physical parametric model, each MCMC sample of the observable posterior corresponds to a sample from the posterior on the parameters.

In this chapter I will introduce the probability theory necessary for parameter inference and uncertainty quantification, then I will present a code I have developed for performing such calculations with general computational models. This code will be applied to practical problems in the chapters that follow.

9.1 Forward and Inverse UQ Propagation

Uncertainty propagation (UQ) with Monte Carlo sampling is a method to inform uncertainty of one variable y using uncertainty of another variable θ. This is simple if we assume some physics model M,

$$y = M(\theta|q), \tag{9.1}$$

and that the probability distribution function (PDF) $p(\theta)$ is known. One can simply draw independent samples $\theta_i \sim p(\theta)$ and evaluate $y_i = M(\theta_i|q)$ in order to generate samples of y. The q indicates that M could be a function of other variables which are held fixed.

If, on the other hand, we have a PDF for y and want to find the corresponding PDF for θ, then we have an inverse problem. For 'interesting' relationships $y = M(\theta|q)$, determining the inverse is non-trivial. In such cases, we can use Markov Chain Monte Carlo (MCMC) to sample some probability distribution for y via Bayes' Theorem (e.g. with a likelihood function defined by experimental uncertainties of measured observables) and propagate that uncertainty backwards into the probability distribution for a set of physics model parameters θ.

9.1.1 Bayes theorem

Bayes' theorem defines a posterior probability distribution for a random variable y by relating some prior probability distribution p to observations D of the random variable:

$$P(y|D) = \frac{L(D|y)p(y)}{\int L(D|y)p(y)dy}, \tag{9.2}$$

where L defines the likelihood of the observations given a certain value of y.

In the context of a physical parameteric model, $y = M(\theta|q)$ for which we wish to solve the inverse problem, Bayes theorem takes the form:

$$P(\theta|D) = \frac{L(D|\theta)p(\theta)}{\int L(D|\theta)p(\theta)d\theta}, \tag{9.3}$$

where D remains observations of the variable y, now related by $y = M(\theta|q)$ to the variable of interest θ, the model parameters. The likelihood function is where the model enters:

$$L(D|\theta) = \tilde{L}(D|M(\theta|q)). \tag{9.4}$$

9.1.2 Standard likelihood function

The likelihood function defines the probability of the observations D given a particular value of the random variable y. The experimental data we deal with are typically reported in terms of a mean value, and an uncertainty: $d_i = \mu_i \pm \sigma_i$. This uncertainty is taken to represent the diagonal matrix element of a covariance matrix. Such a covariance encodes both statistical uncertainty and irreducible systematic uncertainty due to experimental or physical constraints.

Once a set of means and a covariance matrix is defined, we assume that they correspond to a multivariate gaussian probability distribution:

$$P(\boldsymbol{y}|D : \boldsymbol{\mu}, \boldsymbol{\Sigma}) = \mathcal{N}(\boldsymbol{y}; \boldsymbol{\mu}, \boldsymbol{\Sigma}) \equiv \frac{\exp\left(-\frac{1}{2}\boldsymbol{r}^T\boldsymbol{\Sigma}^{-1}\boldsymbol{r}\right)}{\sqrt{(2\pi)^N|\boldsymbol{\Sigma}|}}, \tag{9.5}$$

where $\boldsymbol{r} = \boldsymbol{y} - \boldsymbol{\mu}$. We have made the switch to vector notation to indicate that we are generally dealing with a set of observable data points. Usually these are observables of the same quantity measured at different system energies, e.g. a cross section at different incident energies. The covariance matrix $\boldsymbol{\Sigma}$ describes how the various observations vary with respect

to one another. Until we have complete covariance data from experimental sources, this is a diagonal matrix where the diagonals are the experimental errors, δ_y^2 (δ_y is the standard deviation: experimental error bar). Note, however, that the underlying independent variable such as the incident energy is not encoded in this framework. At best, observables adjacent in energy are adjacent in the covariance matrix.

Once again, as we introduce a parametric model, we substitute $\boldsymbol{y} = \boldsymbol{M}(\boldsymbol{\theta}|q)$, to define our standard inverse-problem (log) likelihood function as the probability that a given model evaluation is consistent with the experimental data D:

$$\log L(D : \boldsymbol{\mu}, \boldsymbol{\Sigma}|\theta) = -\frac{1}{2}(\boldsymbol{r}^T \boldsymbol{\Sigma}^{-1} \boldsymbol{r} + \log |\boldsymbol{\Sigma}| + k \log 2\pi), \tag{9.6}$$

where $\boldsymbol{r} = \boldsymbol{\mu} - \boldsymbol{M}(\boldsymbol{\theta}|q)$ is the residual between the data $\boldsymbol{y}$ and the model $\boldsymbol{M}$. The dimension-N array $\boldsymbol{r}$ and dimension-$N \times N$ array $\boldsymbol{\Sigma}$ include all data for all observables. The parameter vector θ is dimension k.

9.1.3   Including unaccounted for uncertainties

There are two common approaches for dealing with inconsistent experimental uncertainties by including other 'unaccounted-for' sources of uncertainties. The first is by adding a meta-parameter which may renormalize certain datasets or observables with respect to one another. The second is to include meta-parameter for each observable which models an unknown source of uncertainty. This is discussed in [230]. These "unaccounted-for uncertainty parameters" (UAUP) δ_{uaup} add-in-quadrature with the experimental uncertainties δ_{exp} in the covariance matrix:

$$\Delta^2 = \delta_{\text{exp}}^2 + \delta_{\text{uaup}}^2, \tag{9.7}$$

where Δ^2 are the diagonal elements of the covariance matrix $\boldsymbol{\Sigma}$. This approach may help soften issues coming from underestimated experimental uncertainties, or equivalently, underestimated theoretical uncertainties. However, it still does not address the issue of the relative weighting of multiple data sets.

9.1.4 Inverse to Forward UQ Propagation for the Surrogate Reaction Method

This is an extension of the idea of simple inverse UQ propagation. In the inverse-to-forward case, we assume that we have a complementary variable(s)

$$z = G(\theta|q'), \tag{9.8}$$

where G is some other physics model that depends on the same variables θ, which we now constrain with the inverse UQ propagation of $y = F(\theta|q)$. Here, q' could be the same or different from q. To obtain samples of z, we first perform simple inverse UQ propagation to obtain $p(\theta|q)$, then we sample $z_i = G(\theta_i \sim p(\theta|q)|q')$.

9.1.5 Metropolis Hastings for Uncertainty Quantification

In physics we often are concerned not only with a single value of a variable x, but with the probability of observing an aribtrary value. This is best described in the language of probability theory as the probability density function (PDF) of the random variable x. Formally,

$$P(a < x < b) = \int_a^b f(x)dx \tag{9.9}$$

gives the probability of observing a value of x between a and b. And so $f(x)$ is the probability *density* function. Still, it is common to casually refer to $f(x)$ as the probability of a certain value of x.

For a sufficiently complex PDF, a closed functional form may not exist, and yet it is still possible to generate samples from that distribution:

$$X_i \sim f(x). \tag{9.10}$$

And so, by generating a large number of samples $\{X_1, X_2, ..., X_n\}$, one can generate a histogram approximation of the PDF $f(x)$.

In this way, Monte Carlo methods can be used to approximately evaluate Bayes' theorem even when the integral of the prior and likelihood functions may not exist in closed form.

Markov Chain Monte Carlo (MCMC) is a Monte Carlo method [179] for generating samples X_i of an unknown distribution $f(x)$. It begins with a random number which initiates a chain of random numbers stochastically generated by a Markov process. A Markov process being one in which subsequent members of the chain generated depend only on the previous sample. The usefulness of MCMC comes from the fact that it only requires the ability to evaluate some probability density function which is proportional to $f(x)$; we don't need to be able to draw samples directly from f. This is ideal for drawing samples from a posterior distribution given by Bayes' theorem:

$$P(x|D) = \frac{L(D|x)p(x)}{\int L(D|x)p(x)dx}, \tag{9.11}$$

since it means we don't need to evaluate the integral for the normalization constant (the denominator). Instead, we only need to be able to compute the numerator given some data D and a proposal for the random variable x.

The Metropolis Hastings algorithm is perhaps the simplest implementation of the decision step.

Algorithm 3 Metropolis Hastings. To sample from a density $f(x)$ known up to a normalizing constant, initialize with some X_0 for which $f(X_0) > 0$.

> **for** $t = 0, ..., T - 1$ **do**
>> $Y \sim q(y|X_t)$ $\qquad\qquad\qquad\qquad\qquad$ ▷ Y is drawn from the proposal density
>> $U \sim \text{Uniform}(0, 1)$
>> $\alpha(a, b) = min\left(\frac{f(b)q(a,b)}{f(a)q(b,a)}, 1\right)$
>> $X_{t+1} \leftarrow \begin{cases} Y, & U \le \alpha(X_t, Y) \\ X_t, & \text{otherwise} \end{cases}$
> **end for**

This algorithm generates samples X_t from the PDF $f(x)$, i,e, $X_t \sim f(x)$. The PDF $\alpha(x, y)$ is the acceptance probability, determined from the ratio of the target density f evaluated at the current and proposal states, weighted by q. An important requirement of the MH algorithm is that we know the form of f up to a constant, so that we can carry out this evaluation. $q(x, y)$ is the proposal density function, from which the proposal state Y is drawn. This is a local probability density function centered around the current state X_t. The fact that the proposal state Y is sampled from a PDF centered on the current state X_t is what results in a Markov Process.

9.2   Computational Model Monte Carlo Sampler

I have developed a code called the computational model Monte Carlo sampler (COMMCAS) for the Nuclear Data and Theory group at Lawrence Livermore National Laboratory (LLNL) over the past 5 years. In that time, there have been contributions from two former graduate students (now graduated). The majority of the machine learning work was conducted by graduate students Kirana Bergstrom and Emily Shinkle. The more recent integration with Python computational models is due to postdoc Simone Perrotta.
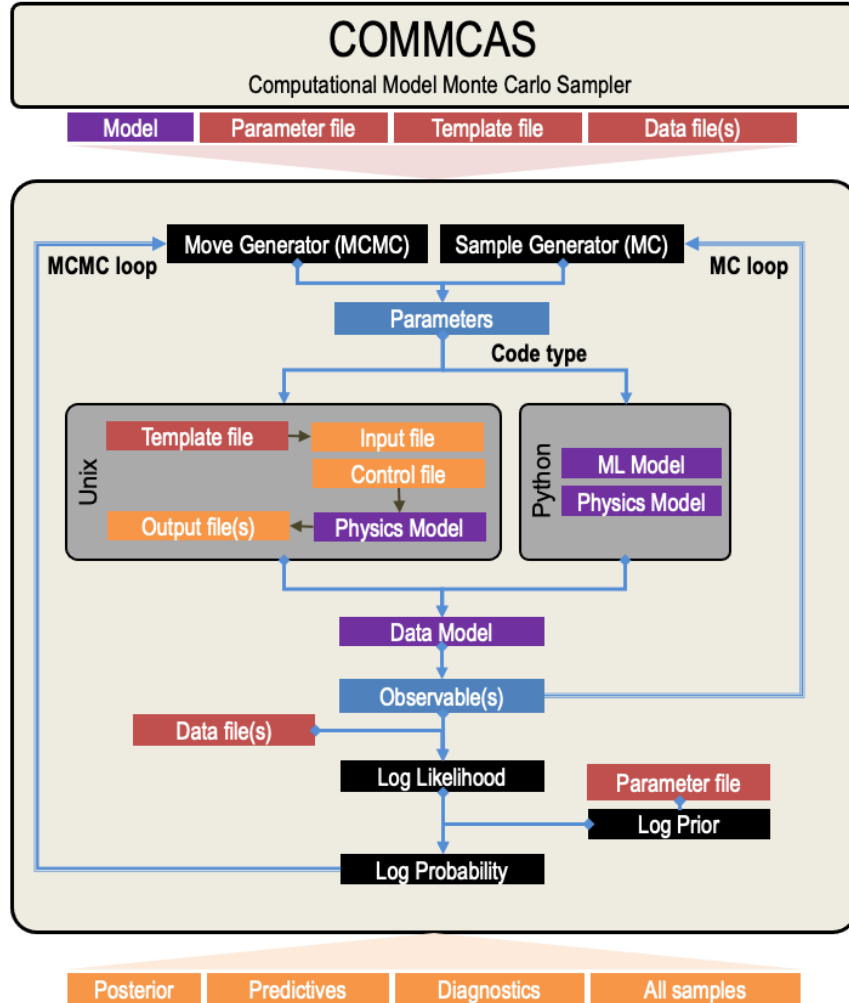
Figure 9.1: Data flow diagram of the COMMCAS code. Sampling of a prior distribution, and computing the predictive of a posterior distribution are done with the MC loop, while sampling of a posterior distribution are done with the MCMC loop.

COMMCAS is both a Monte Carlo sampler and a general computational model Python-wrapper. It uses emcee [91] to sample the input space of parametric computational models and compare to experimental measurements of model observables.

It works with essentially any computational model that meets these criteria:

- Runs on Linux

- Reads its input parameters from a file or Linux redirect

- Writes its results to one or more files in columnated format

or, is a Python function with the appropriate argument signature.

When dealing with linux programs, COMMCAS works by modifying a user-provided template file, running the computational model with system calls, and reading the specified output files. Essentially, it acts as a Python wrapper for generic computational models. With light modification, it can also work with any model with a Python interface.

COMMCAS can sample either a prior distribution of model parameters using Monte Carlo (MC) sampling, or it can sample a Bayesian posterior distribution using Markov chain Monte Carlo (MCMC). In the case of MC, one propagates the uncertainty in the parameter space into uncertainty in the observable space. In the case of MCMC, the likelihood function of Bayes' theorem is defined by experimental uncertainties provided as part of the user-defined experimental measurement data.

It can therefore be used to "fit" a model to experimental data by sampling posterior distribution of the model observables, thus propagating the observable uncertainty into model parameter uncertainty.

A key feature of COMMCAS is the ability to track multiple observables simultaneously. The idea being that a single model calculation generates multiple observables of interest which may be correlated, but conceptually distinct.

Additionally, COMMCAS has the option to train a neural network to serve as an emulator for a unix model. This is ideal if the unix function is computationally expensive and the parameter space is relatively narrow. Once trained, this network can be called in place of the unix function to reduce runtime for other types of sampling. This technique for accelerating MCMC has been employed previously by others, for example Zou et al. [314], Wang et al. [292], and Park et al. [220].

9.2.1 Log-likelihood function

The log likelihood function used by COMMCAS is:

$$\log L(D : \boldsymbol{\mu}, \boldsymbol{\Sigma}|\theta) = -\frac{1}{2}(\boldsymbol{r}^T \boldsymbol{\Sigma}^{-1} \boldsymbol{r} + \log |\boldsymbol{\Sigma}| + k \log 2\pi),$$

where $\boldsymbol{r} = \boldsymbol{\mu} - \boldsymbol{M}(\boldsymbol{\theta}, x|q)$ is the residual between the data means $\boldsymbol{\mu}$ and the parametric model $\boldsymbol{M}$. D is the experimental data defined as pairs of means and standard deviations: (μ_i, σ_i). These values make up the vector $\boldsymbol{\mu}$ and covariance matrix $\boldsymbol{\Sigma}$. The covariance matrix is rescaled (and optionally shifted) so that the diagonals are

$$\Sigma_{ii} = (k/N)(\sigma_i^2 + \delta_{ui}^2).$$

Here k is the number of parameters θ_i in the model and N is the number of data points (μ_i, σ_i). The unaccounted-for uncertainties δ_u^2, if UAUQ parameters u_u are included, are

$$\delta_{ui} = u_u(\mu_i + M(\theta, x_i))/2.$$

9.2.2 Python interface

COMMCAS can be imported as a Python package and run from within your own Python script. As of December 2022, this option has only been tested with MCMC sampling of a Unix executable computational model.

Here is an example where we construct a COMMCAS run. First, we import the necessary packages, including commcas by pointing to the directory where its source code is located.

```
1  import sys
2  sys.path.append("/usr/workspace/pints/shared/commcas/src")
3  import commcas
```

If you are using parallel computing resources, you should add the following line directly after you import commcas:

```
1  pool = commcas.readypool(num_threads=36)
```

Here, `num_threads` is the number of multiprocessing threads to use. If you are using MPI, this parameter is not used and instead an MPI Pool is created automatically.

Next, we set the path to the computational model code to be executed:

```
1  modelname = "~/bin/YAHFC.x"
```

The next step is to create 'Observable' objects. These define the observables which are computed by the model code. If one provides a corresponding 'datafile', then this observable is used to compute the likelihood function. A data file is not required for all observables – those without will be tracked but will not contribute to the likelihood function.

```
1  observable1 = commcas.observables.Observable(
2          name="Gamma_0719_2+2_2+1",
3          outfile="96Mo/Pop/g/gammas/Channel_g_Gammas_i003f001_Egam_0.7196.
    dat",
4          outcoly=6,
5          datafile="./data/Z_Mo96_gam_prob_0719keV.g91",
6          dataformat="1x2y",
7          fitmin=None,
8          fitmax=None,
9          contributes=True,
10         xsigma=0.08)
```

commcas.observables.Observable Arguments

`name` (string) is the name of the observable. Any normal string without spaces is allowed, but there are some constraints if you are using a Python functional model rather than a Unix executable.

`outfile` (string or None) file path/name generated by the executable model, relative to template directory. None if using functional model.

`outcoly` (integer) the number of the column (0-indexed) where the observable can be found in the 'outfile' file. None if using functional model.

`outcolx` (integer) the number of the column (0-indexed) where the observable's x values can be found in the 'outfile' file. None if using functional model.

`datafile` (string or None) filename for existing data on this observable, e.g. experimental data. Path should be relative to current working directory. None if no data; in that case this observable will not contribute to the likelihood function.

`dataformat` (string or None) specially formatted string chosen from: '2x2y', '1x2y', '1x1y', 'none', 'xydxdy'. This string indicated the format of the columns in 'datafile'. For example, '2x2y' means there are 4 columns: x, dx, y, dy. '1x2y' means there are 3 columns: x, y, dy. This implies y = f(x), where x has an uncertainty (standard deviation) dx, and y has an uncertainty dy. None only if 'datafile' is None.

`fitmin` (float or None) minimum x value below which the data in 'datafile' is not used for the likelihood calculation. None means `fitmin = -inf`.

`fitmax` is the maximum x value above which the data in 'datafile' is not used. All data will still be plotted. None means `fitmax = +inf`.

`contributes` (bool) Flag to determine if this observable contributes to the likelihood function. Default `True`.

`interpolate` (bool) Flag to determine if the model is interpolated to the data or not. Default True. If False, the model must provide (x,y) pairs that exactly match the x-values of the data.

`interporder` (integer) Order of the spine used to interpolate the model. A value of 1 would be linear interpolation.

xsigma (float) Standard deviation of Gaussian smoothing for x values. This value is used to account for Gaussian uncertainty in the x values of the observable. After the model is computed, it is folded with a Gaussian kernel with standard deviation xsigma. Has units equal to those of x.

Back to the example

I created several other observables too, not shown. Once we have our observables, we pack them into a dictionary to more easily pass around.

```
1  observable_dict = {}
2  observable_dict.update(
3          {
4                  observable1.name : observable1,
5                  observable2.name : observable2,
6                  observable3.name : observable3,
7                  observable4.name : observable4,
8                  observable5.name : observable5,
9                  observable6.name : observable6,
10                 observable7.name : observable7
11         }
12 )
```

Next is the main object for our calculations, the `Job` object. This holds all of the information necessary for a run. I also create a pool object for parallel execution.

```
1  job = commcas.jobs.Job(
2          jobname = "example2",
3          modeltype='executable',
4          executable=modelname
5          sampletype="posterior",
6          workdir="templates",
7          template="mo95dpg.template",
8          psetfile="mo95dpg.pset",
9          backend_filename=None,
10         nwalkers=36,
11         iterations=10,
12         burnin=0,
13         thin_by=1,
14         warmstartname=None,
15         observable_dict=observable_dict)
```

commcas.jobs.Job Arguments

`jobname` (string) Any string you want to name pre-pend output files with. 'debug' is a special option that will print extra information and save certain files. 'default' is a special option that will automatically generate a name based on the time.

`modeltype` (string) Must be from ('function', 'proxy', 'executable') determining which type of computational model is to be used. If 'executable', user must provide 'executable' argument.

`executable` (string) This is the `/path/name` of the executable model to be used. 'proxy' is a special option that will use a Python functional model instead.

`sampleType` (string) choose the sample type from the options 'posterior', 'prior', 'prior', 'sequential', 'training', 'density'.

`workdir` (string) `/path/` starting from the active directory to the folder containing the template and other (optional) input files.

`template` (string) filename of the template input file. This must be in 'workdir'.

`psetfile` (string) filename of the parameter specification file.

`backend_filename` (string or None) `/path/name` of the (optional) backend file from which to continue a previous calculation, or, from which to read parameters if using 'sequential' sampling.

`nwalkers` (integer) number of walkers used to sample. If using the 'stretchMove', this must be at least twice the number of model parameters. It's a good idea to make this a multiple of the number of processes.

`iterations` (integer) number of iterations to perform during sampling. If you are sequentially sampling a backend file, entering a negative iterations number will begin sampling

224

from the end of the chain progress backwards.

`burnin` (integer) number of samples to ignore from the beginning of the sampling when computing posterior statistics. Samples before the burnin are still saved to the backend.

`thin_by` (integer) factor by which the number of samples will be thinned. e.g. 1 will keep all samples, 10 will keep only every tenth sample.

`warmstartname` (string or None) `/path/name` of file containing initial vector from which to start sampling nearby. `None` will start randomly from the prior.

`observable_dict` (dict) dictionary of `Observable` objects.

`movetype` (emcee move) you can create and set a different 'emcee' package move type here.

`scratch` (bool) option to write temporary executable folders to the system scratch. This is often faster, and doesn't clutter the active directory. Default is False.

Back to the example

We are ready to run. This will create a `emcee` sampler object containing our results which we can then process into preliminary plots and statistics:

```
1  sampler = commcas.run(job,pool)
2  commcas.make_plots(job, sampler)
3  commcas.write_stats(job, sampler)
```


9.2.3 Sampling options

The sampling options are: posterior, prior, sequential, density, training.

'Posterior' uses MCMC.

Table 9.1: COMMCAS arguments for determining the extent of the sampling.

Variable	Description	Recommendation
nwalkers	Number of independent Markov chain samplers, each of which has a different initialization.	Must be at least 2 times the parameter dimension. More is better.
iterations	Number of MCMC/MC steps to take for each walker; total samples will be (nwalkers x iterations). (N+1 model evaluations will be performed if starting fresh).	This will depend on how good your starting point is.
burnin	Number of iterations to throw away for plotting and statistics. The burnin iterations will still be saved in the backend.	You will have to monitor the convergence to determine a reasonable value.

'Prior' uses MC.

'Sequential' draws samples in order from an existing Markov chain stored in a backend file.

'Density' samples from a probability density generated from the kernel density estimate (KDE) of a previously calculated Markov chain. The motivation here is to more efficiently sample a known posterior using Monte Carlo sampling.

'Training' produces a neural network intended to emulate a more computationally expensive function. This neural network can then easily be used in place of the expensive function for any of the other sampling options listed above. More information is provided in the following section.

There are a number of variables that determine the quality of the sampling.

The default move type is the Stretch Move (affine invariant sampler), which is the default for emcee. To change the move type, you can pass a different move from the emcee library to the jobs argument 'movetype'.

If you have an acceptance fraction problem, the first thing to do is increase the number of

walkers, rather than change the move type.

Additional information about training option

If the 'training' option is selected, COMMCAS will train a neural network surrogate/proxy to emulate a unix function (e.g. YAHFC). Once trained, this network can be called in place of the unix function to reduce runtime for other types of sampling. This option runs a self-guided training loop which alternates between running the unix function to generate training data and using the generated data to train the neural network. This loop ends when one of the three following conditions is met:

- MSE goal is met

- loss is no longer decreasing

- max number of data generation steps has been reached

See more information about each condition below.

The user must specify some variables. Read carefully – some variables will look similar to those for different sampling types, but they are different.

For information about how to now use this neural network as a proxy for the unix function with other sampling types, see below.

9.2.4 Sampling with a proxy

COMMCAS can be run with the sampling option 'training' to generate a neural network surrogate/proxy model for a unix function (eg. YAHFC). Once a sufficient proxy has been trained, the proxy can be used in place of the unix function for faster sampling.

Table 9.2: COMMCAS arguments for proxy model training.

Argument	Description	Recommendation
proxy_name	A name for the neural network to distinguish it from any others you train	You might select the jobname or a name describing the network architecture.
layer_info	A list of list of positive integers indicating the number of nodes in hidden layer of the proxy model. The length of the list indicates the number of hidden layers. E.g. Entering '40, 60' will produce a neural network with two hidden layers with sizes 40 and 60.	This will depend on the number of parameters, the number of observables, the size of the parameter space, and complexity of the unix function. I suggest starting with a single hidden layer of size 60 and increasing if the loss is not low enough (see below).
mse_goal	If the network achieves this MSE, the training will terminate. MSE indicates how different the proxy outputs are from the outputs of the unix function. A value of 1 indicates essentially random guessing. Enter -1 to elimate this stop condition.	The default is currently 1e-3. More work is needed to determine the best value for this parameter. Examine the training output files to judge what MSE seems best.
nwalkers	This is the number of evaluations of the unix function that will be run in parallel.	The number of cores available.
max_iters	After the unix function has been evaluated (in parallel) this many times, the training will terminate. In this case, the total number of calls of the unix function is (nwalkers)(max_iters).	I have found that it is good to have $(\text{nwalkers})(\text{max\_iters}) > 2000$

For this option, enter 'proxy' when prompted for the model to use. You will later be asked to provide three additional pieces of information. You will need to provide the 'proxy_name' you chose when creating the proxy, as well as the list of layer sizes. Finally, you must provide the name of a directory containing the following three files:

- `proxy_name_proxy.pt`

- `proxy_name_observables_helper.pkl`

- `proxy_name_parameters_helper.pkl`

When the proxy was trained, these files were deposited into a directory. One can simply provide this filename. Alternatively, one can transfer these three files into the working directory or another directory and provide the name of that directory instead.

Everything else is identical to sampling with a unix function, just (hopefully) much faster.

9.2.5   Prior distribution and parameter specification file (.pset)

This file specifies the parameters that will be fit, and establishes a prior distribution from a range of options. This file ends in '.pset'.

This file should be in the working directory specified in the input file.

Here's an example .pset file 'zr91wNorms.pset':

```
1  # pnames:
2  #    Parameters keywords which should appear in the template input files.
3  #    Spelling and case matter.
4  #
5  # prior:
6  #    The type of prior distribution to use for this parameter. The options
       are:
7  #        none :
8  #            No prior is used.
9  #            Initial state will be within 10% of arg1. arg2 is not used.
10 #        parity:
11 #            No prior is used, except that the sign of the parameter
12 #            is not allowed to change. "normal conservation".
13 #            Initial state will be within 10% of arg1. arg2 is not used.
14 #        uniform:
15 #            Uniform prior, where p(x) = 1 if arg1 < x < arg2 and 0
       otherwise.
16 #            Initial state will be drawn from U(arg1, arg2).
17 #        normal:
18 #            Normal (Gaussian) prior, where p(x) = N(x, mu=arg1, sd=arg2).
19 #            Initial state will be drawn from p(x).
20 #        pnormal:
21 #            Normal (Gaussian) prior multiplied by the parity distribution.
22 #            I.E. a normal distribution that cannot change signs.
23 #        loguniform:
```

```
24 #              Log uniform distribution (parameter appears uniform on a log
       scale).
25 #
26 # arg1 , arg2:
27 #    Arguments for the prior distribution functions. See above for how
       these are
28 #    used in each prior.
29 # pname        prior       arg1        arg2
30 cnLDaa95         pnormal   12.5       6.0
31 cnLDla          pnormal    0.014      0.0042
32 cnLDdel95       pnormal    1.23       1.23
33 cnLDdW95        normal    -0.927     -0.927
34 cnLDgam         pnormal    0.096      0.0288
35 gSFeE1          pnormal   16.6        5.0
36 gSFeG1          pnormal    4.0        4.0
37 gSFeS1          pnormal   200.0       100.0
38 # Model normalizations
39 _NORM_Pg -Sr96 -813    parity      1.0 1.0
```

Each parameter can have its own prior type.

The parameters with the names `_NORM-##_` are special keywords for scaling the model predictions. The two-digit integer $\#\#$ specifies which model observable to scale. `_NORM_-Pg-Sr96 -813_` scales the observable named 'Pg-Sr96-813'.

9.2.6   Parallel Computing

COMMCAS has two parallel computing implementations: pool from multiprocessing and MPIpool from schwimmbad.

By default, running COMMCAS will use Python multiprocessing with the number of threads equal to half the number of detected processors. Half because I assume the CPU has twice as many virtual CPUs as physical CPUs. Python multiprocessing is limited to single-node compute.

To run COMMCAS with MPI, simply call it using srun, etc., and MPIpool will automatically be used instead of multiprocessing pool, enabling multi-node compute.

9.2.7   Sequential sampling

Sequential sampling now properly samples backends in-order by requiring that the user sets the same number of walkers. You can also now set a negative iterations number to start sampling at the end of the sample set in the backend, and progress backwards. The meaning of the various parameters (`nwalkers, iterations, burnin, thinby`) should also be clarified. Figure 9.2 may be useful for visualizing the Markov chains.
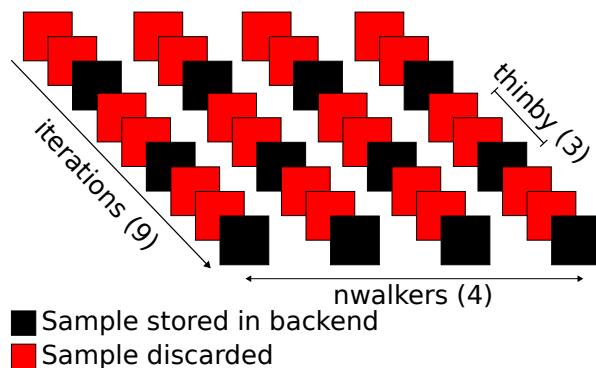

Figure 9.2: Graphical representation of a COMMCAS backend data structure generated from MCMC. In this example, iterations=9, nwalkers=4, thinby=3. As a result, $(9 \times 4)/3 = 12$ net samples will be generated. With a nonzero burnin, only plotting and reported statistics would differ.

When creating a new Markov chain, nwalkers quasi-independent Markov chains are generated. Each chain will take iterations number of steps, creating at most (iterations×nwalkers) samples. If thinby is nonzero, then only every thinby samples will be stored; the rest discarded. Then, the final Markov chain will have (iterations × nwalkers)/thinby samples.

The burnin parameter never effects how many samples are saved when generating a new Markov chain. If nonzero, burnin determines how many samples at the beginning of the final Markov chain will be ignored when computing statistics and generating plots.

When sampling an existing Markov chain, nwalkers must match the number of walkers in the backend. Then, the first burnin number of samples will be ignored, and only every thinby

samples will be used. The iterations number determines how many, and in what order
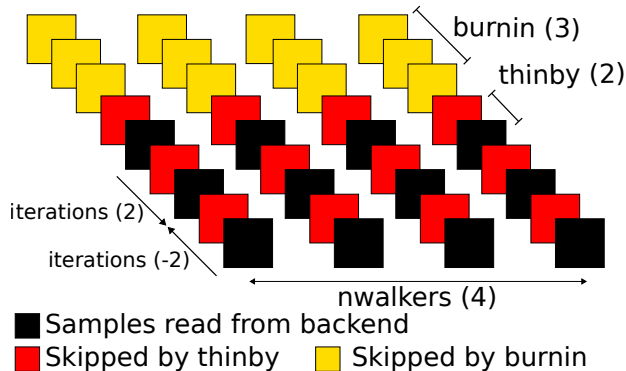

Figure 9.3: Graphical representation of a COMMCAS backend data structure being processed for resampling. In this example, nwalkers=4, thinby=2, and burnin=3, iterations=± 2. As a result, $(2 \times 4)/2 = 8$ net (re)samples will be generated. If iterations is positive, the sampling begins from the beginning of the pruned samples. If negative, it begins from the end.

the samples will be resampled. If positive, sampling begins at the beginning of the chain and proceeds forwards. Each iteration computes one model evaluation for each walker. If iterations is negative, then sampling begins at the end of the chain and proceeds backwards. In both cases, burnin and thinby are always relative to the beginning of the chain; these pruning steps both occur before sampling begins and iterations determines how the remaining samples are treated.

9.2.8   Including unaccounted-for uncertainty parameters (UAUP)

A new set of meta-parameters to account for unaccounted-for uncertainty, called unaccounted-for uncertainty parameters (UAUPs) are included, up to one for each observable type. Meta-parameters do not enter into the model itself: while all parameters $\Theta = \{\theta, \theta_{\mathrm{meta}}\}$ are treated equally for MCMC-purposes, only the regular parameters are fed into the model: $\boldsymbol{M}(\theta)$.

In this case, the meta-parameter is labeled δ_u, and is enters into the covariance matrix as an

additional source of uncertainty:

$$\Delta^2 = \delta_y^2 + \delta_u^2 \tag{9.12}$$

where Δ^2 are the diagonals of $\boldsymbol{\Sigma}$, and δ_y are the uncertainties from experiment (one for each data point). The δ_u uncertainties are unique up to each observable type.

9.2.9 Systematic handling of outliers (future work)

An important remaining feature lacking from COMMCAS which Cole Pruitt explored in his optical model work is systematic exclusion of outliers. By outliers we mean data points which produce model residuals many standard deviations away from the rest of the data, i.e. by having unusually small reported uncertainties. In statistics this is called sigma clipping.

This feature is an important counter-measure to unaccounted-for uncertainty parameters: an outlier in the reported uncertainty will tend to inflate the UAUP.

9.3 Future work: Regularized likelihood functions

There are some problems when it comes to fitting theoretical models to nuclear data:

1. The data lack covariances

2. Multiple data sets cover the same energy domain; covariances between data sets in the same energy domain are generally not well defined

3. Data sets within the same energy region can have incompatible uncertainties

4. It is difficult to weigh the relative uncertainty of multiple observables, each of which has a variable number of experimental data sets constraining them

Discrete covariances of observables at different energies within a given experiment are important ingredients, but really what we want to say is that many of these observables are smooth functions of energy (or angle, etc). Discrete covariances can approximately encode that information within a single data set. But when you add multiple data sets with their own reported covariances, we can see conceptual problems arise. Is simply adding unaccounted for uncertainties or renormalizing data sets or their covariances [230] the right approach?

I want to re-frame this problem to make the solution clear: when we have observables which are smooth functions of an underlying variable X (energy, angle), what is the correct way to deal with uncertainty per unit X? These issues all meet when it comes time to define a likelihood function for an inverse uncertainty quantification (UQ) solver. I claim that Gaussian Processes (GPs) [235] are an ideal tool for addressing these problem. This approach will mostly address problem 4, and to a lesser extent problems 1 and 2. Problem 3 will likely persist.

9.3.1 Datasize-weighted covariances

The issue of the relative weighting of multiple data sets is summarized in the following thought experiment: suppose we are fitting multiple observables simultaneously: should an observable with more data points in a comparable energy range contribute more to the likelihood function than an observable with comparatively little measurements? Without covariances *on uncertainties* between experiments, there is no definite way to decide.

One approach for dealing with this issue, also discussed in [230] is to renormalize the covariance matrix, or sub-blocks thereof, by a weight equal to the number of data points within

that block. For example, by a factor of k/N_{block}, where k is the number of model parameters and N_{block} is the number of data within a block of the covariance, associated with a particular observable or data set. The problem with such an approach is that the covariance tends towards zero as the number of data points becomes large. If the uncertainty were purely statistical then this might be reasonable. However, this is not so for experimental nuclear data.

9.3.2   Generalized Least Squares

This problem of interpreting multiple nuclear data sets is shared with nuclear data evaluation. How do evaluators deal with this problem? Historically it has been with generalized least squares (GLS), with the particular implementation being the GMA (Gauss-Markov-Aitken) method and GMA code originally from Argonne National Lab [223, 49].

The GMA equations give the optimal observable predictions $\boldsymbol{p}$ and their covariances $\boldsymbol{V}_p$ on the new grid given a set of observations (data):

$$\boldsymbol{p} = \boldsymbol{V}_p \boldsymbol{A}^T \boldsymbol{V}_y^{-1} \boldsymbol{y} \tag{9.13}$$

$$\boldsymbol{V}_p = (\boldsymbol{A}^T \boldsymbol{V}_y^{-1} \boldsymbol{A})^{-1}, \tag{9.14}$$

where $\boldsymbol{y}$ are measured values of the observables (containing multiple data sets over the same energy domain), $\boldsymbol{V}_y$ is the corresponding experimental covariance matrix, and $\boldsymbol{A}$ is called the design matrix. The design matrix does the job of mapping (linearly) the measured observables to new values of the observables on an arbitrary grid of points (the design space). The design matrix may simply interpolate, for example.

The great benefit of the GMA method is to 'bin' multiple sets of data onto a desired grid, while best preserving the information carried by the data about the mean values and co-

variances. In fact, this is the discrete version of what I will be proposing. It could be used instead. A possible downside of GMA is the large number of parameters (which scales with the size of the design space) and that it sometimes leads to un-smooth and non-physical features [49].

9.3.3 Proposal

I propose using a Gaussian Process model to turn the collection of experimental data sets into a single, fully co-variate probability distribution to be used as part of the likelihood function in inverse UQ propagation. That GP model, faithfully encoding the joint experimental probability distribution, will be used in place of the data in our existing MCMC framework (obtaining the posterior of the model parameters given the data). This addresses the problems laid out in the introduction by regularizing the data vectors and reducing the dimension of the covariance matrix.

Regularization

The purpose of creating a GP model for the multiple data sets of a single energy-dependent observable is to regularize or 'bin' the multivariate normal distribution which describes it. Unlike the experimental covariance matrix, or even one determined by a GMA method [223], the GP covariance kernel is explicitly aware of the energy-dependence of the covariances. A simple kernel is a Gaussian function [73]:

$$k(x, x'; \sigma_f, l) = \sigma_f \exp\left[\frac{-(x - x')^2}{2l^2}\right], \tag{9.15}$$

where σ_f and l are parameters to be fit to the experimental data.

We assume that each data point of an observable y occurs at some independent variable (e.g.

energy) x,

$$y = f(x), \tag{9.16}$$

that experimental measurements of particular y_i at x_i are noisy,

$$y_i = f(x_i) + \mathcal{N}(0, \boldsymbol{\Sigma}), \tag{9.17}$$

but that experimental measurements can provide good approximations of that noise (uncertainty). An experimental data set will provide a set of measured mean values $\boldsymbol{\mu}_{\mathrm{exp}}$ and estimated covariances $\boldsymbol{\Sigma}_{\mathrm{exp}} \approx \boldsymbol{\Sigma}$ for some set of (y_i, x_i).

The job of the kernel function k of a GP is to estimate the covariance matrix elements at energies on an arbitrary grid: a grid of prediction points x_* for which the GP will predict observable values y_*.

Regularized likelihood

Our new likelihood function is the multivariate Gaussian distribution defined on the predictive (interpolated) grid of q points with means [73, 235]:

$$\boldsymbol{\mu}_* = \boldsymbol{K}_* \boldsymbol{K}^{-1} \boldsymbol{\mu}_{\mathrm{exp}}. \tag{9.18}$$

The matrix $\boldsymbol{K}$ is defined on the grid of experimental data points,

$$\boldsymbol{K} = \boldsymbol{\Sigma}_{\mathrm{exp}} + \boldsymbol{\Sigma}_{\mathrm{GP}} + \boldsymbol{\Sigma}_{\mathrm{theory}} \tag{9.19}$$

where $\boldsymbol{\Sigma}_{\mathrm{GP}}$ has matrix elements equal to the kernel $k(x_i, x_j; \boldsymbol{\kappa})$ evaluated on the experimental data grid x_i. The theory covariance matrix may not be known, in which case it is omitted.

Similarly, $\boldsymbol{K}_*$ is a matrix of kernel values $k(x_*, x_j)$ at prediction grid points x_* against all data grid points x_j. The GP predictive covariance matrix is [73, 235]:

$$\boldsymbol{\Sigma}_* = \boldsymbol{K}_{**} - \boldsymbol{K}_* \boldsymbol{K}^{-1} \boldsymbol{K}_*^T, \tag{9.20}$$

where $\boldsymbol{K}_{**} = k(x_*, x_*)$.

The probability function defined on the predictive-grid of energies $\boldsymbol{x}_*$ is thus:

$$P(\boldsymbol{y}_* | D : \boldsymbol{\mu}_{\text{exp}}, \boldsymbol{\Sigma}_{\text{exp}}) = \mathcal{N}(\boldsymbol{y}_*; \boldsymbol{\mu}_*, \boldsymbol{\Sigma}_*). \tag{9.21}$$

Assuming a model $\boldsymbol{M}(\boldsymbol{\theta}) = \boldsymbol{y}_*$, we define the regularized likelihood as:

$$\tilde{L}(D | \boldsymbol{M}(\boldsymbol{\theta})) = \mathcal{N}(\boldsymbol{M}(\boldsymbol{\theta}); \boldsymbol{\mu}_*, \boldsymbol{\Sigma}_*). \tag{9.22}$$

As a reminder, the crux of this new likelihood function is to be able find an appropriate kernel function $k(x, x'; \boldsymbol{\kappa})$ and subsequently fit its parameters $\boldsymbol{\kappa}$ to represent the experimental $\boldsymbol{\mu}_{\text{exp}}$ and $\boldsymbol{\Sigma}_{\text{exp}}$.

Dimension reduction

In the standard likelihood function, our joint PDF is described by $n + n(n+1)/2$ parameters provided by experiment: n mean-values and $n(n+1)/2$ independent covariance elements. The regularized likelihood function, by contrast, will have only p parameters: the number of parameters describing the kernel function $k(x, x')$.

Generally $p \ll n \ll n(n+1)/2$, so that in most cases we end up with far fewer parameters required to describe the joint PDF describing the experimental data, and therefore also of the likelihood function used in the inverse UQ problem. Of course, the downside of this is

that we risk losing information in the process.

What this proposal is not

This is not a proposal to use a Gaussian Process for nuclear data evaluation, which amongst other requirements sets out to not only interpolate but to extrapolate. In this application the goal of the GP is only to encode the joint experimental uncertainty as a function of energy, thereby avoiding over-prescription of certainty when adding multiple measurements of observables in the same energy region.

Chapter 10

Surrogate Reactions II: Parameter Inference and Uncertainty Quantification

The general concept of the surrogate reaction method was already discussed in the previous chapter on the Weisskopf-Ewing approximation of the surrogate reaction method. Earlier work demonstrated that cross sections for neutron-induced fission and radiative neutron capture can be determined from a combination of surrogate reaction data and theory. For the fission case, it was shown that the Weisskopf-Ewing approximation can be employed, which significantly simplifies the implementation of the surrogate method [80]. This is not true for neutron capture cross sections, where a more sophisticated theoretical evaluation of the data is required using the complete surrogate reaction method [81, 236, 222].

The conclusions of Chapter 8 are similar: while peak cross sections can be estimated using the Weisskopf-Ewing approximation, the shape of the (n, n') and $(n, 2n)$ cross sections, especially for low neutron energies, cannot be reliably determined without accounting for the angular-momentum differences between the neutron-induced and surrogate reaction. To obtain reliable (n, n') and $(n, 2n)$ cross sections from surrogate reaction data, a detailed

description of the surrogate reaction mechanisms is required.

The full surrogate reaction method, as compared to the surrogate reacion method with the Weisskopd-Ewing approximation, requires two additional ingredients. The first is a model to predict the spin-parity distribution of the compound nucleus following its formation in the surrogate reaction entrance channel. The second ingredient is a means to do parameter inference on the model parameters describing the statistical decay of the compound nucleus. In this chapter, I address the second need, and rely on the work of others to supply the first. In particular I demonstrate the application of the COMMCAS code discussed in Chapter 9 to the full surrogate method by providing the framework for parameter inference and uncertainty quantification.

10.1   Theory for the desired reaction

The Hauser-Feshbach (HF) statistical reaction formalism properly accounts for conservation of angular momentum and parity in compound-nuclear reactions. For a reaction with entrance channel $\alpha = a + A$ that forms the CN B^*, which subsequently decays into the exit channel $\chi = c + C$,

$$a + A \rightarrow B^* \rightarrow c + C,$$

the HF cross section can be written as

$$\sigma_{\alpha\chi}(E_a) = \sum_{J,\pi} \sigma_\alpha^{CN}(E_{ex}, J^\pi) G_\chi^{CN}(E_{ex}, J^\pi). \tag{10.1}$$

Here E_a and E_{ex} are the kinetic energy of the projectile a and the excitation energy of the compound nucleus B^*, respectively. They are related to each other via $E_a = \frac{m_A}{m_a + m_A}(E_{ex} - $

S_a), where S_a is the energy needed to separate the particle a from the nucleus B^*. m_a and m_A are the masses of the projectile and target, respectively. J and π are the spin and parity of the compound nucleus and $\sigma_\alpha^{CN}(E_{ex}, J^\pi)$ is the cross section for the forming the compound nucleus B^* with spin and parity J^π at energy E_{ex}. The $\sigma_\alpha^{CN}(E_{ex}, J^\pi)$ and their sum, the compound-formation cross section $\sigma_\alpha^{CN}(E_{ex}) = \sum_{J,\pi} \sigma_\alpha^{CN}(E_{ex}, J^\pi)$, can be determined using an appropriate optical model for the a-nucleus interaction. Width fluctuation corrections have been omitted to simplify the notation in Equation 10.1, but are included in the calculations.

$G_\chi^{CN}(E_{ex}, J^\pi)$ is the probability that the CN decays via the exit channel χ. For reactions that emit one particle (neutron, proton, alpha, etc.) it depends on the convolution of the transmission coefficient $T_{\chi l_c j_\chi}^J$ with the level density $\rho_{j_C}(U)$ for the residual nucleus, divided by analogous terms for all competing decay modes χ':

$$G_\chi^{CN}(E_{ex}, J^\pi) = \frac{\sum_{l_c j_\chi j_C} \int T_{\chi l_c j_\chi}^J \rho_{j_C}(U) dE_\chi}{\sum_{\chi' l_c' j_\chi' j_C'} \int T_{\chi' l_c' j_\chi'}^J (E_{\chi'}) \rho_{j_C'}(U') dE_{\chi'}}. \tag{10.2}$$

The quantities l_c and l_c' are the relative orbital angular momenta in the exit channels. $\vec{j_\chi} = \vec{j_c} + \vec{j_C}$ is the exit channel spin, related to the total spin $\vec{J} = \vec{l_a} + \vec{j_\alpha} = \vec{l_c} + \vec{j_\chi}$ by conservation of momentum with the entrance channel spin, $\vec{j_\alpha} = \vec{j_a} + \vec{j_A}$. $\rho_C(U, j_C)$ is the density of levels of spin j_C at energy U in the residual nucleus.

Contributions from decays to discrete levels and to regions described by a level density have to be accounted for and are implicitly included in the integrals in both the numerator and denominator of Eq. (10.2). For reactions that involve sequential decays, e.g. the emission of two neutrons in (n,2n), Eq. (10.2) is repeatedly applied: First, to determine the possible outcomes of the CN decay in the first step of the emission chain, and second, to follow the subsequent decays of the intermediate compound nuclei created. In HF calculations, the final cross sections are obtained by tracking all possible decays in this manner. All sums over

quantum numbers must respect parity conservation, although this is not explicitly expressed here.

In this chapter, we focus on neutron-induced reactions, *i.e.* $\alpha = n+A$. For such reactions, the optical model potential, used to calculate the first factor in Eq. (10.1), is well approximated by a one-body potential [100]. By far the greatest source of uncertainty comes from the decay probabilities, a fact that can be attributed to uncertainties in the nuclear structure inputs. *Ab initio* shell-model calculations can provide nuclear structure information for nuclei with only a dozen or so nucleons, and traditional shell-model calculations cover a limited number of nuclei, primarily near closed shells, containing up to around 100 nucleons. Mean-field and beyond-mean field approaches cover a wider range of nuclei, but calculating the relevant structure quantities (level densities and gamma-ray strength functions) is nontrivial. While much progress has been made toward achieving microscopic nuclear structure inputs for HF calculations of medium-mass and heavy nuclei, many isotopes needed for applications and for simulating stellar environments are currently out of reach.

In the absence of microscopic predictions of structural properties, phenomenological models are used for nuclear level densities and electromagnetic transition strengths, with parameters that are fitted to available data. Much effort has been devoted to generate global or regional parameter systematics [48] that can be utilized as to perform HF calculations and build nuclear reaction evaluations [177, 175, 215, 45]. Alternatively, it is possible to use surrogate reaction data to obtain experimental constraints on the decay probabilities.

10.2   Benchmark: Zr-90 neutron capture

The following is a modified version of a conference proceedings from the Compound Nuclear Reactions conference of 2018 [114].
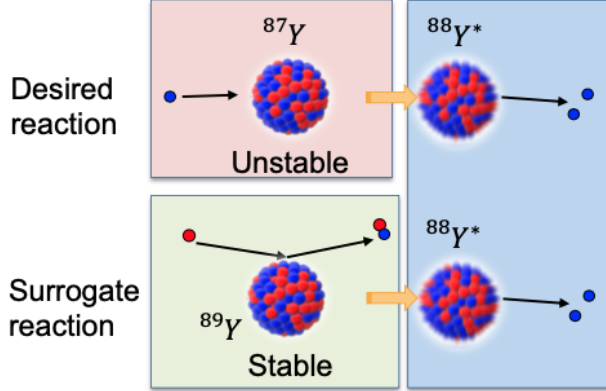
Figure 10.1: In this example shown here, we form the compound nucleus ^{88}Y by choosing the stable target ^{89}Y and performing a (p, d) (proton-deuteron) reaction. This we call the surrogate reaction. Experiments can be conducted to measure the coincidence probabilities $P_{d,p}(E_{ex})$, where emitted deuterons are measured in coincidence with gamma rays emitted from the compound nucleus with specific energies, which identify the compound nucleus formed.

Neutron capture cross sections can be measured by bombarding a sample of target nuclei with neutrons and detecting decay products. Such measurements cannot be completed in the laboratory when the target isotopes have half-lives that are short compared to timescales relevant to the experiment. This leaves critical gaps in nuclear data libraries. To predict the missing data, nuclear cross section calculations can, in principle, be carried out using statistical Hauser-Feshbach (HF) models [48].

In compound nuclear reactions, a compound nucleus (CN) is formed, which then decays through the available decay channels. These channels and the probability of each being taken depends on the nuclear level densities and γ-ray strength functions of the CN. The general lack of nuclear structure information for medium to heavy mass nuclei leads to the need for indirect constraints on the corresponding HF parameters. The surrogate method [80] obtains these constraints using measurements of the same CN decay observed in alternative reactions.

Specifically, in Ref. [81] the decay of the CN ^{91}Zr was modeled using parametrized (phenomenological) forms for the level density and γ-ray strength function. The parameters

were fit to measured ^{92}Zr$(p, d\gamma)$ data from the surrogate experiment and subsequently used to calculate the desired ^{90}Zr(n, γ) cross section. A Bayesian Monte Carlo approach was employed which provided an average (n, γ) cross section, along with a variance, yielding an uncertainty band that is symmetric around the mean.

In this section, we explore a Markov-Chain Monte Carlo approach to fitting the parameters to the surrogate data. MCMC generates a probability distribution for each parameter without visiting every combination of parameters. We chose to implement a Metropolis-Hastings algorithm [128] because it is the most common variety of MCMC. We present preliminary results for the ^{90}Zr(n, γ) neutron capture cross section. This reaction serves as a benchmark case since direct experimental data is available for ^{90}Zr(n, γ). Earlier results [81] for this application of the surrogate method used Bayesian Monte Carlo sampling, which has some disadvantages over the more robust MCMC approach. We sample the HF parameter to constrain five parameters in the composite Gilbert-Cameron level density model, and nine parameters in the γ-ray strength function description. The prior distribution is a finite and flat distribution, centered around recommended parameter values from RIPL-3 [48].

The posterior distribution of parameters is obtained by fitting to experimental data for ^{92}Zr$(p, d\gamma)$ from Ref. [81]. We then generate a HF prediction for the desired ^{90}Zr(n, γ) reaction at each point in the posterior distribution of parameters. The subsequent distribution of ^{90}Zr(n, γ) cross sections is our constraint on the neutron capture cross section. The posterior parameter distribution we obtain is sampled, yielding the ^{90}Zr(n, γ) cross section shown in Figure 10.2. The result is in agreement with the TENDL 2015 and ENDF/B-VII.x evaluations, both of which are based on directly-measured data. In future work we will investigate correlations among the model parameters.
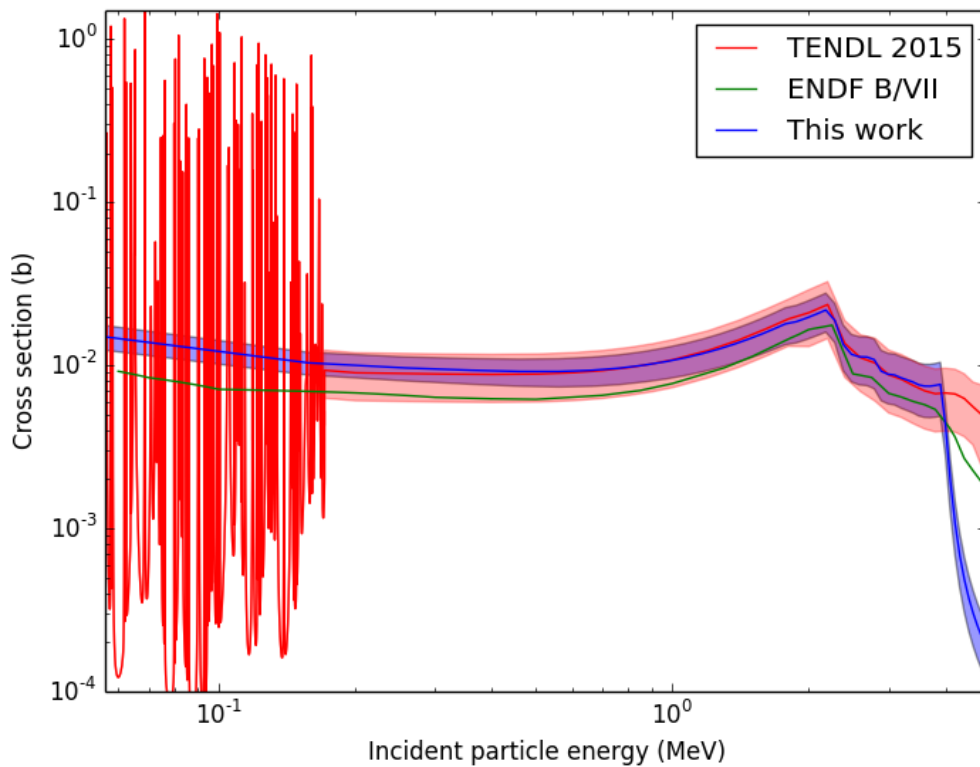
Figure 10.2: (Taken from [114].) ^{90}Zr(n, γ) cross section obtained indirectly from ^{92}Zr$(p, d\gamma)$ data using the newly-developed MCMC approach. The thick solid (blue) curve is the mean value and the thin solid curves indicate the 68% confidence interval. For comparison, the Talys Evaluated Nuclear Data Library (TENDL) [175] and the Evaluated Nuclear Data File (ENDF) library results are shown as well [57].

10.3 Benchmark: neutron capture on Mo-95

In this section I will demonstrate the application of COMMCAS to a specific problem which has already been addressed in [236] and again in a conference proceeding improving on the statistical methods [76]. I contributed to the latter publication.

The application in question is a surrogate reaction evaluation of the ^{96}Mo neutron capture cross section (n, γ) using the reaction ^{95}Mo$(d, p\gamma)$ as a surrogate. This case serves as a valuable benchmark since direct measurements of this cross section are available to validate the surrogate approach. The desired neutron capture cross section is:

$$n +^{95} \text{Mo} \rightarrow^{96} \text{Mo}^* \rightarrow\ ^{96}\text{Mo} + \gamma. \tag{10.3}$$

The surrogate reaction is:

$$d +^{95} \text{Mo} \rightarrow^{96} \text{Mo}^* + p \rightarrow\ ^{96}\text{Mo} + \gamma + p. \tag{10.4}$$

We can see that both reactions form ^{96}Mo* as an intermediate compound nucleus, which is what allows us to use ^{95}Mo$(d, p\gamma)$ to constrain ^{96}Mo(n, γ) indirectly - in particular, the decay branching ratios. A proton-gamma coincidence measurement is made for specific gamma transitions in ^{96}Mo. See [236] for more experimental details. The result is five $P_{p\gamma}(E_x)$, energy-dependent coincidence probability measurements.

The task of the surrogate evaluation is to use these measurements of the surrogate reaction to constrain the desired neutron capture reaction. This requires two UQ propagation steps. First, an inverse UQ propagation to constrain Hauser-Feshbach model parameters using the measured coincidence probabilities $P_{p\gamma}(E_x)$. This produces a distribution of model parameters describing the decay of the compound nucleus shared by both reactions (the surrogate and the desired reaction). Second, a forward UQ propagation to calculate the distribution

of (n, γ) cross sections given the now constrained model parameters. Both of these steps can be done with COMMCAS.

For this benchmark data I use the same five experimental data curves $P_{p\gamma}(E_x)$ from the five best-measured gamma transitions between states and with energies: $2_2^+ \rightarrow 2_1^+$ 7.17 MeV, $2_1^+ \rightarrow 0_1^+$ 7.78 MeV, $6_1^+ \rightarrow 4_1^+$ 8.12 MeV, $4_2^+ \rightarrow 2_1^+$ 1.091 MeV, $3_1^+ \rightarrow 2_1^+$ 1.20 MeV. These are the five 'observables' COMMCAS uses to compute its likelihood function.

For the model parameters describing the decay of the compound nucleus, I focus on the nuclear level densities and gamma-ray strength functions of the compound nucleus ^{96}Mo. I varied four level density parameters, and nine gamma-ray strength function (GSF) parameters, focusing on the giant dipole resonance of the E1 GSF. I also followed the procedure of [236] and included a normalization parameter for each gamma transition channel, which corrects for limited knowledge of individual gamma-decay branching ratios. This constitutes five parameters, one for each coincidence probability. Finally, each observable was assigned its own unaccounted-for uncertainty parameter (UAUQ). The total number of parameters was 23.

For the MCMC sampling, I used a large number of walkers (500), with a relatively short sampling period of about 1000 samples. (This is acceptable because the priors are close to the posterior solution.) All five observables were fit simulaneously over the entire energy range of the available data. A Gaussian smoothing was applied to all coincidence probabilities with a half-width of 0.08 MeV to account for the beam width of the experiment. The posterior model predictions after sampling are are shown in Figure 10.3. Two other observables were also tracked during the sampling which did not contribute to the likelihood function, shown in Figure 10.4. These observables, the E1 gamma-ray strength function and the M1 GSF, are tracked by COMMCAS during the fit, but do not influence the posterior distribution of parameters. There are experimental measurements available for the E1 photoabsorption cross section, which can provide some indication as to the overall shape of the E1 strength

function. We see that the E1 GSF constraints obtained from fitting to the surrogate data yield overall agreement with the data in the energy range where the data was fit, below 11 MeV excitation energy of the compound nucleus ^{96}Mo. Once the surrogate data was fit and the decay parameters were constrained, I conducted the second series of calculations: forward UQ propagation. Using the last few parameter samples from the Markov Chain generated during sampling, I computed the desired cross section ^{96}Mo(n,γ). The results are shown in Figure 10.5. The uncertainty bands in this figure have a specific interpretation: given the uncertainty in the measured surrogate data from the ^{95}Mo$(d,p\gamma)$ experiment, along with our prior limits on the Hauser-Feshbach decay parameters, this is the confidence interval for the ^{96}Mo(n,γ) neutron capture cross section. I find excellent agreement with the directly measured data, and with the previously published surrogate evaluation in [236] using similar methods.
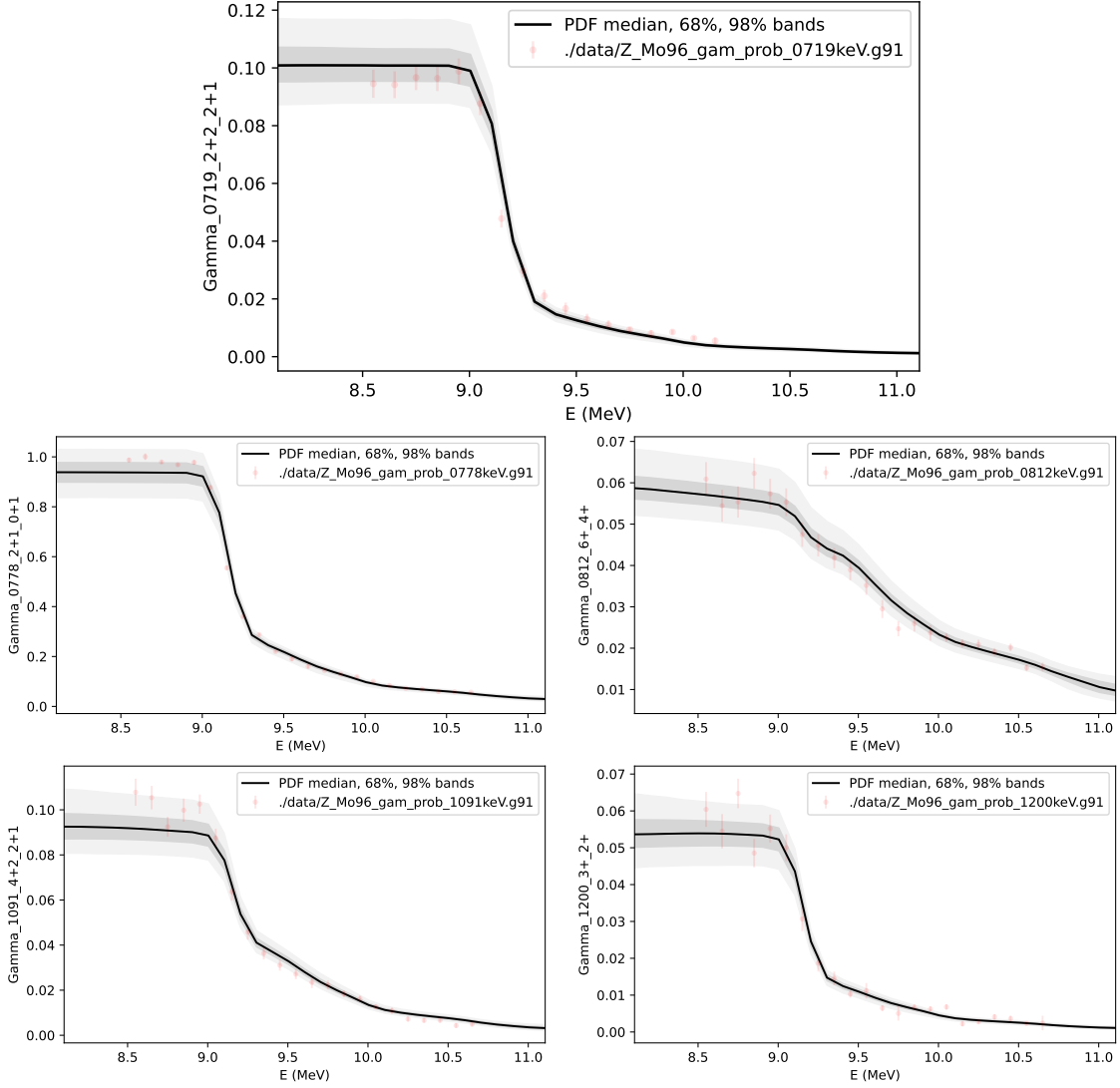
Figure 10.3: The five data sets for $P_{p\gamma}(E_x)$ coincidence probabilities from the five best-measured gamma transitions between states and with energies: $2_2^+ \to 2_1^+$ 7.17 MeV, $2_1^+ \to 0_1^+$ 7.78 MeV, $6_1^+ \to 4_1^+$ 8.12 MeV, $4_2^+ \to 2_1^+$ 1.091 MeV, $3_1^+ \to 2_1^+$ 1.20 MeV. These are the five 'observables' COMMCAS uses to compute its likelihood function. The gray bands are the model posteriors after sampling with MCMC: the black line is the 50-th percentile, the dark grey band is the 68-percent confidence interval, and the light grey band is the 98-percent confidence interval.
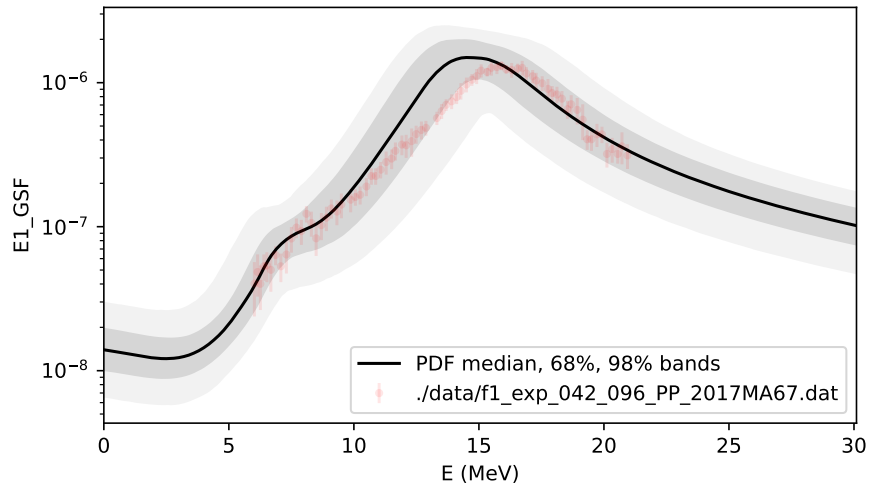
Figure 10.4: This observable, the E1 gamma-ray strength function, was tracked by COMM-CAS during the fit, but not included in the likelihood function. This is useful for understanding the properties of the posterior distribution in the context of a multi-physics model; auxiliary observables can be used to assess the sensibility of the posterior parameters.
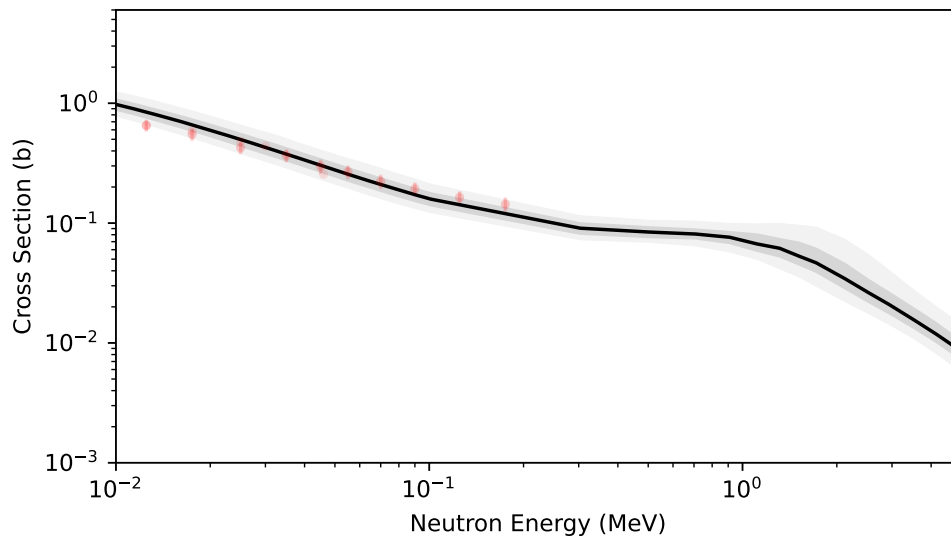
Figure 10.5: The predictive posterior of the desired observable: the ^{96}Mo(n,γ) neutron capture cross section obtained by fitting the compound nucleus decay parameters to the 95Mo$(d,p\gamma)$ surrogate data shown in Figure 10.3. The experimental data (orange dots with error bars) were not used in the calculations. Our results show excellent agreement with those presented in [236], and with the experimental data (see [236] for details).

Chapter 11

Constraints on (γ, p) branch points for the γ-process

This chapter is based on a paper I co-authored, "Measurements of proton capture in the $A = 100 - 110$ mass region: Constraints on the $^{111}In(\gamma, p)/(\gamma, n)$ branching point relevant to the γ-process" by Orlando Olivas-Gomez, et al. [212] Orlando and I met as graduate student interns at LLNL in the summer of 2019, both working with Jutta Escher. After some lunchtime discussions, I realized from Orlando's description of his experimental work that the UQ tool I was developing (which would later be called COMMCAS) was perfect for analyzing his group's data. This led to a collaboration between Orlando and his Ph.D. advisor Anna Simon of Notre Dame, Escher, and myself. Escher and I were fourth and third authors, respectively.

As a principally experimental physics paper, my contribution is mainly centered around the improved interpretation of the results, in particular with respect to quantifying the uncertainties. The contents of this chapter closely follow sections from the original paper [212], with some rewording and reorganization to emphasize my contribution and to avoid discussion of

the experimental aspects with which I was not involved.

11.1 Overview

The γ-process is an explosive astrophysical scenario, which is thought to be the primary source of the rare, proton-rich stable p-nuclei. However, current γ-process models remain insufficient in describing the observed p-nuclei abundances, with disagreements up to two orders of magnitude. A sensitivity study has identified ^{111}In as a model-sensitive $(\gamma, p)/(\gamma, n)$ branching point within the γ-process. Constraining the involved reaction rates may have a significant impact on the predicted p-nuclei abundances. Here we report on measurements of the cross sections for ^{102}Pd$(p, \gamma)^{103}$Ag,^{108}Cd$(p, \gamma)^{109}$In, and ^{110}Cd$(p, \gamma)^{111}$In reactions for proton lab energies 3-8 MeV using HECTOR and the γ-summing technique. These measurements were used to constrain Hauser-Feshbach parameters used in TALYS 1.9, which constrains the ^{111}In$(\gamma, p)^{110}$Cd and ^{111}In$(\gamma, n)^{110}$Ag reaction rates. The newly-constrained reaction rates indicate that the ^{111}In $(\gamma, p)/(\gamma, n)$ branching point occurs at a temperature of 2.71 ± 0.05 GK, well within the temperature range relevant to the γ-process. These findings differ significantly from previous studies, and may impact the calculated abundances.

A key step in the analysis of this work is to take the experimentally measured (p, γ) cross section and to make an inference about the inverse (γ, p) cross section. To do this requires some intermediate theoretical model which can compute both of these. By constraining the model with the new experimental data, we obtain new constraints on the inverse process via the theoretical model. Before my involvement in this work, the group's plan was to try the various pre-programmed statistical decay models in a popular reaction code (TALYS), and choose the one that reproduced the experimental data. This choice would then be used for the inference calculations of the inverse process. My contribution was to improve on this method by first selecting a model, and then using Bayesian statistics to constrain the model

paramters using the data. In the end, both Bayesian and non-Baysian methods were used and are compared in this chapter.

11.2   Introduction

The p-nuclei are the proton-rich stable nuclei between ^{74}Se through ^{196}Hg. As a group they are the rarest of all stable nuclei, with abundances typically two to three orders of magnitude lower than other stable isotopes of the same element [7]. Unlike most nuclei heavier than iron, which can be made through sequential neutron captures in the s- and r- processes, the p-nuclei are shielded from β-decay by the valley of stability, and thus it was determined that an alternative mechanism is needed [47]. Presently, the origin of the p-nuclei remains a mystery.

The most favored and thoroughly investigated model for the production of the p-nuclei is known as the γ-process [304]. The γ-process is based on explosive astrophysical scenarios, in which at temperatures between 2.0-3.0 GK photodisintegration reactions, (i.e., (γ, p), (γ, n), and (γ, α)), on preexisting r-, s-process seed nuclei can produce most of the p-nuclei. This process is illustrated in Fig. 11.1 for the $A = 100 - 110$ mass region.

For many years, the primary astrophysical site for the γ-process was thought to primarily occur within the oxygen-neon rich layers of a massive star undergoing core-collapse type-II supernova [14]. Type-II supernova based γ-process models are mildly successful in predicting most of the solar p-nuclei abundances within about a factor of three. However, there are serious deficiencies, especially in the molybdenum-ruthenium region where the solar abundances are underpredicted by up to two orders of magnitude [241]. Thus, there could be several independent astrophysical scenarios contributing to the production of the p-nuclei (see [238] and the references therein). For example, recent advances in simulations have demonstrated
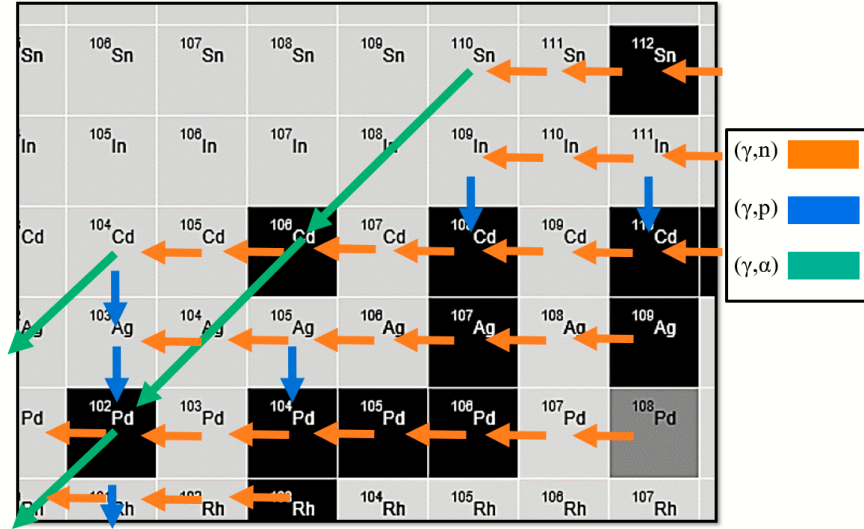
Figure 11.1: (Taken from [212]) The γ-process reaction flow for the $A = 100-110$ mass region where photodisintegration reactions on seed nuclei can produce the p-nuclei (shown here ^{102}Pd, ^{106}Cd, ^{108}Cd, and ^{112}Sn). Colored arrows indicate the dominant photodisintegration reaction. Isotopes with two outgoing arrows are branching points; at a critical temperature, one reaction rate will become stronger than the other.

that the γ-process can also occur within the carbon rich layers of a white dwarf undergoing type-Ia supernova [281].

Therefore, although the γ-process may be the primary candidate for the production of the p-nuclei, it is not clear to what extent each astrophysical site contributes to the p-nuclei abundances. One of the major factors hindering progress is due to uncertainties of the associated nuclear physics. To better understand the γ-process, and the contributions coming from different astrophysical sites, it is imperative to constrain the nuclear input, which is the focus of this work.

Modeling of the γ-process requires input of thousands of nuclear reaction rates, which requires knowledge of the cross section within the appropriate Gamow energy window for each reaction. However, most of these cross sections have not been experimentally measured and thus rely on theoretical calculations. The calculations are done using the Hauser-Feshbach statistical reaction formalism [129], which is implemented in reaction model codes such as

TALYS [173] and NON-SMOKER [239, 240]. However, due to the lack of experimental data, parameters inherent to the Hauser-Feshbach theory are poorly constrained. For example, proton and neutron capture/emission reaction rates calculated by NON-SMOKER have uncertainties of about a factor of two [239].

This becomes an issue primarily when the (γ, n) and (γ, p) reaction rates for an isotope are comparable in magnitude within the γ-process temperature window. As illustrated in Fig. 11.1, the γ-process proceeds through a sequence of (γ, n) reactions, shifting the abundances to the proton-rich side of stability. At some point along a chain of isotopes, the (γ, p) or (γ, α) rate becomes stronger than that of neutron emission, and the mass flow branches into another isotopic chain. These are known as branching points, and establishing their locations is crucial for accurate modeling of the γ-process. However, due to the reaction rate uncertainties, there is an ambiguity in the location of several branching points, and consequently, in the reaction flow of several mass regions which may have a significant impact on the predicted p-nuclei abundances.

In one particular case, a sensitivity study [237] has identified ^{111}In as a potential $(\gamma, p)/(\gamma, n)$ model-sensitive branching point within the γ-process. This is demonstrated in Figure 11.2, which shows the stellar photodisintegration rates for ^{111}In, taken from the JINA REACLIB database [61]. These (γ, p) and (γ, n) rates are based on two versions of the NON-SMOKER code (labeled tsh8-v6 and rath-v2) [240, 61], with tsh8-v6 being the more recent version. The (γ, p) rates from these two versions differ by about a factor of five. The inconsistencies between these two rates, coupled with the uncertainty of the reaction rates, make it unclear at what temperature (γ, n) begins to dominate. If the ths8-v6 version is correct, it could be between 2.3 GK to 3 GK. On the other hand, rath-v2 predicts the branching point above 3 GK and possibly outside the γ-process window.

Above the branch-point temperature, ^{111}In$(\gamma, n)^{110}$In begins to dominate, and the reaction flow would feed into ^{108}Cd through the series of reactions: ^{110}In$(\gamma, n)^{109}$In$(\gamma, p)^{108}$Cd (see

Fig. 11.1). Below the branch-point temperature however, ^{111}In$(\gamma, p)^{110}$Cd would dominate, feeding into ^{110}Cd. So, if the branch-point temperature is determined to be within the γ-process temperature window, the abundance ratio of ^{108}Cd to ^{110}Cd would be sensitive to temperature, which would be a useful metric in constraining the seed-distribution and/or astrophysical conditions necessary for the γ-process. Thus, the purpose of this work is to
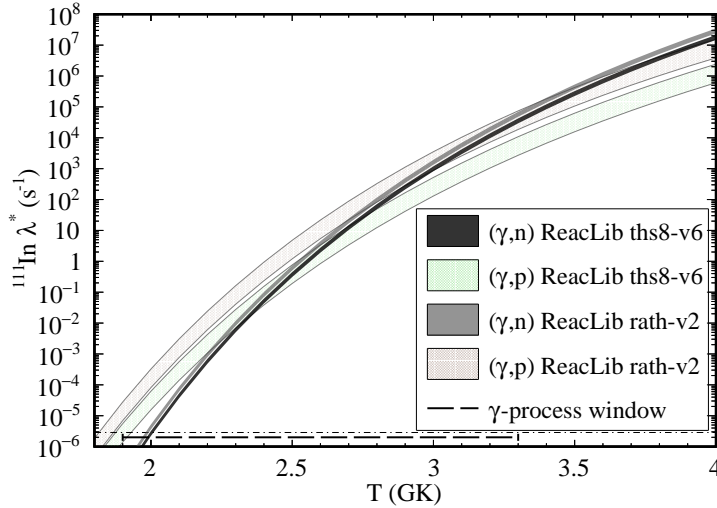

Figure 11.2: (Taken from [212]) Stellar photodisintegration reaction rates for ^{111}In. The light shaded bands are (γ, p) rates taken from the JINA REACLIB database [61]. The labels refer to the version of NON-SMOKER used. The uncertainty of the reaction rates makes it unclear at what temperature (γ, n) begins to dominate (γ, p), which can have a significant impact on γ-process model predictions of p-nuclei abundances.

reduce the nuclear uncertainties of γ-process models by constraining the ^{111}In$(\gamma, n)^{110}$In and ^{111}In$(\gamma, p)^{110}$Cd reaction rates. This constrains the ^{111}In $(\gamma, p)/(\gamma, n)$-temperature branching point, improving our understanding of the reaction flow in this mass region.

To achieve this goal, the cross sections for ^{108}Cd$(p, \gamma)^{109}$In, and ^{110}Cd$(p, \gamma)^{111}$In were measured between lab energies 3-8 MeV, which covers most of the Gamow window for each reaction. By measuring (p, γ) cross sections of nuclei near ^{111}In, the measurements can be used to constrain the Hauser-Feshbach parameters, and consequentially, constrain the inverse reaction rates of interest. In addition, the ^{102}Pd(p, γ) cross section was also measured throughout a similar energy range. The inclusion of this reaction, being a lower mass relative to

to the other two nuclei, helped limit the bias when constraining the set of Hauser-Feshbach parameters used in describing similar reactions in the $A = 100 - 110$ mass region to be discussed later.

In the present dissertation, I will present only the discussion of the constrained Hauser-Feshbach parameters, and constrained $^{111}In(\gamma, n)^{110}In$ and $^{111}In(\gamma, p)^{110}Cd$ reaction rates.

11.3   Bayesian modeling

Each of the models underlying the Hauser-Feshbach cross sections, (i.e., the OMP, γSF, and NLD), has associated with it an uncertainty which contributes to the overall uncertainty of the cross section. For phenomenological models, there are several parameters which are typically fit to nuclear data. For example, the Kopecky-Uhl generalized Lorentzian γSF (KU-γSF) [178], which is a parameterization of a Lorentzian representation of the giant dipole resonance (GDR), depends on the strength, centroids, and widths of the E1 and M1 GDR. The Gilbert-Cameron NLD model (GC-NLD), which is the combination of a constant-temperature model with a Fermi-gas model at higher temperatures [101], depends on an energy-dependent level density parameter a. The values of these parameters depend on the nuclear structure of the nuclei participating in the reaction; when there is no experimental information, they are estimated from systematics and/or extrapolated.

Using the (p, γ) cross sections measured in this work, statistical parameter estimation within γSF and NLD models were carried out using the Hauser-Feshbach code TALYS, version 1.9.

For the NLD, the GC-NLD was used. The internal parameters constrained were the asymptotic level density parameter $\tilde{a}$, and the level density damping parameter γ of the three nuclei in the proton-entrance, neutron-exit, and γ-exit channels of each reaction. For example, in the $^{110}Cd(p, \gamma)^{111}In$ reaction, ^{110}Cd, ^{110}In, and ^{111}In are considered.

For the γSF, E1 transitions were calculated using the KU-γSF. The internal parameters constrained were the centroid, width, and strength of the E1 GDR. The M1 transition were calculated using the Brink-Axel Lorentzian (BA-γSF) [39, 18]. Two M1 peaks were considered, and the internal parameters constrained were the centroids, strengths, and widths of these peaks. Higher-order transitions were left as the TALYS default, which is discussed in [174].

Regarding the OMP, the Koning and Delaroche OMP (KD-OMP) [176] was used for protons and neutrons. For the α OMP — the TALYS default — the alpha potential of Avrigeanu et al. [17] was chosen, which is consistent with the recommendation by [168] for the same mass region. The parameters within these models were not varied and kept as the TALYS default.

In total, fifteen parameters for each reaction were constrained; these parameters were found to be the dominant factors affecting the cross-section predictions. The Hauser-Feshbach model, in this case TALYS, is represented as a parametric model of the cross sections: $\sigma_{th}(\theta)$. To constrain the parameters θ, a Markov Chain Monte Carlo (MCMC) algorithm was used to sample the posterior probability distribution, which was found by combining prior knowledge of the parameters with new knowledge given by the experimental measurements described in this work. This is accomplished with Bayes' theorem:

$$P(\theta|D) = \frac{L(D|\theta)p(\theta)}{\int L(D|\theta)p(\theta)d\theta}, \tag{11.1}$$

where θ is the set of model parameters ($\tilde{a}$, γ, etc.) and D is the set of experimental cross-section measurements (previous measurements in the literature are not included). $p(\theta)$ is the joint prior probability distribution of the parameters, which was taken to be uniform to obtain an unbiased posterior. $L(D|\theta)$ is the likelihood function, which is defined to be a multivariate normal distribution, with means equal to the measured cross sections σ_{exp}

and a diagonal covariance matrix with elements equal to the square of the experimental uncertainties $d\sigma_{exp}^2$:

$$L(D : \sigma, d\sigma|\theta) \propto \exp\left[-\sum_{i \in D}\left(\frac{\sigma_{exp} - \sigma_{th}(\theta)}{d\sigma_{exp}}\right)^2\right]. \tag{11.2}$$

A Metropolis Hastings algorithm [128] serves as the MCMC sampler. For each reaction, 15 independent chains of 1500 steps were computed. The first 500 steps of each chain were considered "burn in", and discarded. In total, the posterior distribution for each reaction contains 15000 samples.

Once the joint posterior probability distribution $P(\theta|D)$ is obtained, a distribution of cross-section predictions can be calculated by sampling from $P(\theta|D)$. The results of this are shown in the left panels of Fig. 11.3. The band represents a 68% confidence interval, while central values are taken as the median. As a comparison, the TALYS 1.9 calculations using the default parameters values for the same NLD and γSF are shown as well. The results are a significant improvement over the TALYS 1.9 default and NON-SMOKER models, as the predictions are in good agreement with the experimental data throughout the energy range measured. In a similar fashion, the inverse cross section and reaction rates of interest can also be calculated by sampling from $P(\theta|D)$.

11.4   Pre-Bayesian modeling

In the previous section, the internal parameters within phenomenological models were constrained, resulting in predictions that agree well with experiment within uncertainties. However, as previously mentioned, the uncertainties of the internal parameters grow with extrapolation from experimental data. In addition to determining the best constrained reaction rates, it is also beneficial to develop a model for the mass region that can be used for nearby

nuclei where there is still little to no experimental data. For this, we turn to microscopic γSF and NLD models.

Microscopic models tend to be less accurate, but are more robust, capable of describing a small mass region with less need for experimental data for re-calibration of their internal parameters. However, there are many microscopic γSF and NLD available within TALYS, and it is unclear which combination best describes the region of interest; random combinations of these models vary the cross-section predictions by over a factor of ten.

Thus, every combination possible for microscopic γSF and NLD models available within TALYS 1.9 was tested. Within TALYS 1.9, there are three microscopic NLDs and six microscopic γSFs for a total of 18 combinations; each model is listed in Table 11.1. For the OMP, the KD-OMP and the semi-microscropic Jeukenne-Lejeune-Mahaux OMP (JMP-OMP) [157] were tested for protons and neutrons. Like the previous method, the α OMP remained as the TALYS default.

Table 11.1: Microscopic NLD and γSF available within TALYS 1.9. The numbering notation is consistent with the TALYS 1.9. manual [174]. The microscopic γSFs calculate the dominant E1 transitions; M1 and all other higher order transitions are calculated using the BA-γSF.

NLD	
ldmodel 4:	Skyrme force from Goriely's tables [113]
ldmodel 5:	Skyrme force from Hilaire's combinatorial tables [111]
ldmodel 6:	Temperature dependent HFB, Gogny force from Hilaire's combinatorial tables [139]
γSF	
strength 3:	Hartree-Fock BCS tables [48]
strength 4:	Hartree-Fock-Bolgubyubov (HFB) tables [48]
strength 5:	Goriely's hybrid tables [109]
strength 6:	Goriely's temperature dependent HFB [139]
strength 7:	temperature dependent relativistic mean field [15]
strength 8:	Gogny D1M HFB and quasiparticle random phase approximation [195]

The total number of combinations tested was then 36. From each combination, theoretical

cross sections for each energy measured in this work were calculated and compared to the experimental values. Unlike the Bayesean modeling method described in the previous section, the default parameters of the microscopic models were not changed. In order to determine the best combination, the chi-square value χ^2 for each model was computed, which is equal to the argument in the exponent of Eq. (11.2), taking σ_{th} as the model prediction, and σ_{exp} as the experimental cross section for a given energy.

The model combination with the smallest χ^2 for each individual reaction is labeled as "Local" and is plotted as a solid line on the right-hand panels of Fig. 11.3 for that reaction. The other reactions are plotted as a dashed line for comparison. From the 36 model combinations, the KD-OMP had a lower χ^2 compared to its JMP-OMP counterpart. From the 18 combinations that used the KD-OMP, model 4-3 was found to have the smallest χ^2 across all three reactions. The two numbers correspond to the NLD-γSF used. This model combination is labeled as "Global", and is shown as a solid red line in all three plots.

The microscopic and phenomenological models discussed in this section were also compared to the experimental partial cross sections (capture to the ground state and meta-stable state) for ^{108}Cd and ^{110}Cd, which is shown in Fig. 11.5. The models are in good agreement with the measurements within the uncertainties.

11.5   Photodisintegration reaction rates

Calculation of the photodisintegration decay rates requires integration of the cross section folded over the photon number density with respect to the incident γ-ray energy:

$$\lambda_{(\gamma,\beta)}(T) = \frac{1}{\pi^2 c^2 \hbar^3} \int_0^\infty \frac{E_\gamma^2}{e^{E_\gamma/kT} - 1} \, \sigma_{(\gamma,\beta)}(E_\gamma) \, dE_\gamma, \tag{11.3}$$

where E_γ is the energy of the incident γ ray and $\sigma_{(\gamma,\beta)}$ is the cross section for the photodisintegration reaction to exit channel β. However, in stellar interiors, nuclei exist not only in their ground states but also in excited states in thermal equilibrium. Therefore, a calculation of the stellar photodisintegration decay rate, which accounts for thermally accessible excited states, is needed. The stellar photodisintegration rate is given by:

$$\lambda^*_{(\gamma,\beta)}(T) = \frac{\sum_\mu \lambda^\mu_{(\gamma,\beta)}(T) e^{-E^\mu_x/kT}}{\sum_\mu (2J^\mu + 1) e^{-E^\mu_x/kT}} \tag{11.4}$$

where $\lambda^\mu_{(\gamma,\beta)}$ is the photodisintegration rate of a nuclei in state μ with excitation energy E^μ_x and spin J.

Using TALYS 1.9 the stellar (γ, p) and (γ, n) decay rates for the inverse reactions measured in this work were calculated for temperatures between 0.001 - 10 GK. The rates are calculated based off the MCMC-fitted model, where each calculation was done using parameters sampled from the posterior distribution. Stellar decay rates below 1 GK in general were below TALYS' precision, and therefore have been omitted from the table. The ^{111}In stellar photodissociation decay rates based off the MCMC fitted model, along with the global and local ^{110}Cd microscopic model are plotted in Fig. 11.4. These rates are in good agreement, within uncertainties, with the predictions from the REACLIB tsh8-v6.

Despite two different approaches used to constrain the Hauser-Feshbach theory, the stellar (γ, p) rates are in good agreement with one another. There is however, some slight variation between model predictions of the stellar (γ, n) rates. This is to be expected, since the reactions were constrained based off (γ, p) cross-section measurements. Furthermore, the MCMC-fitted approach alters the level density of the neutron exit channel.

In the bottom panel of Fig. 11.4, the ratios of the stellar (γ, p) to (γ, n) decay rates are shown. The ratio of rates from the REACLIB ths8-v6 has an uncertainty estimated at about a factor of three, which is shown as a gray band. Within this uncertainty band, the MCMC-fitted

KU-γSF, GC-NLD model constrains the branch-point temperature to 2.71 ± 0.05 GK. While the line thickness of the microscopic-model rate ratios are aesthetic for easier distinguishing, the band of the MCMC-fitted model represents a 68% percentile of the posterior distribution. The ^{110}Cd Micro model is in good agreement while the Global model predicts the branch-point temperature at around 2.6 GK. This discrepancy is somewhat expected as in general the Global model will be less accurate, but serve as a better estimation for other reaction rates in the $A = 100 - 110$ mass region.

Based on our results, the branch-point temperature is indeed within the γ-process temperature window, and the abundance ratio of ^{108}Cd to ^{110}Cd will be temperature sensitive. In addition, it can be seen that the global-microscopic model gives similar predictions to the MCMC-fitted model, helping to validate it as a model useful in investigating other reaction rates in the same mass region.

11.6 Conclusion

In an effort to better model the γ-process, and potentially mitigate discrepancies of the predicted p-nuclei abundances, the ^{111}In$(\gamma, p)^{110}$Cd and ^{111}In$(\gamma, n)^{110}$In reaction rates were constrained, constraining the temperature of the ^{111}In$(\gamma, p),(\gamma, n)$ branching point. This was achieved by measuring the cross sections for ^{102}Pd$(p, \gamma)^{103}$Ag, ^{108}Cd$(p, \gamma)^{109}$In, and ^{110}Cd$(p, \gamma)^{111}$In, and then using the measurements to constrain γSF and NLD models used in Hauser-Feshbach theory within TALYS 1.9. In constraining these models we have adopted two different approaches: in one approach parameters within phenomenological models such as the KU-γSF and GC-NLD were constrained through a MCMC sampling algorithm; another approach investigated various combinations of microscopic γSF and NLD, identifying the combination which best describes the experimental measurements. We recommend using the global-microscopic combination for estimating cross sections/reaction rates for proton

and neutron reactions in the $A = 100-110$ mass region where there are no experimental measurements. Both methods give similar predictions for the $^{111}\mathrm{In}(\gamma,p)^{110}\mathrm{Cd}$ and $^{111}\mathrm{In}(\gamma,n)^{110}\mathrm{In}$ reaction rates.

In conclusion, with a few stable-target experiments, the $^{111}\mathrm{In}(\gamma,p)/(\gamma,n)$ branch-point temperature, for which previously only the lower limit of 2.3 GK was established, has been constrained to 2.71 ± 0.05 GK; this is a reduction of over a factor of 30. However, the uncertainties presented are only systematic, as there may be additional uncertainties inherit to the TALYS code which are difficult to quantify. Based on our results, above the branching-point temperature $^{108}\mathrm{Cd}$ will be fed through $^{109}\mathrm{In}$, while below $^{110}\mathrm{Cd}$ will be fed through $^{111}\mathrm{In}$. This may have an impact on the predicted abundances of these isotopes, as well on the lighter p-nuclei, warranting further investigation. Furthermore, future cross-section measurements to constrain other model-dependant γ-process branching points are desirable, as constraining the nuclear input will likely continue to provide further insight and constraints into the astrophysical conditions necessary to produce the p-nuclei.
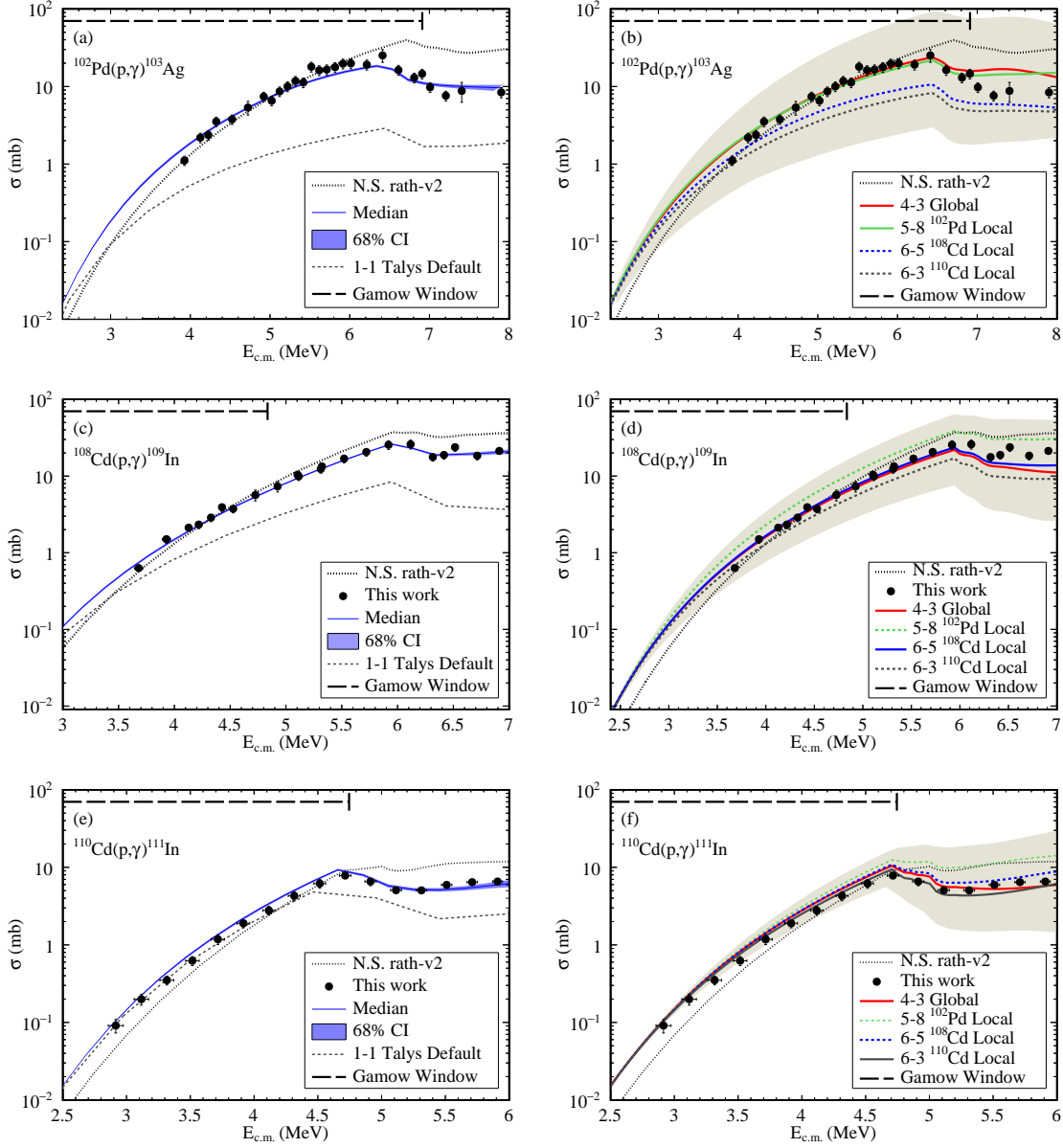
Figure 11.3: (Taken from [212].) Constraining of Hauser-Feshbach statistical parameters used to predict cross sections. The left panels show the MCMC-fitted result based off constrained parameters within the KU-γSF and GC-NLD model. The solid blue line is the median prediction while the band represents a 68% confidence interval. For the panels on the right hand side, predictions based off different combinations of microscopic NLD and γSF are shown. The shaded band represents the total range of predictions from all microscopic model combinations available in TALYS 1.9. The combination that best fits all three reactions from this work is labeled "Global" while the combination that best fits a single reaction is labeled as "Local". The number notation represents NLD and γSF model number consistent with the notation used in the TALYS 1.9 manual [174].
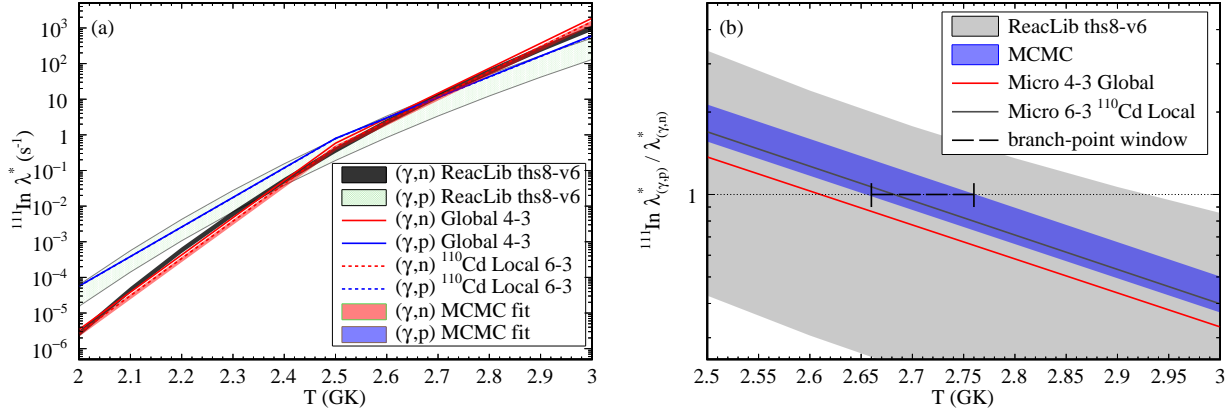
Figure 11.4: (Taken from [212].) Figure (a) shows predicted stellar photodissociation decay rates for ^{111}In based off MCMC fitted and microscopic γSF and NLD models. The previous rates based off of ReacLib-V6 is plotted for comparison. Figure (b) plots the ratio of the $(\gamma, p)/(\gamma, n)$ stellar decay rates. Band thickness of the MCMC fitted (KU-γSF and GC-NLD) reflects a 68% confidence interval band.
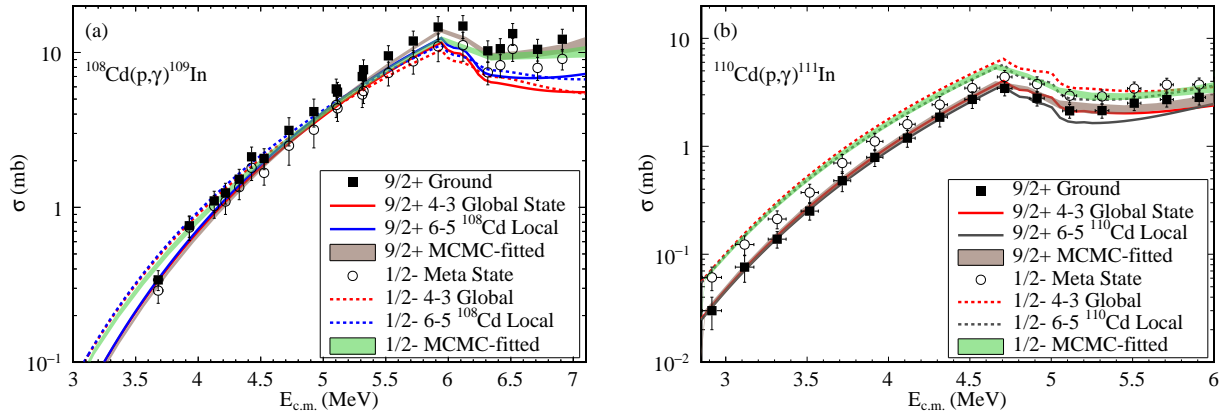

Figure 11.5: (Taken from [212].) Comparison of the MCMC-fitted GC-NLD and KU-γSF model, and microscopic models to the experimentally measured partial cross sections of ^{108}Cd (a) and ^{110}Cd (b).

Part III

BETA-DELAYED NEUTRON

EMISSION

Chapter 12

Introduction

Parts of the discussion in this chapter have already been published in a conference proceeding [117] which I authored for the 15th International Conference on Nuclear Data for Science and Technology (ND2022).

In this chapter I will review the dissertation proposal, laying out the main problem I am addressing in this final part of the dissertation.

Reaction measurements on fission products are being planned at both Argonne National Lab and at the Facility for Rare Isotope Beams. These indirect experiments produce specific short-lived nuclei via beta decay, and the subsequent neutron and gamma emission are studied. Some initial experiments found a surprising overabundance of gamma emission, which theory has yet to explain [274, 286]. To remedy this, we are developing an integrated nuclear data workflow that connects advanced nuclear shell model codes for describing the beta decay with a contemporary nuclear reaction model code.

Beta decay is the mechanism for element transmutation towards stability, and plays an important role in competition with neutron-capture in the formation of heavy elements:

Understanding this is one of the central tasks of the nuclear theory community and the new Facility for Rare Isotope Beams (FRIB) [13, 252]. A less common, yet important [207] process is the emission of one or more neutrons immediately following beta decay in a process called beta-delayed neutron emission (BDNE), depicted in Figure 12.1.

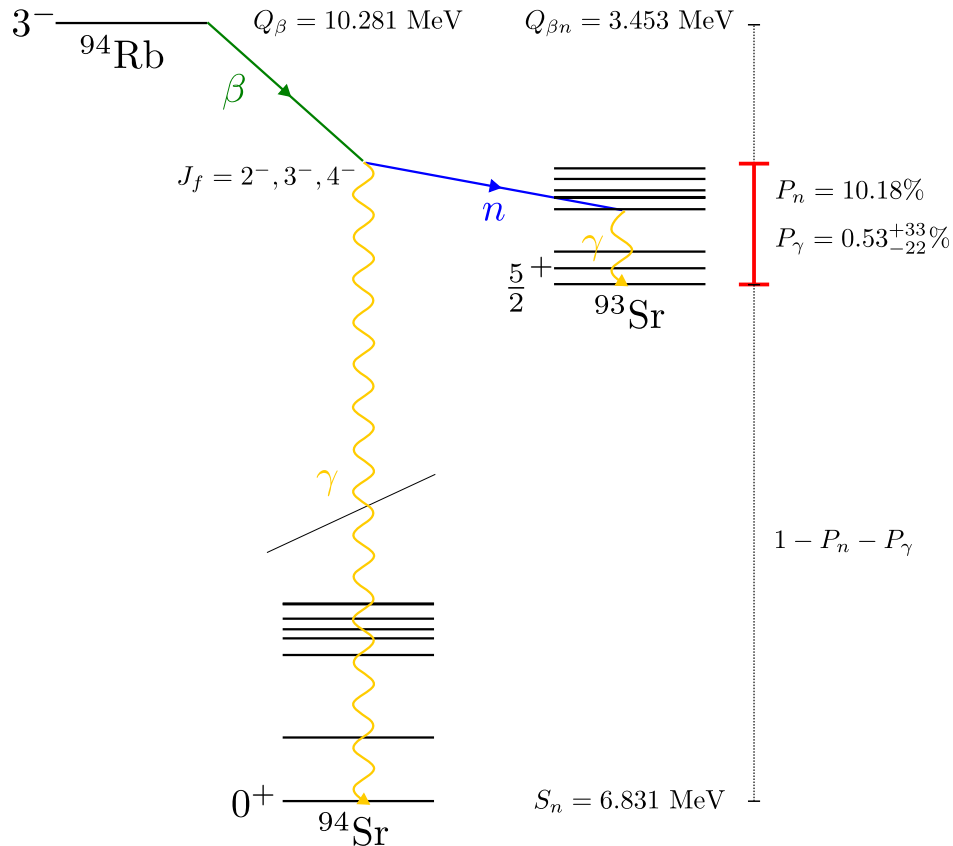Figure 12.1: Schematic depiction of beta-delayed neutron emission for the case of ^{94}Rb. The distribution of states populated by beta decay can be predicted with a microscopic structure model like quasiparticle random-phase approximation or shell model. The decay of the neutron and gamma emitting nucleus (^{94}Sr) is historically described by a statistical model, assuming compound nuclear decay.

12.1 The discrepancy: the statistical model versus the measurement

Theoretical description of BDNE has been an ongoing challenge since the late 1970's [96, 231, 142]. The idea of *selectivity* [96] of states populated by beta decay, leading to non-statistical neutron emission, was proposed to explain peak-features seen in delayed neutron spectra. These effects were almost explained away by the *Pandemonium effect* [126], which indicated that such peaks were artifacts due to detector limitations. Others showed that in some cases, (a) statistical models of BDNE could reproduce the peaks if excited states in the residual nucleus were included [231], and (b) that states populated in beta decay could be strongly connected to excited states in the final nucleus [264], supporting selectivity. At the close of the decade, the nuances were better understood, including the importance beta-decay strength function shape and nuclear level densities [142, 234].

With the development of total absorption gamma-ray spectroscopy (TAGS) [4, 152] and its application to the study of BDNE [274, 286, 121], the Pandemonium effect can be avoided. Even so, the statistical description in some cases significantly under-predicts the intensity of emitted photons from TAGS experiments, e.g. in [286]. Thus, BDNE remains an important and unresolved modeling challenge. There are three hypotheses which may explain this.

12.2 The three hypotheses

I propose three hypotheses which may explain the discrepancy between the statistical reaction model and the observed emission of beta-delayed gammas and neutrons. These will be reffered back to throughout the rest of the dissertation.

Hyp. 1: Gamma-ray strength function is stronger than assumed. This is the simplest ex-

planation: if the photon-strength function is enhanced, the nucleus formed by beta decay will de-excite below the neutron separation energy before delayed neutrons are emitted. If this is the explanation, then many neutron capture rates will also have to be re-evaluated, especially for astrophysical interests.

Hyp. 2: Forbidden beta decay is stronger than assumed, blocking high-l neutron emission. If forbidden transitions play a significant role in these neutron-rich cases, then higher angular momentum states populated by beta decay would block this emission of neutrons to available states in the neighboring nucleus.

Hyp. 3: Beta decay does not lead to a compound nucleus. Essentially, selectivity. This explanation requires the greatest change in our description of beta-delayed neutron emission. It would also have significant implications for the use of beta-decay as a means of indirect cross section measurements such as the beta-Oslo method [269].

In the following chapters, I will address each of these.

12.3   Shell model approach

Some BDNE studies have made progress combining quasiparticle random-phase approximation (QRPA)-type descriptions of beta decay with HF calculations to reasonable effect [167, 124]. We are also aware of recent efforts with the shell model [120]. We want to continue along these lines to incorporate modern shell model methods into HF codes in a self-consistent way, including level densities and gamma-ray strength functions derived from the shell model.

Shell model calculations, treating nuclei at the nucleon-degree-of-freedom, offer the largest model spaces to capture the physics of complex nuclei. Energy levels, binding energies,

nuclear level densities, gamma-ray strength functions, and beta-decay strength functions can all be computed from the same wave functions generated from phenomenological interactions. Even after restricting configurations to a finite valence space, nuclei of interest to BDNE generate basis dimensions several orders of magnitude larger than current computational limits, $O(10^{10})$.

To make these models tractable without discarding important orbitals, we apply an importance truncation in the many-body configuration space. We assign configuration importance, in explicit proton-neutron formalism based, based on the eigenvalues of the "separable" proton and neutron parts of the Hamiltonian. This approach is motivated by the empirical fact that eigenstates of the nuclear Hamiltonian $\hat{H} = \hat{H}^{(p)} + \hat{H}^{(n)} + \hat{H}^{(pn)}$ are well approximated by simple products of eigenstates of the proton-only and neutron-only interactions, $\hat{H}^{(p)}$ and $\hat{H}^{(n)}$ [217, 219], with fidelity increasing exponentially with the number of extremal states taken in combination.

Our code, PANASh (proton and neutron approximate shell-model, unpublished), implements this importance truncation scheme (see Chapter 4). Basis states are constructed by coupling together eigenstates of $\hat{H}^{(p)}$ and $\hat{H}^{(n)}$, up to fixed total angular momentum and parity. The basis is then truncated by using only some fraction of all states, taking the lowest excitations from each subspace. PANASh has been designed and simplified for our purpose, and is ready for extensive application.

Chapter 13

Theory of Beta Decay

This chapter covers the theory necessary for calculating shell model inputs for modeling the of beta-delayed neutron emission. Nuclear level densities, gamma-ray strength functions, and leading order beta decay strength functions are all discussed in previous chapters. What remains is the calculation of beta-decay transitions. A good introductory text is chapter 7 of Suhonen [272]. A complete treatment of the subject, however, is beyond the scope of most textbooks. This is especially true for higher-order beta decay transitions and proper treatment of the interaction of the electron and nuclear wave functions. For the complete treatment, Behrens and Buhring [24] is the definitive reference.

13.1 Beta decay transition probabilities

Beta decay is a weak-nuclear process wherein a neutron decays into a proton (β^- decay), which for a nucleus with Z protons and N neutrons is:

$$(Z, N) \xrightarrow{\beta^-} (Z + 1, N - 1) + e^- + \bar{\nu}_e. \tag{13.1}$$

Alternatively, a proton may decay into a neutron (β^+ decay),

$$(Z, N) \xrightarrow{\beta^+} (Z - 1, N + 1) + e^+ + \nu_e \tag{13.2}$$

(There is also electron capture (EC).)

Beta decay transitions emitting leptons with a total $L = 0$ are called *allowed transitions*, otherwise they are called *forbidden*. Allowed transitions are further categorized into:

- *Fermi* (F) transitions if the emitted electron (positron) and anti-neutrino (neutrino) couple to total spin $S = 0$ (thus the nucleus changes total angular momentum $\Delta J = 0$), and

- *Gamow-Teller* (GT) if the emitted particles couple to $S = 1$ (thus the nucleus changes $\Delta J = 0, 1$).

To do beta decay calculations as part of nuclear reaction theory, the quantity we need is the transition rate, or half-life, of nuclear states. In the usual way:

$$t_{1/2} = \frac{\ln 2}{T_{fi}}, \tag{13.3}$$

where T is the transition probability. For reporting beta decay rates in literature, the $\log ft$ values are typically presented:

$$f_0 t_{1/2} = \frac{\kappa}{B_F + B_{GT}}, \tag{13.4}$$

where f_0 is the energy-independent phase-space integral and B_F and B_{GT} are the reduced transition probabilities:

$$B_F = \frac{g_v^2}{2J_i + 1} |M_F|^2, \tag{13.5}$$

$$B_{GT} = \frac{g_A^2}{2J_i + 1} |M_{GT}|^2. \tag{13.6}$$

κ is a collection of constants:

$$\kappa = \frac{2\pi^3 \hbar^7 \ln(2)}{m_e^5 c^4 G_F^2} \approx 6289 \text{ s}. \tag{13.7}$$

From [272], here is the Fermi beta decay matrix element:

$$M_F = \delta_{J_f J_i} \sum_{ab} M_F(ab) \langle \Psi^f | | [\pi_a^\dagger \tilde{\nu}_b]_{\Delta J = 0} | | \Psi^i \rangle, \tag{13.8}$$

with

$$M_F(ab) = \langle a | | \mathbf{1} \boldsymbol{\tau}^\pm | | b \rangle = \delta_{ab} \hat{j}_a. \tag{13.9}$$

The indices a and b label the single-particle orbitals from which the many-body states $|\Psi\rangle$ are constructed. $\pi_a^\dagger$ is a proton single-particle state creation operator. $\tilde{\nu}_b$ is the time-reversed destruction operator for neutron single-particle states. Recall that:

$$\tilde{c}_{j,-m} = (-1)^{j-m} c_{j,m}. \tag{13.10}$$

The Fermi operator changes only the isospin of the wave function - all other quantum numbers are unchanged; the delta function δ_{ab} enforces this sending a neutron in orbit b to the same proton orbit $a = b$.

The Gamow-Teller (GT) (allowed) beta decay matrix element is:

$$M_{GT} = \langle \Psi^f | | \boldsymbol{\sigma} \boldsymbol{\tau}^\pm | | \Psi^i \rangle = \sum_{ab} M_{GT}(ab) \langle \Psi^f | | [\pi_a^\dagger \tilde{\nu}_b]_{\Delta J = 1} | | \Psi^i \rangle, \tag{13.11}$$

where in the second equality the $\boldsymbol{\tau}^-$ operator is selected for β^- transitions. Here,

$$M_{GT}(ab) = \frac{1}{\sqrt{3}} \langle a| |\boldsymbol{\sigma\tau}^-| |b\rangle = \sqrt{2}\delta_{n_a,n_b}\delta_{l_a,l_b}\hat{j}_a\hat{j}_b(-1)^{l_a+j_a+\frac{3}{2}} \begin{Bmatrix} \frac{1}{2} & \frac{1}{2} & 1 \\ j_a & j_a & l_a \end{Bmatrix}. \tag{13.12}$$

The Gamow-Teller operator acts on the isospin and the intrinsic spin of the nucleons, while the principle quantum number n and orbital angular momentum l remain unchanged.

13.2   Beta decay matrix elements with PANASh

Next we need expressions for the beta decay B-values using PANASh. To compute equations the transition matrix elements for Fermi and Gamow-Teller transitions (13.8) and (13.11) (and all other types of transitions), PANASh will need to supply one-body charge-changing transition matrix elements. These are a simple generalization of one-body transition matrix elements and were defined in section 4.7.2 for the PANASh basis:

$$\langle\Psi^f||[\hat{\pi}_a^\dagger \otimes \tilde{\nu}_b]_K||\Psi^i\rangle = (-1)^{j_{n_f}-j_b-j_{n_i}}[J_f][K][J_i] \sum_{p_f n_f p_i n_i} \psi_{p_f n_f}^f \psi_{p_i n_i}^i$$
$$\times[j_{p_f}][j_{n_i}] \begin{Bmatrix} j_{p_f} & j_{p_i} & j_a \\ j_{n_f} & j_{n_i} & j_b \\ J_f & J_i & K \end{Bmatrix} S_{p_f n_i;a}S_{n_i n_f;b}, \tag{13.13}$$

where $\psi_{p_i n_i}^i$ are the wave function coefficients in the PANASh basis, and $S_{p_f n_i;a}$, $S_{n_i n_f;b}$ are the proton, neutron spectroscopic amplitudes of the PANASh basis factors. The program RHODIUM, a companion code to BIGSTICK takes as input the proton and neutron basis factors used to construct the PANASh basis to compute these spectroscopic amplitudes.

There is a somewhat complicated pipeline connecting these three codes, BIGSTICK, RHODIUM, and PANASh. In summary (See Figure 13.1):

1. **BIGSTICK** computes the proton and neutron wave functions which become the PANASh basis factors

2. **RHODIUM** computes the proton spectroscopic amplitudes and the neutron spectroscopic amplitudes

3. PANASh computes the nuclear wave functions using the proton and neutron wave functions from **BIGSTICK** (actually, it just needs the one-body transition matrix elements)

4. PANASh computes the beta decay matrix elements using its nuclear wave functions and the spectroscopic amplitudes from **RHODIUM**
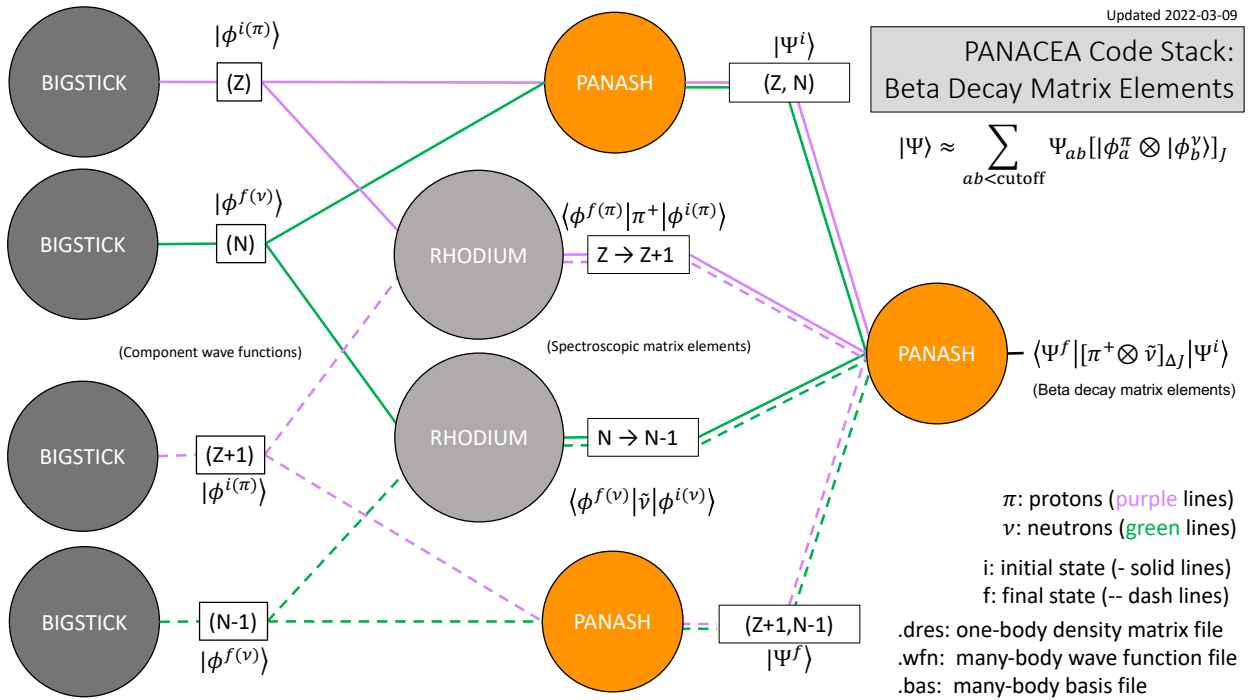
Figure 13.1: Interplay between **BIGSTICK**, **RHODIUM** and PANASh codes. Many-proton and many-neutron wave functions generated with the full configuration interaction (FCI) code, **BIGSTICK**. These proton and neutron factors are used to construct the many-nucleon, truncated basis used by PANASh. The beta decay matrix elements are computed with PANASh using its own approximate wave functions and spectroscopic amplitudes (generalized one-body density matrices) from the utility code **RHODIUM**.

13.3   The electron and the neutrino

So far we have described how to calculate the $\log f_0 t$ value for beta decays by rearranging the relation:

$$t_{1/2} = \frac{\kappa}{f(Q)} = \frac{\kappa}{f_0(B_F + B_{GT})} = \frac{\ln(2)}{T_{fi}}, \tag{13.14}$$

where $f(Q)$ is the phase-space factor which depends on the energy of the transition Q. This is done to avoid treatment of the phase-space factor. But our principle quantity of interest is this total transition probability:

$$T_{fi} = \frac{\ln(2)}{\kappa} f, \tag{13.15}$$

so we must calculate the phase space factor. In general, the phase space factor depends not only on the nuclear structure of the decaying nucleus and its products, but also on the interaction between the emitted electron and the residual nucleus. In this section, I will discuss the details required for us to calculate the beta decay transition probability by taking into account the physics of the emitted electron and antineutrino.

We will assume that the initial and final nuclear states are very heavy compared to the Q-value of the beta decay, so that the three body decay $(Z, N) \to (Z+1, A) + e^- + \bar{\nu}_e$ can be treated mostly non-relativistically. In particular, we assume we can work in the brick-wall frame of reference, where the nuclear mass is infinite and drops out of the kinematics. In terms of the electron energy (in units of $m_e c^2$), the phase space factor is an integral:

$$f(W_0) = \int_1^{W_0} C(W)(W^2 - 1)^{1/2} W (W_0 - W)^2 F_0(Z, W) dW. \tag{13.16}$$

The integrand is proportional to the differential electron energy distribution:

$$P(W)dW = \frac{G_F^2}{(\hbar c)^6}\frac{1}{2\pi^3\hbar}C(W)p_e cW(W_0 - W)^2 F_0(Z,W)dW, \tag{13.17}$$

- $C(W)$ is a shape factor which contains the nuclear structure content

- p_e is the momentum of the out-going electron

- $W = (p_e^2 + 1)^{1/2}$ is the outgoing electron energy in units of $m_e c^2$ ($W = E_e/(m_e c^2)$)

- $W_0 \approx M_i - M_f$ is the maximum electron energy

- $F_0(Z,W)$ is the Fermi function; the effect of the Coulomb interaction between the electron and nucleus

In this way we can see that the partial half-life is just:

$$t_{1/2} = \ln(2)\left(\int P(W)dW\right)^{-1}. \tag{13.18}$$

More usefully, the transition probability from a state i in the precursor nucleus to a state f in the residual nucleus is

$$T_{fi} = \frac{G_F^2}{(\hbar c)^6}\frac{1}{2\pi^3\hbar}\int_1^{W_0} C(W)p_e cW(W_0 - W)^2 F_0(Z,W)dW. \tag{13.19}$$

When the nuclear shape factor $C(W)$ is energy-independent, it is common to denote the phase-space factor as the statistical phase-space factor:

$$f_0(W_0) = \int_1^{W_0} (W^2 - 1)^{1/2}W(W_0 - W)^2 F_0(Z,W)dW, \tag{13.20}$$

since it depends only on the kinematics of the outgoing leptons. The energy-independent

form factor C is nothing but the B-values of the transition. In the case of allowed decay,

$$T_{fi} = \frac{G_F^2}{(\hbar c)^6} \frac{1}{2\pi^3 \hbar} \delta(W_0 - (E_i - E_f)/m_e c^2) f_0(W_0)(B_F(i \to f) + B_{GT}(i \to f)). \quad (13.21)$$

The delta function is included to point out the relation between the maximum electron energy and the energy of the nuclear transition. In the following subsections I will explain each term.

13.3.1 Energy and momentum relations

The kinematic quantities of interest are the energies and momenta of the nucleus, electron, and neutrino before and after the beta decay. The momentum transfer of the processes is

$$\vec{q} = \vec{p}_f - \vec{p}_i = -(\vec{p}_e + \vec{p}_\nu). \quad (13.22)$$

The initial nucleus is usually at rest, so that $\vec{q} = \vec{p}_f$, and $q^2 = p_f^2 = 2 M_f E_R$, where E_R is the kinetic energy of the recoiled nucleus. The limits on the three and four momentum transfer are:

$$0 \leq \boldsymbol{q}^2 \leq \Delta^2 - m_e^2 \quad (13.23)$$

$$-\Delta^2 \leq q^2 \leq -m_e^2, \quad (13.24)$$

where $\Delta = -(M_f - M_i)$ is the mass defect. The maximal energy W_0 of the beta particles is

$$W_0 = -(W_f - M_i) = \Delta - |E_R|_{W_\nu=0} = \Delta \left(1 - \frac{\Delta^2 - m_e^2}{2 M_f \Delta} \right). \quad (13.25)$$

Since the second term (nuclear recoil energy) is of the order $0.01/A$,

$$W_0 \simeq \Delta. \tag{13.26}$$

Note that we are working in units of $m_e c^2$ with $c = 1$.

The rest masses here naturally include the binding energy, not just the bare nucleon masses. Since the particle numbers in the nucleus doesn't change, the Q value here is just the difference in the energies of the nuclear states minus the rest energy of the leptons (we will ignore the neutrino). Assuming we are always decaying from the ground state of the initial nucleus,

$$Q = BE(\Psi_i) - (BE(\Psi_f) + E_{Ex}(\Psi_f)) - m_e c^2, \tag{13.27}$$

where BE are the ground-state binding energies of the initial and final nuclei, and E_f is the excitation energy of the final state. We can write this as $Q = E_i - E_f - m_e c^2$, where $E = BE_{gs} + E_{Ex}$. If E_i and E_f of the nuclear states are in MeV, then,

$$W_0 = M_i - M_f = \frac{E_i}{m_e c^2} - \frac{E_f}{m_e c^2} = \frac{Q}{m_e c^2} + 1. \tag{13.28}$$

This hopefully makes the limits of the phase space integral $(1, W_0)$ clearer; we can think of this as an integral from zero Q-value to the maximum Q value when E_f is the ground state of the residual nucleus.

13.3.2 Phase space factor

How does this phase space factor arise? The staring point is the basic relation between the total decay probability for a state $i \to f$ in terms of an S-matix:

$$P_{fi} = S_{if}^\dagger S_{fi}, \tag{13.29}$$

where

$$S_{fi} = \delta_{fi} + i(2\pi)^4 \delta^4(p_f - p_i) N T_{fi}, \tag{13.30}$$

for a T-matrix T_{fi} and normalization N, depending on the plane wave initial and final states. Taking into account the various conservations of energy and momentum, and in the rest-frame of the initial nucleus ($\vec{p}_i = 0$), the decay probability per unit time can be written,

$$\frac{dW}{dt} = \frac{1}{(2\pi)^5} \sum_{fs} \int T_{if}^\dagger T_{fi} \delta^3(\vec{p}_f + \vec{p}_e + \vec{p}_\nu) \delta(W_f + W + W_\nu - M_i) d^3 p_f d^3 p_e d^3 p_\nu. \tag{13.31}$$

The sum is over all final states f and spins s. We chose the rest frame of the initial nucleus because by also assuming the initial nucleus is infinitely massive compared to the others, we can omit its energy contribution. The T-matrix is connected to the beta decay Hamiltonian through first-order perturbation theory:

$$T_{fi} = -\frac{1}{(2\pi)^4 \delta^4(p_f - p_i)} \langle f | \int H_\beta(x) d^4 x | i \rangle. \tag{13.32}$$

It's useful to look at the case where the T-matrix is energy-independent (constant). This is the case for allowed transitions, for example. In such cases, the transition probability is

dictated by the number of available states. The transition probability density becomes

$$\frac{dW}{dt} \propto \frac{1}{(2\pi)^5} \int \delta^3(\vec{p}_f + \vec{p}_e + \vec{p}_\nu)\delta(W_f + W + W_\nu - M_i)d^3p_f d^3p_e d^3p_\nu = \frac{R}{(2\pi)^5}. \quad (13.33)$$

R is the phase space integral due to the kinematic effects only, and not the dynamics of the decay process. R can be simplified by integrating out the neutrino momentum $\vec{p}_\nu$, and, after a change to spherical variables, also integrating over $d\phi_e$, $d\Omega_f$, and $d(cos\Theta_{fe})$:

$$\begin{aligned} dR &= 8\pi^2 \int (W_f + W - M_i)p_f dp_f W dW \\ &= 16\pi^2 p_e W (W_0 - W)^2 dW \end{aligned} \quad (13.34)$$

with $W_0 = M_i - M_f$. For details on the other physically-motivated substitutions and limits of integration used, see the full discussion in chapter 5 of Behrens and Buhring [24] . This is the probability, under the constant-T-matrix assumption, that the electron is emitted with energy between W and $W + dW$.

The statistical shape factor,

$$P_0(W) = p_e W (W_0 - W)^2 \quad (13.35)$$

is shown in Figure 13.2. Restoring the possible energy dependence of the T-matrix, we obtain:

$$P(W)dW = \frac{1}{2\pi^3} \sum_{fs} |T|^2 p_e W (W_0 - W)^2 dW. \quad (13.36)$$

All that's missing from this expression now is the Coulomb correction $f(Z, W)$ scaling factor.
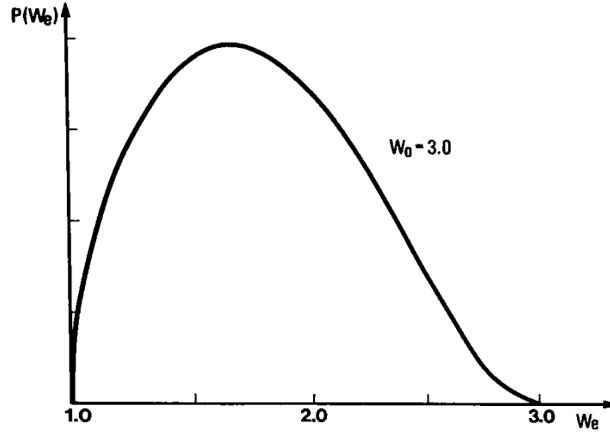
Figure 13.2: The statistical shape factor $P(W) = p_e W(W_0 - W)^2 dW$ for beta decay. Taken from Behrens and Buhring [24] chapter 5.3.

13.3.3 Statistical phase factor with no Fermi factor

If we assume an energy-independent nuclear form factor so that only the statistical phase space factor is considered, and the integral can be carried out *a priori*. Assuming a statistical shape (13.34) and a negligible Coulomb correction, one can obtain [24]:

$$
\begin{aligned}
f_{00}(W_0) &= \int_1^{W_0} (W^2 - 1)^{1/2} W (W_0 - W)^2 dW \\
&= \frac{1}{60}[(2W_0^4 - 9W_0^2 - 8)\sqrt{W_0^2 - m_e^2} + 15W_0 \ln\left(W_0 + \sqrt{W_0^2 - m_e^2}\right)].
\end{aligned}
\tag{13.37}
$$

Recall that the maximum electron energy is $W_0 = (E_i - E_f)/(m_e c^2)$. At the lower limit, $f(1) = 0$, and for large W_0, goes like W_0^5. On a plot the function resembles an exponential function (although it is much slower). This means that the phase space factor suppresses low-energy transitions and greatly enhances higher energy transitions.

13.3.4 Fermi factor (static Coulomb correction)

In addition to the weak interaction leading to the beta decay, there is also the electrostatic interaction between the outgoing electron and the nuclear charge. This distorts the outgoing

electron wave function in a complicated way and is the subject of the first half of the Behrens and Buhring [24] text. We can also see that that will effect the electron energy spectrum. For β^- decay, the outgoing electron will feel an attractive potential from the nucleus. In some approximation, this effect can be factored into the so-called Fermi function $F_0(Z, W)$. The differential electron spectrum is then:

$$P(W)dW = \frac{G_F^2}{(\hbar c)^6}\frac{1}{2\pi^3\hbar}C(W)p_e cW(W_0 - W)^2 F_0(Z, W)dW. \tag{13.38}$$

$F_0(Z, W)$ comes from a ratio of distorted and free electron radial wave functions [272]. (See [24], p 105.) The standard definition of the Fermi factor is:

$$F_0(W, Z) = 4(2p_e R/\hbar)^{2(\gamma-1)}e^{\pi y}\left(\frac{|\Gamma(\gamma + iy)|}{\Gamma(1 + 2\gamma)}\right)^2, \tag{13.39}$$

where the $\gamma = \gamma_1$ function is $\gamma = \sqrt{1 - (\alpha Z)^2}$ (≈ 1 for small Z). The argument $y(W) = (\alpha ZW)/(p_e c)$. The radius R is [256] $R \approx 1.2A^{1/3}$fm. The Fermi function is order unity, and has been tabulated approximately in [119] and less approximately in [256].

Since numerical evaluation of the Fermi function has historically been tedious, there have been several attempts at approximations, e.g. [288]. As a historical note, Suhonen's text [272] attributes the following non-relativistic approximation:

$$F_0(W, Z) \approx \frac{W}{p_e}\frac{2\pi\alpha Z}{1 - e^{-2\pi\alpha Z}}, \tag{13.40}$$

to Primakoff and Rosen [228]; the "Primakoff-Rosen approximation". However, that paper on double beta decay specifically attributes the same expression as a "very approximate" form from Blatt and Weisskopf [31]. An even more true attribution, following [288], would be from Mott and Massey 1933 [206]. In any case, Venkataramaiah [288] points out that for

small Z this has the form

$$F_0(W, Z) \approx 1 + \pi \alpha Z W / p_e. \tag{13.41}$$

The nonrelativistic equation (13.40) can be improved to within one-percent error for large-Z up to Z=84 by multiplying by the factor [288]:

$$[W^2(1 + 4(\alpha Z)^2) - 1]^{\sqrt{1-(\alpha Z)^2}-1}. \tag{13.42}$$

In this work we will use the relativistic formula (13.39).

13.3.5 Finite neutrino mass

As we now know, neutrinos have a nonzero rest mass. This has an effect on the spectrum. I will now revisit the kinematics integral in more detail to show its effect. I follow the development in DeBenedetti [64].

The most general statistical factor for the number of final (momentum) states of a reaction is the product of the differential momentums of each particle:

$$\rho_f = \frac{1}{dW_0} \prod_{i=1}^{N-1} \frac{d^3 p_i}{(2\pi\hbar)^3}, \tag{13.43}$$

where the energy and momentum satisfy:

$$E_0 = \sum_{i=1}^{N} E_i, \text{ and } 0 = \sum_{\alpha=1}^{N} p_\alpha. \tag{13.44}$$

We are dealing with a particle decay rection where the initial nuclear is many orders of magnitude more massive than the emitted electron and neutrino. Working in the rest frame

of the initial particle then,

$$dE_0 = \sum_{\alpha=1}^{N-1} dE_\alpha. \tag{13.45}$$

To obtain the differential momentum distribution of the electron (which is historically what is observed rather than the elusive neutrino), we integrate over all other degrees of freedom. In general, for particle '1' this takes the form:

$$\rho_f(p_1)dp_1 = \frac{d^3p_1}{(2\pi\hbar)^3} \frac{d}{dE_0} \prod_{\alpha=2}^{N-1} \int_0^{E_\alpha/c} \frac{d^3p_\alpha}{(2\pi\hbar)^3}. \tag{13.46}$$

In this case, there is only the neutrino to integrate over. The energy available to the neutrino is the energy available for the reaction (E_0) minus the electron energy:

$$E_\nu^2 = (E_0 - E_e)^2 - m_\nu^2 c^4. \tag{13.47}$$

Substituting spherical coordinates ($d^3p = p^2 dp d\Omega$) with rotational symmetry,

$$\rho_f(p_e)dp_e = \frac{4\pi p_e^2 dp_e}{(2\pi\hbar)^6} \frac{d}{dE_0} \int_0^{[(E_0-E_e)^2 - m_\nu^2 c^4]^{1/2}/c} 4\pi p_\nu^2 dp_\nu \tag{13.48}$$

$$= \frac{16\pi^2 p_e^2 dp_e}{(2\pi\hbar)^6} \frac{1}{3c^3} \frac{1}{dE_0}[(E_0 - E_e)^2 - m_\nu^2 c^4]^{3/2} \tag{13.49}$$

$$= \frac{16\pi^2}{(2\pi\hbar)^6 c^3} p_e^2 [(E_0 - E_e)^2 - m_\nu^2 c^4]^{1/2} dp_e. \tag{13.50}$$

Recent measurements put the neutrino mass < 0.8 ev/c^2 from beta decay measurements [3] or $< 0.2 - 0.4$ ev/c^2 from astronomical measurements [107]. This is at least three orders of magnitude smaller than the first term. We ignore its effects in this work.

13.3.6 Numerical phase space factor

Today it is a trivial task to integrate the phase space integral without any approximation to the Fermi factor (13.39). I have implemented such a routine and plotted a comparison in the following figures. Note that these calculations assume an energy-independent nuclear shape factor $C(W)$, which is the case for Fermi and Gamow-Teller allowed transitions.
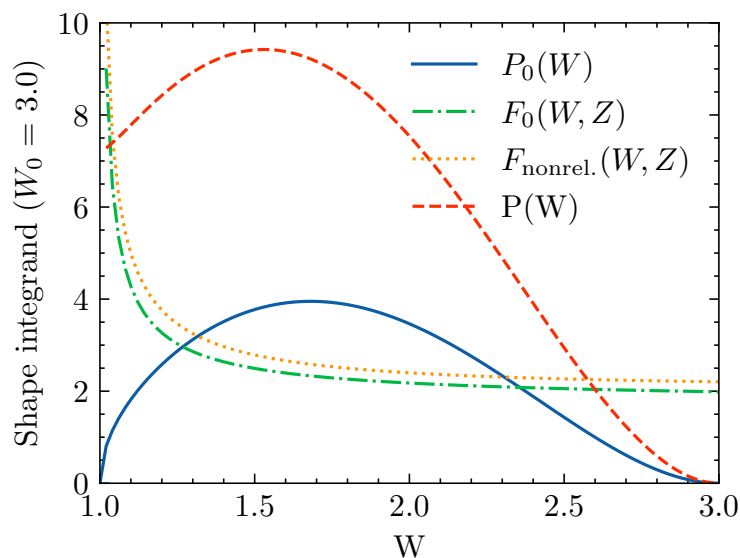

Figure 13.3: Integrand of the phase space integral equation (13.38), which gives the probability density of emitting electrons with energy W (unitless), and its Fermi-factor contribution. The total integrand $P(W)$ is the product of the statistical shape $P_0(W)$ and the Fermi factor $F_0(W, Z)$.

First, it is useful to visualize the relative contributions of the statistical shape (13.35) and the Fermi factor (13.39). Figure 13.3 shows the integrand of the phase space factor f and the individual contributions from the statistical shape and Fermi function $F_0(W, Z)$. The integrand is essentially the probability density function for the number of emitted electrons as a function of the electron energy W [272]. This plot is for a maximum electron energy of $W_0 = 3.0$, which corresponds to a Q-value of 1.02 MeV.

Next, I numerically integrate both the bare statistical factor and the Fermi-corrected phase space integrands. There is perfect agreement with the analytic integral of the statistical

factor given by equation (13.37). The results are shown in Figure 13.4. The values of W_0 range from 1 (zero Q-value) to around 30, which corresponds to a Q-value of 15 MeV. The enhancement of the phase space factor from the Fermi term is significant except for at very low transition energies.
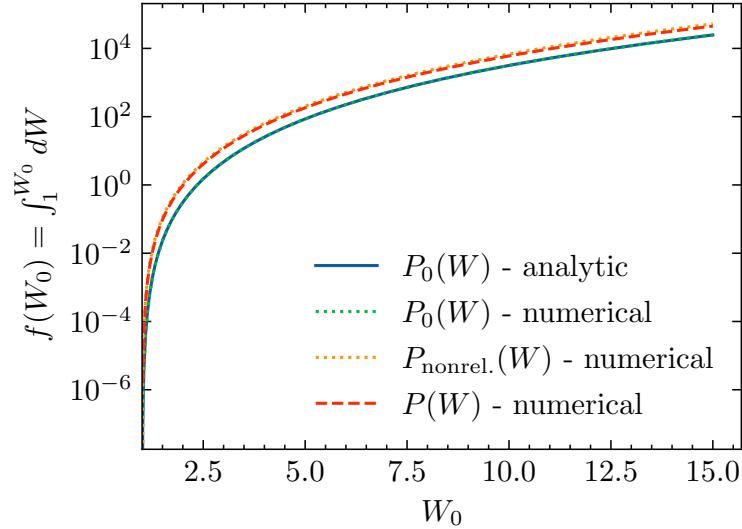

Figure 13.4: Integrated phase space factor as a function of the maximum electron kinetic energy W_0, with $(P(W))$ and without $(P_0(W))$ the Fermi factor $F_0(W, Z)$ correcting the bare statistical shape $P_0(W)$.

Finally, I have also shown in both Figures 13.3 and 13.4 the nonrelativistic approximation to the Fermi function from equation (13.40). Over the range of W_0s in Figure 13.4, the non-relativistic formula over-estimates the phase space integral by about 17%.

13.4 Spin-parity distribution of the residual nucleus

Before we can run our statistical reaction code, we need to know which states will be populated in the residual nucleus. Assuming a fixed excitation energy, the remaining degrees of freedom (as far as the reaction code is concerned) are the spins and parities of the states populated. This is what our shell model calculations must provide.

We can compute the spin parity distribution of the residual nucleus as a ratio of transition probabilities. At each excitation energy $E_x = E_f - BE_{\text{gs}f}$ of the residual nucleus, we want to know what fraction of states will be populated with a given spin J, and parity π:

$$F(E_x, J, \pi) = \frac{\sum_f \delta_{J_f J} \delta_{\pi_f \pi} \delta(E_x - E_f + BE_{\text{gs}f}) T_{fi}}{\sum_{f'} \delta(E_x - E_{f'} + BE_{\text{gs}f}) T_{f'i},} \tag{13.51}$$

The state i is always the ground state of the initial nucleus. Note also that T_{fi} has its own restrictions regarding conservation of energy, and spin and parity depending on the type of transition. Since we are taking a ratio, a number of constants drop out. For allowed transitions, we obtain:

$$F(E_x, J, \pi) = \frac{\sum_f \delta_{J_f J} \delta_{\pi_f \pi} \delta(E_x - Q_0 - m_e c^2 W_0) f_0(W_0)[B_F(i \to f) + B_{GT}(i \to f)]}{\sum_{f'} \delta(E_{f'} - E_f) f_0(W_0)[B_F(i \to f') + B_{GT}(i \to f')],} \tag{13.52}$$

where $Q_0 \equiv BE_{\text{gs}i} - BE_{\text{gs}f}$ is the difference in ground state binding energies.

In the shell model where all of the states are discrete, (13.51) will either be 1 where there is a state, or 0 where there is not. This is evident from the delta functions on E_x. In reality what we are describing are neutron unbound states, i.e. resonances, which are not actually discrete. In fact, for the statistical decay description to be valid, these resonances must be densely packed and overlapping. To model this we can convolute our function (13.52) (or (13.51)) with a Lorentzian as in [285], or Gaussian as in [52].

13.5 Summary

I have presented the theory required to describe the beta decay process and the probabilities with which it populates particular states in the residual nucleus. This can be calculated for individual states in the final nucleus using equation (13.19), which takes into account the phase space of the outgoing electron and antineutrino and depends on the energy of the

transition $Q = E_i - E_f - m_e c^2$. If we are interested in statistically averaged quantities, we can instead use equation (13.51) to determine the distribution of spin-parity combinations populated in the residual nucleus as a function of its excitation energy E_x. This is what is required as input for a statistical reactions description of beta-delayed neutron emission, which is the subject of the next two chapters.

Chapter 14

The Decay of ^{94}Rb: Statistical Reactions

The primary case study of this work is the beta-delayed neutron emission of ^{94}Rb and its competition with beta-delayed gamma emission. It has been shown that a standard statistical treatment of the decay with existing models does not reproduce the experimentally observed channel branching ratios [286]. In this chapter I will use the methods presented earlier in the dissertation to to provide an integrated shell model and statistical reaction description of the beta-delayed neutron emission of ^{94}Rb. The goal is to correctly predicts the competition between the gamma and neutron emission channels, or to explain why the statistical treatment is not sufficient.

14.1   Reviewing the experimental literature

The relevant experimental results from a 2017 paper by Valencia et al. [286] are shown in Figure 14.1. In this experiment, ^{94}Rb spontaneously beta decayed from its ground state, forming ^{94}Sr with excitation energies between zero and the beta-decay Q-value of 10.281 MeV. Since $Q_\beta > S_n$, the neutron separation energy of ^{94}Sr, both gammas and neutrons were
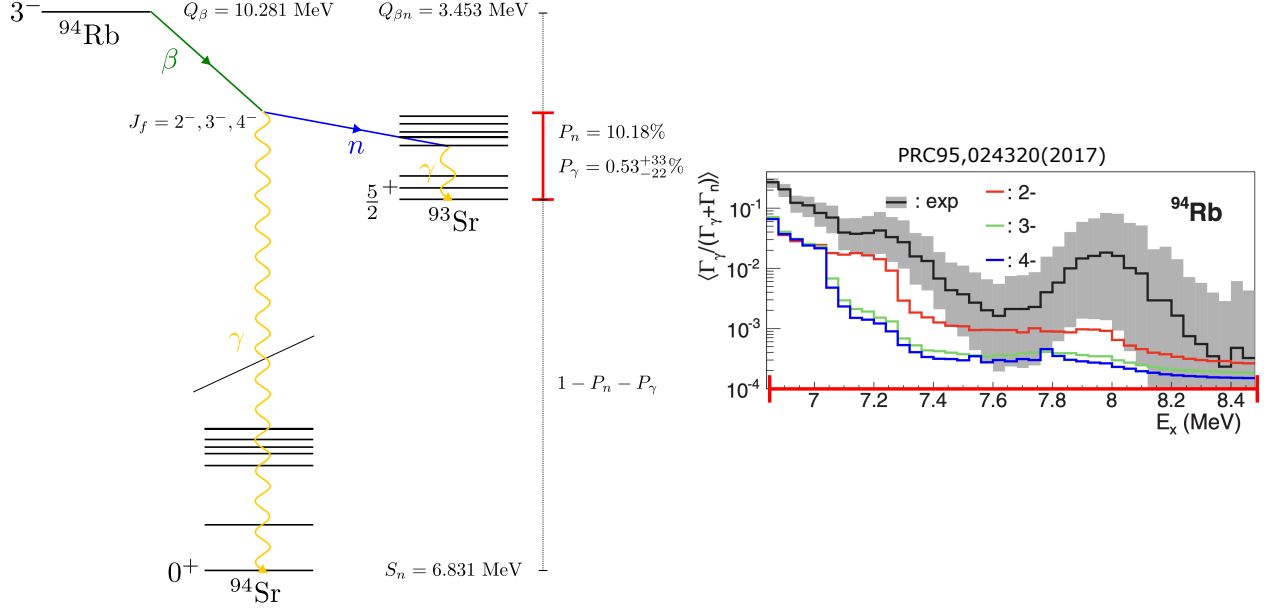
Figure 14.1: The discrepancy between the measured and predicted beta delayed gamma-neutron branching ratios. The diagram on the left depicts the process leading to the measurement. The solid red line in the diagram corresponds to the horizontal axis E_x in the graph on the right (taken from [286]), which is the excitation energy of ^{94}Sr. See text for discussion.

observed. The competition between the emitted gammas and neutrons above the neutron separation energy was studied. In this work, the quantity of interest is the average total-gamma-width as a ratio of the total decay width of ^{94}Sr:

$$\left\langle \frac{\Gamma_{\gamma:i}}{\Gamma_{\gamma:i} + \Gamma_{n:i}} \right\rangle = \left\langle \frac{\sum_{f=1}^{n_\gamma} \Gamma_{\gamma:fi}}{\sum_{f=1}^{n_\gamma} \Gamma_{\gamma:f'i} + \sum_{f=1}^{n_n} \Gamma_{n:fi}} \right\rangle, \tag{14.1}$$

where $\Gamma_{\gamma:fi}$ is the partial decay width for a gamma transition from a level $i \rightarrow f$, and similarly for the partial neutron decay widths $\Gamma_{n:fi}$. ($\Gamma = \hbar T$ for a transition probability T.) The sums extend over all final states allowed by energy, angular momentum, and parity rules. The averages extend over all initial states in some initial energy bin.

In principle, equation (14.1) can be calculated with a Hauser-Feshbach (HF) reaction code.

However, HF theory assumes that:

$$\left\langle \frac{\Gamma_{\gamma:i}}{\Gamma_{\gamma:i} + \Gamma_{n:i}} \right\rangle \approx \frac{\langle \Gamma_{\gamma:i} \rangle}{\langle \Gamma_{\gamma:i} \rangle + \langle \Gamma_{n:i} \rangle}. \tag{14.2}$$

The authors of [286] found that this greatly under-predicts the data and that a significant improvement is obtained by including the effects of Porter-Thomas fluctuations, by assuming that the partial decays widths are random numbers distributed according to a Porter-Thomas (PT) distribution (a chi-squared distribution with 1 degree of freedom). Still, the statistical model based on these PT distribution results in the solid lines plotted in the right side of Figure 14.1 – under-predicting the experimentally measured values.

My goal in this chapter is to shed light on the remaining discrepancy between the statistical model and the experimental measurement by testing the three hypotheses laid out in Chapter 12. I begin by first reproducing the results of [286] using the tools available to me. This is discussed in the next section.

14.2   Initial statistical reaction calculations

The first thing to check is that we can reproduce the published results. This is essentially a nuclear data evaluation task. I first checked the RIPL-3 library [48] to source reasonable priors for the gamma-ray strength function parameters. These are shown in Tables 14.1 and 14.2. There is no experimental data in the database for our specific nucleus ^{94}Sr, but there are systematic theoretical predictions from a simple model [103], as well as experimental data for nearby nuclei.

I used the default settings for the Gilbert and Cameron level density parameters, and all other parameters for the YAHFC calculation. Then, I populated ^{94}Sr with each of the possible spins for allowed, then forbidden, beta decay from ^{94}Rb. This leads to a decay

Table 14.1: Giant dipole resonance parameters for ^{93,94}Sr. Assuming a Lorentzian (RIPL-3) or enhanced generalized Lorentzian (YAHFC) shape with one or two peaks with energies E, width G, and strength S.

Nucleus	E1 (MeV)	G1 (MeV)	S1 (mb)	E2 (MeV)	G2 (MeV)	S1 (mb)
RIPL-3						
^{93}Sr	17.54	7.48	-	15.25	4.43	
^{94}Sr	17.64	6.99	-	14.89	4.10	
YAHFC Default						
^{93}Sr	16.84	4.5	206	-	-	-
^{94}Sr	16.84	4.5	206	-	-	-

Table 14.2: Magnetic strength function parameters for ^{93,94}Sr.

Nucleus	E (MeV)	G (MEV)	S (mb)
YAHFC Default			
^{93}Sr	9.05	4.0	0.48
^{94}Sr	9.01	4.0	0.47

with competition between gammas and neutrons above the neutron separation energy of $S_n = 6.832$ MeV. Since the ground state of ^{94}Rb is accepted to be 3^- [286], allowed beta decays ($\Delta J = 0, 1$) will result in ^{94}Sr nuclei with 2^-, 3^-, and 4^-. Figure 14.2 shows the results of this using the YAHFC defaults for the GSF. I find that the agreement with the experimental data is worse than reported by [286].

There are a few measurements of some strontium gamma-ray strength functions using various different methods for different isotopes. These are compared in Figure 14.3 with some theoretical models from systematic studies of gamma-ray strength functions across the nuclear chart.

In order constrain our GSF model using this data while accounting for uncertainty in the model, I used COMMCAS to fit the GSF parameters in the statistical reaction code YAHFC to the data. I assumed an enhanced generalized Lorentzian (EGLO) model with two peaks: the standard dominant GDR around 17 MeV, plus another peak around 10 MeV to reproduce the structure seen in the NRF data. I included all three data sets in the fit, excluding the anomalous data in the NRF data set (measurements taken above the neutron separation
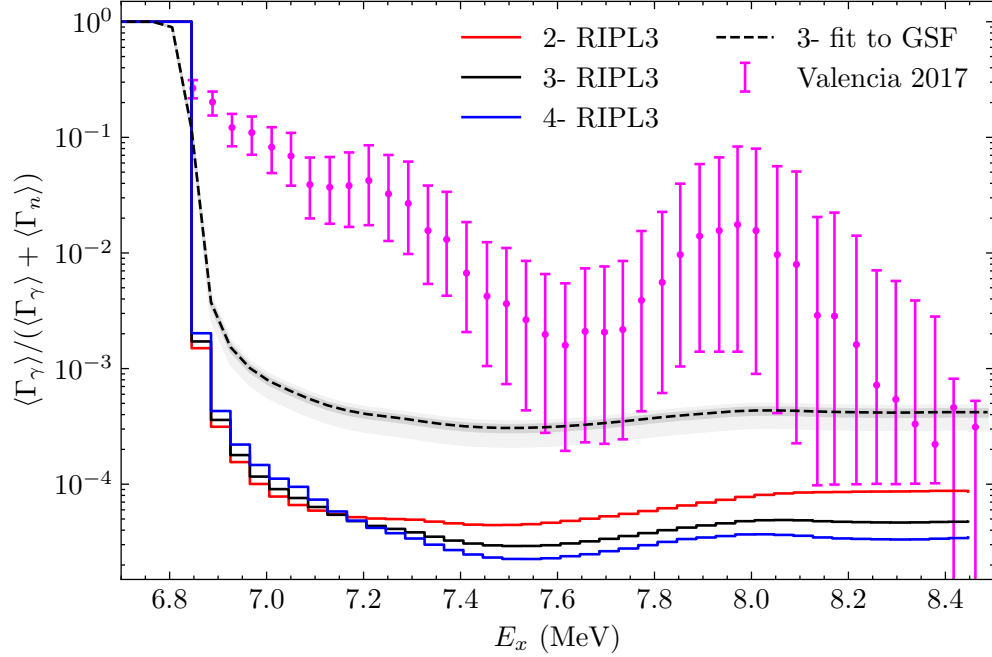
Figure 14.2: Comparison of the initial statistical calculations of the beta-delayed neutron emission of ^{94}Rb compared to the experimental data of Valencia 2017 [286]. The data from the paper was estimated using graphical software. The solid lines show decays from a ^{94}Sr nucleus populated by allowed decay and using the RIPL-3 [48] parameters used by default in the YAHFC Hauser-Feshbach code. The grey bands show the decay from 3^- states in ^{94}Sr using GSF parameters fit to available experimental data and systematic models.

energy, see [261] for discussion).

It is well known that neutron capture is sensitive to the low-energy part of the gamma ray strength function, and that experimental and theoretical evidence suggests that the low energy part of the GSF may be enhanced by M1 electromagnetic transitions. The same will be true for BDNE; a low energy enhancement of the GSF from the M1 component may contribute to the enhanced gamma emission probability. I therefore included a simple M1 model with two peaks: one primary and the second placed near zero energy to model possible low-energy components. I fit M1 GSF to the SMLO systematic model of [110] to which I assigned an arbitrary 10% uncertainty. Both models were assigned an un-accounted for uncertainty parameter (see Chapter 9). Since none of the data used polarized beams to excite the nucleus, the polarization of the transitions in each data set is unknown. As
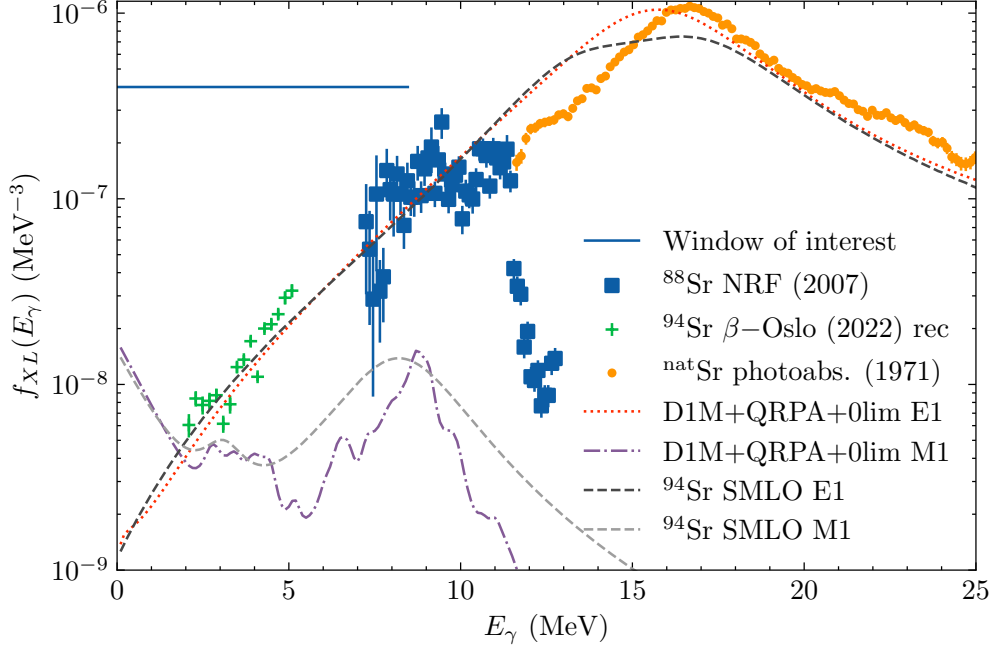
Figure 14.3: Gamma-ray strength functions for Strontium isotopes from various experimental and theoretical models. The window of interest indicates the energies relevant for gamma emission from ^{94}Sr. Nuclear resonance florescence (NRF) data from [261]. β-Oslo data from database [110] sourced from unpublished data from A. Sweet. Photo-absorption data on natural strontium from [189]. D1M plus quasiparticle random phase approximation (QRPA) plus emperical low-energy enhancement from [110, 112]. Simple modified Lorentzian (SMLO) from global fits from the same database.

a rough approximation, I assume that the data are dominated by E1 transitions, although this is possibly wrong below 5 MeV where the M1 and E1 of the systematic models predict roughly equal magnitude from M1 and E1.

The results of the fit are shown in Figure 14.4. The assumptions described above result in a reasonable total GSF. Examining Figure 14.2, we can see that this fit significantly increases the gamma channel in the BDNE of ^{94}Rb. The gray band shows calculations of the normalized Γ_γ from 3^- states in ^{94}Sr.

In summary, by improving the phenomonological GSF's using available measurements and global systematic models, I was able to greatly increase the agreement with the data compared to the default parameterizations. This used the parameter inference and uncertainty
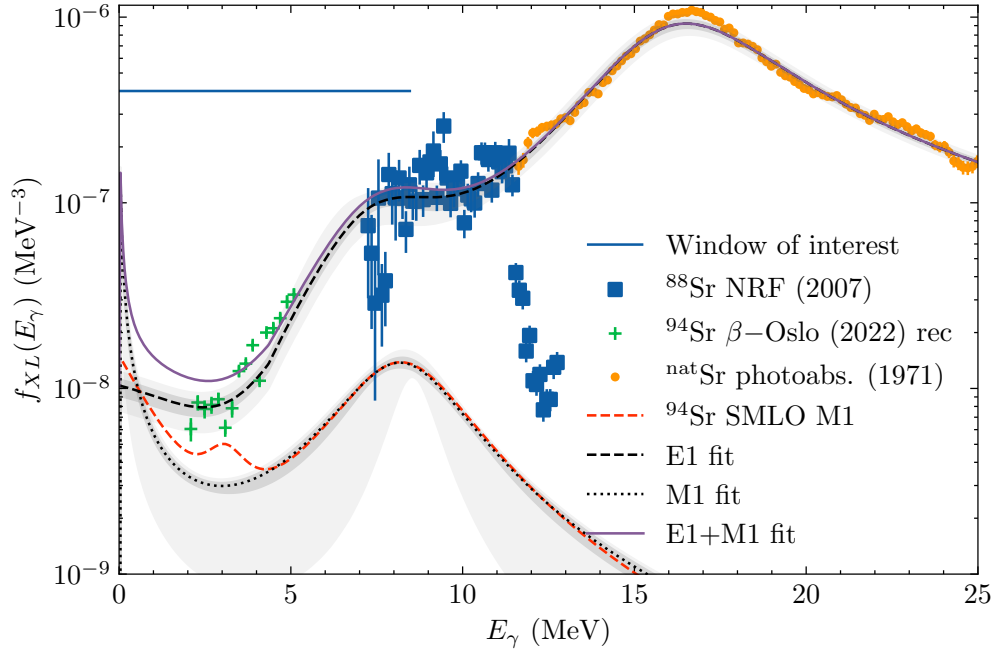
Figure 14.4: Gamma-ray strength functions fit to experimental data and models using COMMCAS markov chain monte carlo sampling.

quantification tools developed in Part II. Second, this improvement is not sufficient. Following the investigation of Valencia 2017 [286], this is likely due to contributions from random fluctuations in the neutron partial widths. This will be addressed in the next section.

14.3   Porter-Thomas fluctuations

The calculations performed in the previous section do not match the results from Valencia et al. [286]. The missing gamma strength in our statistical calculations can be partly attributed to the effects of Porter-Thomas (PT) width fluctuations. Put simply, the distribution of individual-level gamma-decay widths has a long tail: a small number of very strong transitions (from the tail of a PT distribution of decay widths) dominate the statistics and the energy averaged Hauser-Feshbach calculation does not reproduce the correct decay

pattern. In terms of the average ratio of widths, this means that

$$\left\langle \frac{\Gamma_\gamma}{\Gamma_\gamma + \Gamma_n} \right\rangle \neq \frac{\langle \Gamma_\gamma \rangle}{\langle \Gamma_\gamma \rangle + \langle \Gamma_n \rangle}. \tag{14.3}$$

The classic paper on the topic of this effect is by Porter and Thomas [224]. A review of evidence for and against this model can be found in the proceedings by Weidenmuller [295]. More recent work has reinforced the evidence that neutron resonances indeed follow a Porter-Thomas distribution [85]. Shell model calculations have provided evidence that M1 and E2 transition intensities (specifically, the reduced B-values) follow a PT distribution [2, 125]. And successful application to compound nucleus decay [286, 273] (e.g. see DICEBOX [29] or RAINIER [170]) has provided further justification.

The authors of the Valencia paper [286] addressed this effect with a custom program similar to DICEBOX [29] or RAINIER [170], but including the effects of neutron width fluctuations (e.g. DICEBOX handles only gamma width fluctuations). In this section I will attempt to avoid such a step, and instead seek a novel solution inspired by the Hauser-Feshbach solution to width fluctuation corrections (WFCs) for correlations between the entrance channel and all outgoing decay channels [215, 203]. This will enable us to take into account this effect without a single-purpose code while maintaining the full suite of capabilities of a complete Hauser-Feshbach code.

14.3.1 Random partial widths

The basic theory of Porter-Thomas fluctuations goes like this: the partial widths (whether electromagnetic or neutron) are proportional to squared matrix elements,

$$\Gamma_{fi} \propto |\langle \Psi_f | \hat{\mathcal{O}} | \Psi_i \rangle|^2, \tag{14.4}$$

for some transition operator $\hat{\mathcal{O}}$. The total decay width for the initial level i is the sum:

$$\Gamma_i = \sum_{f=1}^{n} \Gamma_{fi}. \tag{14.5}$$

Now, we consider the matrix elements to be random numbers following a Gaussian distribution (more specifically, a Gaussian orthogonal ensemble, viz. [311]). A sum of n squared-Gaussian random variables is a chi-squared distribution with n degrees of freedom. The probability density function for such a variable is:

$$P(x,n) = \Gamma(r)^{-1} r (rx)^{r-1} e^{-rx}, \tag{14.6}$$

where Γ here is the gamma-function, $r = n/2$, and in our context $x = \Gamma_{fi}/\bar{\Gamma}_{fi}$ is a dimensionless quantity in terms of the average partial width. (Note that this differs from the common definition $\chi_n^2 = 2^{-r} \Gamma(r)^{-1} x^{r-1} e^{-x/2}$ which has a mean of $n = 2r$.) So if we assume that the matrix elements have a Gaussian distribution, the individual partial widths will have a chi-squared distribution with $n = 1$. In nuclear physics this is called the Porter-Thomas (PT) distribution:

$$P_{\mathrm{PT}}(x) = P(x, n = 1) = \frac{e^{-x/2}}{\sqrt{2\pi x}}. \tag{14.7}$$

The physical implications of this analysis is that the individual level widths Γ_i will fluctuate around their mean value $\bar{\Gamma}_{fi}$ with a distribution given by a PT distribution.

Continuing the assumption of Gaussian matrix elements, the total level widths are also chi-squared distributions, but now with n degrees of freedom. As n increases, the variance of the total width of the resonance tends to decrease ($P(x; n)$ approaches a delta function as $n \to \infty$, see Figure 14.5). In other words, the total width approaches a constant (the average). This mean that the effects of PT distributed widths are only significant when there are a small number of final states (small n). Otherwise, all widths behave the same.
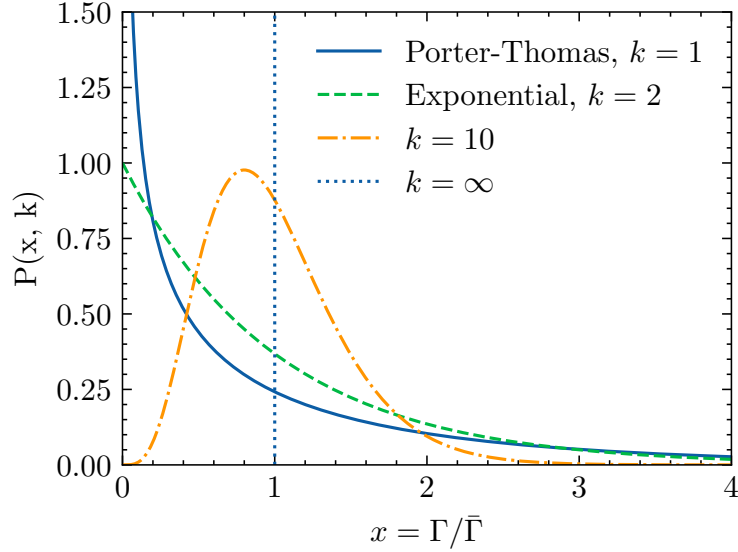
Figure 14.5: The Porter-Thomas distribution and related distributions which approach a delta function at $x = 1$ as $n \to \infty$.

On a related note, PT fluctuations are not sufficient to explain other instances of apparent non-statistical decay. For examples, see the work by Koehler et al. [171] and Fanto et al. [84] concerning the case of neutron capture on ^{96}Mo. So the remaining discrepancy of [286] is not a new trouble.

In our specific case of beta-delayed neutron emission, we are interested in decays near the neutron separation energy. In this regime, there is a large number of final states for the gamma decay, and a small number of final states for the neutron decay. This means that the total neutron widths will follow a low-n chi-squared distribution, while the total gamma decay widths will be roughly constant. I therefore focus on implementing PT fluctuations of the neutron partial widths only.

14.3.2 Porter-Thomas numerical experiment

It is not at all obvious that including Porter-Thomas fluctuations will increase the average gamma widths with respect to the neutron widths. Although one would expect that as

the number of neutron partial widths (i.e. the number of accessible excited states in the neighboring nucleus) increases, the effect should disappear and return the Hauser-Feshbach prediction. To illustrate, I conducted a numerical experiment to analyze the effects of assuming PT neutron widths on the quantity $\langle \Gamma_\gamma / \Gamma_t \rangle$, where $\Gamma_t = \Gamma_\gamma + \Gamma_n$.

I assume standard normal matrix elements for both types of transitions and work in units of the mean so that $\Gamma_n = x$. Equivalently, $P(\Gamma_n) = P(x, k)$. I further assume the gamma total widths include many terms, so that $P(\Gamma_\gamma) \approx \delta(\Gamma_\gamma - 1)$. Thus, the purely Hauser-Feshbach estimate of $\langle \Gamma_\gamma / \Gamma_t \rangle$ for any k neutron partial widths is exactly $1/2$:

$$\frac{\langle \Gamma_\gamma \rangle}{\langle \Gamma_\gamma \rangle + \langle \Gamma_n \rangle} = \frac{1}{1 + \langle P(\Gamma_n, k) \rangle} = \frac{1}{2}. \tag{14.8}$$

In other words, equal odds for either channel regardless of the number of neutron partial widths. Next, I numerically simulate the "true" ratio assuming randomly distributed neutron widths. I generate random samples of the ratio,

$$\frac{\Gamma_\gamma}{\Gamma_t} = \frac{1}{1 + \Gamma_n}, \tag{14.9}$$

by generating random values of Γ_n from the appropriate chi-squared distribution $P(x, k)$ for the desired number of neutron partial widths k. To generate one sample, k random numbers are drawn $y_i \sim N(0, 1)$, $i = 1, ..., k$, then I compute $\Gamma_n = \sum_{i=1}^{k} y_i^2 / \langle y_i^2 \rangle$, where $\langle y^2 \rangle$ is the sample mean of y_i^2. After sampling, I compute the mean ratio $\langle \Gamma_\gamma / \Gamma_t \rangle$ of all the samples.

I generated 10^6 samples representing the initial states of the compound nucleus in some fixed energy bin. The final results are fairly insensitive to the number of samples, but I generated a large number to produce smooth histograms. The results of the numerical simulations for $k = 1$ and $k = 100$ are shown in Figure 14.6. The gamma total widths are constant (black dashed line) while the neutron total widths are randomly distributed (blue histograms). The resulting distribution of width ratios are shown in the narrow green histograms.
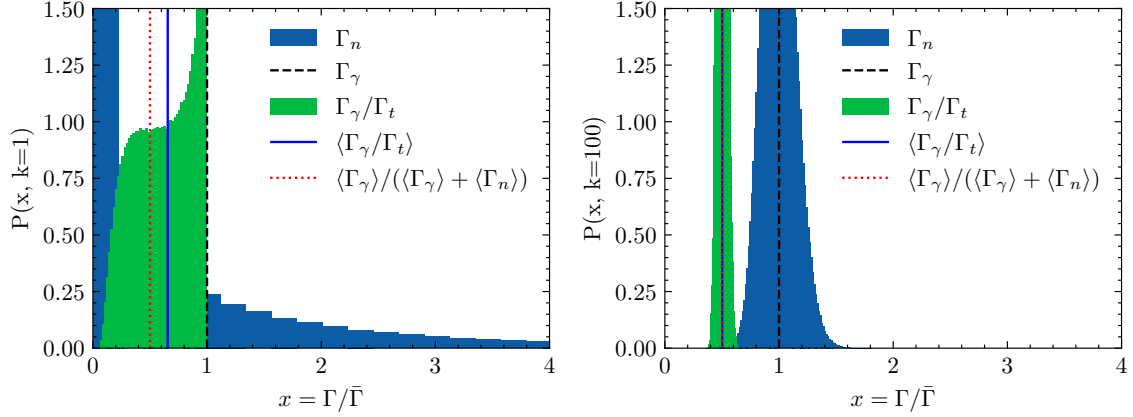
303

Figure 14.6: Porter-Thomas fluctuation toy model wherein the average neutron and gamma widths are equal. See text for discussion.

The left panel of Figure 14.6 shows a simulation with one neutron partial width. The total neutron width Γ_n follows a PT distribution. The ratio of the gamma total width to the combined total width is shown in the green histogram with thin bars. The average of these width ratios (blue solid line) is enhanced with respect to the HF estimate (red dotted line).

The right panel of Figure 14.6 shows a simulation with 100 neutron partial widths. The neutron total widths are centered around 1.0 (broad, blue histogram). The distribution of neutron total widths is narrow and centered around the average near 0.5. The average of these width ratios (solid blue line) is indistinguishable from the HF prediction (red dotted line).

At $k = 1$ we observe the maximum effect of PT fluctuations. I obtain $\langle \Gamma_\gamma / \Gamma_t \rangle = 0.66$. As anticipated, the gamma width is enhanced with respect to the HF prediction of 0.5. The increase is about 33 percent.

For the $k = 100$ simulation, $\langle \Gamma_\gamma / \Gamma_t \rangle = 0.50(3)$, which is close to the HF prediction. As expected, the PT fluctuations are strongly suppressed as the number of partial widths in-creases.

14.3.3 Porter-Thomas enhancement factor

We have shown how Porter-Thomas fluctuations of the neutron partial widths can enhance the average gamma total width. But how many partial widths are required before the PT result reduces to the HF approximation? And how strong can the PT enhancement be when it is ignored? To answer these questions, I varied the number of neutron partial widths from $k = 1$ to $k = 100$ and repeated the above experiment for each. For each k, I computed $\langle \Gamma_\gamma / \Gamma_t \rangle$ and divided by the HF prediction to compute a PT enhancement factor:

$$W_{PT} = \text{PT enhancement factor} = \frac{\langle \Gamma_\gamma / \Gamma_t \rangle}{\langle \Gamma_\gamma \rangle / (\langle \Gamma_\gamma \rangle + \langle \Gamma_n \rangle)}. \tag{14.10}$$

Figure 14.7 shows the smooth decay of the PT enhancement factor from its maximum at $k = 1$.
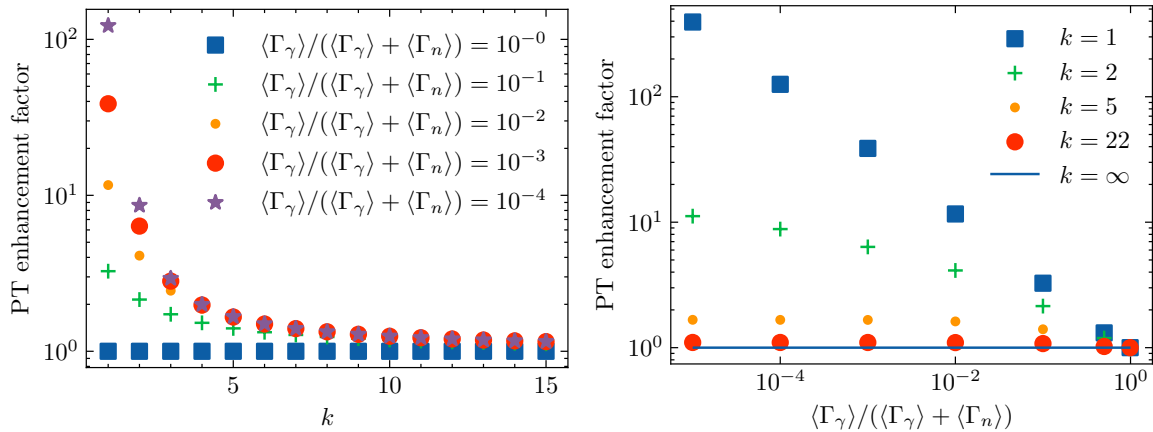
Figure 14.7: Reduction of the Porter-Thomas (PT) enhancement factor as a function of increasing number of neutron partial widths k and for different Hauser-Feshbach width ratios $\langle \Gamma_\gamma \rangle / (\langle \Gamma_\gamma \rangle + \langle \Gamma_n \rangle)$. The vertical axis is the factor by which PT fluctuations of the neutron partial widths increase the average relative gamma total widths with respect to the Hauser-Feshbach approximation.

Finally, I repeat the whole experiment for different values of the fixed total gamma width. Recall that so far the gamma width was a constant equal to the average neutron width, 1.0. Now I vary $P(\Gamma_\gamma) = \delta(\Gamma_\gamma - g)$ for some variable constant g. The sampled ratios are now

given by:

$$\frac{\Gamma_\gamma}{\Gamma_t} = \frac{g}{g + \Gamma_n}. \tag{14.11}$$

Since $\langle \Gamma_n \rangle = 1$ by construction, changing g is equivalent to changing the ratio

$$h \equiv \frac{\langle \Gamma_\gamma \rangle}{\langle \Gamma_\gamma \rangle + \langle \Gamma_n \rangle} = \frac{g}{g + 1}, \tag{14.12}$$

which is the HF estimate of the width ratio and is the denominator of the PT enhancement factor. In all previous simulations we had $g = 1$, which is $h = 1/2$. Now I include ratios of $h = 10^0$, 10^{-1}, 10^{-2}, 10^{-3}, and 10^{-4}. This spans the range of values of the Hauser-Feshbach ratios in Figure 14.2.

Figure 14.7 shows that for $k = 1$, the PT enhancement can be up to two orders of magnitude. By $k = 5$, all curves are below an enhancement of 2. For all curves to be below an enhancement of 1.1, one requires $k > 22$.

To summarize these numerical experiments, we have learned that fluctuations of the neutron partial widths from highly excited states to low-lying levels in the neighboring nucleus produce a strong enhancement of the gamma width. This assumes that we have many available partial gamma widths. This effect is independent of any energy dependence of the neutron partial widths (which are known to have an approximately $\sqrt{E}$ dependence [294, 85, 84]) and depends only on the number of neutron partial widths k and the ratio of average widths h (eq. (14.12)). Normalizing to the ratio h removes the energy dependence from our simulations. We can therefore compute a correction factor $W_{PT}(k, h)$ relating the Hauser-Feshbach estimate to the true ratio $\langle \Gamma_\gamma / \Gamma_n \rangle$:

$$\langle \Gamma_\gamma / \Gamma_t \rangle = W_{PT}(k, h) \frac{\langle \Gamma_\gamma \rangle}{\langle \Gamma_\gamma \rangle + \langle \Gamma_n \rangle}. \tag{14.13}$$

There are publicly available codes to model the effects of PT fluctuations for gamma cascades. The same is not true for neutron decays where Hauser-Feshbach models are assumed to be sufficient. However, it may be possible that including the PT enhancement factor is sufficient.

Figure 14.8 shows the calculations from Figure 14.2 with the PT width fluctuation corrections applied. At each energy bin of the HF calculation, I apply equation (14.13). k at each energy is calculated according to the discrete levels used by the HF code. It is equal to the cumulative number of levels in the residual nucleus available for neutron emission. h is equal to the original HF ratio of average widths.
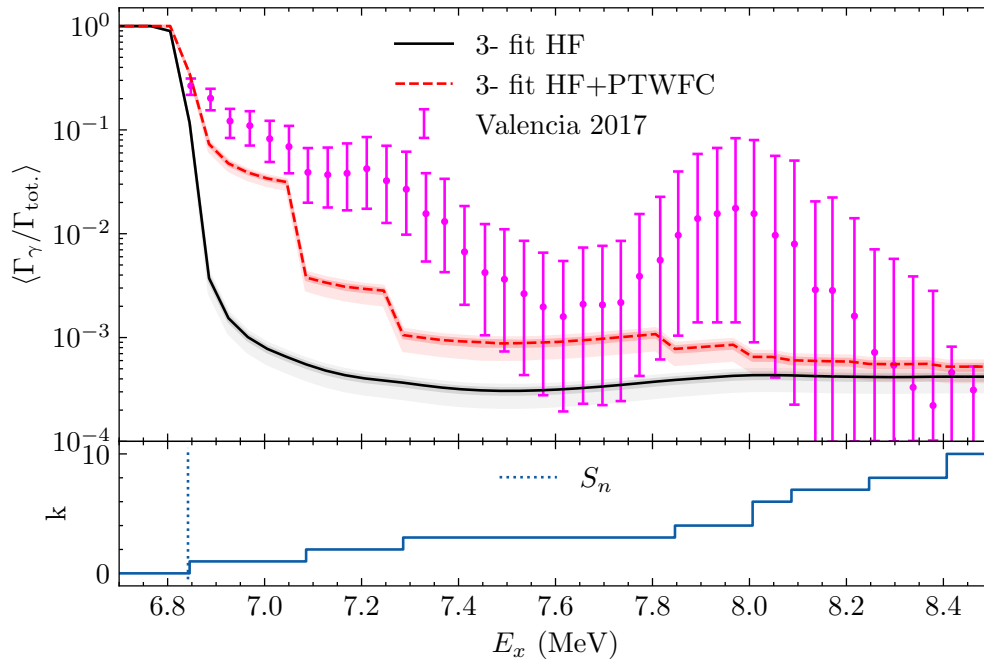
Figure 14.8: Same as Figure 14.2 with and without the Porter-Thomas width fluctuation correction (PTWFC) factor. The lower panel shows the number of partial widths k available for neutron emission (neutron decay to ^{93}Sr). The discontinuities in the HF+PTWFC calculation line up with changes in k.

I believe this is the first time a correction factor for Porter-Thomas width fluctuations has been applied within the framework of a Hauser-Feshbach code. However, the basic idea is conceptually equivalent to width-fluctuation corrections [204] for particle-induced reactions. These types of width fluctuations are usually only applied to account for correlations be-

tween two competing channels, but Moldauer [205] pointed out the "second and less widely discussed" enhancement due to fluctuations of the total widths.

In future studies, one should generalize the assumptions made in this study to test the sensitivity to those assumptions. For example, the gamma partial widths could also be modeled as random numbers, with a large k value which could be estimated based on the level density or from shell model calculations. Additionally, distributions of the partial widths with different degrees of freedom ($n \neq 1$) could be tested.

Summarizing the findings so far, we have shown that improvements to the gamma-ray strength functions using existing measurements combined with a correction factor for (neutron) Porter-Thomas width fluctuations significantly improves the statistical model's agreement with the data. In agreement with the conclusions of Valencia [286], we have independently verified that the current statistical model is not sufficient to explain the strong gamma emission observed in the measurements of [286]. In the final section of this chapter, we will continue to work within the framework of statistical nuclear reactions to test one of the hypotheses for this discrepancy proposed in Chapter 12.

14.4 Forbidden decays

Let us restate the second hypothesis presented in Chapter 12 for explaining the model discrepancy:

Hyp. 2: Forbidden beta decay is stronger than assumed, blocking high-l neutron emission. If forbidden transitions play a significant role in these neutron-rich cases, then higher angular momentum states populated by beta decay would block this emission of neutrons to available states in the neighboring nucleus.

In theory, we can compute the relative strength of forbidden decays from ^{94}Rb into ^{94}Sr using a microscopic model such as the shell model. The method for such a calculation is shown in section 13.4. Prior to such an undertaking, however, we can test the plausibility of this hypothesis by modeling the decay of ^{94}Sr from artificial spin populations with a fixed J^π. This is completely analogous to the study performed in Chapter 8: Surrogate Reactions I: Weisskopf-Ewing Approximation. If the decay of ^{94}Sr shows only weak dependence on the spin and parity J^π of the decaying states, then it would not matter whether the beta decay populating those states were allowed with transitions $\Delta J^\pi = 0^+, 1^+$, or first-forbidden with transitions $\Delta J^\pi = 0^-, 1^-, 2^-$. This is equivalent to the Weisskopf-Ewing approximation.

I performed such a study by simulating the decay of ^{94}Sr from three sets of single-J^π spin-parity populations. The possible spin-parity combinations populated in ^{94}Sr following the beta decay of the 3^- ground state of ^{94}Rb are summarized in Table 14.3.

Table 14.3: Possible spin-parity combinations populated in ^{94}Sr following the beta decay of the 3^- ground state of ^{94}Rb.

Type of beta decay	ΔJ^π	J^π populated in ^{94}Sr
Allowed, Fermi	0^+	3^-
Allowed, Gamow-Teller	$0^+, 1^+$	$2^-, 3^-, 4^-$
First-forbidden, non-unique	$0^-, 1^-$	$2^+, 3^+, 4^+$
First-forbidden, unique	2^-	$1^+, 5^+$

I used the gamma-ray strength function parameters obtained by fitting to the available data, as described in section 14.2. I also applied PTWFC factors, as described in section 14.3.3. The results are shown in Figure 14.9. What is clear from panel (a) of Figure 14.9 is the conclusion reached by [286], that the present statistical model, even including the effects of Porter-Thomas flucuations, cannot account for the observed gamma-width ratio. Panels (b) and (c), however, indicate that an appropriate combination of the effects of first-forbidden decay may in fact account for the missing gamma strength. Recall that in the real beta decay from ^{94}Rb to ^{94}Sr, there is some mix of allowed and forbidden decays, and the assumption so far has been the the allowed decays dominate. But recent work in the field of reactor
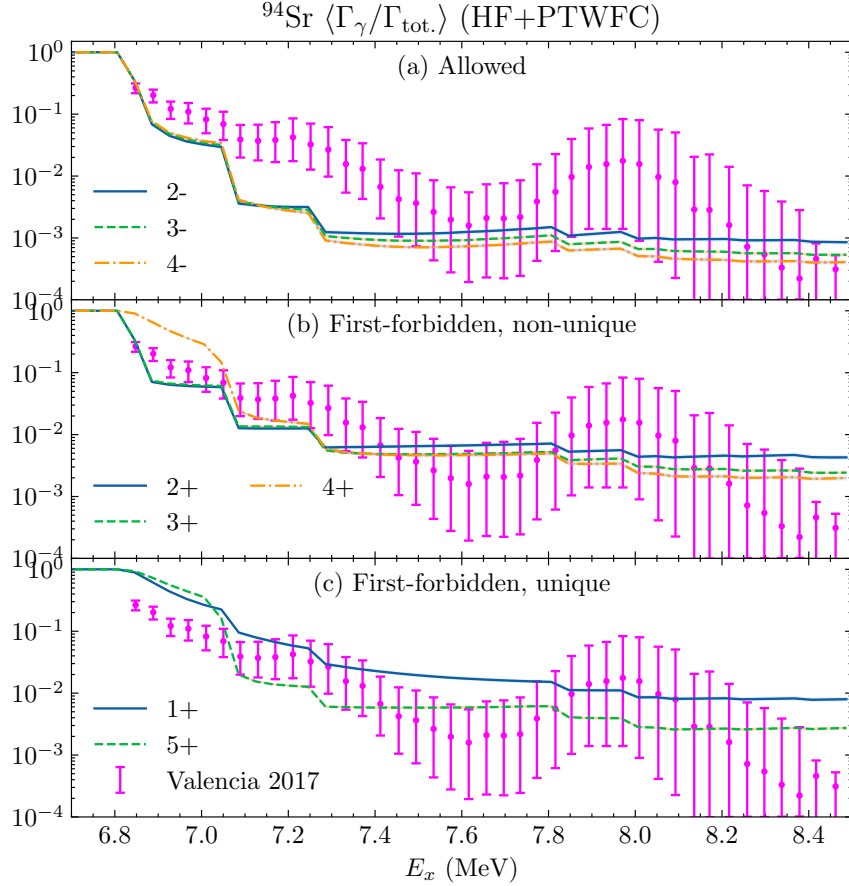
Figure 14.9: Each panel shows the HF+PTWFC calculations for decays from states populated by a different beta-decay mode: (a) allowed (Fermi and Gamow-Teller), (b) first-forbidden, non-unqie, and (c) first-forbidden, unique. Without any other modifications, decays from allowed state cannot explain the data. However, some energy-dependent combination of contributions from (a), (b), and (c) may provide a solution.

anti-neutrino monitoring has shown that nuclei in this region can have a nontrivial forbidden decay contribution [83, 131]. The true spin-parity distribution will be energy dependent, as indicated by equation (13.51).

With this simple study, I have shown that *hypothesis 2* is feasible: statistical calculations akin to a Weisskopf-Ewing test show that nonzero forbidden decays are a viable explanation of the discrepancy. What remains is to use our theoretical models to assess the likelihood that these forbidden decays have sufficient strength. In principle, this can be done using the shell model. In the following chapter I will recount progress towards this goal.

Chapter 15

The Decay of ^{94}Rb: Shell Model

I call the reader's attention back to the three hypotheses proposed in Chapter 12:

Hyp. 1: Gamma-ray strength function is stronger than assumed.

Hyp. 2: Forbidden beta decay is stronger than assumed, blocking high-l neutron emission.

Hyp. 3: Beta decay does not lead to a compound nucleus.

In Chapter 14 we used statistical reactions calculations to show that hypothesis 2 is at least plausible. In this chapter I will lay the groundwork to test all three hypotheses using the shell model. First, by providing a microscopic calculation of both the gamma-ray strength functions (hyp. 1). Using the methods developed in Chapter 6, we will be able to propose a new statistical reaction prediction using modified gamma-ray strength functions. Then, I will explain what next steps are necessary to test the forbidden beta decay strength (hyp. 2), and finally the possibility of non-statistical decay by analyzing the correlations between the electromagnetic and electroweak transition probabilities (hyp. 3).

All three investigations can be carried out with the nuclear shell model. But because the

nuclei involved ^{94}Rb and ^{94}Sr require large model spaces, we will have to employ the basis reduction methods developed in Part I of this dissertation.

The first section will cover an initial analysis of the shell model interaction to be used for our calculations, followed by calculations of the shell model gamma-ray strength function. The reduced-basis provided by our PANASh code will be crucial for testing this hypothesis since the dimensions for ^{94}Sr are too large for the number of states we require for computing the gamma-ray strength function. I begin this section with both full configuration interaction (FCI) calculations with `BIGSTICK` and truncated shell model calculations with PANASh, with the former being important for testing the phenomenological interaction we will be using.

15.1   Validating the interaction

I validated the shell model interaction *glepn* defined in 1990 by Mach et al. [191] against published results to make sure it behaved in `BIGSTICK` (and by extension PANASh) as expected.

The *glepn* interaction was developed for a shell model description of the beta decay of ^{96}Y to ^{96}Zr. The authors also evaluated their results against other zirconium isotopes. It's worth noting that the paper concludes saying that a major goal should be obtaining a better interaction for the spectroscopy in the $A = 96$ region, and one which better describes both allowed and forbidden transition rates. Despite this, it has been applied in recent literature to a broad range of nuclei in a systematic study of allowed and forbidden beta decay [131]. It will be used here until a better interaction can be created in future work.

The single particle space involves orbits from the $N = 3$ and $N = 4$ major shells. The frozen core is ^{56}Ni, and seven active orbits are included from the pf and gds shells: $2p3/2$,

$1f5/2$, $2p1/2$, $1g9/2$, $2d5/2$, $3s1/2$, and $2d3/2$. The Mach paper [191] indicates that the $1f7/2$ orbit is included, but in available implementations of the interaction, the $1f7/2$ orbit is omitted. This valence space can fit up to 34 protons and 34 neutrons. I will use this notation to descibe the full single-particle valence space which couples together the proton π and neutron ν single particle spaces:

$$
\begin{aligned}
glepn77 = \pi^{Z_v}(2p_{3/2}, 1f_{5/2}, 2p_{1/2}, 1g_{9/2}, 2d_{5/2}, 3s_{1/2}, 2d_{3/2}) \\
\otimes \nu^{N_v}(2p_{3/2}, 1f_{5/2}, 2p_{1/2}, 1g_{9/2}, 2d_{5/2}, 3s_{1/2}, 2d_{3/2}),
\end{aligned}
\tag{15.1}
$$

where Z_v and N_v are the number of protons and neutrons in each valence subspace. I decorated the *glepn* model space name with "77" to indicate 7 proton orbits and 7 neutron orbits, which will be reduced in later calculations.

The interaction itself consists of 14 single particle energies $\epsilon_{i=1,..,7}^{x=p,n}$, and 1621 two-body matrix elements. The single-particle energies are given in Table 15.1.

The model space truncation described in the original paper for *glepn* is not easily implemented in modern large-scale shell model codes such as BIGSTICK. (Essentially, it took only a small number of possible configurations within the selected single-particle space, e.g. a single 1p-1h configuration relative to a frozen core.) Instead, I used results from a more recent paper [233] to validate usage of the interaction.

The nucleus used for validation was ^{92}Sr, which has 10 valence protons and 26 valence neutrons. The calculation done in [233] blocked protons from exciting to the $2d$ orbits ($2d_{3/2}$ and $2d_{5/2}$), and forced the neutron orbits up to $1g_{9/2}$ ($2p_{3/2}$, $1f_{5/2}$, $2p_{1/2}$, $1g_{9/2}$) to remain filled. This restriction on the neutrons means that there is effectively an additional soft core with 22 frozen neutrons. The model space is

$$
glepn53 = \pi^{10}(2p_{3/2}, 1f_{5/2}, 2p_{1/2}, 1g_{9/2}, 3s_{1/2}) \otimes \nu^{4}(2d_{5/2}, 3s_{1/2}, 2d_{3/2}).
\tag{15.2}
$$

I implemented this space in `BIGSTICK` using the weight-factor truncation method described in section 1.3.3. The w-truncation used is shown in Table 15.1 with $W_{\text{max}} = 0$. This leads to M-scheme dimensions of more than 33 million.

Table 15.1: The single-particle energies $\epsilon^{x=p,n}$ of the *glepn* model space and the w-truncation scheme used to implement the model space given in equation (15.2).

Orbit	ϵ^p	w^p	ϵ^n	w^n
$2p3/2$	-0.387	0	-6.032	0
$1f5/2$	-3.090	0	-7.882	0
$2p1/2$	-1.078	0	-4.809	0
$1g9/2$	-0.647	0	-4.156	0
$2d5/2$	8.742	1	3.983	1
$3s1/2$	8.780	0	4.721	1
$2d3/2$	9.815	1	8.471	1

Using the model space (15.2) and the *glepn* interaction, I was able to reproduce the energies of the first several states in ^{92}Sr to at least the first three decimal places. To reproduce the energies of Ramahlo [233] I had to assume two-body matrix elements (TBMEs) were in un-normalized (upn) format:

$$V_{abcd;J}^{\text{xpn}} = \frac{1}{2}\sqrt{(1 + \delta_{ab})(1 + \delta_{cd})}V_{abcd;J}^{\text{upn}}. \tag{15.3}$$

See `BIGSTICK` manual [165] for discussion of normalized and unnormalized TBME conventions. Further, the TBME's were not re-scaled by any factor of A, as is the case for some interactions.

15.2 ^{94}Rb low-lying structure with *glepn*53 FCI

For beta-delayed neutron emission, we need only the ground state information for ^{94}Rb. The nuclear data sheets evaluated spin assignment for the ground state is 3^- [1]. The experiment responsible for the spin assignment was a beta decay detected optical pumping method [36].

Table 15.2: Low lying excitation energies of ^{92}Sr from experiment and the shell model calculations described in the text. This work is shown in columns UPN, assuming un-normallized TBMEs, and XPN, assuming normalized TBMEs.

State	Ramahlo 2022 [233]	UPN	Exp.	XPN
0^+_1	0	0	0	0
2^+_1	0.848	0.848	0.815	0.813
2^+_2	1.793	1.793	1.385	1.693
2^+_3	2.074	2.074	1.778	1.844
0^+_2	*	1.657	2.088	1.294
1^+_1	2.552	**	2.141	1.788

*Not reported
**Did not converge

The parity was assumed based on shell model calculations [1].

With such a high level density it's expected that our model may not correctly predict the order of the states, and indeed this is the case. We will therefore compute the first few states and take the lowest 3^- to be our ground state.

We begin with the same model space used for the benchmark calculation of ^{92}Sr, since ^{94}Rb is not too far away with one fewer proton and three extra neutrons. Rubidium-94 has $(Z, N) = (37, 57)$. With a ^{56}Ni core, this leaves $(9, 29)$ valence particles, and with the soft 22-neutron core due to the truncation, an effective valence count of $(9, 7)$. The model space is:

$$glepn53 = \pi^9(2p_{3/2}, 1f_{5/2}, 2p_{1/2}, 1g_{9/2}, 3s_{1/2}) \otimes \nu^7(2d_{5/2}, 3s_{1/2}, 2d_{3/2}). \tag{15.4}$$

The M-scheme dimension for the negative parity states in this model space is 35,673,448.

The results of the calculation for the first few levels is shown in Table 15.3. The spin assignments of the experimentally observed levels are not well constrained. The parenthesis around the parity assignments indicate that the parity is assumed, but not confirmed. The first 3^- state in the *glepn* calculation is 354 keV above the predicted ground state. This is

large compared to the 'rule of thumb' shell model error of 100 keV.

Table 15.3: Low lying excitation energies and spin assignments of ^{94}Rb from experiment and the shell model calculation described in the text. The 3^- ground state is in bold font.

Excitation	Experiment		UPN		XPN	
	J_i^π	E_x	J_i^π	E_x	J_i^π	E_x
1	$\mathbf{3_1^{(-)}}$	$\mathbf{0.000}$	2_1^-	0.000	2_1^-	0.000
2	*	0.005	2_2^-	0.229	$\mathbf{3_1^-}$	$\mathbf{0.060}$
3	*	0.191	$\mathbf{3_1^-}$	$\mathbf{0.354}$	0_1^-	0.133
4	(4^-)	0.217	1_1^-	0.447	1_1^-	0.691
5	*	0.223	0_1^-	0.653	2_2^-	0.769
6	*	0.293	1_2^-	0.927	4_1^-	0.832
7	(5^-)	0.328	4_1^-	0.950	2_3^-	0.837

*Unknown spin assignment

Calculating the single particle occupancies shows that the 3^- state has zero occupation of the $3s_{1/2}$ orbit:

$$\hat{N}[\pi^9(2p_{3/2}, 1f_{5/2}, 2p_{1/2}, 1g_{9/2}, 3s_{1/2})] = (3.4, 4.7, 0.4, 0.5, 0.0) \tag{15.5}$$

$$\hat{N}[\nu^7(2d_{5/2}, 3s_{1/2}, 2d_{3/2})] = (5.7, 1.1, 0.2). \tag{15.6}$$

An approximate diagram of these single-particle occupancies is shown in Figure 15.1. This is not surprising since the single particle energy of the $3s_{1/2}$ orbit is 9 MeV higher in single-particle energy (see Table 15.1). As a check, I also ran another calculation with the $3s_{1/2}$ removed from the proton space:

$$glepn43 = \pi^9(2p_{3/2}, 1f_{5/2}, 2p_{1/2}, 1g_{9/2}) \otimes \nu^7(2d_{5/2}, 3s_{1/2}, 2d_{3/2}). \tag{15.7}$$

The dimension was reduced to 13.4 million, and the low-lying energies were unchanged to the third digit.
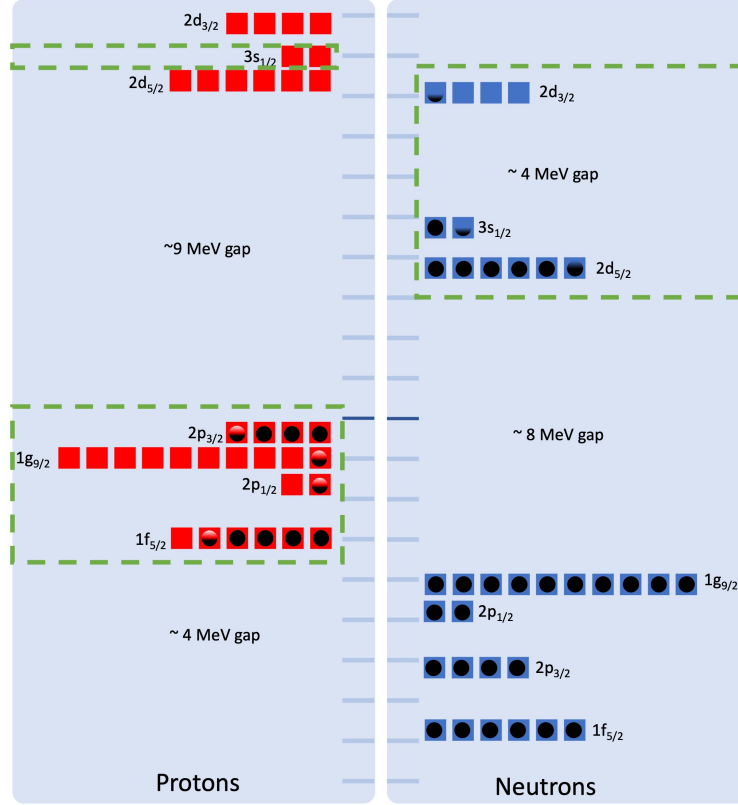
Figure 15.1: Ground state single-particle occupancy of ^{94}Rb resulting from the FCI calculation described in the text and given by equations (15.5) and (15.6). The green dashed boxes indicate the active orbits in the *glepn53* truncation. The order and spacing of the orbits in the figure are based on the effective single-particle energies (SPEs) of the interaction, and differ from the usual order. We can see that the $2p_{3/2}$ orbit fills before the $1g_{9/2}$ despite its higher SPE - this is in line with the expected ordering of the orbits and is realized by the residual two-body interaction.

15.3 ^{94}Sr low-lying structure with *glepn53* FCI

The M-scheme dimension of ^{94}Sr in the *glepn53* model space is 122,689,148 ($1.2 \cdot 10^8$). The low-lying spectra of this model can be extracted with commodity resources. BIGSTICK obtained the lowest 10 states in about 1.5 hrs on 1 HPC node with 36 cores. The proton and neutron spaces and their dimensions in the *glepn*53 model space are:

$$\pi^{10}(2p_{3/2}, 1f_{5/2}, 2p_{1/2}, 1g_{9/2}, 3s_{1/2})_{146,144} \tag{15.8}$$

$$\nu^{6}(2d_{5/2}, 3s_{1/2}, 2d_{3/2})_{142}. \tag{15.9}$$

Table 15.4: Low lying excitation energies and spin assignments of ^{94}Sr from experiment and the *glepn*53 FCI shell model calculation described in the text.

Excitation	Experiment		UPN		XPN	
	J_i^π	E_x	J_i^π	E_x	J_i^π	E_x
1	0_1^+	0.000	0_1^+	0.000	0_1^+	0.000
2	2_1^+	0.837	2_1^+	1.280	2_1^+	1.087
3	(3_1^-)	1.926	0_2^+	2.020	0_2^+	1.903
4	4_1^+	2.146	3_1^+	2.233	2_1^+	2.314
5	(2_2^+)	2.271	2_3^+	2.498	5_3^-	2.494
6	(3_2^-)	2.414	0_3^+	2.638	6_3^-	2.542
7	(4_1^-)	2.614	5_1^-	2.648	4_1^-	2.566
8	$*$	2.650	2_3^+	2.663	4_3^+	2.674
9	$4_2^{(+)}$	2.704	4_1^+	2.779	3_1^+	2.757
10	$*$	2.711	4_1^-	2.836	2_1^+	2.788

*Unknown spin assignment

15.4 Applying PANASh

Next, we can apply PANASh. There are two distinct strategies we can take. First, we can use the same truncated model space described above (15.2), and use the PANASh truncation to further reduce the dimension. For example, for ^{94}Rb the $Z_v = 9$ proton factors are computed in the proton-only part of the single particle space (15.4) with dimension 98,775. The $N_v = 7$ neutron factors are computed in the neutron-only space with dimension 119. The advantage of this is we will reach a much higher excitation level under the same computational limits. This strategy is not so useful for our needs since we only need the 3^- ground state. For the beta decay product ^{94}Sr we need levels up to around 8.5 MeV, thousands of levels.

The second strategy is to calculate the proton and neutron factors in the untruncated *glepn*77 model space (15.1), and to rely entirely on the PANASh truncation. The main advantage of this approach is to include the higher orbits which are fairly close in single-particle energy. The untruncated M-scheme dimension of the full *glepn* model space for ^{94}Rb is 442 billion.

The proton and neutron spaces and their dimensions are:

$$\pi^9(2p_{3/2}, 1f_{5/2}, 2p_{1/2}, 1g_{9/2}, 2d_{5/2}, 3s_{1/2}, 2d_{3/2})_{4,014,532} \tag{15.10}$$

$$\nu^{29}(2p_{3/2}, 1f_{5/2}, 2p_{1/2}, 1g_{9/2}, 2d_{5/2}, 3s_{1/2}, 2d_{3/2})_{26,566}. \tag{15.11}$$

The M-scheme dimension of ^{94}Sr in the *glepn*77 model space is 10,177,374,468,286, or about $1.0 \cdot 10^{13}$. The proton and neutron factor spaces and their dimensions are:

$$\pi^{10}(2p_{3/2}, 1f_{5/2}, 2p_{1/2}, 1g_{9/2}, 2d_{5/2}, 3s_{1/2}, 2d_{3/2})_{9,757,466} \tag{15.12}$$

$$\nu^{28}(2p_{3/2}, 1f_{5/2}, 2p_{1/2}, 1g_{9/2}, 2d_{5/2}, 3s_{1/2}, 2d_{3/2})_{119,994}. \tag{15.13}$$

Figure 15.2 shows a comparison of the low-lying states of ^{94}Sr computed with three different shell model truncations: (1) a PANASh calculation with *glepn*53 using 500 of 146k proton components and 142 of 142 neutron components, (2) a PANASh calculation with *glepn*77 using 500 of 9.8 M proton components and 500 of 120k neutron components, and finally (3) a FCI calculation *glepn*53 using the equivalent of all components for both protons and neutrons. Also shown are the limited number of experimentally observed levels. All three calculations reproduce the 2^+ first excited state, and show some variation of a deformed rotational spectra. All three predict a low-lying 3^+ state where the experiment asigns a 3^- state. The experiment reporting the parity of that state should be re-examined to investigate this discrepancy. Between the two PANASh calculations, the *glepn*53 model is showing a much higher level density below 4 MeV. This could be an indication that the space is more converged with the given fraction of basis components used in each calculation.

We can use the methods of Chapter 6 to compute the nuclear level density (NLD) and gamma-ray strength functions (GSF) of ^{94}Sr. In principle these can both be used as inputs to our Hauser-Feshbach calculations. However, the nuclear level densities obtained in our
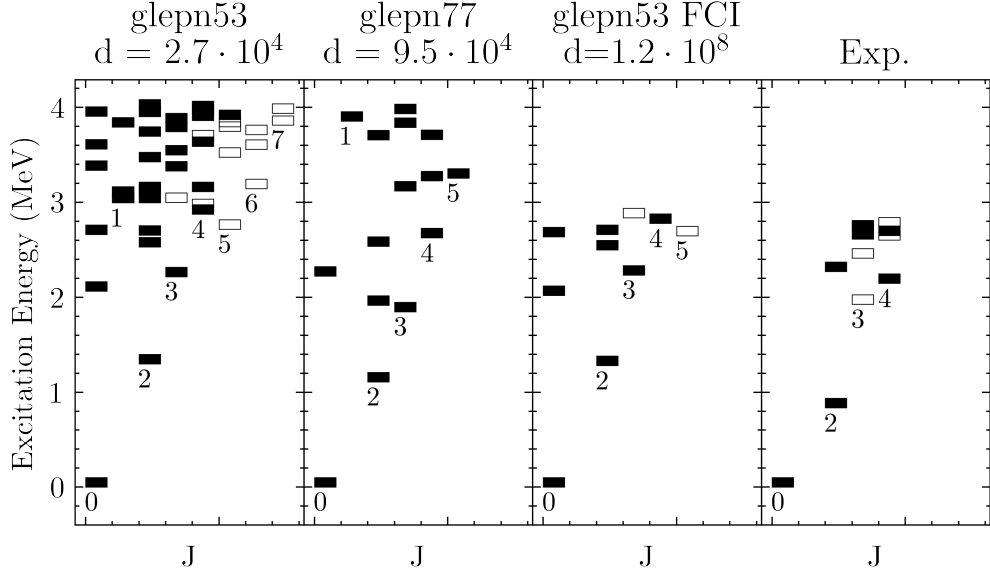
Figure 15.2: Low-lying evels in ^{94}Sr computed with three different truncation schemes, and compared to experiment. From left to right, the first two panels are PANASh calculations. *glepn*53 uses 500 of 146k proton components and 142 of 142 neutron components. glepn77 uses 500 of 9.8 M proton components and 500 of 120k neutron components. Finally, *glepn*53 FCI (untruncated model) uses the equivalent of all components for both protons and neutrons.

basis-reduced method do not perform as well as other methods such as the Lanczos moments method [214]. Instead, the real utility of our weak entanglement approximation and the PANASh code is to calculate the gamma-ray strength functions, which appear to be much more robust to basis reduction (see Figure 6.9).

We can still use the cumulative level density produced by our calculations as an indicator of the convergence of many states by comparing to experimentally measured levels. Figure 15.3 shows the nuclear level densities for our PANASh *glepn*53 with $m_p = 500$, $m_n = 142$ and *glepn*77 calculations with $m_p = 500$, $m_n = 500$. Also plotted are the cumulative number of known (experimentally measured) levels, and a constant temperature (CT) model with RIPL-3 parameters fit to the same data [48]. Since the CT model agrees well with the data, and we have reason to believe the truncated models will under-predict the level density, we use the CT model as a reference. Both of our PANASh models agree quite well with the
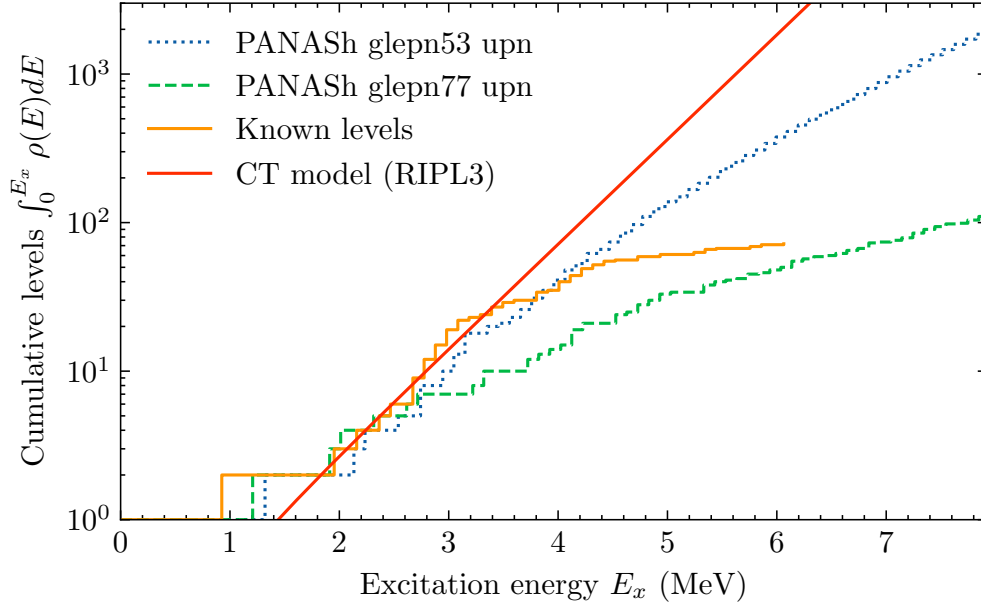
Figure 15.3: Cumulative number of levels in ^{94}Sr as computed by the nuclear shell model calculations described in the text. *glepn*53 uses 500 of 146 k proton components and 142 of 142 neutron components. *glepn*77 uses 500 of 9.8 M proton components and 500 of 120 k neutron components. The constant temperature (CT) model was computed using recommended parameters from the RIPL-3 database [48], which were fit to the known (measured) levels.

data up to about 2.8 MeV, and then begin to deviate.

Figure 15.4 presents the shell model M1 gamma-ray strength functions I calculated using the lowest 4,000 states of ^{94}Sr in the *glepn*53 model space with $f_p = 500/146k = 10^{-3}$ and $f_n = 142/142 = 1$. This generated more than 1.3 million downward transitions, which were processed into gamma-ray strength functions according to the methods of Chapter 6. Also included are the phenomenological GSF models (E1 and M1) which were fit to available data and global models in section 14.2. Two shell model gamma ray strength functions (M1) are shown. These are the two formulas for the GSF discussed in 6: the Oslo-experiment formula (M1 SM Oslo (*glepn*53)), and the proposed Hauser-Feshbach formula (M1 SM HF (*glepn*53)). Both use exactly the same set of shell model transition probabilities, and the only difference lies in the formula used to take the sums and averages.
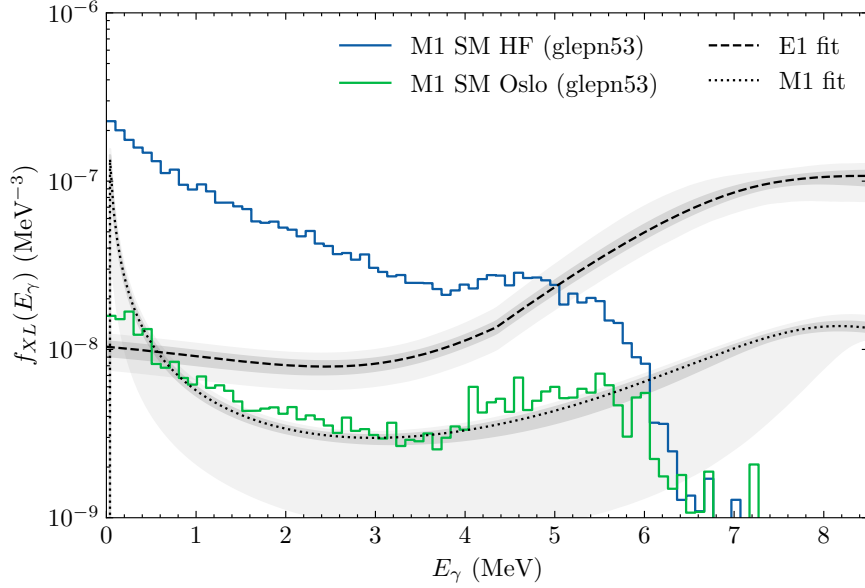
Figure 15.4: Gamma-ray strength functions for ^{94}Sr as computed by the nuclear shell model calculations described in the text. The shell model (SM) M1 gamma-ray strength functions are computed using the methods described in Chapter 6. In particular, I show both the Oslo-experiment formula from recent literature [97, 208, 184, 40, 260] and our proposed Hauser-Feshbach formula proposed in section 6.2.7. The grey bands are the same calculations from Figure 14.4 from the MCMC fit to experimental E1 data and M1 models.

The shell model GSF calculated using the Oslo-experiment formula (equation (6.43)) shows excellent agreement with the phenomenological model fit to agree with the global SMLO and D1M+QRPA models shown in Figure 14.3. This is expected because those models were modified with a low-energy enhancement to match established M1 shell model calculations [112]. As discussed in Section 6.2.7, however, this may not be the correct form of the GSF to use in Hauser-Feshbach calculations. If our proposed formula (6.50), plotted as "M1 SM HF *glepn*53" turns out to be the correct one, then Figure 15.4 shows how significant the modification to the GSF could be.

The next step is to use this M1 SM GSF in the Hauser-Feshbach calculation to see how it affects the BDNE of ^{94}Rb. I repeated the calculations described in section 14.4: I use the same E1 GSF parameters as before, but replace the phenomonological M1 GSF with the microscopic M1 GSF computed with the shell model. I run the HF decays from each group

of spin-parity combinations for allowed and forbidden decay, and finally I apply the PTWFC factors. The results are shown in Figure 15.5. The results are promising. The allowed decays
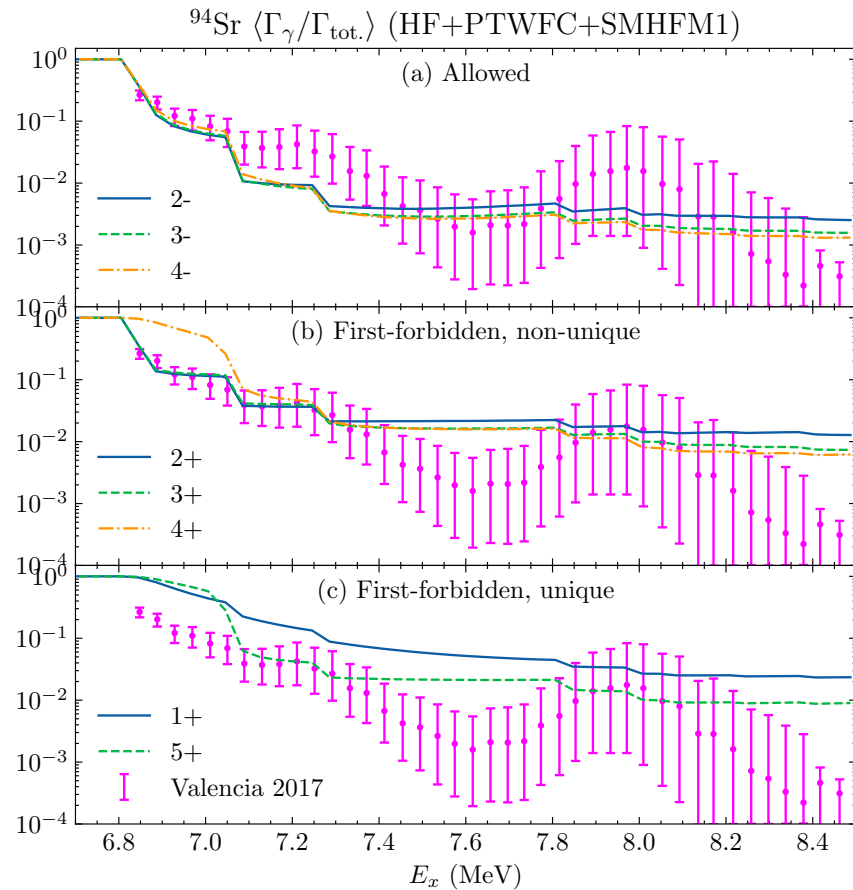

Figure 15.5: Same as Figure 14.9 except the M1 GSF is replaced with the shell model GSF "M1 SM HF (*glepn*53)" shown in Figure 15.4. Compared to calculations performed with the published M1 GSF based on the Oslo-measurement formula, calculations performed with the proposed GSF greatly enhance the gamma emission in ^{94}Sr.

are now consistent with the experimental error bars everywhere except between 7.1 MeV and 7.4 MeV, whereas with the previous GSF the discrepancy was between 6.9 MeV and 7.5 MeV (Figure 14.9). The agreement for the allowed decays is also improved across the entire energy range. Overall, the effect is to increase the agreement of the statistical model with the data, and to reduce the need for changes to the forbidden decay contribution.

In summary, a change to the definition of the shell model gamma ray strength function proposed in Chapter 6, if validated, explains most of the remaining discrepancy between

the statistical model and the measured beta-delayed gamma emission. This would support hypothesis 1 given in Chapter 12 and would reduce the contributions required from forbidden decays to make up the difference (hypothsis 2). Further investigation is needed on both fronts: a rigorous test of microscopic gamma-ray strength functions for or against the proposed modification, and a microscopic calculation of the contribution from forbidden beta decays. These are beyond the scope of this dissertation, but a path forward is discussed in the next chapter.

Chapter 16

Summary and Outlook

The objective of this final part of the dissertation has been to improve our understanding of beta-delayed neutron emission, using the decay of ^{94}Rb as a case study.

I have successfully combined the nuclear shell model methods from Part I with the statistical nuclear reaction methods from Part II. This has enabled a treatment of beta delayed neutron emission by directly interfacing shell model structure calculations with a Hauser-Feshbach reaction code. Along the way, I introduce a new method for implementing Porter-Thomas width fluctuations of neutron widths, which to my knowledge is a unique approach and generally applicable. This effect is important for proper treatment of gamma emission above the neutron emission threshold and can increase the gamma emission probability by two order of magnitude. I intent to work with developers of the `YAHFC` HF code to implement these corrections in their code.

Additionally, the newly proposed form of the microscopic gamma-ray strength function from Chapter 6 greatly improves the statistical model's ability to reproduce the data of Valencia et al. [286]. Further work is required to test this new proposal before a final conclusion can be made. If this new method for determining gamma ray strength functions turns out to be

valid, it will have significant impact on other areas of nuclear reactions. In particular, neutron capture reactions will be greatly enhanced, with important implications for astrophysical simulations. These findings support hypothesis 1: that the gamma-ray strength function is stronger than previously assumed. However, this does not completely resolve the discrepancy. The analysis presented in Chapter 15 suggests that it must be combined with hypothesis 2: that there is some forbidden decay strength, which I have shown would enhance the emission of beta-delayed gammas and reduce the model discrepancy. To make a final conclusion on this, further investigation is required.

These developments and the case study of beta-delayed neutron emission of ^{94}Rb have demonstrated the potential for a unified approach combining nuclear structure and statistical nuclear reactions relying on advanced shell model basis reduction methods. The shell model calculations performed for these nuclear structure inputs were made possible using basis-reduction techniques in Part I, and I have made significant progress towards a fully microscopic description of the relevant nuclear structure. In the rest of this chapter, I will detail ongoing and future work that will continue this effort, including thorough investigations of hypotheses 2 and 3.

16.1 ^{94}Rb to ^{94}Sr beta decay distribution

All calculations of the γ and neutron total widths in the previous chapters have assumed that the compound nucleus (^{94}Sr) is populated by beta decay with states of energy E_x, spin J, and parity π. We selected specific J, π combinations to model corresponding to particular types of beta decay transitions (allowed, forbidden, etc.). This dependence can be expressed as $\Gamma(E_x, J, \pi)$. In an actual beta decay, the distribution of the states populated, $F(E_x, J, \pi)$,

will determine the actual total widths by the relation:

$$\Gamma(E_x) = \sum_{J,\pi} F(E_x, J, \pi)\Gamma(E_x, J, \pi), \qquad (16.1)$$

where $\sum_{J,\pi} F(E_x, J, \pi) = 1$. To calculate the distribution of spins and parities $F(E_x, J, \pi)$ populated in ^{94}Sr following the beta decay of ^{94}Rb, one would use the formalism discussed in section 13.4. We have left this to future work for two reasons.

First, the distribution of spin-parity combinations accessible by allowed decays (Fermi and Gamow-Teller) shows very little dependence on the spins. This means that determining the exact distribution of the allowed decays will not provide any additional insight. However, if we wanted to calculate this distribution, we would also need to expand the single-particle model space beyond *glepn*53. Essentially, the *glepn*53 proton and neutron single particle states are orthogonal below 9 MeV. The only orbital shared between the proton and neutron subspaces is the $3s_{1/2}$. (See Figure 15.1.) A neutron can only transfer to this orbit by allowed decay if the transition is Fermi ($\Delta J = 0$ and no spin change). Our shell model calculations show very little occupation of this orbit in ^{94}Sr in the window of interest up to 8.5 MeV, which is not surprising considering the 9 MeV gap between the $2p_{3/2}$ and $2d_{5/2}$ proton single particle states.

The most straightforward remedy would be to use the full *glepn*77 space. But if this turns out to be too costly even with the PANASh basis reduction, *glepn*57 may also prove fruitful. This model space would keep the proton space unchanged and open up the lower 4 neutron orbits. The approach is supported by evidence that Gamow-Teller transitions in this region proceed through the decay of a neutron in the ^{78}Ni-core [192].

The second reason for postponing this calculation is that the formalism required to properly treat forbidden decays is beyond the scope of this work. It requires implementation of:

1. additional momentum-dependent electroweak operators

2. modification of some operators by perturbation from the charge-distribution of the nucleus

3. careful treatment of the small parameters which are, in addition to the lepton momenta, the electron rest mass, the electron kinetic energy, and αZ, which for rubidium is $37/137 \approx 0.27$

Nonetheless, in Chapter 17 I have aggregated the necessary formalism, constants, and approximations. Importantly, I have expressed the general energy-dependent shape factor $C(W)$ in terms of electroweak operators from Chapter 2. This means that the core subroutiens from the `dmscatter` can be reused in a new code capable of computing high-precision beta decay transition probabilities for medium to heavy mass nuclei.

16.2 Beta decay selectivity: compound nuclear versus direct reactions

The final *hypothesis. 3: Beta decay does not lead to a compound nucleus* can be tested within the framework of the nuclear shell model by analyzing correlations between states populated by beta decay and their electromagnetic decay properties.

In order for a compound nucleus to form, it must evolve from some asymptotic initial state with special structure (e.g. a nuclear ground state plus a plane wave projectile, or simply a nuclear ground state in the case of beta decay) to a randomized, statistical state with very low probability for one particular nuclear configuration. When this is not the case, and only a small number of degrees of freedom are excited in the target nucleus, we are dealing with a direct reaction process. This can be the case if there is a strong overlap between

the asymptotic initial state and (through an electromagnetic transition) a low-lying state in the $A + 1$ system [306]. Statistical reaction codes describe the intermediate process between direct and compound nucleus processes in the context of pre-equilibrium decay [100]. This process is modeled using an exiton model [243, 100, 215]: the first configurations of neutron capture are imagined as a one-particle excitation of the $A+1$ system. Two-body interactions then evolve this state adiabatically to configurations with more and more $n + 1$-particle n-hole configurations, until the energy of the incoming neutron is evenly spread amongst all nucleons. There is a chance for one nucleon to escape at each step in the process, hence "pre-equilibrium emission", with the probability declining as the energy is distributed amongst the nucleons At the end of the pre-equilibrium process, the system reaches equilibrium: a compound nuclear state.

By using Hauser-Feshbach theory to describe beta-delayed neutron emission, and decay of beta decay products in general, we are implicitly assuming this transition from the special structure of the asymptotic initial state to a statistical, equilibrated compound nucleus. In the case of beta decay, the initial state is even simpler than the asymptotic state of neutron capture: it is a nuclear ground state. The beta decay transition operators also have relatively simple structure, and can appear as one-particle one-hole excitations in the final state nucleus. This raises the possibility that (1) beta decay may selectively populate states with simple particle-hole structure, (2) these states may have especially strong electromagnetic character, so that (3) the beta decay products may decay by a process more analogous to direct reactions than to compound nuclear reactions. If this is the case, then it would point to a non-statistical nature of beta-delayed neutron emission. This is known to be the case for at least some systems near closed shells [120, 135].

The shell model can test this idea. The beta decay transition probabilities can be represented as a transition matrix F_{fi} where i is the ground state in ^{94}Rb and f are all possible final states in ^{94}Sr. The matrix elements F_{fi} are simply the transition probabilities given by

equation (13.19). We would then matrix multiply this with the matrix $G_{f'i'}$ of gamma-decay transition probabilities given by equation (6.18) to obtain the total probability of beta-delayed gamma decay to final states f' in ^{94}Sr:

$$P_{f'i}^{(\gamma)} = \sum_f \delta_{i'f} G_{f'i'} F_{fi}. \tag{16.2}$$

This is the probability of beta-delayed gamma emission in the absence of other decay channels. Most notably it omits competition with neutron emission. However, if $P_{f'i}^{(\gamma)}$ is highly localized to a small number of final states f', that would indicate strong correlations between states populated by beta decay and states with strong electromagnetic collectivity. This alone would support the possibilities (1) and (2) from the previous paragraph. To investigate point (3), one could estimate the mixing of these selective states with nearby states via the Hamiltonian two-body matrix elements $\hat{V}_{2b}$:

$$\text{two-body mixing} = \rho(E_{f'} + \delta E)|\langle(\Psi_{f'} + \delta E)|\hat{V}_{2b}|\Psi_{f'}\rangle|^2, \tag{16.3}$$

where $\rho(E_{f'} + \delta E)$ is the density of states that can be reached by the two-body matrix elements. If these two-body mixing amplitudes are strong compared to the $P_{f'i}^{(\gamma)}$ matrix elements, then formation of compound nuclear states is likely.

16.3   Shell model uncertainty quantification

Another avenue to improve this analysis is to account for the uncertainty in the nuclear shell model. Efforts to do uncertainty quantification (UQ) with the nuclear shell model is a relatively new venture [94, 95]. I expect the future of shell model uncertainty quantification will begin at interaction creation. For example, MCMC methods could be applied when fitting phenomenological interactions to observables, whether that be with direct shell model

methods or model emulators. Having an uncertainty quantified shell model interaction would make UQ of observables like the GSF straightforward.

16.4   Discrete branching ratios

Our approach so far has been to use the shell model to compute the statistical behaviour of the decaying nucleus by computing averages over many branching ratios. This inevitably introduces some approximation because it ignores correlations and the distribution of individual widths that give rise to Porter-Thomas fluctuations. Furthermore, it is an artificial restriction within the framework of the nuclear shell model.

An alternative approach is to use the shell model to compute the branching ratios of all levels (simply a matter of normalizing the transition probabilities). This would allow seamless integration with a Monte Carlo Hauser Feshbach codes like `YAHFC` which can read-in discrete levels and branching ratios. From the HF code perspective, we would treat the shell model levels and branching ratios as if they were experimentally measured levels. Of course, known levels and branching ratios should be used first where available.

Chapter 17

Future work: Higher Order Corrections to Beta Decay

This chapter reviews and aggregates the theory necessary for calculating higher order corrections to nuclear beta decay using the shell model.

The definitive text on beta decay formalism is the book by Behrens and Burhing [24], a 600-page treatise on the subject. For some time, the only competing formalism was that of Holstein [143]. In a recent review of the subject by Hayen et al. [132], the two formalisms are compared. To summarize, Behrens and Buhring provide the more complete and rigorous treatment, while Holstein's treatment benefits from its more transparent presentation of different terms - yet is ultimately hindered by its approximations. Some effects like Coulomb corrections need to be added back in, which confuses the interaction of various small terms. I therefore adopt the formalism of Behrens and Buhring.

In this chapter I (1) present the main results relevant for first forbidden decay of medium-mass nuclei to first order, and (2) express the relevant nuclear operators in terms of those of Chapter 2: the search for dark matter. In this way, I have prepared the way for imple-

mentation of a new code to calculate forbidden bet decay transition probabilities using our existing shell model framework.

17.1 Weak interaction

Assuming a pure vector plus axial-vector current, the beta decay Hamiltonian density can be written as [24]:

$$H_\beta = -\frac{G_\beta}{\sqrt{2}} \left[J_\mu^\dagger(x) L_\mu(x) + h.c. \right],$$ (17.1)

where G_β is the coupling constant of a single nucleon, $J_\mu(x)$ is the nuclear current,

$$J_\mu^\dagger(x) = i\bar{\psi}_p(x)\gamma_\mu(1 + g_A\gamma_5)\psi_n(x),$$ (17.2)

and the lepton current is:

$$L_\mu(x) = i\bar{\psi}_{\nu_e}\gamma_\mu(1 + \gamma_5)\psi_e(x).$$ (17.3)

γ_λ are Dirac matrices. The field operators $\psi(x)$ can be written in terms of plane waves of momentum creation and annihilation operators.

The nuclear current must recieve special treatment due to a number of theoretical challenges due to the strong force:

1. The nucleons in a nucleus are not plane waves, but bound states

2. Many body effects complicate the Hamiltonian, adding additional terms

The following generalization is therefore adopted:

$$J_\mu^\dagger(x) = \langle f | V_\mu(x) + A_\mu(x) | i \rangle = e^{i(p_i - p_f)x} \langle f | V_\mu(0) + A_\mu(0) | i \rangle, \tag{17.4}$$

where the second equality is due to translational invariance of the interaction.

The next development is to make a multipole expansion of the interaction.

17.2   Multipole expansion

A well known expansion is a plane wave in terms of spherical functions:

$$e^{i\boldsymbol{q}\cdot\boldsymbol{r}} = 4\pi \sum_{LM} (i)^L j_L(\boldsymbol{q}\cdot\boldsymbol{r}) Y_L^{M*}(\hat{q}) Y_L^M(\hat{r}). \tag{17.5}$$

The spherical Bessel functions have the expansion:

$$j_L(qr) = \frac{(qr)^L}{(2L+1)!!} \sum_{n=0} \frac{(-1)^n (2L+1)!!}{(2n)!!(2L+2n+1)!!} (qr)^{2n}. \tag{17.6}$$

The first two terms are:

$$j_L(qr) = \frac{(qr)^L}{(2L+1)!!} \left(1 - \frac{(qr)^2}{2(2L+3)} + \dots \right). \tag{17.7}$$

I have included a plot of the spherical Bessel functions in figure 17.1.

Stech and Schulke [270, 259] first introduced such an expansion for beta decay:

$$\langle i | V_0(0) + A_0(0) | i \rangle = \sum_{LM} (-1)^{J_f - M_f} [J_i] \sqrt{4\pi} \tag{17.8}$$
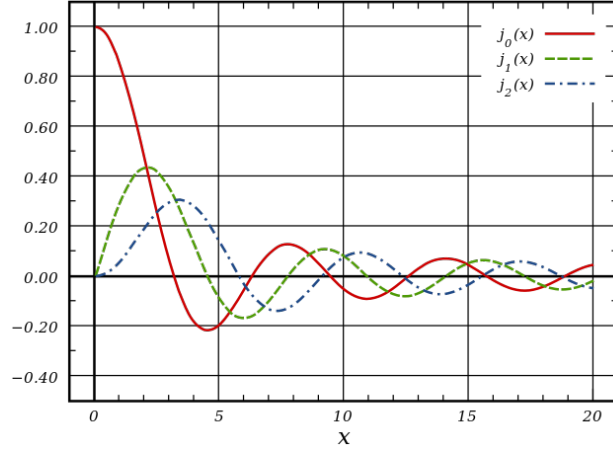
Figure 17.1: The first few spherical Bessel functions $j_L(x)$.

$$\times \begin{pmatrix} J_f & L & J_i \\ -M_f & M & M_i \end{pmatrix} Y_L^{*M}(\hat{q}) \frac{(qR)^L}{(2L+1)!!} F_L(q^2) \tag{17.9}$$

$$\langle i| \vec{V}(0) + \vec{A}(0) |i\rangle = \sum_{KLM} (-1)^{J_f - M_f} [J_i] \sqrt{4\pi} \tag{17.10}$$

$$\times \begin{pmatrix} J_f & K & J_i \\ -M_f & M & M_i \end{pmatrix} \vec{Y}_{KL}^{*M}(\hat{q}) \frac{(qR)^L}{(2L+1)!!} F_{KL}(q^2), \tag{17.11}$$

where the form factors $F_L(q^2)$ and $F_{KL}(q^2)$ are related to reduced matrix elements of the interaction. They have the form:

$$F_L(q^2) = \sqrt{4\pi} [J_i]^{-1} \frac{(2L+1)!!}{(qR)^L}$$
$$\times \langle \Psi_f || \sum_k i^L j_L(qx_k) Y_L(\hat{x}_k) \left[1 + \frac{g_A}{2m_p i} \vec{\nabla}_k \cdot \vec{\sigma}_k \right] \tau_+^k || \Psi_i \rangle, \tag{17.12}$$

$$F_{KL}(q^2) = \sqrt{4\pi}[J_i]^{-1}\frac{(2L+1)!!}{(qR)^L}$$

$$\times \langle\Psi_f||\left\{\sum_k i^L j_L(qx_k)\vec{Y}_{KL}(\hat{x}_k)\left[\frac{1}{2m_p i}\vec{\nabla}_k + g_A\vec{\sigma}_k\right]\tau^k_+\right.$$

$$+ i\sqrt{6}\sum_j(-1)^{L-K}[j]C(1jL|00)\begin{Bmatrix}1 & 1 & 1\\ j & L & K\end{Bmatrix}$$

$$\left.\times \sum_k qj_j(qx_k)(i)^j\vec{Y}_{Kj}(\hat{x}_k)\cdot\left(\frac{\mu}{2m_p i}\sigma_k\right)\tau^k_+\right\}||\Psi_i\rangle. \tag{17.13}$$

By an intermediate step not shown, irreducible tensor operators are substituted, adding an index to the form factors:

$$F_{KLs} = \begin{cases}F_L\delta_{KL}, & s = 0\\ F_{KL}, & s = 1.\end{cases} \tag{17.14}$$

The form factor coefficients can be then expanded in power of (qR) as:

$$F_{KLs}(\boldsymbol{q}^2) = \sum_n \frac{(-1)^n(2L+1)!!}{(2n)!!(2L+2n+1)!!}(qR)^{2n}F^{(n)}_{KLs}. \tag{17.15}$$

Usually $qR << 1$, and so one can truncate the series:

$$F_{KLs}(\boldsymbol{q}^2) = F^{(0)}_{KLs} - \frac{(qR)^2}{2(2L+3)}F^{(1)}_{KLs} + ... \tag{17.16}$$

For light cases, only the first term need be retained. But for large-Z systems [270],

$$qR \sim W_0R + \frac{3}{2}\alpha Z, \tag{17.17}$$

and so the second term in the expansion may also be needed.

17.3 Behrens and Buhring $M_K(k_e, k_\nu)$ and $m_K(k_e, k_\nu)$

The shape factor $C(W)$ is a sum of terms $M_K(k_e, k_\nu)$ and $m_K(k_e, k_\nu)$, which I denote as M_{K,k_e,k_ν} and m_{K,k_e,k_ν}:

$$C(W) = \sum_{k_e,k_\nu,K} \lambda_{k_e} \left[M^2_{K,k_e,k_\nu} + m^2_{K,k_e,k_\nu} - \frac{2\gamma_{k_e}}{k_e W} M_{K,k_e,k_nu} m_{K,k_e,k_\nu} \right]. \tag{17.18}$$

These M_{K,k_e,k_ν} and m_{K,k_e,k_ν} quantities are functions of the (shape) form factors $F^{(N)}_{KLs}$. The indices k_e and k_ν ($k = 1, 2, 3, ...$) are for the momentum expansions of the electron and neutrino, respectively. The index K is the order of forbiddeness of the transition. The most dominant terms are those with the lowest $K = K_{min}, K_{min} + 1$; $K_{min} = \Delta J$, and the lowest k_e and k_ν:

$$k_e + k_\nu = K + 1, K + 2. \tag{17.19}$$

The leading order terms are the well-known Fermi ($J^{\Delta\pi} = 0^+$),

$$M_{0,1,1} = {}^V F^{(0)}_{000}; \tag{17.20}$$

Gamow-Teller ($J^{\Delta\pi} = 0^+, 1^+$):

$$M_{1,1,1} = -{}^A F^{(0)}_{101}; \tag{17.21}$$

first-forbidden non-unique ($J^{\Delta\pi} = 0^-, 1^-$):

$$M_{0,1,1} = {}^A F^{(0)}_{000} - \frac{1}{3}\alpha Z \, {}^A F^{(0)}_{011}(1,1,1,1) - \frac{1}{3}W_0 R \, {}^A F^{(0)}_{011} \tag{17.22}$$

$$m_{0,1,1} = -\frac{1}{3}m_e R \, {}^A F^{(0)}_{011} \tag{17.23}$$

and first-forbidden unique ($J^{\Delta\pi} = 2^-$):

$$M_{2,1,2} = -\frac{1}{3}p_\nu R\ ^A F_{211}^{(0)} \tag{17.24}$$

$$M_{2,2,1} = -\frac{1}{3}p_e R\ ^A F_{211}^{(0)}. \tag{17.25}$$

We have the Coulomb function ratio:

$$\lambda_{k_e} = \frac{f_{k_e-1}(Z,W)}{f_0(Z,W)}, \tag{17.26}$$

as a function of the generalized Fermi function:

$$f_{k_e-1}(Z,W) = 4^{k_e-1}(2k_e)(k_e + \gamma_{k_e})[(2k_e - 1)!!]^2(2(W^2 - 1)^{1/2}R/\hbar)^{2(\gamma_{k_e} - k_e)}$$
$$\times \left(\frac{|\Gamma(\gamma_{k_e} + iy)|}{\Gamma(1 + 2\gamma_{k_e})}\right)^2 \tag{17.27}$$

The helper functions used are $\gamma_{k_e} = [k_e^2 - (\alpha Z)^2]^{1/2}$ and $y = \frac{\alpha ZW}{pc}$. Besides [23, 24], the full expressions for M and m are reproduced in [123].

The general approach to calculations using the BB formalism is to identify the relevant approximations one can take for the nucleus of interest (e.g. infinite mass, or small Z approximations), then throw out the corresponding small terms.

17.3.1   Form factor integral forms

Additional notation is used to as a shorthand for integrals correcting the nuclear form factors for the nuclear charge distribution. We define form factor coefficients [23]:

$$F_{KLs}^{(N)}(k_e, m, n, \rho) = \int_0^\infty J(q)F_{KLs}(q^2)q^2 dq, \tag{17.28}$$

where

$$J(q) = \frac{2}{\pi} \frac{(qR)^L}{(2L+1)!!} \int_0^\infty \left(\frac{r}{R}\right)^{L+2N} I(k_e, m, n, \rho, r) j_L(qr) r^2 dr. \tag{17.29}$$

The quantities $I(k_e, m, n, \rho; r)$ are lengthy functions of the radial coordinate r and the nuclear radius parameter R. When $\rho = 0$ (equivalently $Z = 0$), $I(k_e, m, n, \rho = 0; r) = 1$. As an example of the type of functions I take, in the case of a uniform charge distribution,

$$I(k, 1, 1, 1; r) = \begin{cases} \frac{3}{2} - \frac{2k+1}{2(2k+3)} \left(\frac{r}{R}\right)^2, & 0 \le r \le R \\ \frac{2k+1}{2k} \frac{R}{r} - \frac{3}{2k(2k+3)} \left(\frac{R}{r}\right)^{2k+1} & R \le r. \end{cases} \tag{17.30}$$

BB tabulate these functions for various charge distribution models.

17.3.2 Relation between Behrens and Buhring and CLEM operators

Modern EFT theories interested in electroweak forces (e.g. [118]) have used the formalism following Walecka (e.g. see [67]), which I refer to as the CLEM (Coulomb, longitudinal, transverse-electric, and transverse-magnetic) operators. Behrens and Buhring (BB) [24] provide the relation between the two multipole expansions, which I will repeat here in the notation of [67].

The BB form factors with the impulse approximation in terms of nuclear matrix elements is expressed as:

$$F_{JLs}(\boldsymbol{q}^2) = (-1)^{J-L} \mathcal{M}_{JLs}(\boldsymbol{q}^2). \tag{17.31}$$

The multipole operators of Walecka being the Coulomb, longitudinal, transverse-electric,

and transverse-magnetic are all defined in terms of the spherical Bessel functions, spherical harmonics, and vector spherical harmonics [67]:

$$M_J^{M_J}(q\boldsymbol{x}) \equiv j_J(qx)Y_J^{M_J}(\Omega_x), \tag{17.32}$$

$$\mathbf{M_{JL}^{M_J}}(\mathbf{qx}) \equiv j_L(qx)\boldsymbol{Y}_{JL1}^{M_J}(\Omega_x). \tag{17.33}$$

We have, in terms of the vector and axial-vector currents $\hat{\boldsymbol{\mathcal{J}}} = \hat{\boldsymbol{V}} + \hat{\boldsymbol{A}}$ [24], with $q = |\boldsymbol{q}|$,

$$\hat{C}_J^M(q) = \int d\boldsymbol{x} M_J^{M_J} \hat{\mathcal{J}}_0(\boldsymbol{x}) \tag{17.34}$$

$$\hat{L}_J^{M_J}(q) = \int d\boldsymbol{x} [\frac{i}{q}\nabla M_J^{M_J}(q\boldsymbol{x})] \cdot \hat{\boldsymbol{\mathcal{J}}}(\boldsymbol{x}) \tag{17.35}$$

$$\hat{E}_J^{M_J}(q) = \int d\boldsymbol{x} [\frac{1}{q}\nabla \times \boldsymbol{M}_{JJ}^{M_J}(q\boldsymbol{x})] \cdot \hat{\boldsymbol{\mathcal{J}}}(\boldsymbol{x}) \tag{17.36}$$

$$\hat{M}_J^{M_J}(q) = \int d\boldsymbol{x} \boldsymbol{M}_{JJ}^{M_J}(q\boldsymbol{x}) \cdot \hat{\boldsymbol{\mathcal{J}}}(\boldsymbol{x}). \tag{17.37}$$

The relations to the BB form factors $F_{JLs}(\boldsymbol{q}^2)$ are (Eqs. (9.74) - (9.77) in [24]):

$$\langle J_f||i^J\hat{C}_J||J_i\rangle = \sqrt{\frac{2J_i+1}{4\pi}}\frac{(qR)^J}{(2J+1)!!}F_{JJ0}(\boldsymbol{q}^2) \tag{17.38}$$

$$\langle J_f||i^J\hat{L}_J||J_i\rangle = -\sqrt{\frac{2J_i+1}{4\pi}}\left\{\frac{(qR)^{J-1}}{(2J-1)!!}\sqrt{\frac{J}{2J+1}}F_{J,J-1,1}(\boldsymbol{q}^2)\right. \tag{17.39}$$

$$\left. -\frac{(qR)^{J+1}}{(2J+3)!!}\sqrt{\frac{J+1}{2J+1}}F_{J,J+1,1}(\boldsymbol{q}^2)\right\} \tag{17.40}$$

$$\langle J_f||i^J\hat{E}_J||J_i\rangle = -\sqrt{\frac{2J_i+1}{4\pi}}\left\{\frac{(qR)^{J-1}}{(2J-1)!!}\sqrt{\frac{J+1}{2J+1}}F_{J,J-1,1}(\boldsymbol{q}^2)\right. \tag{17.41}$$

$$\left. +\frac{(qR)^{J+1}}{(2J+3)!!}\sqrt{\frac{J}{2J+1}}F_{J,J+1,1}(\boldsymbol{q}^2)\right\} \tag{17.42}$$

$$\langle J_f||i^J\hat{M}_J||J_i\rangle = \sqrt{\frac{2J_i+1}{4\pi}}\frac{(qR)^J}{(2J+1)!!}F_{JJ1}(\boldsymbol{q}^2). \tag{17.43}$$

Note that the i^J and i^{K-1} factors on the LHS is needed if single particle wave functions on both sides are used.

To use the single-particle matrix elements from Donnelly and Haxton [67], we will want to invert the relations of (17.38)-(17.43).

$$F_{JJ0}(\boldsymbol{q}^2) = \sqrt{4\pi}[J_i]^{-1}\frac{(2J+1)!!}{(qR)^J}\langle J_f||i^J\hat{C}_J||J_i\rangle \tag{17.44}$$

$$F_{J,J-1,1}(\boldsymbol{q}^2) = -\sqrt{4\pi}[J_i]^{-1}\frac{(2J+1)!!}{(qR)^{J-1}}\left[\sqrt{\frac{J}{2J+1}}\langle J_f||i^J\hat{L}_J||J_i\rangle\right. \tag{17.45}$$

$$\left.+\sqrt{\frac{J+1}{2J+1}}\langle J_f||i^J\hat{E}_J||J_i\rangle\right] \tag{17.46}$$

$$F_{J,J+1,1}(\boldsymbol{q}^2) = -\sqrt{4\pi}[J_i]^{-1}\frac{(2J+1)!!}{(qR)^{J+1}}\left[\sqrt{\frac{J+1}{2J+1}}\langle J_f||i^J\hat{L}_J||J_i\rangle\right. \tag{17.47}$$

$$\left.-\sqrt{\frac{J}{2J+1}}\langle J_f||i^J\hat{E}_J||J_i\rangle\right] \tag{17.48}$$

$$F_{JJ1}(\boldsymbol{q}^2) = \sqrt{4\pi}[J_i]^{-1}\frac{(2J+1)!!}{(qR)^J}\langle J_f||i^J\hat{M}_J||J_i\rangle\,. \tag{17.49}$$

17.4   Matrix elements of the CLEM operators

The seven basic electroweak operators M, Δ, Δ', Σ, Σ', Σ'', and Ω can be used in a harmonic oscillator basis to obtain closed-form matrix elements of such transitions. And, since the weak interaction density is related to the electromagnetic interaction density, a common choice is to use the Coulomb, Longitudinal, Electric, and Magnetic operators from standard multipole analysis of, e.g. electron scattering on nuclei [68]. (Conserved-vector-current (CVC) theory tells us that the matrix elements in the weak processes due to vector current are identical to those in the electromagnetic process.) In this section I will restate these expressions, while realizing them with relevant values to this study.

The relevant equations from Donnelly and Haxton [67] are (20a-g), which I will first list, and then digest. Other references are [211, 67].

Vector (General)

$$C_{JM_J;TM_T}(qr) = F_1^{(T)} M_J^{M_J}(qr) I_T^{M_T} \tag{17.50}$$

$$L_{JM_J;TM_T}(qr) = \frac{q_0}{q} C_{JM_J;TM_T}(qr) \tag{17.51}$$

$$E_{JM_J;TM_T}(qr) = \frac{q}{m_N} \left[F_1^{(T)} \Delta_J'^{M_J}(qr) + \frac{1}{2} \mu^{(T)} \Sigma_J^{M_J}(qr) \right] I_T^{M_T} \tag{17.52}$$

$$iM_{JM_J;TM_T}(qr) = \frac{q}{m_N} \left[F_1^{(T)} \Delta_J^{M_J}(qr) - \frac{1}{2} \mu^{(T)} \Sigma_J'^{M_J}(qr) \right] I_T^{M_T} \tag{17.53}$$

where, besides the coupling constants $F_X^{(T)}$, we have used the isospin operator:

$$I_T^{M_T} \equiv \frac{1}{2} \begin{cases} 1 & T = 0, M_T = 0 \\ \tau_0 = \tau_3 & T = 1, M_T = 0 \\ \tau^{\pm 1} = \pm \frac{1}{\sqrt{2}}(\tau_1 \pm i\tau_2) & T = 1, M_T = \pm 1 \end{cases} \tag{17.54}$$

Axial-vector (General)

$$iC_{JM_J;TM_T}(qr) = \frac{q}{m_N} \left[F_A^{(T)} \Omega_J'^{M_J}(qr) + \frac{1}{2} q_0 F_P^{(T)} \Sigma_J''^{M_J}(qr) \right] I_T^{M_T} \tag{17.55}$$

$$-iL_{JM_J;TM_T}(qr) = \left(F_A^{(T)} - \frac{q^2}{2m_N} F_P^{(T)} \right) \Sigma_J''^{M_J}(qr) I_T^{M_T} \tag{17.56}$$

$$-iE_{JM_J;TM_T}(qr) = F_A^{(T)} \Sigma_J'^{M_J}(qr) I_T^{M_T} \tag{17.57}$$

$$M_{JM_J;TM_T}(qr) = F_A^{(T)} \Sigma_J^{M_J}(qr) I_T^{M_T} \tag{17.58}$$

The $q_0 = -E$ factor is the time-component of the momentum transfer four-vector [67]. The expression for the Coulomb operator, taken from Donnely and Haxton [67], differs in convention from the expression of both Connell [211] and Glick and Magic [102]. The above

uses $\Omega' = \Omega + \frac{1}{2}\Sigma''$. I will switch to the convention of the latter, leading to:

$$iC_{JM_J;TM_T}(qr) = \frac{q}{m_N}\left[F_A^{(T)}\Omega_J^{M_J}(qr) + \frac{1}{2}(F_A^{(T)} + q_0 F_P^{(T)})\Sigma_J''^{M_J}(qr)\right]I_T^{M_T}. \tag{17.59}$$

Another difference between the sources is conventional: whether the isospin operator is included in the definition of the CLEM operators.

17.4.1   Coupling constants

For the coupling constants $F_X^{(T)}$ and $\mu^{(T)} = F_1^{(T)} + 2m_N F_2^{(T)}$, Donnely and Haxton [67] refer us to Connell [211]. There is also a discussion of these coupling constants in [68]. Each coupling constant has momentum dependence:

$$F_X^{(T)}(q^2) \propto \left[1 + \frac{q^2}{(855\text{MeV})^2}\right]^{-2}, \tag{17.60}$$

which is essentially constant for any momentum we will be interested in. For the axial-vector coupling,

$$F_A^{(T)} = g_A \approx -1.276. \tag{17.61}$$

The vector coupling constants are equal to their electromagnetic counterparts [68, 67, 211]:

$$F_1^{(T=0,1)} = g_V = 1 \tag{17.62}$$

$$\mu^{(0)} = F_1^{(0)} + 2m_N F_2^{(0)} = \mu_p + \mu_n = 0.890 \tag{17.63}$$

$$\mu^{(1)} = F_1^{(1)} + 2m_N F_2^{(1)} = \mu_p - \mu_n = 4.706. \tag{17.64}$$

In the above, μ_p and μ_n are the proton and neutron magnetic moments. From early experiments [31],

$$\mu_p = (2.7934 \pm 0.0003)\frac{e\hbar}{2m_p c} \tag{17.65}$$

$$\mu_n = (-1.9135 \pm 0.0003)\frac{e\hbar}{2m_p c}. \tag{17.66}$$

From Connell [211], the pseudoscalar coupling constant is

$$F_P(q^2) = \frac{2m_N F_A(q^2)}{q^2 + m_\pi^2} = g_P, \tag{17.67}$$

which, according to contemporary measurements [106], is estimated to be

$$g_P = 349(9). \tag{17.68}$$

17.4.2   Reduced matrix operators

I now write down the reduced and simplified matrix elements, assuming a sum over all single-particle states, and ignoring orientation in space to drop the M_J dependence (J_z reduced matrix elements will be used, summing over all orientations). I also use the assumptions about the coupling constants discussed in the previous sections to express the operators in terms of the well-known coupling constants g_V, g_A, g_P, μ.

Vector (Simplified)

Under CVC theory, the vector-longitudinal operator can be expressed in terms of the Coulomb operator.

$$C_{JM}(qr) = g_V M_J^{M_J}(qr)\tau^\pm \tag{17.69}$$

$$L_{JM}(qr) = -\frac{E}{q}C_{JM}(qr) \tag{17.70}$$

$$E_{JM}(qr) = \frac{q}{m_N}\left[g_V \Delta_J'^{M_J}(qr) + \frac{1}{2}\mu \Sigma_J^{M_J}(qr)\right]\tau^\pm \tag{17.71}$$

$$M_{JM}(qr) = -i\frac{q}{m_N}\left[g_V \Delta_J^{M_J}(qr) - \frac{1}{2}\mu \Sigma_J'^{M_J}(qr)\right]\tau^\pm \tag{17.72}$$

Axial-vector (Simplified)

$$C_{JM}(qr) = -i\frac{q}{m_N}\left[g_A \Omega_J^{M_J}(qr) + \frac{1}{2}(g_A + q_0 g_P)\Sigma_J''^{M_J}(qr)\right]\tau^\pm \tag{17.73}$$

$$L_{JM}(qr) = i\left(g_A - \frac{q^2}{2m_N}g_P\right)\Sigma_J''^{M_J}(qr)\tau^\pm \tag{17.74}$$

$$E_{JM}(qr) = ig_A\Sigma_J'^{M_J}(qr)\tau^\pm \tag{17.75}$$

$$M_{JM}(qr) = g_A\Sigma_J^{M_J}(qr)\tau^\pm \tag{17.76}$$

17.4.3 Nuclear electroweak operators

There are six basic operators, $M_J, \Delta_J, \Sigma_J', \Sigma_J'', \tilde{\Phi}_J', \Phi_J''$, describing the electro-weak coupling of the WIMPs to the nucleon degrees of freedom. These are constructed from Bessel spherical and vector harmonics [67]:

$$M_{JM}(q\vec{x}) \equiv j_J(qx)Y_{JM}(\Omega_x) \tag{17.77}$$

$$\vec{M}_{JLM}(q\vec{x}) \equiv j_L(qx)\vec{Y}_{JLM}(\Omega_x), \tag{17.78}$$

where, using unit vectors $\vec{e}_{\lambda=-1,0,+1}$,

$$Y_{JLM}(\Omega_x) = \sum_{m\lambda} \langle Lm1\lambda| \, |(L1)JM_J\rangle \, Y_{Lm}(\Omega_x)\vec{e}_\lambda. \tag{17.79}$$

The multipole operators are defined as:

$$M_{JM} \tag{17.80}$$

$$\Delta_{JM} \equiv \vec{M}_{JJM} \cdot \frac{1}{q}\vec{\nabla} \tag{17.81}$$

$$\Delta'_{JM} \equiv -i\left[\frac{1}{q}\vec{\nabla} \times \vec{M}_{JJM}\right] \cdot \frac{1}{q}\vec{\nabla} \tag{17.82}$$

$$\Sigma_{JM} \equiv \vec{M}_{JJM} \cdot \vec{\sigma} \tag{17.83}$$

$$\Sigma'_{JM} \equiv -i\left(\frac{1}{q}\vec{\nabla} \times \vec{M}_{JJM}\right) \cdot \vec{\sigma} \tag{17.84}$$

$$\Sigma''_{JM} \equiv \left(\frac{1}{q}\vec{\nabla}M_{JM}\right) \cdot \vec{\sigma} \tag{17.85}$$

$$\Omega_{JM} \equiv M_{JM}\vec{\sigma} \cdot \frac{1}{q}\vec{\nabla} \tag{17.86}$$

$$\tilde{\Phi}'_{JM} \equiv \left(\frac{1}{q}\vec{\nabla} \times \vec{M}_{JJM}\right) \cdot \left(\vec{\sigma} \times \frac{1}{q}\vec{\nabla}\right) + \frac{1}{2}\vec{M}_{JJM} \cdot \vec{\sigma} \tag{17.87}$$

$$\Phi''_{JM} \equiv i\left(\frac{1}{q}\vec{\nabla}M_{JM}\right) \cdot \left(\vec{\sigma} \times \frac{1}{q}\vec{\nabla}\right) \tag{17.88}$$

The last two are not used for beta decay. Some of these can be calculated as combinations of the others. First, the Δ' operator:

$$\Delta'_{JM} = \left[-\left(\frac{J}{2J+1}\right)^{1/2}\vec{M}_{J,J+1,M} + \left(\frac{J+1}{2J+1}\right)^{1/2}\vec{M}_{J,J-1,M}\right] \cdot \frac{1}{q}\vec{\nabla}. \tag{17.89}$$

The first factor being identical in form, the Σ' operator:

$$\Sigma'_{JM} = \left[-\left(\frac{J}{2J+1}\right)^{1/2}\vec{M}_{J,J+1,M} + \left(\frac{J+1}{2J+1}\right)^{1/2}\vec{M}_{J,J-1,M}\right] \cdot \vec{\sigma}. \tag{17.90}$$

Similar in form, the Σ'' operator:

$$\Sigma''_{JM} = \left[\left(\frac{J+1}{2J+1} \right)^{1/2} \vec{M}_{J,J+1,M} + \left(\frac{J}{2J+1} \right)^{1/2} \vec{M}_{J,J-1,M} \right] \cdot \vec{\sigma}. \qquad (17.91)$$

17.4.4 Nuclear electroweak matrix elements

The matrix elements of the nuclear electroweak operators can be calculated for standard wave functions from second-quantized shell model calculations:

$$\langle \Psi_f | |X_J| | \Psi_i \rangle = \sum_{a,b} \langle a | |X_J| | b \rangle \, \rho_J^{fi}(ab), \qquad (17.92)$$

where single-particle orbital labels a imply shell model quantum number n_a, l_a, j_a, and the double-bar $||$ indicates reduced matrix elements [74]. For elastic collisions, only the ground state is involved, i.e. $\Psi_f = \Psi_i = \Psi_{g.s.}$.

We will need explicit representations of the matrix elements. In this section, I mostly just reproduce results from old papers for convenience. The important original papers are [68, 67, 211], and for a recent review with a modern Mathematica implementation, see [130].

First I will state the operator matrix elements in terms of spherical Bessel functions and related single-particle operators, and then present the explicit expressions for those single-particle matrix elements in a harmonic oscillator basis. The single particle states have labels n, l, and j, as per usual. The matrix elements are reduced, using the Wigner-Eckart theorem to remove M_J dependence [74],

$$\langle j'm' | T_{JM} | jm \rangle = (-1)^{j'-m'} \begin{pmatrix} j' & J & j \\ -m' & M & m \end{pmatrix} \langle j' | |T_J| | j \rangle . \qquad (17.93)$$

The coupling symbol here is the 3-j symbol.

The M_J reduced matrix elements are [67]:

$$\langle a| \, |M_J(y)| \, |b\rangle = \frac{1}{\sqrt{4\pi}}(-1)^{J+j+1/2}[l'][l][j'][j][J] \begin{Bmatrix} l' & j' & \frac{1}{2} \\ j & l & J \end{Bmatrix} \begin{pmatrix} l' & J & l \\ 0 & 0 & 0 \end{pmatrix} \langle a| \, j_J(y) \, |b\rangle,$$

(17.94)

where $y = qx$, $|a\rangle = |n'l'j'\rangle$ and $|b\rangle = |nlj\rangle$.

Next are the matrix elements related to the Σ_{JM} operator, in terms of the general $\vec{M}_{JLM}$ vector function (which in Σ_{JM} has $L = J$):

$$\langle a| \, |\vec{M}_{JL}(y) \cdot \vec{\sigma}| \, |b\rangle = \frac{1}{\sqrt{4\pi}}(-1)^{l'}\sqrt{6}[l'][l][j'][j][J][L] \begin{Bmatrix} l' & l & L \\ \frac{1}{2} & \frac{1}{2} & 1 \\ j' & j & J \end{Bmatrix} \begin{pmatrix} l' & L & l \\ 0 & 0 & 0 \end{pmatrix} \langle a| \, j_J(y) \, |b\rangle.$$

(17.95)

The next matrix elements are related to the Δ_{JM} operator:

$$\langle a| \, |\vec{M}_{JL}(y) \cdot \frac{1}{q}\vec{\nabla}| \, |b\rangle = \frac{1}{\sqrt{4\pi}}(-1)^{L+j+1/2}[l'][j'][j][J][L] \begin{Bmatrix} l' & j' & \frac{1}{2} \\ j & l & J \end{Bmatrix}$$

$$\left[-(l+1)^{1/2}[l+1] \begin{Bmatrix} L & 1 & J \\ l & l' & l-1 \end{Bmatrix} \begin{pmatrix} l' & L & l+1 \\ 0 & 0 & 0 \end{pmatrix} \right.$$

$$\left. \times \langle a| \, j_L(y) \left(\frac{d}{dy} + \frac{l+1}{y} \right) |b\rangle \right]$$

(17.96)

348

The matrix elements related to the Ω_{JM} operator:

$$\langle a| |M_J(y)\vec{\sigma} \cdot \frac{1}{q}\vec{\nabla}| |b\rangle = \frac{1}{\sqrt{4\pi}}(-1)^{l'}[l'][j'][j][2j-l][J] \begin{Bmatrix} l' & j' & \frac{1}{2} \\ j & 2j-l & J \end{Bmatrix} \begin{pmatrix} l' & J & 2j-l \\ 0 & 0 & 0 \end{pmatrix}$$

$$\times \left[-\delta_{j,l+1/2} \langle a| j_L(y) \left(\frac{d}{dy} - \frac{l}{y} \right) |b\rangle \right.$$

$$\left. + \delta_{j,l-1/2} \langle a| j_L(y) \left(\frac{d}{dy} + \frac{l+1}{y} \right) |b\rangle \right].$$

$$(17.97)$$

17.4.5 Bessel function harmonic oscillator matrix elements

To compute the matrix elements of the basic electroweak operators, we need the matrix elements of the spherical Bessel function, and related operators, in a basis of harmonic oscillator states $|b\rangle = |nlj\rangle$. These are listed below, taken from [67, 130]. In the following, the definition of y differs from that in previous sections. Here, $y = (qb/2)^2$, where $b = \sqrt{\hbar/m\omega}$ is the harmonic oscillator length scale.

The confluent hyper-geometric functions $_1F_1$ are described in the Appendix.

$$\langle a| j_L(y) |b\rangle$$

$$= \frac{2^L}{(2L+1)!!} y^{L/2} e^{-y} \sqrt{(n'-1)!(n-1)!} \sqrt{\Gamma(n'+l'+1/2)\Gamma(n+l+1/2)}$$

$$\times \sum_{m=0}^{n-1} \sum_{m'=0}^{n'-1} \frac{(-1)^{m+m'}}{m!m'!(n-m-1)!(n'-m'-1)!}$$

$$\times \frac{\Gamma[(l+l'+L+2m+2m'+3)/2]}{\Gamma(l+m+3/2)\Gamma(l'+m'+3/2)} \, _1F_1[(L-l'-l-2m'-2m)/2; L+3/2; y].$$

$$(17.98)$$

$$\langle n'l'j'| j_L(y)(\frac{d}{dy} - \frac{l}{y}) |nlj\rangle$$

$$= \frac{2^{(L-1)}}{(2L+1)!!} y^{(L-1)/2} e^{-y} \sqrt{(n'-1)!(n-1)!} \sqrt{\Gamma(n'+l'+1/2)\Gamma(n+l+1/2)}$$

$$\times \sum_{m=0}^{n-1} \sum_{m'=0}^{n'-1} \frac{(-1)^{m+m'}}{m!m'!(n-m-1)!(n'-m'-1)!} \frac{\Gamma[(l+l'+L+2m+2m'+2)/2]}{\Gamma(l+m+3/2)\Gamma(l'+m'+3/2)}$$

$$\times \left\{ -\frac{1}{2}(l+l'+L+2m+2m'+2) \, _1F_1[(L-l'-l-2m'-2m-1)/2; L+3/2; y] \right.$$

$$\left. + 2m \, _1F_1[(L-l'-l-2m'-2m+1)/2; L+3/2; y] \right\}.$$

$$(17.99)$$

$$\langle n'l'j'| j_L(y)(\frac{d}{dy} + \frac{l+1}{y}) |nlj\rangle$$

$$= \frac{2^{L-1}}{(2L+1)!!} y^{(L-1)/2} e^{-y} \sqrt{(n'-1)!(n-1)!} \sqrt{\Gamma(n'+l'+1/2)\Gamma(n+l+1/2)}$$

$$\times \sum_{m=0}^{n-1} \sum_{m'=0}^{n'-1} \frac{(-1)^{m+m'}}{m!m'!(n-m-1)!(n'-m'-1)!} \frac{\Gamma[(l+l'+L+2m+2m'+2)/2]}{\Gamma(l+m+3/2)\Gamma(l'+m'+3/2)}$$

$$\times \left\{ -\frac{1}{2}(l+l'+L+2m+2m'+2) \, _1F_1[(L-l'-l-2m'-2m-1)/2; L+3/2; y] \right.$$

$$\left. + (2l+2m+1) \, _1F_1[(L-l'-l-2m'-2m+1)/2; L+3/2; y] \right\}.$$

$$(17.100)$$

17.5 Special formulas

17.5.1 First forbidden non-unique to first order

In most applications of BB formalism, only a select number of terms are relevant for a given set of approximations and required precision. To see an example of a reduction of the full

theory, see the 1972 paper [26] in which Behrens et al. apply the BB formalism to the first forbidden decay of ^{209}Pb.

In a first forbidden non-unique decay, the nuclear angular momentum and parity change by $\Delta J^\pi = 0^-, 1^-$. The shape factor for first forbidden decays is found in BB [24] section 14.3, which highest order coefficients given (in slightly opaque notation) in equations (14.452 - 14.460). An expanded version is given in Table 4 of [23], and in equation (5) of [26]. Both provide:

$$C(W) = M_{011}^2 + m_{011}^2 - 2\frac{\mu_1\gamma_1}{W}M_{011}m_{011} + M_{111}^2 + m_{111}^2 - 2\frac{\mu_1\gamma_1}{W}M_{111}m_{111} \tag{17.101}$$

$$+ M_{112}^2 + \lambda_2 M_{121}^2 + M_{212}^2 + \lambda_2 M_{221}^2, \tag{17.102}$$

where μ_1 and λ_2 are Coulomb functions, and $\gamma_1 = \sqrt{1-(\alpha Z)^2}$. The $M_{Kk_e k_\nu}$ and $m_{Kk_e k_\nu}$ quantities are, to first order in the expansion of small parameters [23], αZ, WR, $m_e R$ (αZ, $WR/\hbar c$, $m_e cR/\hbar$ in SI units):

$$M_{011} = {}^AF_{000} - \frac{1}{3}\alpha Z\,{}^AF_{011}(1,1,1,1) - \frac{1}{3}W_0R\,{}^AF_{011} \tag{17.103}$$

$$m_{011} = -\frac{1}{3}R\,{}^AF_{011} \tag{17.104}$$

$$M_{111} = -{}^VF_{101} - \frac{1}{3}\alpha Z\sqrt{\frac{1}{3}}\,{}^VF_{110}(1,1,1,1) - \frac{1}{3}W_0R\sqrt{\frac{1}{3}}\,{}^VF_{110} \tag{17.105}$$

$$-\frac{1}{3}\alpha Z\sqrt{\frac{2}{3}}\,{}^AF_{111}(1,1,1,1) - \frac{1}{3}(W-q)R\sqrt{\frac{2}{3}}\,{}^AF_{111} \tag{17.106}$$

$$m_{111} = -\frac{1}{3}R\left[\sqrt{\frac{1}{3}}\,{}^VF_{110} + \sqrt{\frac{2}{3}}\,{}^AF_{111}\right] \tag{17.107}$$

$$M_{112} = \frac{1}{3}qR\left[\sqrt{\frac{2}{3}}\,{}^VF_{110} + \sqrt{\frac{1}{3}}\,{}^AF_{111}\right] \tag{17.108}$$

$$M_{121} = \frac{1}{3}pR\left[\sqrt{\frac{2}{3}}\,{}^VF_{110} - \sqrt{\frac{1}{3}}\,{}^AF_{111}\right] \tag{17.109}$$

$$M_{212} = -\frac{1}{3}qR\,{}^AF_{211} \tag{17.110}$$

$$M_{221} = -\frac{1}{3}pR \, ^AF_{211}. \tag{17.111}$$

We have:

$$\alpha = \text{fine structure constant}$$

$$q = (W_0 - W) = \text{neutrino momentum}$$

$$R \approx r_0 A^{1/3} \text{ nuclear radius}$$

$$Z = \text{proton number of the daughter}$$

Furthermore, terms with qR and pR are small (on the order of 0.04 in natural units) and only their squares enter $C(W)$; these terms can be dropped [26]. We are left with:

$$C(W) = M_{011}^2 + m_{011}^2 - 2\frac{\mu_1\gamma_1}{W}M_{011}m_{011} + M_{111}^2 + m_{111}^2 - 2\frac{\mu_1\gamma_1}{W}M_{111}m_{111}; \tag{17.112}$$

$$M_{011} = \, ^AF_{000} - \frac{1}{3}\alpha Z \, ^AF_{011}(1,1,1,1) - \frac{1}{3}W_0 R \, ^AF_{011} \tag{17.113}$$

$$m_{011} = -\frac{1}{3}R \, ^AF_{011} \tag{17.114}$$

$$M_{111} = -\, ^VF_{101} - \frac{1}{3}\alpha Z\sqrt{\frac{1}{3}} \, ^VF_{110}(1,1,1,1) - \frac{1}{3}W_0 R\sqrt{\frac{1}{3}} \, ^VF_{110} \tag{17.115}$$

$$-\frac{1}{3}\alpha Z\sqrt{\frac{2}{3}} \, ^AF_{111}(1,1,1,1) - \frac{1}{3}(W-q)R\sqrt{\frac{2}{3}} \, ^AF_{111} \tag{17.116}$$

$$m_{111} = -\frac{1}{3}R\left[\sqrt{\frac{1}{3}} \, ^VF_{110} + \sqrt{\frac{2}{3}} \, ^AF_{111}\right]. \tag{17.117}$$

These expressions require the following form factor coefficients F_{KLs}^N which can be related to standard CLEM operators:

$$^AF_{000}, \; ^AF_{011}, \; ^AF_{111}, \; ^VF_{101} \; ^VF_{110}, \tag{17.118}$$

as well as the following shape form factor coefficients $F_{KLs}^N(k_e, m, n, \rho)$ which require special

integrals to compute:

$$^{A}F_{011}(1,1,1,1), \ ^{A}F_{111}(1,1,1,1), \ ^{V}F_{110}(1,1,1,1). \tag{17.119}$$

Since we are only computing to leading order, I have dropped the N label in F^{N}_{KLs}; where needed it is set to zero. If the nucleus is sufficiently small, the small Z approximation may apply, in which case

$$\alpha Z << 1, \tag{17.120}$$

so that the shape form factors may be neglected. For our nuclei of interest, however, $Z = 35 - 40$, so

$$0.26 \leq \alpha Z \leq 0.29. \tag{17.121}$$

Using the relations from section 17.3.2, we can express the operators not requiring special integrals in terms of the standard CLEM operators. For both of the following, we set $J = 0$ and obtain:

$$^{A}F_{000} = \sqrt{4\pi}[J_{i}]^{-1} \langle J_{f}||\hat{C}^{A}_{0}||J_{i}\rangle , \tag{17.122}$$

$$^{A}F_{011} = -\sqrt{4\pi}[J_{i}]^{-1} \frac{1}{qR} \left[\langle J_{f}||i^{J}\hat{L}^{A}_{0}||J_{i}\rangle \right]. \tag{17.123}$$

For the next three relations, we set $J = 1$:

$$^{V}F_{110} = F_{JJ0}(\boldsymbol{q}^{2}) = \sqrt{4\pi}[J_{i}]^{-1} \frac{3}{qR} \langle J_{f}||i\hat{C}^{V}_{1}||J_{i}\rangle , \tag{17.124}$$

$$^{V}F_{101} = F_{J,J-1,1}(\boldsymbol{q}^{2}) = -\sqrt{4\pi}[J_{i}]^{-1}3\left[\sqrt{\frac{1}{3}} \langle J_{f}||i\hat{L}^{V}_{1}||J_{i}\rangle + \sqrt{\frac{2}{3}} \langle J_{f}||i\hat{E}^{V}_{1}||J_{i}\rangle \right], \tag{17.125}$$

$$^A F_{111} = F_{JJ1} = \sqrt{4\pi}[J_i]^{-1} \frac{3}{qR} \langle J_f| |i\hat{M}_1^A| |J_i\rangle. \tag{17.126}$$

The shape form factor coefficients $F_{KLs}^N(k_e, m, n, \rho)$ can be calculated as integral transforms of the previously listed formulas via the relation (17.28). For the order we are computing, we only need $N = 0$ and $L = 1$ terms:

$$F_{K1s}^{(0)}(1, 1, 1, 1) = \int_0^\infty J_{L=1}^{(N=0)}(q) F_{KL=1s}(q^2) q^2 dq. \tag{17.127}$$

We can write down the geometric factor for the specific case of $I(k = 1, 1, 1, 1)$:

$$I(1, 1, 1, 1; r) = \begin{cases} \frac{3}{2} - \frac{3}{10}\left(\frac{r}{R}\right)^2, & 0 \le r \le R \\ \frac{3}{2}\frac{R}{r} - \frac{3}{10}\left(\frac{R}{r}\right)^3 & R \le r. \end{cases} \tag{17.128}$$

Then the kernel simplifies to:

$$J_{L=1}^{(N=0)}(q) = \frac{2}{\pi}\frac{qR}{3}\int_0^\infty \left(\frac{r}{R}\right) I(1, 1, 1, 1; r) j_{L=1}(qr) r^2 dr. \tag{17.129}$$

Note that we cannot use the small-qr expansion of the spherical Bessel function here because we are integrating $r \to \infty$. The asymptotic form of the Bessel functions for all L are some phase shift of $\cos(qr)/(qr)$. $I(1, 1, 1, 1; r)$ goes like $1/r$. Thus, the integrand appears to have asymptotic behaviour as $r\cos(x)$, which would not converge. However, Behrens and Buhring [24] claim (BB 6.162) that in fact the integral $J(q)$ is equivalent to q-derivatives of

$$\tilde{J}(q) = \frac{2}{\pi}q\int_0^\infty I(k_e, m, n, \rho; r) j_0(qr) r^2 dr, \tag{17.130}$$

which, by a similar argument as above, does converge.

17.5.2 First forbidden unique to first order

In a first forbidden unique decay, the nuclear angular momentum and parity change by $\Delta J^\pi = 2^-$. The shape factor in this case is, to a first approximation, of the 'normal' unique shape [25]:

$$C(W) = M_{212}^2 + \lambda_2 M_{221}^2, \tag{17.131}$$

where the dominant terms are:

$$M_{212} = -\frac{1}{3} p_\nu R \,^A F_{211} \tag{17.132}$$

$$M_{221} = -\frac{1}{3} p_e R \,^A F_{211} \tag{17.133}$$

so that

$$C(W) = \frac{1}{9} R^2 (\,^A F_{211})^2 (p_\nu^2 + \lambda_2 p_e^2). \tag{17.134}$$

The next leading corrections to the normal shape scale like $W_0 R$ and αZ and include the form factors and shape form factors $^A F_{220}$ and $^V F_{221}$.

Using equations (17.44) and setting $J = 2$, we obtain the expression for $^A F_{211}$:

$$^A F_{2,1,1}(\boldsymbol{q}^2) = \sqrt{4\pi} [J_i]^{-1} \frac{15}{qR} \left[\sqrt{\frac{2}{5}} \langle J_f || \hat{L}_2^A || J_i \rangle + \sqrt{\frac{3}{5}} \langle J_f || \hat{E}_2^A || J_i \rangle \right]. \tag{17.135}$$

17.5.3 As a correction to allowed shape

A common approximation for computing first forbidden decays is by approximating the energy spectrum $C(W)$ as a correction to the allowed-shape spectrum. In this way, the form

is:

$$C(W) = k \left[1 + aW + \frac{b}{W} + cW^2 \right], \tag{17.136}$$

where the coefficients are related to the nuclear matrix elements. Some papers like [202, 313] attribute the following definition to a Behrens and Buhring 1971 paper [23] (which does not appear to contain that definition), but a paper by Towner and Hardy (1972) [280] indicates that the definition is from the text by Schopper (1966) [257]. There is a footnote in BB [24] on page 594 which briefly mentions this notation. The formulas are:

$$k = (\zeta_0^2 + \frac{1}{9}w^2) + (\zeta_1^2 + \frac{1}{9}(x+u)^2 - \frac{4}{9}\mu_1\gamma_1 u(x+u) \tag{17.137}$$

$$+ \frac{1}{18}W_0^2(2x+y)^2 - \frac{1}{18}\lambda_2(2x-u)^2] + \frac{1}{12}z^2(W_0^2 - \lambda_2), \tag{17.138}$$

$$ka = -\frac{4}{3}uY - \frac{1}{9}W_0(4x^2 + 5u^2) - \frac{1}{6}z^2W_0, \tag{17.139}$$

$$kb = \frac{2}{3}\mu_1\gamma_1[-\zeta_0 w + \zeta_1(x+u)], \tag{17.140}$$

$$kc = \frac{1}{18}[8u^2 + (2x+u)^2 + \lambda_2(2x-u)^2] + \frac{1}{12}z^2(1+\lambda_2) \tag{17.141}$$

- $\zeta_0 = V + \frac{1}{3}wW_0$

- $\zeta_1 = Y + \frac{1}{3}(u-x)W_0$

- $V = \xi'v + \xi w'$

- $Y = \xi'y - \xi(u' + x')$

- $\xi = \frac{\alpha Z}{2R}$

The functions $\gamma_{k=1}$, $\mu_{k=1}$, and λ_2 are Coulomb functions, and for sufficiently light nuclei, $\gamma_1 = \mu_1 = \lambda_2 = 1$.

The factors w, x, u, z are non-relativistic electroweak matrix elements, which are expressed in terms of operators like the isospin operator $\boldsymbol{\tau}$, the spin operator $\boldsymbol{\sigma}$, and the vector spherical

harmonic,

$$\boldsymbol{C}_{lm} = \sqrt{\frac{4\pi}{2l+1}}\boldsymbol{Y}_{lm}. \tag{17.142}$$

From [313], using the Condon and Shortley phase convention and reduced matrix elements (assumed sum over all nucleons):

$$w = -R\ ^{A}F_{011}^{0} = -g_{A}\sqrt{3}[J_{i}]^{-1}\langle f||r[\boldsymbol{C_{1}}\times\sigma]^{\boldsymbol{0}}\tau||\mathbf{i}\rangle\boldsymbol{C} \tag{17.143}$$

$$x = -\frac{1}{\sqrt{3}}R\ ^{V}F_{110}^{0} = -[J_{i}]^{-1}\langle f||r\boldsymbol{C_{1}}\tau||\mathbf{i}\rangle \tag{17.144}$$

$$u = -\sqrt{\frac{2}{3}}R\ ^{A}F_{111}^{0} = -g_{A}\sqrt{2}[J_{i}]^{-1}\langle f||r[\boldsymbol{C_{1}}\times\sigma]^{\boldsymbol{1}}\tau||\mathbf{i}\rangle \tag{17.145}$$

$$z = \frac{2}{\sqrt{3}}R\ ^{A}F_{211}^{0} = 2g_{A}[J_{i}]^{-1}\langle f||[\boldsymbol{C_{1}}\times\sigma]^{\boldsymbol{2}}\tau||\mathbf{i}\rangle. \tag{17.146}$$

In the above and below, $[J] = \sqrt{2J+1}$ and the axial-vector coupling constant is approximately $g_{A} = -1.27$. M is the nucleon mass. The necessary primed expressions (derivatives with respect to r) in terms of the nuclear charge distribution (uniform sphere),

$$I(1,1,1,1,r) = \frac{3}{2}\begin{cases} 1 - \frac{1}{5}\left(\frac{r}{R}\right)^{2}, & 0 \leq r \leq R \\ \frac{R}{r} - \frac{1}{5}\left(\frac{R}{r}\right)^{3}, & r \geq R \end{cases}, \tag{17.147}$$

are given by:

$$w' = -\frac{2}{3}R\ ^{A}F_{011}^{0}(1,1,1,1) = -g_{A}\sqrt{3}[J_{i}]^{-1}\langle f||\frac{2}{3}rI(1,1,1,1,r)[\boldsymbol{C_{1}}\times\sigma]^{\boldsymbol{0}}\tau||\mathbf{i}\rangle\boldsymbol{C} \tag{17.148}$$

$$x' = -\frac{2}{3\sqrt{3}}R\ ^{V}F_{110}^{0}(1,1,1,1) = -[J_{i}]^{-1}\langle f||\frac{2}{3}rI(1,1,1,1,r)\boldsymbol{C_{1}}\tau||i\rangle \tag{17.149}$$

$$u' = -\frac{2}{3}\sqrt{\frac{2}{3}}R\ ^{A}F_{111}^{0}(1,1,1,1) = -g_{A}\sqrt{2}[J_{i}]^{-1}\langle f||\frac{2}{3}rI(1,1,1,1,r)[\boldsymbol{C_{1}}\times\boldsymbol{\sigma}]^{\boldsymbol{1}}\boldsymbol{\tau}||i\rangle \tag{17.150}$$

Finally, $\xi'v$ and $\xi'y$ are relativistic operators with non-relativistic reductions:

$$\xi'v =^A F^0_{000} = \frac{1}{M}g_A\sqrt{3}[J_i]^{-1}\langle f||[\boldsymbol{\sigma}\times\boldsymbol{\nabla}]^0\boldsymbol{\tau}||i\rangle \tag{17.151}$$

$$\xi'y =^V F^0_{101} = -\frac{1}{M}[J_i]^{-1}\langle f||\boldsymbol{\nabla}\boldsymbol{\tau}||i\rangle. \tag{17.152}$$

Large Z (ξ) approximation; allowed shape

Following the arguments retold in Towner [280], we can neglect certain terms in the above expansion when

$$\xi = \frac{\alpha Z}{2R} >> W_0, \tag{17.153}$$

where W_0 is the maximum electron energy and R is the nuclear charge radius. It can be shown that in this limit,

- $k \sim O(\xi^2)$

- $ka \sim O(\xi)$

- $kb \sim O(\xi)$

- $kc \sim O(1)$

Thus, keeping only the leading term in ξ,

$$C(W) \sim k. \tag{17.154}$$

BB mention the large-Z approximation in a footnote on page 594 in the context of this 'historical' notation: for large Z (and if cancellations do not occur), the quantities V and Y

are approximated by:

$$V \approx A_0 \tag{17.155}$$

$$Y \approx -C_0, \tag{17.156}$$

which, expanding using BB formalism to leading order, is equivalent to:

$$V \approx {}^A F_{000} \mp \frac{1}{3}\alpha Z \; {}^A F_{011}(1,1,1,1) - \frac{1}{3}W_0 R \; {}^A F_{011} \tag{17.157}$$

$$Y \approx -\left(-{}^V F_{101} \mp \frac{1}{3}\alpha Z \sqrt{\frac{1}{3}} \; {}^V F_{110}(1,1,1,1) \right. \tag{17.158}$$

$$\left. -\frac{1}{3}W_0 R \sqrt{\frac{1}{3}} \; {}^V F_{110} \mp \frac{1}{3}\alpha Z \sqrt{\frac{2}{3}} \; {}^A F_{111}(1,1,1,1) \right. \tag{17.159}$$

$$\left. +\frac{1}{3}W_0 R \sqrt{\frac{2}{3}} \; {}^A F_{111} \right). \tag{17.160}$$

17.6   Coulomb correction

Because the electron (lepton) emitted during beta decay will interact with the residual nuclear charge, the beta decay interaction must include weak and electromagnetic terms. Since the electromagnetic interaction is strong compared to the weak interaction, it cannot be included as a simple perturbation. There are two main effects of the Coulomb correction, static and radiative:

1. Static distortion of the electron wave functions, modifying the beta spectrum by an overall scaling factor (i.e. the Fermi function $f(Z, E)$)

2. Radiative correction terms (things like bremsstrahlung) which alter the normalization of the shape function as well as the form of the multipole operators

17.6.1 Static corrections

The static effects are the main concern of Behrens and Buhring [24], and is fully incorporated into their treatment of the electron radial wave functions. A schematic Feynman diagram is shown in Figure 17.2 for the dominant terms static terms.
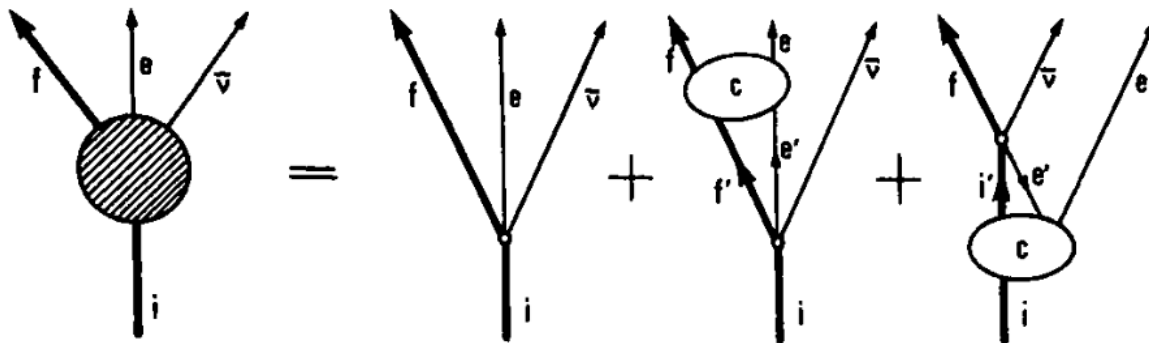

Figure 17.2: Figure from Behrens and Buhring [24] showing the (static) electromagnetic interaction (c) correction to nuclear beta decay.

The physical interpretation of static corrections is that the electron radial wave functions are distorted by the presence of the nuclear charge from simple plane waves to Coulomb wave functions. We will see in the following sections covering the Behrens and Buhring (BB) formalism that a number of functions are needed which encode this distortion in the calculation of beta decay form factors. These are called the Coulomb functions: μ_k, γ_k, λ_k, which to leading order are close to unity.

First, we have the Fermi function γ_k:

$$\gamma_{k_e} = \sqrt{k_e^2 - (\alpha Z)^2},\tag{17.161}$$

where Z is the atomic number of the residual nucleus, and $k_e = k$ is the wave number of the

outgoing electron. α is the fine structure constant.

$$\mu_{k_e} = \frac{k_e W}{\gamma_{k_e} m} \frac{\alpha^2_{-k_e} - \alpha^2_{k_e}}{\alpha^2_{-k_e} + \alpha^2_{k_e}}, \tag{17.162}$$

$$\lambda_{k_e} = \frac{\alpha^2_{-k_e} + \alpha^2_{k_e}}{\alpha^2_{-1} + \alpha^2_1}, \tag{17.163}$$

where α_{k_e} are called the Coulomb-amplitudes, which are solutions to the electron radial wave function equations in the presence of a uniform nuclear charge. They generally have the form (to leading order in $WR << 1$):

$$\alpha_k \simeq (2W)^{-1/2} (2p)^\gamma e^{(\pi/2)y} |E^{-1}| \frac{|\Gamma(\gamma + iy)|}{\Gamma(1 + 2\gamma)}, \tag{17.164}$$

where $y = \frac{\alpha ZW}{pc}$ and E is a normalization factor. This can be expressed in terms of the generalized Fermi function, introduced elsewhere, which has the form $f_{k-1} \sim 1 + O(\alpha Z)$ when $\alpha Z \to 0$. With this shorthand,

$$\alpha_\kappa \simeq \frac{p}{k\sqrt{2W}} \sqrt{f_{k-1}} \begin{cases} \sqrt{(k+\gamma)(kW - \gamma m)}, & \kappa = k \\ \sqrt{(k+\gamma)(kW + \gamma m)}, & \kappa = -k. \end{cases} \tag{17.165}$$

Using

$$\alpha^2_{-k_e} + \alpha^2_{k_e} \simeq f_{k-1} p^2 \frac{k + \gamma}{k} \tag{17.166}$$

$$\alpha^2_{-k_e} - \alpha^2_{k_e} \simeq f_{k-1} p^2 \frac{(k+\gamma)\gamma}{k^2} \frac{m}{W}, \tag{17.167}$$

we find

$$\gamma_{k_e} = \sqrt{k_e^2 - (\alpha Z)^2} \tag{17.168}$$

$$\mu_{k_e} \simeq 1 \tag{17.169}$$

$$\lambda_{k_e} = \frac{f_{k_e - 1}}{f_0} \frac{k_e + \gamma_{k_e}}{k_e(1 + \gamma_1)} \approx 1 + O\{(\alpha Z)^2\}. \tag{17.170}$$

Tabulated values for the Fermi functions, as a function of Z, r_0 ($R = r_0 A^{1/3}$), and p, can be found in [256]. I include some of the relevant values in Table 17.1. As a reminder, the relation between the important quantities are:

$$W = \sqrt{p^2 + 1} \tag{17.171}$$

$$E = (W - 1)m_e c^2 \tag{17.172}$$

$$m_e c^2 = 511.006\text{keV}. \tag{17.173}$$

Table 17.1: Coulomb functions as a function of Z and the electron momentum p (in units of $m_e c$) for $r_0 = 1.2$ fm reported by [256]. $p = 1$ corresponds to $E \approx 0.21$ MeV and $p = 20$ to $E \approx 9.7$ MeV. The underlying Coulomb amplitudes α_k and Coulomb phases Δ_k were computed by solving the equation for a nucleus with a uniform charge distribution and without screening effects.

μ_1	$p = 1$	$p = 20$
$Z = 20$	0.9994	0.9832
$Z = 50$	0.9971	0.9297
$Z = 80$	0.9893	0.8376
λ_2	$p = 1$	$p = 20$
$Z = 20$	0.9804	1.0099
$Z = 50$	0.8880	1.0486
$Z = 80$	0.7201	1.1859

17.6.2   Radiative corrections

Radiative corrections can further be categorized into 'inner' and 'outer' radiative corrections, depending on whether the correction deals with the structure of the strong interaction. Inner radiative corrections are typically incorporated into effective coupling constants, while the outer corrections are energy dependent [132, 24]. The first few orders of radiative corrections are shown in Figure 17.3.

In light nuclei and for low-precision applications, the effect of the static Coulomb interaction
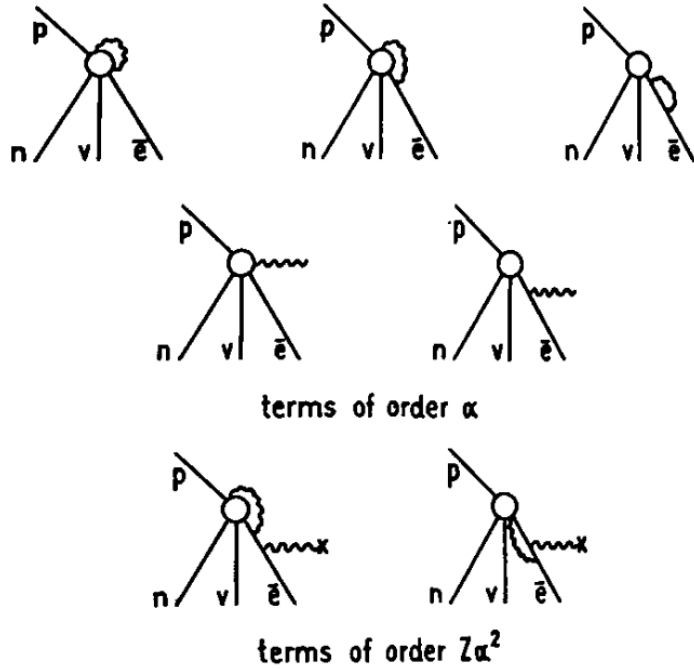
Figure 17.3: Figure from Behrens and Buhring [24] showing the (radiative) electromagnetic corrections to nuclear beta decay for the first few orders in the smallness parameters: α, $Z\alpha^2$. The final two order α diagrams show inner bremsstrahlung corrections [132].

can be ignored. The smallness parameter is of the order:

$$\epsilon_C \sim \alpha Z_f = \frac{1}{4\pi\epsilon_0} \frac{e^2}{\hbar c} Z_f \approx \frac{1}{137} Z_f, \tag{17.174}$$

where Z_f is the nuclear charge of the residual nucleus.

The correction to the spectrum shape has the form

$$C_R(W) = C(W)(1 + \Delta_R^{V/A})(1 + \delta_R(W, W_0)), \tag{17.175}$$

where $\Delta_R^{V/A}$ ($\approx 2.4\%$ [193]) is the inner radiative correction term, and $\delta_R(W, W_0)$ is the outer. For $\Delta_R^V \approx 2.4\%$ [193], while the axial-vector component is incorporated into g_A [132]. The energy-dependent outer radiative correction has scaling factors of α, $Z\alpha^2$, and $Z^2\alpha^3$. The effect is of the order of a percent, at least for super-allowed transitions [24].

17.7 Glick-Magid and Gazit Formalism

Glick-Magid and Gazit [102] have renewed the beta decay formalism, providing an alternative to the formalisms by Behrenes and Burhing [23, 24] and Holstein [143]. The GD formalism is essentially equivalent to the formalism of Connel, Donnelly, and Walecka [211] and related work in terms of the Walecka operators. In this section, I restate the important results from their paper. In each case, I reduce to the leading order for the cases we are interested in: medium-to-heavy mass nuclei.

An important note is that the formalism in this section ignores corrections due to the Coulomb force between the nucleus and the β particle, which is dominated by a factor [102]:

$$\epsilon_c \sim \alpha Z_f. \tag{17.176}$$

However, this term may become important for the nuclei we are interested in here.

Spectra

Switching now to the notation of [102], where the spectrum remains differential in the electron and neutrino momenta, we begin with:

$$\frac{d^5\omega}{dE \frac{d\hat{k}}{4\pi} \frac{d\hat{\nu}}{4\pi}} = \frac{4}{\pi^2} k E (E_0 - E)^2 F^{\mp}(Z_f, E) C_{\text{corr}} \frac{1}{2J_i + 1} \Theta(q, \vec{\beta} \cdot \vec{\nu}), \tag{17.177}$$

- E, $\vec{k}$, $\vec{\beta} = \vec{k}/E$ are the energy, momentum, direction of the emitted electron with $E_0 =$

- ν, $\vec{\nu}$ are the energy and momentum of the emitted neutrino

- $(E_0, \vec{q}) = (E, \vec{k}) + (\nu, n\vec{u})$ is the momentum transfer

- C_corr contains corrections such as: radiative corrections, finite-mass and electrostatic finite-size effects, atomic and chemical effects

- $F^\mp(Z_f, E)$ is the Fermi function describing the interaction of the residual nucleus with the emitted electron

- $\Theta(q, \vec{\beta} \cdot \vec{\nu})$ contains the nuclear form factors

At leading order, the (point-charge) Fermi function is taken to be [132]:

$$F^\mp(Z_f, E) = 4(2kR_f)^{2(\gamma_0 - 1)} \frac{|\Gamma(\gamma_0 + iy)|^2}{\Gamma^2(2\gamma_0 + 1)} e^{\pi y}, \tag{17.178}$$

- $\gamma_0 = \sqrt{1 - (\alpha Z_f)^2}$

- $y = \pm \alpha Z_f E / k$

- $\Gamma(z)$ is the complex gamma function

Small parameters

The formalism proceeds by expanding the nuclear form factors in a number of small parameters, which can be used to determine which terms are important for a given situation. I collected those terms in the Table 17.2, along with their approximate sizes depending on the system.

β-decay multipole expansion

Within the standard model, only vector (V) and axial-vector (A) couplings contribute to the weak force. By assuming an infinitely massive nucleus, the form factors can be written in

Table 17.2: Small parameters and their sizes in the Glick-Magid and Gazit formalism

Small parameter	Scaling	Approximate size
ϵ_{NR}: non-relativistic expansion	P_{Fermi}/m_N	0.2
ϵ_{qr}: leptonic wavefunction expansion	qR	$0.02A^{1/3}$
ϵ_{recoil}	$\frac{q}{m_N}$	0.003
ϵ_{M_π}: pion correction	$\frac{q}{m_\pi}$	0.02
ϵ_M: nuclear recoil	$\frac{\Delta M}{M_{min}}$	$0.003A^{-1}$
ϵ_c: Coulomb correction	αZ_f	$Z_f/137$
ϵ_{NM}: nuclear model	Q/Λ_b	

the expansion:

$$
\begin{aligned}
\Theta(q, \vec{\beta} \cdot \hat{\nu}) = \sum_{J=1}^{\infty} & \left[(1 - (\hat{\nu} \cdot \hat{q})(\vec{\beta} \cdot \hat{q}))(|\langle ||\hat{E}_J|| \rangle|^2 + |\langle ||\hat{M}_J|| \rangle|^2) \right. \\
& \left. \pm \hat{q} \cdot (\hat{\nu} - \vec{\beta}) 2 \operatorname{Re} \left(\langle ||\hat{E}_J|| \rangle \langle ||\hat{M}_J|| \rangle^* \right) \right] \\
+ \sum_{J=0}^{\infty} & \left[(1 - \vec{\beta} \cdot \hat{\nu} + 2(\hat{\nu} \cdot \hat{q})(\vec{\beta} \cdot \hat{q})) |\langle ||\hat{L}_J|| \rangle|^2 \right. \\
& \left. + (1 + \vec{\beta} \cdot \hat{\nu}) |\langle ||\hat{C}_J|| \rangle|^2 - \hat{q} \cdot (\hat{\nu} + \vec{\beta}) 2 \operatorname{Re} \left(\langle ||\hat{L}_J|| \rangle \langle ||\hat{C}_J|| \rangle^* \right) \right],
\end{aligned}
\tag{17.179}
$$

in terms of the multipole operators, i.e. the Coloumb, longitudinal, electric, and magnetic operators:

$$
\hat{C}_J(q) = \int d^3r \; j_J(qr) Y_J(\hat{r}) \mathcal{J}_0(\vec{r}) \tag{17.180}
$$

$$
\hat{L}_J(q) = \frac{i}{q} \int d^3r \; \left[\vec{\nabla}(j_J(qr) Y_J(\hat{r})) \right] \cdot \vec{\mathcal{J}}(\vec{r}) \tag{17.181}
$$

$$
\hat{E}_J(q) = \frac{1}{q} \int d^3r \; \left[\vec{\nabla} \times (j_J(qr) \vec{Y}_{JJ1}(\hat{r})) \right] \cdot \vec{\mathcal{J}}(\vec{r}) \tag{17.182}
$$

$$
\hat{M}_J(q) = \int d^3r \; j_J(qr) \vec{Y}_{JJ1}(\hat{r}) \cdot \vec{\mathcal{J}}(\vec{r}). \tag{17.183}
$$

- $j_J(qr)$ are spherical Bessel functions

- $Y_J(\hat{r})$, $\hat{Y}_{Jl1}$ are spherical harmonics, vector spherical harmonics

- $\vec{\mathcal{J}}(\vec{r})$, $\mathcal{J}_0(\vec{r})$ is the nuclear current, nuclear charge

These correspond to equations (13a-d) in [67], which Behrens and Burhing point out in Section 9.3 of their text comparing different formalisms [24].

Impulse approximation, leading order multipole operators

The next solidifying step in the formalism is to express the multipole expansion of the operators in terms of single-particle matrix elements of well known operators, namely those of [67]. For that to happen, one has to apply the impulse approximation to the nuclear currents; writing the current density operator as one body currents. A non-relativistic expansion is made, taking the low-momentum limit of nucleonic motion within the nucleus, and the current density operator is written as a sum of first-quantization, location-independent operators [102]:

$$\mathcal{J}(\vec{r}) = \sum_{j=1}^{A} \hat{\mathcal{J}}^{(1)}(j)\delta^{(3)}(\vec{r} - \vec{r}_j) \tag{17.184}$$

There are separate expressions for the V and A currents, listed in equations (A3a - A.3d) of [102]. The operators from equations (17.179), now with the non-relativistic and impulse-approximated currents, become:

Vector:

$$\hat{C}_J^V(q) = g_V \sum_{j=1}^{A} M_J(q\vec{r}_j)\tau_j^{\pm} + \mathcal{O}(\epsilon_{qr}^J \epsilon_{NR}^2) \tag{17.185}$$

$$\hat{L}_J^V(q) = -\frac{q}{2m_N}g_V \sum_{j=1}^{A} \left\{ M_J(q\vec{r}_j) - 2\left[\frac{1}{q}\vec{\nabla}M_J(q\vec{r}_j)\right] \cdot \frac{1}{q}\vec{\nabla} \right\}\tau_j^{\pm} + \mathcal{O}(\epsilon_{qr}^{J-1}\epsilon_{NR}^2) \tag{17.186}$$

$$\hat{E}_J^V(q) = \frac{q}{m_N} \sum_{j=1}^{A} \left\{ -ig_V \left[\frac{1}{q}\vec{\nabla} \times \vec{M}_{JJ1}(q\vec{r}_j)\right] \cdot \frac{1}{q}\vec{\nabla} \right. \tag{17.187}$$

$$\left. + \frac{g_V + \tilde{g}_{T(V)}}{2}\vec{M}_{JJ1}(q\vec{r}_j) \cdot \vec{\sigma}_j \right\}\tau_j^{\pm} + \mathcal{O}(\epsilon_{qr}^{J-1}\epsilon_{NR}^2) \tag{17.188}$$

$$\hat{M}_J^V(q) = -\frac{iq}{m_N} \sum_{j=1}^{A} \left\{ g_V \vec{M}_{JJ1}(q\vec{r}_j) \cdot \frac{1}{q}\vec{\nabla} \right. \tag{17.189}$$

$$\left. + i\frac{g_V + \tilde{g}_{T(V)}}{2} \left[\frac{1}{q}\vec{\nabla} \times \vec{M}_{JJ1}(q\vec{r}_j) \right] \cdot \vec{\sigma}_j \right\} \tau_j^{\pm} + \mathcal{O}(\epsilon_{qr}^J \epsilon_{NR}^2). \tag{17.190}$$

Axial-vector:

$$\hat{C}_J^A(q) = -\frac{iq}{m_N} \sum_{j=1}^{A} \left\{ g_A M_J(q\vec{r}_j)\vec{\sigma}_j \cdot \frac{1}{q}\vec{\nabla} + \frac{1}{2}\left[g_A - \frac{\tilde{g}_P}{2m_N}(E_0 \pm \Delta E_c) \right] \right. \tag{17.191}$$

$$\left. \times \left[\frac{1}{q}\vec{\nabla}M_J(q\vec{r}_j)\right] \cdot \vec{\sigma}_j \right\} \tau_j^{\pm} + \mathcal{O}(\epsilon_{qr}^J \epsilon_{NR}^2) \tag{17.192}$$

$$\hat{L}_J^A(q) = i\left(g_A + \frac{q^2}{(2m_N)^2}\tilde{g}_P \right) \sum_{j=1}^{A}[\frac{1}{q}\vec{\nabla}M_J(q\vec{r}_j)] \cdot \vec{\sigma}_j\tau_j^{\pm} + \mathcal{O}(\epsilon_{qr}^{J-1} \epsilon_{NR}^2) \tag{17.193}$$

$$\hat{E}_J^A(q) = \left(g_A + \frac{q^2}{(2m_N)^2}\tilde{g}_P \right) \sum_{j=1}^{A}[\frac{1}{q}\vec{\nabla} \times \vec{M}_{JJ1}(q\vec{r}_j)] \cdot \vec{\sigma}_j\tau_j^{\pm} + \mathcal{O}(\epsilon_{qr}^{J-1} \epsilon_{NR}^2) \tag{17.194}$$

$$\hat{M}_J^A(q) = \left(g_A + \frac{q^2}{(2m_N)^2}\tilde{g}_P \right) \sum_{j=1}^{A} \vec{M}_{JJ1}(q\vec{r}_j) \cdot \vec{\sigma}_j\tau_j^{\pm} + \mathcal{O}(\epsilon_{qr}^J \epsilon_{NR}^2) \tag{17.195}$$

- $M_J(q\vec{r}) = j_J(qr)Y_J(\hat{r})$

- $\vec{M}_{JL1}(q\vec{r}) = j_L(qr)\vec{Y}_{JL1}(\hat{r})$

Fermi Transition $J^{\Delta\pi} = 0^+$

The operator for the Fermi transition, i.e. for $J^{\Delta\pi} = 0^+$, to leading order is

$$\Theta^{0^+}(q, \vec{\beta} \cdot \vec{\nu}) = (1 + \vec{\beta} \cdot \hat{\nu})|\langle||\hat{C}_0^V||\rangle|^2$$

$$= (1 + \vec{\beta} \cdot \hat{\nu})|\langle||\hat{1}||\rangle|^2, \tag{17.196}$$

where I have taken the NLO shape-correction term $\delta_1^{0^+} \approx 0$, the nuclear-structure-depednent factor $b^{0^+} \approx 0$, and the recoiled-nucleus correction $a^{0^+} \approx 1$.

Gamow-Teller $J^{\Delta\pi} = 1^+$

The operator for the Gamow-Teller transition, i.e. for $J^{\Delta\pi} = 1^+$, to leading order is

$$\Theta^{1^+}(q, \vec{\beta} \cdot \vec{\nu}) = 3|\langle||\hat{L}_1^A||\rangle|^2$$
$$= 3|\langle||\hat{\boldsymbol{\sigma}}||\rangle|^2.$$
(17.197)

Non-unique first-forbidden transition $J^{\Delta\pi} = 0^-$

We are interested in medium-to-heavy mass nuclei, so I set the recoil terms to zero: $\delta_1^{0^-} = 0$, $\delta_{\beta^2}^{0^-} = 0$, and $\delta_{(\beta\nu)^2}^{0^-} = 0$. The angular correlation coefficient is likewise negligible, so $a^{0^-} = 1$. Finally, the Fierz term is ignored, $b^{0^-} = 0$. The operator for non-unique first-forbidden transitions is then:

$$\Theta^{0^-}(q, \vec{\beta} \cdot \hat{\nu}) = (1 + \vec{\beta} \cdot \hat{\nu}) \left[|\langle||\hat{C}_0^A||\rangle|^2 - \frac{E_0}{q} 2\,\mathrm{Re}(\langle||\hat{L}_0^A||\rangle\langle||\hat{C}_0^A||\rangle^*) + |\langle||\hat{L}_0^A||\rangle|^2 \right]$$
$$+ 2\frac{E(E_0 - E)}{q^2}[\beta^2 - (\vec{\beta} \cdot \hat{\nu})^2]|\langle||\hat{L}_0^A||\rangle|^2.$$
(17.198)

Bibliography

[1] D. Abriola and A. Sonzogni. Nuclear data sheets for A = 94. *Nuclear Data Sheets*, 107(9):2423–2578, 2006.

[2] A. Adams, G. Mitchell, W. Ormand, and J. Shriner. Distribution of shell model reduced transition probabilities in 22Na. *Physics Letters B*, 392(1–2):1–6, Jan. 1997.

[3] M. Aker, A. Beglarian, J. Behrens, A. Berlev, U. Besserer, B. Bieringer, F. Block, S. Bobien, M. Böttcher, B. Bornschein, L. Bornschein, T. Brunst, T. S. Caldwell, R. M. D. Carney, L. La Cascio, S. Chilingaryan, W. Choi, K. Debowski, M. Deffert, M. Descher, D. Díaz Barrero, P. J. Doe, O. Dragoun, G. Drexlin, K. Eitel, E. Ellinger, R. Engel, S. Enomoto, A. Felden, J. A. Formaggio, F. M. Fränkle, G. B. Franklin, F. Friedel, A. Fulst, K. Gauda, W. Gil, F. Glück, R. Grössle, R. Gumbsheimer, V. Gupta, T. Höhn, V. Hannen, N. Haußmann, K. Helbing, S. Hickford, R. Hiller, D. Hillesheimer, D. Hinz, T. Houdy, A. Huber, A. Jansen, C. Karl, F. Kellerer, J. Kellerer, M. Kleifges, M. Klein, C. Köhler, L. Köllenberger, A. Kopmann, M. Korzeczek, A. Kovalík, B. Krasch, H. Krause, N. Kunka, T. Lasserre, T. L. Le, O. Lebeda, B. Lehnert, A. Lokhov, M. Machatschek, E. Malcherek, M. Mark, A. Marsteller, E. L. Martin, C. Melzer, A. Menshikov, S. Mertens, J. Mostafa, K. Müller, H. Neumann, S. Niemes, P. Oelpmann, D. S. Parno, A. W. P. Poon, J. M. L. Poyato, F. Priester, S. Ramachandran, R. G. H. Robertson, W. Rodejohann, M. Röllig, C. Röttele, C. Rodenbeck, M. Ryšavý, R. Sack, A. Saenz, P. Schäfer, A. Schaller née Pollithy, L. Schimpf, K. Schlösser, M. Schlösser, L. Schlüter, S. Schneidewind, M. Schrank, B. Schulz, A. Schwemmer, M. Šefčík, V. Sibille, D. Siegmann, M. Slezák, F. Spanier, M. Steidl, M. Sturm, M. Sun, D. Tcherniakhovski, H. H. Telle, L. A. Thorne, T. Thümmler, N. Titov, I. Tkachev, K. Urban, K. Valerius, D. Vénos, A. P. Vizcaya Hernández, C. Weinheimer, S. Welte, J. Wendel, J. F. Wilkerson, J. Wolf, S. Wüstling, J. Wydra, W. Xu, Y. R. Yen, S. Zadoroghny, and G. Zeller. Direct neutrino-mass measurement with sub-electronvolt sensitivity. *Nature Physics*, 18(2):160–166, Feb. 2022.

[4] A. Algora, D. Cano-Ott, B. Rubio, J. Tain, J. Agramunt, J. Blomqvist, L. Batist, R. Borcea, R. Collatz, A. Gadea, J. Gerl, M. Gierlik, M. Górska, O. Guilbaud, H. Grawe, M. Hellström, Z. Hu, Z. Janas, M. Karny, R. Kirchner, P. Kleinheinz, W. Liu, T. Martinez, F. Moroz, A. Plochocki, M. Rejmund, E. Roeckl, K. Rykaczewski, M. Shibata, J. Szerypo, and V. Wittmann. The GT resonance revealed in $\beta+$-decay using new experimental techniques. *Nuclear Physics A*, 654(1, Supplement 1):727c–730c, 1999.

[5] L. Amico, R. Fazio, A. Osterloh, and V. Vedral. Entanglement in many-body systems. *Reviews of Modern Physics*, 80(2):517–576, May 2008.

[6] N. Anand, A. L. Fitzpatrick, and W. C. Haxton. Weakly interacting massive particle-nucleus elastic scattering response. *Physical Review C*, 89(6), June 2014.

[7] E. Anders and N. Grevesse. Abundances of the elements: Meteoritic and solar. *Geochimica et Cosmochimica Acta*, 53(1):197–214, Jan. 1989.

[8] E. Anderson, Z. Bai, C. Bischof, L. S. Blackford, J. Demmel, J. Dongarra, J. Du Croz, A. Greenbaum, S. Hammarling, A. McKenney, et al. *LAPACK Users' Guide*. SIAM, 1999.

[9] F. Andreozzi, N. L. Iudice, and A. Porrino. An importance sampling algorithm for generating exact eigenstates of the nuclear Hamiltonian. *Journal of Physics G: Nuclear and Particle Physics*, 29(10):2319–2333, Sept. 2003.

[10] F. Andreozzi and A. Porrino. Truncation of large shell-model eigenproblems by model space partitioning, 1999.

[11] F. Andreozzi and A. Porrino. A redundancy-free approach to the use of correlated bases in the truncation of large shell-model eigenproblems. *Journal of Physics G: Nuclear and Particle Physics*, 27(4):845–853, Mar. 2001.

[12] F. Andreozzi, A. Porrino, and N. L. Iudice. A simple iterative algorithm for generating selected eigenspaces of large matrices. *Journal of Physics A: Mathematical and General*, 35(5):L61–L66, Jan. 2002.

[13] A. Arcones, D. W. Bardayan, T. C. Beers, L. A. Bernstein, J. C. Blackmon, B. Messer, B. A. Brown, E. F. Brown, C. R. Brune, A. E. Champagne, A. Chieffi, A. J. Couture, P. Danielewicz, R. Diehl, M. El-Eid, J. E. Escher, B. D. Fields, C. Fröhlich, F. Herwig, W. R. Hix, C. Iliadis, W. G. Lynch, G. C. McLaughlin, B. S. Meyer, A. Mezzacappa, F. Nunes, B. W. O'Shea, M. Prakash, B. Pritychenko, S. Reddy, E. Rehm, G. Rogachev, R. E. Rutledge, H. Schatz, M. S. Smith, I. H. Stairs, A. W. Steiner, T. E. Strohmayer, F. Timmes, D. M. Townsley, M. Wiescher, R. G. Zegers, and M. Zingale. White paper on nuclear astrophysics and low energy nuclear physics Part 1: Nuclear astrophysics. *Progress in Particle and Nuclear Physics*, 94:1–67, 2017.

[14] M. Arnould and S. Goriely. The p-process of stellar nucleosynthesis: Astrophysics and nuclear physics status. *Physics Reports*, 384(1):1–84, 2003.

[15] D. P. Arteaga and P. Ring. Relativistic random-phase approximation in axial symmetry. *Physical Review C*, 77(3), Mar. 2008.

[16] P. Athron, C. Balázs, A. Beniwal, S. Bloor, J. E. Camargo-Molina, J. M. Cornell, B. Farmer, A. Fowlie, T. E Gonzalo, F. Kahlhoefer, et al. Global analyses of Higgs portal singlet dark matter models using GAMBIT. *The European Physical Journal C*, 79(1):1–28, 2019.

[17] V. Avrigeanu, M. Avrigeanu, and C. Mănăilescu. Further explorations of the α-particle optical model potential at low energies for the mass range $A \approx 45$–209. *Phys. Rev. C*, 90:044612, Oct 2014.

[18] P. Axel. Electric dipole ground-state transition width strength function and 7-mev photon interactions. *Physical Review*, 126(2):671–683, Apr. 1962.

[19] C. Bahri, D. J. Rowe, and W. Wijesundera. Phase transition in the pairing-plus-quadrupole model. *Physical Review C: Nuclear Physics*, 58(3):1539–1550, Sept. 1998.

[20] C. Bahri and DJ. Rowe. SU(3) quasi-dynamical symmetry as an organizational mechanism for generating nuclear rotational motions. *Nuclear Physics A*, 662(1):125–147, 2000.

[21] G. A. Bartholomew, E. D. Earle, A. J. Ferguson, J. W. Knowles, and M. A. Lone. Gamma-ray strength functions. In M. Baranger and E. Vogt, editors, *Advances in Nuclear Physics: Volume 7*, pages 229–324. Springer US, Boston, MA, 1973.

[22] G. Baur and H. Rebel. Coulomb breakup of nuclei - Applications to astrophysics. *Annual Review of Nuclear and Particle Science*, 46:321–350, 1996.

[23] H. Behrens and W. Bühring. Nuclear beta decay. *Nuclear Physics A*, 162(1):111–144, 1971.

[24] H. Behrens and W. Bühring. *Electron Radial Wave Functions and Nuclear Beta-Decay*. International Series of Monographs on Physics. Clarendon Press, 1982.

[25] H. Behrens, M. Kobelt, L. Szybisz, and W. G. Thies. The unique first-forbidden β-DECAY OF 86Rb. *Nuclear Physics A*, 245(3):515–527, 1975.

[26] H. Behrens, M. Kobelt, WG. Thies, and H. Appel. The first forbidden beta decay of Pb209. *Zeitschrift für Physik A Hadrons and nuclei*, 252(4):349–361, 1972.

[27] G. Bertone and D. Hooper. History of dark matter. *Reviews of Modern Physics*, 90(FERMILAB-PUB-16-157-A):045002, 2018.

[28] F. E. Bertrand, G. R. Satchler, D. J. Horen, J. R. Wu, A. D. Bacher, G. T. Emery, W. P. Jones, D. W. Miller, and A. van der Woude. Giant multipole resonances from inelastic scattering of 152-MeV alpha particles. *Physical Review C: Nuclear Physics*, 22(5):1832–1847, Nov. 1980.

[29] F. Bečvář. Simulation of γ cascades in complex nuclei with emphasis on assessment of uncertainties of cascade-related quantities. *Nuclear Instruments and Methods in Physics Research Section A: Accelerators, Spectrometers, Detectors and Associated Equipment*, 417(2–3):434–449, Nov. 1998.

[30] G. Blanchon, M. Dupuis, and H. F. Arellano. Prospective study on microscopic potential with Gogny interaction. *The European Physical Journal A*, 51(12), Dec. 2015.

[31] J. Blatt and V. Weisskopf. *Theoretical Nuclear Physics*. Dover Books on Physics Series. Dover Publications, 1991.

[32] J. Blomqvist and A. Molinari. Collective 0- vibrations in even spherical nuclei with tensor forces. *Nuclear Physics A*, 106(3):545–569, 1968.

[33] G. R. Blumenthal, S. Faber, J. R. Primack, and M. J. Rees. Formation of galaxies and large scale structure with cold dark matter. *Nature*, 311(SLAC-PUB-3307):517–525, 1984.

[34] A. Bohr and B. Mottelson. *Nuclear Structure, Vol. 1.* World Scientific, Singapore, 1998.

[35] R. Bonetti, L. Colombo, and K.-I. Kubo. Inelastic α-scattering to the continuum: A probe of α-clustering in nuclei. *Nuclear Physics*, A420:109–123, 1984.

[36] J. Bonn, F. Buchinger, P. Dabkiewicz, H. Fischer, SL. Kaufman, H.-J. Kluge, H. Kremmling, L. Kugler, R. Neugart, EW. Olten, et al. Determination of nuclear spins of short-lived Rb and Cs isotopes by β radiation detected optical pumping. *Hyperfine Interactions*, 4(1-2):174–178, 1978.

[37] G. Boutoux, B. Jurado, V. Méot, O. Roig, L. Mathieu, M. Aïche, G. Barreau, N. Capellan, I. Companis, S. Czajkowski, K.-H. Schmidt, J. Burke, A. Bail, J. Daugas, T. Faul, P. Morel, N. Pillet, C. Théroine, X. Derkx, O. Sérot, I. Matéa, and L. Tassan-Got. Study of the surrogate-reaction method applied to neutron-induced capture cross sections. *Physics Letters B*, 712(4–5):319–325, 2012.

[38] T. Bringmann, J. Conrad, J. M. Cornell, L. A. Dal, J. Edsjö, B. Farmer, F. Kahlhoefer, A. Kvellestad, A. Putze, C. Savage, et al. DarkBit: A GAMBIT module for computing dark matter observables and likelihoods. *The European Physical Journal C*, 77(12):1–57, 2017.

[39] D. Brink. *Some aspects of the interaction of light with matter*. PhD thesis, University of Oxford, 1955.

[40] B. A. Brown and A. C. Larsen. Large low-energy M1 strength for ^{56,57}Fe within the nuclear shell model. *Physical Review Letters*, 113(25):252502, Dec. 2014.

[41] B. A. Brown and W. D. M. Rae. The shell-model code NuShellX@MSU. *Nuclear Data Sheets*, 120:115–118, 2014.

[42] B. A. Brown and W. A. Richter. New "USD" Hamiltonians for the sd shell. *Physical Review C: Nuclear Physics*, 74(3):034315, Sept. 2006.

[43] B. A. Brown, N. J. Stone, J. R. Stone, I. S. Towner, and M. Hjorth-Jensen. Magnetic moments of the 2_1^+ states around ^{132}Sn. *Physical Review C: Nuclear Physics*, 71(4):044317, Apr. 2005.

[44] B. A. Brown and BH. Wildenthal. Status of the nuclear shell model. *Annual Review of Nuclear and Particle Science*, 38(1):29–66, 1988.

[45] D. Brown, M. Chadwick, R. Capote, A. Kahler, A. Trkov, M. Herman, A. Sonzogni, Y. Danon, A. Carlson, M. Dunn, D. Smith, G. Hale, G. Arbanas, R. Arcilla, C. Bates, B. Beck, B. Becker, F. Brown, R. Casperson, J. Conlin, D. Cullen, M.-A. Descalle, R. Firestone, T. Gaines, K. Guber, A. Hawari, J. Holmes, T. Johnson, T. Kawano, B. Kiedrowski, A. Koning, S. Kopecky, L. Leal, J. Lestone, C. Lubitz, J. Marquez Damian, C. Mattoon, E. McCutchan, S. Mughabghab, P. Navratil, D. Neudecker, G. Nobre, G. Noguere, M. Paris, M. Pigni, A. Plompen, B. Pritychenko, V. Pronyaev, D. Roubtsov, D. Rochman, P. Romano, P. Schillebeeckx, S. Simakov, M. Sin, I. Sirakov, B. Sleaford, V. Sobes, E. Soukhovitskii, I. Stetcu, P. Talou, I. Thompson, S. van der Marck, L. Welser-Sherrill, D. Wiarda, M. White, J. Wormald, R. Wright, M. Zerkle, G. Žerovnik, and Y. Zhu. ENDF/B-VIII.0: The 8th major release of the nuclear reaction data library with CIELO-project cross sections, new standards and thermal scattering data. *Nuclear Data Sheets*, 148:1–142, 2018.

[46] P. Brussard and P. Glaudemans. *Shell-Model Applications in Nuclear Spectroscopy.* North-Holland Publishing Company, Amsterdam, 1977.

[47] E. M. Burbidge, G. R. Burbidge, W. A. Fowler, and F. Hoyle. Synthesis of the elements in stars. *Reviews of Modern Physics*, 29(4):547–650, Oct. 1957.

[48] R. Capote, M. Herman, P. Obložinský, P. Young, S. Goriely, T. Belgya, A. Ignatyuk, A. Koning, S. Hilaire, V. Plujko, M. Avrigeanu, O. Bersillon, M. Chadwick, T. Fukahori, Z. Ge, Y. Han, S. Kailas, J. Kopecky, V. Maslov, G. Reffo, M. Sin, E.Sh. Soukhovitskii, and P. Talou. RIPL – reference input parameter library for calculation of nuclear reactions and nuclear data evaluations. *Nuclear Data Sheets*, 110(12):3107–3214, 2009.

[49] Capote, R., Smith, D.L., and Trkov, A. Nuclear data evaluation methodology including estimates of covariances. *EPJ Web of Conferences*, 8:04001, 2010.

[50] B. V. Carlson, R. Capote, and M. Sin. Inclusive proton emission spectra from deuteron breakup reactions. *Few-Body Systems*, 57(5):307–314, May 2016.

[51] R. T. Carpenter. The electric-dipole gamma-ray strength function for heavy even-even nuclei, Aug. 1962.

[52] E. Caurier. Shell model and nuclear structure. *Progress in Particle and Nuclear Physics*, 59(1):226–242, July 2007.

[53] E. Caurier, G. Martinez-Pinedo, F. Nowacki, A. Poves, and A. P. Zuker. The shell model as a unified view of nuclear structure. *Reviews of Modern Physics*, 77(2):427–488, 2005.

[54] E. Caurier, J. Menéndez, F. Nowacki, and A. Poves. Influence of pairing on the nuclear matrix elements of the neutrinoless $\beta\beta$ decays. *Physical Review Letters*, 100(5):052503, Feb. 2008.

[55] E. Caurier, F. Nowacki, A. Poves, and K. Sieja. Collectivity in the light xenon isotopes: A shell model study. *Physical Review C: Nuclear Physics*, 82(6):064304, Dec. 2010.

[56] E. Caurier, A. Poves, and AP. Zuker. A full 0h?ω description of the $2\nu\beta\beta$ decay of 48 Ca. *Physics Letters B*, 252(1):13–17, 1990.

[57] M. Chadwick, P. Obložinský, M. Herman, N. Greene, R. McKnight, D. Smith, P. Young, R. MacFarlane, G. Hale, S. Frankle, A. Kahler, T. Kawano, R. Little, D. Madland, P. Moller, R. Mosteller, P. Page, P. Talou, H. Trellue, M. White, W. Wilson, R. Arcilla, C. Dunford, S. Mughabghab, B. Pritychenko, D. Rochman, A. Sonzogni, C. Lubitz, T. Trumbull, J. Weinman, D. Brown, D. Cullen, D. Heinrichs, D. McNabb, H. Derrien, M. Dunn, N. Larson, L. Leal, A. Carlson, R. Block, J. Briggs, E. Cheng, H. Huria, M. Zerkle, K. Kozier, A. Courcelle, V. Pronyaev, and S. van der Marck. ENDF/B-VII.0: Next generation evaluated nuclear data library for nuclear science and technology. *Nuclear Data Sheets*, 107(12):2931–3060, 2006.

[58] S. Chiba and O. Iwamoto. Verification of the surrogate ratio method. *Physical Review C: Nuclear Physics*, 81(4):044604, Apr. 2010.

[59] S. Cohen and D. Kurath. Effective interactions for the 1p shell. *Nuclear Physics*, 73(1):1–24, 1965.

[60] B. J. Cole. Predicted proton and two-proton decay energies for nuclei in the upper fp shell. *Physical Review C: Nuclear Physics*, 59(2):726–730, Feb. 1999.

[61] R. H. Cyburt, A. M. Amthor, R. Ferguson, Z. Meisel, K. Smith, S. Warren, A. Heger, R. D. Hoffman, T. Rauscher, A. Sakharuk, H. Schatz, F. K. Thielemann, and M. Wiescher. The JINA REACLIB database: Its recent updates and impact on type-I X-ray bursts. *The Astrophysical Journal Supplement Series*, 189(1):240–252, June 2010.

[62] D. Dashdorj, T. Kawano, P. E. Garrett, J. A. Becker, U. Agvaanluvsan, L. A. Bernstein, M. B. Chadwick, M. Devlin, N. Fotiades, G. E. Mitchell, R. O. Nelson, and W. Younes. Effect of preequilibrium spin distribution on ^{48}Ti +n cross sections. *Physical Review C: Nuclear Physics*, 75(5):054612, May 2007.

[63] P. J. Davis and P. Rabinowitz. Appendix 2 - FORTRAN programs. In *Methods of Numerical Integration (Second Edition)*, pages 480–508. Academic Press, second edition edition, 1984.

[64] S. DeBenedetti. *Nuclear Interactions*. Wiley, 1964.

[65] W. Dickhoff and R. Charity. Recent developments for the optical model of nuclei. *Progress in Particle and Nuclear Physics*, 105:252–299, 2019.

[66] F. S. Dietrich, I. J. Thompson, and T. Kawano. Target-state dependence of cross sections for reactions on statically deformed nuclei. *Physical Review C: Nuclear Physics*, 85(4):044611, Apr. 2012.

[67] T. Donnelly and W. Haxton. Multipole operators in semileptonic weak and electromagnetic interactions with nuclei: Harmonic oscillator single-particle matrix elements. *Atomic Data and Nuclear Data Tables*, 23(2):103–176, 1979.

[68] T. W. Donnelly and J. D. Walecka. Electron scattering and nuclear structure. *Annual Review of Nuclear Science*, 25(1):329–405, 1975.

[69] A. K. Drukier, K. Freese, and D. N. Spergel. Detecting cold dark-matter candidates. *Physical Review D: Particles and Fields*, 33(12):3495–3508, June 1986.

[70] G. Duhamel-Chrétien, G. Perrin, C. Perrin, V. Comparat, E. Gerlic, S. Galès, and C. P. Massolo. Neutron hole states in ^{89}Zr via the (p→,d) reaction at 58 mev. *Phys. Rev. C*, 43:1116–1126, Mar 1991.

[71] J. Dukelsky and S. Pittel. The density matrix renormalization group for finite fermi systems. *Reports on Progress in Physics*, 67(4):513, Mar. 2004.

[72] E. Escher, J., T. Burke, J., J. Casperson, R., O. Hughes, R., and D. Scielzo, N. One-nucleon pickup reactions and compound-nuclear decays. *Epj Web of Conferences*, 178:03002, 2018.

[73] M. Ebden. Gaussian processes: A quick introduction, 2015.

[74] A. Edmonds. *Angular Momentum in Quantum Mechanics*. Investigations in Physics Series. Princeton University Press, 1957.

[75] D. R. Entem and R. Machleidt. Accurate charge-dependent nucleon-nucleon potential at fourth order of chiral perturbation theory. *Physical Review C: Nuclear Physics*, 68(4):041001, Oct. 2003.

[76] J. Escher, K. Bergstrom, E. Chimanski, O. Gorton, E. J. In, M. Kruse, S. Péru, C. Pruitt, R. Rahman, E. Shinkle, A. Thapa, and W. Younes. Improving nuclear data evaluations with predictive reaction theory and indirect measurements. *EPJ Web of Conferences*, 284:03012, 2023.

[77] J. E. Escher. 87Y(n,g) and 90Zr(n,g) cross sections from surrogate reactions: Theoretical tools and illustration of the approach. Technical Report LLNL-TR-701412, Lawrence Livermore National Laboratory, 2016.

[78] J. E. Escher and F. S. Dietrich. Determining (n,f) cross sections for actinide nuclei indirectly: Examination of the surrogate ratio method. *Physical Review C: Nuclear Physics*, 74(5):054601, Nov. 2006.

[79] J. E. Escher and F. S. Dietrich. Cross sections for neutron capture from surrogate measurements: An examination of weisskopf-ewing and ratio approximations. *Phys. Rev. C*, 81:024612, Feb 2010.

[80] J. E. Escher, J. T. Harke, F. S. Dietrich, N. D. Scielzo, I. J. Thompson, and W. Younes. Compound-nuclear reaction cross sections from surrogate measurements. *Reviews of Modern Physics*, 84(1):353–397, Mar. 2012.

[81] J. E. Escher, J. T. Harke, R. O. Hughes, N. D. Scielzo, R. J. Casperson, S. Ota, H. I. Park, A. Saastamoinen, and T. J. Ross. Constraining neutron capture cross sections for unstable nuclei with surrogate reaction data and theory. *Physical Review Letters*, 121(5):052501, July 2018.

[82] N. W. Evans, C. A. J. O'Hare, and C. McCabe. SHM^{++}: A refinement of the standard halo model for dark matter searches in light of the gaia sausage, 2018.

[83] D.-L. Fang and B. A. Brown. Effect of first-forbidden decays on the shape of neutrino spectra. *Physical Review C: Nuclear Physics*, 91(2):025503, Feb. 2015.

[84] P. Fanto, Y. Alhassid, and H. A. Weidenmüller. Statistical-model description of γ decay from compound-nucleus resonances. *Phys. Rev. C*, 101:014607, Jan 2020.

[85] P. Fanto, G. F. Bertsch, and Y. Alhassid. Neutron width statistics in a realistic resonance-reaction model. *Physical Review C*, 98(1), July 2018.

[86] J. L. Feng. Dark matter candidates from particle physics and methods of detection. *Annual Review of Astronomy and Astrophysics*, 48(1):495–545, Aug. 2010.

[87] A. Fetter and J. Walecka. *Quantum Theory of Many-Particle Systems*. Dover Books on Physics. Dover Publications, 2012.

[88] R. B. Firestone. *Deconvolution of the Photon Strength Function*, page 179–184. Springer International Publishing, Sept. 2020.

[89] A. L. Fitzpatrick, W. Haxton, E. Katz, N. Lubbers, and Y. Xu. The effective field theory of dark matter direct detection. *Journal of Cosmology and Astroparticle Physics*, 2013(02):004–004, Feb. 2013.

[90] A. L. Fitzpatrick and K. M. Zurek. Dark moments and the DAMA-CoGeNT puzzle. *Physical Review D: Particles and Fields*, 82(7):075004, Oct. 2010.

[91] D. Foreman-Mackey, D. W. Hogg, D. Lang, and J. Goodman. Emcee: The MCMC hammer. *Publications of the Astronomical Society of the Pacific*, 125(925):306, Mar. 2013.

[92] C. Forssén, B. D. Carlsson, H. T. Johansson, D. Sääf, A. Bansal, G. Hagen, and T. Papenbrock. Large-scale exact diagonalizations reveal low-momentum scales of nuclei. *Phys. Rev. C*, 97:034328, Mar 2018.

[93] C. Forssén, F. Dietrich, J. Escher, R. Hoffman, and K. Kelley. Determining neutron capture cross sections via the surrogate reaction technique. *Physical Review C: Nuclear Physics*, 75:055807, 2007.

[94] J. M. R. Fox, C. W. Johnson, and R. N. Perez. Uncertainty quantification of an empirical shell-model interaction using principal component analysis. *Physical Review C: Nuclear Physics*, 101(5):054308, May 2020.

[95] J. M. R. Fox, C. W. Johnson, and R. N. Perez. Uncertainty quantification of transition operators in the empirical shell model. *Phys. Rev. C*, 108:054310, Nov 2023.

[96] H. Franz, J. V. Kratz, K. L. Kratz, W. Rudolph, G. Herrmann, F. M. Nuh, S. G. Prussin, and A. A. Shihab-Eldin. Delayed-neutron spectra following decay of ^{85}As and ^{135}Sb. *Physical Review Letters*, 33(14):859–862, Sept. 1974.

[97] S. Frauendorf and R. Schwengner. Evolution of low-lying M1 modes in germanium isotopes. *Physical Review C: Nuclear Physics*, 105(3):034335, Mar. 2022.

[98] K. Freese, J. Frieman, and A. Gould. Signal modulation in cold-dark-matter detection. *Physical Review D: Particles and Fields*, 37(12):3388–3405, June 1988.

[99] P. Fröbrich and R. Lipperheide. *Theory of Nuclear Reactions*. Clarendon Press, Oxford, 1996.

[100] E. Gadioli and P. E. Hodgson. *Pre-Equilibrium Nuclear Reactions*. Clarendon Press, Oxford, 1992.

[101] A. Gilbert and A. G. W. Cameron. A composite nuclear-level density formula with shell corrections. *Canadian Journal of Physics*, 43(8):1446–1496, Aug. 1965.

[102] A. Glick-Magid and D. Gazit. A formalism to assess the accuracy of nuclear-structure weak interaction effects in precision β-decay studies. *Journal of Physics G: Nuclear and Particle Physics*, 49(10):105105, Sept. 2022.

[103] M. Goldhaber and E. Teller. On nuclear dipole vibrations. *Physical Review*, 74(9):1046–1049, Nov. 1948.

[104] G. Golub. *Matrix Computations*. Johns Hopkins University Press, 2013.

[105] G. Golub and R. Underwood. The block lanczos method for computing eigenvalues. In J. R. Rice, editor, *Mathematical Software*, pages 361–377. Academic Press, 1977.

[106] M. González-Alonso and J. Martin Camalich. Isospin breaking in the nucleon mass and the sensitivity of β decays to new physics. *Physical Review Letters*, 112(4):042501, Jan. 2014.

[107] A. Goobar, S. Hannestad, E. Mörtsell, and H. Tu. The neutrino mass bound from WMAP 3 year data, the baryon acoustic peak, the SNLS supernovae and the Lyman-α forest. *Journal of Cosmology and Astroparticle Physics*, 2006(06):019, 2006.

[108] M. W. Goodman and E. Witten. Detectability of certain dark-matter candidates. *Physical Review D: Particles and Fields*, 31(12):3059–3063, June 1985.

[109] S. Goriely. Radiative neutron captures by neutron-rich nuclei and the r-process nucleosynthesis. *Physics Letters B*, 436(1-2):10–18, 1998.

[110] S. Goriely, P. Dimitriou, M. Wiedeking, T. Belgya, R. Firestone, J. Kopecky, M. Krtička, V. Plujko, R. Schwengner, S. Siem, H. Utsunomiya, S. Hilaire, S. Péru, Y. S. Cho, D. M. Filipescu, N. Iwamoto, T. Kawano, V. Varlamov, and R. Xu. Reference database for photon strength functions. *The European Physical Journal A*, 55(10), Oct. 2019.

[111] S. Goriely, S. Hilaire, and A. J. Koning. Improved microscopic nuclear level densities within the hartree-fock-bogoliubov plus combinatorial method. *Physical Review C*, 78(6), Dec. 2008.

[112] S. Goriely, S. Hilaire, S. Péru, and K. Sieja. Gogny-HFB+QRPA dipole strength function and its application to radiative nucleon capture cross section. *Physical Review C: Nuclear Physics*, 98(1):014327, July 2018.

[113] S. Goriely, F. Tondeur, and J. M. Pearson. A Hartree–Fock nuclear mass table. *Atomic Data and Nuclear Data Tables*, 77(2):311–381, Mar. 2001.

[114] O. Gorton and J. E. Escher. *Neutron Capture Cross Sections from Surrogate Reaction Data and Theory: Connecting the Pieces with a Markov-Chain Monte Carlo Approach*, page 229–231. Springer International Publishing, Sept. 2020.

[115] O. C. Gorton. Efficient modeling of nuclei through coupling of proton and neutron wavefunctions. Master's thesis, San Diego State University, 2018.

[116] O. C. Gorton and J. E. Escher. Cross sections for neutron-induced reactions from surrogate data: Reexamining the Weisskopf-Ewing approximation for (n,n') and (n,2n) reactions. *Physical Review C: Nuclear Physics*, 107(4):044612, Apr. 2023.

[117] O. C. Gorton, C. W. Johnson, and J. E. Escher. A problem in the statistical description of beta-delayed neutron emission. *EPJ Web of Conferences*, 284:03013, 2023.

[118] O. C. Gorton, C. W. Johnson, C. Jiao, and J. Nikoleyczik. Dmscatter: A fast program for WIMP-nucleus scattering. *Computer Physics Communications*, 284:108597, 2023.

[119] NB. Gove and MJ. Martin. Log-f tables for beta decay. *Atomic Data and Nuclear Data Tables*, 10(3):205–219, 1971.

[120] R. Grzywacz, J. Heideman, M. Madurga, Z. Xu, T. Kawano, J. Escher, T. King, and R. Lica. Evidence of non-statistical neutron emission following beta-decay near doubly magic 132Sn. *Bulletin of the American Physical Society*, 2022.

[121] V. Guadilla, J. L. Tain, A. Algora, J. Agramunt, D. Jordan, M. Monserrate, A. Montaner-Pizá, E. Nácher, S. E. A. Orrigo, B. Rubio, E. Valencia, M. Estienne, M. Fallot, L. Le Meur, J. A. Briz, A. Cucoanes, A. Porta, T. Shiba, A.-A. Zakari-Issoufou, A. A. Sonzogni, J. Äystö, T. Eronen, D. Gorelov, J. Hakala, A. Jokinen, A. Kankainen, V. S. Kolhinen, J. Koponen, I. D. Moore, H. Penttilä, I. Pohjalainen, J. Reinikainen, M. Reponen, S. Rinta-Antila, K. Rytkönen, V. Sonnenschein, A. Voss,

L. M. Fraile, V. Vedia, E. Ganioğğlu, W. Gelletly, M. Lebois, J. N. Wilson, and T. Martinez. Total absorption γ-ray spectroscopy of the β-delayed neutron emitters ^{137}I and ^{95}Rb. *Physical Review C: Nuclear Physics*, 100(4):044305, Oct. 2019.

[122] P. Gysbers, G. Hagen, JD. Holt, G. R. Jansen, T. D. Morris, P. Navrátil, T. Papenbrock, S. Quaglioni, A. Schwenk, SR. Stroberg, et al. Discrepancy between experimental and theoretical β-decay rates resolved from first principles. *Nature Physics*, 15(5):428–431, 2019.

[123] M. Haaranen, J. Kotila, and J. Suhonen. Spectrum-shape method and the next-to-leading-order terms of the β-decay shape factor. *Physical Review C: Nuclear Physics*, 95(2):024327, Feb. 2017.

[124] O. Hall, T. Davinson, A. Estrade, J. Liu, G. Lorusso, F. Montes, S. Nishimura, V. Phong, P. Woods, J. Agramunt, D. Ahn, A. Algora, J. Allmond, H. Baba, S. Bae, N. Brewer, C. Bruno, R. Caballero-Folch, F. Calviño, P. Coleman-Smith, G. Cortes, I. Dillmann, C. Domingo-Pardo, A. Fijalkowska, N. Fukuda, S. Go, C. Griffin, R. Grzywacz, J. Ha, L. Harkness-Brennan, T. Isobe, D. Kahl, L. Khiem, G. Kiss, A. Korgul, S. Kubono, M. Labiche, I. Lazarus, J. Liang, Z. Liu, K. Matsui, K. Miernik, B. Moon, A. Morales, P. Morrall, M. Mumpower, N. Nepal, R. Page, M. Piersa, V. Pucknell, B. Rasco, B. Rubio, K. Rykaczewski, H. Sakurai, Y. Shimizu, D. Stracener, T. Sumikama, H. Suzuki, J. Tain, H. Takeda, A. Tarifeño-Saldivia, A. Tolosa-Delgado, M. Wolińska-Cichocka, and R. Yokoyama. β-delayed neutron emission of r-process nuclei at the N=82 shell closure. *Physics Letters B*, 816:136266, 2021.

[125] A. Hamoudi, R. G. Nazmitdinov, E. Shahaliev, and Y. Alhassid. Statistical fluctuations of electromagnetic transition intensities and electromagnetic moments in pf-shell nuclei. *Phys. Rev. C*, 65:064311, Jun 2002.

[126] J. Hardy, L. Carraz, B. Jonson, and P. Hansen. The essential decay of pandemonium: A demonstration of errors in complex beta-decay schemes. *Physics Letters B*, 71(2):307–310, 1977.

[127] H. Hasper. Large scale shell-model calculations in the upper part of the sd shell: General description and energy levels for A=36-39. *Physical Review C: Nuclear Physics*, 19(4):1482–1497, Apr. 1979.

[128] W. K. Hastings. Monte Carlo sampling methods using Markov chains and their applications. *Biometrika*, 57(1):97–109, Apr. 1970.

[129] W. Hauser and H. Feshbach. The inelastic scattering of neutrons. *Physical Review*, 87(2):366–373, July 1952.

[130] W. Haxton and C. Lunardini. SevenOperators, a Mathematica script for harmonic oscillator nuclear matrix elements arising in semileptonic electroweak interactions. *Computer Physics Communications*, 179(5):345–358, 2008.

[131] L. Hayen, J. Kostensalo, N. Severijns, and J. Suhonen. First-forbidden transitions in the reactor anomaly. *Physical Review C: Nuclear Physics*, 100(5):054323, Nov. 2019.

[132] L. Hayen, N. Severijns, K. Bodek, D. Rozpedzik, and X. Mougeot. High precision analytical description of the allowed β spectrum shape. *Reviews of Modern Physics*, 90(1):015008, Mar. 2018.

[133] A. C. Hayes. Applications of nuclear physics. *Reports on Progress in Physics*, 80(2):026301, Jan. 2017.

[134] C. Hebborn, F. Nunes, G. P. Potel Aguilar, W. H. Dickhoff, J. W. Holt, M. C. Atkinson, R. B. Baker, C. Barbieri, G. Blanchon, M. Burrows, R. Capote Noy, P. Danielewicz, M. Dupuis, Ch. Elster, J. Escher, L. Hlophe, A. Idini, H. Jayatissa, B. P. Kay, K. Kravvaris, J. J. Manfredi, A. Mercenne, B. Morillon, G. Perdikakis, C. D. Pruitt, G. H. Sargsyan, I. J. Thompson, M. Vorabbi, and T. R. Whitehead. Optical potentials for the rare-isotope beam era. *Journal of Physics G: Nuclear and Particle Physics*, 2023.

[135] J. Heideman, R. Grzywacz, Z. Y. Xu, M. Madurga, J. E. Escher, T. Kawano, A. Algora, A. N. Andreyev, J. Benito, T. Berry, M. J. G. Borge, C. Costache, H. De Witte, A. Fijalkowska, L. M. Fraile, H. O. U. Fynbo, A. Gottardo, C. Halverson, L. J. Harkness-Brennan, A. Illana, L. Janiak, D. S. Judson, T. T. King, A. Korgul, T. Kurtukian-Nieto, I. Lazarus, R. Lică, R. Lozeva, N. Marginean, R. Marginean, C. Mazzocchi, C. Mihai, R. E. Mihai, A. I. Morales, R. D. Page, J. Pakarinen, M. Piersa-Siłkowska, Z. Podolyák, M. Singh, C. Sotty, M. Stepaniuk, O. Tengblad, A. Turturica, P. Van Duppen, V. Vedia, S. Viñals, N. Warr, R. Yokoyama, and C. X. Yuan. Evidence of nonstatistical neutron emission following β decay near doubly magic ^{132}Sn. *Phys. Rev. C*, 108:024311, Aug 2023.

[136] M. Herman, R. Capote, B. V. Carlson, P. Oblozinsky, M. Sin, A. Trkov, H. Wienke, and V. Zerkin. EMPIRE: Nuclear reaction model code system for data evaluation. *Nuclear Data Sheets*, 108(12):2655–2715, 2007.

[137] R. A. Herrera, C. W. Johnson, and G. M. Fuller. Modified brink-axel hypothesis for astrophysical gamow-teller transitions. *Physical Review C: Nuclear Physics*, 105(1):015801, Jan. 2022.

[138] S. Hilaire, M. Girod, P. Demetriou, R. Julin, and S. V. Harissopulos. The amedee nuclear structure database. In *AIP Conference Proceedings*. AIP, 2008.

[139] S. Hilaire, M. Girod, S. Goriely, and A. J. Koning. Temperature-dependent combinatorial level densities with the d1m gogny force. *Physical Review C*, 86(6), Dec. 2012.

[140] S. Hilaire, Ch. Lagrange, and A. J. Koning. Comparisons between various width fluctuation correction factors for compound nucleus reactions. *Annals of Physics*, 306(2):209–231, 2003.

[141] M. Hoferichter, J. Menéndez, and A. Schwenk. Coherent elastic neutrino-nucleus scattering: EFT analysis and nuclear responses. *Physical Review D: Particles and Fields*, 102(INT-PUB-20-026):74018, July 2020.

[142] P. Hoff. The population of excited states in residual nuclei via delayed neutrons. *Nuclear Physics A*, 359(1):9–35, 1981.

[143] B. R. Holstein. Electromagnetic corrections to allowed nuclear beta decay. *Physical Review C: Nuclear Physics*, 9(5):1742–1747, May 1974.

[144] M. Honma, T. Otsuka, B. A. Brown, and T. Mizusaki. Effective interaction for pf-shell nuclei. *Physical Review C: Nuclear Physics*, 65(6):061301, May 2002.

[145] M. Honma, T. Otsuka, B. A. Brown, and T. Mizusaki. New effective interaction for pf-shell nuclei and its implications for the stability of the N=Z=28 closed core. *Physical Review C: Nuclear Physics*, 69(3):034335, Mar. 2004.

[146] M. Honma, T. Otsuka, BA. Brown, and T. Mizusaki. Shell-model description of neutron-rich pf-shell nuclei with a new effective interaction GXPF1. *The European Physical Journal A: Hadrons and Nuclei*, 25(1):499–502, 2005.

[147] M. Honma, T. Otsuka, T. Mizusaki, and M. Hjorth-Jensen. New effective interaction for f_5pg_9-shell nuclei. *Physical Review C: Nuclear Physics*, 80(6):064323, Dec. 2009.

[148] R. Horodecki, P. Horodecki, M. Horodecki, and K. Horodecki. Quantum entanglement. *Reviews of Modern Physics*, 81(2):865–942, June 2009.

[149] M. Horoi, B. A. Brown, and V. Zelevinsky. Truncation method for shell model calculations. *Physical Review C: Nuclear Physics*, 50(5):R2274–R2277, Nov. 1994.

[150] M. Horoi, B. A. Brown, and V. Zelevinsky. Exponential convergence method: Nonyrast states, occupation numbers, and a shell-model description of the superdeformed band in ^{56}Ni. *Physical Review C: Nuclear Physics*, 67(3):034303, Mar. 2003.

[151] M. Horoi, A. Volya, and V. Zelevinsky. Chaotic wave functions and exponential convergence of low-lying energy eigenvalues. *Physical Review Letters*, 82(10):2064–2067, Mar. 1999.

[152] Z. Hu, L. Batist, J. Agramunt, A. Algora, B. A. Brown, D. Cano-Ott, R. Collatz, A. Gadea, M. Gierlik, M. Górska, H. Grawe, M. Hellström, Z. Janas, M. Karny, R. Kirchner, F. Moroz, A. Płochocki, M. Rejmund, E. Roeckl, B. Rubio, M. Shibata, J. Szerypo, J. L. Tain, and V. Wittmann. β decay of ^{97}Ag: Evidence for the Gamow-Teller resonance near ^{100}Sn. *Physical Review C: Nuclear Physics*, 60(2):024315, July 1999.

[153] R. O. Hughes, C. W. Beausang, T. J. Ross, J. T. Burke, R. J. Casperson, N. Cooper, J. E. Escher, K. Gell, E. Good, P. Humby, M. McCleskey, A. Saastimoinen, T. D. Tarlow, and I. J. Thompson. ^{236}Pu(n,f), ^{237}Pu(n,f), and ^{238}Pu(n,f) cross sections deduced from (p,t), (p,d), and (p,p') surrogate reactions. *Physical Review C: Nuclear Physics*, 90(1):014304, July 2014.

[154] R. O. Hughes, J. T. Burke, and J. E. Escher. Toward (n,n') and (n,2n) cross sections for 155Gd using the surrogate reaction method and the NeutronSTARS detector. Technical report, Lawrence Livermore National Laboratory, (in progress) 2020.

[155] Y. Iwata, N. Shimizu, T. Otsuka, Y. Utsuno, J. Menéndez, M. Honma, and T. Abe. Large-scale shell-model analysis of the neutrinoless $\beta\beta$ decay of ^{48}Ca. *Physical Review Letters*, 116(11):112502, Mar. 2016.

[156] I. Jeong, S. Kang, S. Scopel, and G. Tomar. WimPyDD: An object-oriented Python code for the calculation of WIMP direct detection signals. *arXiv preprint arXiv:2106.06207*, 2021.

[157] J.-P. Jeukenne, A. Lejeune, and C. Mahaux. Optical-model potential in finite nuclei from Reid's hard core interaction. *Physical Review C: Nuclear Physics*, 16(1):80–96, July 1977.

[158] L. F. Jiao, Z. H. Sun, Z. X. Xu, F. R. Xu, and C. Qi. Correlated-basis method for shell-model calculations. *Physical Review C: Nuclear Physics*, 90(2):024306, Aug. 2014.

[159] H. T. Johansson and C. Forssén. Fast and accurate evaluation of wigner 3-j, 6-j, and 9-j symbols using prime factorization and multiword integer arithmetic. *SIAM Journal on Scientific Computing*, 38(1):A376–A384, 2016.

[160] C. W. Johnson. Systematics of strength function sum rules. *Physics Letters B*, 750:72–75, 2015.

[161] C. W. Johnson, G. F. Bertsch, and D. J. Dean. Orderly spectra from random interactions. *Physical Review Letters*, 80(13):2749–2753, Mar. 1998.

[162] C. W. Johnson and O. C. Gorton. Proton-neutron entanglement in the nuclear shell model. *Journal of Physics G: Nuclear and Particle Physics*, 50(4):045110, Mar. 2023.

[163] C. W. Johnson, K. D. Launey, N. Auerbach, S. Bacca, B. R. Barrett, C. R. Brune, M. A. Caprio, P. Descouvemont, W. H. Dickhoff, C. Elster, P. J. Fasano, K. Fossez, H. Hergert, M. Hjorth-Jensen, L. Hlophe, B. Hu, R. M. I. Betan, A. Idini, S. König, K. Kravvaris, D. Lee, J. Lei, A. Mercenne, R. N. Perez, W. Nazarewicz, F. M. Nunes, M. Płoszajczak, J. Rotureau, G. Rupak, A. M. Shirokov, I. Thompson, J. P. Vary, A. Volya, F. Xu, R. G. T. Zegers, V. Zelevinsky, and X. Zhang. White paper: From bound states to the continuum. *Journal of Physics G: Nuclear and Particle Physics*, 47(12):123001, Nov. 2020.

[164] C. W. Johnson, W. E. Ormand, and P. G. Krastev. Factorization in large-scale many-body calculations. *Computer Physics Communications*, 184(12):2761–2774, 2013.

[165] C. W. Johnson, W. E. Ormand, K. S. McElvain, and H. Shan. BIGSTICK: A flexible configuration-interaction shell-model code, 2018.

[166] T. Kawano. *CoH3: The Coupled-Channels and Hauser-Feshbach Code*, page 27–34. Springer International Publishing, Sept. 2020.

[167] T. Kawano, P. Möller, and W. B. Wilson. Calculation of delayed-neutron energy spectra in a quasiparticle random-phase approximation–Hauser-Feshbach model. *Physical Review C: Nuclear Physics*, 78(5):054601, Nov. 2008.

[168] R. Kelmar, A. Simon, O. Olivas-Gomez, P. Millican, C. S. Reingold, E. Churchman, A. M. Clark, S. L. Henderson, S. E. Kelly, D. Robertson, E. Stech, and W. P. Tan. Searching for $(\gamma,\alpha)/(\gamma,n)$ branching points in the γ-process path near $a = 100$. *Phys. Rev. C*, 101:015801, Jan 2020.

[169] M. Kerveno, M. Dupuis, A. Bacquias, F. Belloni, D. Bernard, C. Borcea, M. Boromiza, R. Capote, C. De Saint Jean, P. Dessagne, J. C. Drohé, G. Henning, S. Hilaire, T. Kawano, P. Leconte, N. Nankov, A. Negret, M. Nyman, A. Olacel, A. J. M. Plompen, P. Romain, C. Rouki, G. Rudolf, M. Stanoiu, and R. Wynants. Measurement of ^{238}U(n,n'γ) cross section data and their impact on reaction models. *Physical Review C: Nuclear Physics*, 104(4):044605, Oct. 2021.

[170] L. Kirsch and L. Bernstein. Rainier: A simulation tool for distributions of excited nuclear states and cascade fluctuations. *Nuclear Instruments and Methods in Physics Research Section A: Accelerators, Spectrometers, Detectors and Associated Equipment*, 892:30–40, June 2018.

[171] P. E. Koehler, A. C. Larsen, M. Guttormsen, S. Siem, and K. H. Guber. Extreme nonstatistical effects in γ decay of ^{95}mo neutron resonances. *Phys. Rev. C*, 88:041305, Oct 2013.

[172] A. Koning and M. Duijvestijn. A global pre-equilibrium analysis from 7 to 200 MeV based on the optical model potential. *Nuclear Physics A*, 744:15–76, 2004.

[173] A. Koning, S. Hilaire, and S. Goriely. Global and local level density models. *Nuclear Physics A*, 810(1-4):13–76, 2008.

[174] A. Koning, S. Hilaire, and S. Goriely. TALYS-1.9 *A nuclear reaction program* user manual, 2017.

[175] A. Koning, D. Rochman, J. Kopecky, J. Ch. Sublet, E. Bauge, S. Hilaire, P. Romain, B. Morillon, H. Duarte, S. van der Marck, S. Pomp, H. Sjostrand, R. Forrest, H. Henriksson, O. Cabellos, S. Goriely, J. Leppanen, H. Leeb, A. Plompen, and R. Mills. TENDL-2015: TALYS-based evaluated nuclear data library, 2015.

[176] A. J. Koning and J.-P. Delaroche. Local and global nucleon optical models from 1 keV to 200 MeV. *Nuclear Physics*, A713:231, 2003.

[177] A. J. Koning, S. Hilaire, and M. C. Duijvestijn. TALYS: Comprehensive nuclear reaction modeling. *AIP Conference Proceedings*, 769(1):1154–1159, 2005.

[178] J. Kopecky and M. Uhl. Test of gamma-ray strength functions in nuclear reaction model calculations. *Physical Review C*, 41(5):1941–1955, May 1990.

[179] D. P. Kroese, T. Taimre, and Z. I. Botev. *Handbook of Monte Carlo Methods*. John Wiley & Sons, 2013.

[180] A. T. Kruppa, J. Kovács, P. Salamon, Ö. Legeza, and G. Zaránd. Entanglement and seniority. *Physical Review C: Nuclear Physics*, 106(2):024303, Aug. 2022.

[181] M. K. G. Kruse. The no core shell model. In *Extensions to the No-Core Shell Model: Importance-truncation, Regulators and Reactions*, pages 9–32. Springer International Publishing, Cham, 2013.

[182] A. Larsen, A. Spyrou, S. Liddick, and M. Guttormsen. Novel techniques for constraining neutron-capture rates relevant for r-process heavy-element nucleosynthesis. *Progress in Particle and Nuclear Physics*, 107:69–108, 2019.

[183] A. C. Larsen, M. Guttormsen, M. Krtičcka, E. Běěták, A. Bürger, A. Görgen, H. T. Nyhus, J. Rekstad, A. Schiller, S. Siem, H. K. Toft, G. M. Tveten, A. V. Voinov, and K. Wikan. Analysis of possible systematic errors in the Oslo method. *Physical Review C: Nuclear Physics*, 83(3):034315, Mar. 2011.

[184] A. C. Larsen, J. E. Midtbø, M. Guttormsen, T. Renstrøm, S. N. Liddick, A. Spyrou, S. Karampagia, B. A. Brown, O. Achakovskiy, S. Kamerdzhiev, D. L. Bleuel, A. Couture, L. C. Campo, B. P. Crider, A. C. Dombos, R. Lewis, S. Mosby, F. Naqvi, G. Perdikakis, C. J. Prokop, S. J. Quinn, and S. Siem. Enhanced low-energy γ-decay strength of ^{70}Ni and its robustness within the shell model. *Physical Review C: Nuclear Physics*, 97(5):054329, May 2018.

[185] Ö. Legeza and J. Sólyom. Optimizing the density-matrix renormalization group method using quantum information entropy. *Physical Review B*, 68(19):195116, Nov. 2003.

[186] Ö. Legeza, L. Veis, A. Poves, and J. Dukelsky. Advanced density matrix renormalization group method for nuclear structure calculations. *Physical Review C: Nuclear Physics*, 92(5):051303, Nov. 2015.

[187] J. Lei and A. M. Moro. Numerical assessment of post-prior equivalence for inclusive breakup reactions. *Physical Review C: Nuclear Physics*, 92(6):061602, Dec. 2015.

[188] J. Lei and A. M. Moro. Reexamining closed-form formulae for inclusive breakup: Application to deuteron- and ^{6}Li-induced reactions. *Physical Review C: Nuclear Physics*, 92(4):044616, Oct. 2015.

[189] A. Lepretre, H. Beil, R. Bergere, P. Carlos, A. Veyssiere, and M. Sugawara. The giant dipole states in the A = 90 mass region. *Nuclear Physics A*, 175(3):609–628, 1971.

[190] J. Lewin and P. Smith. Review of mathematics, numerical factors, and corrections for dark matter experiments based on elastic nuclear recoil. *Astroparticle Physics*, 6(1):87–112, 1996.

[191] H. Mach, E. K. Warburton, R. L. Gill, R. F. Casten, J. A. Becker, B. A. Brown, and J. A. Winger. Meson-exchange enhancement of the first-forbidden ^{96}Y^g(0^-)$\rightarrow^{96}$Zr^g (0^+) β transition: β decay of the low-spin isomer of ^{96}Y. *Physical Review C: Nuclear Physics*, 41(1):226–242, Jan. 1990.

[192] M. Madurga, S. V. Paulauskas, R. Grzywacz, D. Miller, D. W. Bardayan, J. C. Batchelder, N. T. Brewer, J. A. Cizewski, A. Fijałkowska, C. J. Gross, M. E. Howard, S. V. Ilyushkin, B. Manning, M. Matoš, A. J. Mendez, K. Miernik, S. W. Padgett, W. A. Peters, B. C. Rasco, A. Ratkiewicz, K. P. Rykaczewski, D. W. Stracener, E. H. Wang, M. Woli ńska Cichocka, and E. F. Zganjar. Evidence for gamow-teller decay of ^{78}Ni core from beta-delayed neutron emission studies. *Phys. Rev. Lett.*, 117:092502, Aug 2016.

[193] W. J. Marciano and A. Sirlin. Improved calculation of electroweak radiative corrections and the value of V$_{ud}$. *Physical Review Letters*, 96(3):032002, Jan. 2006.

[194] P. Martin, Y. Gaillard, P. de Saintignon, G. Perrin, J. Chauvin, G. Duhamel, and J. Loiseaux. Excitation of low-lying levels and giant resonances in ^{90}Zr via 57.5 MeV polarized proton inelastic scattering. *Nuclear Physics A*, 315(3):291–309, 1979.

[195] M. Martini, S. Hilaire, S. Goriely, A. Koning, and S. Péru. Improved nuclear inputs for nuclear model codes based on the gogny interaction. *Nuclear Data Sheets*, 118:273–275, 2014.

[196] V. Maslov, Yu.V. Porodzinskij, N. Tetereva, M. Baba, and A. Hasegawa. 238U–nucleon–nucleus optical potential up to 200 MeV. *Nuclear Physics A*, 736(1):77–92, 2004.

[197] C. McCabe. Astrophysical uncertainties of dark matter direct detection experiments. *Physical Review D: Particles and Fields*, 82(2):023530, July 2010.

[198] J. E. Midtbø. *The Low-Energy Enhancement*. PhD thesis, University of Oslo, 2019.

[199] J. E. Midtbø, A. C. Larsen, T. Renstrøm, F. L. Bello Garrote, and E. Lima. Consolidating the concept of low-energy magnetic dipole decay radiation. *Physical Review C: Nuclear Physics*, 98(6):064321, Dec. 2018.

[200] J. E. Midtbø, F. Zeiser, E. Lima, A.-C. Larsen, G. M. Tveten, M. Guttormsen, F. L. Bello Garrote, A. Kvellestad, and T. Renstrøm. A new software implementation of the oslo method with rigorous statistical uncertainty propagation. *Computer Physics Communications*, 262:107795, May 2021.

[201] B. Mihaila. Matrix elements of the Argonne v18 potential. *arXiv preprint arXiv:1111.4018*, 2011.

[202] D. J. Millener, D. E. Alburger, E. K. Warburton, and D. H. Wilkinson. Decay scheme of ^{11}Be. *Physical Review C: Nuclear Physics*, 26(3):1167–1185, Sept. 1982.

[203] P. Moldauer. Statistics and the average cross section. *Nuclear Physics A*, 344(2):185–195, Aug. 1980.

[204] P. A. Moldauer. Why the hauser-feshbach formula works. *Phys. Rev. C*, 11:426–436, Feb 1975.

[205] P. A. Moldauer. Evaluation of the fluctuation enhancement factor. *Phys. Rev. C*, 14:764–766, Aug 1976.

[206] N. Mott and H. Massey. *The Theory of Atomic Collision*. International Series of Monographs on Physics. Clarendon Press, 1933.

[207] M. Mumpower, R. Surman, G. McLaughlin, and A. Aprahamian. The impact of individual nuclear properties on r-process nucleosynthesis. *Progress in Particle and Nuclear Physics*, 86:86–126, 2016.

[208] F. Naqvi, A. Simon, M. Guttormsen, R. Schwengner, S. Frauendorf, C. S. Reingold, J. T. Harke, N. Cooper, R. O. Hughes, S. Ota, and A. Saastamoinen. Nuclear level densities and γ-ray strength functions in samarium isotopes. *Physical Review C: Nuclear Physics*, 99(5):054331, May 2019.

[209] G. Nobre, A. Palumbo, D. Brown, M. Herman, S. Hoblit, and F. Dietrich. Towards a coupled-channel optical potential for rare-earth nuclei. *Nuclear Data Sheets*, 118:266–269, 2014.

[210] G. P. A. Nobre, A. Palumbo, M. Herman, D. Brown, S. Hoblit, and F. S. Dietrich. Derivation of an optical potential for statically deformed rare-earth nuclei from a global spherical potential. *Physical Review C: Nuclear Physics*, 91(2):024618, Feb. 2015.

[211] J. S. O'Connell, T. W. Donnelly, and J. D. Walecka. Semileptonic weak interactions with C^{12}. *Physical Review C: Nuclear Physics*, 6(3):719–733, Sept. 1972.

[212] O. Olivas-Gomez, A. Simon, O. Gorton, J. E. Escher, E. Churchman, P. Millican, R. Kelmar, C. S. Reingold, A. M. Clark, N. Cooper, C. Harris, S. L. Henderson, S. E. Kelly, F. Naqvi, A. Palmisano, D. Robertson, E. Stech, A. Spyrou, and W. P. Tan. Measurements of proton capture in the A=100–110 mass region: Constraints on the ^{111}In$(\gamma,p)/(\gamma,n)$ branching point relevant to the γ process. *Physical Review C: Nuclear Physics*, 102(5):055806, Nov. 2020.

[213] J. Orear, E. Fermi, A. Rosenfeld, and R. Schluter. *Nuclear Physics: A Course given by Enrico Fermi at the University of Chicago*. Midway Reprints. University of Chicago Press, 1950.

[214] W. E. Ormand and B. A. Brown. Microscopic calculations of nuclear level densities with the lanczos method. *Phys. Rev. C*, 102:014315, Jul 2020.

[215] WE. Ormand. Monte Carlo Hauser-Feshbach computer code system to model nuclear reactions: YAHFC. Technical report, Lawrence Livermore National Lab.(LLNL), Livermore, CA (United States), 2021.

[216] S. Ota, J. T. Burke, R. J. Casperson, J. E. Escher, R. O. Hughes, J. J. Ressler, N. D. Scielzo, I. J. Thompson, R. A. E. Austin, B. Abromeit, N. J. Foley, E. McCleskey, M. McCleskey, H. I. Park, A. Saastamoinen, and T. J. Ross. Spin differences in the ^{90}Zr compound nucleus induced by (p,p') inelastic scattering and (p,d) and (p,t) transfer reactions. *Physical Review C: Nuclear Physics*, 92(5):054603, Nov. 2015.

[217] T. Papenbrock and D. J. Dean. Factorization of shell-model ground states. *Physical Review C: Nuclear Physics*, 67(5):051303, May 2003.

[218] T. Papenbrock and D. J. Dean. Density matrix renormalization group and wave-function factorization for nuclei. *Journal of Physics G: Nuclear and Particle Physics*, 31(8):S1377, 2005.

[219] T. Papenbrock, A. Juodagalvis, and D. J. Dean. Solution of large scale nuclear structure problems by wave function factorization. *Physical Review C: Nuclear Physics*, 69(2):024312, Feb. 2004.

[220] S.-C. Park, J.-W. Ha, K.-S. Park, and Y.-H. Song. Sensitivity analysis and bayesian MCMC based on artificial neural network surrogate model for input variable uncertainty calibration. *Journal of Korean Institute of Architectural Sustainable Environment and Building Systems*, 15(4):326–337, 2021.

[221] A. Pérez-Obiol, S. Masot-Llima, A. M. Romero, J. Menéndez, A. Rios, A. García-Sáez, and B. Juliá-Díaz. Quantum entanglement patterns in the structure of atomic nuclei within the nuclear shell model, 2023.

[222] R. Pérez Sánchez, B. Jurado, V. Méot, O. Roig, M. Dupuis, O. Bouland, D. Denis-Petit, P. Marini, L. Mathieu, I. Tsekhanovich, M. Aïche, L. Audouin, C. Cannes, S. Czajkowski, S. Delpech, A. Görgen, M. Guttormsen, A. Henriques, G. Kessedjian, K. Nishio, D. Ramos, S. Siem, and F. Zeiser. Simultaneous determination of neutron-induced fission and radiative capture cross sections from decay probabilities obtained with a surrogate reaction. *Physical Review Letters*, 125(12):122502, Sept. 2020.

[223] WP. Poenitz and SE. Aumeier. The simultaneous evaluation of the standards and other cross sections of importance for technology. Technical report, Argonne National Lab.(ANL), Argonne, IL (United States), 1997.

[224] C. E. Porter and R. G. Thomas. Fluctuations of nuclear reaction widths. *Phys. Rev.*, 104:483–491, Oct 1956.

[225] G. Potel, F. M. Nunes, and I. J. Thompson. Establishing a theory for deuteron-induced surrogate reactions. *Physical Review C: Nuclear Physics*, 92(3):034611, Sept. 2015.

[226] G. Potel, G. Perdikakis, B. V. Carlson, M. C. Atkinson, W. Dickhoff, J. E. Escher, M. S. Hussein, J. Lei, W. Li, A. O. Macchiavelli, A. M. Moro, F. Nunes, S. D. Pain, and J. Rotureau. Toward a complete theory for predicting inclu- sive deuteron breakup away from stability. *The European Physical Journal A: Hadrons and Nuclei*, 53:178, 2017.

[227] J. R. Primack, D. Seckel, and B. Sadoulet. Detection of cosmic dark matter. *Annual Review of Nuclear and Particle Science*, 38(1):751–807, Dec. 1988.

[228] H. Primakoff and S. P. Rosen. Double beta decay. *Reports on Progress in Physics*, 22(1):121, Jan. 1959.

[229] C. D. Pruitt, R. J. Charity, L. G. Sobotka, J. M. Elson, D. E. M. Hoff, K. W. Brown, M. C. Atkinson, W. H. Dickhoff, H. Y. Lee, M. Devlin, N. Fotiades, and S. Mosby. Isotopically resolved neutron total cross sections at intermediate energies. *Physical Review C: Nuclear Physics*, 102(3):034601, Sept. 2020.

[230] C. D. Pruitt, J. E. Escher, and R. Rahman. Uncertainty-quantified phenomenological optical potentials for single-nucleon scattering. *Physical Review C: Nuclear Physics*, 107(1):014602, Jan. 2023.

[231] S. Prussin, Z. Oliveira, and K.-L. Kratz. Does the simple statistical model describe delayed neutron emission?: The cases of 85As, 87Br, 135Sb and 137I. *Nuclear Physics A*, 321(2):396–414, 1979.

[232] Qi, Chong. Shell model description of heavy nuclei and abnormal collective motions. *Epj Web of Conferences*, 178:02015, 2018.

[233] M. Ramalho, J. Suhonen, J. Kostensalo, G. A. Alcalá, A. Algora, M. Fallot, A. Porta, and A.-A. Zakari-Issoufou. Analysis of the total β-electron spectrum of ^{92}Rb: Implications for the reactor flux anomalies. *Physical Review C: Nuclear Physics*, 106(2):024315, Aug. 2022.

[234] S. Raman, B. Fogelberg, J. A. Harvey, R. L. Macklin, P. H. Stelson, A. Schröder, and K. L. Kratz. Overlapping β decay and resonance neutron spectroscopy of levels in ^{87}Kr. *Physical Review C: Nuclear Physics*, 28(2):602–622, Aug. 1983.

[235] C. E. Rasmussen, C. K. Williams, et al. *Gaussian Processes for Machine Learning*, volume 1. Springer, 2006.

[236] A. Ratkiewicz, J. A. Cizewski, J. E. Escher, G. Potel, J. T. Burke, R. J. Casperson, M. McCleskey, R. A. E. Austin, S. Burcher, R. O. Hughes, B. Manning, S. D. Pain, W. A. Peters, S. Rice, T. J. Ross, N. D. Scielzo, C. Shand, and K. Smith. Towards neutron capture on exotic nuclei: Demonstrating (d,pγ) as a surrogate reaction for (n,γ). *Physical Review Letters*, 122(5):052502, Feb. 2019.

[237] T. Rauscher. Branchings in the γ process path revisited. *Physical Review C: Nuclear Physics*, 73:015804, 2006.

[238] T. Rauscher, N. Dauphas, I. Dillmann, et al. Constraining the astrophysical origin of the p-nuclei through nuclear physics and meteoritic data. *Reports On Progress in Physics*, 76:066201, 2013.

[239] T. Rauscher and F.-K. Thielemann. Astrophysical reaction rates from statistical model calculations. *Atomic Data and Nuclear Data Tables*, 75(1–2):1–351, May 2000.

[240] T. Rauscher and F.-K. Thielemann. Tables of nuclear cross sections and reaction rates: An addendum to the paper "astrophysical reaction rates from statistical model calculations". *Atomic Data and Nuclear Data Tables*, 79(1):47–64, Sept. 2001.

[241] M. Rayet, N. Prantzos, and M. Arnould. The p-process revisted. *Astron. Astrophysics*, 227:271, 1990.

[242] J. J. Ressler, J. T. Burke, J. E. Escher, C. T. Angell, M. S. Basunia, C. W. Beausang, L. A. Bernstein, D. L. Bleuel, R. J. Casperson, B. L. Goldblum, J. Gostic, R. Hatarik, R. Henderson, R. O. Hughes, J. Munson, L. W. Phair, T. J. Ross, N. D. Scielzo, E. Swanberg, I. J. Thompson, and M. Wiedeking. Surrogate measurement of the ^{238}Pu(n,f) cross section. *Physical Review C: Nuclear Physics*, 83(5):054610, May 2011.

[243] I. Ribanský, P. Obložinský, and E. Běták. Pre-equilibrium decay and the exciton model. *Nuclear Physics A*, 205(3):545–560, May 1973.

[244] W. A. Richter, S. Mkhize, and B. A. Brown. sd-shell observables for the USDA and USDB Hamiltonians. *Physical Review C: Nuclear Physics*, 78(6):064302, Dec. 2008.

[245] P. Ring and P. Schuck. *The Nuclear Many-Body Problem*. Springer Science & Business Media, New York, 2004.

[246] C. Robin, M. J. Savage, and N. Pillet. Entanglement rearrangement in self-consistent nuclear structure calculations. *Physical Review C: Nuclear Physics*, 103(3):034325, Mar. 2021.

[247] R. Roth. Importance truncation for large-scale configuration interaction approaches. *Physical Review C: Nuclear Physics*, 79(6):064324, June 2009.

[248] J. Rotureau, N. Michel, W. Nazarewicz, M. Płoszajczak, and J. Dukelsky. Density matrix renormalization group approach for many-body open quantum systems. *Physical Review Letters*, 97(11):110603, Sept. 2006.

[249] D. J. Rowe. Quasi-Dynamical Symmetry:a new use of symmetry in nuclear physics. In *The Nucleus*, pages 379–395. Springer, Boston MA, 2000.

[250] B. Sadoulet. Deciphering the nature of dark matter. *Reviews of Modern Physics*, 71(2):S197–S204, Mar. 1999.

[251] D. Savran, T. Aumann, and A. Zilges. Experimental studies of the pygmy dipole resonance. *Progress in Particle and Nuclear Physics*, 70:210–245, May 2013.

[252] H. Schatz, A. D. B. Reyes, A. Best, E. F. Brown, K. Chatziioannou, K. A. Chipps, C. M. Deibel, R. Ezzeddine, D. K. Galloway, C. J. Hansen, F. Herwig, A. P. Ji, M. Lugaro, Z. Meisel, D. Norman, J. S. Read, L. F. Roberts, A. Spyrou, I. Tews, F. X. Timmes, C. Travaglio, N. Vassh, C. Abia, P. Adsley, S. Agarwal, M. Aliotta, W. Aoki, A. Arcones, A. Aryan, A. Bandyopadhyay, A. Banu, D. W. Bardayan, J. Barnes, A. Bauswein, T. C. Beers, J. Bishop, T. Boztepe, B. Côté, M. E. Caplan, A. E.

Champagne, J. A. Clark, M. Couder, A. Couture, S. E. de Mink, S. Debnath, R. J. de-Boer, J. den Hartogh, P. Denissenkov, V. Dexheimer, I. Dillmann, J. E. Escher, M. A. Famiano, R. Farmer, R. Fisher, C. Fröhlich, A. Frebel, C. Fryer, G. Fuller, A. K. Ganguly, S. Ghosh, B. K. Gibson, T. Gorda, K. N. Gourgouliatos, V. Graber, M. Gupta, W. Haxton, A. Heger, W. R. Hix, W. C. G. Ho, E. M. Holmbeck, A. A. Hood, S. Huth, G. Imbriani, R. G. Izzard, R. Jain, H. Jayatissa, Z. Johnston, T. Kajino, A. Kankainen, G. G. Kiss, A. Kwiatkowski, M. La Cognata, A. M. Laird, L. Lamia, P. Landry, E. Laplace, K. D. Launey, D. Leahy, G. Leckenby, A. Lennarz, B. Longfellow, A. E. Lovell, W. G. Lynch, S. M. Lyons, K. Maeda, E. Masha, C. Matei, J. Merc, B. Messer, F. Montes, A. Mukherjee, M. Mumpower, D. Neto, B. Nevins, W. G. Newton, L. Q. Nguyen, K. Nishikawa, N. Nishimura, F. M. Nunes, E. O'Connor, B. W. O'Shea, W.-J. Ong, S. D. Pain, M. A. Pajkos, M. Pignatari, R. G. Pizzone, V. M. Placco, T. Plewa, B. Pritychenko, A. Psaltis, D. Puentes, Y.-Z. Qian, D. Radice, D. Rapagnani, B. M. Rebeiro, R. Reifarth, A. L. Richard, N. Rijal, I. U. Roederer, J. S. Rojo, J. S. K, Y. Saito, A. Schwenk, M. L. Sergi, R. S. Sidhu, A. Simon, T. Sivarani, A. Skuladottir, M. S. Smith, A. Spiridon, T. M. Sprouse, S. Starrfield, A. W. Steiner, F. Strieder, I. Sultana, R. Surman, T. Szücs, A. Tawfik, F. Thielemann, L. Trache, R. Trappitsch, M. B. Tsang, A. Tumino, S. Upadhyayula, J. O. V. Martínez, M. Van der Swaelmen, C. V. Vázquez, A. Watts, B. Wehmeyer, M. Wiescher, C. Wrede, J. Yoon, R. G. T. Zegers, M. A. Zermane, and M. Zingale. Horizons: Nuclear astrophysics in the 2020s and beyond, 2022.

[253] L. I. Schiff. Quantum mechanics 3rd. *New York: M cGraw-Hill*, pages 283–285, 1968.

[254] A. Schiller, L. Bergholt, M. Guttormsen, E. Melby, J. Rekstad, and S. Siem. Extraction of level density and γ strength function from primary γ spectra. *Nuclear Instruments and Methods in Physics Research Section A: Accelerators, Spectrometers, Detectors and Associated Equipment*, 447(3):498–511, 2000.

[255] U. Schollwöck. The density-matrix renormalization group. *Reviews of Modern Physics*, 77(1):259–315, Apr. 2005.

[256] H. Schopper, H. Behrens, and J. Jänecke. Numerical tables for beta-decay and electron Capture/Numerische tabellen für beta-zerfall und elektronen-einfang. In *Landolt-Börnstein: Numerical Data and Functional Relationships in Science and Technology-New Series*. Springer, 1969.

[257] H. F. Schopper. *Weak Interactions and Nuclear Beta Decay*. North-Holland Publishing Company, 1966.

[258] D. V. Schroeder. Entanglement isn't just for spin. *American Journal of Physics*, 85(11):812–820, 2017.

[259] L. Schülke. Nuclear β-decay. II. *Zeitschrift für Physik*, 179(3):331–342, 1964.

[260] R. Schwengner, S. Frauendorf, and A. C. Larsen. Low-energy enhancement of magnetic dipole radiation. *Physical Review Letters*, 111(23):232504, Dec. 2013.

391

[261] R. Schwengner, G. Rusev, N. Benouaret, R. Beyer, M. Erhard, E. Grosse, A. R. Junghans, J. Klug, K. Kosev, L. Kostov, C. Nair, N. Nankov, K. D. Schilling, and A. Wagner. Dipole response of ^{88}Sr up to the neutron-separation energy. *Physical Review C: Nuclear Physics*, 76(3):034321, Sept. 2007.

[262] N. D. Scielzo, J. E. Escher, J. M. Allmond, M. S. Basunia, C. W. Beausang, L. A. Bernstein, D. L. Bleuel, J. T. Burke, R. M. Clark, F. S. Dietrich, P. Fallon, J. Gibelin, B. L. Goldblum, S. R. Lesher, M. A. McMahan, E. B. Norman, L. Phair, E. Rodriquez-Vieitez, S. A. Sheets, I. J. Thompson, and M. Wiedeking. Measurement of γ-emission branching ratios for ^{154,156,158}Gd compound nuclei: Tests of surrogate nuclear reaction approximations for (n,γ) cross sections. *Physical Review C: Nuclear Physics*, 81(3):034608, Mar. 2010.

[263] V. Semkova, E. Bauge, A. Plompen, and D. Smith. Neutron activation cross sections for zirconium isotopes. *Nuclear Physics A*, 832(3-4):149–169, 2010.

[264] A. Shihab-Eldin, W. Halverson, F. Nuh, S. Prussin, W. Rudolph, H. Ohm, and K. Kratz. Nonstatistical interpretation of delayed neutron emission — simple shell model approach. *Physics Letters B*, 69(2):143–146, 1977.

[265] N. Shimizu, T. Mizusaki, Y. Utsuno, and Y. Tsunoda. Thick-restart block Lanczos method for large-scale shell-model calculations. *Computer Physics Communications*, 244:372–384, 2019.

[266] AM. Shirokov, IJ. Shin, Y. Kim, M. Sosonkina, P. Maris, and JP. Vary. N3LO NN interaction adjusted to light nuclei in ab exitu approach. *Physics Letters B*, 761:87–91, 2016.

[267] E. Sh. Soukhovitskiĩ, R. Capote, J. M. Quesada, S. Chiba, and D. S. Martyanov. Nucleon scattering on actinides using a dispersive optical model with extended couplings. *Physical Review C: Nuclear Physics*, 94(6):064605, Dec. 2016.

[268] E. Sh. Soukhovitskiĩ, R. Capote, J. M. Quesada, S. Chiba, and D. S. Martyanov. Erratum: Nucleon scattering on actinides using a dispersive optical model with extended couplings [Phys. Rev. C 94, 064605 (2016)]. *Physical Review C: Nuclear Physics*, 102(5):059901, Nov. 2020.

[269] A. Spyrou, S. N. Liddick, A. C. Larsen, M. Guttormsen, K. Cooper, A. C. Dombos, D. J. Morrissey, F. Naqvi, G. Perdikakis, S. J. Quinn, T. Renstrøm, J. A. Rodriguez, A. Simon, C. S. Sumithrarachchi, and R. G. T. Zegers. Novel technique for constraining r-Process (n, γ) reaction rates. *Physical Review Letters*, 113(23):232502, Dec. 2014.

[270] B. Stech and L. Schülke. Nuclear β-decay. I. *Zeitschrift für Physik*, 179(3):314–330, 1964.

[271] F. W. Strauch. Resource letter QI-1: Quantum information. *American Journal of Physics*, 84(7):495–507, 2016.

[272] J. Suhonen. *From Nucleons to Nucleus: Concepts of Microscopic Nuclear Theory.* Theoretical and Mathematical Physics. Springer, Berlin, Germany, 2007.

[273] J. Tain and D. Cano-Ott. The influence of the unknown de-excitation pattern in the analysis of -decay total absorption spectra. *Nuclear Instruments and Methods in Physics Research Section A: Accelerators, Spectrometers, Detectors and Associated Equipment*, 571(3):719–727, Feb. 2007.

[274] J. L. Tain, E. Valencia, A. Algora, J. Agramunt, B. Rubio, S. Rice, W. Gelletly, P. Regan, A.-A. Zakari-Issoufou, M. Fallot, A. Porta, J. Rissanen, T. Eronen, J. Äystö, L. Batist, M. Bowry, V. M. Bui, R. Caballero-Folch, D. Cano-Ott, V.-V. Elomaa, E. Estevez, G. F. Farrelly, A. R. Garcia, B. Gomez-Hornillos, V. Gorlychev, J. Hakala, M. D. Jordan, A. Jokinen, V. S. Kolhinen, F. G. Kondev, T. Martínez, E. Mendoza, I. Moore, H. Penttilä, Zs. Podolyák, M. Reponen, V. Sonnenschein, and A. A. Sonzogni. Enhanced γ-Ray emission from neutron unbound states populated in β decay. *Physical Review Letters*, 115(6):062502, Aug. 2015.

[275] I. Talmi. *Simple Models of Complex Nuclei.* CRC Press, Boca Raton, 1993.

[276] B. Thakur, S. Pittel, and N. Sandulescu. Density matrix renormalization group study of ^{48}Cr and ^{56}Ni. *Physical Review C: Nuclear Physics*, 78(4):041303, Oct. 2008.

[277] I. Thompson and J. Escher. Theory of (3He,alpha) surrogate reactions for deformed uranium nuclei. Technical Report UCRL-TR-225984, Lawrence Livermore National Laboratory, 2006.

[278] I. J. Thompson and F. M. Nunes. *Nuclear Reactions for Astrophysics: Principles, Calculation and Applications of Low-Energy Reactions.* Cambridge University Press, 2009.

[279] A. Tichai, S. Knecht, AT. Kruppa, Ö. Legeza, CP. Moca, A. Schwenk, MA. Werner, and G. Zarand. Combining the in-medium similarity renormalization group with the density matrix renormalization group: Shell structure and information entropy. *arXiv preprint arXiv:2207.01438*, 2022.

[280] I. Towner and J. Hardy. First-forbidden non-unique β-transitions and mirror comparisons in light nuclei. *Nuclear Physics A*, 179(2):489–503, 1972.

[281] C. Travaglio, F. K. Röpke, R. Gallino, and W. Hillebrandt. Type Ia supernovae as sites of the p-process: Two-dimensional models coupled to nucleosynthesis. *The Astrophysical Journal*, 739(2):93, Sept. 2011.

[282] S. Typel and G. Baur. Theory of the Trojan–Horse method. *Annales de Physique*, 305:228, 2003.

[283] M. Uhl and B. Strohmaier. STAPRE, a computer code for particle induced activation cross sections and related quantities. Technical Report IRK 76/01, rev. 1978, Institut für Radiumforschung und Kernphysik, Vienna, Austria, 1976.

[284] Y. Utsuno, T. Otsuka, B. A. Brown, M. Honma, T. Mizusaki, and N. Shimizu. Shape transitions in exotic Si and S isotopes and tensor-force-driven Jahn-Teller effect. *Physical Review C: Nuclear Physics*, 86(5):051301, Nov. 2012.

[285] Y. Utsuno, N. Shimizu, T. Otsuka, S. Ebata, and M. Honma. Photonuclear reactions of calcium isotopes calculated with the nuclear shell model. *Progress in Nuclear Energy*, 82:102–106, 2015.

[286] E. Valencia, J. L. Tain, A. Algora, J. Agramunt, E. Estevez, M. D. Jordan, B. Rubio, S. Rice, P. Regan, W. Gelletly, Z. Podolyák, M. Bowry, P. Mason, G. F. Farrelly, A. Zakari-Issoufou, M. Fallot, A. Porta, V. M. Bui, J. Rissanen, T. Eronen, I. Moore, H. Penttilä, J. Äystö, V.-V. Elomaa, J. Hakala, A. Jokinen, V. S. Kolhinen, M. Reponen, V. Sonnenschein, D. Cano-Ott, A. R. Garcia, T. Martínez, E. Mendoza, R. Caballero-Folch, B. Gomez-Hornillos, V. Gorlichev, F. G. Kondev, A. A. Sonzogni, and L. Batist. Total absorption γ-ray spectroscopy of the β-delayed neutron emitters ^{87}Br, ^{88}Br, and ^{94}Rb. *Physical Review C: Nuclear Physics*, 95(2):024320, Feb. 2017.

[287] R. Varner, W. Thompson, T. McAbee, E. Ludwig, and T. Clegg. A global nucleon optical model potential. *Physics Reports*, 201(2):57–119, 1991.

[288] P. Venkataramaiah, K. Gopala, A. Basavaraju, S. S. Suryanarayana, and H. Sanjeeviah. A simple relation for the Fermi function. *Journal of Physics G: Nuclear Physics*, 11(3):359, Mar. 1985.

[289] L. Vietze, P. Klos, J. Menéndez, W. Haxton, and A. Schwenk. Nuclear structure aspects of spin-independent WIMP scattering off xenon. *Physical Review D: Particles and Fields*, 91(4):043520, 2015.

[290] T. von Egidy and D. Bucurescu. Spin distribution in low-energy nuclear level schemes. *Physical Review C: Nuclear Physics*, 78(5):051301, Nov. 2008.

[291] T. von Egidy and D. Bucurescu. Experimental energy-dependent nuclear spin distributions. *Physical Review C: Nuclear Physics*, 80(5):054310, Nov. 2009.

[292] J. Wang, Z. Zhou, K. Lin, C. K. Law, and B. Yang. Facilitating Bayesian analysis of combustion kinetic models with artificial neural network. *Combustion and Flame*, 213:87–97, 2020.

[293] L. Wei. Unified approach for exact calculation of angular momentum coupling and recoupling coefficients. *Computer Physics Communications*, 120(2):222–230, 1999.

[294] H. A. Weidenmüller. Distribution of partial neutron widths for nuclei close to a maximum of the neutron strength function. *Physical Review Letters*, 105(23), Dec. 2010.

[295] H. A. Weidenmüller. Limitations of the porter-thomas distribution. In *AIP Conference Proceedings*. Author(s), 2017.

[296] M. Weinstein, A. Auerbach, and V. R. Chandra. Reducing memory cost of exact diagonalization using singular value decomposition. *Physical Review E: Statistical Physics, Plasmas, Fluids, and Related Interdisciplinary Topics*, 84(5):056701, Nov. 2011.

[297] S. R. White. Density matrix formulation for quantum renormalization groups. *Physical Review Letters*, 69(19):2863–2866, Nov. 1992.

[298] S. R. White. Density-matrix algorithms for quantum renormalization groups. *Physical Review B*, 48(14):10345–10356, Oct. 1993.

[299] R. R. Whitehead and A. Watt. On the lanczos method and the method of moments. *Journal of Physics G: Nuclear Physics*, 4(6):835–842, June 1978.

[300] T. R. Whitehead, Y. Lim, and J. W. Holt. Global microscopic description of nucleon-nucleus scattering with quantified uncertainties. *Physical Review Letters*, 127(18):182502, Oct. 2021.

[301] BH. Wildenthal. Empirical strengths of spin operators in nuclei. *Progress in particle and nuclear physics*, 11:5–51, 1984.

[302] K. G. Wilson. The renormalization group: Critical phenomena and the Kondo problem. *Reviews of Modern Physics*, 47(4):773–840, Oct. 1975.

[303] R. B. Wiringa, VGJ. Stoks, and R. Schiavilla. Accurate nucleon-nucleon potential with charge-independence breaking. *Physical Review C*, 51(1):38, 1995.

[304] S. E. Woosley and W. M. Howard. The p-process in supernovae. *The Astrophysical Journal Supplement Series*, 36:285, Feb. 1978.

[305] J. Xia, A. Abdukerim, W. Chen, X. Chen, Y. Chen, X. Cui, D. Fang, C. Fu, K. Giboni, F. Giuliani, et al. PandaX-II constraints on spin-dependent WIMP-nucleon effective interactions. *Physics Letters B*, 792:193–198, 2019.

[306] Y. Xu and S. Goriely. Systematic study of direct neutron capture. *Physical Review C*, 86(4), Oct. 2012.

[307] W. Younes and H. C. Britt. Neutron fission of ^{235,237,239}U and ^{241,243}Pu: Cross sections, integral cross sections and cross sections on excited states. Technical Report UCRL-ID-154206, Lawrence Livermore National Laboratory, Livermore, CA, 2003.

[308] W. Younes and H. C. Britt. Simulated neutron-induced fission cross sections for various Pu, U, and Th isotopes. *Physical Review C: Nuclear Physics*, 68(3):034610, Sept. 2003.

[309] R. M. Zbikowski and C. W. Johnson. Bootstrapped block Lanczos for large-dimension eigenvalue problems. *Computer Physics Communications*, 291:108835, 2023.

[310] F. Zeiser. *Uncertainty Quantification for Nuclear Level Densities and Y-Ray Strength Functions from the Oslo Method and Beyond.* PhD thesis, University of Oslo, 2021.

[311] V. Zelevinsky, B. Brown, N. Frazier, and M. Horoi. The nuclear shell model as a testing ground for many-body quantum chaos. *Physics Reports*, 276(2–3):85–176, Nov. 1996.

[312] V. Zerkin and B. Pritychenko. The experimental nuclear reaction data (EXFOR): Extended computer database and Web retrieval system. *Nuclear Instruments and Methods in Physics Research Section A: Accelerators, Spectrometers, Detectors and Associated Equipment*, 888:31–43, 2018.

[313] Q. Zhi, E. Caurier, J. J. Cuenca-García, K. Langanke, G. Martínez-Pinedo, and K. Sieja. Shell-model half-lives including first-forbidden contributions for r-process waiting-point nuclei. *Physical Review C: Nuclear Physics*, 87(2):025803, Feb. 2013.

[314] Z. Zhou and D. M. Tartakovsky. Markov chain Monte Carlo with neural network surrogates: Application to contaminant source identification. *Stochastic Environmental Research and Risk Assessment*, 35:639–651, 2021.

Appendix A

Functions and Algorithms

This appendix goes over some functions used in the text, but whose details aren't necessary to understand on a first pass.

A.1 Matrix elements of Bessel functions in a harmonic oscillator basis

To compute the matrix elements of the electroweak operators in a harmonic oscillator basis, we use the derivations from [67]. Namely, equations (1a) - (1f) and (3a) - (3d), which express the necessary geometric matrix elements in terms of matrix elements of the spherical Bessel functions. Here, we write out the remaining explicit formulas for obtaining matrix elements of the Bessel functions $j_L(y)$ in a harmonic oscillator basis in terms of the confluent hyper-geometric function:

$$_1F_1(a, b, z) = \sum_{n=0}^{\infty} \frac{a^{(n)} z^n}{b^{(n)} n!},$$

(A.1)

which makes use of the rising factorial function:

$$m^{(n)} = \frac{(m+n-1)!}{(m-1)!}.$$ (A.2)

The first additional relation is for the matrix elements of the Bessel function:

$$\langle n'l'j'| j_L(y) |nlj\rangle = \frac{2^L}{(2L+1)!!} y^{L/2} e^{-y} \sqrt{(n'-1)!(n-1)!}$$

$$\times \sqrt{\Gamma(n'+l'+1/2)\Gamma(n+l+1/2)} \sum_{m=0}^{n-1}\sum_{m'=0}^{n'-1} \frac{(-1)^{m+m'}}{m!m'!(n-m-1)!(n'-m'-1)!}$$ (A.3)

$$\times \frac{\Gamma[(l+l'+L+2m+2m'+3)/2]}{\Gamma(l+m+3/2)\Gamma(l'+m'+3/2)} \, {}_1F_1[(L-l'-l-2m'-2m)/2; L+3/2; y].$$

The two additional relations are needed:

$$\langle n'l'j'| j_L(y)(\frac{d}{dy} - \frac{l}{y}) |nlj\rangle =$$

$$\frac{2^{(L-1)}}{(2L+1)!!} y^{(L-1)/2} e^{-y} \sqrt{(n'-1)!(n-1)!}\sqrt{\Gamma(n'+l'+1/2)\Gamma(n+l+1/2)}$$

$$\times \sum_{m=0}^{n-1}\sum_{m'=0}^{n'-1} \frac{(-1)^{m+m'}}{m!m'!(n-m-1)!(n'-m'-1)!} \frac{\Gamma[(l+l'+L+2m+2m'+2)/2]}{\Gamma(l+m+3/2)\Gamma(l'+m'+3/2)}$$ (A.4)

$$\times \Big\{ -\frac{1}{2}(l+l'+L+2m+2m'+2) \, {}_1F_1[(L-l'-l-2m'-2m-1)/2; L+3/2; y]$$

$$+2m \, {}_1F_1[(L-l'-l-2m'-2m+1)/2; L+3/2; y]\Big\}.$$

And finally:

$$\langle n'l'j'| j_L(y)(\frac{d}{dy} + \frac{l}{y}) |nlj\rangle =$$

$$\frac{2^{(L-1)}}{(2L+1)!!} y^{(L-1)/2} e^{-y} \sqrt{(n'-1)!(n-1)!}\sqrt{\Gamma(n'+l'+1/2)\Gamma(n+l+1/2)}$$

$$\times \sum_{m=0}^{n-1}\sum_{m'=0}^{n'-1} \frac{(-1)^{m+m'}}{m!m'!(n-m-1)!(n'-m'-1)!} \frac{\Gamma[(l+l'+L+2m+2m'+2)/2]}{\Gamma(l+m+3/2)\Gamma(l'+m'+3/2)}$$ (A.5)

$$\times \Big\{ -\frac{1}{2}(l+l'+L+2m+2m'+2) \, {}_1F_1[(L-l'-l-2m'-2m-1)/2; L+3/2; y]$$

$$+(2l+2m+1) \, {}_1F_1[(L-l'-l-2m'-2m+1)/2; L+3/2; y]\Big\}.$$

All remaining electroweak matrix elements can be computed in terms of these Bessel elements, combined with vector coupling coefficients, etc., as set forth in the aforementioned reference.

A.2 Vector coupling coefficients

A.2.1 Basic Computation

I implemented a standard set of functions and subroutines for computing the vector-coupling 3-j, 6-j, and 9-j symbols using the Racah algebraic expressions found in Edmonds [74].

For an analysis of relative error compared to more modern methods, see Johansson and C. Forssen [159]. A more accurate but slower method involves prime factorization of integers. In old Fortran, see work by Wei (1999) [293]

For the 3-j symbol, we use the relation to the Clebsh-Gordon vector-coupling coefficients:

$$
\begin{pmatrix} j_1 & j_2 & J \\ m_1 & m_1 & M \end{pmatrix} = (-1)^{j_1 - j_2 - M}(2J+1)^{-1/2}(j_1 j_2 m_1 m_2 | j_1 j_2; J, -M). \tag{A.6}
$$

The vector coupling coefficients are computed as:

$$
(j_1 j_2 m_1 m_2 | j_1 j_2; J, M) = \delta(m_1 + m_1, m)(2J+1)^{1/2}\Delta(j_1 j_2 J) \tag{A.7}
$$

$$
\times [(j_1 + m_1)(j_1 - m_1)(j_2 + m_2)(j_2 - m_2)(J + M)(J - M)]^{1/2} \sum_z (-1)^z \frac{1}{f(z)}, \tag{A.8}
$$

where

$$f(z) = z!(j_1 + j_2 - J - z)!(j_1 - m_2 - z)! \tag{A.9}$$

$$\times (j_2 + m_2 - z)!(J - j_2 + m_1 + z)!(J - m_1 - m_2 + z)!, \tag{A.10}$$

and

$$\Delta(abc) = \left[\frac{(a + b - c)!(a - b + c)!(-a + b + c)!}{(a + b + c + 1)!} \right]^{1/2}. \tag{A.11}$$

The sum over z is over all integers such that the factorials are well-defined (non-negative-integer arguments).

Similarly, for the 6-j symbols:

$$\begin{Bmatrix} j_1 & j_2 & j_3 \\ m_1 & m_1 & m_3 \end{Bmatrix} = \Delta(j_1 j_2 j_3)\Delta(j_1 m_2 m_3)\Delta(m_1 j_2 m_3)\Delta(m_1 m_2 j_3)\sum_z (-1)^z \frac{(z+1)!}{g(z)}, \tag{A.12}$$

with

$$g(z) = (\alpha - z)!(\beta - z)!(\gamma - z)!(z - \delta)!(z - \epsilon)!(z - \zeta)!(z - \eta)! \tag{A.13}$$

$$\alpha = j_1 + j_1 + m_1 + m_2 \qquad\qquad \beta = j_2 + j_3 + m_2 + m_3 \tag{A.14}$$

$$\gamma = j_3 + j_1 + m_3 + m_1 \tag{A.15}$$

$$\delta = j_1 + j_2 + j_3 \qquad\qquad \epsilon = j_1 + m_2 + m_3 \tag{A.16}$$

$$\zeta = m_1 + j_2 + m_3 \qquad\qquad \eta = m_1 + m_2 + j_3. \tag{A.17}$$

For the 9-j symbol, we use the relation to the 6-j symbol:

$$\begin{Bmatrix} j_1 & j_2 & j_3 \\ j_4 & j_5 & j_6 \\ j_7 & j_8 & j_9 \end{Bmatrix} = \sum_k (-1)^{2k}(2k+1) \begin{Bmatrix} j_1 & j_4 & j_7 \\ j_8 & j_9 & k \end{Bmatrix} \begin{Bmatrix} j_2 & j_5 & j_8 \\ j_4 & k & j_6 \end{Bmatrix} \begin{Bmatrix} j_3 & j_6 & j_9 \\ k & j_1 & j_2 \end{Bmatrix}. \quad (A.18)$$

The 6-j symbols used to calculate the 9-j symbol are first taken from any tabulated values. Otherwise, they are computed as previously described.

A.3 Array spooling

A.3.1 Spooling

A sewing machine bobbin is a cylindrical object onto which thread is *spooled* before the machine is operated.

In computing, there are many cases where your data is multi-dimensional. But multi-dimensional arrays are unwieldy, especially in distributed memory systems. One dimensional arrays are best.

If you choose to *spool* your data into a one-dimensional array, you ought to know where your data ends up, and ideally, be able to access it efficiently. These notes help me do that.

Note that the term spooling, which I might have been the first to apply in the context of arrays, is array *flattening* with the additional feature that the mapping of indices is chosen to optimize data locality. Of course, high performance computing eventually reduces to understanding the layout of data in memory, so this is not a novel concept.

To spool an n-dimensional array into a 1-d array, we need to map an arbitrary number of

indices into a single index y:

$$\text{spool}(y) \leftarrow \text{array}[i, j, k, l, m, n, o, p, ...], \tag{A.19}$$

To create a one-to-one correspondence, we have to assign an order to the n indices:

$$x_n > x_{n-1} > ... > x_1. \tag{A.20}$$

This ordering, or hierarchy, is arbitrary; it doesn't have anything to do with the meaning of the indices or their ranges, but it does have consequences, discussed later.

Let's further suppose that each index x runs from x^{min} to x^{max}. With these constraints, we can use the following mapping:

$$y = x_n + \sum_{i<n}(x_i - x_i^{min}) \prod_{j>i}(x_j^{max} - x_j^{min} + 1). \tag{A.21}$$

The inequalities under the sum and product symbols are with respect to the ordering. For example, $i < n$ means "those indices x_i with lesser order than x_n".

With this mapping, incrementing x_n will change y by the least amount. In fact, it will be incremented by one. Going up one index in the ordering we have defined will increase the amount y is incremented.

Our choice of ordering should therefore be informed by the *access pattern* we expect for this array. Indices which will be incremented more frequently (e.g. deeper inside a nested-loop structure) should appear higher in the ordering.

2-d example

Let's take a two dimensional array $\text{array}[x_2, x_1]$ where $x_1 = 1, ..., m$, and $x_2 = 0, ..., n - 1$. We have to choose an ordering, so let's take $x_2 > x_1$.

Applying the formula, we have

$$y = x_2 + (x_1 - x_1^{min}) \times (x_2^{max} - x_2^{min} + 1) \tag{A.22}$$

Substituting our particulars we have:

$$y = x_2 + (x_1 - 1)(n - 1 - 0 + 1) \tag{A.23}$$
$$= x_2 + (x_1 - 1)n. \tag{A.24}$$

If instead we take $x_1 > x_2$ then,

$$y = x_1 + (x_2 - x_2^{min}) \times (x_1^{max} - x_1^{min} + 1), \tag{A.25}$$

which is:

$$y = x_1 + (x_2 - 0)(m - 1 + 1) \tag{A.26}$$
$$= x_1 + x_2 m. \tag{A.27}$$

3-d example

Suppose a three dimensional array $\text{array}[x_1, x_2, x_3]$ where $x_1 = 1, ..., r$, $x_2 = 0, ..., s$, and $x_3 = 1, ..., 2t$. We take the ordering $x_2 > x_3 > x_1$.

$$y = x_2 + (x_3 - 1)(s - 0 + 1) + (x_1 - 1)(2t - 1 + 1)(s - 0 + 1) \tag{A.28}$$

$$= x_2 + (x_3 - 1)(s + 1) + (x_1 - 1)2t(s + 1). \tag{A.29}$$

Again, changing the ordering will change the expression. This ordering would be most efficient for a nested loop such as:

```
do x1 = 1, r:
  do x3 = 1, 2t:
    do x2 = 0, s:
      y = x2 + (x3-1)(s+1) + (x1-1)*2*t*(s+1)
      access spool[y]
```

This requires $10(s + 1)(2t)r$ integer operations to compute.

Sectors

The 3-d example in the previous section can be improved by pre-computing parts of the index further up in the loop hierarchy.

$$y = x_n + \text{sector}(x_{n-1}, ..., x_1), \tag{A.30}$$

where

$$\text{sector}(x_{n-1}, ..., x_1) \equiv \sum_{i<n}(x_i - x_i^{min})\text{sectorsize}(i). \tag{A.31}$$

The sectorsize quantities do not depend on the loop variable x_i, and can therefore be pre-computed beforehand:

$$\text{sectorsize}(i) \equiv \prod_{j>i}(x_j^{max} - x_j^{min} + 1). \tag{A.32}$$

Or, recursively:

$$\text{sectorsize}(i) = (x_i^{max} - x_i^{min} + 1)\text{sectorsize}(i-1), \tag{A.33}$$

with $\text{sectorsize}(1) = 1$.

Improved 3-d example

Taking the same 3-d example as before, we can improve the performance by computing sectors in shallower loops and by pre-computing sector sizes. Recall that:

$$y = x_2 + (x_3 - 1)(s + 1) + (x_1 - 1)2t(s + 1). \tag{A.34}$$

In this case:

```
secsize1 = 1
secsize2 = (s+1) # * secsize1
secsize3 = (2*t) * secsize2
```

```
do x1 = 1, r:

   sector1 = (x1 - 1) * secsize3

   do x3 = 1, 2t:

      sector31 = (x3 - 1) * secsize2 + sector1

      do x2 = 0, s:

         y = x2 + sector31

         access spool[y]
```

This requires $(2t)(s + 1)r + 3(2t)r + 2r + 3$ operations to compute. Assuming $2t$, s, and r are all similarly large, this is a speedup of approximately $\frac{20str}{2str} = 10$.

Upper-triangular

Suppose we have some symmetry which allows us to only store the upper triangular part of a two-dimensional array. I.e. $i <= j$ for all rows i and columns j. Then the access pattern of the array might look like the following:

```
   column j

r  1  2  4  7 11

o     3  5  8 12

w        6  9 13

            10 14

i              15
```

and so on. In this case, the spooling is different. Importantly, we no longer need to know the size of the array, because the number of labeled rows in each column is always equal to the column number. Further, we always know that the largest index in the previous column

$j' = j - 1$ is the sum of all integers up to j', which is $j'(j' + 1)/2$. Thus:

$$y = i + j(j - 1)/2. \tag{A.35}$$

This can be combined with higher dimensional square blocks.

A.3.2   Un-spooling

Suppose we have a single do-loop which addresses a two-dimensional array. How do we invert the map?

It depends on the access pattern. We could have a row-major access pattern: "' 1 4 7 2 5 8 3 6 9 "' In which case the mapping is

$$x_1 = (y - 1)/s_{x_1} + 1 \tag{A.36}$$

$$x_2 = \quad \bmod (y - 1, s_{x_1}) + 1 \tag{A.37}$$

Upper triangular

Suppose the desired access pattern is upper triangular:

```
1 2 4 .
  3 5 .
    6 .
      .
```

Then the mapping is:

$$j = \text{ceiling}((\sqrt{8y+1} - 1)/2) \tag{A.38}$$

$$i = y - j(j-1)/2 \tag{A.39}$$

Here, i is fast and j is slow. A nice aspect of this layout is that the mapping does not depend on the size of the array. However, it does rely on real-type arithmetic (but there's a way around that).

The compute cost of the j index is at least 5 FLOPS plus the cost of the ceiling function. The cost of the i index is 4 FLOPS. The former is reduced to 4 FLOPS with:

$$j = \text{ceiling}(\sqrt{2y + 0.25} - 0.5) \tag{A.40}$$

$$i = y - j(j-1)/2 \tag{A.41}$$

To see why this seemingly arbitrary map works, notice from the label pattern above that we are trying to map the first N integers onto the first n columns, where the j-th column has j consecutive labels. The maximum label which n rows can support is:

$$\sum_{j=1}^{n} j = \frac{n(n+1)}{2}. \tag{A.42}$$

The index y maps to the column with at least as many labels:

$$y \le \frac{j(j+1)}{2}. \tag{A.43}$$

The positive solution for j is:

$$j \le \frac{\sqrt{8y+1} - 1}{2}. \tag{A.44}$$

408

Finally, by demanding that j be an integer, we find the first part of the mapping:

$$j = \text{ceiling} \left(\frac{\sqrt{8y + 1} - 1}{2} \right).$$ (A.45)

Since the label y increases by one when increasing the row index i, all we need is to subtract the maximum label from the previous column from y to get i. But this is just the sum of all integers up to the previous column number $j' = j - 1$. A simple substitution gives us the final result for the row i:

$$i = y - \frac{j(j-1)}{2}.$$ (A.46)

A word of caution: Since this map relies on real numbers, it is susceptible to rounding errors. In particular, if $1/j$ is small compared to the precision of the real data type, then the ceiling function may go the wrong way.

Appendix B

Shell Model Supplemental

B.1 Nucleon-nucleon interaction

The nuclear strong force is a screened version of the full strong force between quarks within a nucleon. The residual force between nucleons is what matters for nuclear physics. Fetter and Walecka's book [87] has a succinct summary of the main features this force has, from empirical investigation: (1) attractive and short range (a few fermi fm= 10^{-15}m), (2) hard core (repulsive at short distances 1/2 fm), (3) spin dependent, (4) non-central (has a tensor component), (5) spin-orbit force, (6) charge-independent. The potential with these properties is called the nucleon-nucleon (NN) potential. As a Hamiltonian invariant under translation, rotation, and reflection, whatever operators are combined must result in a scalar valued operator. The seven possible base operators are [303, 201]:

$$1 \qquad\qquad \text{purely central} \qquad\qquad \text{(B.1)}$$

$$\boldsymbol{\sigma}_i \cdot \boldsymbol{\sigma}_j \qquad\qquad \text{spin dependent} \qquad\qquad \text{(B.2)}$$

$$S_{ij} = 3(\boldsymbol{\sigma}_i \cdot \boldsymbol{r})(\boldsymbol{\sigma}_j \cdot \boldsymbol{r}) - \boldsymbol{\sigma}_i \cdot \boldsymbol{\sigma}_j \qquad\qquad \text{tensor force (non-central)} \qquad\qquad \text{(B.3)}$$

$$l \cdot S \qquad\qquad\qquad\qquad \text{spin-orbit} \qquad\qquad \text{(B.4)}$$

$$l^2 \qquad\qquad\qquad\qquad \text{quadratic in momentum} \qquad\qquad \text{(B.5)}$$

$$l^2(\sigma_i \cdot \sigma_j) \qquad\qquad\qquad\qquad\qquad\qquad\qquad \text{(B.6)}$$

$$(l \cdot S)^2, \qquad\qquad\qquad\qquad\qquad\qquad\qquad \text{(B.7)}$$

where σ are the Pauli spin matrices, $l = r \times p$ is the orbital angular momentum of the two particles, $r = r_i - r_j$ is their relative position, and $S = (\hbar/2)\sigma$.

If we include isospin dependence, the most general NN potential with constant and linear terms in momentum takes the form:

$$V_{NN}(r) = [V_0(r) + V_s(r)\sigma_1 \cdot \sigma_2 + V_{ls}(r)l \cdot S + V_T(r)S_{12}](1 + \tau_1 \cdot \tau_2). \qquad \text{(B.8)}$$

To fit experimental data, its common to also include terms quadratic in momentum [303].

B.2   Simple models

B.2.1   Extreme single-particle model

The so-called extreme single-particle model is the simplest possible shell model wherein we consider filling the lowest energy single-particle states first and taking no other combinations. The approximate wave function is a single Slater determinant (product wave function) consisting of the occupation of the lowest energy single-particle states only. Assuming some set of single-particle energies ϵ_i, the Hamiltonian would be:

$$H_{\mathrm{ESP}} = \sum_i \epsilon_i \hat{a}_i^\dagger \hat{a}_i \qquad\qquad\qquad\qquad \text{(B.9)}$$

which essentially just counts up the number of particles in each orbit with weights equal to the single-particle energies.

B.2.2   Mean field models

General mean field models extend the idea of the extreme single-particle model from a non-interacting set of particles with a constant potential, to a non-interacting set of particles with a central potential. The usual development is to start with a 1+2 body Hamiltonian, and to shift by a constant central potential until the Hamiltonian looks like a strong mean field plus a weak residual two-body interaction:

$$H = H_{MF} + H_{RES}, \tag{B.10}$$

where we then solve just the mean field part:

$$H_{MF} = \sum_i h(\mathbf{r}), \tag{B.11}$$

which is a model in which each particle i experiences only a mean-field, central potential $h(\boldsymbol{r})$ from the rest of the particles.

The most well-known mean field method is the Hartree-Fock method wherein the approximate wave functions are pure Slater determinants. The single-particle wave functions composing the product are varied until a minimum in the energy is found.

B.2.3   Mean field Hamiltonian

Here I follow the material of Suhonen's textbook [272], but the material can be found in any introductory text on the nuclear many-body physics.

The single particle Hamiltonian is a mean-field Hamiltonian, that is, it approximates the central potential felt by any given nucleon due to the effects of all other nucleons in its vicinity. In terms of a nucleon mass $m_N c^2 \approx 940$ MeV, it has the form:

$$h(r) = -\frac{\hbar^2}{2m_N}\nabla^2 + v(r) + v_C(r) + v_{LS}(r)\boldsymbol{L}\cdot\boldsymbol{S} \tag{B.12}$$

where $v(r)$ is some suitable central potential for the nuclear force. Typically either a Harmonic oscillator (HO) or Woods-Saxon potential (WS) it considered. In the rest of this section a WS will be used for illustration. The WS potential performs better than a HO potential at reproducing single-particle energies, but usually HO basis functions are assumed when computing analytic single-particle operator matrix elements.

The mean field potential has three major terms. The first is the spin-independent WS potential already discussed. To improve this model, one also includes a Coulomb repulsion term for the protons,

$$v_C(r) = \frac{Ze^2}{4\pi\epsilon_0} \begin{cases} \frac{3-(r/R)^2}{2R}, & r \leq R \\ \frac{1}{r}, & r > R, \end{cases} \tag{B.13}$$

which is just the static Coulomb force from a uniformly charged sphere of charge.

The Woods-Saxon potential has the form:

$$v_{WS}(r) = \frac{-V_0}{1 + e^{(r-R)/a}}, \tag{B.14}$$

with parameters describing the potential well depth, surface diffuseness, and nuclear radius:

$$V_0 = \left(51 \pm 33\frac{N-Z}{A}\right) \text{MeV}, \tag{B.15}$$

$$a = 0.67\text{fm}, \tag{B.16}$$

$$R = r_0 A^{1/3} \text{fm} = 1.27 A^{1/3}. \tag{B.17}$$

A drawing of this function is shown in comparison to a similar Harmonic oscillator potential in Figure B.1.
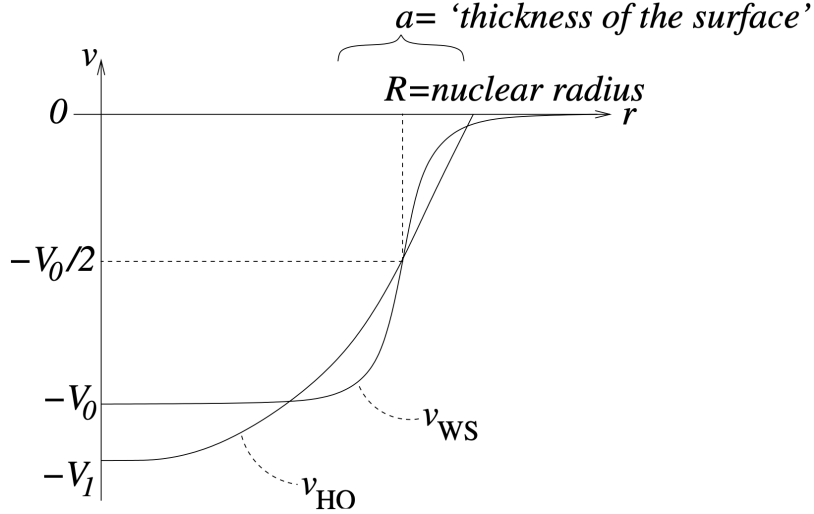

Figure B.1: Suhonen's [272] drawing of a Woods-Saxon and Harmonic oscillator potential with similar integrated energies. Typical values for the parameters are (^{40}Ca) $a = 0.67$fm, $R = 4.3$fm, $V_0 = 51$ MeV.

To obtain the experimentally observed magic numbers, one has to include a spin-orbit interaction. This is an attractive, spin-dependent interaction of the form:

$$v_{LS}(r)\vec{L} \cdot \vec{S}, \tag{B.18}$$

where $\vec{L}$ is the orbital angular momentum of the nucleon, and $\vec{S}$ is its spin vector. This force will break the degeneracy of levels of a given n and l into states with total angular momentum j. The total angular momentum of a particle is $\vec{J} = \vec{L} + \vec{S}$. This central potential peaks at the nuclear surface,

$$v_{LS}(r) = -v_{LS}^{(0)} \left(\frac{r_0}{\hbar}\right)^2 \frac{1}{r}\frac{d}{dr}v_{WS}(r), \tag{B.19}$$

with $v_{Ls}^{(0)} = 0.44$. The spin-orbit operator $\vec{L} \cdot \vec{S}$ satisfies

$$\vec{L} \cdot \vec{S} \, |l\tfrac{1}{2}jm\rangle = \frac{1}{2}[j(j+1) - l(l+1) - \frac{3}{4}]\hbar^2 \, |l\tfrac{1}{2}jm\rangle \,, \tag{B.20}$$

which shows us the j-dependence: states with higher j are more-strongly bound.

The solution to the single-particle Hamiltonian would be the single-particle wave functions ψ_i with energies ϵ_i. In this context of the configuration interaction model, these ϵ_i are the single-particle energies.

B.3 Phenomenological interactions

Here I include some practical information about a number of phenomenological interactions used in this work.

Model space	$0d_{3/2}$, $0d_{5/2}$, $1s_{1/2}$
.int	usdb
.spo	sd
$Z_0 = N_0$	8
Core	^{16}O
Max occ.	12
Largest nucleus	^{40}Ca
xspe, A, B, X	1.0 18.0 A 0.3
Single particle orbits (3):	

n	l	π	j	E (MeV)	max occ.
0	2	+1	3/2	2.1117	4
0	2	+1	5/2	-3.9257	6
1	0	+1	1/2	-3.2079	2

Authors	Brown, Richter (2006)
Citation [42]	`https://doi.org/10.1103/PhysRevC.74.034315`

Model space	$0f_{7/2}$, $1p_{3/2}$, $0f_{5/2}$, $1p_{1/2}$
.int	gx1a
.spo	fp
$Z_0 = N_0$	20
Core	^{40}Ca
Max occ.	20
Largest nucleus	^{80}Zr
xspe, A, B, X	1.0 42.0 A 0.3
Single particle orbits (4):	

n	l	π	j	E (MeV)	max occ.
0	3	-1	7/2	-8.6240	8
1	1	-1	3/2	-5.6793	4
0	3	-1	5/2	-1.3829	6
1	1	-1	1/2	-4.1370	2

Authors	Honma, Otsuka, Brown, Mizusaki (2004)
Citation [145]	`https://doi.org/10.1103/PhysRevC.69.034335`

Model space	$0f_{5/2}$, $1p_{3/2}$, $1p_{1/2}$, $0g_{9/2}$
.int	jun45
.spo	jj44
$Z_0 = N_0$	28
Core	^{56}Ni
Max occ.	22
Largest nucleus	^{100}Sn
xspe, A, B, X	1.0 58.0 A 0.3
Single particle orbits (4):	

n	l	π	j	E (MeV)	max occ.
0	3	-1	5/2	-8.7087	6
1	1	-1	3/2	-9.8280	4
1	1	-1	1/2	-7.8388	2
0	4	+1	9/5	-6.2617	10

Author(s)	Honma, Otsuka, Mizusaki, Hjorth-Jensen (2009)
Citation [147]	`https://doi.org/10.1103/PhysRevC.80.064323`

Model space	$0g_{7/2}$, $1d_{5/2}$, $1d_{3/2}$, $2s_{1/2}$, $0h_{11/2}$
.int	GCN5082
.spo	GCN5082
$Z_0 = N_0$	50
Core	^{100}Sn
Max occ.	32
Largest nucleus	^{164}Pb
xspe, A, B, X	1.0 1.0 1.0 1.0
Single particle orbits (5):	

n	l	π	j	x	E (MeV)	max occ.
0	4	+1	7/2	4	-10.416450	8
1	2	+1	5/2	4	-10.602300	6
1	2	+1	3/2	4	-8.915810	4
2	0	+1	1/2	4	-9.057190	2
0	5	-1	11/2	5	-8.205680	12

Author(s)	Brown, Stone, Stone, Towner, Hjorth-Jensen
Citation [43]	(Unpublished.)

Model space	$0f_{5/2},\ 1p_{3/2},\ 1p_{1/2},\ 0g_{9/2},\ 1d_{5/2},\ 1d_{3/2},\ 2s_{1/2}$
.int	glepn
.spo	glepn
$Z_0 = N_0$	28
Core	^{56}Ni
Max occ.	34
Largest nucleus	^{124}Gd
xspe, A, B, X	1.0 1.0 1.0 1.0
Single particle orbits (5):	

n	l	π	j	x	E (MeV)	max occ.
0	4	+1	7/2	4	-10.416450	8
1	2	+1	5/2	4	-10.602300	6
1	2	+1	3/2	4	-8.915810	4
2	0	+1	1/2	4	-9.057190	2
0	5	-1	11/2	5	-8.205680	12

Author(s)	Mach, Warburton, Gill, Casten, Becker, Brown, Winger
Citation [191]	https://doi.org/10.1103/PhysRevC.41.226

B.4 BIGSTICK OBTD format specification

This document specifies the format of the one-body density matrix files produced by the many-body code `BIGSTICK`.

```
1    State        E           Ex          J         T
2      1    -330.17116    0.00000       1.500   11.500
3    Single particle state quantum numbers
4  ORBIT        N       L    2 x J
5       1       0       2       3
6       2       0       2       5
7       3       1       0       1
8   Initial state #    1 E = -330.17117 2xJ, 2xT =    3   23
9   Final state   #    1 E = -330.17117 2xJ, 2xT =    3   23
10  Jt =    0, proton      neutron
11     1    1   1.55844    5.40558
```

B.4.1 Definition

One-body density matrices between many-body eigenstates $|\Psi\rangle$ are defined as

$$\rho_K^{fi}(ab) = \frac{1}{\sqrt{2K+1}}\langle\Psi_f||[\hat{c}_a^\dagger \otimes \tilde{c}_b]_K||\Psi_i\rangle, \tag{B.21}$$

where $\hat{c}_a^\dagger$ is the fermion-creation operator (with good angular momentum quantum numbers), $\tilde{c}_b$ is the time-reversed fermion-destruction operator. The creation/destruction operators refer to single-particle states in a harmonic oscillator basis.

Each state $|\Psi_i\rangle$ and has an energy eigenvalue and two quantum numbers: total angular momentum J_i and total isospin T_i. The angular momentum K of the density matrix operator $\rho_K(ab)$ must satisfy conservation of angular momentum according to the triangle inequality rule for both the many-body states and the single-particle states:

$$|J_f - J_i| \leq K \leq |J_f + J_i|, \tag{B.22}$$

$$|j_a - j_b| \leq K \leq |j_a + j_b|. \tag{B.23}$$

B.4.2 Symmetry

Two space saving measures may be taken in the storage of these matrix elements which must be taken into account. The first is trivial: matrix elements equal to zero are not stored in the file. The second is more subtle and can be confused with the first measure. One-body

density matrices obey the following symmetry relation:

$$\rho_{K,T}^{i,f}(ba) = (-1)^{j_a-j_b+J_i-J_f+T_i-T_f}\rho_{K,T}^{f,i}(ab), \tag{B.24}$$

only matrix elements with $a < b$ (or $a > b$) need to be stored in order fully specify the nonzero matrix elements.

B.4.3 Filename

The density matrix file ends in ".dres".

B.4.4 Format

The file is written with standard plain text.

B.4.5 Three blocks

The density matrix file has three consecutive blocks: (1) many-body state information, (2) single-particle state quantum numbers, (3) density matrix element blocks.

B.4.6 First block: States

The f and i indices on the $\rho_J^{f,i}(ab)$ object refer to the many-body states involved.

The states section of the file is identified by the following line:

```
  State      E        Ex        J        T
```

This line begins with exactly two blank spaces. Each state is specified by 5 numbers:

1. State number (i.e, 1, 2, 3, 4. 1 is the ground state.)

2. State eigenvalue/energy in MeV

3. State excitation energy (eigenvalue/energy minus the ground state (1st state) eigenvalue/energy)

4. State total angular momentum quantum number

5. State total isospin quantum number

Each number should be in its own column separated by one or more spaces.

Example with five states:

```
1    State        E           Ex          J        T
2      1      -330.17116    0.00000     1.500   11.500
3      2      -330.13419    0.03697     0.500   11.500
4      3      -329.77492    0.39624     2.500   11.500
5      4      -329.70014    0.47102     1.500   11.500
6      5      -329.42771    0.74346     3.500   11.500
```

B.4.7   Second block: Single particle state quantum numbers

The single particle state quantum numbers section begins with the following two lines:

```
1    Single particle state quantum numbers
2  ORBIT      N      L    2 x J
```

Each single particle state (SPS) is specified by 4 numbers:

1. SPS number (i.e. 1, 2, 3, ...)

2. SPS nodal quantum number

3. SPS orbital angular momentum

4. SPS twice the total angular momentum

Each number should be in its own column separated by one or more spaces.

Example with five SPS:

```
1    Single  particle  state  quantum  numbers
2 ORBIT       N      L     2 x J
3       1        0        4        7
4       2        1        2        5
5       3        1        2        3
6       4        2        0        1
7       5        0        5       11
```

B.4.8 Third block: Density matrix element blocks

Density matrix blocks have three nested sub-blocks:

1. States involved

2. Transition angular momentum value

3. SPS labels and matrix elements

States involved

The states involved in a block are specified by two lines. The first specifies the initial (ket) state and the second specifies the final (bra) state.

By example:

```
1  Initial  state  #     1 E =  -330.17117  2xJ,  2xT =     3   23
2  Final  state    #     1 E =  -330.17117  2xJ,  2xT =     3   23
```

Both lines are preceded by a space. "Initial" and "Final" are capitalized.

Transition angular momentum (operator momentum)

The operator connecting a given initial and final states is constrained by conservation of angular momentum, but can otherwise take any integer value. The line specifying this sub-block is as follows:

```
1   Jt =    1, proton       neutron
```

The line begins with one space. The two strings at the end of the line indicate the coupling of the second two columns of density matrix elements that follow. For isospin format density matrix files, this line would be:

```
1   Jt =    1, Tt = 0           1
```

Single particle state labels and matrix elements

The inner-most block of data store the actual one-body density matrix elements for each allowed combination of single-particle states. There are four numbers per line in the inner-most block:

1. Creation SPS label (a)

2. Destruction SPS label (b)

3. Proton (isospin-0) coupling one-body density matrix element $\rho_{K,(p)}^{f,i}(a,b)$ (if isospin format then $\rho_{K,T=0}^{f,i}(a,b)$)

4. Neutron (isospin-1) coupling one-body density matrix element $\rho_{K,(n)}^{f,i}(a,b)$ (if isospin format then $\rho_{K,T=1}^{f,i}(a,b)$)

For example:

```
1     1     1     1.55844     5.40558
2     2     2     0.82990     4.64991
3     3     3     0.33371     2.66182
4     4     4     0.15089     2.19140
5     5     5     0.19585     5.45541
```

Matrix elements which are identically zero are not stored in the file to save space.

B.4.9 Example density matrix file with one state

From the following example file one should be able to find that (examples):

$$\rho_{K=0,(p)}^{f=1,i=1}(a = 3, b = 3) = 0.33371 \tag{B.25}$$

$$\rho_{K=2,(n)}^{f=1,i=1}(a = 2, b = 1) = -0.00432 \tag{B.26}$$

```
1     State          E          Ex          J          T
2       1     -330.17116     0.00000     1.500    11.500
3     Single  particle  state  quantum  numbers
4  ORBIT        N       L     2 x J
5       1       0       4       7
6       2       1       2       5
7       3       1       2       3
8       4       2       0       1
9       5       0       5      11
10  Initial  state #     1 E =  -330.17117 2xJ, 2xT =     3   23
11  Final  state    #     1 E =  -330.17117 2xJ, 2xT =     3   23
12  Jt =    0, proton        neutron
13      1     1     1.55844     5.40558
14      2     2     0.82990     4.64991
15      3     3     0.33371     2.66182
16      4     4     0.15089     2.19140
17      5     5     0.19585     5.45541
18  Jt =    1, proton        neutron
19      1     1     0.01905     0.02637
20      1     2    -0.00378     0.01404
21      2     1     0.00378    -0.01404
22      2     2     0.01022     0.00476
23      2     3     0.00387     0.00942
24      3     2    -0.00387    -0.00942
25      3     3    -0.00075     0.82318
26      3     4     0.00046     0.01952
27      4     3    -0.00046    -0.01952
28      4     4    -0.00194    -0.01399
29      5     5     0.00030     0.00399
```